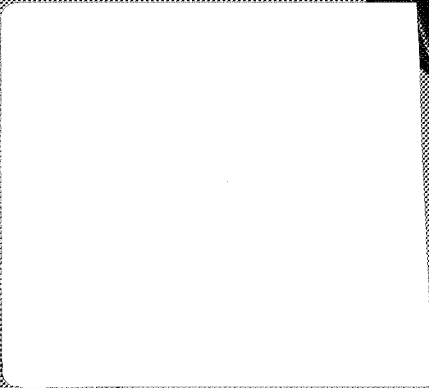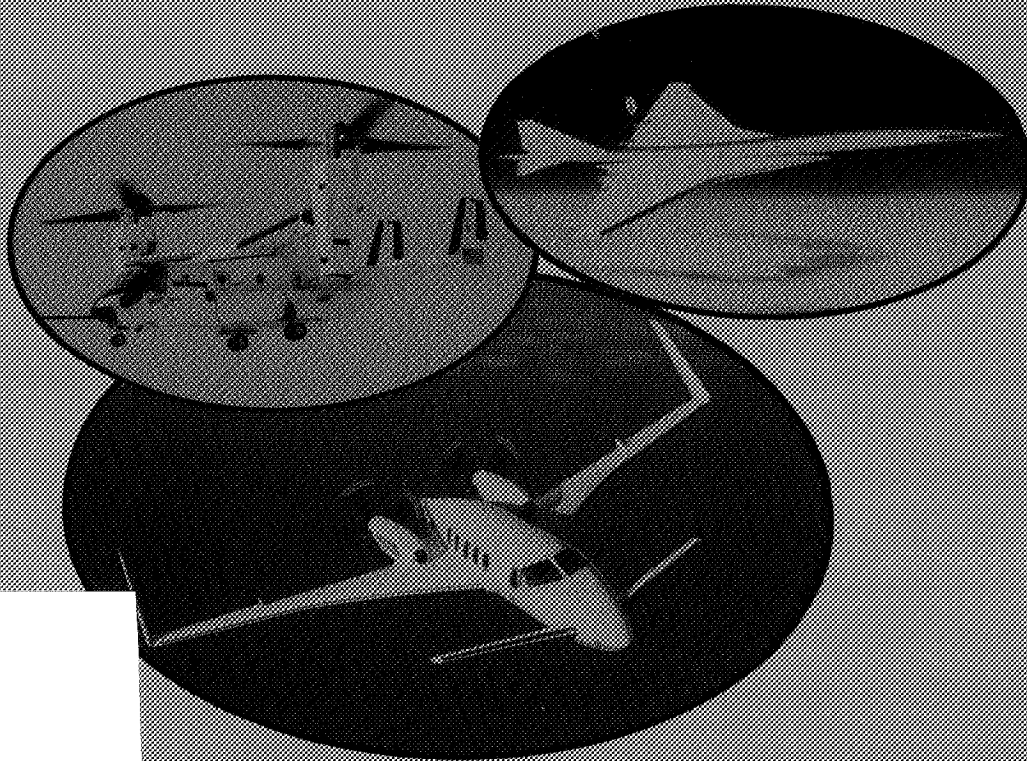NASA Conference Publication 3087
Part 2

Eighth DoD/NASA/FAA Conference on Fibrous Composites in Structural Design

Proceedings of a conference held in
Norfolk, Virginia
November 28–30, 1989

522256

NASA

Eighth DoD/NASA/FAA Conference on Fibrous Composites in Structural Design

Compiled by
James H. Starnes, Jr.
NASA Langley Research Center
Hampton, Virginia

Herman L. Bohon
Lockheed Engineering & Sciences Company
Hampton, Virginia

Sherry B. Garzon
NASA Langley Research Center
Hampton, Virginia

NASA

National Aeronautics and
Space Administration

Office of Management

Scientific and Technical
Information Division

1990

PREFACE

The Eighth DoD/NASA/FAA Conference on Fibrous Composites in Structural Design is one of a series of conferences jointly sponsored by the National Aeronautics and Space Administration, the U.S. Air Force, the U.S. Army, the U.S. Navy (Department of Defense), and the Federal Aviation Administration. The purpose of this series of conferences is to convene periodically key government and industry research and design engineers to present and discuss the status, problems, and requirements in the technical disciplines related to the design of composite structures. This series of conferences provides a forum for the scientific community to exchange composite structures design information and an opportunity to observe recent progress in composite structures design and technology.

The Eighth DoD/NASA/FAA Conference on Fibrous Composites in Structural Design was held in Norfolk, Virginia during November 28–30, 1989. The conference consisted of 42 presentations by senior managers and experts in the field of composite structures. The conference was organized into six sessions that emphasized perspectives in composites (one session), applications in design (one session), concepts in design (one session), methodology in design (two sessions), and reliability in design (one session). This publication contains the papers presented in the applications in design, methodology in design, and reliability in design sessions of the conference.

Certain materials are identified in this publication in order to specify adequately which materials were used in the structural design or research efforts. In no case does such identification imply recommendation or endorsement of a product by NASA, DoD, or FAA, nor does it imply that the materials are necessarily the only ones or the best ones available for the purpose. In many cases equivalent materials are available and would probably produce equivalent results.

The Conference Organizing Committee would like to take this opportunity to thank all the authors and presenters for their outstanding contributions to the conference technical program as well as the conference attendees, whose contributions to the conference discussions helped to make the conference a successful technology exchange forum for current composite structural design issues.

James H. Starnes, Jr.
Herman L. Bohon
Sherry B. Garzon

James H. Starnes, Jr.
General Chairman
NASA Langley Research Center
Hampton, Virginia

Herman L. Bohon
Technical Chairman
Lockheed Engineering
 & Sciences Company
Hampton, Virginia

Sherry B. Garzon
Administrative Assistant
NASA Langley Research Center
Hampton, Virginia

Conference Organizing Committee

James H. Starnes, Jr.   NASA Langley Research Center
Thomas E. Hess   Naval Air Development Center
Don W. Oplinger   Army Materials Technology Laboratory
J. David Oetting   Wright Research and Development Center
Danny E. Good   Army Aviation Applied Technology Directorate
Joseph R. Soderquist   Federal Aviation Committee

CONTENTS

Part 1*

Applications in Design
Chairman: Dan Good
Aviation Applied Technology Directorate
USAARTA (AVSCOM)

Concepts in Design
Chairman: Dave Oetting
Wright Research and Development Center

*Part 1 is presented under separate cover

Methodology in Design (A)
Chairman: Don Oplinger
Army Materials Technology Laboratory

Part 2

Reliability in Design
Chairman: Joe Soderquist
Federal Aviation Administration

Methodology in Design (B)
Chairman: Thomas Hess
Naval Air Development Center

PART 2

Reliability in Design

Chairman: Joe Soderquist
Federal Aviation Administration

EVALUATION OF COMPOSITE COMPONENTS
ON THE BELL 206L AND SIKORSKY S-76 HELICOPTERS

Donald J. Baker

Aerostructures Directorate
U. S. Army Research and Technology Activity(AVSCOM)
Langley Research Center
Hampton,VA

ABSTRACT

Progress on two programs to evaluate structural composite components in flight service on Bell 206L and Sikorsky S-76 commercial helicopters is described. Forty ship sets of composite components that include the litter door, baggage door, forward fairing, and vertical fin have been installed on Bell Model 206L helicopters that are operating in widely different climates. Component installation started in 1981 and selected components are being removed and tested at prescribed intervals over a ten year evaluation. Four horizontal stabilizers and eleven tail rotor spars that are production components on the S-76 helicopter are being tested after prescribed periods of service to determine the effects of the operating environment on their performance. Concurrent with the flight evaluation, materials used to fabricate the components are being exposed in ground racks and tested at specified intervals to determine the effects of outdoor environments. In this paper results achieved from 123,000 hours of accumulated service on the Bell 206L components and 53,000 hours on the Sikorsky S-76 components are reported. Seventy-eight Bell 206L components have been removed and tested statically. Results of seven years of ground exposure of materials used to fabricate the Bell 206L components are presented. Results of tests on four Sikorsky S-76 horizontal stabilizers and eleven tail rotor spars will be presented. Panels of material used to fabricate the Sikorsky S-76 components that were exposed for six years have been tested and results are presented.

INTRODUCTION

Over the past fifteen years, NASA has sponsored programs to build a data base and establish confidence in the long-term durability of advanced composite materials in transport aircraft structures (reference 1). Primary and secondary components have been installed on commercial aircraft and world-wide flight service experience is being obtained. Flight environments for transport aircraft and helicopters are quite different and the behavior of composite components in the two environments may differ substantially.

Therefore, in 1978 NASA and the U.S. Army Research and Technology Activity (AVSCOM) initiated the first major program to evaluate helicopter composite components in flight service. A contract was awarded to design, fabricate, certify, and install forty ship sets of composite litter doors, baggage doors, forward fairings and vertical fins on Bell Helicopter Textron, Inc. (Bell) Model 206L helicopters. The specific objective of this program is to determine the long-term durability of composite airframe structures in the operational environment of light commercial helicopters. Such helicopters often operate for extended periods in remote areas with primitive maintenance facilities and near unimproved areas where damage from tree limbs, rocks, sand and other debris is commonly encountered.

In 1979 NASA and the U. S. Army Research and Technology Activity initiated a second research program to determine the residual strength of composite helicopter components after specified periods of flight service. A contract was awarded to Sikorsky Aircraft Co. to evaluate the flight service performance of four horizontal stabilizers and eleven tail rotor paddles on Sikorsky S-76 helicopters and to determine the residual strength of each composite component after removal from service. The composite components are production parts for the S-76.

The S-76 composite components were chosen to compare real-time in-service environmental effects with accelerated laboratory test results and analytical predictions for both static and dynamic loaded primary structures. The tail rotor is designed primarily for cyclic fatigue loading, whereas the horizontal stabilizer is designed for static loading. Realistic environmental factors established through flight service and residual strength testing of these components will allow more efficient design of composite components for future helicopters. Concurrent with these flight service programs, materials used to fabricate the components are being exposed in ground racks at seven sites and are tested at prescribed intervals to determine the effects of outdoor environments.

This paper describes the design, flight service experience and post service testing of each composite component and ground based exposure of material specimens. Residual strength of components after flight service and strength of specimens after outdoor exposure are reported and compared with baseline values.

Use of commercial products or names of manufacturers in this report does not constitute official endorsement of such products of manufacturers, either expressed or implied, by the National Aeronautics and Space Administration or the U.S. Army Research and Technology Activity.

BELL 206L PROGRAM

Component Description

A total of forty-five (45) ship sets of litter doors, baggage doors, forward fairings and vertical fins were manufactured for the Bell 206L helicopter (figure 1). A detailed description of the design, fabrication, and certification of each component is reported in reference 2. A brief description of each component follows.

Litter Door - The litter door is located on the left side of the aircraft as shown in figure 1. The door is 26.0 in. wide by 46.0 in. high. Schematics of the litter door are shown in figure 2. The door consists of outer and inner skins of Kevlar-49® fabric/F-185[1] epoxy composite material. Each skin contains areas that are reinforced with unidirectional Kevlar-49/F-560[1] epoxy composite material. Each skin was fabricated separately and then the two skins were secondarily bonded together to form the door. A plexiglass window was bonded directly to the door with EC3549[2] adhesive. The weight of the metal door is 13.10 lbm, whereas the composite door weight is 8.20 lbm for a weight saving of 37.4 percent. Bell Helicopter was responsible for the design and fabrication of the litter door.

Design of the litter door was controlled primarily by two loading conditions required for FAA certification: 1.) An outward aerodynamic load that includes the reaction loads from the hinge points of the cabin door; and 2.) the weight of the litter door and cabin door plus a 50 lbf downward force at the cabin door handle. The latter loading condition simulates a person pulling on the cabin door when both doors are open.

Baggage Door - The baggage door is also located on the left side of the aircraft as shown in figure 1. The door is 37.5 in. long by 23.4 in. wide. A photograph of the baggage door is shown in figure 3. The door consists of Kevlar-49 fabric/LRF-277[3] epoxy composite material facesheets bonded on 3.1 lbm/ft^3 Nomex honeycomb core. Areas around the hinges and latches were reinforced with additional plies of Kevlar-49 fabric/LRF-277 epoxy. Weights of both the composite and metal baggage door are 2.90 lbm. The baggage door offered no weight savings but remained in the program to assess the effects of long-term durability. Brunswick Corp. was responsible for the design and fabrication of the baggage door.

Design of the baggage door was based primarily on two loading conditions required for FAA certification: an outward aerodynamic load and a downward load caused by pulling on the door latch in the open position.

® Registered trademark of Dupont Corporation

[1] Manufactured by Hexcel Corp., Dublin, CA.

[2] Manufactured by 3M Co., St. Paul, MN.

[3] Manufactured by Brunswick Corp., Lincoln, NB

394

Forward Fairing - Location of the forward fairing on the aircraft is shown in figure 1. The fairing is 35.9 in. long, 29.0 in. wide and 13.0 in. high at the aft end. A photograph of the fairing is shown in figure 4. Most of the fairing consists of single-ply Kevlar-49 fabric /CE-306[4] epoxy composite material skin that was cocured on a 4.5 lbm/ft^{3} Klegecell[5] foam core. Areas around the hinges and latches were reinforced with additional plies of Kevlar-49/CE-306 epoxy. Weight of the metal forward fairing is 8.60 lbm, whereas the composite fairing weighs 7.26 lbm for a 15.6 percent weight saving. Bell Helicopter was responsible for the design and fabrication of the forward fairing.

Design and certification tests of the fairing were based on an outward aerodynamic pressure load.

Vertical Fin - The vertical fin is used for directional stability in forward flight and is located on the aircraft as shown in figure 1. A photograph of the fin is shown in figure 5. The fin is 79.0 in. high and the chord varies between 12.0 in. and 19.0 in. The vertical fin is a full-depth sandwich structure with T-300/E-788[6] graphite/epoxy composite material facesheets on a Fibertruss[7] core. Fibertruss is a high strength and high stiffness fiberglass core. An aluminum alloy screen was bonded to the exterior surface of the skin to provide lightning protection. The leading edge of the vertical fin is a 2-ply Kevlar-49 fabric/epoxy skin attached to the structural box. The tail skid is a tapered filament-wound S-glass/epoxy tube with a short length of steel tubing and standard abrasion pad attached at the tip. The weight of a metal vertical fin is 15.30 lbm, and the weight of the composite vertical fin is 12.30 lbm. This results in a 19.6 percent weight saving. Bell Helicopter was responsible for the design and fabrication of the vertical fin.

Design and certification of the vertical fin was based on three design conditions, two static and one fatigue loading. The first static test condition simulated aerodynamic loading only. The second static test condition simulated an aircraft landing in the tail down attitude. Fatigue tests were conducted on specimens that simulate the fin-to-fuselage attachment structure of the fin. The fatigue tests were conducted at room temperature after the specimen had been conditioned at 120 °F and 95 percent relative humidity for 42 days (1000 hours).

Ground Exposure Specimens

Concurrent with the flight service program, material test specimens are being exposed at five locations on the North American Continent (figure 6). The selected locations are in the general areas where the composite components are being flown. Each location contains one rack as shown in figure 7. The racks were installed in 1980 and contain five trays each for removal after 1, 3, 5, 7, and 10 years of exposure. A tray contains 24 each of tension, short-beam-shear (SBS), and IITRI-compression specimens and four 2.0-in.-wide specimens to provide information on the weathering characteristics of each material system. The tension, compression and SBS specimens are painted with a polyurethane paint (IMIRON[8]) that is used on the flight service helicopters.

The four composite material systems in the ground exposure program are 1.) Kevlar-49 fabric (style 281)/F-185 epoxy $[0/45/0]_s$; 2.) Kevlar-49 fabric (style 120)/LRF-277 epoxy $[0/90/\pm45]_s$; 3.) Kevlar-49 fabric (style 281)/CE-306 $[0/90]_s$; and 4.) T-300/E-788 $[0/\pm45/0]_s$ graphite/epoxy. The material systems correspond to those used for the litter door, baggage door, forward fairing, and vertical fin, respectively.

Flight Service Evaluation

A total of forty (40) ship sets of composite components have been supplied to operators as kits for installation on aircraft that are located in the four geographical areas shown in figure 8. The areas selected include a hot, humid, salt-spray environment (U.S. Gulf Coast); a cold rocky environment (Alaska); a

---

[4] Manufactured by Ferro Corp., Culver City, CA.

[5] Manufactured by Klegecell Corp., Grapevine, TX

[6] Manufactured by U. S. Polymetric Co., Santa Ana, CA.

[7] Manufactured by Hexcel Corp., Dublin, CA

[8] Manufactured by Dupont Corp.,Wilmington, DE.

cold, damp pollution-prone environment (East Canada and N.E. United States); and a hot, dry environment (S.W. United States). Each component is inspected annually or after 1200 hours of service for evidence of damage, repair, excessive wear or weathering. At the conclusion of the first, third, fifth, seventh, and tenth year of flight service selected components are removed and returned to Bell Helicopter Textron, Inc. for static testing. Prior to testing, each component receives the same nondestructive inspection that was required during manufacturing. Test results are compared to design strength requirements.

Ground Exposure Specimen Evaluation

A tray of ground exposure specimens is removed at a prescribed interval of time, sealed in a plastic bag and shipped to the Langley Research Center. The tray remains in the sealed bag until static testing is initiated. All tests are performed at room temperature on six replicates for each specimen type. The tests are performed in accordance with the following ASTM standards: 1.) Tension-D3039; 2.) SBS-D2344; and 3.) Compression-D3410 using the IITRI test fixture.

Specimens used to characterize moisture absorption were cut from the tested tension specimens. A 0.5-inch-long section was cut from the undamaged area of the tension specimen as soon as possible after completion of testing. The paint was removed by sanding, using caution not to remove an excessive amount of the outer ply. Each specimen was weighed after the paint removal. A 0.5-inch-long specimen was also removed from the unpainted exposure specimen and weighed prior to being used for moisture content determination. All specimens were stored in sealed plastic bags between the different operations.

All specimens used to characterize moisture absorption were placed in a vacuum oven at 140 °F. Each specimen was weighed periodically to determine weight loss as a function of time.

Results and Discussion

Flight Service Components - Installation of the composite components on the Bell 206L began in March 1981. Aircraft flying these components had accumulated 122,355 hours through the end of 1988. The aircraft with the highest flight time has flown 9606 hours. Over one-half (67,919 hours) of the total time has been accumulated by aircraft flying in the Gulf of Mexico area. Next in flying time is Northeast USA and East Canada with 38,195 hours followed by Alaska with 8321 flight hours. Aircraft in Southwest USA have flown 7920 hours. As of April 1989, 51 components were flying, 78 components were removed for testing, 9 components were being reinstalled, 15 components were lost due to crashes or damaged beyond repair, and 11 components could not be located.

The litter door has had very few problems with the composite material skins. However, a major problem occured with the metal hinges. These metal hinges are used to hold the cabin door and were underdesigned and failed in service when someone pushed the cabin door too far open. New high strength hinges have been installed and the litter doors are back in service.

Buckling occurred in the outer skin of the litter door on four helicopters parked in the Southwest U.S. desert during the summer. The probable cause of buckling is the thermal mismatch between the Kevlar-49/epoxy skins and the plexiglass window. This window was bonded to the exterior skin. The coefficient of thermal expansion of the plexiglass window is 4.5×10^{-6} in./in./°F and the coefficient of thermal expansion for the Kevlar/epoxy skin is near zero. Personnel at this desert facility have taken surface temperature measurements on aluminum helicopter structures with the same external paint scheme as the composite skins and the temperatures typically reach 200 °F to 225 °F during the summer. The bond between the door structure and window was broken near the buckle on the four doors. The doors were modified and a rubber seal was bonded between the door structure and window to permit relative thermal expansion. Other normal service problems have occured, such as broken windows, bumps and scratches, which were repaired at the operator's repair facilities per repair instructions received with the kits.

Of the four components, the baggage door has the poorest service record. All baggage doors have been removed from service due to large, unrepairable voids between the outer skin and the Nomex core. Destructive inspection of doors that were removed from service indicate very little filleting between the outer skin and core, resulting in a poor bond between the outer skin and core. During manufacture, the

396

outside skin was co-cured with the Nomex core while the inner skin had an adhesive layer between the skin and the core.

Another service problem with the baggage door is cracking of the unsupported corners. This corner cracking of the baggage doors is caused by people accidently hitting the corners of the door with baggage and other gear to be stowed in the baggage compartment. This is an aesthetic problem rather than a functional problem but it does distract from the appearance of a commercial vehicle. The door and some of the adjacent structure would have to be redesigned to eliminate this corner cracking.

The forward fairing has had the fewest service problems. Until the 1985 inspection, the only service-related problem was associated with the use of the fairing as an antenna base. Field operators use the flat upper surface of the fairing to mount their communications antennas and they had to bond a metal plate to the underside of the fairing for grounding. The 1985 field inspection revealed that two helicopters operating in the Gulf Coast area had developed cracks on the inside surface near each latch. Both aircraft have been in service since 1981 and have flown 4193 hours and 5409 hours, respectively. The fairings were repaired with fiberglass, per maintenance instructions, at the operator's repair facility.

The graphite/epoxy vertical fin has an excellent service record. Its only problem has been cracking of paint on the two-ply Kevlar unsupported leading edge. This cracked paint was caused by field personnel using the fin as a handhold in ground handling. Two fins have been struck by lightning and one fin was repaired and returned to service. The other fin was returned to Bell for analysis and residual strength testing.

One of the most severe effects of the Gulf Coast environment on metallic components is corrosion. Operators typically start to repair corrosion on metal fins after 1 1/2 to 2 years of service. By six years in service, the leading edge, trailing edge, and several other parts of the metal fins have been rebuilt. The graphite fins on aircraft flying in the Gulf Coast area have been in service for up to seven years without a single maintenance problem related to corrosion.

As part of the flight service program, selected components are removed from service and tested to the same simulated aerodynamic loading as was used in FAA certification. Seventy-eight components have been removed for testing. The exposure region, exposure time, flight hours, and post service failure loads for each component are given in Tables 1 through 4. The exposure times range from 12 to 84 months and the flight times range from 386 to 6750 hours.

Failure loads (Table 1) for fifteen litter doors vary from 901 to 1768 lbs. These failure loads are the total loads on the door including the hinge reaction from the cabin door. Failure loads as a function of flight hours are shown in figure 9. Each open symbol type represents the failure load for a different exposure area. Also shown in figure 9 are two strength requirements, ultimate strength and design strength. The ultimate strength is the usual strength that an aircraft component must meet or exceed at all times. The design strength shown is the strength that an unconditioned component (as-fabricated) must meet or exceed. The design strength is intentionally greater than the ultimate strength and is the product of the ultimate strength and the environmental factor determined from the environmentally conditioned material coupon specimens (reference 2). This strength is shown for reference only, since the components tested are between as-fabricated and fully conditioned. The filled symbol represents the average baseline failure load. This baseline failure load, reported in reference 2, is the average of five components selected at random from the production lot of 45 components. The range of failure loads for the baseline tests are also shown in the figure. All litter doors had failure loads that exceeded the ultimate strength requirement of 635 lbs. (reference 2) and nine of the doors had failure loads that exceeded the design strength of 1229 lbs. It is acceptable for the failure load of doors that have been environmentally exposed to be below the design strength, so long as it is higher than the ultimate strength. Failure loads do not appear to be a function of exposure time. Initially in the post-service testing (reference 3), only the failure load was to be determined and compared with the baseline and certification loads. During testing of the third set of components the recording of deflections to limit load was started. From this load-deflection data for each component a stiffness could be determined for each component. This stiffness for each component gives another indication of composite material response to environmental effects since some of the failure loads are determined by metal hinge failures or latch pins slipping from the test fixtures. The stiffness of the litter

door as a function of flight time is shown in figure 10. The stiffness is calculated using measurements for the deflection at mid-span of the small post (Sec C-C in figure 2) as the load was applied. The stiffness shown for certification is the average of three tests used for certification. Large scatter in the measured stiffness is shown in figure 10. This large scatter is acceptable when considering that the door is installed in a fixture that simulates the aircraft attach points and loaded to limit load with water bags to simulate the uniform aerodynamic loading. A difference of only 0.025 inch deflection at limit load will change the stiffness by a factor of two. It is unfortunate that the deflections for the baseline tests were not recorded for comparison with components from the same production run. The doors that have been tested have accumulated a total of 23,087 hours of flight service.

Failure loads (Table 2) for 26 baggage doors vary from 0.31 to 1.57 psi and service times for the doors vary from 386 to 6750 hours. Failure loads as a function of flight hours are shown in figure 11. Each open symbol type represents the failure load for a different exposure area. The filled symbol represents the average baseline strength. These baggage doors are the components that developed large disbonds and have been removed from service. Most of the test points represent baggage doors that have some disbond between the core and the outer skin. Twenty-one of the doors had failure loads that were below the design strength of 0.70 psi and nine doors had failure loads that were below the ultimate strength requirement of 0.50 psi (reference 2). The stiffness of the baggage door as a function of the flight hours is shown in figure 12. The stiffness was determined by measuring the deflection at the center of the door as the loads were applied. The disbonds do not appear to affect the stiffness as much as the strength. The baggage doors that have been tested have accumulated a total of 51,798 hours of flight service.

Failure loads (Table 3) for 15 forward fairings vary from 1.8 to 3.93 psi and service times for these components vary from 386 to 6750 hours. Failure loads as a function of flight hours are shown in figure 13. Each open symbol type represents the failure load for a different exposure area. Failure loads vary from 1.89 to 3.93 psi and exceed the design strength of 0.49 psi (reference 2), by more than a factor of three. Failure loads for forward fairings tested to determine the baseline strength (reference 2) varied between 2.2 psi and 3.4 psi. Failure loads for eight of the fifteen forward fairings tested are between 2.2 psi and 3.4 psi. The large scatter in the failure load could be the result of variations in the fabrication process. Considerable variation could result from putting down the single ply of Kevlar fabric (style 281) on a compound contoured surface. The lay-up requires cutting and overlapping the fabric at many places to prevent wrinkling on the surface. The stiffness of the forward fairing as a function of the flight hours is shown in figure 14. The stiffness was calculated using measurements for the deflection of the upper surface at a point 14.5 inches from the aft end as the load was applied. The stiffness of all fairings, except one, exceeded the stiffness of the certification fairings. The fairings that have been tested accumulated a total of 23,730 hours of flight time.

Failure loads (Table 4) for fifteen vertical fins vary from 1.12 to 1.80 psi and service times for these fins vary from 306 to 6750 hours. Failure loads as a function of flight hours is shown in figure 15. All fins exceed the design strength of 1.05 psi. Failure loads for twelve of the fifteen fins are between 1.35 and 1.57 psi which is the range of failure loads for the baseline tests (reference 2). One fin that was struck by lightning is identified in Table 4. The fin was damaged at the top with no damage in the structural box. This fin failed at 1.23 psi with no apparent effect from the lightning strike. The environment does not appear to affect the failure load of the vertical fins. The stiffness of the vertical fin as a function of flight time is shown in figure 16. Stiffness was calculated using measurements for the tip deflection as the simulated aerodynamic load was applied. The certification deflection data for the fin are not available. The vertical fins that have been tested have accumulated 26,139 flight hours.

Ground Exposure Specimens - In the summer of 1985 the exposure racks (figure 7) located at Cameron, LA and on the off shore oil platform were destroyed by hurricanes. All the following data for five and seven years of exposure are from the three remaining sites: Hampton, VA; Toronto Canada; and Ft. Greely, AK.

The baseline strengths for the as-fabricated ground exposure specimens are given in Table 5. Each table entry is the mean strength of the six replicates tested. The residual compressive and short beam shear

strengths of exposed painted specimens are shown in figures 17 and 18, respectively. Each point shown on the figures for one year or three years of exposure is the mean of thirty tests (5 racks and 6 replicates of each material), while each point for five years and seven years of exposure is the mean of eighteen tests (3 racks and 6 replicates of each material). The mean strength results shown in each figure are normalized by the mean baseline strength. Scatter bands in the baseline strength are also shown in figures 17 and 18. The residual compression strength of exposed painted specimens shown in figure 17 varies between 88 and 101 percent of baseline. Kevlar-49/LRF-277 material has the lowest strength retention of 88 to 90 percent of baseline. For the first five years of exposure the other materials exceeded the lower baseline scatter band of 96 percent. At seven years of exposure Kevlar-49/F-185 and T-300/E-788 materials retained 93 percent of the baseline strength. The short beam shear strength of exposed painted specimens (figure 18) varies between 89 and 104 percent of baseline. Like the compression strength results, the Kevlar-49/LRF-277 material has retained the lowest short beam shear strength of 89 to 92 percent. The T-300/E-788 material retained the highest strength of 100 to 104 percent of baseline. All materials, except Kevlar-49/LRF-277, exceeded the baseline scatter minimum of 93 percent. The residual tension strength of the exposed specimens after exposure equals or exceeds the baseline strength.

A summary of moisture absorption data for each material as a fraction of composite specimen weight for painted specimens that were exposed for three, five and seven years is shown in figures 19 through 22. Each symbol type represents a different exposure location and the filled symbols represent the unpainted specimens. Each data point for painted specimens is the average of six replicates. Summaries of the moisture absorption data for the unpainted specimens are also shown in figures 19 through 22. Each data point for the unpainted specimens is from a single specimen. Moisture absorption data for the Kevlar-49/CE-306 material are shown in figure 19. No trend is evident after three years of exposure. After five and seven years of exposure the painted specimens absorb 0.15 to 0.38 percent(average) more moisture than the unpainted specimens. The painted Kevlar-49/CE-306 specimens appear to be reaching an equilibrium condition of 2.1 percent moisture absorption. Moisture absorption data for the Kevlar-49/F-185 material are shown in figure 20. This figure indicates that painted specimens absorb more moisture than the unpainted specimens. The painted specimens absorb up to 0.63 percent (average) more moisture than the unpainted specimens. Moisture absorption data for the Kevlar-49/LRF-277 material are shown in figure 21. The trend in this material is the opposite from the other two Kevlar materials in this program. For the Kevlar-49/LRF-277 material the unpainted specimens absorb more moisture than the painted specimens. By the seventh year of exposure the unpainted specimens are approaching an equilibrium condition of 2.3 percent moisture absorption. Moisture absorption data for the T-300/E-788 graphite/epoxy material are shown in figure 22. The 0.74 percent absorption for three year exposure at the Gulf of Mexico does appear high. There is no method to determine if this high moisture absorption would continue in the Gulf of Mexico since the rack was destroyed before the removal of specimens after five years of exposure. No trend is evident after three years of exposure. After five and seven years of exposure the painted specimens absorbed approximately 0.10 percent more moisture than the unpainted specimens, the same trend followed by two of the Kevlar/epoxy systems. Kevlar-49/epoxy materials absorb four to five times more moisture than graphite/epoxy materials because the Kevlar fibers absorb moisture. The average values, for each material, compare well with published values for other Kevlar/epoxy and graphite/epoxy systems (reference 1).

SIKORSKY S-76 PROGRAM

Component Description

A total of fifteen S-76 composite components were used in this evaluation: four horizontal stabilizers; and eleven tail rotor spars. The location of the horizontal stabilizer and tail rotor paddles, which contain the tail rotor spars, on the S-76 is shown in figure 23. A detailed description is given in reference 4. A brief description of each component follows.

Horizontal Stabilizer - A sketch of the left half of the horizontal stabilizer is shown in figure 24. The

stabilizer is a full depth sandwich structure with crossplied Kevlar-49 fabric/5143[9] epoxy composite material skins and Nomex honeycomb core. The torque tube that joins the left and right sides of the stabilizer is full depth aluminum honeycomb construction with unidirectional AS1[10] graphite/6350[11] epoxy composite material in the spar caps. The torque tube is overwrapped with cross plies of Kevlar-49 fabric/5143 epoxy to provide additional torsional rigidity. The composite horizontal stabilizer weighs 40.0 lbm.

Design of the stabilizer was controlled primarily by static load requirements. All production parts are proof load tested at room temperature prior to installation. For proof load testing the stabilizer is supported at ±25.0 in. from the centerline and a 2400 lbf downward load is applied at the centerline. The deflection of the torque tube is measured and recorded. FAA certification and baseline strengths were achieved by supporting the stabilizer at the aircraft attachment points and applying load through pads bonded to the stabilizer skin at ±40.0 in. from the centerline. The design limit loads (DLL) for static tests and baseline loads for fatigue testing are shown in figure 25. Static tests are performed with the structure at 160 °F. Fatigue tests are performed at room temperature.

Tail Rotor Spar - The tail rotor spar is a solid laminate constructed with AS1 graphite/6350 epoxy composite material. The spar is shown in figure 26 and is 52.9 in. long by 3.5 in. wide. Weight of the spar is 14.6 lbm. Two glass/epoxy blades are attached to the spar to form the tail rotor paddle as shown in figure 27.

The tail rotor spar was designed to withstand a high number of cyclic loads. The tail rotor was fatigue tested using the edgewise moment, flatwise moment, torsion, and centrifugal loads illustrated in figure 28. The centrifugal load is kept constant and represents the centrifugal force for a rotor operating at 110 percent of the normal rotor speed. The cyclic loadings are in phase and held in the same proportions, as the absolute values are varied to produce a fatigue fracture in the range of 10^5 to 5×10^6 cycles.

Material Allowables

Using the projected aircraft usage, Sikorsky predicted (reference 4) the saturation moisture levels in Kevlar-49/5143 to be 2.2 percent and AS1/6350 to be 1.1 percent. To expedite the development of design allowables for the S-76 program, Sikorsky used accelerated conditioning on coupon specimens for determining material properties. All conditioning was conducted at 87 percent relative humidity and 190 °F.

Ground Exposure Panels

Panels of AS1/6350 and Kevlar-49/5143 are being subjected to outdoor ground based exposure at Stratford, CT and West Palm Beach (WPB), FL. The Kevlar-49/epoxy panels are 5-plies thick and the graphite/epoxy panels are 6-, 14-, and 33-plies thick. Each year, three panels of each material and thickness combination are removed for evaluation. Sizes of panels are 8.0 in. by 22.0 in., 6.0 in. by 8.0 in., and 2.0 in. by 6.0 in. The 2.0 in. by 6.0 in. panels were left unpainted for determining the effects of weathering on bare composites and the other panels were painted with a polyurethane aircraft paint. The 6-ply graphite/epoxy panels are machined into compression and flexure specimens. The 14- and 33-ply graphite/epoxy panels are machined into compression, short beam shear static, flexure and short beam shear fatigue specimens. The 5-ply Kevlar-49/epoxy panels are machined into tension specimens. All exposed specimens are tested at room temperature and the test data are compared with baseline data for room temperature dry specimens. Moisture content is determined by cutting the 6.0 in. by 8.0 in. panel into four specimens which are dried at 150 °F.

---

[9] Manufactured by American Cyanamid, Havre de Grace, MD

[10] Manufactured by Hercules. Inc., Magna, UT.

[11] Manufactured by Ciba Geigy, Fountain Valley, CA.

Flight Service Evaluation

Four horizontal stabilizers and eleven tail rotor spars have been removed from aircraft in service over an eight-year period. Since these components are production parts, they receive the normal maintenance inspection for surface damage every 100 flight hours and inspection for structural damage annually or after 1000 flight hours. One of the stabilizers has been static tested and the remaining stabilizers have been fatigue tested.

Seven of the tail rotor spars have been fatigue tested and the remaining four spars have been cut into short beam shear specimens that have been subjected to the following tests: (1) Room temperature static; (2) 170°F static; and (3) room temperature fatigue. After full-scale component testing, coupons have been removed from the components to determine their moisture content.

Results and Discussion

Flight Service Components

The horizontal stabilizers and tail rotor spars were removed from aircraft operating in the Gulf Coast region of Louisana. The components have accumulated a combined total of 53,146 hours; 15,496 hours for the stabilizers; and 37,650 hours for the tail rotor spars. All components scheduled for testing have been removed from service. The flight hours and exposure times at removal are given in Table 6.

Horizontal Stabilizers -The first horizontal stabilizer (serial no. 00076, see Table 6) removed from service had accumulated 1600 flight hours over a 17 month period. Prior to full scale testing, the stabilizer was proof load tested in accordance with the procedure required for production acceptance. The proof load deflection for this stabilizer was the same as the corresponding deflection for the stabilizer used for the initial acceptance test. The flight service stabilizer was static tested to failure. Data for strain as a function of percent limit load are shown in figure 29. The tension strain response was linear up to 160 percent of design limit load (DLL) and then increased at reduced slope until the maximum applied load of 220 percent of DLL was reached. The compression strain response was linear to 120 percent of DLL and then increased at a reduced slope until 170 percent of DLL was reached. The compression strain did not increase after 170 percent of DLL. At 220 percent of DLL the stabilizer made a loud "snap" and the load dropped to 150 percent of DLL. Attempts to increase the load beyond 150 percent DLL resulted in increased deflection until the test fixture limit was reached. Visual inspection of the stabilizer indicated a buckle in the splice plate on the left hand leading edge of the torque box. Teardown of the component revealed a loss of shear transfer capabilities between the composite material and the metal honeycomb. The stabilizer tested for certification did not fail but reached the maximum deflection allowed by the fixture at 268 percent of DLL.

The second stabilizer (serial no. 00009) was subjected to proof loading and fatigue loading after 56 months of exposure and 3999 hours of flight time. The deflection for this stabilizer at proof load was the same as the corresponding deflection for the stabilizer used for the acceptance test. The same loads for fatigue testing were applied as were used for certification (figure 25). When no fracture occured after 5 x 10^5 cycles the test was stopped and the loads increased by five percent. At 3 x 10^5 additional cycles at the higher loads, a fracture occurred in the torque box.

The third stabilizer (serial no. 00021) was subjected to proof loading, static loading, and fatigue loading after 66 months and 4051 flight hours. Visual inspection and coin tapping revealed two small disbond areas in the torque box. One disbond measured approximately 0.75 in. long by 1.50 in. wide and was located at left Buttline 3 (3 in. to left of aircraft centerline). The other disbond measured approximately 1.0 in. long by 3.0 in. wide, located at right Buttline 3. An acceptable deflection was measured during proof load testing indicating no loss of stiffness. The stabilizer was loaded to design limit load, at 160°F, followed by fatigue testing at room temperature. Due to an error in loading the applied fatigue loads were 23 percent higher than the baseline loads. After 59,980 cycles fracture occurred in the torque box. The fractured area was located between right and left Buttline 3.

The fourth stabilizer (serial no. 00027) was subjected to proof loading and fatigue loading after 91 months and 5846 flight hours. The deflection for this stabilizer at proof load was the same as the corre-

sponding deflection for the stabilizer used for the acceptance test. The same loads for fatigue were applied as were used for certification (figure 25). After 437,340 cycles fracture occurred in the torque box.

Tail Rotor Spars - Eleven tail rotor spars have been removed for testing. No defects were found during inspections of the spars. Seven of the spars were fatigue tested and the remaining spars used to obtain specimens for coupon tests. A summary of data for the tail rotor spars is given in Table 7 along with data from spars labeled serial numbers 00046 and 00064 (reference 5). These two spars were removed from a Sikorsky flight test aircraft that was located at West Palm Beach, FL. The points designated "a"(Table 7) represent the first fracture on one side of the spar. On spars that did not have a complete failure, testing was continued on the other side until fracture occurred and the results are designated "b". Cyclic shear stress as a function of cycles to crack initiation is shown in figure 30 along with the strength of dry spars tested at room temperature for FAA certification. These results indicate a 94 percent strength retention for the exposed spars when compared to strength data from certification tests.

A predicted moisture-time profile (reference 6) for the tail rotor spars (reference 5) operating in the Louisiana Gulf coast region is shown in figure 31. Weather data from Lake Charles, LA were used in predicting the absorbed moisture. Measured moisture values (Table 7) are shown in figure 31 on a plot of percent moisture as a function of calendar time. As can be seen in figure 31, the measured moisture values are below the predicted moisture values for the low calendar time (30-40 months) while the measured moisture values for exposure time of 70 months is higher than the predicted values.

Ground Exposure Specimens

A summary of the moisture absorption results for exposed panels with two through six years of exposure is presented in Table 8. These results indicate that the 6-ply AS1/6350 panels exposed at West Palm Beach, FL have exceeded the predicted saturation levels of 1.1 percent moisture while panels exposed at Stratford, CT have reached the predicted levels. The 14-ply and 33-ply panels are not expected to reach saturation for several years. A predicted moisture-time profile (reference 6) for the 6-ply panels exposed at Stratford, CT is shown in figure 32. The measured moisture for each panel (Table 8) are also shown in figure 32. The results in the figure show that the measured moisture values are in good agreement with the predicted values. Plots of residual strength as a function of moisture content for flexure, short beam shear, and tension specimens are shown in figures 33 through 35, respectively. Each individual data point is the mean strength of 18 tests. The solid line in each figure is the residual strength after the accelerated conditioning of the specimens (reference 4). Residual flexure strengths in figure 33 for exposed 6-ply AS1/6350 laminates exceed 95 percent of baseline strength and also meet (5 years at West Palm Beach, FL) or exceed the strength of the accelerated conditioned specimens. Residual short beam shear strengths in figure 34 for exposed AS1/6350 laminates vary between 72 and 89 percent of baseline and are within one percent of the strength of the accelerated conditioned specimens. Residual tension strengths in figure 35 of the Kevlar-49/5143 material vary from 99 to 107 percent of the baseline strength and exceed the strength of the accelerated conditioned specimens by 11 to 24 percent. This material follows the same trend as the tension strength of Kevlar-49 fabric materials used in the Bell 206L program.

CONCLUSIONS

Bell 206L Program

Aircraft flying the Bell 206L components have accumulated approximately 123,000 hours. The high time aircraft has accumulated over 9000 hours. Over one-half of the total flight hours have been accumulated in the Gulf of Mexico area. The use of composite material eliminates the metal corrosion problem which is significant on aircraft that fly in the Gulf of Mexico area. The baggage door has the poorest service record resulting from poor bonding between the exterior skin and the core. This bond could not be repaired, and the baggage doors were removed from flight service. The other components have had problems from ground handling or underdesigned metal parts. In general the composites components have performed well in flight service. Individual components that have been tested have accumulated up to 6750 flight hours and 69 months of exposure time. With the exception of the baggage door, post-service strengths exceed the ultimate strength.

Residual short beam shear and compression strengths for ground exposure specimens after 5 years of exposure exceeded 88 percent of baseline strengths. The Kevlar-49/LRF-277 material had the lowest retained strength of 88 to 92 percent of baseline strength after exposure. Residual strength of all other materials exceed 93 percent of baseline strength after exposure. Tension strength of all specimens after exposure equaled or exceeded the baseline strength.

The Kevlar-49/CE-306 and Kevlar-49/F-185 materials absorb up to 0.6 percent more moisture when painted. The Kevlar/epoxy materials appear to be approaching an equilibrium condition at 2.1 to 2.3 percent moisture content. The T-300/E-788 painted material absorb approximately 0.1 percent more moisture than the similar unpainted materials.

Sikorsky S-76 Program

The fifteen components evaluated in the Sikorsky S-76 program have accumulated over 53,000 flight hours. The four horizontal stabilizers removed from service passed the proof load test. A horizontal stabilizer with 17 months of exposure failed at 220 percent of design ultimate load. Two horizontal stabilizers with 56 and 66 months of service have been fatigue tested and failed at 300,000 and 59,980 cycles, respectively, at applied loads exceeding loads used for FAA certification.

The tail rotor spars retained 94 percent of the baseline fatigue strength after eight years of exposure. Predicted moisture content for the spars is high for low exposure time (30-40 months) but low for the high exposure time (over 70 months).

The six-ply AS1/6350 panels exposed at West Palm Beach, FL have exceeded the predicted design moisture level of 1.1 percent while the panels at Stratford, CT have reached the predicted level. Residual compression and short beam shear strengths of AS1/6350 exceed 72 percent of baseline strength after six years of exposure. Residual tension strength of Kevlar-49/5143 exceeded baseline strength. The residual strength after outdoor exposure equals or exceeds the strengths from laboratory-conditioned specimens for all material systems.

REFERENCES

1. Dexter, H. Benson: *Long-term Environmental Effects and Flight Service Evaluation of Composite Materials.* NASA TM 89067, January 1987.
2. Zinberg, H.: *Flight Service Evaluation of Composite Components on the Bell Helicopter Model 206L: Design, Fabrication, and Testing.* NASA CR 166002, November 1982.
3. Zinberg, H.: *Flight Service Evaluation of Composite Components on the Bell Helicopter Model 206L: First Annual Flight Service Report.* NASA CR 172296, March 1984.
4. Rich, M. J.; and Lowry, D. W.: *Flight Service Evaluation of Composite Helicopter Components: First Annual Report March 1981 through April 1982.* NASA CR 165952, June 1982.
5. Rich, M. J.; and Lowry, D. W.: *Flight Service Evaluation of Composite Helicopter Components: Second Annual Report May 1982 through September 1983.* NASA CR-172562, April 1985.
6. Mardoian, G. H.; and Ezzo, M. B.: *Flight Service Evaluation of Composite Helicopter Components: Third Annual Report, October 1983 through December 1985.* NASA CR-178149, September 1986.

Table 1. History of litter doors that have been removed for testing

Exposure Region	Serial Number	Start of Service, mo/yr	End of Service, mo/yr	Time, mo	Flight hours	Failure Load, lbs
Gulf	45373	6/81	5/82	12	879	1009
of	45378	2/82	11/84	34	3387	988
Mexico	45367	10/81	1/87	64	6750	1618
	ML-A83	*	*	*	*	1262
Southwest	45614	5/82	10/83	17	386	901
USA	45418	5/82	1/85	32	1235	1768
	45607	5/82	11/87	58	1992	1592
	45609	5/82	8/83	16	802	1644
N.E. USA	45141	5/81	7/82	15	870	980
and	45028	4/82	11/84	32	1160	1302
Canada	45101	8/81	6/83	23	1413	1115
	45017	3/82	11/84	33	902	1750
	45085	4/82	11/84	32	1369	1492
Alaska	45115	5/82	10/84	29	668	931
	45109	7/84	3/88	45	1284	1643

* Unknown

Table 2. History of baggage doors that have been removed for testing

Exposure Region	Serial Number	Start of Service, mo/yr	End of Service, mo/yr	Time, mo	Flight hours	Failure Load, psi
Gulf of Mexico	45373	6/81	5/82	12	879	.91
	45378	2/82	11/84	34	3387	1.39
	*	*	*	*	*	.60
	45378	2/82	4/87	29	2500	.43
	45524	3/82	3/87	60	4828	.69
	45449	11/82	3/87	53	5837	.46
	45546	8/82	4/88	69	6027	.71
	45367	10/81	1/87	64	6750	.60
Southwest USA	45614	5/82	10/83	17	386	.46
	45418	5/82	1/85	32	1235	.49
	45607	4/83	12/87	66	1992	.55
	45608	5/82	11/87	64	1317	.49
N.E. USA and Canada	45141	5/81	7/82	14	870	.50
	45028	4/82	11/84	32	1160	1.57
	45101	8/81	6/83	22	1413	.32
	45017	3/82	11/84	26	902	1.37
	46607	4/83	12/87	56	1824	.50
	45083	6/82	1/88	67	2195	.57
	45085	4/82	11/84	33	1369	.54
	ML-112	*	*	*	*	.55
	ML-13	*	*	*	*	.37
Alaska	45115	5/82	10/84	29	668	1.39
	45108	12/81	3/88	76	2004	.43
	45109	7/84	3/88	45	1284	.60
	45113	11/81	1/87	63	1772	.54
	45114	3/84	3/88	48	1199	.54

* Unknown

Table 3. History of forward fairings that have been removed for testing

Exposure Region	Serial Number	Start of Service mo/yr	End of Service mo/yr	Time, mo	Flight hours	Failure Load, psi
Gulf of Mexico	45373	6/81	5/82	12	879	1.80
	45378	2/82	11/84	34	3387	2.34
	45367	10/81	1/87	64	6750	2.70
	45535	*	*	20	500	2.11
	ML-03	*	*	*	*	3.68
Southwest USA	45614	5/82	10/83	17	386	2.80
	45418	5/82	1/85	32	1235	3.68
	45607	5/82	11/87	58	1992	3.73
N.E. USA and Canada	45141	5/81	7/82	15	870	2.50
	45028	4/82	11/84	32	1160	2.47
	45101	8/81	6/83	23	1413	1.89
	45017	3/82	11/84	33	902	2.46
	45085	4/82	11/84	32	1369	3.44
Alaska	45115	5/82	10/84	29	668	2.69
	45113	11/81	11/88	84	2219	3.93

* Unknown

Table 4. History of vertical fins that have been removed for testing

Exposure Region	Serial Number	Start of Service, mo/yr	End of Service, mo/yr	Time, mo	Flight hours	Failure Load, psi
Gulf of Mexico	45378	2/82	4/87	34	3387	1.12
	45373	6/81	5/82	12	879	1.80
	*	*	*	*	*	1.48
	45367	10/81	1/87	63	6750	1.44
Southwest USA	45608	5/82	11/87	66	2213	1.57
	45614	5/82	10/83	18	386	1.41
	45607	5/82	11/87	66	1992	1.49
	45418	5/82	1/85	32	385	1.50
N.E. USA and Canada	45028	4/82	11/87	32	1160	1.37
	45450+	9/81	7/84	36	2661	1.23
	45141	5/81	7/82	15	870	1.60
	45101	8/81	6/83	23	1413	1.51
	45085	4/82	11/84	32	1369	1.49
	45017	3/82	11/84	33	902	1.39
Alaska	45113	1/81	1/87	63	1772	1.49

* Unknown
+ Struck by lightning

Table 5. Strengths of as-fabricated ground exposure
material specimens

Material	Strength, ksi		
	SBS*	Compression	Tension
Kevlar-49/F-185	6.0	20.2	57.4
Kevlar-49/LRF-277	3.9	22.4	83.7
Kevlar-49/CE-306	5.3	18.3	61.1
T-300/E-788	11.2	126.3	126.5

* Short Beam Shear

Table 6. Flight times of S-76 components
removed from service

Component	Serial Number	Flight Hours	Exposure Time, mo
Horizontal Stabilizer	00076	1600	17
	00009	3999	56
	00021	4051	66
	00027	5846	91
Tail Rotor Spars	00094	2390	29
	00283	1884	37
	00150	2385	38
	00237	2128	42
	00172	2533	39
	00114	3358	52
	00178	3753	51
	00069	4940	69
	00415	5138	68
	00493	5858	97
	00480	5816	100

Table 7. Summary of data for S-76 tail
rotor spars

Serial Number	Exposure Time, mo	Flight Hours	Cyclic Shear Stress, psi	Cycles to crack	Moisture Content, percent
00046	25[1,2]	150	(a) 3980	$.25 \times 10^6$	.29
			(b) 3980	$.38 \times 10^6$	
00064	25[1,2]	150	(a) 4320	$.035 \times 10^6$	.32
			(b) 4320	$.071 \times 10^6$	
00094	29[3]	2390	(a) 3890	$.286 \times 10^6$	.26
			(b) 3920	$.174 \times 10^6$	
00283	37[3]	1884		coupon tests	.36
00150	38[3]	2385		coupon tests	.40
00237	42[3]	2128	4520	$.267 \times 10^6$	.47
00172	39[3]	2533	4270	$.218 \times 10^6$	.49
00114	52[3]	3358	4416	$.839 \times 10^6$	.56
00178	51[3]	3753		coupon tests	.60
00069	69[3]	4940	3820	$.146 \times 10^6$	.66
00415	68[3]	5138		coupon tests	.78
00493	97[3]	5858		coupon tests	*
00480	100[3]	5816	4640	$.140 \times 10^6$	*

[1] reference 5
[2] In-service location: West Palm Beach, FL
[3] In-service location: Gulf Coast Region, LA
* Desorption in progress
(a) First failure
(b) Final failure

Table 8. Summary of moisture content
for exposed panels

Material	Number of Plies	Exposure Location	Exposure Time, mo	Percent Moisture (by weight)
AS1/6350 graphite/epoxy	6	WPB[1]	26	1.02
			35	1.23
			48.5	1.15
			60.5	1.40
			72.5	1.34
			84	*
		Stratford	25	0.86
			36	1.00
			49	0.99
			62	1.13
			73	1.07
			85	*
AS1/6350 graphite/epoxy	14	Stratford	25	0.37
			34.5	0.48
			48	0.44
			61	0.64
			72	0.57**
			84.5	*
AS1/6350 graphite/epoxxy	33	WPB	26	0.27
			35	0.37
			48.5	0.35
			60.5	0.42
			72.5	0.44**
			84	*
		Stratford	25	0.18
			36	0.22
			49.5	0.24
			62	0.30
			73.5	0.25**
			85	*
285/5143 Kevlar/epoxy	5	WPB	26	1.56
			35	2.08
			48.5	1.90
			60.5	1.88
			72.5	2.02
			84	*
		Stratford	26	1.53
			37	1.72
			50	1.75
			63	1.92
			74	1.70
			85.5	*

[1] West Palm Beach, FL
*   Desorption in progress
** estimated

Graphite/epoxy vertical fin

Kevlar/epoxy forward fairing

Kevlar/epoxy baggage door

Kevlar/epoxy litter door
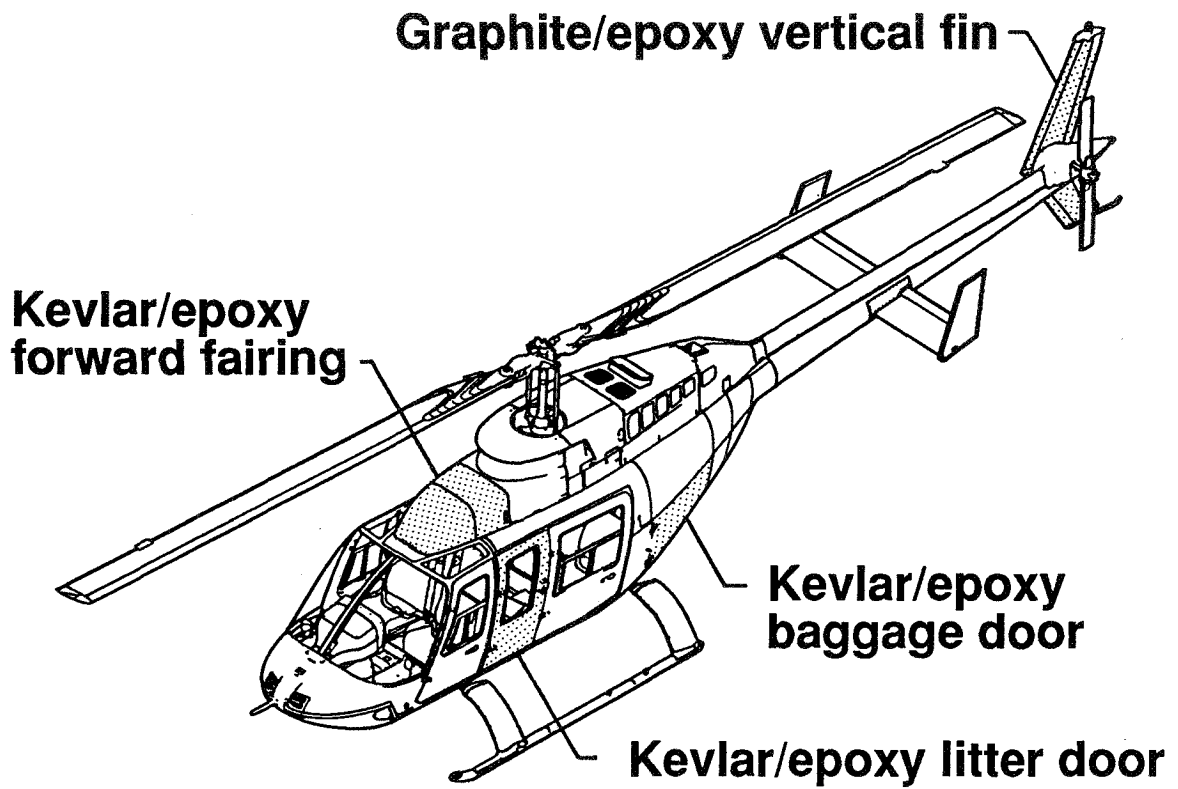
Figure 1. Composite components in flight service on Bell 206L helicopters.

26 in.

46 in.

Unidirectional Kevlar

Sec B-B (rotated)

Sec C-C

Door post

C C

B

A

A

B

Inner skin

Unidirectional Kevlar

Sec A-A
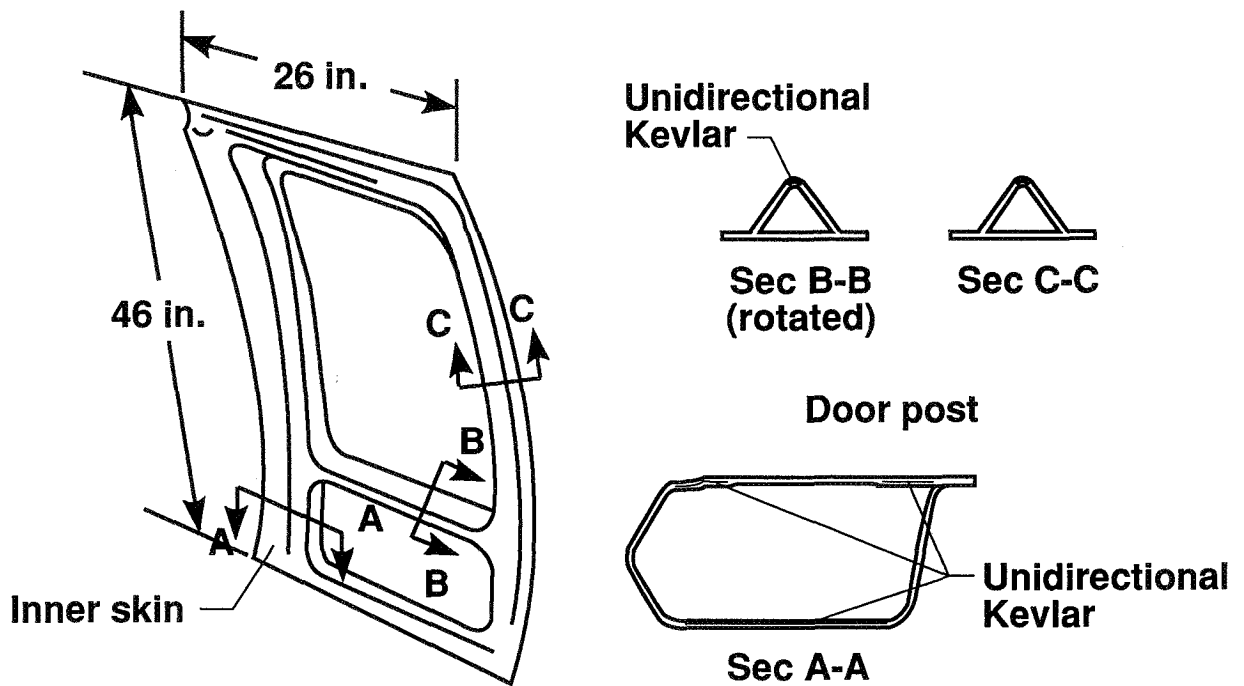
Figure 2. Bell 206L Kevlar/epoxy litter door.
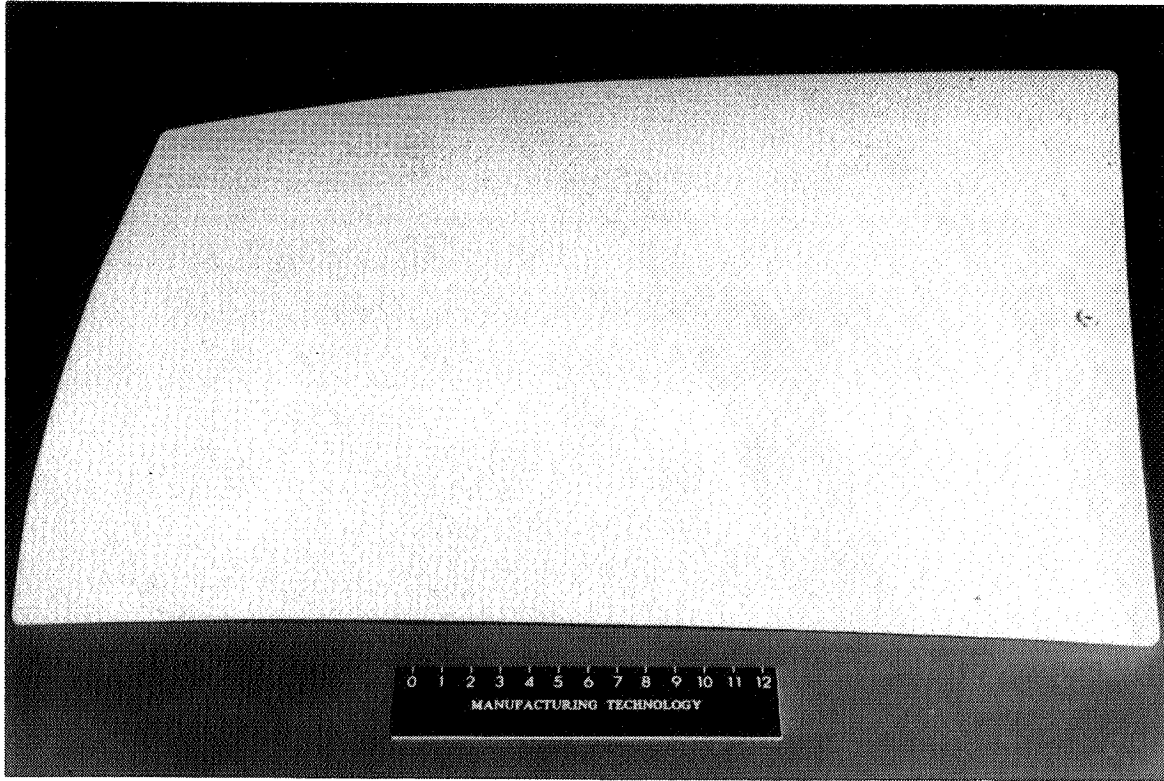
Figure 3. Bell 206L Kevlar/epoxy baggage door.
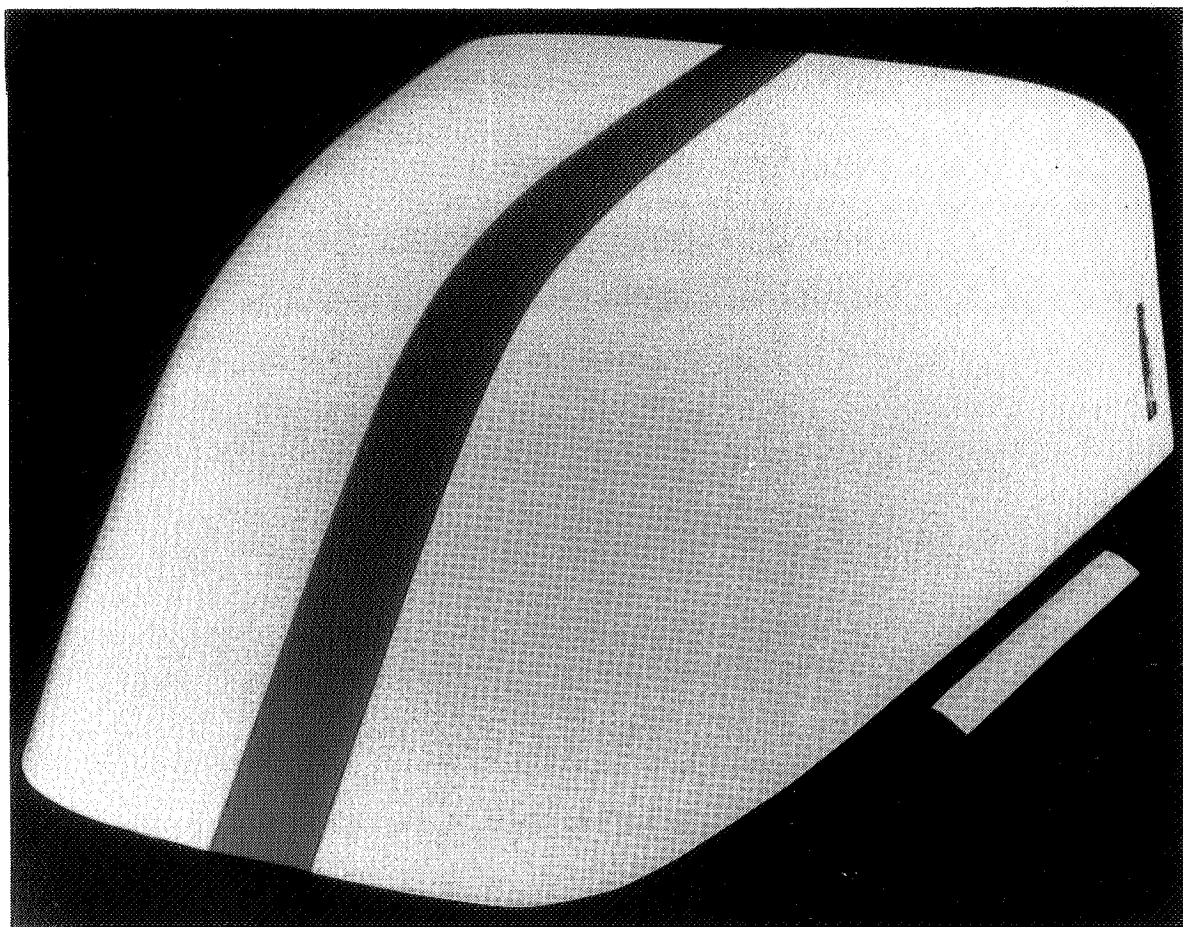
Figure 4. Bell 206L Kevlar/Epoxy forward fairing.
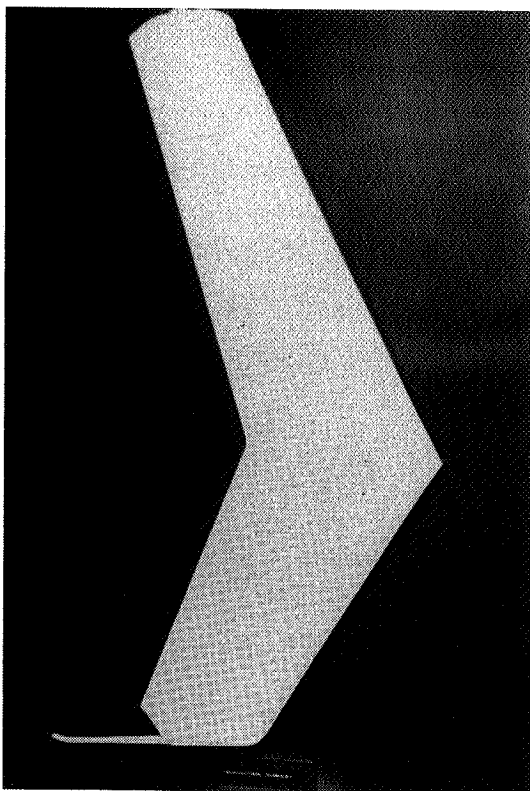
Figure 5. Bell 206L Graphite/Epoxy vertical fin.
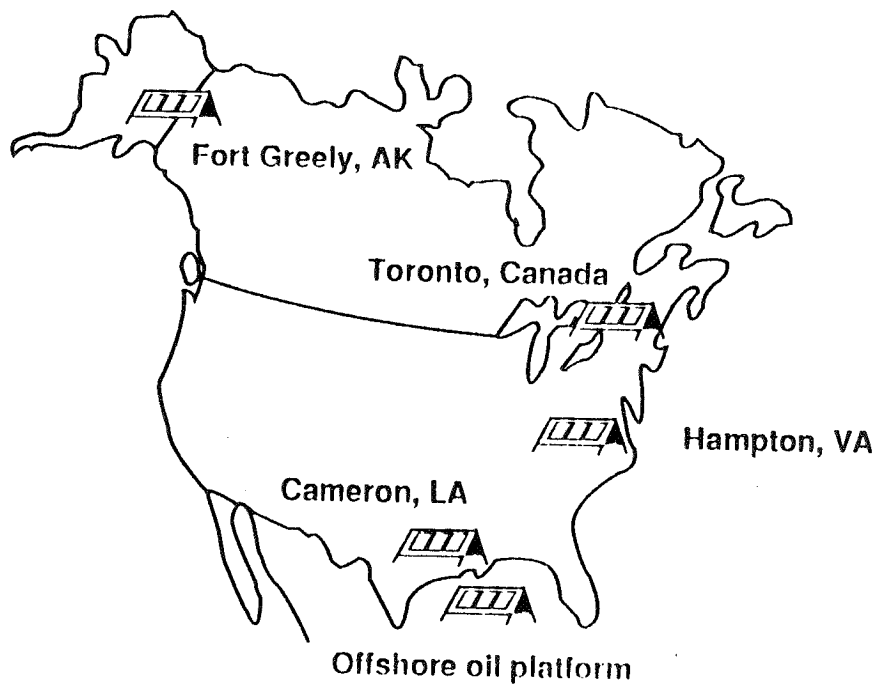
Figure 6. Location of environmental specimen exposure racks.

413
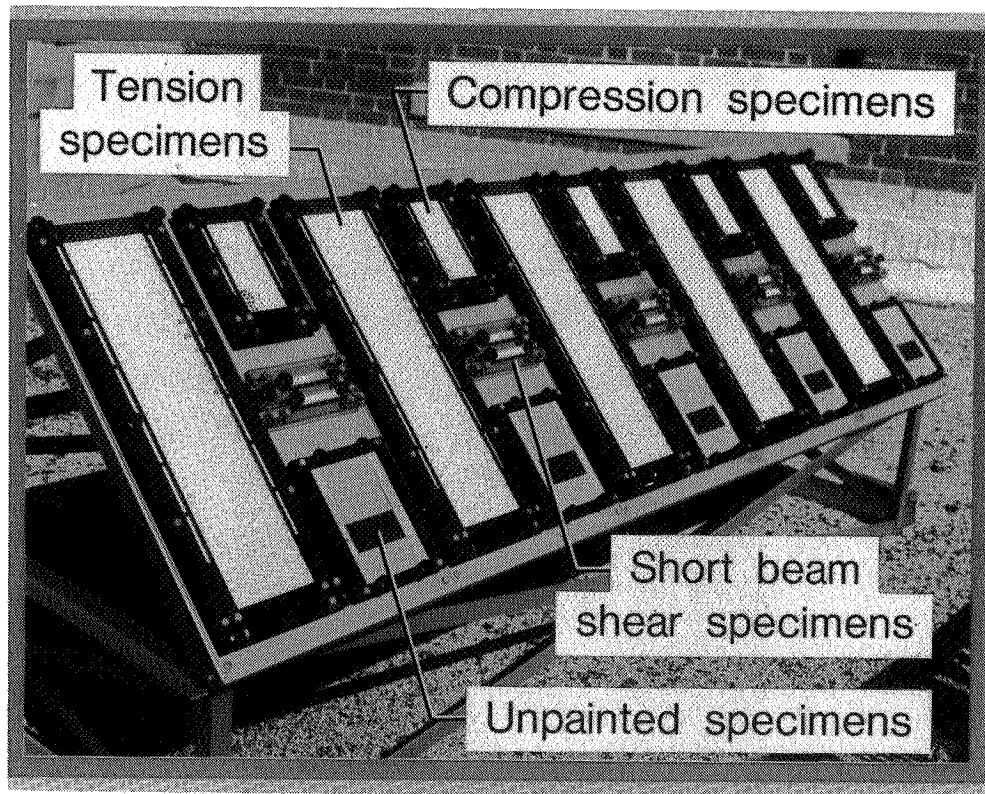
Figure 7. Environmental exposure rack with specimens installed.
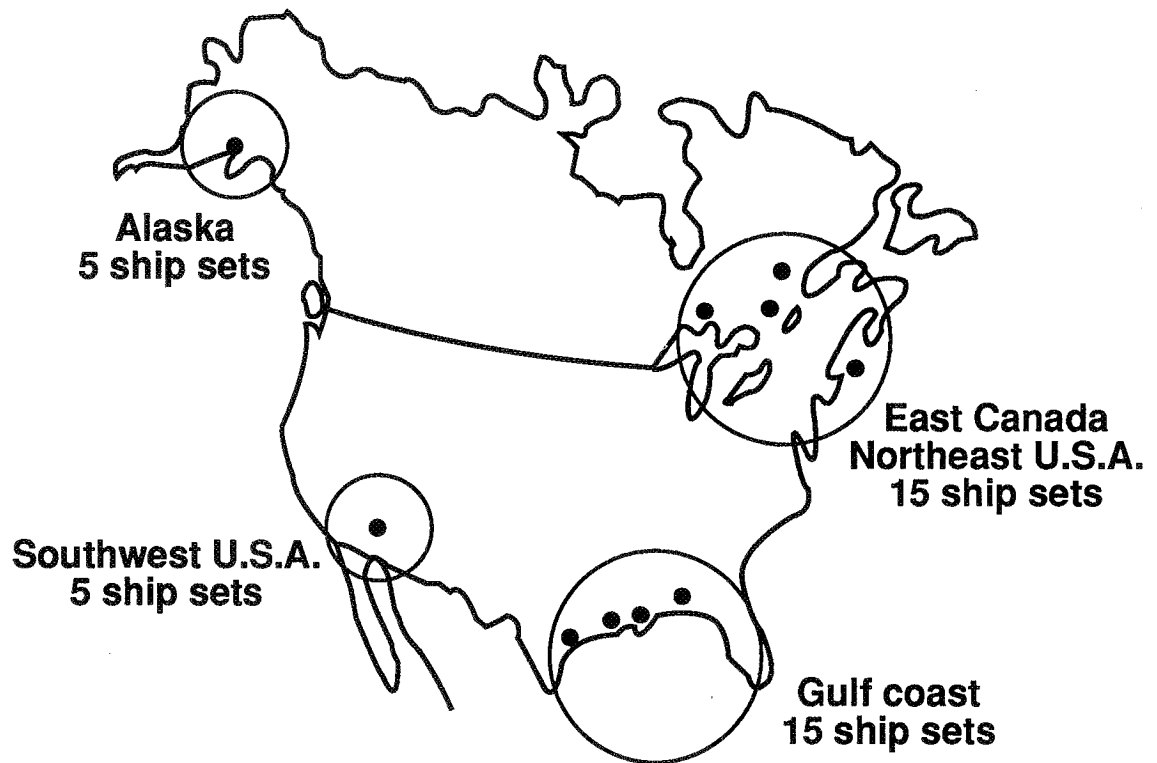
Figure 8. Distribution of Bell 206L helicopters with composite components.
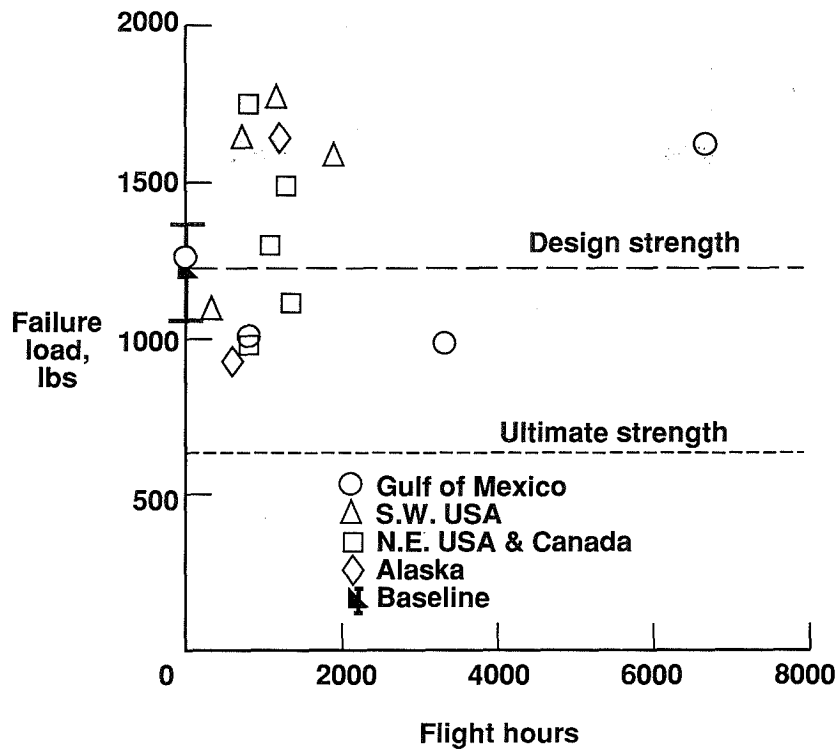
Figure 9. Failure load of litter doors after exposure.
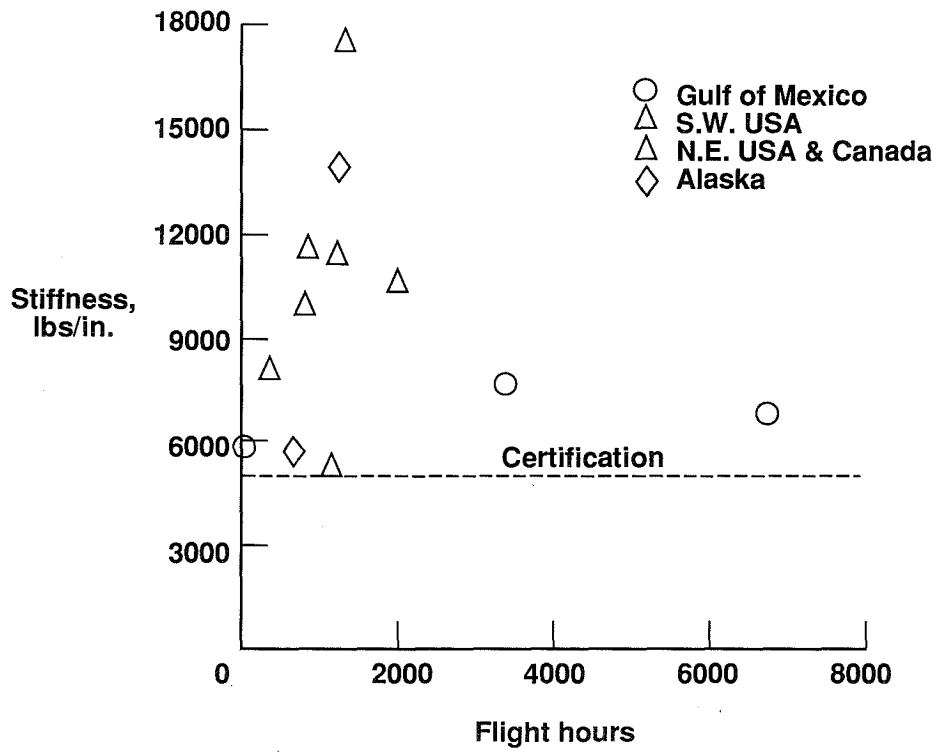
Figure 10. Stiffness of litter doors after exposure.
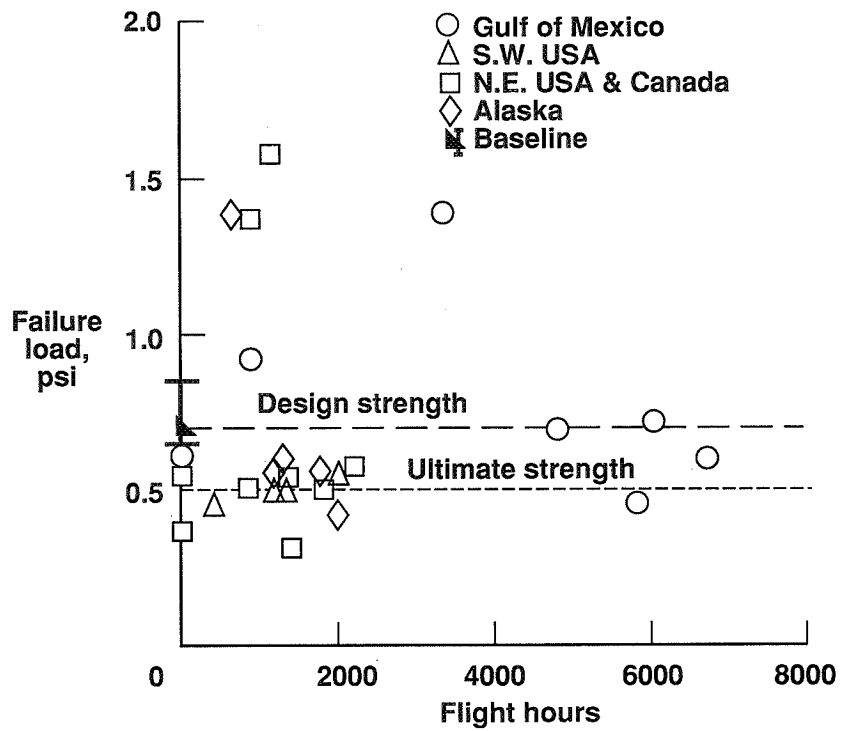
Figure 11. Failure load of baggage doors after exposure.

Figure 12. Stiffness of baggage doors after exposure.
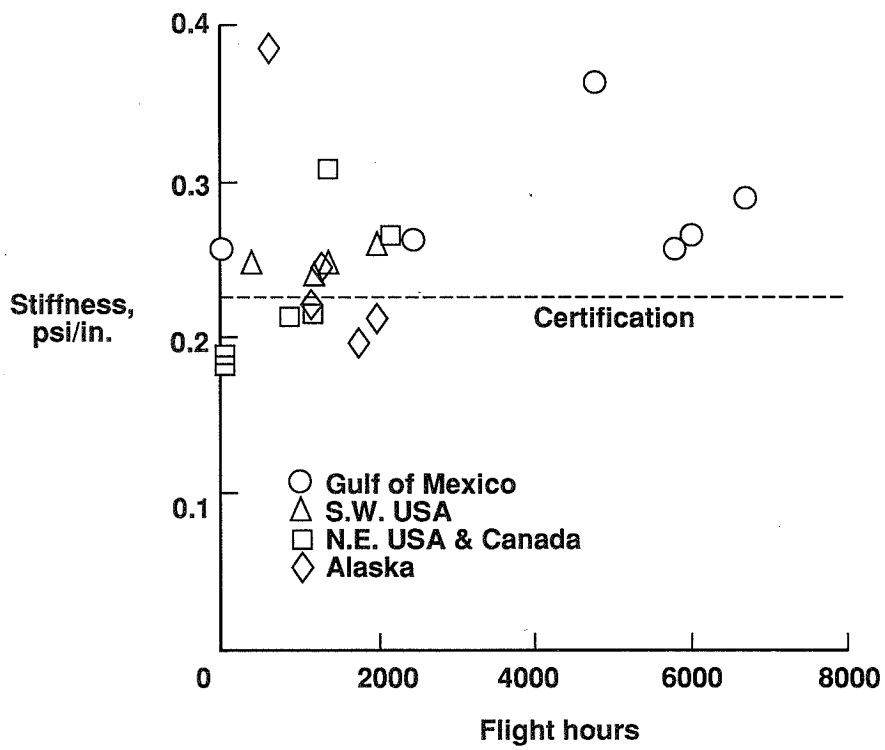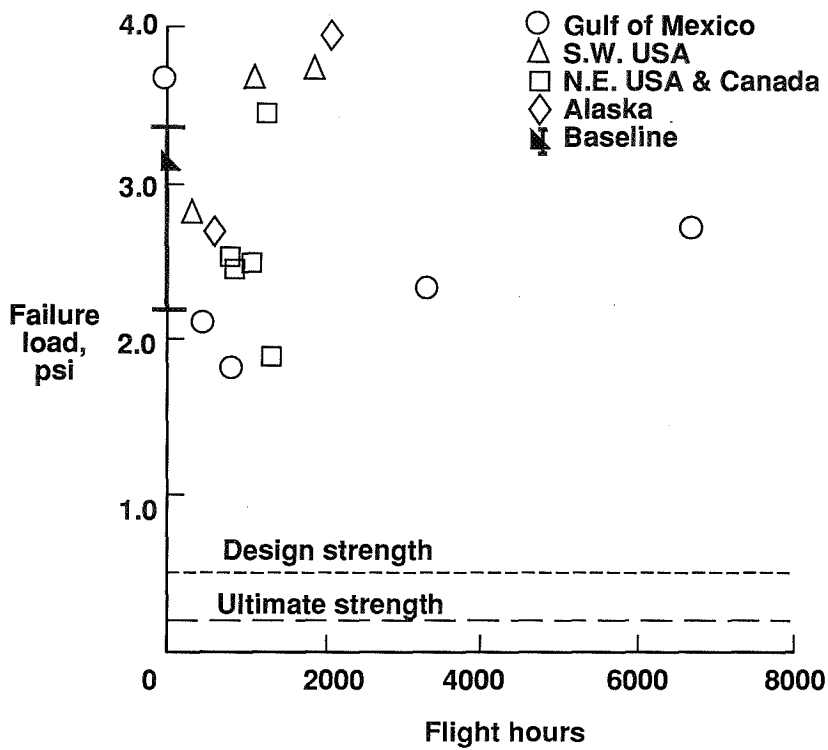
Figure 13. Failure load of forward fairings after exposure.
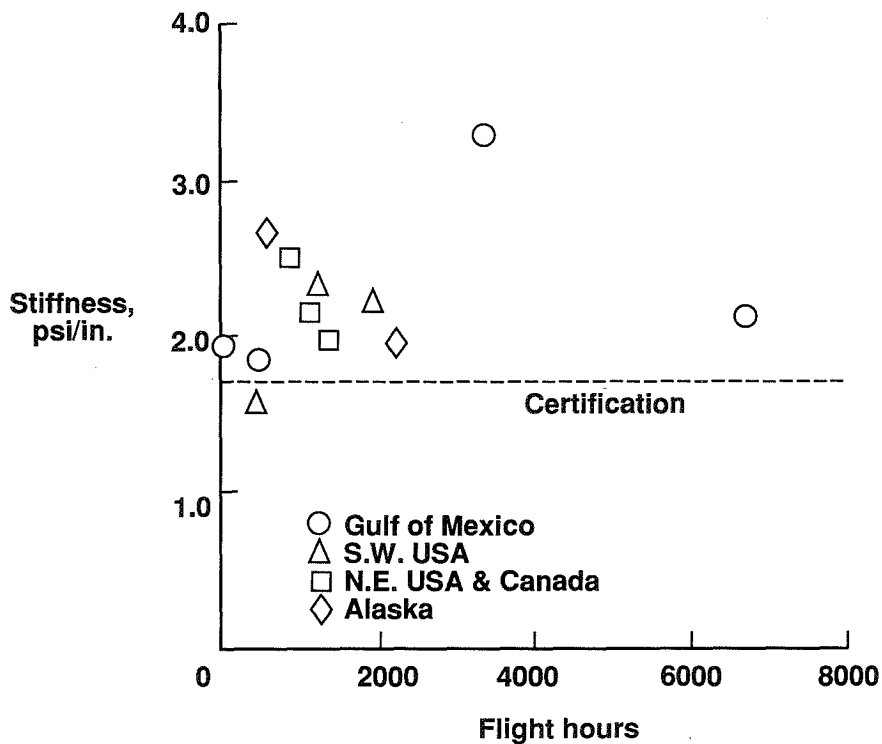
Figure 14. Stiffness of forward fairings after exposure.
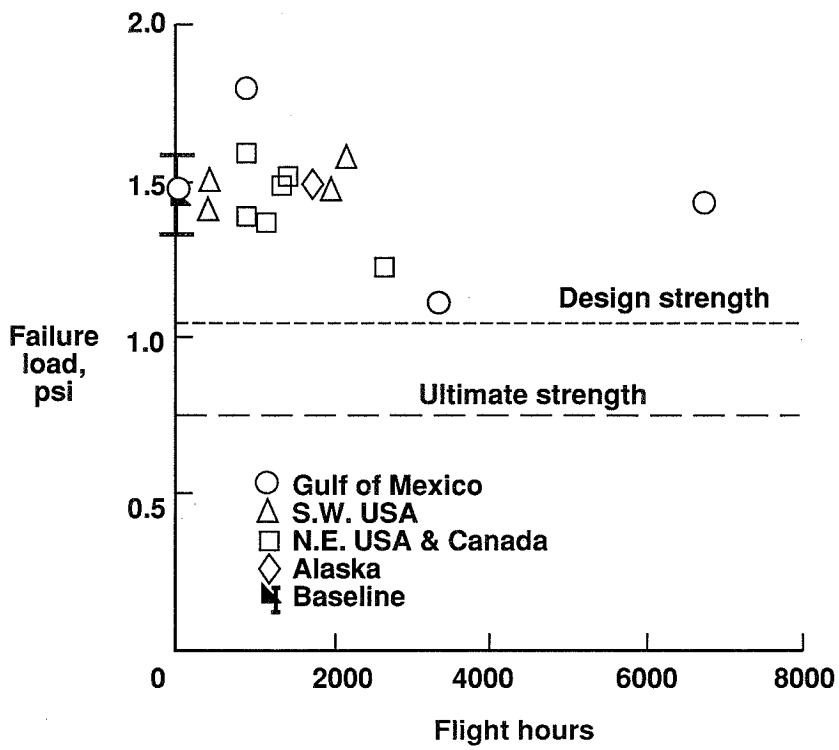
Figure 15. Failure load of vertical fins after exposure.
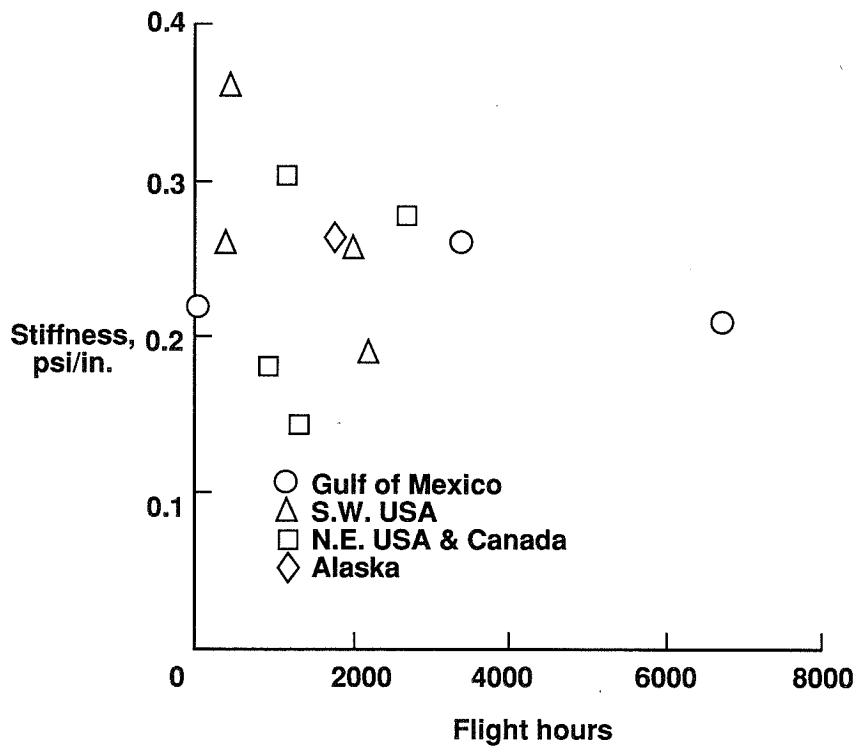
Figure 16. Stiffness of vertical fins after exposure.

120

100

80

Residual strength, percent baseline 60

40

20

Baseline scatter band

o Kevlar fabric (281)/CE-306 epoxy
△ Kevlar fabric (120)/LRF-277 epoxy
□ Kevlar fabric (281)/F-185 epoxy
◇ T-300 graphite/E-788 epoxy

0   2   4   6   8   10

Exposure time, years
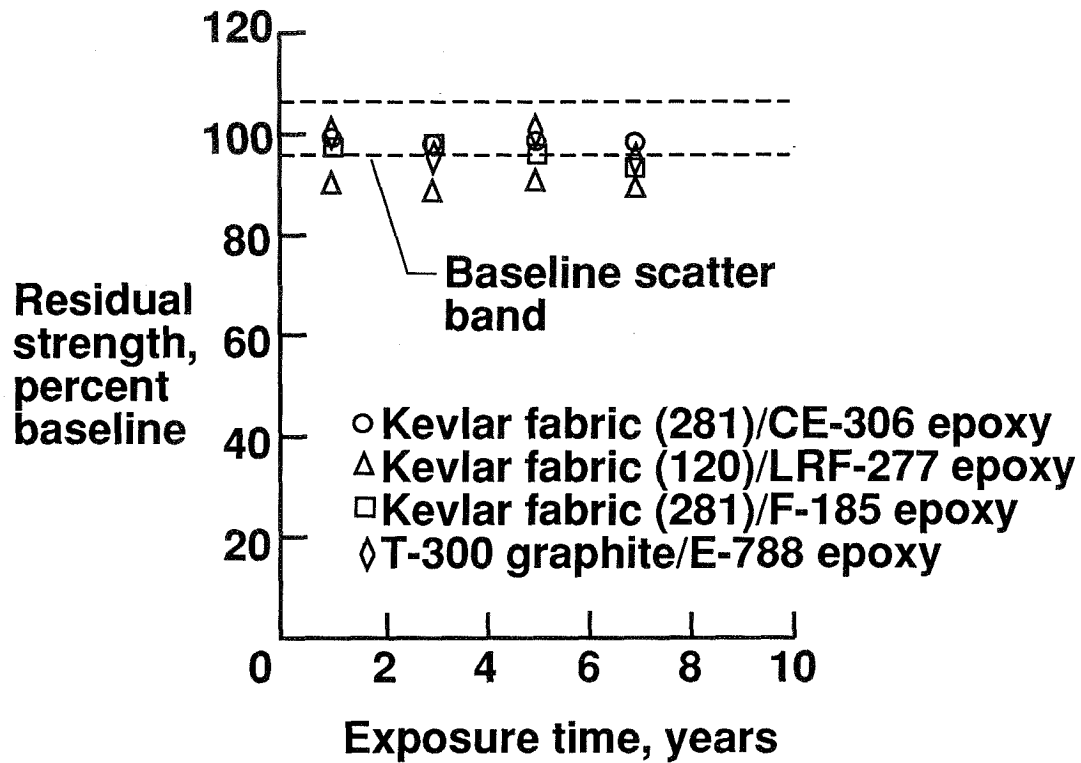
Figure 17. Residual compressive strength of composite materials after exposure.

120

100

80

Residual strength, percent baseline 60

40

20

Baseline scatter band

o Kevlar fabric (281)/CE-306 epoxy
△ Kevlar fabric (120)/LRF-277 epoxy
□ Kevlar fabric (281)/F-185 epoxy
◇ T-300 graphite/E-788 epoxy

0   2   4   6   8   10

Exposure time, years
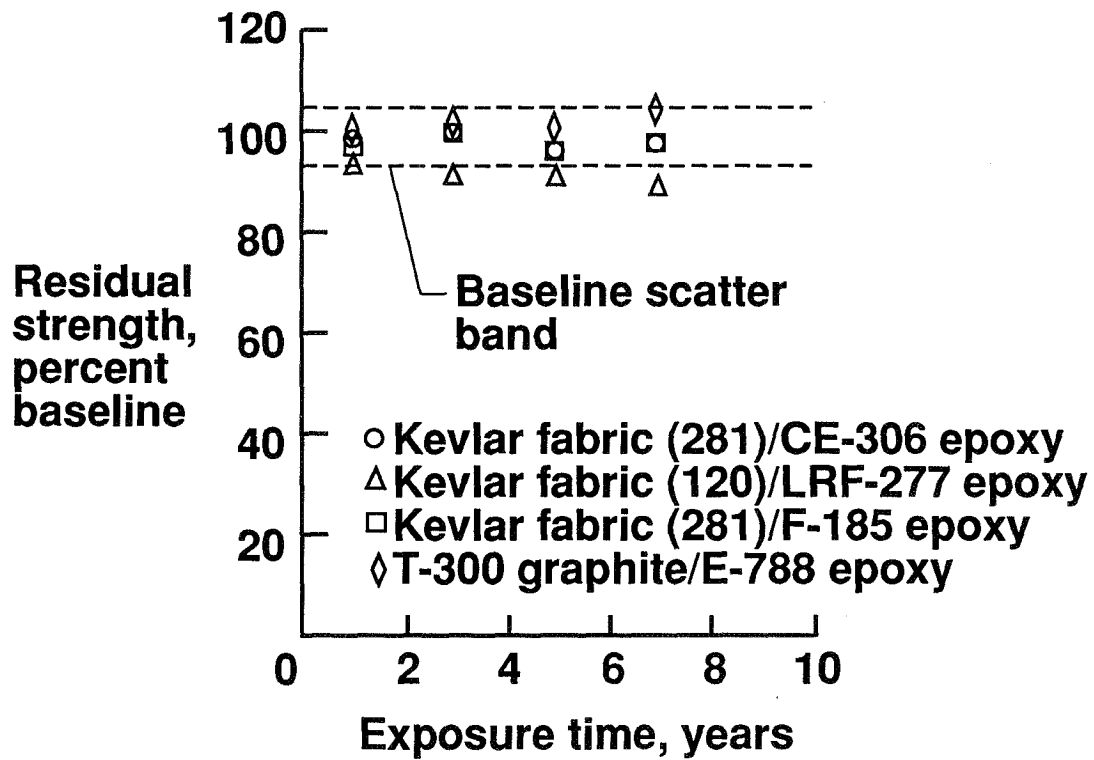
Figure 18. Residual short beam shear strength of composite materials after exposure.
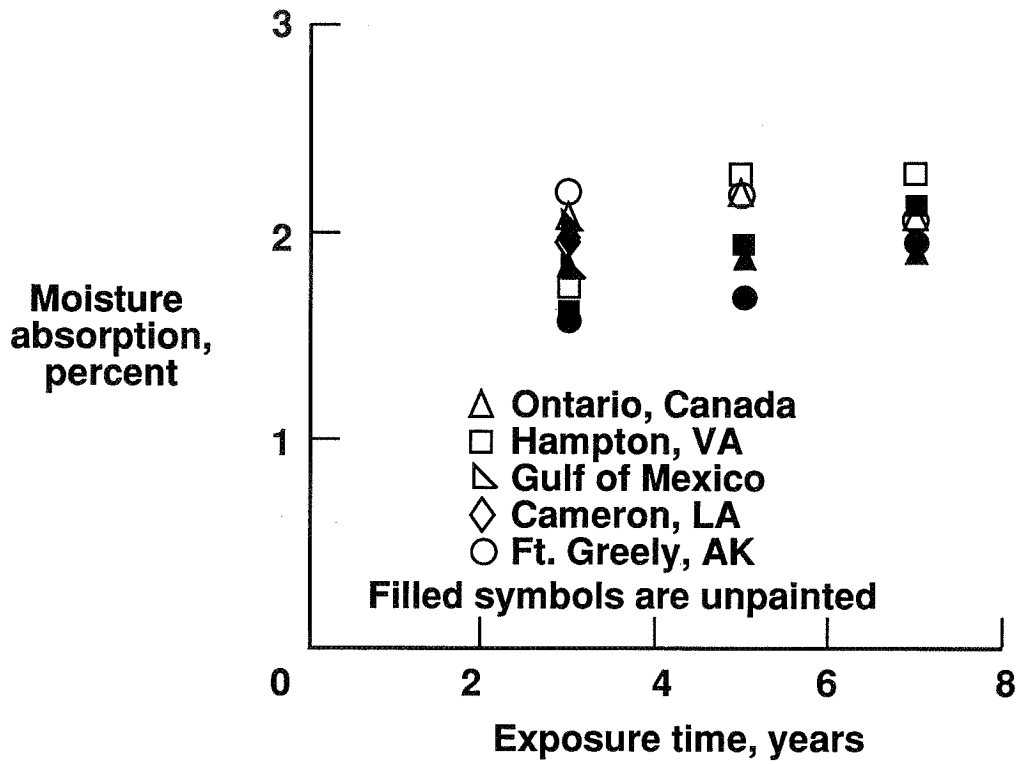
Figure 19. Moisture absorption of Kevlar-49/CE-306 composite material.
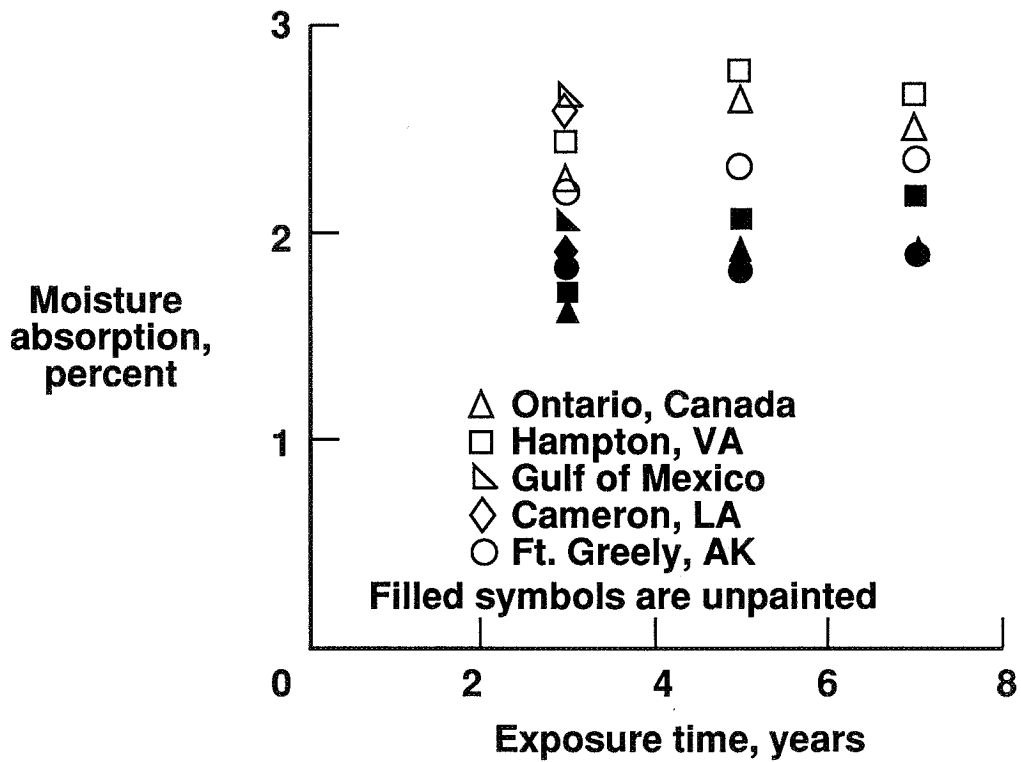
Figure 20. Moisture absorption of Kevlar-49/F-185 composite material.
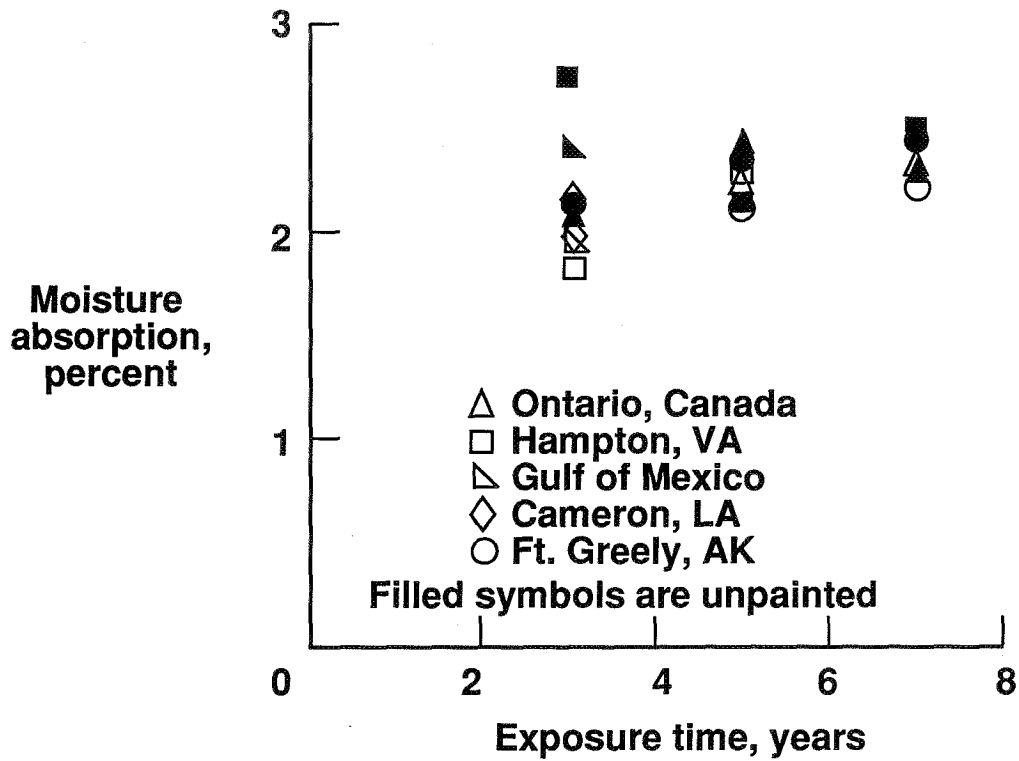
Figure 21. Moisture absorption of Kevlar-49/LRF-277 composite material.
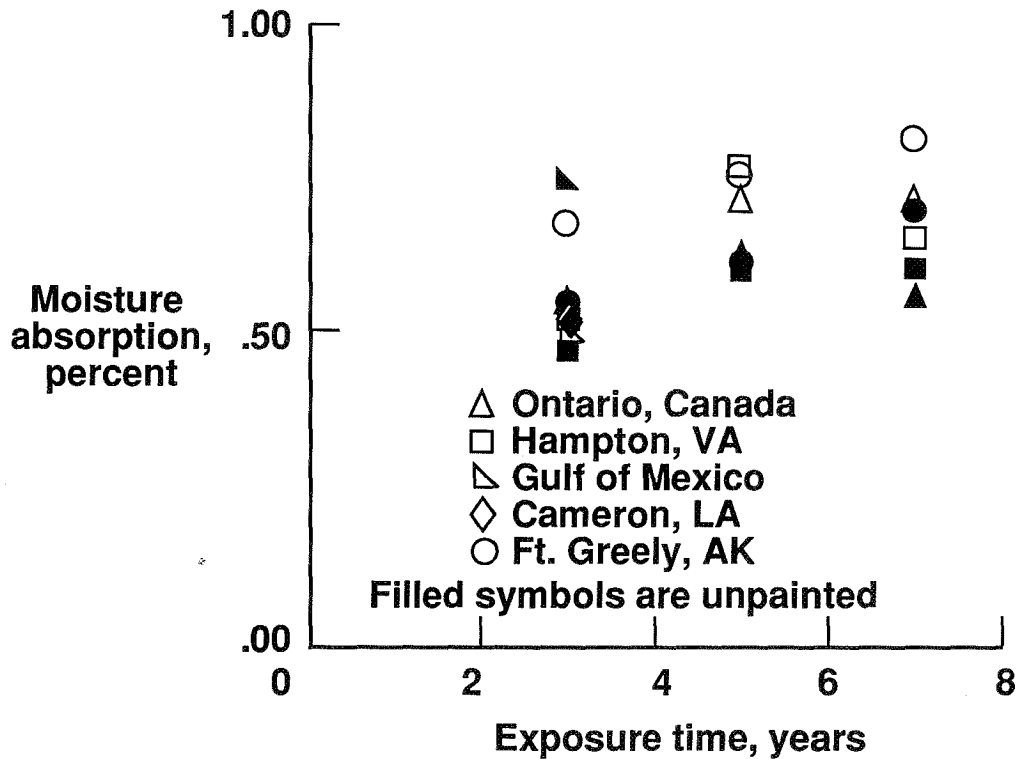
Figure 22. Moisture absorption of T-300/E-788 graphite/epoxy composite material.
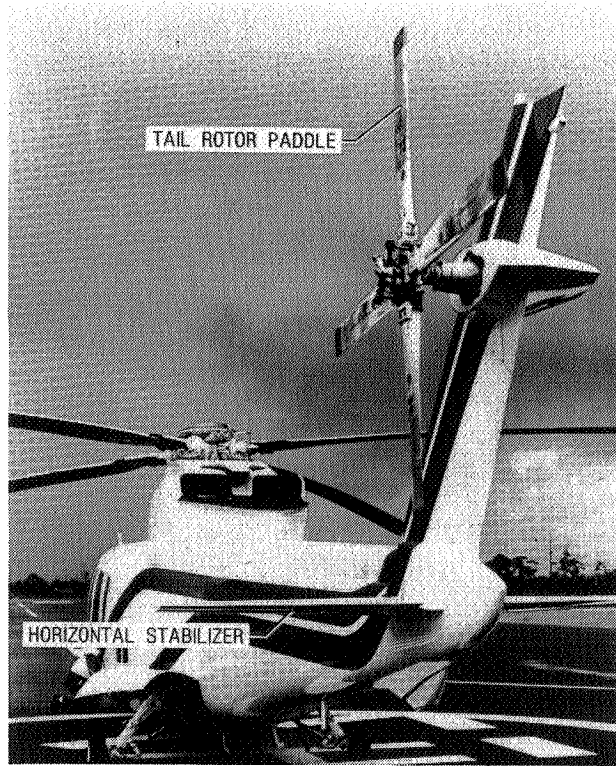
Figure 23. Composite components in flight service on Sikorsky S-76 helicopter.
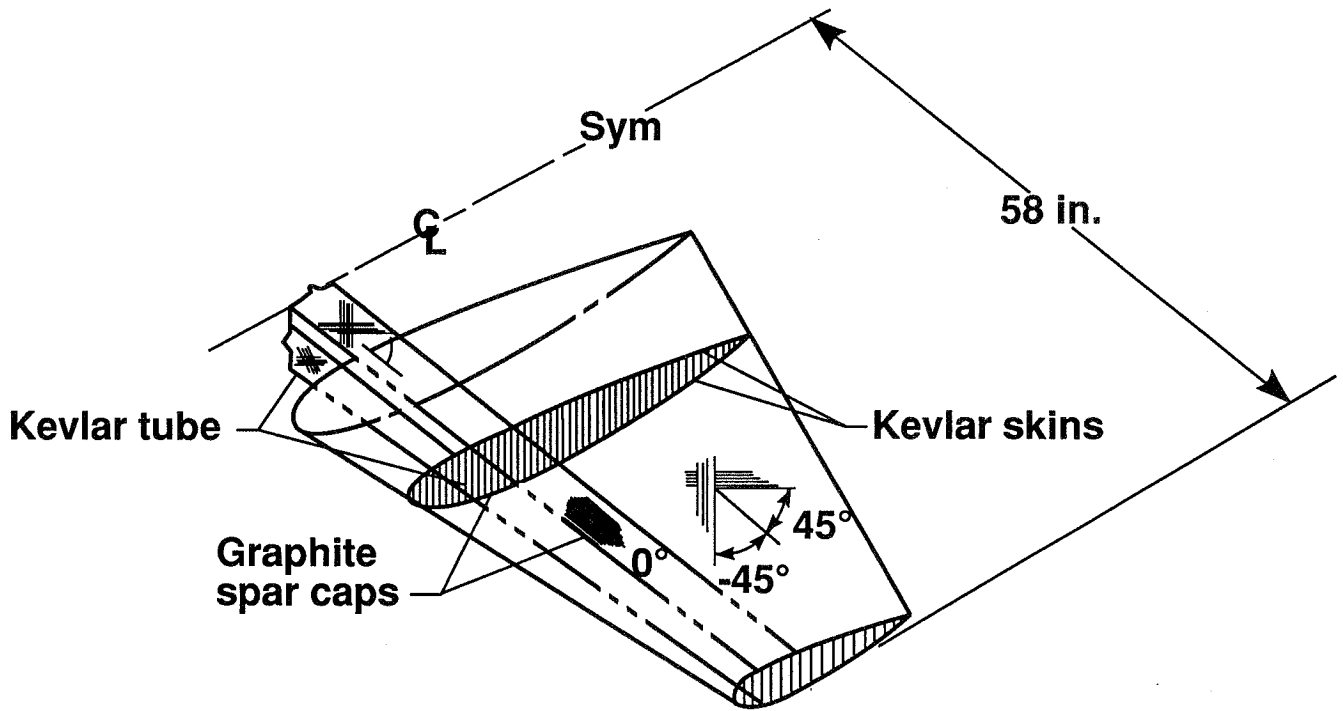
Figure 24. Composite stabilizer for the S-76.
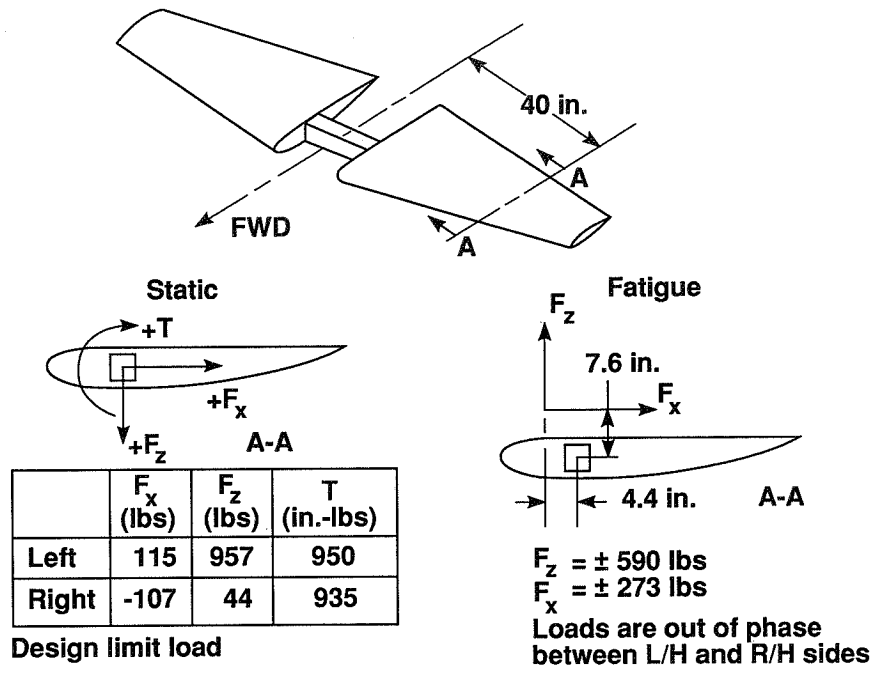
Figure 25.` Load conditions for the S-76 horizontal stabilizer.

Static

+T

+Fx

+Fz   A-A

	Fx (lbs)	Fz (lbs)	T (in.-lbs)
Left	115	957	950
Right	-107	44	935

Design limit load

Fatigue

Fz

7.6 in.

Fx

4.4 in.   A-A

Fz = ± 590 lbs
Fx = ± 273 lbs
**Loads are out of phase
between L/H and R/H sides**

52.9

Ç
L

3.5

6.5

3.5

Plan view

.45   .18   .39   **All dimensions in inches**

Edge view
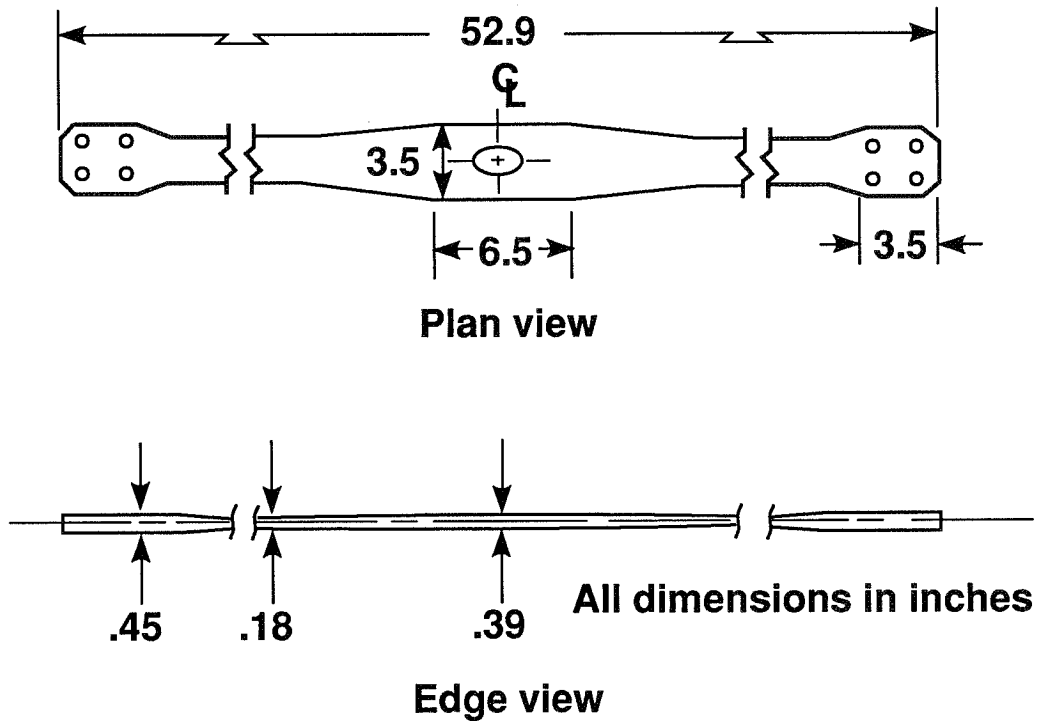
Figure 26. Composite tail rotor spar for the S-76.
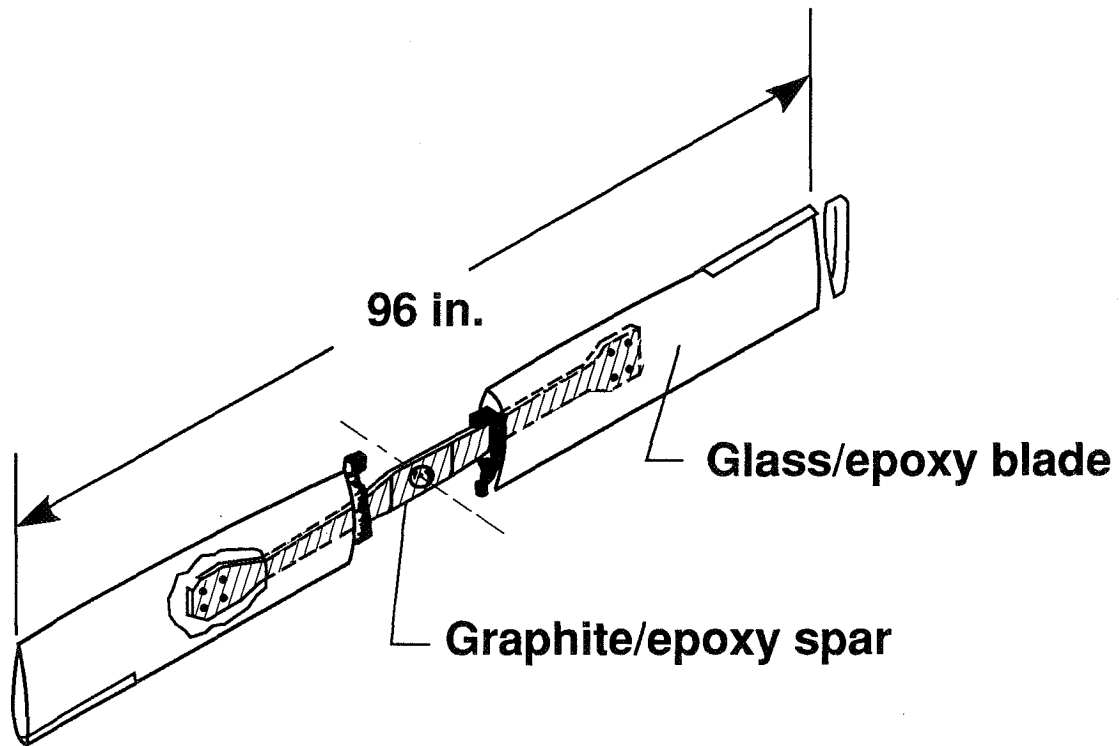
Figure 27. Sikorsky S-76 tail rotor paddle.
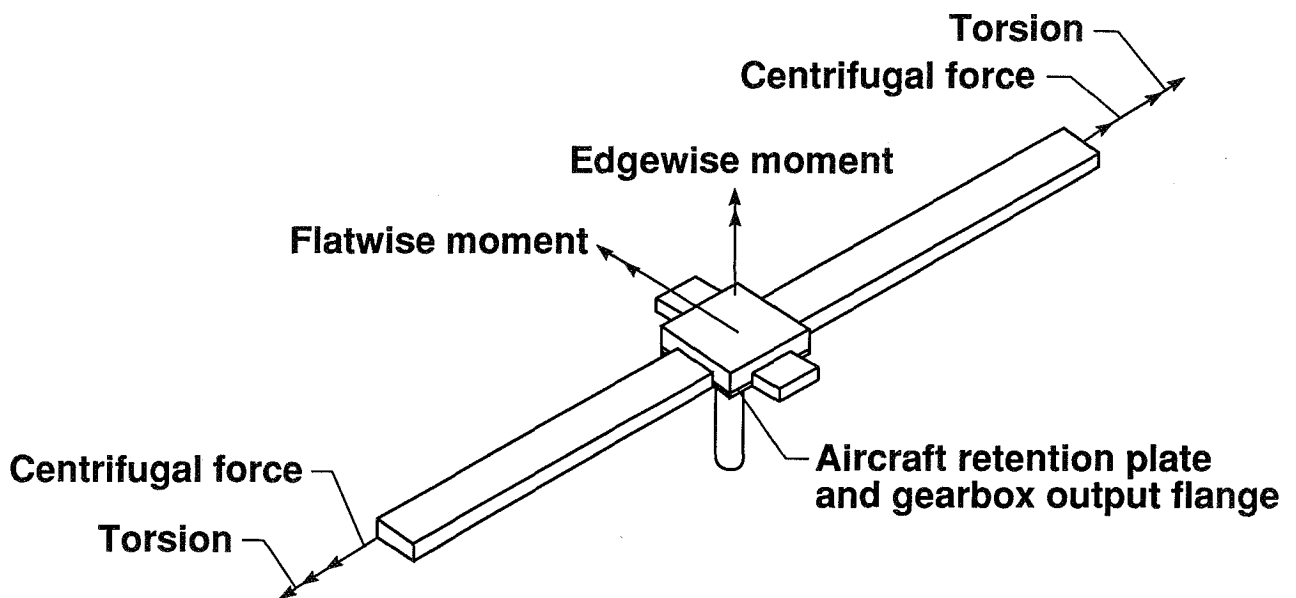
Figure 28. Schematic diagram of S-76 tail rotor spar loadings.
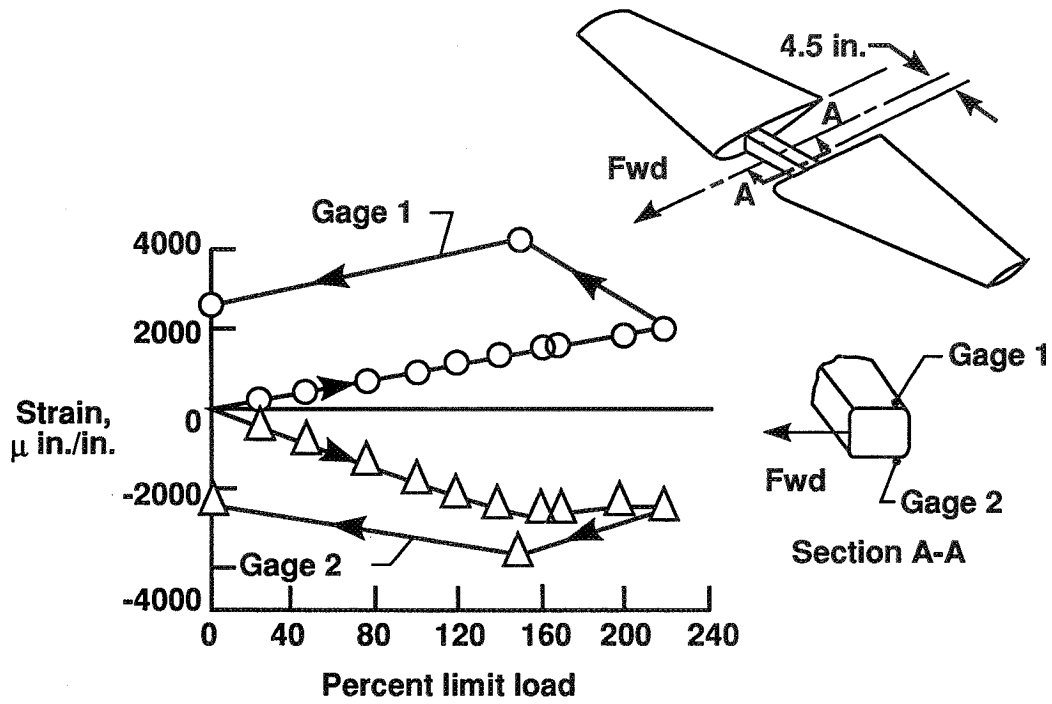
Figure 29. Strain as a function of limit load on the S-76 stabilizer.
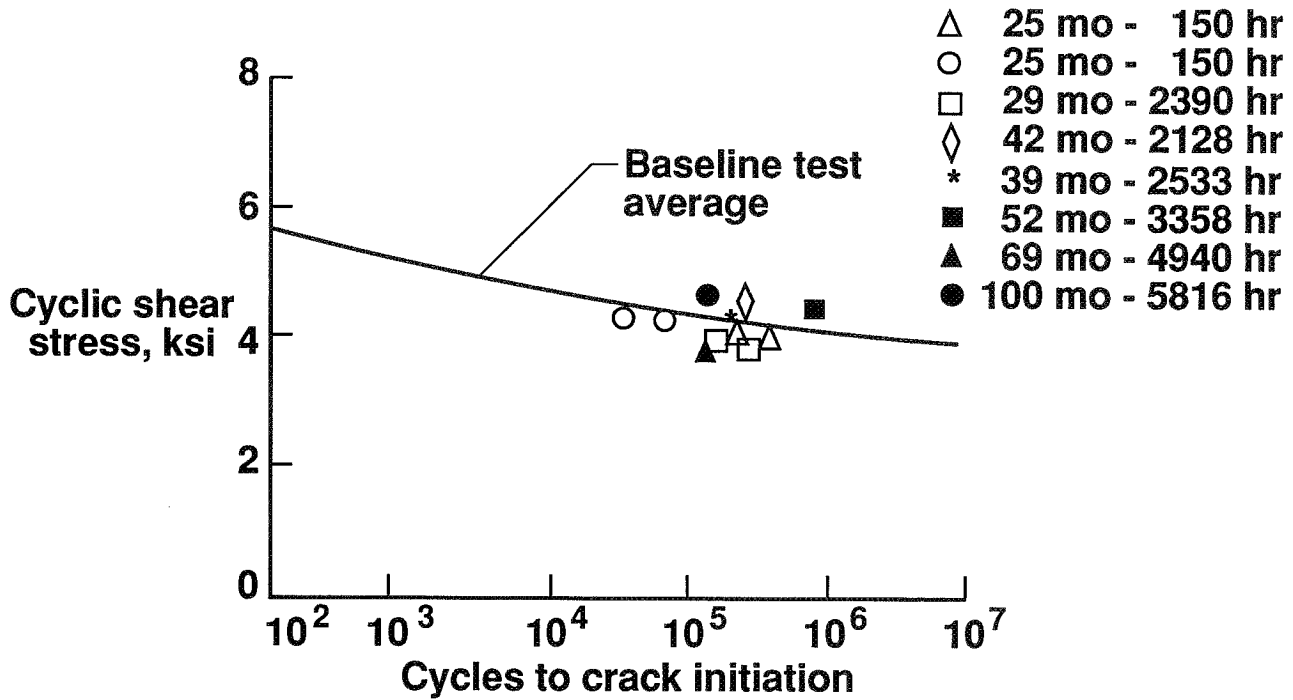
Figure 30. Effect of service environment on S-76 composite tail rotor spars.
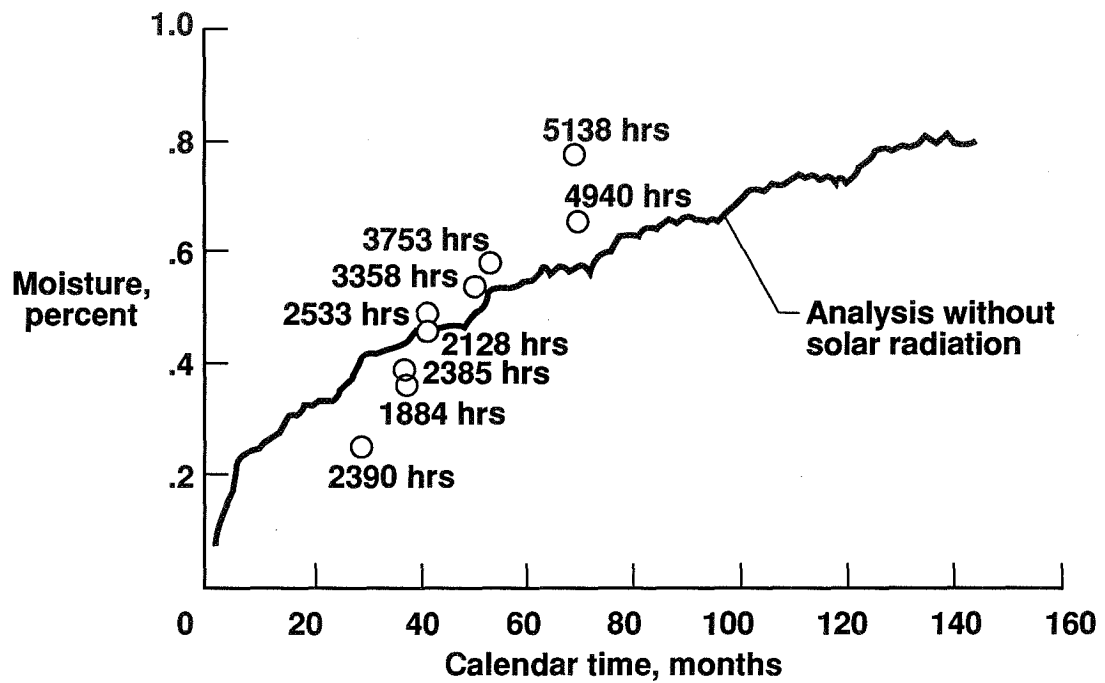
Figure 31. Predicted and measured moisture content for S-76 tail rotor spars exposed at Lake Charles, LA.
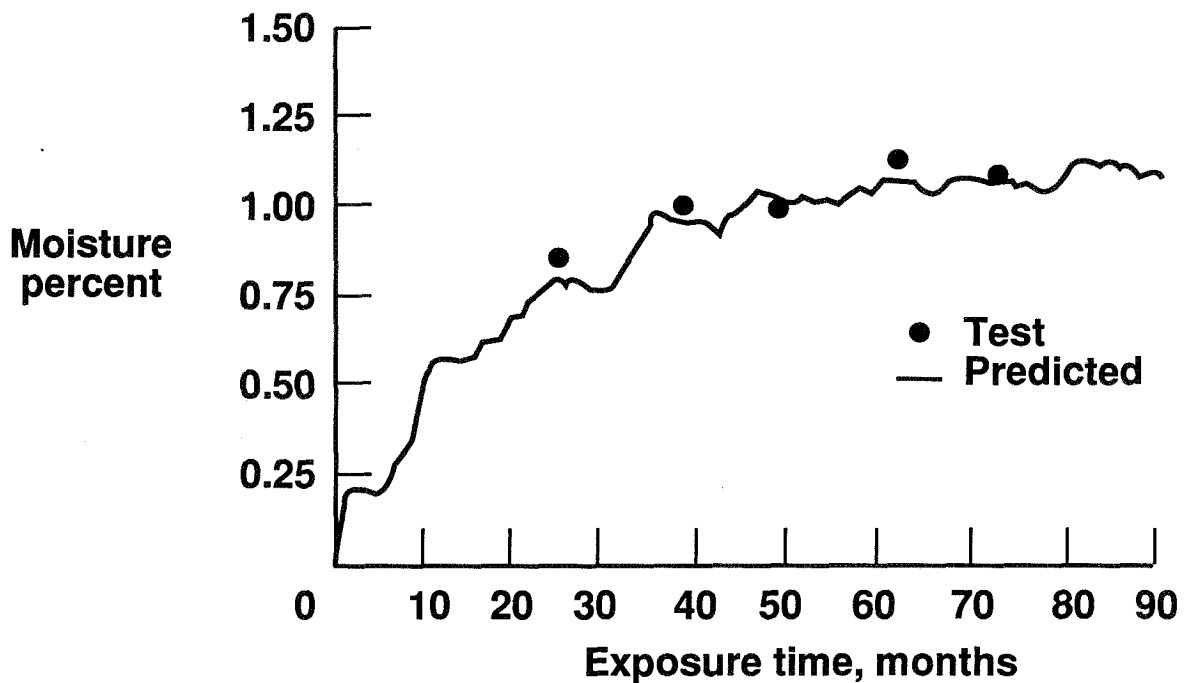
Figure 32. Measured and predicted moisture content for 6-ply AS1/6350 material exposed at Stratford, CT.
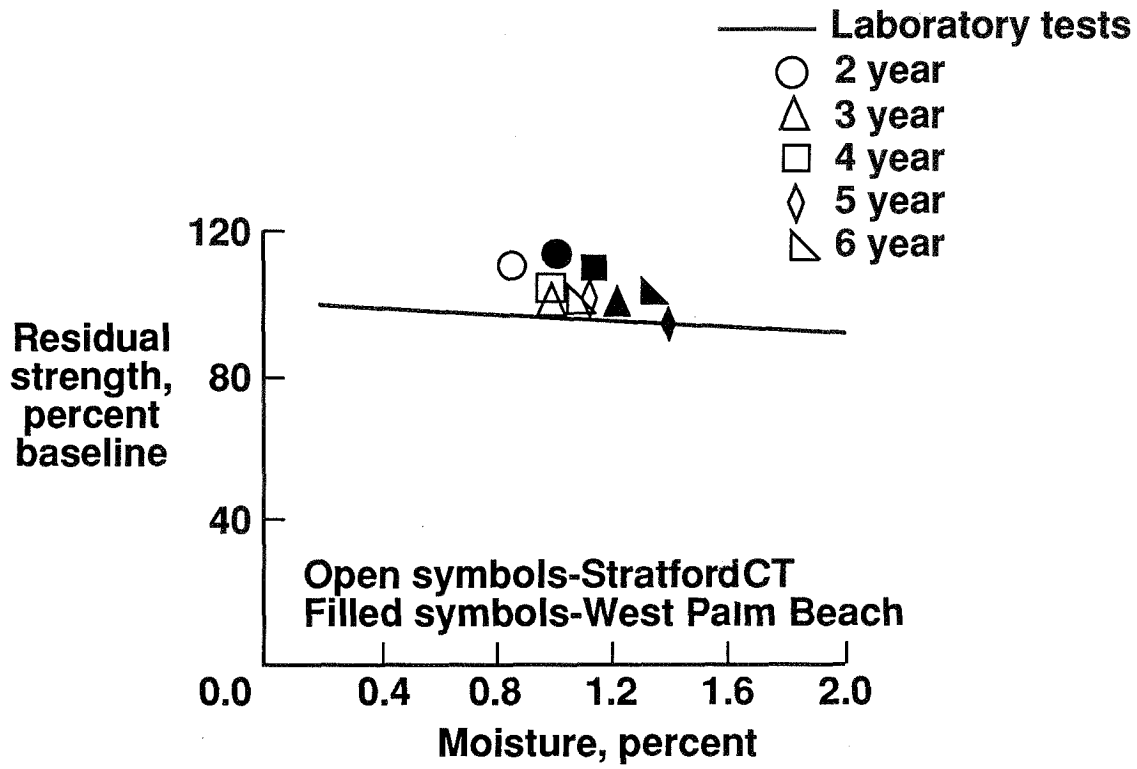
Figure 33. Effect of moisture on the residual flexure strength of 6-ply AS1/6350 material.
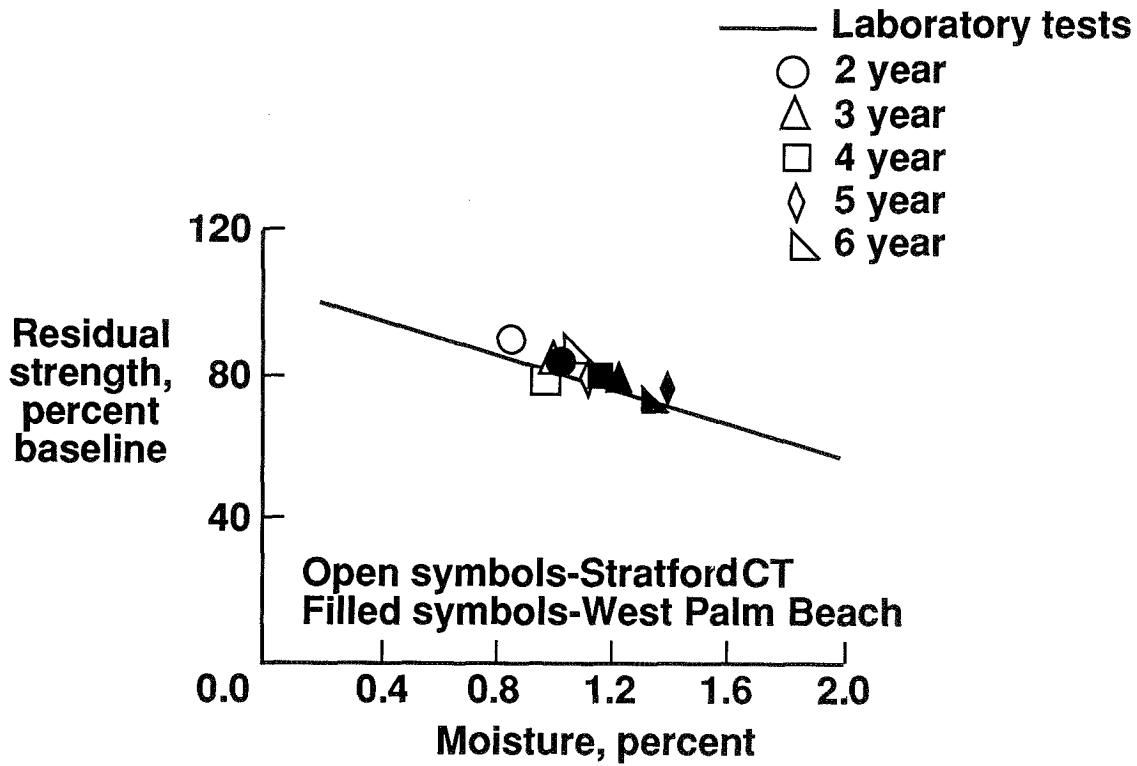
Figure 34. Effect of moisture on the residual short beam shear strength of 6-ply AS1/6350 material.
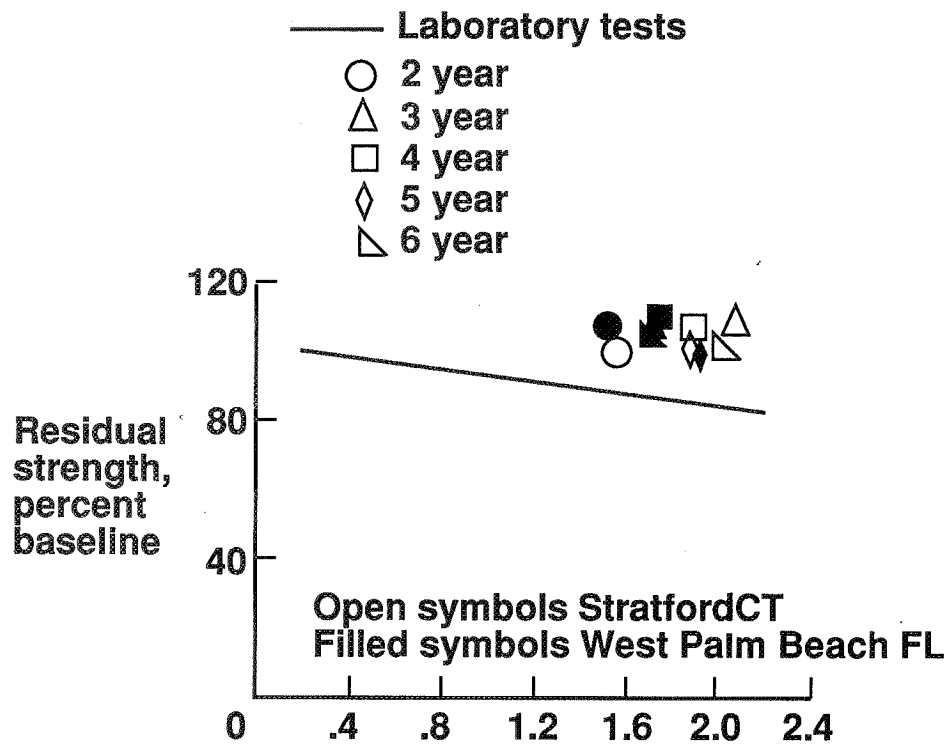
Figure 35. Effect of moisture on the residual tension strength of 6-ply AS1/6350 material.

SUPPORTABILITY EVALUATION OF THERMOPLASTIC AND THERMOSET COMPOSITES

G.R. Chanani, D. Boldi, S.G. Cramer, M.W. Heimerdinger
Northrop Corporation, Aircraft Division
Hawthorne, California

ABSTRACT

Nearly 300 advanced composite components manufactured by Northrop Corporation are flying on U.S. Air Force and U.S. Navy supersonic aircraft as part of a three-year Air Force/Navy/Northrop supportability evaluation. Both thermoplastic and high-temperature thermoset composites are being evaluated for their in-service performance on 48 USAF and Navy F-5E fighter and USAF T-38 trainer aircraft in the first large-scale, long-term maintenance evaluation of these advanced materials. Northrop manufactured four types of doors for the project — avionics bay access, oil fill, inlet duct inspection, and a main landing gear door. The doors are made of PEEK (polyetheretherketone) thermoplastic, which is tougher and potentially less expensive to manufacture than conventional composites; and 5250-3 BMI (bismaleimide) thermoset, which is manufactured like a conventional epoxy composite but can withstand higher service temperatures. Results obtained so far indicate that both the BMI and PEEK are durable with PEEK being somewhat better than BMI.

1. INTRODUCTION

The performance requirements for next generation fighter aircraft are much more demanding than those for current and earlier generations. Additionally, mission requirements demand that the structural weight be a smaller percentage of aircraft maximum gross take-off weight. For these reasons, high performance composite materials will be required in both primary and secondary fighter airframe structures to a much higher degree than in present day aircraft.

USAF and USN in-service experience with graphite epoxy (AS4/3501-6) and other early composite systems has proven the potential for structural weight reduction. However, high material, fabrication, and maintenance costs preclude more extensive use of composite structures. Delaminations, fastener pull throughs, and impact damage are typical types of composite in-service damage. Additionally, structural damage may not be visible, and the lack of clear repair/no-repair criteria may result in unnecessary maintenance actions. Finally, because conventional thermoset composite raw materials require refrigeration and have a limited shelf life, they are difficult and expensive to stock on board ship or at an operational base.

The new generation of advanced composite materials, including bismaleimides (BMI) and toughened epoxies and thermoplastics (TP), show significant potential to reduce the maintenance work load associated with composite materials. ~~These materials~~ ~~ther~~ than AS4/3501-6, ~~which~~ should translate into less in-service damage. In addition, TP materials do not require refrigeration, have an unlimited shelf life, and have unique processing characteristics that promise to make TP structures cheaper to manufacture than thermoset structures. Thermoplastic repairs also appear to be much quicker and simpler than thermoset repairs.

2. PROGRAM APPROACH

To confirm the potential of TP materials, Northrop, jointly with the USAF Wright Research and Development Center, initiated the "Design to Cost, Producibility and Supportability of Thermoplastic Composite Structures" project in March of 1987. The basic project approach follows:

1. Install a statistically significant number of TP and BMI panels on USAF aircraft.

2. Track the performance of these parts over the course of an extended in-service test.

3. Quantify the relative performance of the materials to allow prediction of associated life-cycle costs.

4. Compare the in-service data base to laboratory test data to establish correlation factors in order to extend the results to other advanced composite materials.

The thermoplastic material selected for this program was AS4/Poly-ether-ether-ketone (PEEK) which is also known as APC-2. APC-2 is an extremely tough material with a maximum service temperature of approximately 250 degrees F. The selected thermoset material was AS4/5250-3, a toughened BMI with a maximum service temperature of approximately 370 degrees F. These materials were selected because they were well characterized at Northrop with established procurement and manufacturing specifications.

The T-38 and F-5E aircraft were selected for the in-service evaluation for the following reasons:

1. A substantial in-service data base exists for each of these two aircraft.

2. Existing tooling was available to ensure interchangeability.

3. Most required hardware was available in Northrop stock.

4. Baseline part cost and weight data were available.

5. All loft lines and original design and analysis data were readily accessible.

The criteria used to select the parts are given in Figure 1. Due to the nature and objectives of this project, it was necessary to select simple parts that were easy to manufacture. To minimize impact on routine operations at the subject bases, only highly accessible and readily inspectable parts were selected. Parts on both the left and right hand sides of the aircraft made it possible to fly each configuration/material combination on each aircraft. Doors and panels were selected because these structures experience the most

430

PRODUCIBILITY	SUPPORTABILITY	OTHER
• SHAPE • CONTOUR • THICKNESS • REPRODUCIBILITY	• MAINTENANCE HISTORY • ACCESSIBILITY • INSPECTABILITY • ENVIRONMENT • FREQUENCY OF REMOVAL AND REINSTALLATION	• LEFT AND RIGHT COMPONENTS • STRUCTURAL AND NONSTRUCTURAL

972.34

FIGURE 1. COMPONENT SELECTION CRITERIA

severe handling and are the predominant sites of induced maintenance actions. This approach is expected to allow for the accumulation of a usable data base in the shortest amount of time.

3. PART SELECTIONS FOR IN-SERVICE EVALUATION

The selected parts are detailed in Figure 2. The part locations on the aircraft are shown in Figures 3 and 4. A brief description of each part and the rationale for its selection follow.

3.1 Oil Fill Door

The oil fill door is an access panel located on the underside of the aircraft at the manufacturing break between the aft fuselage and the boat tail. The panel is attached to the aircraft with a piano hinge and two quarter-turn, quick-release fasteners. The door is nonstructural. The baseline consists of a flat chem-milled aluminum sheet with a mechanically attached extruded angle stiffener. The stiffener prevents the panel from gapping during flight due to external pressure loading. The composite designs are very similar to the

metal baseline, consisting of a flat laminate reinforced by an angle section stiffener. In the thermoplastic version, the stiffener is coconsolidated; in the BMI version, it is cocured. In service, the door is constantly in contact with hydraulic fluid and engine oil. The metal doors are frequently damaged through impact during engine removals and reinstallations.

DESCRIPTION	DIMENSIONS (IN.) MATERIAL	COMMENTS
T-38 OIL FILL DOOR FS 479.5 TO 483.0	0.068x2.7x8.7 Al 7075-T6 APC-2 AS4/5250-3	• NONSTRUCTURAL • FLAT CONTOUR • PIANO HINGE • 'L' STIFFENER • QUICK RELEASE FASTENERS • HIGH F.O.D. POTENTIAL • CORROSIVE ENVIRONMENT • EASILY ACCESSIBLE
F-5E OIL FILL DOOR FS 494.5 TO 498.0	0.094x2.7x8.0 Al 7075-T6 APC-2 AS4/5250-3	
F-5E AVIONICS BAY ACCESS PANEL FS CANT 253.5 TO FS 277.75	0.083x14.0x23.0 Al 7075-T6 APC-2 AS4/5250-3	• STRUCTURAL • DOUBLE CONTOUR • HAT STIFFENER • REMOVAL DIFFICULTIES • T-38 BASELINE DIMPLED
T-38 AVIONICS BAY ACCESS PANEL FS CANT 264.0 TO FS 284.0	0.062x11.0x17.0 Al 7075-T6 APC-2 AS4/5250-3	
T-38 INLET DUCT INSPECTION DOOR FS 451.2 TO 458.5	0.094x7.3x8.7 Al 7075-T6 APC-2 AS4/5250-3	• STRUCTURAL • SINGLE CONTOUR • REMOVED EVERY FLIGHT DAY • SUGGESTED BY SAN ANTONIO AIR TRAINING COMMAND (SA-ATC)
F-5E INLET DUCT INSPECTION DOOR FS 486.5 TO 494.5	0.073x8.0x10.0 Al 7075-T6 APC-2 AS4/5250-3	
F-5E MAIN LANDING GEAR DOOR	0.75x15.0x43.0 Al 7075-T6 IM6/PEEK	• STRUCTURAL • DOUBLE CONTOUR • Al HONEYCOMB • PRELOADED • FREQUENT USE

972.37

FIGURE 2. FLIGHT COMPONENTS TO EVALUATE SUPPORTABILITY

DIMENSIONS IN INCHES

LANDING GEAR DOOR

42

20

AVIONICS BAY ACCESS PANEL

OIL FILL DOOR

12.9

8.5

20.8

10.0

2.6

INLET DUCT INSPECTION DOOR

8.0
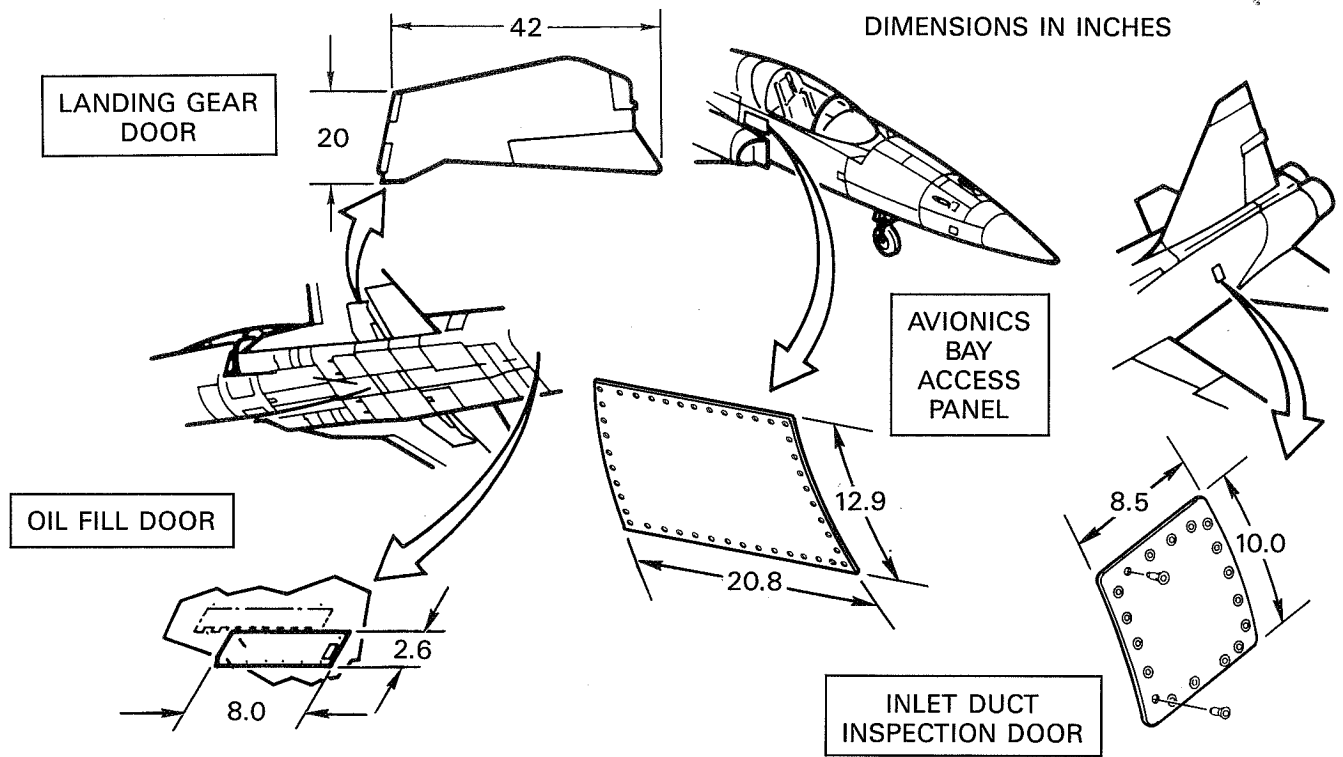
972.39

FIGURE 3. F-5E COMPONENTS SELECTED FOR FLIGHT TESTING

DIMENSIONS IN INCHES

7

7.6

8.3

11

2.6

AVIONICS BAY ACCESS PANEL

8.6

OIL FILL DOOR

INLET DUCT INSPECTION DOOR
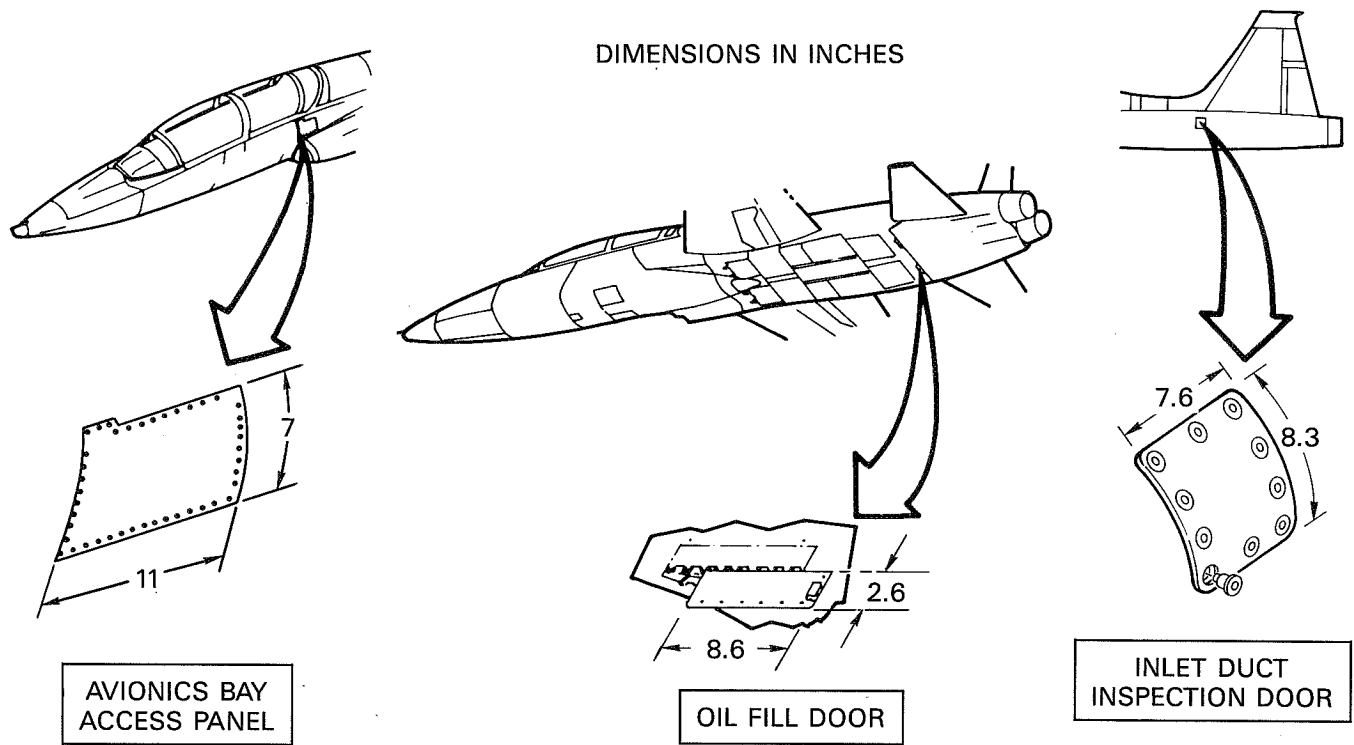
972.40

FIGURE 4. T-38 COMPONENTS SELECTED FOR FLIGHT TESTING

3.2 Avionics Bay Access Panels

The avionics bay access panels are structural panels located below and aft of the aircraft canopies. In flight, these doors are subjected to combined shear, burst pressure, and axial tension/compression loading. The T-38 panel is stiffened by one mechanically attached angle extrusion; the F-5E panel, two. Both panels have chem milled pockets to reduce weight. The F-5E panel is attached to the aircraft with zip-lock fasteners, and the T-38 panel with screws. The F-5E panel holes are protected by a swaged A-286 steel sleeve. This sleeve resists hole elongations and prevents galvanic corrosion. The baseline T-38 avionics bay access panel is dimpled because the door is too thin to be countersunk for flush fasteners. As it was not possible to dimple the composite doors, a steel bushing was designed for these panels. This bushing fills the countersinks in the substructure of the aircraft. A baseline and composite fastener installation are shown in Figure 5.
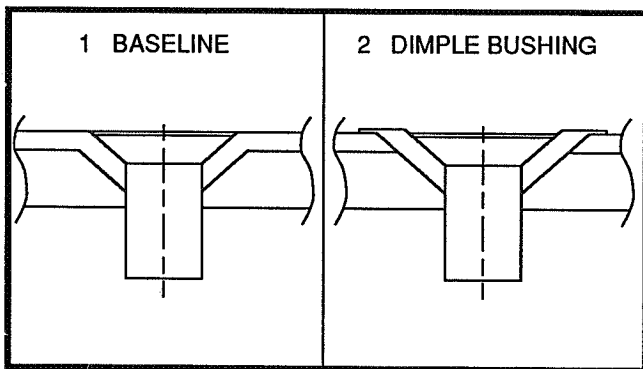
T89-17/7/A

FIGURE 5. T-38 AVIONICS BAY ACCESS PANEL FASTENER MODIFICATION

The composite designs are each reinforced with a single, centrally located hat-section stiffener. The BMI stiffeners are cocured to the skins, the TP stiffeners are mechanically attached. Because the avionics bays are pressurized, the panels are sealed with a form-in-place gasket.

In-service damage to the avionics bay access panels occurs primarily during panel removal and reinstallation. The panels are frequently dropped and occasionally stepped on. On first removal after a new form-in-place gasket has been installed, a screwdriver or putty knife is often used to pry the panels loose. Although this did not damage the aluminum panels, it can cause damage to the composite panels.

Both the F-5E and T-38 composite designs have below-standard fastener edge distance (e/D) and fastener pitch (w/D) geometries. This was unavoidable in a retrofit design where existing fastener arrangements had to be picked up. Coupon tests were conducted to validate the fastener conditions for the avionics bay access panel designs. Coupons were fabricated from both TP and BMI that were representative of the T-38 and F-5E laminates and geometries. The minimum ultimate loads achieved by these tests for the F-5E and T-38 conditions were used as respective design ultimate allowables in the composite panel analyses.

3.3 Inlet Duct Inspection Doors

The inlet duct inspection doors are located on the aft fuselage of the aircraft, below the vertical tail. These doors are structural and are subjected to combined shear, axial tension, and internal pressure. The T-38 panel is removed from the aircraft every flight day. The F-5E panel is also frequently removed. For this reason, the panels are subjected to appreciable handling damage in service. They were selected for this test at the recommendation of engineering and maintenance personnel at the San Antonio Air Logistics Center and Randolph Air Force Base.

The composite designs are essentially identical to the metallic baselines. Both F-5E and T-38 versions are attached to the airframe with ziplock type panel fasteners. As in the F-5E avionics bay access panels, an A-286 steel sleeve was swaged into each fastener hole on the T-38 composite panels. The F-5E panel was too thin to install a sleeve. Both the F-5E and T-38 composite designs had low e/D and w/D conditions. The results of the avionics bay fastener coupon tests were sufficient to validate these designs.

3.4 Main Landing Gear Door

One F-5E main landing gear door was fabricated for flight test. The outer and inner surfaces of the door are shown in Figures 6 and 7, respectively. With the exception of the skins, the door is identical to the existing aluminum door, using the same core, hinges, and other hardware. The skins are IM6/PEEK thermoplastic. The outer skin was consolidated in an autoclave; the inner skin was diaphragm formed. The assembly was adhesively bonded. In service, the door is subjected to foreign object impact damage. This door was installed on a Nellis Air Force Base F-5E in
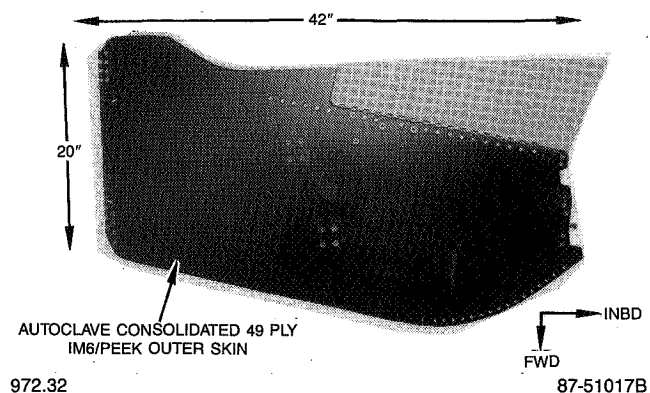
FIGURE 6. TPC OUTER SKIN OF THE F-5E MAIN LANDING GEAR DOOR

December of 1987; this was the first flight (pictured in Figure 8) of a thermoplastic primary structure.
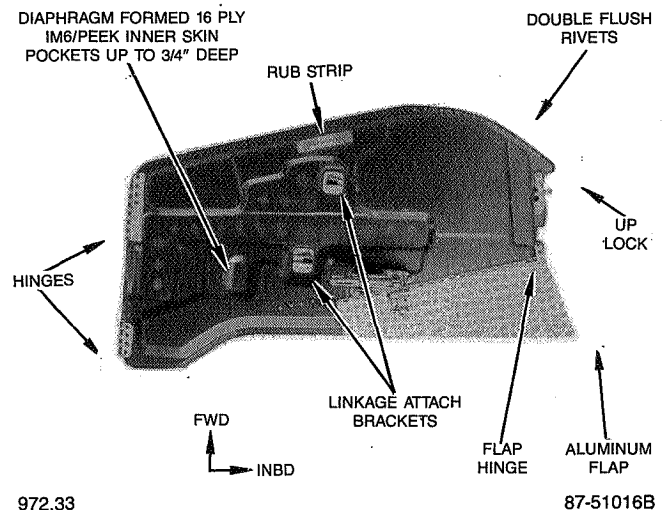
FIGURE 7. TPC INNER SKIN OF THE F-5E MAIN LANDING GEAR DOOR

4. IN-SERVICE EVALUATION

The criteria used for test base selection were as follows:

1. Temperature, humidity, and precipitation variations.
2. Mission profile (fighter and trainer)
3. Maintenance environment (USAF or contractor maintenance).
4. High annual flight hours.
5. Number of available aircraft.

Nellis AFB, Nevada, was selected as the F-5E base, and Williams AFB, Arizona, and Reese AFB, Texas, were selected as the T-38 bases. In April of 1989, the Nellis AFB F-5Es were transferred to the United States Navy. The test panels were left in place and the aircraft are currently based at NAS Fallon, Nevada, and MCAS Yuma, Arizona. The installation summary is given in Figure 9.
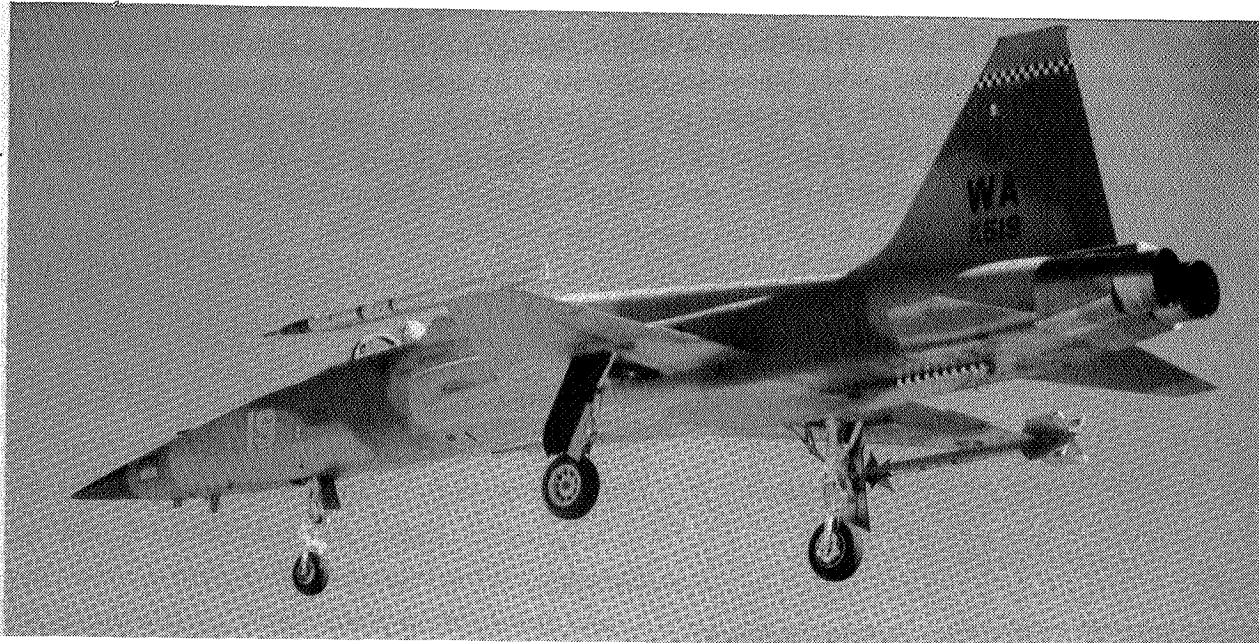
T89-17/5/B

87-03606-6

FIGURE 8. FIRST FLIGHT OF THERMOPLASTIC F-5E MAIN LANDING GEAR STRUT DOOR

To provide a usable data base, Northrop performs regularly scheduled ultrasonic inspections at all bases. As can be seen from the program inspection schedule (shown in Figure 10), the inspection intervals were initially very small, and were relaxed only as the confidence level was increased in part performance. Currently, inspections are performed on a monthly basis.

A typical inspection in progress is shown in Figure 11. For each part, a full size inspection mylar is maintained, noting all defects, dates, and flight hours. A mylar is shown being updated in Figure 12.

To date, the flight test program has accumulated over 20,000 flight hours. A base-by-base flight-hour/sortie summary is given in Figure 13. The types of defects noted are summarized in Figure 14.

LOCATION	TYPE	NUMBER OF AIRCRAFT	INSTALLATION DATE	REMOVAL DATE
NELLIS AFB	F-5E	16	MARCH 88	MARCH 89
WILLIAMS AFB	T-38	16	JUNE 88	NA
REESE AFB	T-38	16	JULY 88	NA
NAS FALLON	F-5E	6	APRIL 89	NA
MCAS YUMA	F-5E	10	APRIL 89	NA

T-38 — 6 PARTS PER AIRCRAFT = 192 PARTS
F-5E — 6 PARTS PER AIRCRAFT + 1 MAIN LANDING GEAR
      STRUT DOOR = 97 PARTS
TOTAL = 289 PARTS

972.36

FIGURE 9. SUMMARY OF IN-SERVICE TEST PART INSTALLATIONS

	FREQUENCY, FLIGHT HOURS					
	PRE- AND POST-FLIGHT	~10	~20	~30	~50	EVERY ~50
• VISUAL						
— EXTERNAL SURFACES	✓					
— INTERNAL SURFACES		✓	✓	✓	✓	✓
• ULTRASONIC*		✓	✓	✓	✓	✓
• RADIOGRAPHIC		AS REQUIRED				

*PERIMETER AND 0.25-in. AROUND FASTENER HOLES

972.35

FIGURE 10. INSPECTION SCHEDULE

435
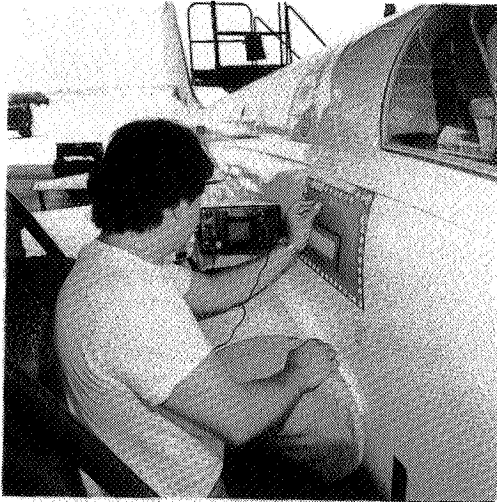
T89-17/37/A   88-01742-10

FIGURE 11. INSPECTION IN PROGRESS
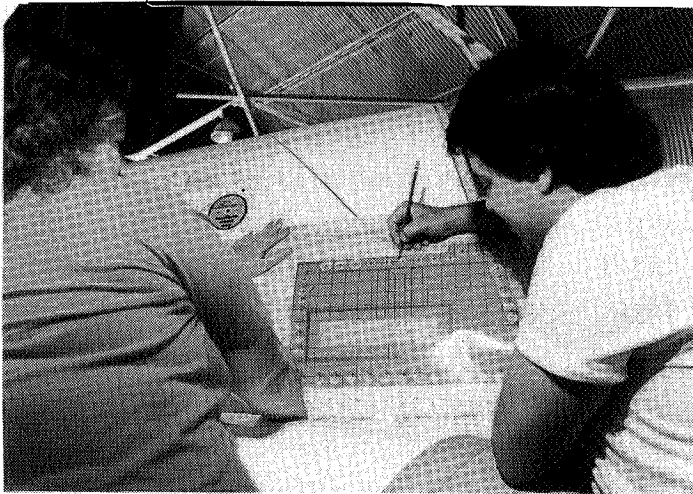
T89-17/6/A   88-01742-11

FIGURE 12. INSPECTION MYLAR

BASE	FLIGHT HOURS	SORTIES
YUMA*	2,613	3,266
FALLON*	1,694	2,117
WILLIAMS	10,103	7,772
REESE	9,477	7,290
TOTALS	23,887	20,445
122,670 PANEL SORTIES		

*INCLUDES NELLIS DATA

972.51

FIGURE 13. FLIGHT HOUR/SORTIE SUMMARY
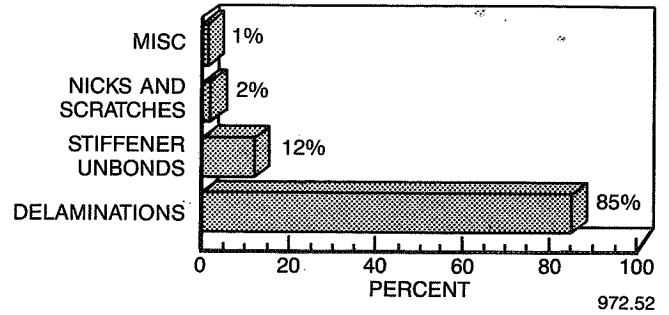
FIGURE 14. DEFECT TYPES IDENTIFIED....

Delaminations are the predominant defect and have many causes. Delaminations noted in the lower corners of the panels are most likely due to the panels being dropped. Delaminations along the edges of the inlet duct doors and avionics bay access panels occur primarily when the panels are first removed from a fresh form-in-place gasket. As previously mentioned, typical maintenance procedure is to use a spatula or putty knife under the lip of the panel to free it. In one case, a delamination in the exact shape of a screwdriver head was noted. Delaminations also occur at fastener holes, and in the body of the panels.

Stiffener unbonds are the second most frequent defect. Because the stiffeners of the TP avionics bay access panels are mechanically attached, stiffener unbonds have been noted only in the BMI panels. The unbonds appear to occur when the panels are off the aircraft. Also, typical maintenance practice is to use the F-5E avionics bay access panel as a tool tray. This did not affect the aluminum doors but may damage the composite panels. To date, three F-5E avionics bay access panels, and one T-38 avionics bay access panel, have been removed from service for repair. Both bonded and mechanical repairs have been successfully performed. All repaired panels were returned to service, and none has suffered additional damage in the repair area.

436

Nicks, gouges, and scratches have been noted on the surface of several panels. The primary cause of this damage appears to be tool impact during removal and reinstallation.

Overall, the thermoplastic parts have proven to be more resistant to maintenance induced damage than the bismaleimide parts, demonstrating the field applicability of laboratory data.

The rates of defect accumulation with respect to flight hours are shown in Figure 15 for the F-5Es and T-38s combined and in Figure 16 for the T-38s only. Figure 15 illustrates the large difference in defect accumulation between the F-5Es and T-38s. This is due, in part, to the F-5E part designs and to the differences in maintenance environment between a tactical base and a training base. It has not been determined at this time if the higher mission severity factors experienced by the F-5Es are a contributing factor. Figure 16 is very interesting in that it compares identical numbers and types of parts in two locations. It is anticipated that defect accumulation versus variation in climate will be characterized by the end of the flight test program.
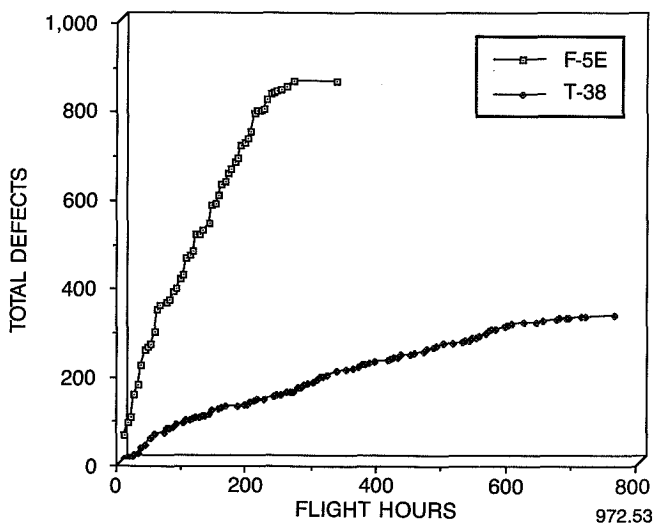
FIGURE 15. DEFECT ACCUMULATION FOR F-5E AND T-38 AIRCRAFT
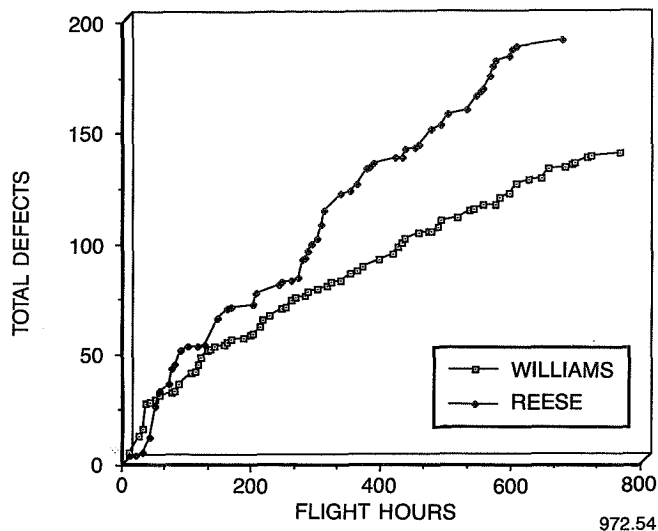
FIGURE 16. DEFECT ACCUMULATION FOR T-38 AIRCRAFT

It is possible to draw several preliminary conclusions concerning the in-service performance of TP and BMI hardware:

1. Laboratory testing does provide a good general indicator of in-service performance.

2. Additional training of maintenance personnel regarding the do's and don'ts of composite maintenance will reduce in-service damage.

3. Design can play a major role in improving the maintainability of composite hardware by selecting the proper material for a given application, selecting proper attach hardware, and by having a general awareness of the maintenance environment.

437

RESIDUAL STRENGTH OF REPAIRED GRAPHITE/EPOXY LAMINATES

AFTER 5 YEARS OF OUTDOOR EXPOSURE

Jerry W. Deaton
Langley Research Center
Hampton, Virginia

INTRODUCTION

The NASA Langley Research Center has sponsored research (reference 1) to develop generic repair techniques and processes for advanced graphite/epoxy (Gr/Ep) composites applicable to secondary structures for commercial transport aircraft. The long-term durability of such repairs is being addressed in a 10-year outdoor exposure program at the Langley Research Center. This paper presents details of the program and results of residual strength tests after 5 years of outdoor exposure.

Four repair methods are being evaluated. These include: (1) externally bolted aluminum-plus adhesive, (2) precured, bonded external Gr/Ep, (3) cure-in-place external Gr/Ep, and (4) cure-in-place flush Gr/Ep. Repaired specimens as well as undamaged and damaged unrepaired controls are being exposed outdoors for 1, 3, 5, 7, and 10 years. The residual tensile strength of stressed, unstressed, and fatigue specimens from each group is reported herein and compared with the tensile strength of baseline specimens which received no outdoor exposure. Figure 1 summarizes the objective and approach of this program.

Identification of the commercial products and companies in this report is used to describe adequately the test materials. The identification of these commercial products does not constitute endorsement, expressed or implied, of such products by the National Aeronautics and Space Administration.

TABBED LAMINATE SPECIMEN

A sketch of an exposure specimen is shown in figure 2. The laminates from which these specimens were obtained consisted of 16 plies of T300[a]/5208[b] Gr/Ep having a $(\pm45/0/\pm45_2/0)_s$ layup. Laminates were cured using the following cure cycle: (1) apply full vacuum, (2) heat to 275 $\pm 5°F$ at 2 to 3°F/minute, (3) dwell at 275 $\pm 5°F$ for 45 minutes, (4) apply 100 ± 5 psi, venting vacuum at 20 psi, (5) heat to 355 $\pm 5°F$ at 2 to 4°F/minute, (6) cure for 120 +10, -0 minutes at 355 $\pm 5°F$, and (7) cool to 175°F under pressure.

Each repair specimen is 27-inches long and 8-inches wide. Fiberglass tabs 0.14-inch thick, fabricated from Narmco[b] 8517/1581 prepreg, were bonded to each end on both surfaces of the specimen. Each tab was beveled to a feather edge extending in 0.5 inch from the edge adjacent to the test section. All four tabs were bonded to the specimen with Metlbond 329 (M-329) supported film adhesive in a single operation using the following bonding cycle: (1) apply full vacuum then apply 35 psi autoclave pressure and vent the vacuum, (2) heat to 350°F at 6°F/minute or greater, (3) cure at 350°F for 1 hour, and (4) cool to 180°F under full pressure.

The damage to be repaired consisted of a 3.75-inch diameter hole located in the center of the test section. This specimen provides a realistic geometric representation of an actual repair and permits the

439

testing of a damaged, unrepaired control specimen. All repair specimens were prepared for bonding by sanding lightly with 180-grit abrasive paper and wiping clean with a rag soaked with MEK.* Prior to any outdoor exposure all specimens received an aircraft finish coat of polyurethane paint.

(a) Manufactured by Union Carbide Corporation, Danbury, CT

(b) Manufactured by Narmco Materials Inc., Anaheim, CA

BOLTED EXTERNAL ALUMINUM REPAIR

Details of the bolted external aluminum patch with supplemental adhesive are shown in figure 3. The 3.75-inch diameter hole was filled with the circular piece obtained from the hole forming operation, and the remainder of the hole was filled with a room temperature curing epoxy and cured for 24 hours. A circular patch was cut from 0.080-inch thick aluminum and fastened to the basic laminate with 3/16-inch diameter MS 21140 stainless steel blind fasteners as shown in the figure. Metlbond 329 supported film adhesive (0.06 psf) was placed between the aluminum patch and the basic laminate, and all fasteners were installed with adhesive to minimize galvanic reactions. After all fasteners were installed, the repair specimen was cured 1 hour at 350°F with pressure applied by the fasteners. A completed bolted external aluminum repair specimen is shown at the bottom of the figure.

PRECURED BONDED EXTERNAL GRAPHITE/EPOXY REPAIR

Figure 4 shows the configuration of the precured bonded external Gr/Ep repair. The 3.75-inch diameter hole was filled using the same procedure described for the previous repair. A 4-ply $(0/90_2/0)$ laminate was fabricated from T300/5208 Gr/Ep material to be used as the repair patch. This laminate was cured using the same bagging procedure and cure cycle as the basic laminate. Each precured layer was cut from the 4-ply laminate using pinking shears to minimize peel stresses at the patch edges. The repair consists of five layers, two layers having $(0/90_2/0)$ orientation and three layers cut from the laminate such that their orientation was $(+45/-45_2/+45)$ relative to the 0-degree direction of the basic laminate being repaired. The size of each layer was decreased in 1/4-inch steps from the surface of the basic laminate. Each layer was separated by M-329, 0.06 psf supported film adhesive as shown in the figure. The bonding cure cycle consisted of covering the layup with one layer of porous Teflon[c]-coated glass and (1) apply full vacuum, (2) heat to 350°F at 6°F/minute or greater, (3) cure at 350°F for 1 hour, and (4) cool to 180°F under full vacuum. A completed precured bonded external Gr/Ep repair specimen is shown at the bottom of the figure.

(c) Teflon is a trade name of E. I. duPont de Nemours & Co. Inc.

CURE-IN-PLACE EXTERNAL GRAPHITE/EPOXY REPAIR

The configuration of the cure-in-place external Gr/Ep repair is illustrated in figure 5. Again, the 3.75-inch diameter hole was filled using the same procedure previously described. One layer of M-329, 0.06 psf supported film adhesive was placed on the basic laminate and ten layers (two plies each layer) of T300/5208 prepreg tape, orientated as shown, were stacked over the damaged area of the basic laminate. Each step was approximately 5/32 inch. The cure cycle consisted of covering the layup with one layer of porous Teflon-coated glass and then: (1) apply full vacuum, (2) heat to 350°F

*MEK (methyl ethyl ketone)

at 2 to 6°F/minute, (3) cure at 350°F for 1 hour, and (4) cool to 180°F under full vacuum. A completed cure-in-place external Gr/Ep repair is shown at the bottom of the figure.

CURE-IN-PLACE FLUSH GRAPHITE/EPOXY REPAIR

Figure 6 shows how the cure-in-place flush graphite repair was achieved in the 16-ply basic laminate. The repair is classified as a flush repair because the projection of the repair material beyond the mold line of the laminate being repaired was kept to a minimum. Scarf surfaces were prepared using sanding discs and belt sanders and have a taper of approximately 18:1 in the lengthwise direction. Gr/Ep (T300/5208) prepreg tape material was then laid-up onto the tapered bond line matching the orientation, ply-by-ply, of the basic laminate. A layer of the M-329, 0.06 psf supported film adhesive was used between the prepreg patch and the scarfed basic laminate surfaces. Three additional cover plies of (0/±45) prepreg were used outside the mold line. Two additional cover plies (±45) inside the mold line extending beyond the repair area were used to increase the strength of the repair. The 0-degree outer mold line plies were serrated at the edges by cutting with pinking shears to reduce peel stresses. The entire repair assembly was then oven cured without bleeding using the following cycle: (1) apply full vacuum, (2) heat to 350°F at 3 to 6°F/minute, (3) cure at 350°F for 1 hour, and (4) cool to 150°F under full vacuum. A completed cure-in-place flush Gr/Ep repair specimen is shown at the bottom of the figure.

REPAIRED GRAPHITE/EPOXY SPECIMEN TEST PLAN

The repaired Gr/Ep specimen exposure test plan is shown in figure 7. A total of 108 specimens are included in the test program. The test program includes 18 undamaged control specimens, 18 damaged unrepaired control specimens, and 18 repaired specimens for each of the four repair concepts previously described. One specimen type is included for each outdoor exposure condition and time shown. The baseline static strength control specimens were the same size (8-inches wide by 27-inches long) as the repair specimens. However, the control specimens for the residual static strength after exposure were standard 1-inch by 12-inch composite tension specimens (reference 2).

The baseline specimens identified as fatigue specimens were exposed to 2.5 lifetimes of the fully-reversed fatigue loading of the L-1011 fin spectrum given in reference 1 for similar 16-ply Gr/Ep specimens. Briefly, the L-1011 fin spectrum is defined for a 36,000 flight lifetime and consists of blocks of climb, cruise, and descent flight spectra typically experienced by the L-1011 aircraft and applied in a random manner. Maximum loads in the spectra were set to cause maximum tensile strains of 0.2 percent, which represents limit load design strains for the L-1011 fin skin. The residual static strength fatigue specimens received 0.25 lifetime of fatigue (9000 flights) each year as indicated in the figure. Baseline static strength tests were performed in May 1983, residual static strength tests after 1 year of outdoor exposure in June 1984, 3-year outdoor exposure residual strength tests in June 1986, and 5-year outdoor exposure residual strength tests in June 1988. Additional residual static strength tests are planned after 7 and 10 years of outdoor exposure.

OUTDOOR EXPOSURE TEST SETUP

Figure 8 shows the outdoor exposure test setup for the control and repaired specimens. The rack of specimens shown in the upper left is for the no load condition. Another rack of specimens (not shown) is for the no load plus fatigue exposure condition. Each rack was positioned so that the specimens were oriented longitudinally, facing south, at an angle of approximately 45 degrees to the

horizontal. The sustained load test setups for the control and repaired specimens are shown in the upper right and the bottom of the figure, respectively. Load was applied to the specimens by a screw driven jack and load cell aligned along the horizontal axis of the specimens. All sustained load specimens are stressed to a load corresponding to limit load strain (0.2 percent) of the L-1011 vertical fin skin which is equivalent to 22 percent of ultimate load for the laminate under consideration. The loading frames also face south and the repaired specimens were at an angle of approximately 45 degrees to the horizontal. The smaller sustained load control specimens were exposed in a horizontal plane because of interference between the clamping fixtures and the loading frame structure.

FATIGUE AND RESIDUAL STRENGTH TEST SETUP

Test equipment used to perform the fatigue and residual static strength tests is shown in figure 9. The console shown on the left of the figure contains the fatigue spectrum data on magnetic tape which were used to control the 100 kip capacity closed-loop electro hydraulic testing system. A repaired specimen is shown clamped in the grips of the test frame, and a fixture to prevent compression buckling of the specimen is shown attached to the specimen. Each type of repair required a different set of fixtures because of the differences in the repair profiles. In general, a 0.004-inch clearance between the fixture bars and repair surface was achieved using shims. All fixture surfaces in contact with the specimen were covered with Teflon tape to minimize load introduction to the fixture. Each fixture had an approximate 1/4-inch space between the ends of the fixture and the beveled ends of the fiberglass tabs when centered over the repair area. Residual tensile strength tests were performed at a load rate of 6000 lbf/minute with the fixture removed. A 20 kip capacity closed-loop electro hydraulic testing system was used for the fatigue and residual strength test of the smaller 1-inch by 12-inch control specimens. Residual tensile strength tests of these specimens were performed at a load rate of 2000 lbf/minute and all fatigue cycles were applied at a frequency of 10 Hertz.

FAILURES OF BASELINE REPAIRED GRAPHITE/EPOXY LAMINATES

Photographs of the failure of the baseline repaired Gr/Ep laminates are shown in figure 10. Failure of the bolted external aluminum repair specimen initiated through the fastener holes. In reference 1, it was observed that the residual strength was low due to premature pull-out of the blind fasteners for similar external metal doubler repairs. It has been demonstrated that significant strength recovery can be provided by a metal patch repair using standard titanium screws and plate nuts, (references 3 and 4). The failure of the precured bonded external Gr/Ep repair was due to disbonding of the repair patch. A similar failure was obtained for the cure-in-place external Gr/Ep repair along with fiber splitting in the outermost ply of the repair. The sawtooth appearance along the edges of these repairs is due to the cutting of the repair materials with pinking shears as previously described. The cure-in-place flush Gr/Ep repair failed in tension outside the repair area.

RELATIVE BASELINE STRENGTHS OF REPAIRED GRAPHITE/EPOXY

LAMINATES

Figure 11 shows the relative baseline strengths for each of the four repair concepts for no outdoor exposure and after 2.5 lifetimes of fully-reversed fatigue cycling. The precured bonded external Gr/Ep repair is the only repair which indicates a loss (approximately 19 percent) in residual tensile strength due to the fatigue cycling. However, it should be noted that only one specimen has been tested at each condition and thus may be within the scatter band for this type of test. The cure-in-

place flush Gr/Ep repair exceeded the control specimen strength by approximately 10 percent and is the only repair which failed outside the repair area. The cure-in-place external Gr/Ep repair was next in bond efficiency at approximately 79 percent of control specimen strength. The precured bonded external Gr/Ep and the bolted external aluminum repairs were about 67 percent and 55 percent effective, respectively, in restoring control specimen strength.

FAILURES OF REPAIRED GRAPHITE/EPOXY LAMINATES AFTER

5 YEARS OF OUTDOOR EXPOSURE

Figure 12 shows failure photographs of the repaired Gr/Ep laminates that were tested after 5 years of outdoor exposure. Failures of the bolted external aluminum, precured bonded external Gr/Ep, and the cure-in-place external Gr/Ep repairs were similar to those of the baseline repaired specimens previously shown in figure 10. The cure-in-place flush Gr/Ep repair failure occurred through the repair area with severe fiber splitting in all plies of the Gr/Ep patch.

RESIDUAL TENSILE STRENGTH OF REPAIRED GRAPHITE/EPOXY

T300/5208 AFTER OUTDOOR EXPOSURE

The residual tensile strengths of repaired Gr/Ep T300/5208 specimens, after outdoor exposure, are shown in figure 13. The data shown on the ordinate (no exposure) are repeated from figure 11 for comparison with the 1-year, 3-year, and 5-year exposure data. The 1-year, 3-year, and 5-year exposure data shown for the control specimens are from the smaller (1-inch by 12-inch) specimen size and may exhibit some scale effect. Comparison of the exposure data for each of the four repair concepts indicates that only the precured bonded external Gr/Ep repair experienced a loss in residual tensile strength due to outdoor exposure. A 10 percent loss is indicated after 1 and 5 years of exposure, and a loss of about 18 percent in residual tensile strength after 3 years of outdoor exposure is indicated. The residual tensile strength of the other three repair methods is essentially unchanged after 5 years of outdoor exposure. Again, it should be noted that each data point represents a single test.

FAILURES OF REPAIRED GRAPHITE/EPOXY LAMINATES AFTER

5 YEARS SUSTAINED STRESS OUTDOOR EXPOSURE

Failure photographs of repaired Gr/Ep laminates for each repair concept tested after 5 years of sustained stress outdoor exposure are shown in figure 14. Again, the bolted external aluminum, precured bonded external Gr/Ep, and the cure-in-place external Gr/Ep repairs had failures similar to the baseline repaired specimens shown in figure 10. However, the cure-in-place flush Gr/Ep repair specimen failed in tension through the repair whereas the failure of the baseline specimen failed outside the repair area.

RESIDUAL TENSILE STRENGTH OF REPAIRED GRAPHITE/EPOXY

T300/5208 AFTER SUSTAINED STRESS OUTDOOR EXPOSURE

Figure 15 shows the residual tensile strength of repaired Gr/Ep T300/5208 after sustained stress outdoor exposure. All specimens were subjected to a sustained stress of 22 percent of ultimate for the undamaged control specimen which corresponds to a strain level of 0.2 percent. Again, the data shown on the ordinate are repeated from figure 11 to assess data trends due to the sustained stress outdoor exposure. The 1-, 3-, and 5-year data shown for the control specimens are again from the smaller (1-inch by 12-inch) specimen size. An indication of the amount of scatter in the data can be obtained by comparing the 1-year exposure data of the undamaged control with the 3- and 5-year data. The measured value of residual tensile strength of the control specimen is about 8 percent less than the baseline strength after 1 year of sustained stress outdoor exposure and about 14 and 10 percent greater than the baseline strength after 3 and 5 years of exposure, respectively. Since control specimen strength is not expected to increase due to the sustained stress outdoor exposure, the difference between the 1-year (-8 percent) and the 3- and 5-year (+14 and +10 percent) residual strength data for the control specimen is probably due to data scatter. Therefore, data scatter of ±10 percent is probably not unreasonable for these types of tests. Comparison of the sustained stress exposure data for each of the four repair concepts indicates that residual tensile strength is essentially unchanged after 5 years of sustained stress outdoor exposure.

FAILURE OF REPAIRED GRAPHITE/EPOXY LAMINATES AFTER

5 YEARS OF OUTDOOR EXPOSURE AND FATIGUE

Figure 16 shows failure photographs of repaired Gr/Ep laminates for each repair method tested after 5 years of outdoor exposure and 1.25 lifetimes of fatigue. Again, the bolted external aluminum, precured bonded external Gr/Ep, and the cure-in-place flush Gr/Ep repairs had failures similar to those of the baseline repaired specimens shown in figure 10. The cure-in-place flush Gr/Ep repaired specimen failed in tension through the repair. This failure is similar to that of the cure-in-place flush Gr/Ep repair failure after 5 years of sustained stress outdoor exposure but without any fatigue cycling, shown in figure 14.

RESIDUAL TENSILE STRENGTH OF REPAIRED GRAPHITE/EPOXY

T300/5208 AFTER OUTDOOR EXPOSURE AND FATIGUE

The effects of combined outdoor exposure and fatigue cycling on the residual tensile strength of repaired Gr/Ep T300/5208 is shown in figure 17. The data shown (shaded symbols) on the ordinate are repeated from figure 11 for the specimens subjected to 2.5 lifetimes of fully-reversed fatigue cycling previously described. A double scale is shown for the abscissa, one for the outdoor exposure time in years, and the other for the amount of fatigue cycles in lifetimes. The 1-, 3-, and 5-year data shown for the control specimens are again from the smaller (1-inch by 12-inch) specimens. The measured value of tensile strength of the undamaged control specimen is about 8 percent less than the baseline strength after 1 year of outdoor exposure and 0.25 lifetime of fatigue and about 4 percent less after 5 years of exposure and 1.25 lifetimes of fatigue. However, after 3 years of outdoor exposure and 0.75 lifetime of fatigue, the measured value is about 15 percent greater than the baseline strength, which again illustrates the amount of data scatter which can be expected from these types of tests. The cure-in-place external Gr/Ep repair is the only repair concept being evaluated which shows a loss in

residual tensile strength after 5 years of outdoor exposure plus 1.25 lifetimes of fatigue (16 percent loss of strength). The other three repair concepts remain essentially unchanged after 5 years of outdoor exposure plus 1.25 lifetimes of fatigue.

CONCLUDING REMARKS

A 10-year outdoor exposure program to assess the long-term durability of repaired Gr/Ep laminates has been described. Specimens representing four repair concepts are being exposed outdoors at the Langley Research Center. Exposure conditions include unstressed, constant sustained stress, and unstressed plus a yearly imposition of 0.25 lifetime of fatigue. Prior to exposure, one repair concept, cure-in-place flush Gr/Ep, was determined to be greater than 100 percent effective in restoring baseline strength. The other three concepts and their effectiveness in restoring baseline strength before exposure are: cure-in-place external Gr/Ep (79 percent), precured bonded external Gr/Ep (67 percent), and bolted external aluminum (55 percent). Test results have been presented which indicate that the residual strengths for all repairs evaluated are not significantly affected after 2.5 lifetimes of fatigue, 5 years of outdoor exposure, 5 years of sustained stress outdoor exposure, or 5 years of outdoor exposure plus 1.25 lifetimes of fatigue.

REFERENCES

1. Stone, R. H.: Repair Techniques for Graphite/Epoxy Structures for Commercial Transport Applications. NASA CR-159056, 1983.

2. ASTM D 3039-76, Standard Test Method for Tensile Properties of Fiber-Resin Composites, 1976.

3. Labor, J. D.: Large Area Composite Structure Repair, AFFDL-TR-77-5, AFFDL-TR-77-121, AFFDL-TR-78-83, Northrop Corporation, Hawthorne, California.

4. Griffin, C. F.; Fogg, L. D.; and Dunning, E. G.: Advanced Composite Aileron for L-1011 Transport Aircraft Design and Analysis. NASA CR-165635, 1981.

Objective

- **Determine environmental durability of repaired graphite/epoxy composite laminates**

Approach

- **Four repair concepts**
  - **Bolted external aluminum**
  - **Precured bonded external Gr/Ep**
  - **Cure-in-place external Gr/Ep**
  - **Cure-in-place flush Gr/Ep**

- **10 year environmental exposure plus tension/compression fatigue**

- **Residual strength tests**

Figure 1 - Objective and approach for repair durability program
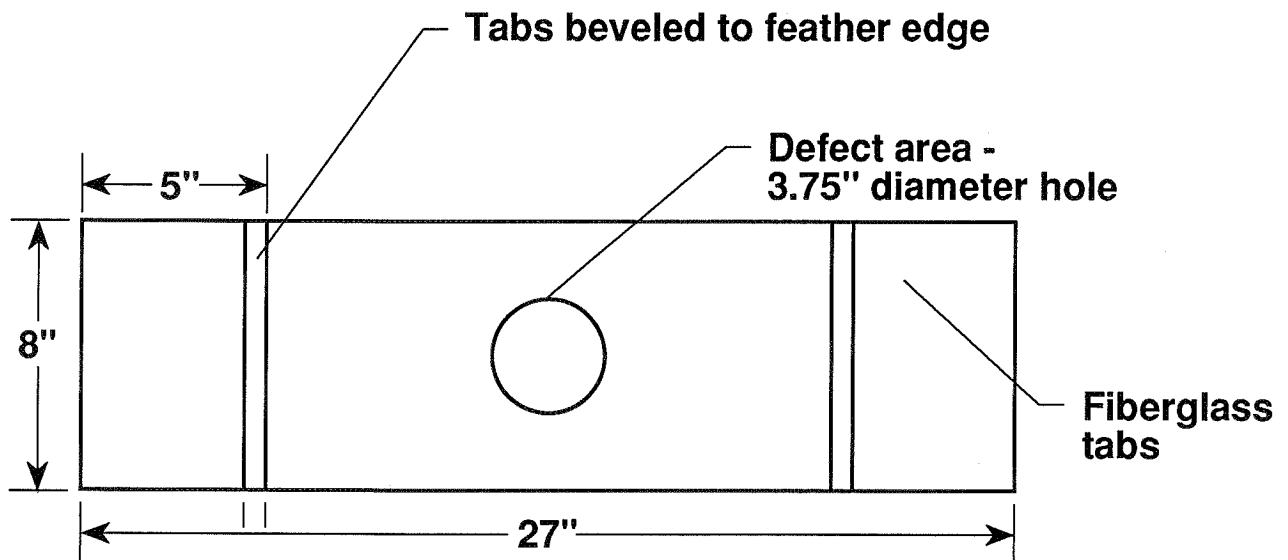
Figure 2 - Tabbed laminate specimen
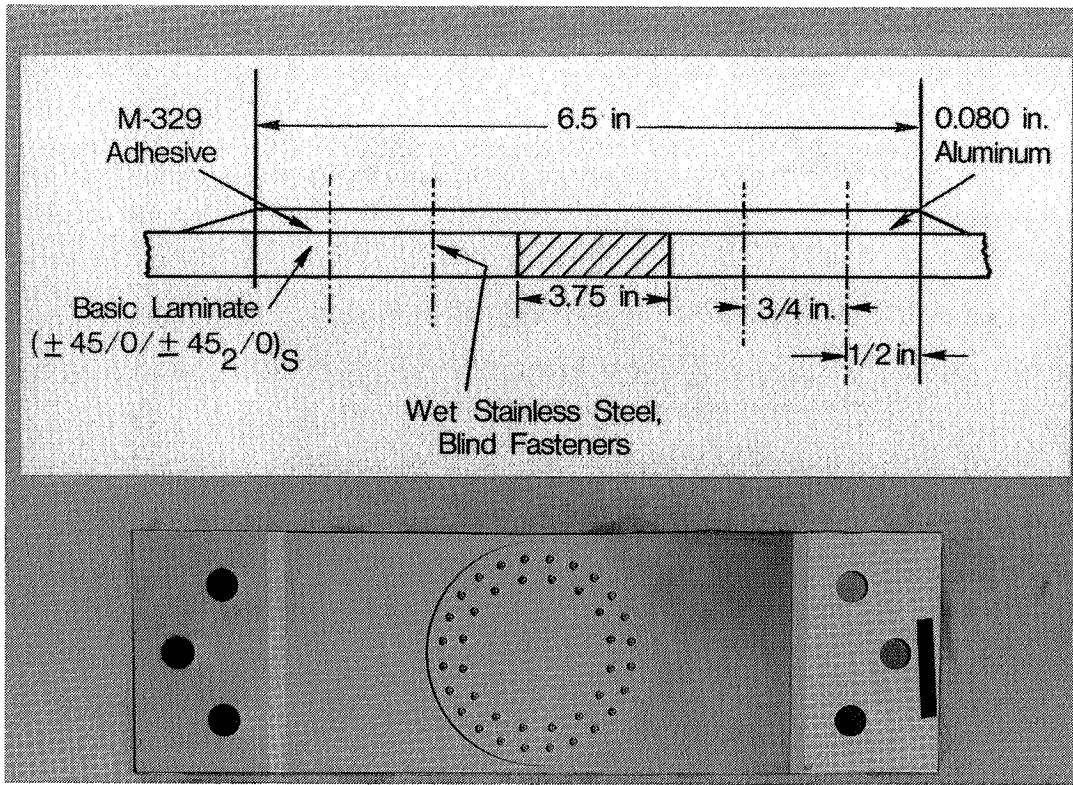
Figure 3 - Bolted external aluminum repair
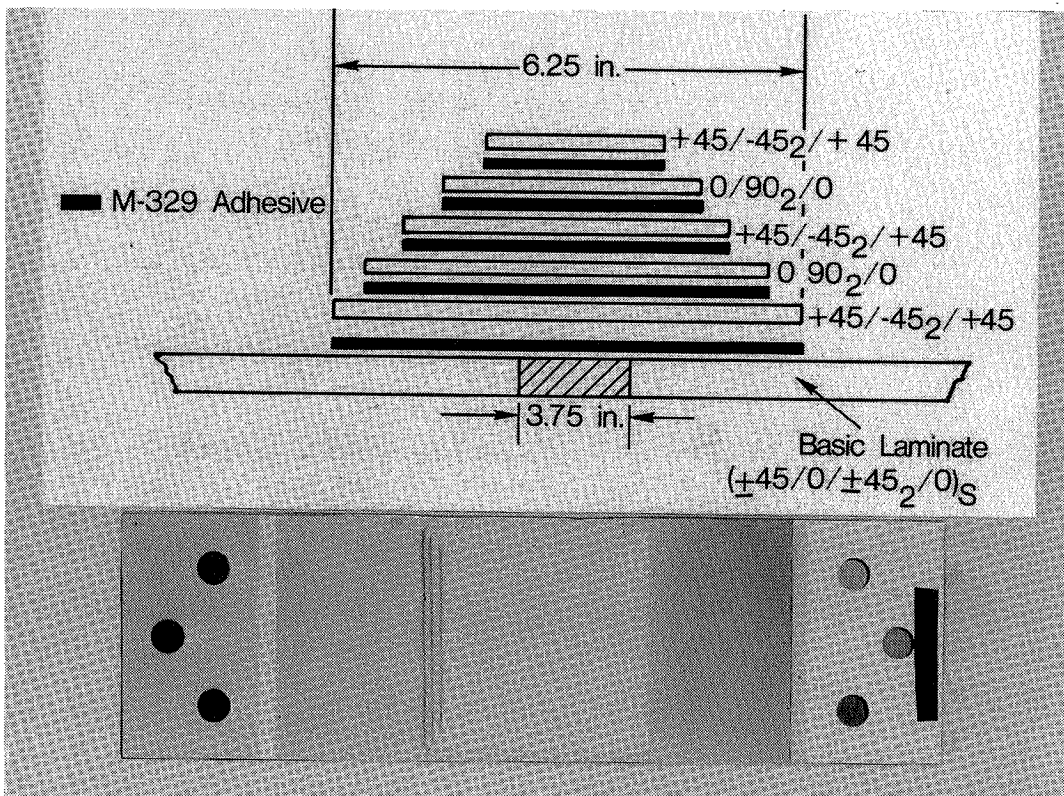
Figure 4 - Precured bonded external graphite/epoxy repair
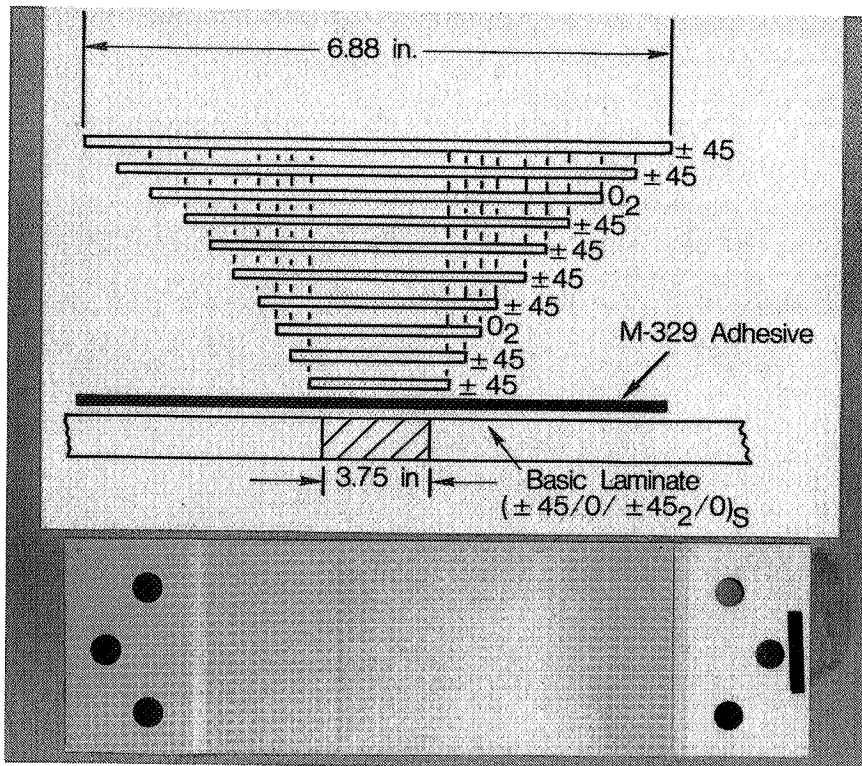
Figure 5 - Cure-in-place external graphite/epoxy repair
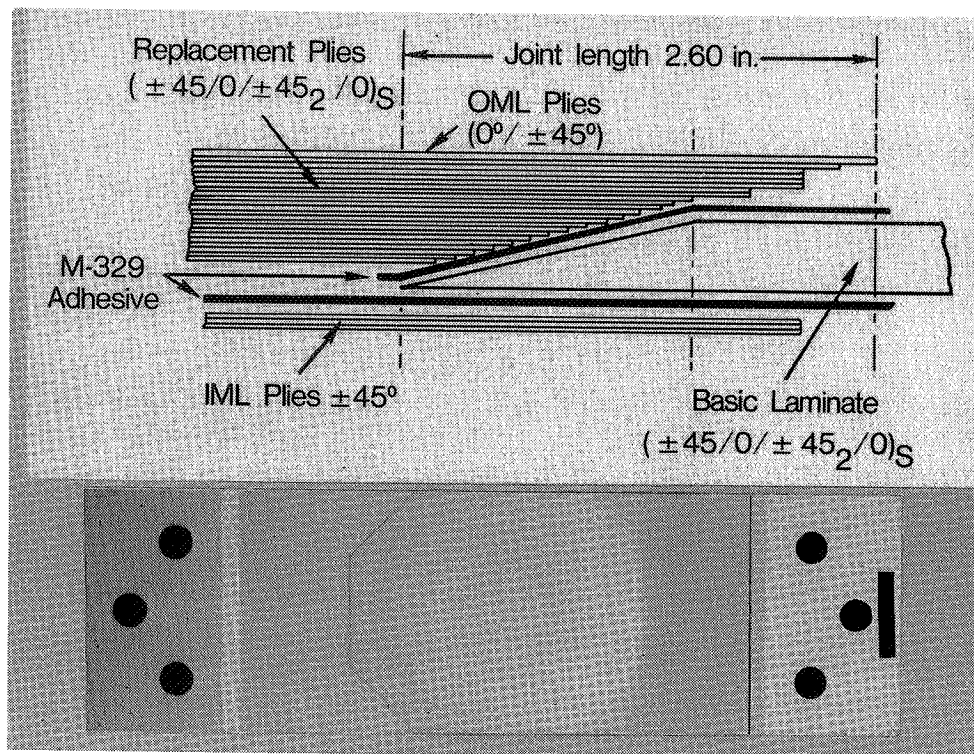
Figure 6 - Cure-in-place flush graphite/epoxy repair

Static Strength	Outdoor Exposure Condition				Test Date
	No Load, Years	Constant Load, Years	No Load + Fatigue,		
			Years	Lifetimes	
Baseline	0	0	0	2.5	5/83
Residual strength ↓	1	1	1	0.25	6/84
	3	3	3	0.75	6/86
	5	5	5	1.25	6/88
	7	7	7	1.75	6/90
	10	10	10	2.50	6/93

Figure 7 -   Repaired graphite/epoxy specimen test plan
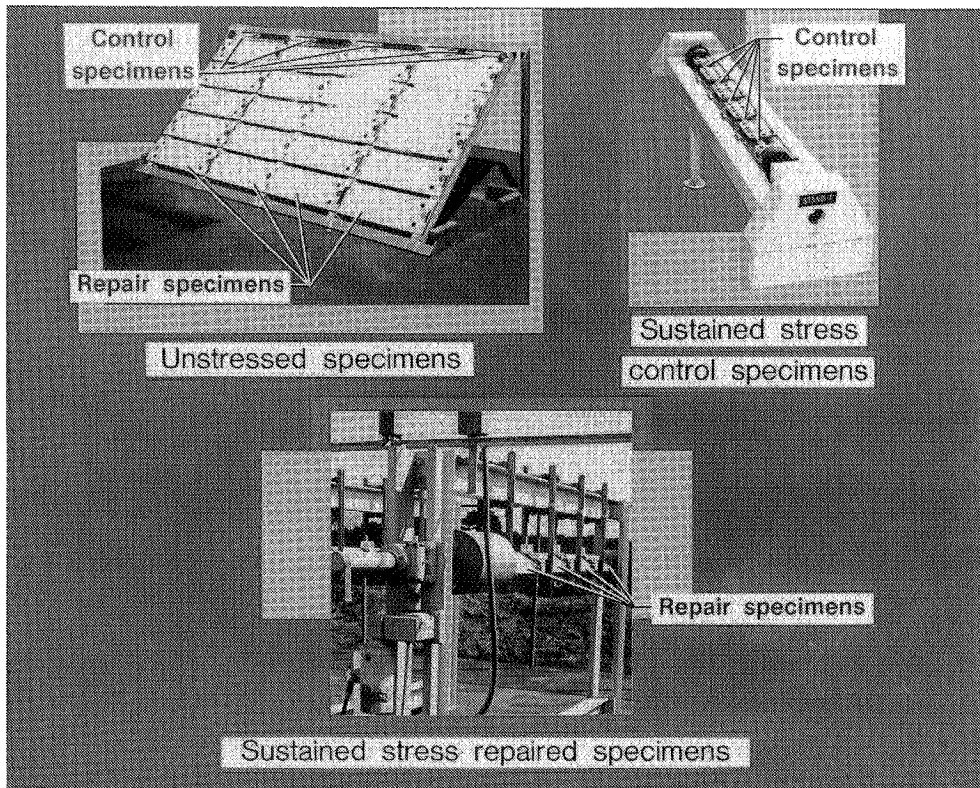
Figure 8 -   Outdoor exposure test setup
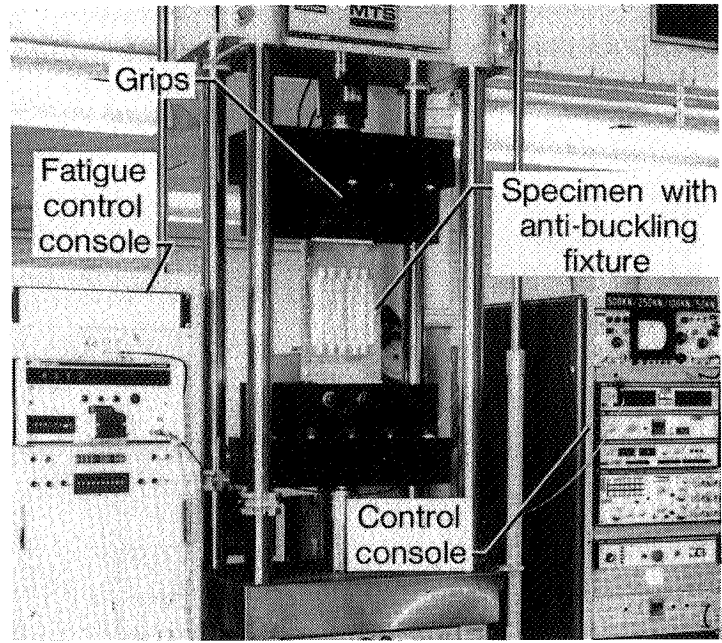
Figure 9 - Fatigue and residual strength test setup
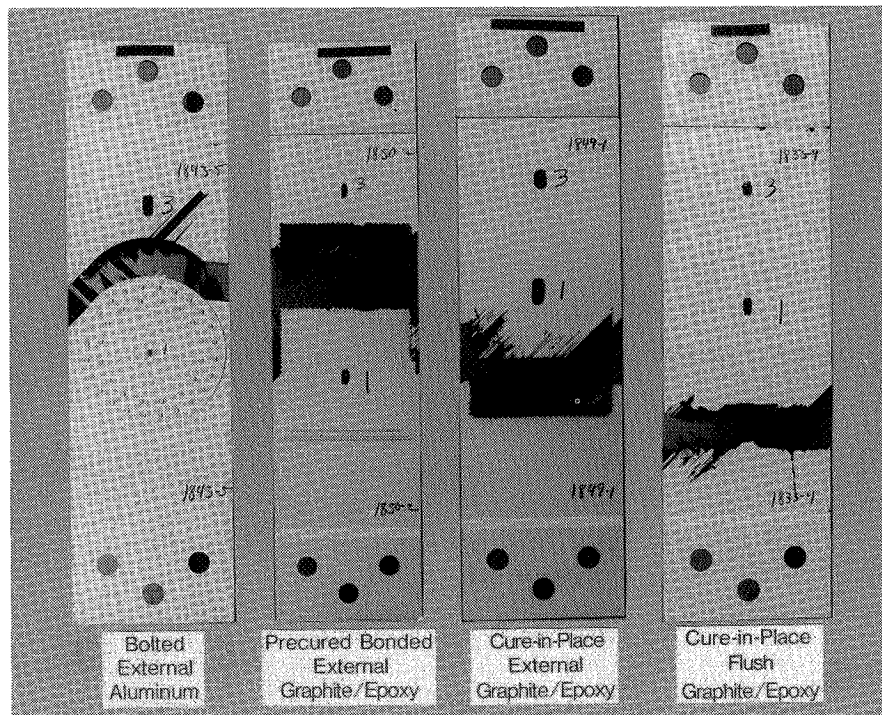
Figure 10 - Failures of baseline repaired graphite/epoxy laminates
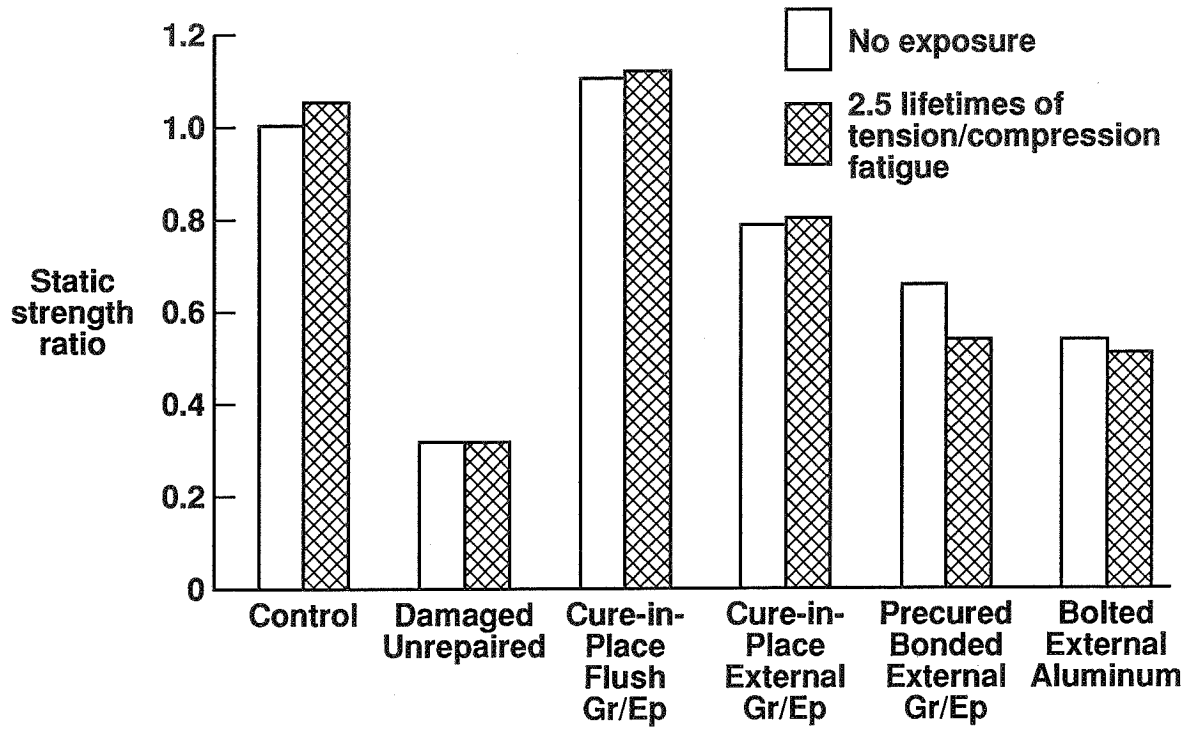
Figure 11 - Relative baseline strengths of repaired graphite/epoxy laminates
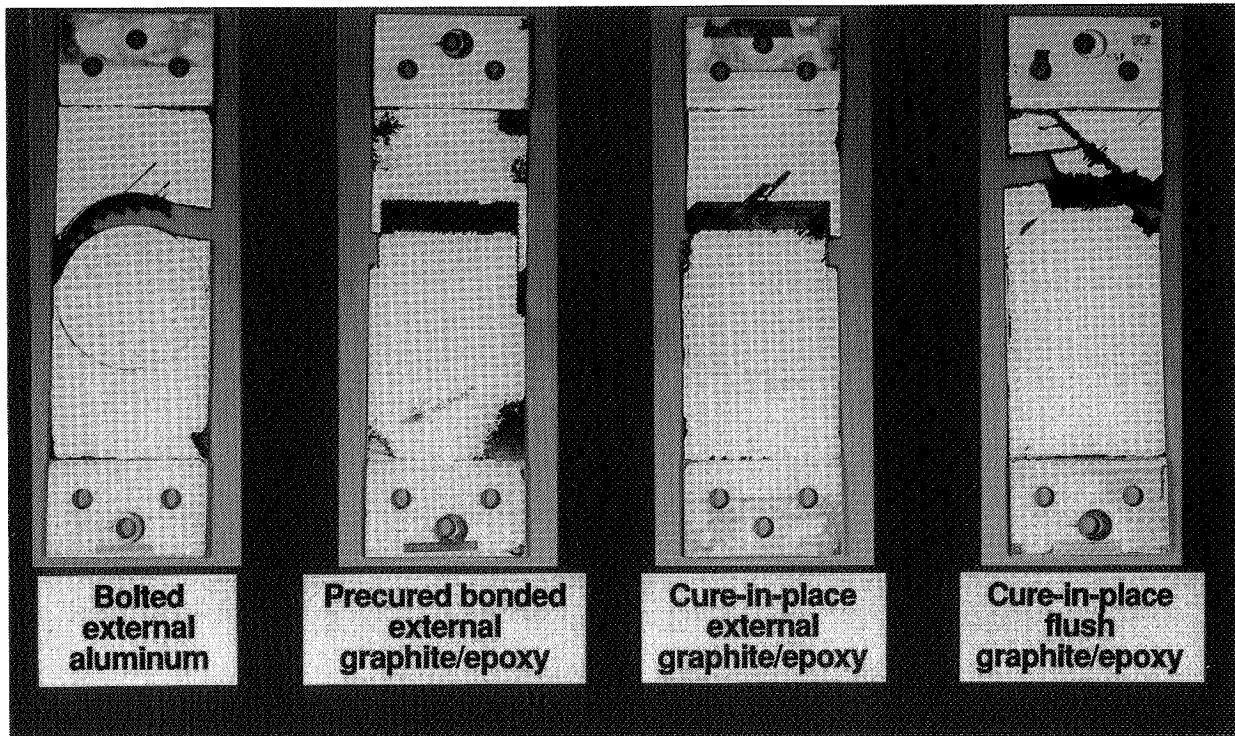
Figure 12 - Failures of repaired graphite/epoxy laminates after 5 years of outdoor exposure
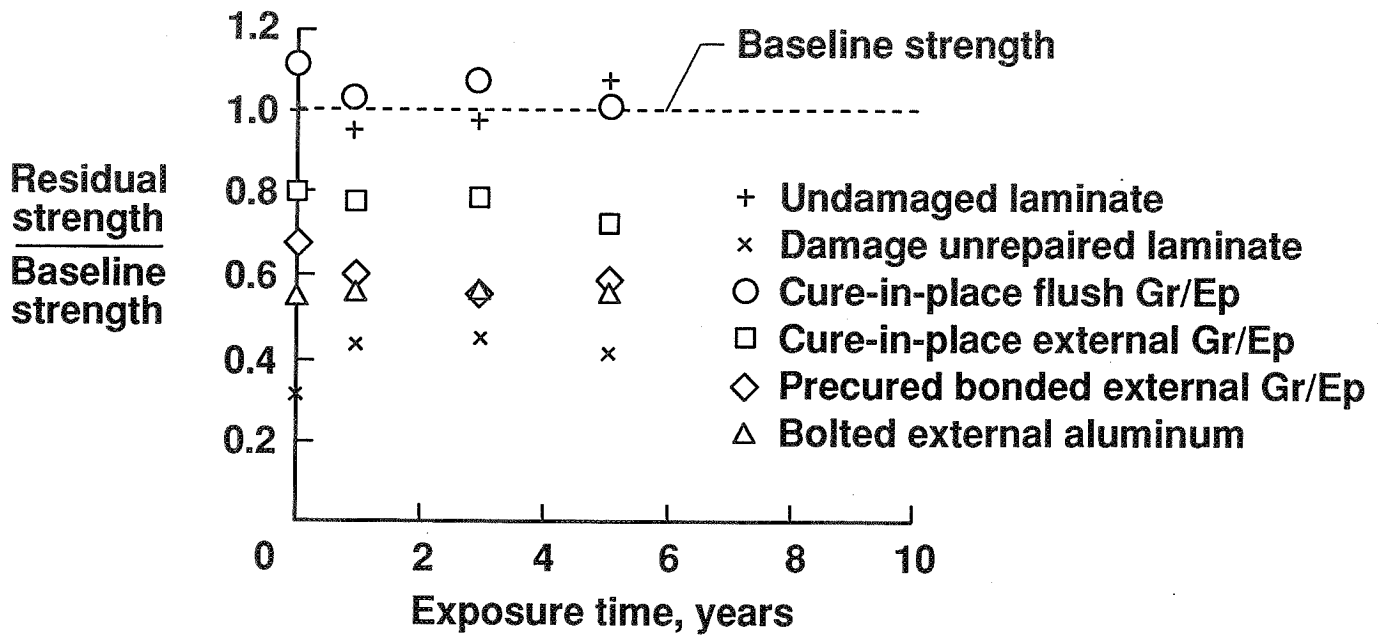
Figure 13 - Residual tensile strength of repaired graphite/epoxy T300/5208 after outdoor exposure
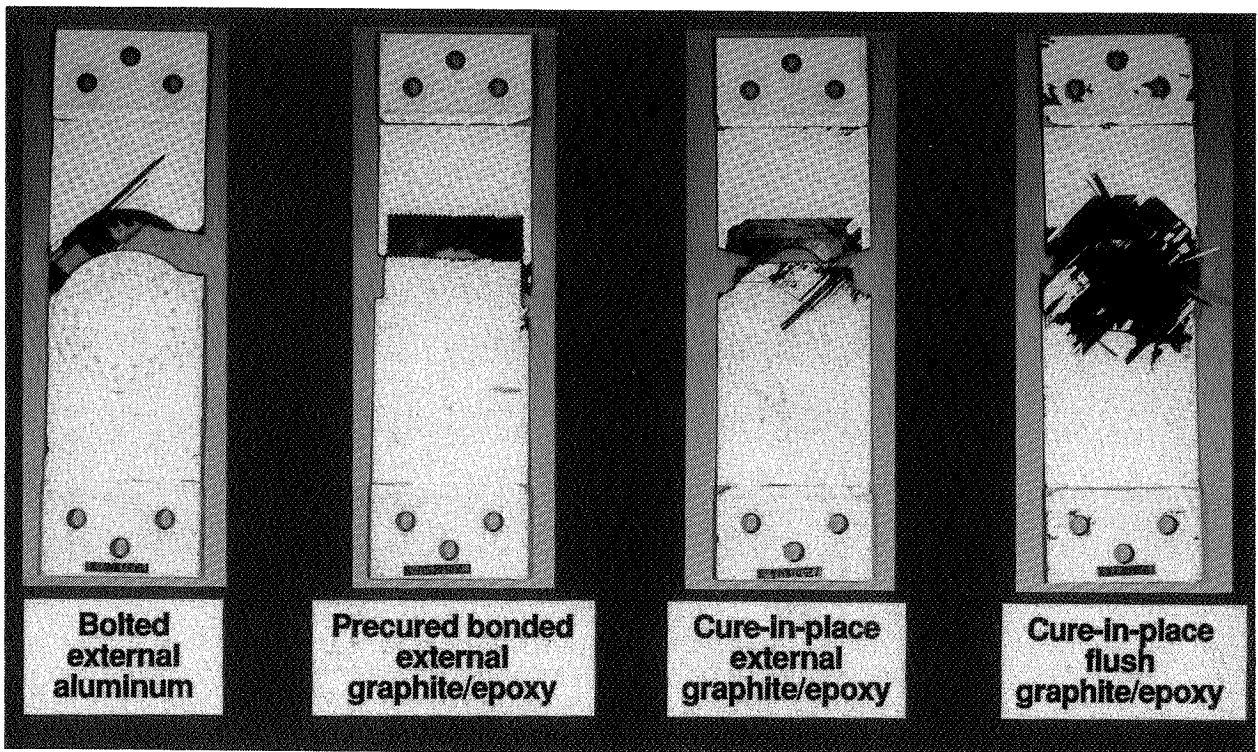
Figure 14 - Failures of repaired graphite/epoxy laminates after 5 years sustained stress outdoor exposure
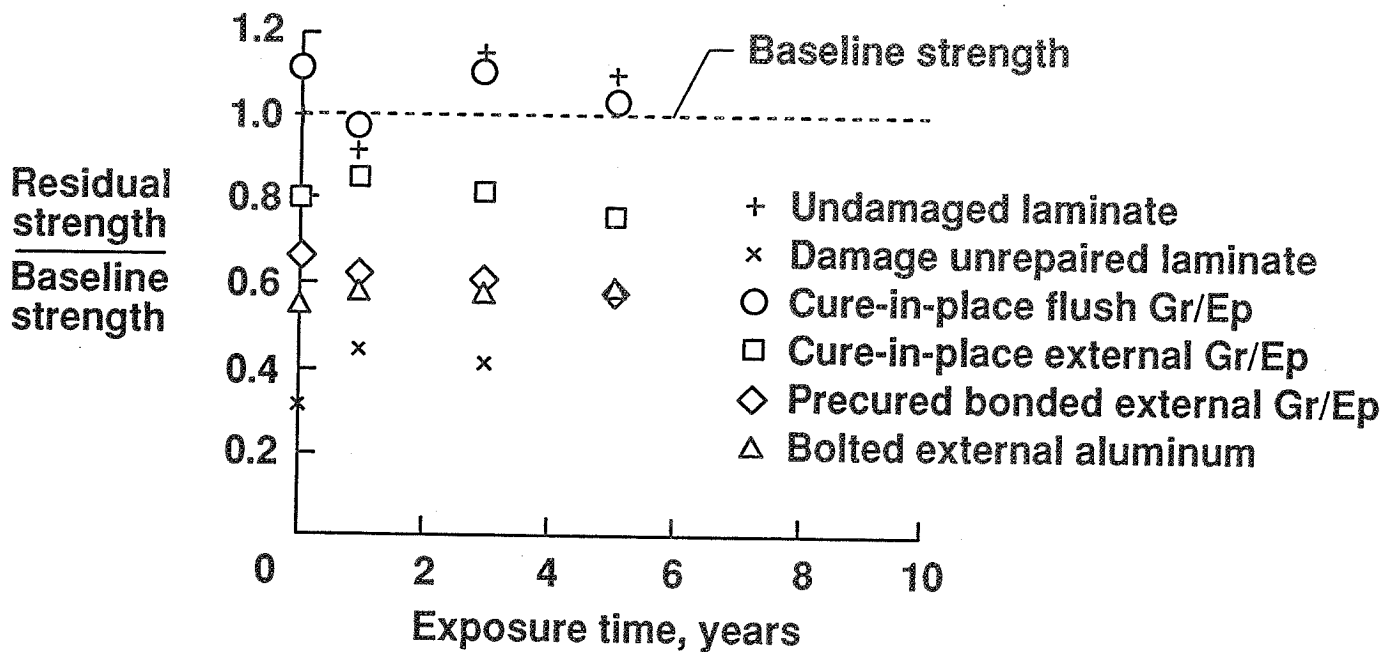
Figure 15 - Residual tensile strength of repaired graphite/epoxy T300/5208 after outdoor exposure stressed at 22 percent of ultimate
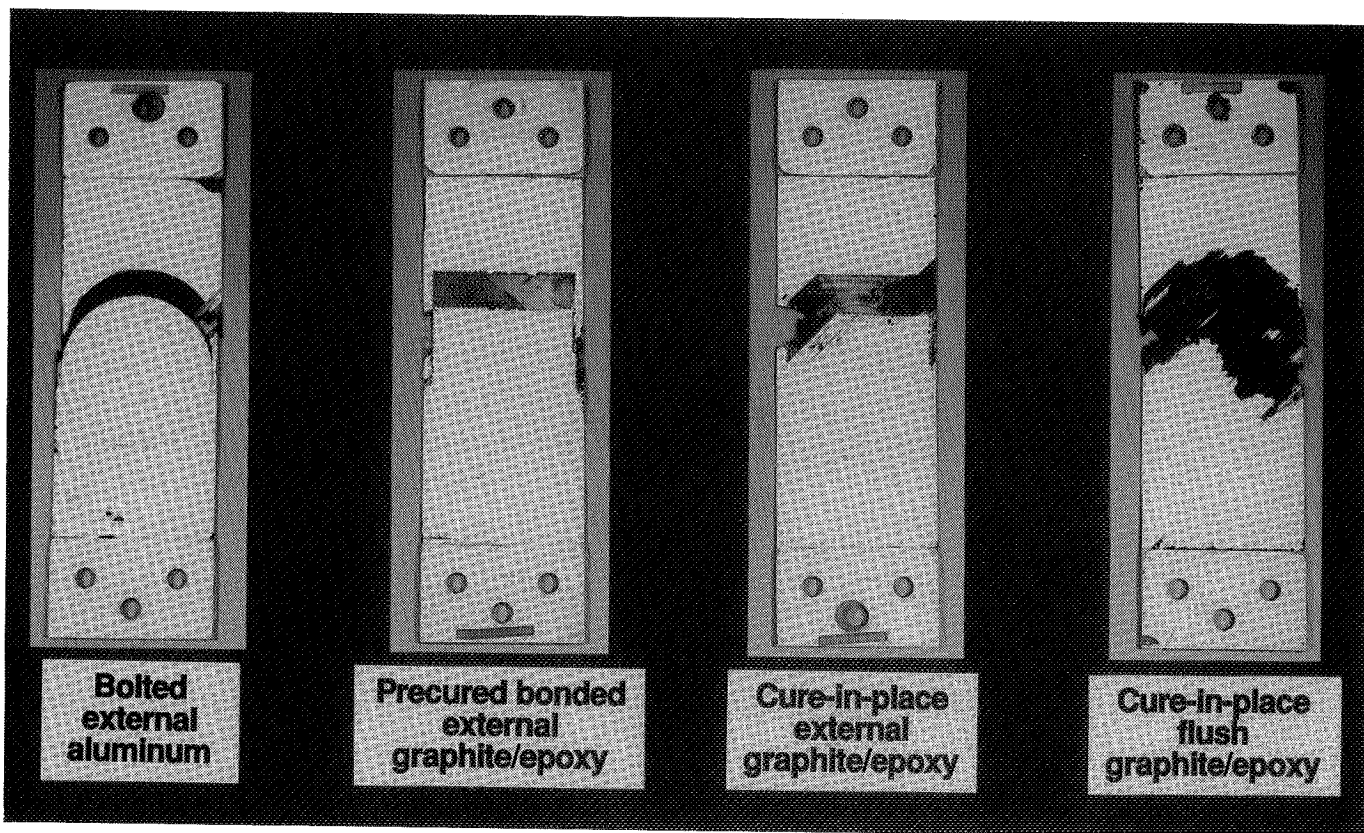
Figure 16 - Failures of repaired graphite/epoxy laminates after 5 years of outdoor exposure and fatigue
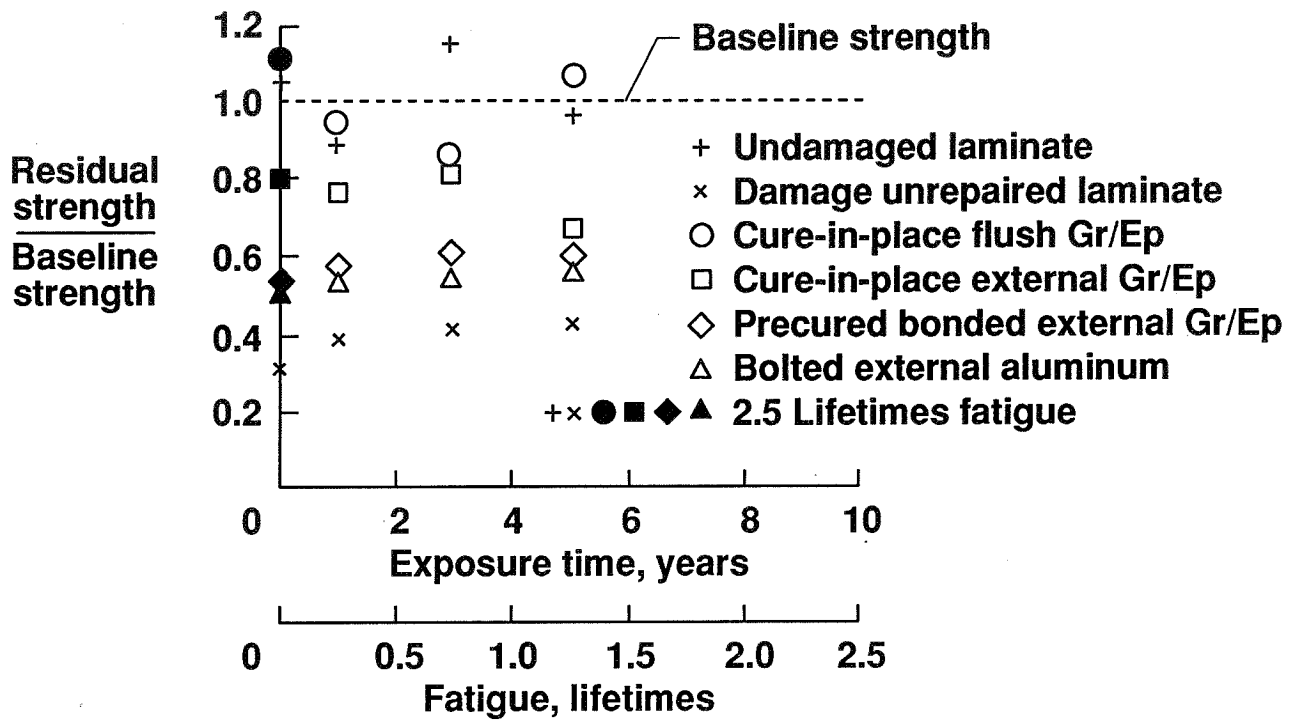
Figure 17 - Residual tensile strength of repaired graphite/epoxy T300/5208 after outdoor exposure and fatigue

Survivability Characteristics Of Composite Compression Structure*

J. Avery, M.R. Allen, D. Sawdy, S. Avery**

Boeing Military Airplanes
Wichita, Kansas

SUMMARY

Test and evaluation was performed to determine the compression residual capability of graphite reinforced composite panels following perforation by high-velocity fragments representative of combat threats. Assessments were made of the size of the ballistic damage, the effect of applied compression load at impact, damage growth during cyclic loading and residual static strength. Several fiber/matrix systems were investigated including high-strain fibers, tough epoxies, and APC-2 thermoplastic. Additionally, several laminate configurations were evaluated including hard and soft laminates and the incorporation of buffer strips and stitching for improved damage resistance or tolerance. Both panels (12 x 20-inches) and full scale box-beam components were tested to assure scalability of results. The evaluation generally showed small differences in the responses of the material systems tested. The soft laminate configurations with concentrated reinforcement exhibited the highest residual strength. Ballistic damage did not grow or increase in severity as a result of cyclic loading, and the effects of applied load at impact were not significant under the conditions tested.

INTRODUCTION

Future combat aircraft will increasingly employ graphite fiber reinforced polymers in primary structure. In order to assure effective operation in conventional threat environments, design criteria and guidelines must be established for these structures when exposed to impacts from high-energy penetrators, including fragments from missile warheads and antiaircraft artillery.

455

This paper presents key results from a recently completed Air Force contract, AFWAL F33615-83-C-3228, sponsored by the Flight Dynamics Laboratory. Mr. J. D. Oetting was the Air Force project manager. The program addressed the lack of data pertaining to the high-energy ballistic impact performance of compression loaded fiber composite structure. Reference 1 cites the final report for the investigation.

Boeing Military Airplanes was the prime contractor. Grumman Aerospace Corporation (GAC) was the subcontractor under the direction of Sam Dastin and Jim Suarez.

Important work has been performed in past years to characterize the static compression strength and fatigue performance of composite structure containing low-energy impact damage, fastener holes, and delaminations. However, there has been a lack of validated design information addressing compression degradation induced by the unique damage mechanisms induced by high-energy projectile perforation.

The approach taken under this program was designed to provide the information needed for assessing the combat damage tolerance of structural members as shown in Figure 1. When an aircraft is impacted by a kinetic-energy penetrator, a near-instantaneous degradation occurs under dynamic conditions. At this instant, stresses due to flight loads interact with those induced by the impact. Immediately after impact, structural capability is controlled by the residual static strength of the damaged member. The effects of short-term fatigue cycling on damage growth and residual strength must be assessed in order to assure safe return-to-base following the combat engagement. The testing conducted under this program provided the data needed to evaluate these critical elements of performance.

This 51-month program was conducted in two parts, as shown in Figures 2 and 3. Part I established and compared the survivability performance of several composite materials and survivable concepts by testing flat panels under compression load against multiple fragment impacts. Part II extended and validated these results for application to full-scale multi-loadpath structure by ballistically testing the most promising survivable design concepts as compression covers on a box-beam component.

At the conclusion of the component testing, a technology consolidation effort was undertaken to correlate key program results with wing design issues. Emphasis was

placed on the cost/benefits associated with using survivable concepts. Consolidation addressed the impact of the program output on the "Design Guide for Survivable Combat Aircraft Structures," (AFWAL-TR-84-3015) reported in Reference 2.

EXPERIMENTAL PROCEDURES

A two part experimental program was accomplished to establish and compare the survivability performance of advanced composite materials and survivable concepts. Flat panels and component covers were impacted under compression load by multiple fragments. These tests established key survivability design and assessment parameters including

- ballistic damage size and type
- residual strength and failure mode
- impact fracture threshold
- strength degradation due to damage growth under cyclic loading

This data was obtained for each of five composite material systems and four candidate damage tolerant concepts using flat panel test specimens. These results were then validated for full-scale multi-loadpath structure by ballistically testing box-beam components.

Three 230-grain steel fragments impacting in a prescribed pattern were employed for the ballistic tests, as shown in Figure 4. Fragment size, pattern and velocity were chosen so that the resulting damage represents a worst-case flaw for these projectiles. The resulting effective damage is approximately equivalent to a 6-7-inch sharp-edged notch with regard to strength degradation. The three-fragment launch system shown in Figure 5 employs three barrels bore-sighted to induce the desired impact pattern on the target. This technique permitted rapid and repeatable launchings that provided consistent damage for comparing material and concept performance.

Part I - Flat Panels. Approximately 100 flat panels were fabricated and tested, employing five fiber/resin systems and four concepts designed for improved survivability. The nominal panel size was 12- by 20- by 1/4 inches.

Ballistic damage tolerance testing of the flat panels was performed in two phases. Phase I evaluated the composite material systems employing a 48-ply laminate having the following distribution of ply orientations: 42% – 0° plies, 50% ±45° plies, and 8% – 90° plies. Phase 2 evaluated the survivable concepts. In this manner, knowledge gained from the materials evaluation was available for use in formulating the survivable designs.

Selection of the composite material systems for testing was based on several factors, including (1) Boeing and Grumman experience with the products as of 1983, (2) degree of government and industry interest in the product for fighter wing structural applications, (3) availability of properties test data and (4) product availability. The goal was to include a broad range of fiber and resin properties in order to assess their importance in ballistic damage tolerance response. The materials evaluated were

	CATEGORY	SELECTION (Fiber/Resin)
a.	Current-day graphite/epoxy	AS1/3501-5A
b.	High modulus graphite/epoxy	IM6/3501-5A
c.	High strain graphite/advanced epoxy	Celion-ST/5245C
d.	Graphite/bismaleimide	IM6/HX1518
e.	Graphite/thermoplastic	AS4/PEEK (APC-2)

The candidate survivable designs evaluated in Phase 2 are illustrated in Figures 6, 7, 8 and 9. They included foam interlayers for energy absorption, compliant (soft) skins with integral stiffening, and intraplies of glass (buffer strips) for crack growth arrestment. The concepts were designated as follows: Energy Absorbing Structure (EAS), Hard Skin with Buffer Strips (HSBS), Compliant Skin with Integral Stiffening (CSIS) and Compliant Skin with Integral Stiffening, Buffer Strips and Stitching (CSIS/BS). These concepts were selected as a result of their previously demonstrated tolerance/resistance to damage in tension, or in compression when containing low energy impact damage. Nine panels of each concept were subjected to the same ballistic impact conditions.

Ballistic impact tests were performed by the Boeing Weapon Effects Laboratory in Wichita and Impact Mechanics Laboratory in Seattle. The majority of tests were

conducted with panels loaded in compression at the time of ballistic impact. Figure 10 shows a typical panel under load. The case shown is fatigue cycling following ballistic damage. The specimen holding fixture provided restraint of overall panel buckling. Two uniaxial strain gages were mounted near the bottom end of each panel as shown in the figure. A potting compound was applied to both the gages and attachment wires to increase their resistance to disbonding from the panel surface during ballistic impact.

Each panel was impacted with three 230-grain fragments traveling approximately 2500 feet/second in a pattern providing the most severe damage. After impact, the preload was removed and measurements of the resulting damage were recorded. Residual strength testing was accomplished by incrementally loading each specimen in compression until failure. Load/strain data and loads at damage growth initiation and/or arrestment were recorded during the test. Figure 11 shows representative panels after ballistic impact and after residual compression strength testing. The testing was designed to measure parameters that are significant for design sizing and combat damage tolerance assessment, including

- Ultimate strain, undamaged
- Threshold strain for catastrophic impact fracture under applied load
- Residual static critical strain for three levels of operational strain at impact
- Residual static critical strain, after a 200 combat sortie truncated flight spectrum

The three best performers from the original four were then selected for component testing in Part II. As discussed later, these concepts were the two compliant skin designs (CSIS, CSIS/BS) and the hardskin with buffer strips (HSBS).

Part II - Components. In Part II, the performance of the three most promising survivable compression cover concepts and the hard skin baseline was verified by ballistic testing large-scale, multi-loadpath components. A reusable box-beam test component, illustrated in Figure 12, was designed to be representative of a fighter wing-box configuration. A graphite/epoxy (AS1/3501) baseline tension cover was employed on all tests. The test panels were installed as compression covers. The substructure was aluminum, with four spars and eight ribs. The box beam test component, approximately 6- by 30- by 114-inches total size, including a 40-inch

central test section, was designed for 4-point load application as shown in Figure13. The test panels were environmentally stabilized prior to ballistic testing.

Each cover was designed to a distributed end loading of approximately 16 kips/inch at 0.006 inch/inch ultimate strain. Two of the cover designs were uniform thickness (HSBS and the baseline) while the compliant skin designs contained planks located along the spar/cover interface to provide the integral stiffening. The 48-ply layup in the web regions on all covers eliminated thickness as a variable and permitted correlation of subcomponent test results with test results from earlier flat panel tests also using 48-ply laminates. Prior work reported in Reference 2 showed a strong correlation between laminate thickness and ballistic damage size.

The predicted failure strain for each cover design was based on the residual strength data from the panel tests of Part I. The baseline cover was expected to fail at the lowest strain: 0.0023 inch/inch. Critical buckling strain was predicted to be 0.0028 inch/inch, 22-percent above the notched failure strain induced by the ballistic damage. The Hard Skin with Buffer Strip cover was predicted to fail at a strain of 0.0027 inch/inch and to buckle at 0.003 inch/inch. The other two cover concepts were predicted to buckle considerably above the limit test strain of 0.004 inch/inch.

All covers were tested identically to provide comparisons of concept performance using the following procedure:

- Apply load to 0.0016 inch/inch strain
- Impact central bay with 3-fragments
- Unload, inspect and record damage
- Apply fatigue spectrum loading representing return to base and limited action
- Apply limit strain (0.004 in/in)

PROGRAM RESULTS

Flat Panel Results

Material System
There was considerable variation in the extent of visible and internal damage from one material system to another. As shown in Figure 14, the area of internal delaminations

460

resulting from fragment impact varied by as much as a factor of two. Internal delamination for all material systems are compared in Figure 15. Generally, the AS1/3501-5A baseline graphite/epoxy sustained the least damage of the material systems tested.

Residual compression strength depends on the notch-sensitivity of the laminate as well as damage size. The ballistic damage resulting from the 3-fragment impacts caused an average strength reduction of 84-percent as shown in Figure 16. The test results in the figure have been normalized by the undamaged ultimate strength obtained from coupon tests. The observed differences in damage size exhibited by the several material systems did not translate to comparable variations in residual strength. APC-2 for example incurred appreciable physical damage but retained higher residual strength.

As all panels employed the same stacking configuration, the results indicate that the influence of fiber/resin system on residual compression strength following this type of damage was small for the composite materials evaluated. This is in contrast to the effects of low-energy impact damage (LEID) for which there is extensive evidence that tough resin systems (PEEK, for example) provide significant improvements in residual compression strength, primarily as a result of reduced impact damage.

The test results also provided information on the effects of impacting panels loaded in compression at the time of impact. The tests show that applied stress has little effect unless its magnitude is approximately 80-percent of the residual static strength of the laminate impacted without preload. In other words, the compression impact fracture threshold (sufficient preload at impact to cause catastrophic failure) for all materials was above 80 percent of the static residual strength. This is consistent with results reported in Reference 3 for tension and shear loaded composite panels tested in a similar fashion.

Cyclic compression loading after impact did not cause noticeable damage growth nor did it reduce residual compression strength. A comparison of residual strengths for both fatigue-cycled and non-fatigue-cycled test panels is shown in Figure 17. The fatigue spectrum employed for these tests simulated 200 fighter sorties and produced compression loads in excess of 80-percent of the static residual strength.

Survivable Concepts

Three of the four concepts evaluated showed significant improvements in compression ballistic damage tolerance relative to the hard skin AS1/3501 baseline. As shown in Figure 18, the compliant skin concepts with integral stiffening (CSIS and CSIS/BS) achieved much greater failure strains than the baseline laminate. The incorporation of buffer strips into hard skin laminates (HSBS) provided improvement in residual failure strain. Stitching within the buffer strip provided further improvement. The Energy Absorbing Structure concept demonstrated no improvements in compression ballistic damage tolerance over the baseline.

Compliant (soft-skin) laminates in compression were shown to be very tolerant of ballistic damage. These laminates have a high percentage of ±45-degree plies with only a small percentage of 0-degree plies distributed within the skin or web region. Such concepts have previously demonstrated good damage tolerance in tension loading (References 4, 5) providing significantly higher failure strains than achieved with laminates having distributed 0-degree plies.

The CSIS/BS concept, a soft-skin design with no 0-degree plies in the soft region, performed particularly well. This concept is being developed by Grumman under their High Strain Wing Development program for Naval Air Development Center. Results from seven residual compression strength tests substantiated the high level of ballistic damage tolerance in compression. It was noted during the residual strength testing that damage growth initiated from the ballistic damaged region and slowed at the soft skin/buffer strip interface, but final failure was only a few percent above the initial damage growth threshold.

HSBS was the only concept tested which exhibited a capability to arrest propagating damage. Following arrestment, the panels sustained load until the applied load was increased sufficiently to cause extension of the local delamination buckles beyond the outermost edge of the buffer strip. Arrestments were equally effective when catastrophic damage growth initiated from high preloads (less than 85 percent static residual strength) at impact or from subsequent residual static strength testing.

The compression impact fracture threshold for all concepts was above 85 percent of the static residual strength. Compression loads at impact below 85 percent of the static residual strength did not affect residual compression strength. Only one concept, HSBS, demonstrated a distinct progressive decline in static residual strength with a progressive increase in preload above 85 percent.

Compression load cycling (characteristic of 200 fighter sorties) following ballistic impact did not degrade the residual static strength of any concept tested. Neither internal nor external damage growth was detected even though the regions around the flaws exhibited substantial local deformation during the cyclic test.

Component Cover Evaluation

The performance of the three best-performing survivable concepts (CSIS, CSIS/BS, HSBS) was verified by ballistic testing large covers attached to a multi-loadpath box-beam component. Figure 19 shows representative ballistic impact damage and final panel failure for box-beam tests. In general, the box-beam tests confirmed the results obtained from the 12 x 20-inch panel tests as the small panels were designed to minimize boundary effects and test results were corrected for finite-width effects. On this basis, Figure 20 shows the good correlation between small-scale and large-scale results. Failure strains were identical between small-scale and large-scale for the baseline and hard-skin with buffer strip (HSBS) concepts. The soft-skin concepts did not fail under the 0.004 limit strain applied during component testing. This latter result was predictable based on the small panel tests.

The failure mode for the four covers was buckled delaminations, identical to the failure mode observed in flat panel tests. The failure lines extended across the cover, normal to the load direction. Preload of the component to 0.0016 inch/inch strain at fragment impact and load cycling after damage produced no degradation of residual strength. The box beam load response was not affected by the damage in the test cover.

Damage growth arrestment was observed for the HSBS cover design as observed in the 12 x 12-in panel tests. Arrestment occurred at the stitch line border of the buffer strip exposed to damage. Figure 21 shows arrestment of propagating damage at the buffer strips, and also shows the final failure induced under higher load.

DISCUSSION

Several conclusions can be drawn from the analysis and testing performed under this program. The following conclusions apply only to the fragment impact conditions and composite configurations tested in this investigation.

- None of the advanced material systems evaluated offered significant improvements in residual compression strength relative to the baseline graphite/epoxy system. This conclusion pertains to hard skin (42/50/8) laminates approximately 1/4-inch thick.

- Within the constraints of the design criteria utilized in this program, soft skin configurations demonstrated significantly better compression ballistic damage tolerance than the baseline hard skin laminate.

- The hard skin with buffer strip configuration demonstrated moderate improvement in failure strain over the baseline and was the only concept tested that exhibited a failure arrestment feature.

- Compression load cycling representative of 200 fighter sorties was not detrimental to the residual compression strength of any configuration tested.

- Results of component testing demonstrated the potential for achieving operational strain levels up to 0.004 in/in in full-scale wing skins containing large ballistic damage. These results have also shown that testing carefully designed panels can adequately simulate the residual strength performance of large scale structure.

- The HSBS, CSIS and CSIS/BS concepts are weight and cost effective for battle damage tolerance enhancements compared with the hard skin baseline. No single configuration achieved the highest damage tolerance at the least weight and manufacturing cost. Concept selection must therefore rely on weight, cost, and performance penalities traded against desired battle damage tolerance.

REFERENCES

1. M. R. Allen, D. T. Sawdy, S. J. Bradley and J. G. Avery,"Survivability Characteristics of Composite Compression Structures," Final Report AFWAL-TR-88-3014, JTCG/AS-87-T-005.

2. S. J. Bradley and J. G. Avery, "Design Guide For Survivable Structures in Combat Aircraft," Final Report AFWAL-TR-84-3015.

3. S. J. Bradley, J. G. Avery, "Survivable Composite Structure, Test and Analysis Report," AFWAL-TR-84-3014.

4. J. G. Avery, S. J. Bradley and K. M. King, "Battle Damage Tolerant Wing Structural Development Program," Final Report, Navy Contract N00019-75-C-0178, Boeing Document D180-26069-1, 1979.

5. Bruno, J., "Conceptual Design of a Composite High Strain Wing for Multi-Mission-Type Aircraft," NADC-81088-60, February 1981.

ACKNOWLEDGMENTS

COMBAT SURVIVABLE STRUCTURE

- LOAD AT IMPACT
- RESIDUAL STRENGTH
- CYCLIC LOADING
- ABDR

CAPABILITY

DYNAMIC THRESHOLD

STRESS

REQUIREMENTS

TAKE OFF

MISSION TIME

LANDING
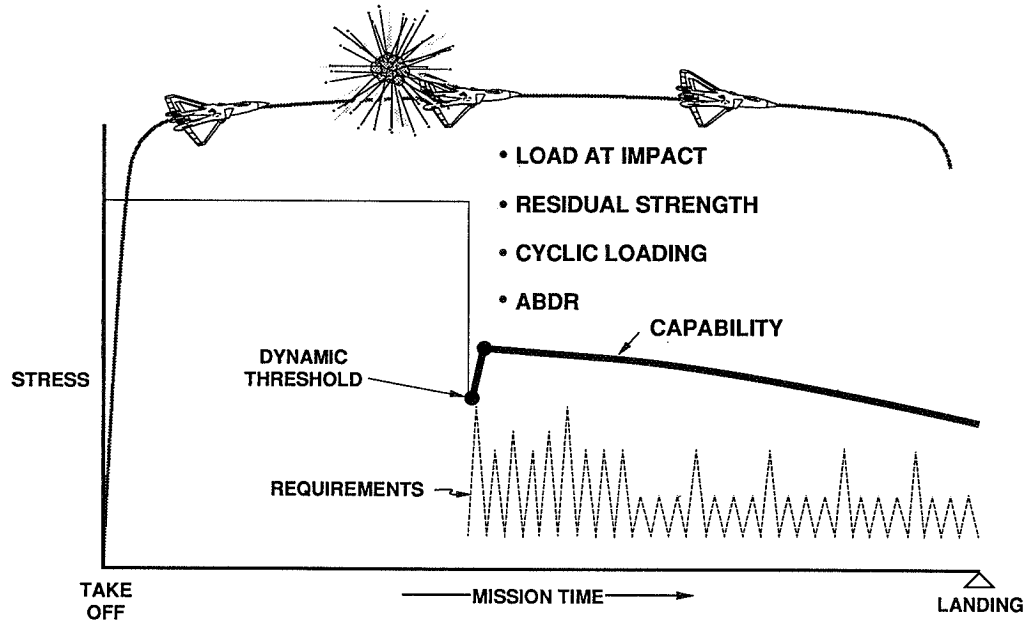
Figure 1   Combat Damage Tolerance Requirements

PROGRAM APPROACH
MULTIPLE FRAGMENT BALLISTIC IMPACTS UNDER LOAD

PART I - PANELS	PART II - COMPONENTS
MATERIAL EVALUATION	
CONCEPT EVALUATION	SCALE-UP VERIFICATION
-12 X 20 - IN PANELS	- 30 X 114 - IN BOX - BEAMS (71 - IN TEST SECTION)
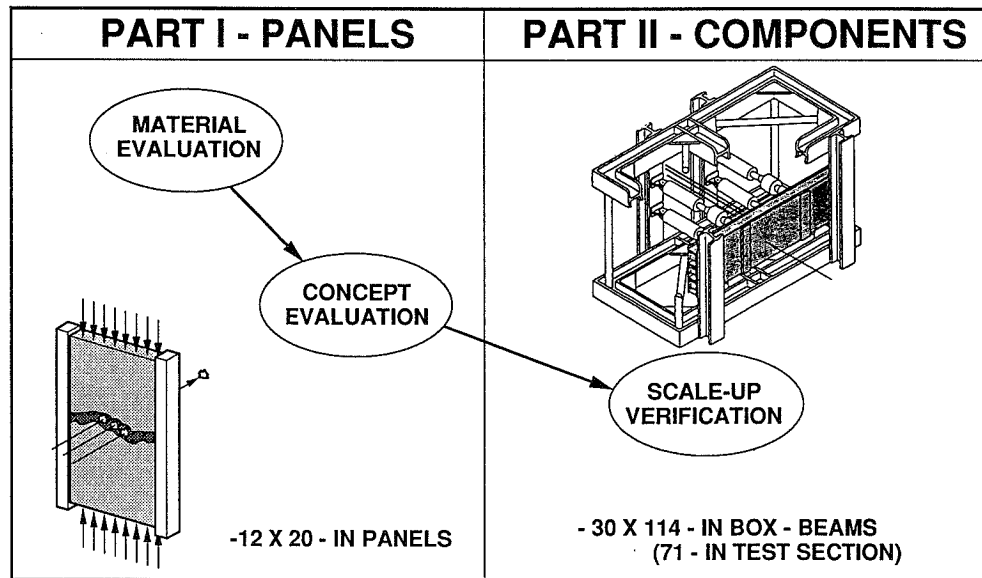
Figure 2   Program Included Panel and Component Evaluation

466

PROGRAM SCHEDULE

1984	1985	1986	1987	1988
PART I - PANELS				
		PART II - COMPONENTS		
				TECHNOLOGY CONSOLIDATION

Figure 3

BALLISTIC TEST CONDITIONS

CYLINDRICAL FRAGMENTS

TYPICAL PATTERN

1.7

1.3

26°
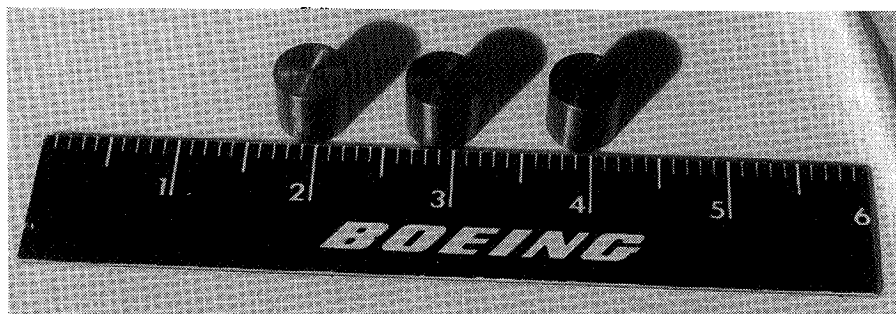
- 230 - GRAIN
- STEEL
- 2500 - FPS
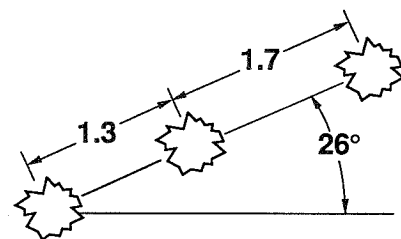
Figure 4   Multiple-Fragment Impact Test Conditions
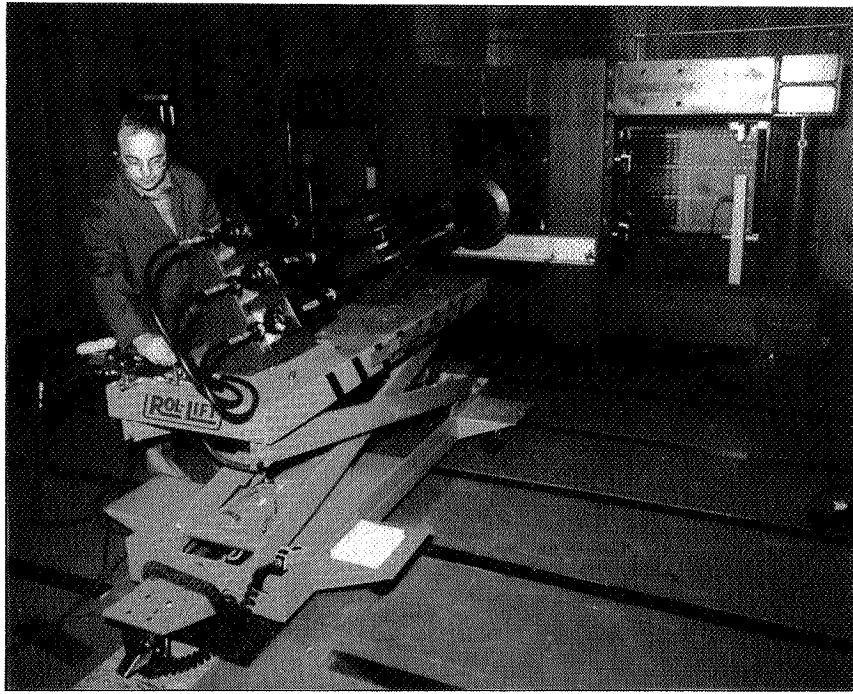
Figure 5   Three-Barrel Launcher System

ENERGY ABSORBING CONCEPT

COMPRESSED FOAM
PLIES (FOR HYD-RAM
DAMAGE RESISTANCE)

HARD SKIN
AS1/3501-5A
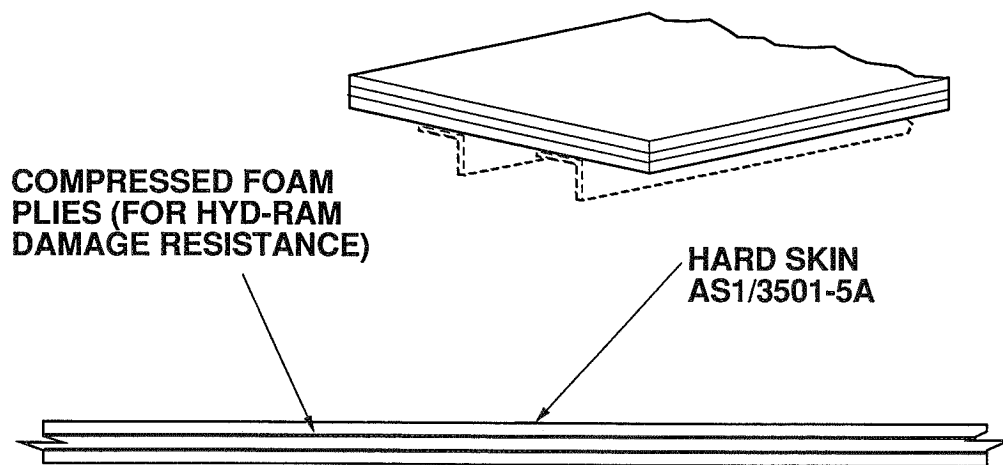
Figure 6   Energy Absorbing Structure (EAS)

HARD SKIN
BUFFER STRIPS AND STITCHING

S-GLASS BUFFER STRIP

**HARD SKIN
IM6/3501-6**

KEVLAR STITCHING
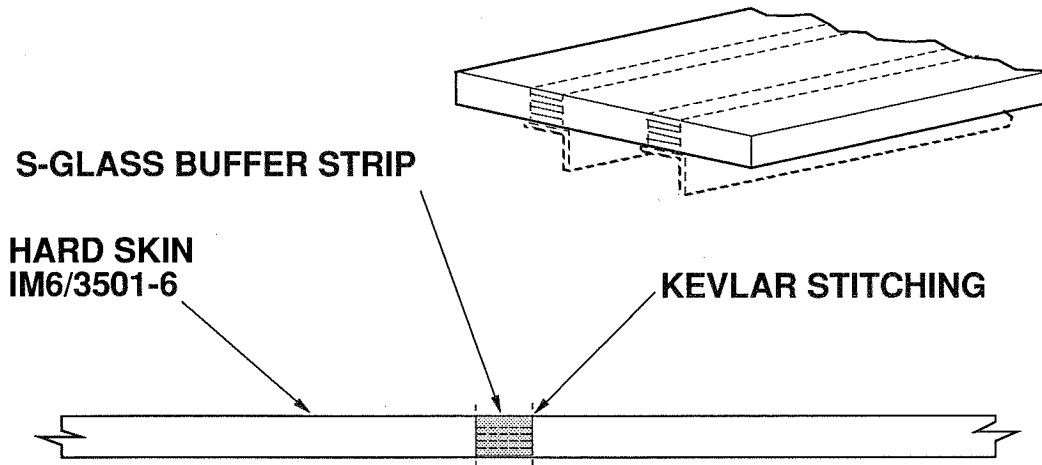
Figure 7   Hard Skin with Buffer Strips (HSBS)

SOFT SKIN

0-DEG "PLANKS

**SOFT SKIN
AS4/PEEK
(APC-2)**
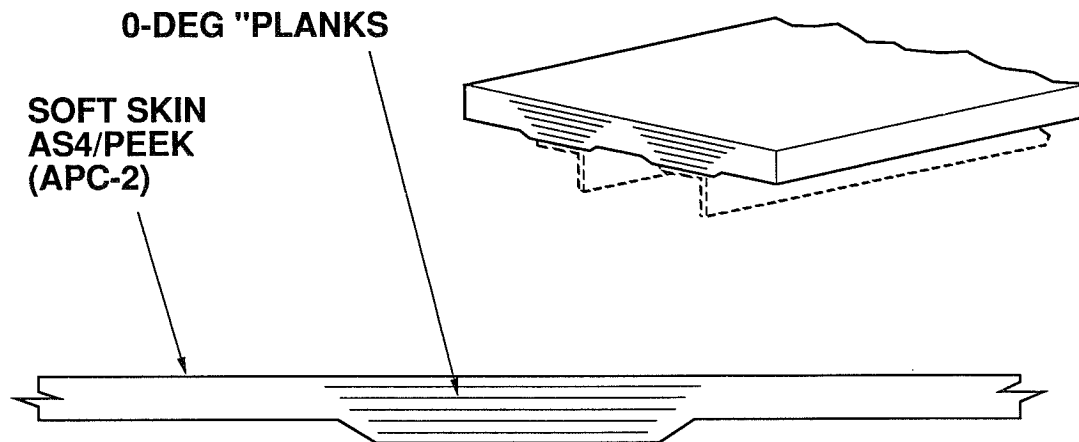
Figure 8   Compliant Skin with Integral Stiffening (CSIS)

469

SOFT SKIN
BUFFER STRIPS AND STITCHING

HIGH STRAIN WING DESIGN
GRUMMAN/NADC

S-GLASS BUFFER STRIP

KEVLAR STITCHING

SOFT SKIN
AS1/3501-5A
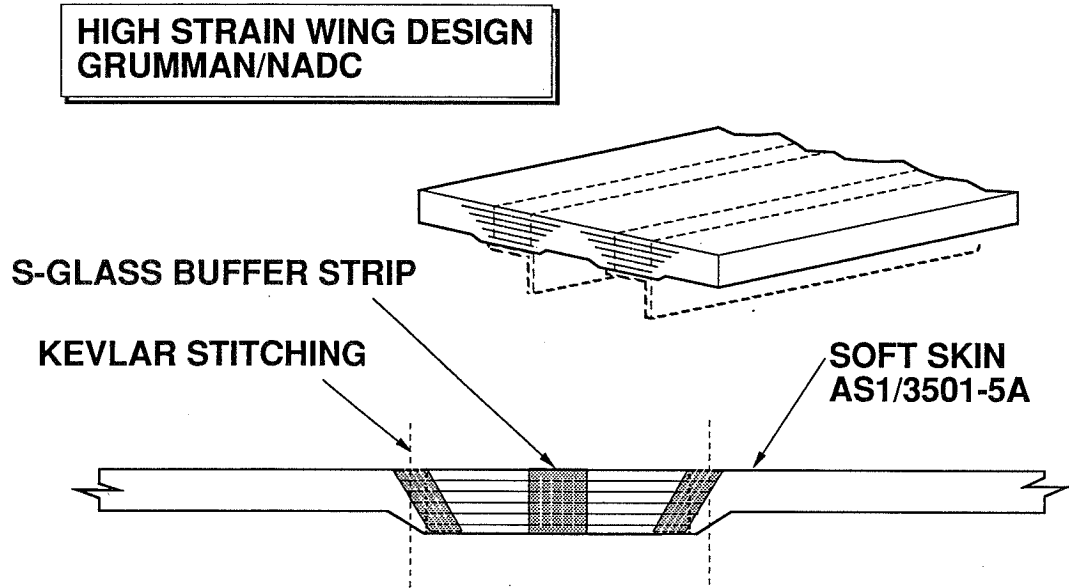
Figure 9   Compliant Skin with Integral Stiffening/Buffer Strips
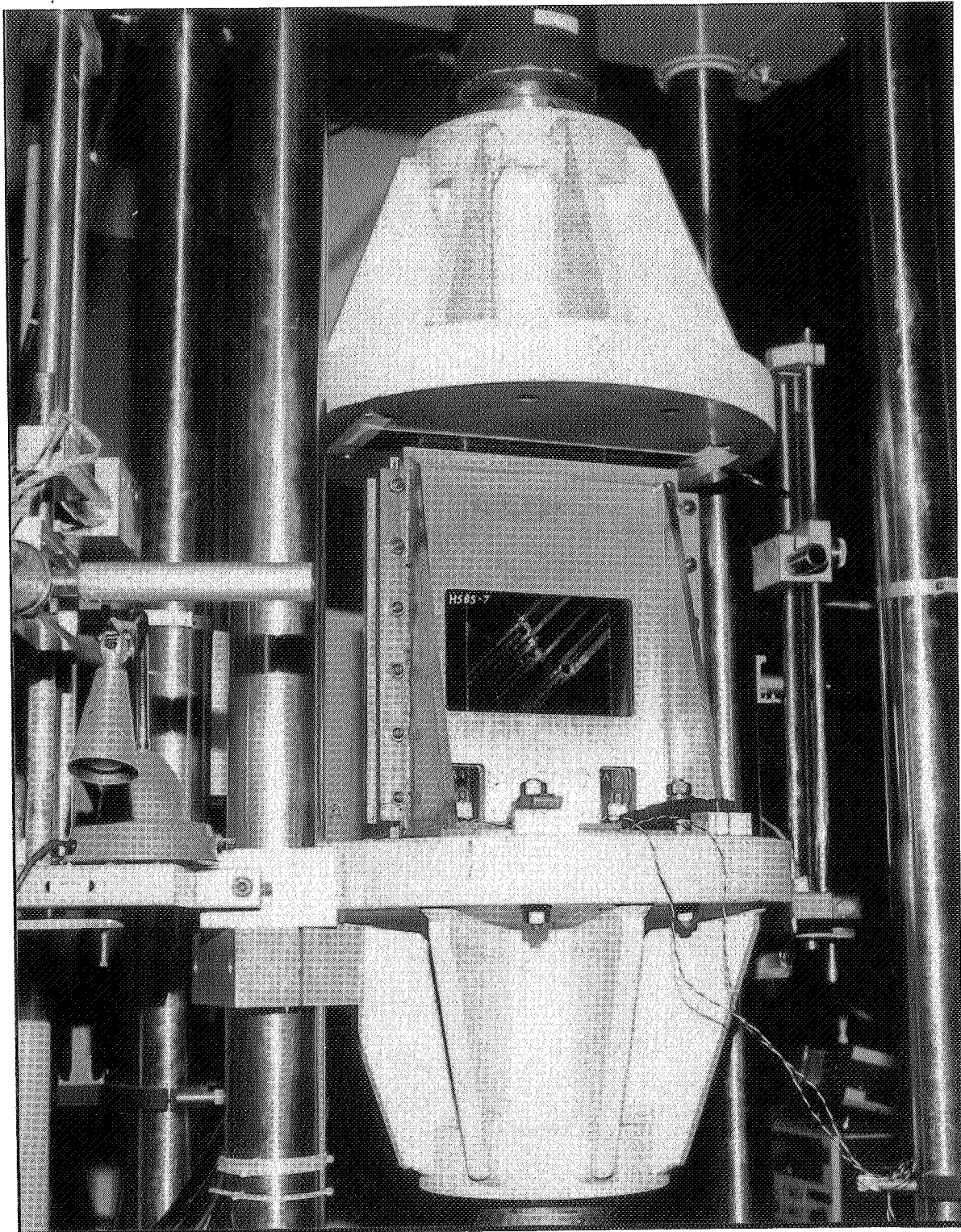
Figure 10   Typical Panel Test-Fatigue Cycling

471
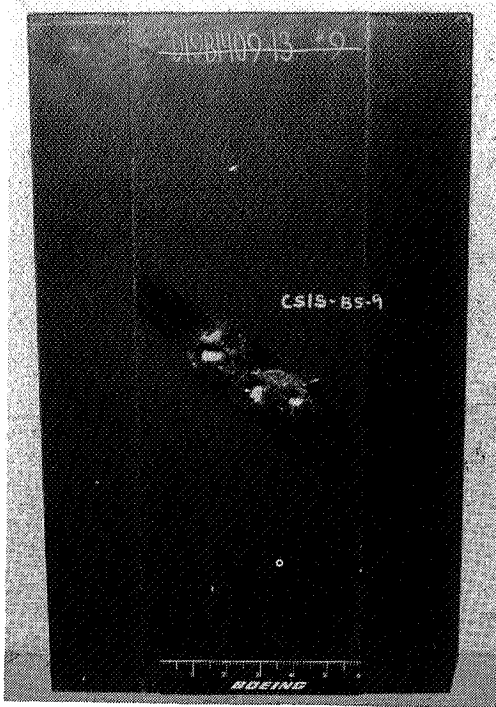
TEST PANELS

IMPACTED PANEL
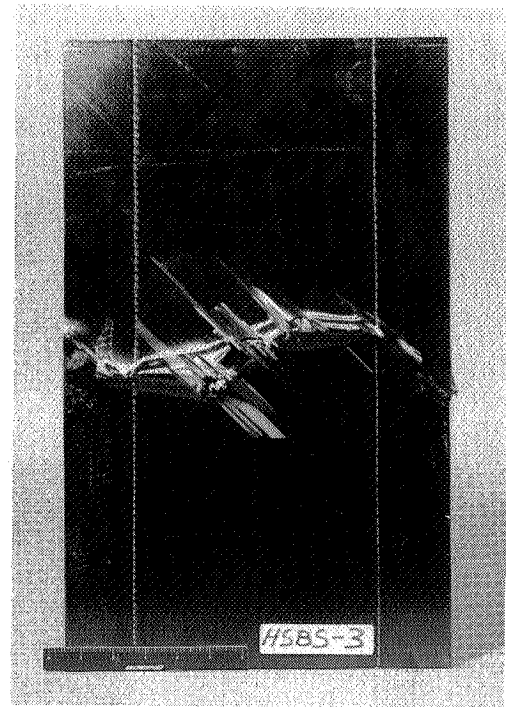
FAILED PANEL

Figure 11   Representative Test Panels Following Impact or Compression Failure

ORIGINAL PAGE
BLACK AND WHITE PHOTOGRAPH
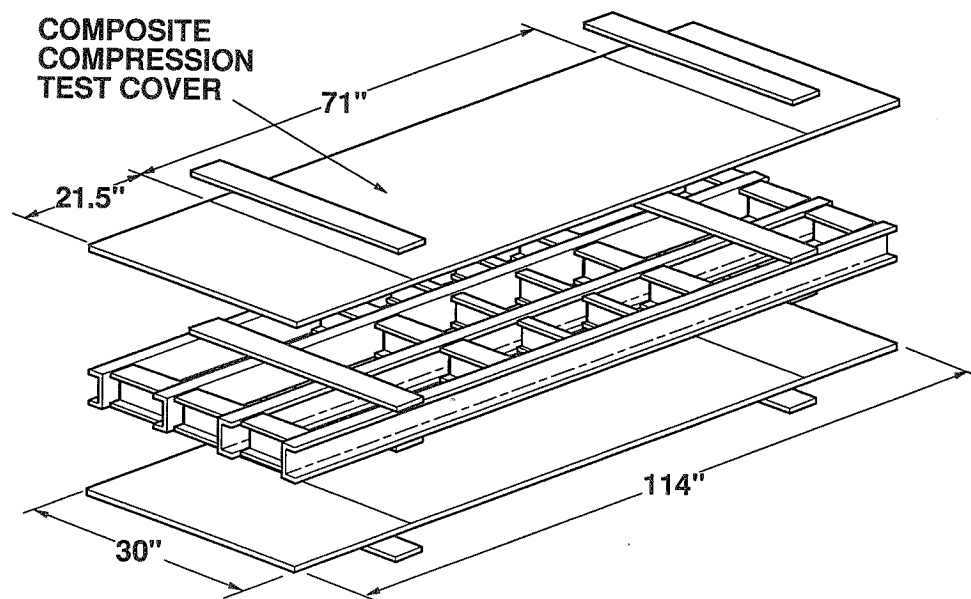
Figure 12   Box-Beam Test Component

472

TEST FIXTURE AND COMPONENT
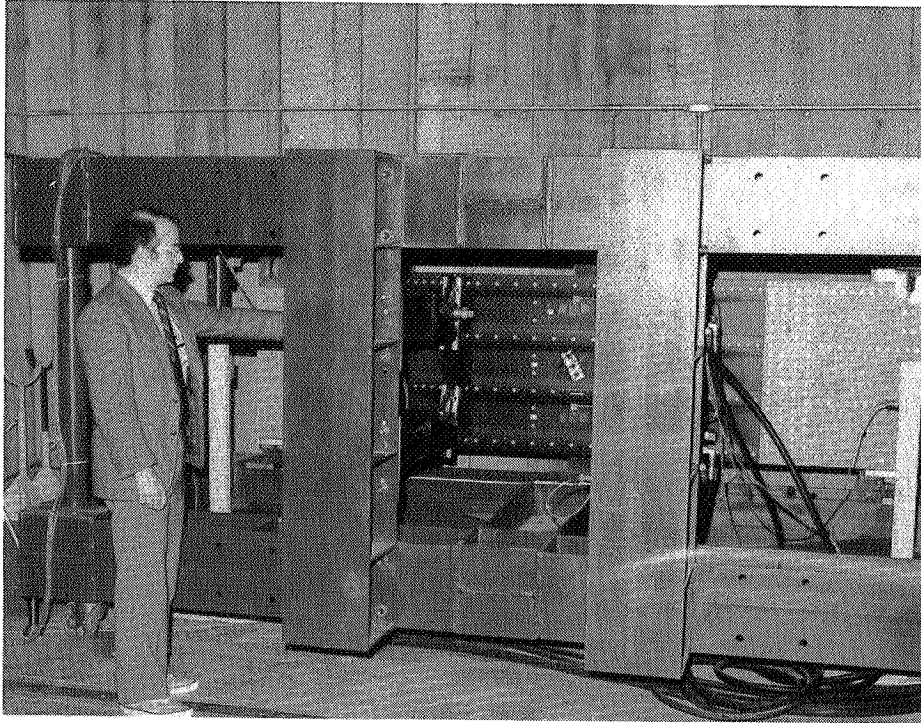
Figure 13   Test Components in Load Fixture

AS1/3501-5A
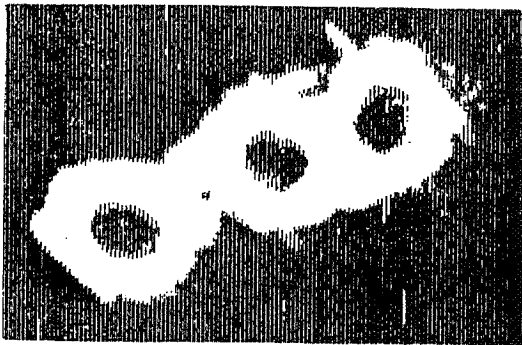
8 INCHES^2

IM6/HX1518

15 INCHES^2

Figure 14   Damage Size Variation - C-Scan Results

473

Figure 15   Damage Size Variation – Comparison of Materials
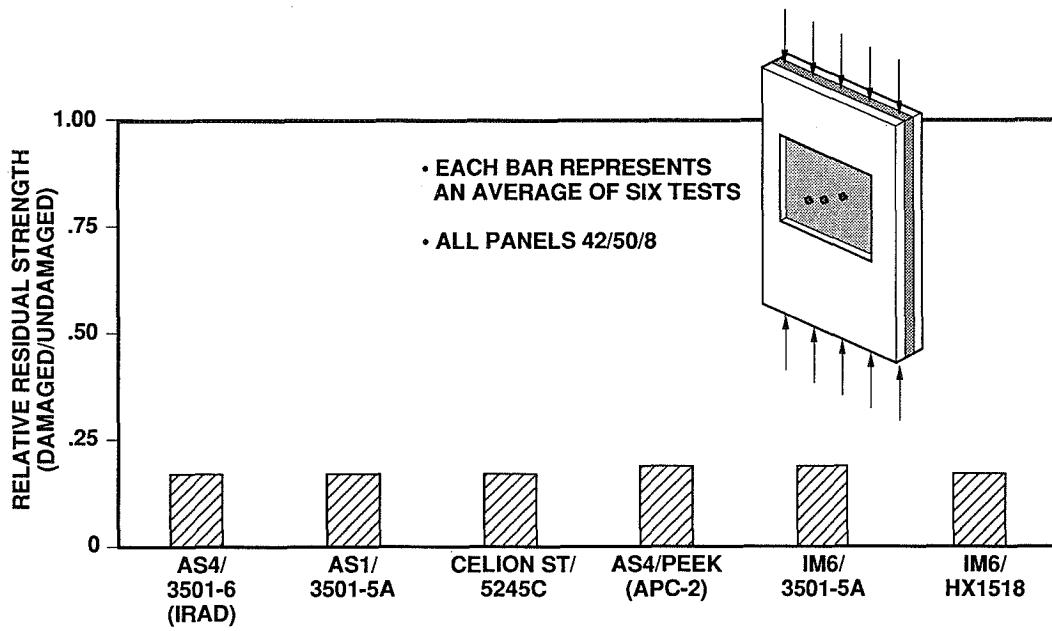
Figure 16   Residual Compression Strength Results

474
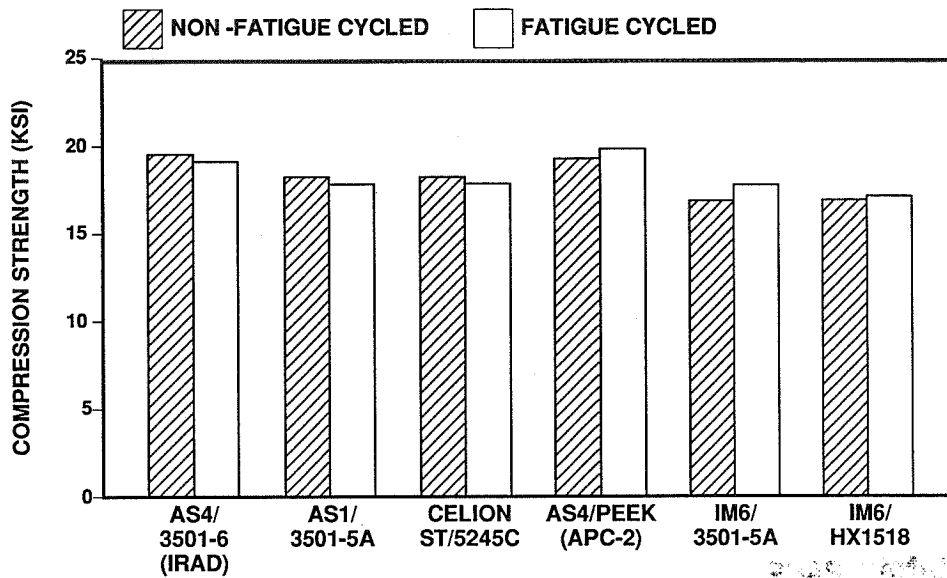
Figure 17   Effect of Fatigue Cycling on Residual Compression Strength
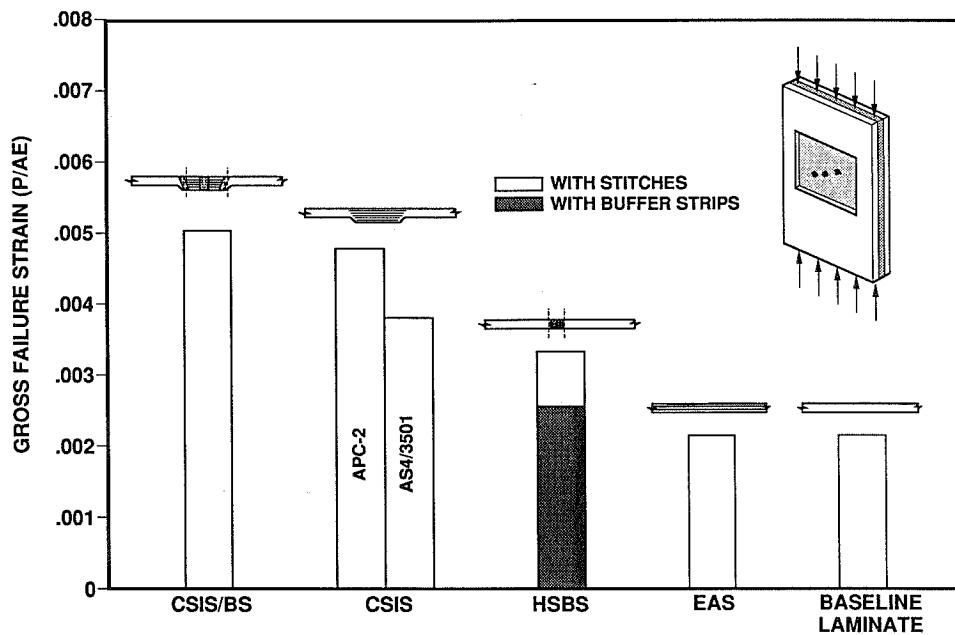
Figure 18   Residual Strength Comparison of Concepts

475

BASELINE COMPRESSION COVER TEST

BALLISTIC IMPACT DAMAGE

ORIGINAL PAGE
BLACK AND WHITE PHOTOGRAPH
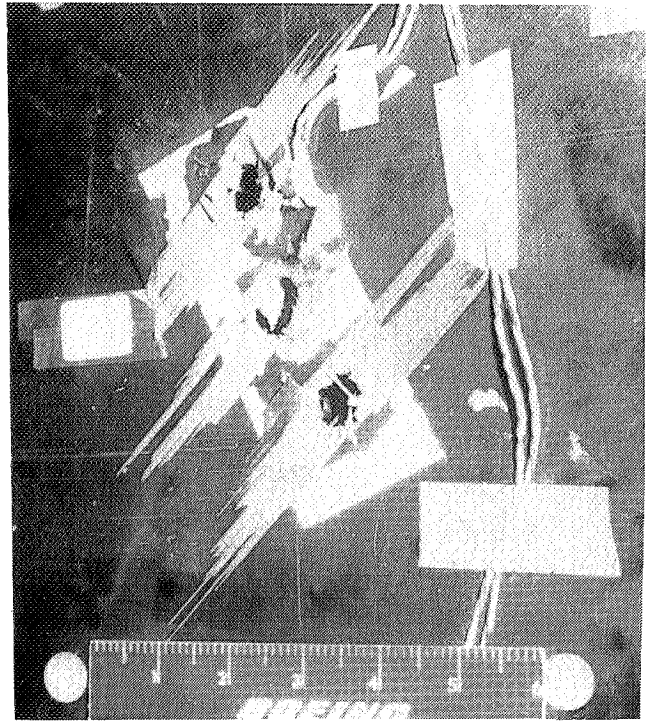
ORIGINAL PAGE IS
OF POOR QUALITY

FAILED COVER
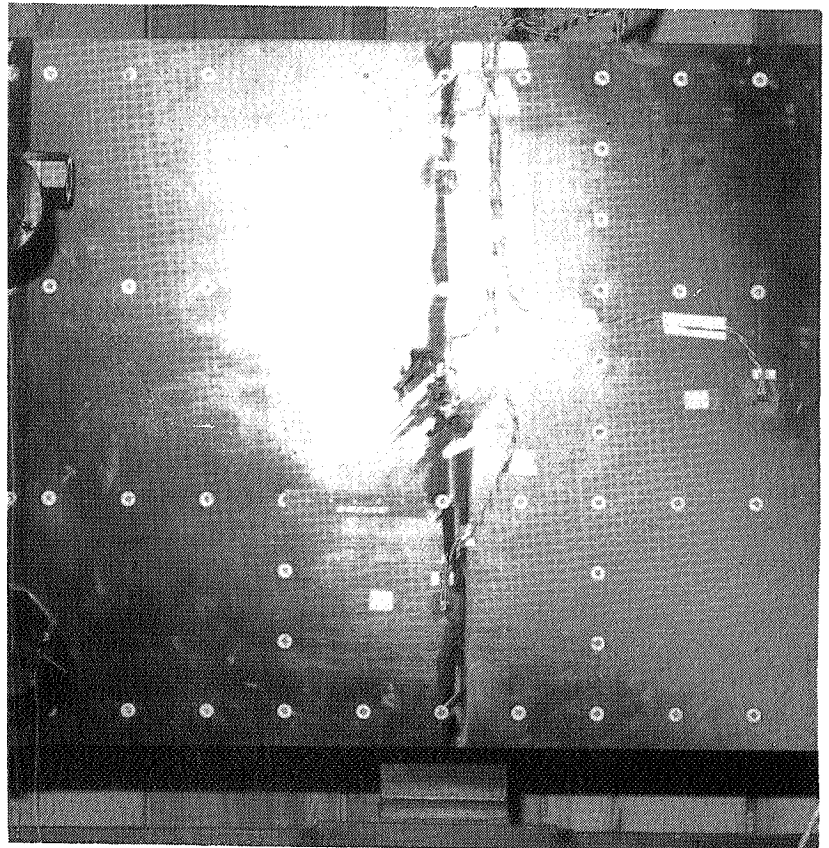
Figure 19   Representative Component Damage and Failure

476

COMPRESSION COVER TESTS
PERFORMANCE COMPARISON
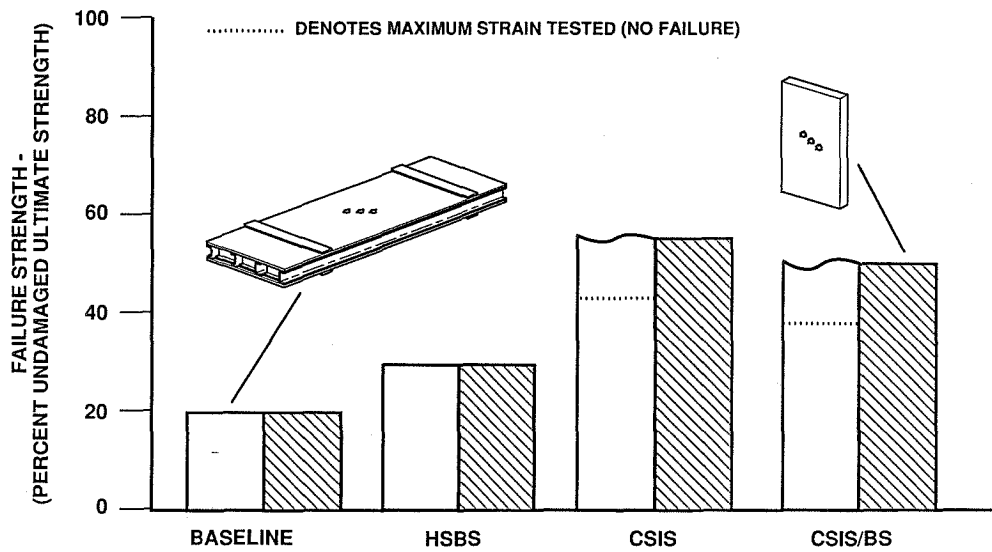
Figure 20   Comparison of Component Test Results

COMPRESSION COVER TEST
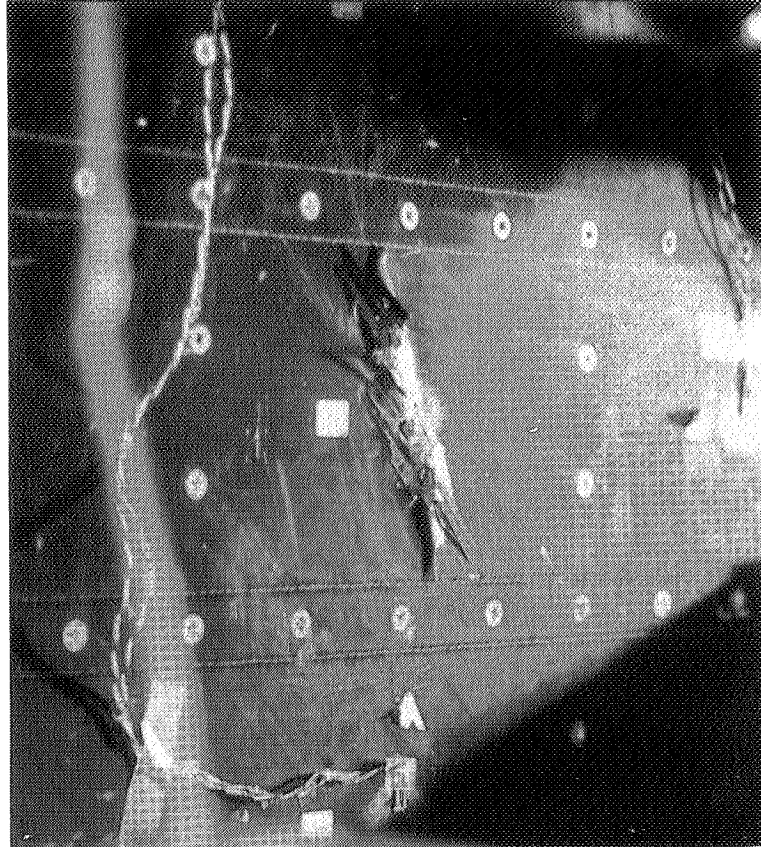
DAMAGE GROWTH AND ARRESTMENT AT BUFFER STRIP
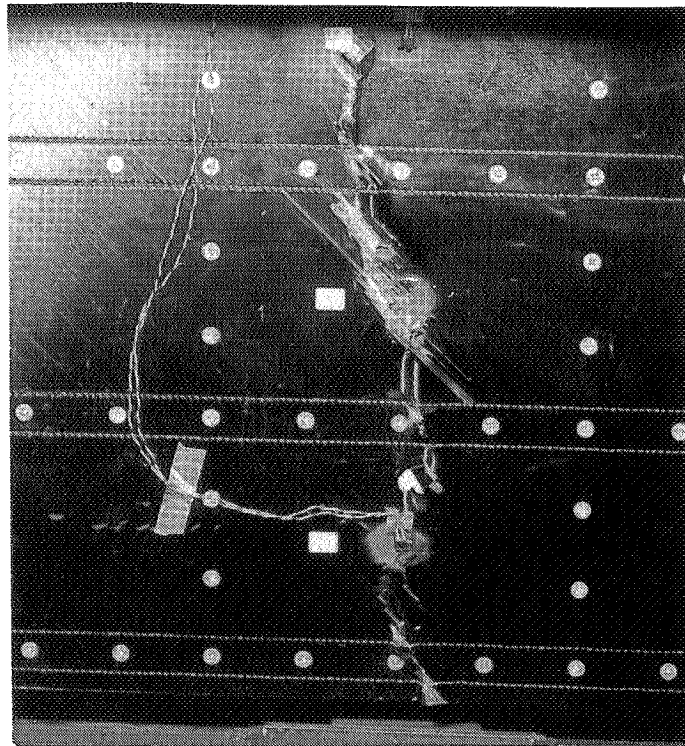
FAILED COVER

Figure 21   Failure Arrestment at Buffer Strips

478

DAMAGE TOLERANCE CERTIFICATION METHODOLOGY FOR COMPOSITE STRUCTURES*

Han Pin Kan and Robin S. Whitehead
Northrop Corporation

Edward Kautz
Naval Air Development Center

ABSTRACT

An advanced certification methodology has been developed for composite structures to include the effects of impact damage. The methodology has the capability to determine the reliability of impact damaged structure at any prescribed load level and impact threat, which may be specified in terms of impact energy or C-scan damage area. In addition, the methodology can also calculate the allowable impact threat level at a given applied load and specified reliability. The developed damage tolerance certification methodology was demonstrated on the F/A-18 inner wing. The results of the methodology demonstration showed that the F/A-18 inner wing has excellent damage tolerance capability.

INTRODUCTION

The application of composite materials to primary aircraft structures requires proven certification procedures to demonstrate their structural integrity. The problem of a certification methodology is to demonstrate, with a high degree of confidence, adequate static strength, fatigue life and damage tolerance capability by test and analysis. For metal structures, a successful structural certification methodology that provides this confidence has evolved over the years. Because of the inherent differences between composites and metals, direct application of the metallics certification methodology to composites is limited. Consequently, the Navy funded two programs (References 1 and 2) to address the issue of certifying undamaged composite structures. In these programs, various approaches to static strength and fatigue life certification were evaluated to determine their capability to certify composite structures. The results of these studies were used to develop a certification methodology for undamaged composite aircraft structures.

Subsequently, the Navy funded two additional programs (References 3 and 4) to account for the effects of impact damage on the static strength and fatigue life of composite structure. The objective of these programs was to expand the previously developed certification procedures for composite structures (References 1 and 2) to include the effects of in-service impact damage on the static strength and fatigue life of composite structures. Specifically, the objective was to establish impact damage requirements for structural certification, which were then integrated into an advanced certification methodology for composite structures. This improved methodology permits certification of impact damaged composite structures with the same level of confidence as undamaged structures and ensures that the threat of in-service low-velocity impact is adequately addressed.

METHODOLOGY DEVELOPMENT

The integrated damage tolerance reliability analysis method developed in Reference 3 was an extension of the previously developed methodology for undamaged structures (Reference 1). A summary of the analysis methodology is presented in Figure 1. The method integrates a post-impact strength prediction analysis (Figure 1a), post-impact strength data scatter (Figure 1a), and the impact threat distribution (Figure 1b) into a single reliability computation (Figure 1c). The following sections describe the development

Post Impact Strength Prediction

The static strength prediction of full scale composite structure containing impact damage was based on the analysis methodology developed by Northrop in Reference 5. A summary of this analysis is shown in Figure 2. The analysis is conducted in two parts because the overall post-impact strength of full scale composite structures can be significantly influenced by structural configuration. It was observed in Reference 5 during static compression tests of impact damaged built-up structure, that failure, in many cases, occurred in two stages. At a certain applied load, local failure initiated at the impact damage followed by damage propagation to the closest spars, where it was positively arrested. After further applied loading, final structural failure occurred.

Initial failure was predicted in Reference 5 using a semi-empirical elastic stiffness reduction technique. It combines all internal damages resulting from a low-velocity impact into an equivalent region of reduced elastic stiffness. The localized stiffness reduction caused a stress concentration effect, which perturbs the local stress field, thereby reducing the overall laminate strength. The severity of stiffness reduction, for a given material system and impact condition, depends on the impact energy level. The influence of other parameters that affect the post-impact compression strength of a laminate were empirically incorporated. The parameters considered were laminate lay-up, laminate thickness, material toughness (G_{IC}), support conditions, and impactor size.

The empirical relationship between the post-impact compression strength and each parameter was obtained in a single functional form through extensive data correlation. The model is expressed as

$$\sigma_f = \sigma_o/[1 + C_1C_2C_3C_4C_5W_e] \tag{1}$$

where

σ_f is the failure stress of the impact-damaged laminate
σ_o is the failure stress of the undamaged laminate
C_1 is the laminate lay-up parameter
C_2 is the full penetration stress concentration parameter
C_3 is the laminate thickness parameter
C_4 is the material toughness parameter
C_5 is the impact energy parameter
W_e is the impactor size parameter.

To examine the overall predictive capability of the model, the failure strength in Equation (1) was expressed in terms of a single independent variable, Z, and written as

$$\sigma_f = \sigma_o/(1 + Z) \tag{2}$$

where

$$Z = C_1C_2C_3C_4C_5W_e.$$

The experimental data are then correlated in terms of the compounded variable Z. Measured failure strains are plotted against the variable Z in Figure 3. The prediction using Equation (2) is also shown in the figure. The figure shows that the semi-empirical model describes the general data trend very well.

This energy based stiffness reduction model for post-impact compression strength prediction was further modified (Reference 3) to allow C-scan damage area as the independent parameter. In its original form, the stiffness reduction model is given by Equation (1). For the damage area based model, it was assumed that the influence of C_1, C_2, and C_3, remain unchanged. That is, the post-impact strength based on damage area is influenced by the laminate lay-up, thickness and full penetration stress concentration in the same manner as post-impact strength based on impact energy. The parameters C_4, C_5 and W_e in the damage area based model are refined as a single parameter, which depends on the damage size and material fracture toughness (G_{IC}). Let $\lambda = C_4C_5W_e$, then Equation (1) can be rewritten as

$$\sigma_f = \sigma_o/(1+C_1C_2C_3\lambda) \tag{3}$$

the parameter λ is determined as a function of damage area by fitting strength data for each material to the expression

$$\lambda = m_1 A^{m_2} \tag{4}$$

where A is the damage area, and m_1 and m_2 are material dependent fitting constants.

The parameter λ is determined by writing Equation (3) as

$$\lambda = \left[\frac{\sigma_o}{\sigma_f} - 1\right] / C_1 C_2 C_3. \tag{5}$$

A fitting technique was applied to post-impact strength data of several materials to determine the values of m_1 and m_2, which showed that m_1 decreases as the material fracture toughness increases; however, m_2 did not change significantly with G_{IC}. The overall data are then fitted into the equation

$$\lambda = m_1 A^{m_2} (G_{IC})^{m_3} \tag{6}$$

where the values of m_1, m_2 and m_3 were obtained by using the least squares method
thus,

$$\sigma = \sigma_o / \left[1 + C_1 C_2 C_3 m_1 A^{m_2} (G_{IC})^{m_3}\right]. \tag{7}$$

To examine the overall predictive capability of the C-scan damage area based model, the failure strength in Equation (1) was expressed in terms of a single independent variable, D, and written as

$$\sigma_f = \sigma_o / (1 + D) \tag{8}$$

where

$$D = C_1 C_2 C_3 m_1 A^{m_2} (G_{IC})^{m_3}. \tag{9}$$

The experimental data were then correlated in terms of the compounded variable D. Measured failure strains are plotted against the variable D in Figure 4. The prediction using Equation (8) is also shown in the figure. The figure shows that the semi-empirical model describes the general data trend well.

The damage propagation arrestment mechanism, shown in Figure 2, is provided by the stiffeners through increased local stiffness due to the presence of the stiffeners and the clamping force of the fastener that prevents out-of-plane displacement of the delaminations. After the initial failure, further increase in the applied load causes load redistribution within the structure. With the arrested damage zone acting as a stress concentrator, severe concentration builds up near the spars, and the final failure mode is compression failure outside the damaged bay. The failure load is controlled by the severity of the stress concentration, similar to the failure of specimens with an open hole.

Structural configuration effects on post-impact strength were incorporated semi-empirically in the stiffness reduction model in Reference 5. In this extension of the stiffness reduction model, the impact damage is assumed to act as a slit after initial failure and arrest as shown in Figure 2. After the initial failure and arrest, the damaged bay is assumed to be totally ineffective, with the slit (representing the arrested impact damage) causing strain concentration in the spar and adjacent bays. Loss of load-carrying capacity of the damaged bay is a conservative assumption, since experimental data (Reference 5) indicate that some load continues to be transferred through the damaged area. From this assumption, the overall equilibrium of the structure requires that

$$P_{TOT} = P_{sp} + P_1 + P_2 + P_3 \tag{10}$$

where

PTOT is the total applied load
Psp is the amount of load carried by the spars
P1 is the amount of load carried by the adjacent partial bay
P2 is the amount of load carried by the adjacent full bay
P3 is the amount of load carried by the remote partial bay.

The load distribution (P_1, P_2, P_3) is obtained by integrating the stresses along the x-axis in Figure 2 with the stress distribution empirically determined from strain data generated in Reference 5. Final failure is then predicted using an average stress (strain) criterion. As shown in Figure 2, final failure strain is given by

$$\epsilon_0 = \frac{\lambda_1}{a_o} \int_b^{b+a_o} \epsilon_f \left[1 + \lambda_2 \left(\frac{b}{x} \right)^4 \right] dx. \tag{11}$$

Figure 5 shows the overall comparison of the measured and predicted post-impact structural strength. Both the initial and final strains are shown in the figure. The data represent tests from six different materials, three impact locations, three structural geometries and four energy levels. The figure also shows a ± 10 percent band about the predicted strain. It can be seen from the figure that the band covers a majority of the experimental data. This verifies the prediction capability of the model.

Post-Impact Compression Strength Data Scatter

The post-impact compression strength test data generated in Reference 5 and under a Northrop IR&D program (Reference 6) were statistically analyzed to determine the data scatter. Individual and joint Weibull methods were used for the analysis. Post-impact compression failure strains were obtained after the specimens were impacted at energy levels between 20 to 100 ft-lb. The materials tested in the references included six composite systems.

The AS4/3501-6 material was more thoroughly tested; therefore, it was used because it provided the most reliable statistics. Strength data for this material were obtained after 20, 40, 50, 60, 70, 75 and 100 ft-lb of impact. The average post-impact compression failure strain and the individual Weibull distribution of the strength after different levels of impact are shown in Figure 6. The figure also shows the predicted post-impact strength using the stiffness reduction model. In addition, the B-basis strength computed from the joint Weibull analysis is also given in the figure. The results of the individual Weibull analysis show that the shape parameter, a, ranges from 8.2 to 22.9. Figure 6 shows that the scatter varies randomly with the impact energy. No relation could be established between a and impact energy. Based on the above scatter analysis, a Weibull shape parameter $a = 12.0$ was selected for use in the reliability analysis.

Impact Threat Distribution

At the start of the Navy program (Reference 3), no detailed data existed on the actual impact threat encountered by in-service composite structures. Consequently, some scenarios for impact threat distributions were developed. It is clear that the impact threat scenario depends on the location of the structure and its structural configuration. In order to establish realistic impact damage requirements, a structural zoning procedure was selected to categorize the structure. Based on the available data, the impact threat was tentatively divided into three levels — high, medium and low. The probabilistic distributions of these impact threats are discussed below.

To quantify the different levels of impact threat, the probability that a structure is exposed to a given impact was assumed to be described by a two-parameter Weibull distribution in terms of the impact energy. Instead of expressing the distribution by the usual scale (β) and shape (a) parameters, the threat was characterized by two impact energy levels. These are the modal energy level associated with a high

possibility of occurrence (X_m), and the higher energy level associated with a low probability of occurrence (X_p). The relationships between the energy parameters and the Weibull scale and shape parameters can be expressed by the following two equations.

$$X_m = \left(\frac{\alpha - 1}{\alpha}\right)^{1/\alpha} \beta \tag{12}$$

and

$$\beta = \frac{X_p}{[-\ln(p)]^{1/\alpha}} \tag{13}$$

where p is the probability of occurrence of the impact energy X_p.

Combining equations (12) and (13), one obtains

$$\frac{X_m}{X_p} = \left[\frac{\alpha - 1}{-\alpha \ln(p)}\right]^{1/\alpha} . \tag{14}$$

Equation (14) can be solved for α by iteration and β is then obtained from Equation (13). The Weibull distribution for the impact threat on a structure is then defined from the values of α and β obtained.

The three scenarios of impact threats, denoted as high, medium and low, were defined as shown in Table I. The table also shows the computed Weibull parameters corresponding to these threats. The high threat distribution has a modal energy of 15 ft-lb with probability of occurrence for a 100 ft-lb or higher energy impact of 0.1. This is considered to be a conservative estimate of the impact threat imposed on a structure. The medium threat has a modal energy of 6 ft-lb. The impact energy of 100 ft-lb or higher is likely, but small (p = 0.01) for this threat. The low threat is a more realistic estimate of the impact damage threat for composite structures. The low threat has a modal energy of 4 ft-lb, and the likelihood of 100 ft-lb impact is remote (p = 0.0001).

Recently, under a Northrop/MCAIR collaborative program, MCAIR conducted a field survey of in-service impact damage to quantify the impact threat to aircraft structures. In this survey, impact data, in terms of dent depth, from four different in-service aircraft types (F-4, F-111, A-10, and F/A-18) were collected. The dent depth data for the four aircraft types surveyed were for metallic aircraft structures. In order to apply this information to composite structures, an impact threat expressed in terms of impact energy is needed. This was accomplished by using an experimentally established impact energy versus dent depth relationship, which was used to generate an impact energy based exceedance curve. The impact energy based exceedances were converted into a probability distribution and compared with the three threats defined earlier. This comparison is shown in Figure 7. This figure shows that all three assumed threat scenarios are conservative compared to the MCAIR in-service survey results.

An additional impact damage scenario considered was design to a barely visible damage criterion (BVD). This criterion was developed from a series of impact tests conducted by the Navy on F/A-18 composite upper wing skin. The BVD criterion selected was 0.05-inch depth dent with a 100 ft-lb cut-off. The results are shown in Figure 8. In this figure, the BVD energy is expressed in terms of skin thickness. The skin thickness is divided into three regions. For laminates of 0.05-inch thick or thinner, a 0.05-inch deep dent would be a through-penetration damage and the cut-off energy is 30 ft-lb. For skin thicknesses between 0.05- and 0.40-inch the BVD energy is between 30 and 100 ft-lb. Beyond a skin thickness of 0.4 inch, the BVD energy increases rapidly with skin thickness. In this region, the cut-off energy of 100 ft-lb is used as the BVD energy.

The post-impact strength analysis and impact threat scenarios discussed above can now be used to calculate the reliability of impact damaged structure, as shown in Figure 1. By integrating $p(\epsilon)$, the post-impact probability of survival of a structure under an applied strain, ϵ, and P(E), the probability of occurrence of energy level, E, under a given impact threat, over the entire range of impact energies, the impact damaged strength reliability is then given by the joint probability function:

$$R(\epsilon) = \int_0^\infty p(\epsilon)\, P(E)\, dE. \qquad (15)$$

The reliability $R(\epsilon)$ in Equation (15) is evaluated using a numerical integration technique.

Reliability Calculations

Example reliability calculations were conducted on a 21-inch three-spar panel with a spar spacing of 7 inches. The panel represented a typical upper skin/spar attachment for a fighter aircraft. The skin and spare material was AS4/3501-6 with a fracture toughness of 0.75 in-lb/in^2. Skin lay-up was (53/35/12) with a thickness of 0.35 inches. Details of the test article are presented in Figure 9, which was subjected to compression loading.

Figures 10 and 11 show example reliability calculations for this structure. The influence of the impact threat scenario on structural reliability is shown in Figure 10. The figure shows that the reliability is highest when the structure is exposed to a low impact threat. The applied compression strains for B-basis reliability are 3,090, 3,220, and 3,510 micro-in/in for the high, medium and low impact threat, respectively. The influence of fracture toughness (G_{IC}) on damaged structural reliability is shown in Figure 11 for the medium threat scenario. The value of G_{IC} varies from 0.75 to 6.5 in-lb/in^2. This range covers most of the commonly used composite material systems. As shown in the figure, G_{IC} has an influence on the damaged structural reliability. The B-basis applied strain increases from 3,220 micro-in/in for $G_{IC} = 0.75$ in-lb/in^2 to 4,170 micro-in/in for $G_{IC} = 6.5$ in-lb/in^2.

METHODOLOGY DEMONSTRATION

The F/A-18 upper inner wing skin was selected for damage tolerance evaluation. The methodology discussed above was applied to evaluate the reliability of this structure when exposed to an impact threat. A baseline study was conducted, followed by a sensitivity study to examine the influence of various parameters on the impact damaged structural reliability of the upper wing skin.

The F/A-18 inner wing span, from wing root to wing fold, is approximately 106 inches. The skin width at the wing root is approximately 45 inches and at the wing fold is 31 inches. The skin material is AS4/3501-6 with a thickness ranging from 0.36 to 0.78 inches. The skin layup is basically (48/48/4) and varies from (39/50/11) to (48/48/4). The substructure consists of the front, rear and four intermediate spars. The compression strain, at the maximum design ultimate load (DUL), in the inner wing upper skin ranges from below 2,500 micro-in/in to 3,500 micro-in/in. The strain distribution is shown in Figure 12. The inner wing skin was subdivided into forty-five regions for damage tolerance evaluation. The subdivision was based on the substructure arrangement and the thickness distribution of the skin. These subdivisions are shown in Figure 13.

The baseline damage tolerance reliability evaluation was conducted using the medium impact threat scenario. The damage tolerance design requirement use was no structural failure below design ultimate load in the presence of impact damage. The damage tolerance reliability analysis was used to determine

1. Reliability at design ultimate load (DUL)

2. B-Basis damage tolerance strain allowable

3. B-Basis margin of safety at DUL

4. B-Basis damage area allowable at DUL.

Figure 14 shows the 95 percent confidence structural reliability of the upper wing skin at DUL. As shown in the figure, the reliability at DUL is very high for the entire upper skin. The majority of the area has a reliability between 0.95 and 0.99, and the reliability of the entire skin exceeds 0.90. This indicates that the F/A-18 inner wing upper skin can reliability withstand the medium impact threat when subjected to design ultimate load. Figure 15 shows the 95 percent confidence, 0.9 reliability (B-Basis) strain contours for the upper wing skin against the medium impact threat. The compression strains shown in this figure range from 3,100 to 4,000 micro-in/in. Comparing the strains in Figure 12 and Figure 15, it can be seen that the strains in Figure 15 are higher than those shown in Figure 12. This comparison is shown in Figure 16 in terms of margin of safety (M.S.). The M.S. was computed for each subdivision using the values shown in Figure 15 as B-basis allowables and the values shown in Figure 13 as ultimate strain. Figure 16 shows the margin of safety ranges from 0.02 to 0.52. This again indicates the high damage tolerance capability of the F/A-18 inner wing upper skin.

Figure 17 shows the 95 percent confidence, 0.9 reliability damage area allowables for the inner wing upper skin. B-Basis damage area allowables range from 3.6 to 33.2 square inches.

Sensitivity Studies

Sensitivity studies were conducted to examine the influence of various parameters on the impact damage tolerance capability of the F/A-18 inner wing. The influence of different threat scenarios and the influence of changing the damage tolerance design requirements were examined separately.

For the impact threat scenario sensitivity studies, the following threats were evaluated:

1. 100 ft-lb mid-bay impact

2. Barely visible impact damage

3. High threat scenario

4. Medium threat scenario

5. Low threat scenario

6. MCAIR survey threat.

Two subdivisions from the F/A-18 inner wing were selected for this study. Analyses were conducted on these subdivisions for each of the impact threat scenarios to compute the B-basis allowables. The results of this study are shown in Figure 18, which shows a general trend for the severity of the impact threat. As can be seen from the figure, the 100 ft-lb impact is the most severe threat and the MCAIR survey threat is the least severe threat. The B-basis allowable for Subdivision 1 ranges from 2,900 micro-in/in for the 100 ft-lb impact to 5,000 micro-in/in for the MCAIR survey threat. This shows that a factor of 1.7 in the design allowable may result depending on the imposed threat. This trend is similar for Subdivision 2. The barely visible impact damage threat is equally severe as the 100 ft-lb impact for the thickness range of this subdivision. The B-basis allowable based on the high threat scenario ranges from 1.08 to 1.09 times higher than that based on the 100 ft-lb impact. The slight difference in this ratio is due to structural configuration effects. The B-basis strain determined based on the medium threat ranges from 1.15 to 1.17

times higher than that based on 100 ft-lb impact. This ratio increases from 1.29 to 1.34 for the low threat, and further increases from 1.69 to 1.71 for the MCAIR survey threat.

The damage tolerance design requirement sensitivity study was conducted by examining the influence of damage tolerance requirements on the margin of safety of the structure. This was done by analyzing the same two subdivisions for the F/A-18 inner wing upper skin. The damage tolerance design requirements selected were

1. No catastrophic structural failure below DUL (Baseline)

   or $$P_F^S \geq DUL \tag{16}$$

   where P_F^S is the structure failure load.

2. No catastrophic structural failure below maximum service load (MSL) with maximum service load defined as 20 percent above design limit load (DLL)

   or $$P_F^S \geq 1.2 \ DLL. \tag{17}$$

3. No catastrophic structural failure below DUL for structure containing barely visible impact damage (BVD)

   or $$P_{BVD} \geq DUL. \tag{18}$$

4. No catastrophic structural failure below MSL for structure containing BVD

   or $$P_{BVD} \geq 1.2 \ DLL. \tag{19}$$

5. No local failure below DLL and no catastrophic structural failure below MSL

   or $$P_{IF} \geq DLL \ and \ P_F^S \geq 1.2 \ DLL \tag{20}$$

   where P_{IF} is the initial (or local) failure load.

6. No local failure at DUL

   or $$P_{IF} \geq DUL. \tag{21}$$

7. No catastrophic structural failure below DUL for structure containing a 2-inch diameter circular internal damage (C-scan damage area)

   or $$P \ (2\text{-}in.dia) \geq DUL. \tag{22}$$

Requirements 1, 2, 5, and 6 depend on the impact threat assumed in the analysis. In this study, the baseline medium threat scenario was used. The results of this study are shown in Figure 19. In this figure, both the margins of safety computed based on the B-basis allowable strain and on the average value are shown. The results in Figure 19 show consistently that the margin of safety is lowest for the BVD requirement (Requirement 3). They also show that Requirements 2 and 5 result in the highest M.S. and they are in general, equal.

The results presented in Figure 19 show that the imposed damage tolerance design requirement has a very significant effect on the design allowable strain level and calculated margin of safety. The B-basis allowable margins of safety vary from 0.09 to 0.64 for the seven design requirements considered.

An interesting observation can be made from Figures 18 and 19. The F/A-18 inner wing has a positive M.S. for impact damage tolerance for the wide range of threat scenarios and design requirements used in the sensitivity study, including the B-Basis requirements. It can be concluded that the F/A-18 inner wing has excellent damage tolerance capability. However, the F/A-18 wing was designed, in the seventies, to no specified impact threat. The reason for the excellent inherent damage tolerance of the inner wing is that the sizing/strain levels in the wing are driven by other factors (strength, stiffness), which tend to automatically build in damage tolerance capability.

· Since the imposed damage tolerance design requirements significantly influence the structural reliability of impact damaged composite structures, a comparison was made of the USAF, Navy and FAA requirements. These requirements are summarized in Table II.

The impact damage requirements of the three agencies are similar. However, the residual static strength requirement (DUL) specified by the Navy and FAA is more severe than that specified by the USAF (DLL $\geq P_{XX} \geq 1.2$ x DLL). The effect of these different residual strength requirements on the impact damage strain allowable is presented in Figure 20. Strain allowables are shown for the seven residual strength requirements discussed above using the medium threat scenario. In all three agency requirements, no statistical knockdown is applied to the specified residual strength load. Therefore, the average strain allowables in Figure 20 would be applicable. Damage tolerance requirement number 3 represents the Navy and FAA residual load requirement, that is $P_{BVD} \geq DUL$. Damage tolerance requirement number 5 represents the USAF requirement ($P_{IF} \geq DLL$, $P_F^S \leq 1.2$ x DLL) for fighter aircraft. Figure 20 shows that for the F/A-18 inner wing the Navy/FAA impact damage design strain is 3,500 micro-in/in, and the USAF design strain is 5,700 micro-in/in, a difference of 60 percent. For all fourteen requirements shown in Figure 20, impact damage design strain range from 3,000 micro-in/in to 5,700 micro-in/in, a difference of 90 percent.

The results presented in Figures 18 to 20 show that it is very important to realistically assess impact damage tolerance design requirements for an airframe. Damage tolerance is one of many requirements applied to the design of an airframe. Realistic assessments of the damage tolerance threat scenario and residual strength requirements must be made in order to avoid unnecessary weight penalties.

CONCLUSIONS

1. The damage tolerance certification methodology developed can be used for preliminary design, trade studies, impact damage scenario sensitivity studies, and in-service damage assessment.

2. Application of the damage tolerance certification methodology to the F/A-18 composite inner wing showed that it possessed excellent damage tolerance capability.

3. Damage tolerance reliability, strain allowable, and margin of safety are sensitive to both the prescribed impact damage threat scenario and residual static strength load requirements.

REFERENCES

1. Whitehead, R.S., Kan, H.P., Cordero, R., and Saether, E.S., "Certification Testing Methodology for Composite Structures," Report No. NADC-87042-60, October 1986, Volumes I and II.

2. Sanger, K.B., "Certification Testing Methodology for Composite Structures," Report No. NADC-86132-60, January 1986.

3. Kan, H.P., Cordero, R., and Whitehead, R.S., "Advanced Certification Methodology for Composite Structure," Draft Final Report, NADC Contract No. N62269-87-C-0259, September 1989.

4. Rapoff, A.J., et al., "An Improved Certification Methodology for Composite Structures," Draft Final Report, NADC Contract No. N62269-87-C-0258, August 1989.

5. Horton, R.E., Whitehead, R.S., et al., "Damage Tolerance of Composites," Volumes I, II and III, Report No. AFWAL-TR-87-3030, July 1988.

6. Whitehead, R.S., et al., "Advanced Materials Development Program," Northrop IR&D Project No. D-1913, January 1985 through December 1987.

Table I. Impact Threat Scenarios.

	HIGH THREAT	MEDIUM THREAT	LOW THREAT
MODAL ENERGY X_m (ft-lb)	15	6	4
PROBABILITY AT 100 ft-lb $p(100)$	0.1	0.01	0.0001
α	1.264	1.192	1.221
β (ft-lb)	51.7	27.8	16.2

T89-24/27/A

Table II. Comparison of USAF, NAVY and FAA Impact Damage and Residual Strength Load Requirements.

REQUIREMENT	USAF	NAVY	FAA
Impact Damage	• 0.1" Dent Depth	• Clearly Visible Damage at 5 Feet	• Detectable Damage
	• 100 ft-lb Cut-Off	• 100 ft-lb Cut-Off	• No Specified Energy Cut-Off
Residual Strength Load (RSL)	• No Damage Growth to Failure in 2 Lifetimes	• No Damage Growth to Failure in 1 Lifetime	• Apply Required Load Cycling
	• RSL $\geq P_{XX}$ Where: DLL $\leq P_{XX} \leq$ 1.2 x DLL	• RSL $\geq$ DUL	• RSL $\geq$ DUL

T89-24/26/A

(a) POST-IMPACT STRENGTH

$$\epsilon_f = \epsilon_o / (1 + Z)$$

$p(\epsilon)$

Mean

B-Basis

IMPACT ENERGY

(b) IMPACT THREAT DISTRIBUTION

$$P(E) = Exp\left[-(E/\beta_E)^{\alpha_E}\right]$$

OCCURRENCE FREQ.

IMPACT ENERGY

(c) RELIABILITY

R = 0.90 (B-Basis)

$$R(\epsilon) = \int_0^\infty p(\epsilon)\, P(E)\, dE$$

95% RELIABILITY

APPLIED STRAIN
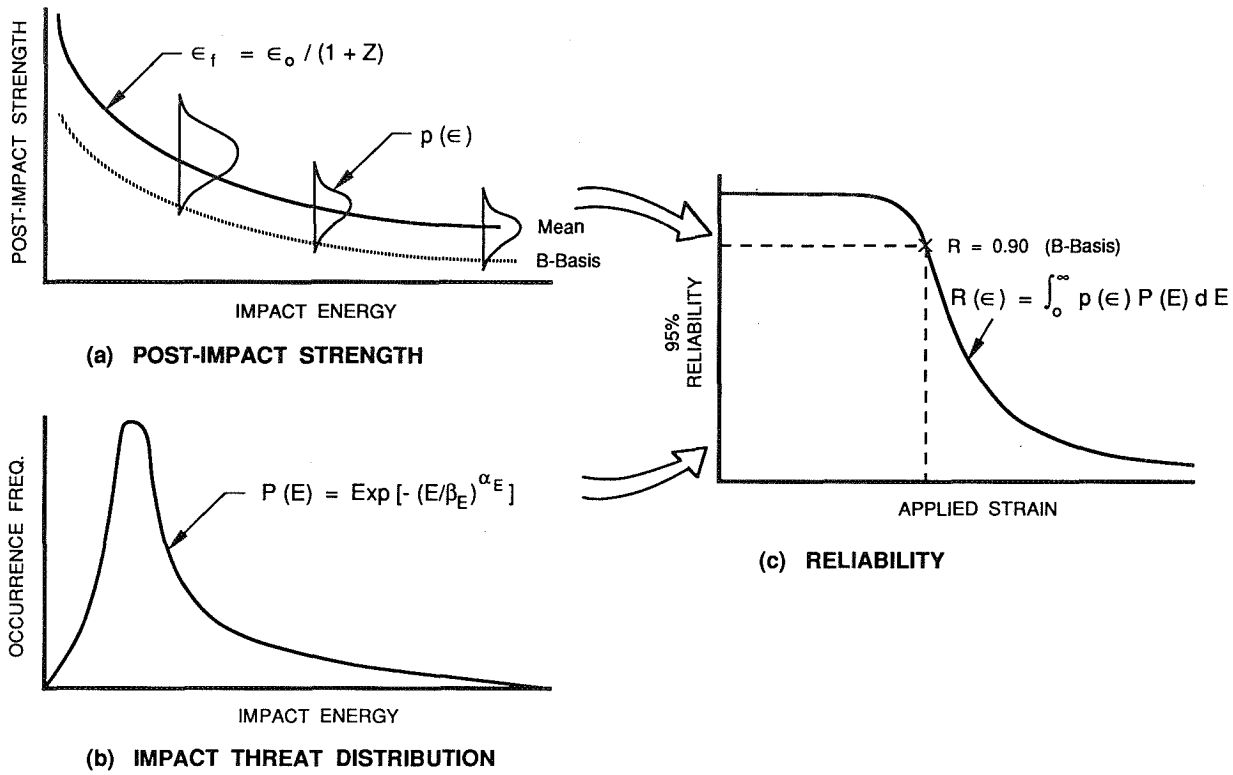
Figure 1. Summary of Integrated Damage Tolerance Reliability Analysis Methodology.

INITIAL FAILURE

$$\epsilon_f = \epsilon_o / (1 + Z)$$

$$Z = \alpha_1 (E_X / E_L)^{\alpha_2} \cdot A(kE)^B \cdot W_e / t^{\alpha_3}$$

$$A = \beta_1 / G_{IC} + \beta_2$$

$$B = \beta_3 + \beta_4 G_{IC} - \beta_5 G_{IC}^2$$

$$W_e = \frac{2 + (1 - d/w)^3}{3(1 - d/w)}$$

$\alpha_1, \alpha_2, \alpha_3, \beta_1, \beta_2, \beta_3, \beta_4, \beta_5$
ARE CONSTANTS

FINAL FAILURE

$$P_{TOT} = P_{SP} + P_1 + P_2 + P_3$$

$$\epsilon_o = \frac{\lambda_1}{a_o} \int_b^{b + a_o} \epsilon_f \left[1 + \lambda_2 \left(\frac{b}{x}\right)^4\right] dx$$

ϵ_f Failure Strain

ϵ_o Ultimate Strain (Undamaged)

λ_1, λ_2 Empirical Constants

T89-24/8/A
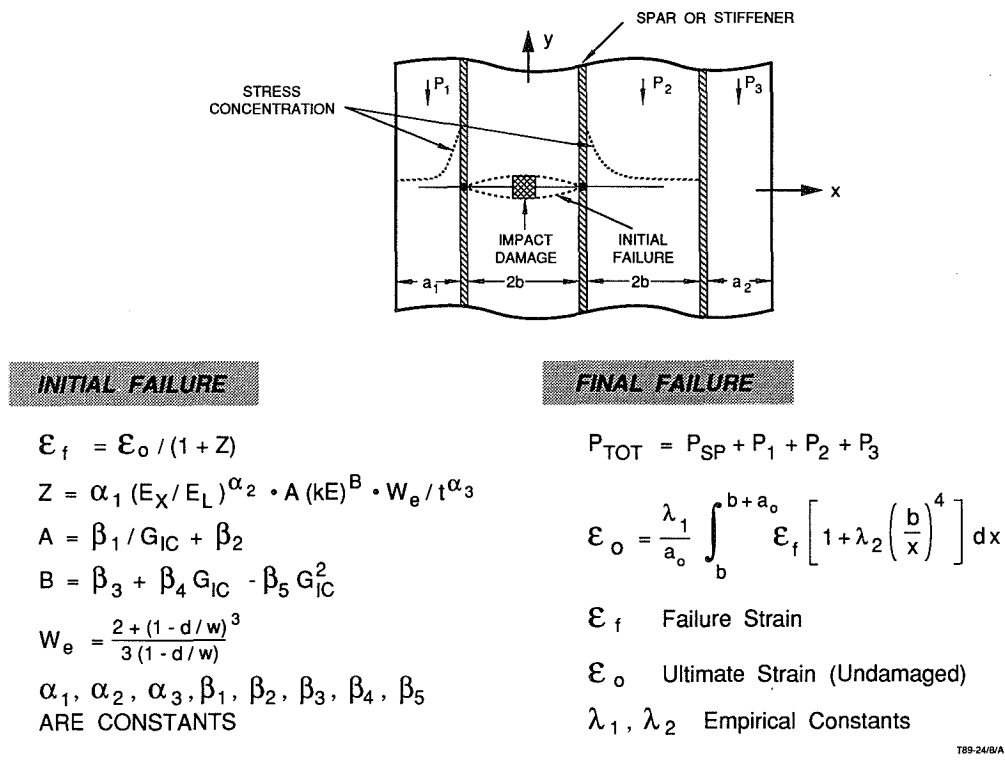
Figure 2. Damage Tolerance Analysis Methodology

489

POST-IMPACT FAILURE STRAIN (μIn/In)

- 12,000
- 10,000
- 8,000
- 6,000
- 4,000
- 2,000
0

0.0   1.0   2.0   3.0   4.0   5.0

COMPOUNDED IMPACT PARAMETER, Z

ALL AS4 FIBERS

● 3501-6
△ 5245C
□ APC2
○ F650
✕ 5050-3

$Z = C_1C_2C_3C_4C_5W_e$
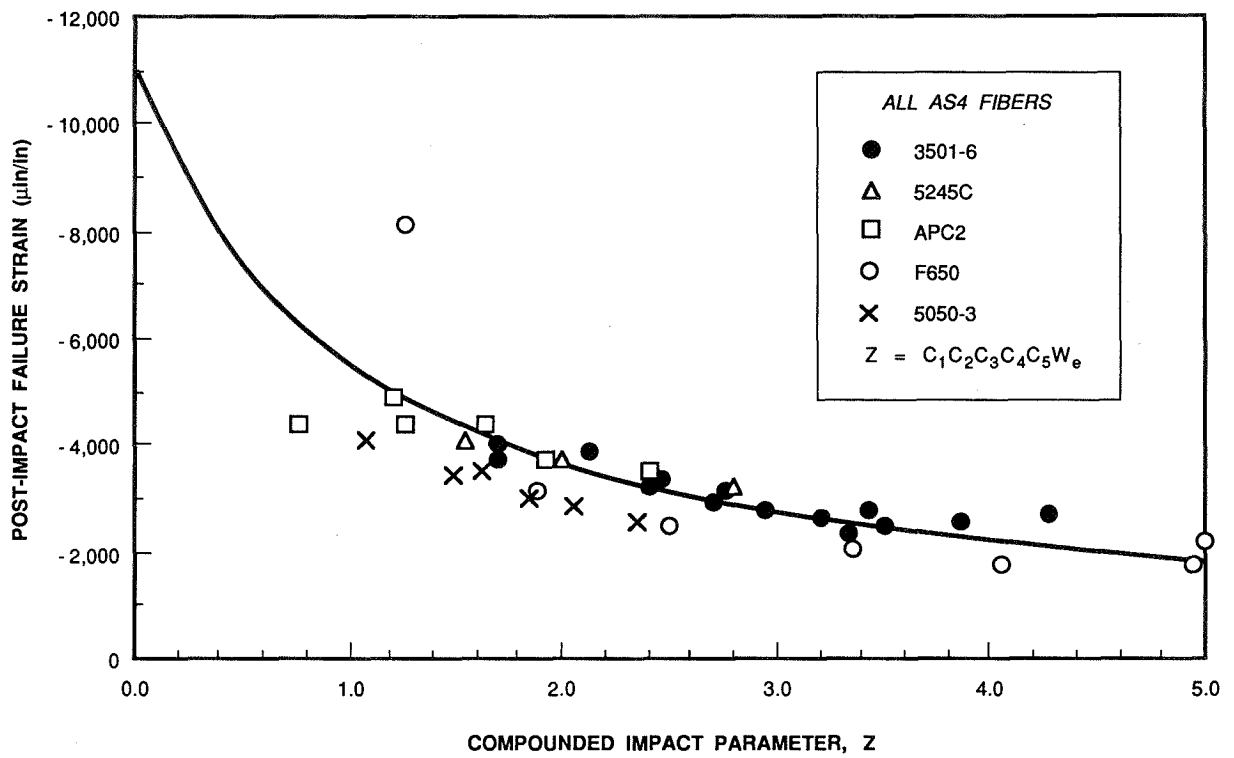
T89-24/9/A

Figure 3. Comparison of Predicted and Observed Strength.

POST-IMPACT STRENGTH (μIn/In)

-12,000
-11,000
-10,000
-9,000
-8,000
-7,000
-6,000
-5,000
-4,000
-3,000
-2,000
-1,000
0

0.0   1.0   2.0   3.0   4.0   5.0   6.0

COMPOUNDED IMPACT PARAMETER, D

$\epsilon_f = \epsilon_0 / (1 + D)$

$D = C_1C_2C_3 \lambda$

$\lambda = m_1 A^{m2} (G_{IC})^{m3}$

ALL AS4 FIBERS

○ 3501-6
△ F650
□ 5250-3   TEST
✕ 5245C   DATA
◇ APC2
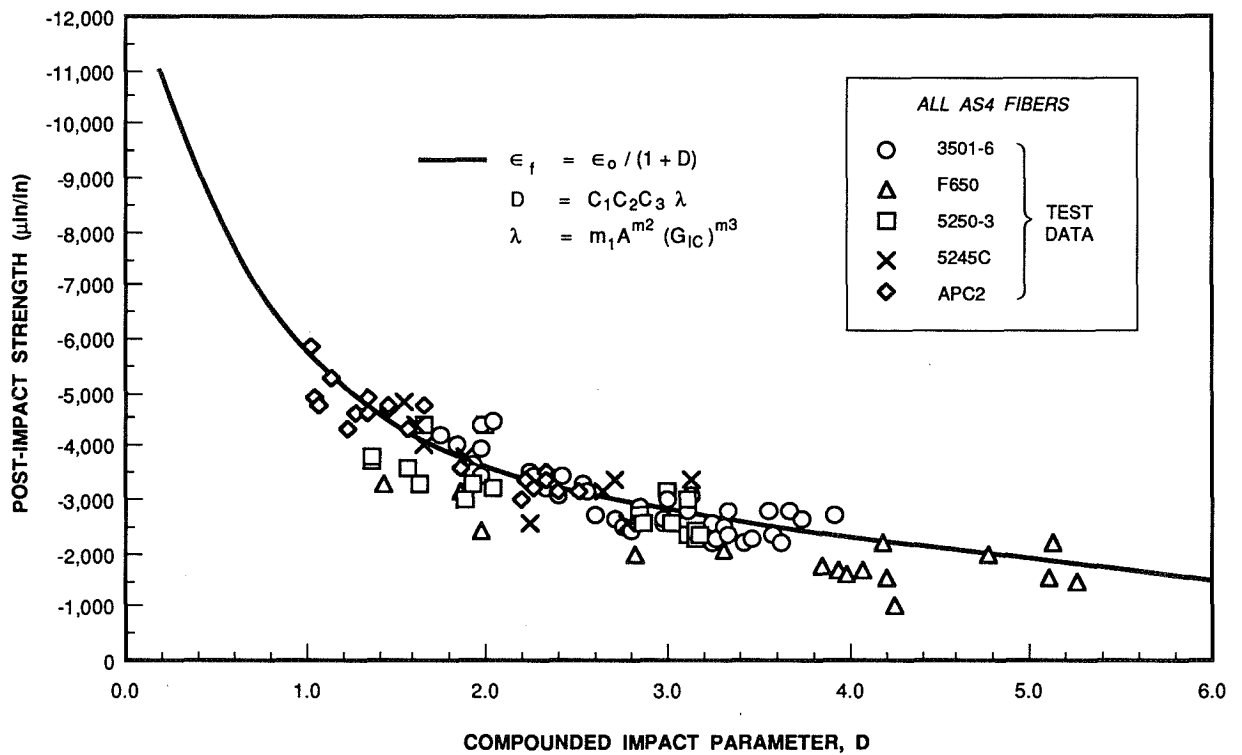
Figure 4. Comparison of Predicted and Measured Initial Failure Strains for Damage Area Based Stiffness Reduction Model.
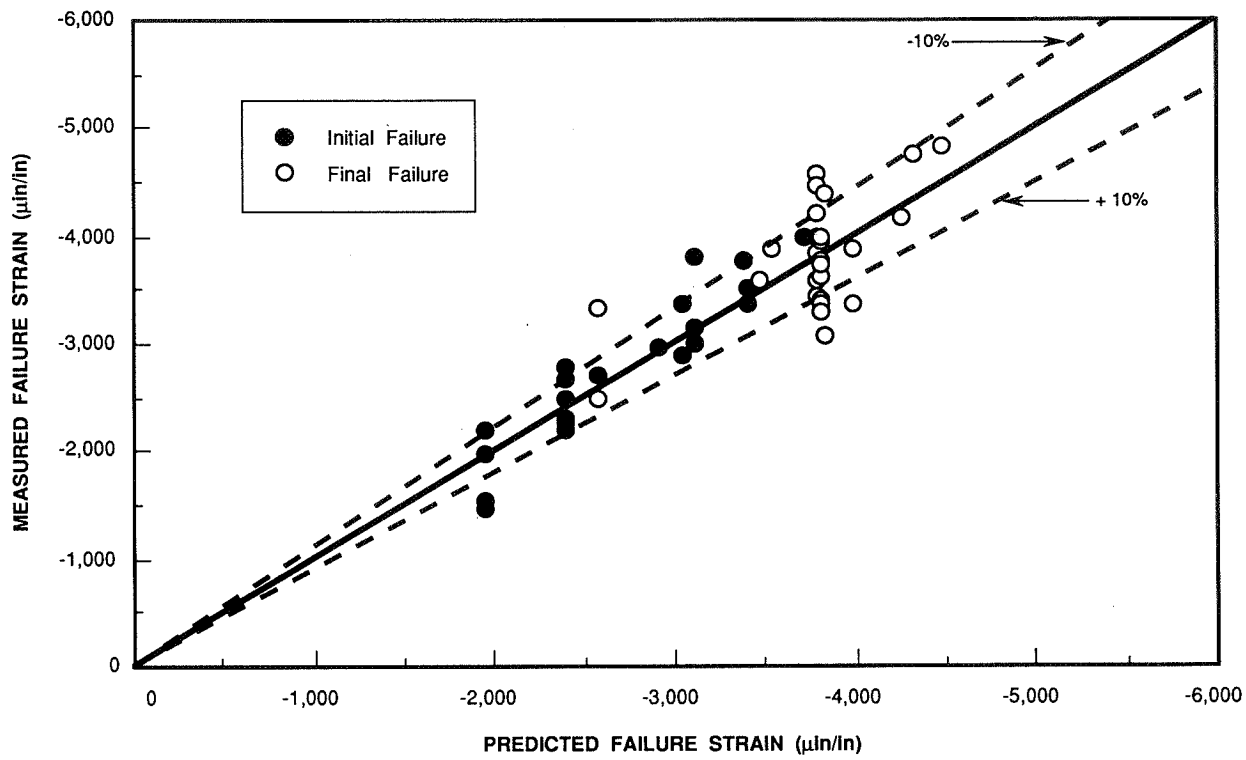
Figure 5. Overall Comparison of Measured and Predicted Structural Strength.
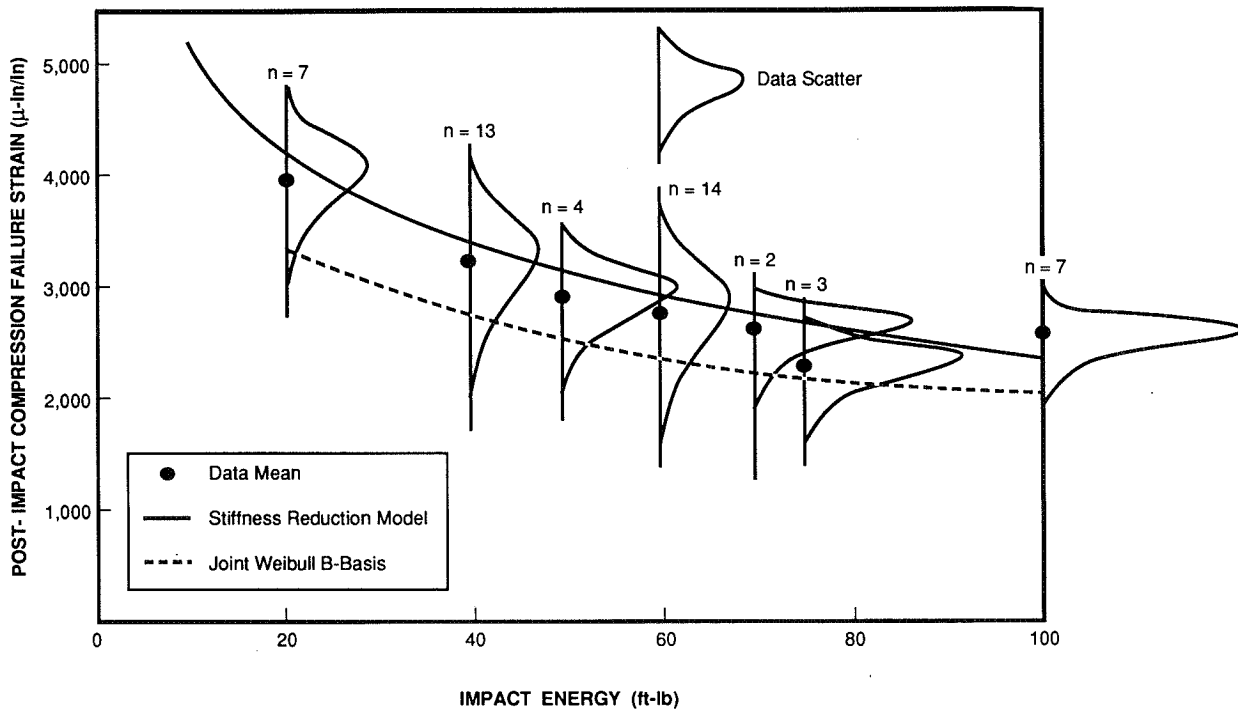
Figure 6. Post-Impact Initial Failure Strain Distribution for AS4/3501-6.
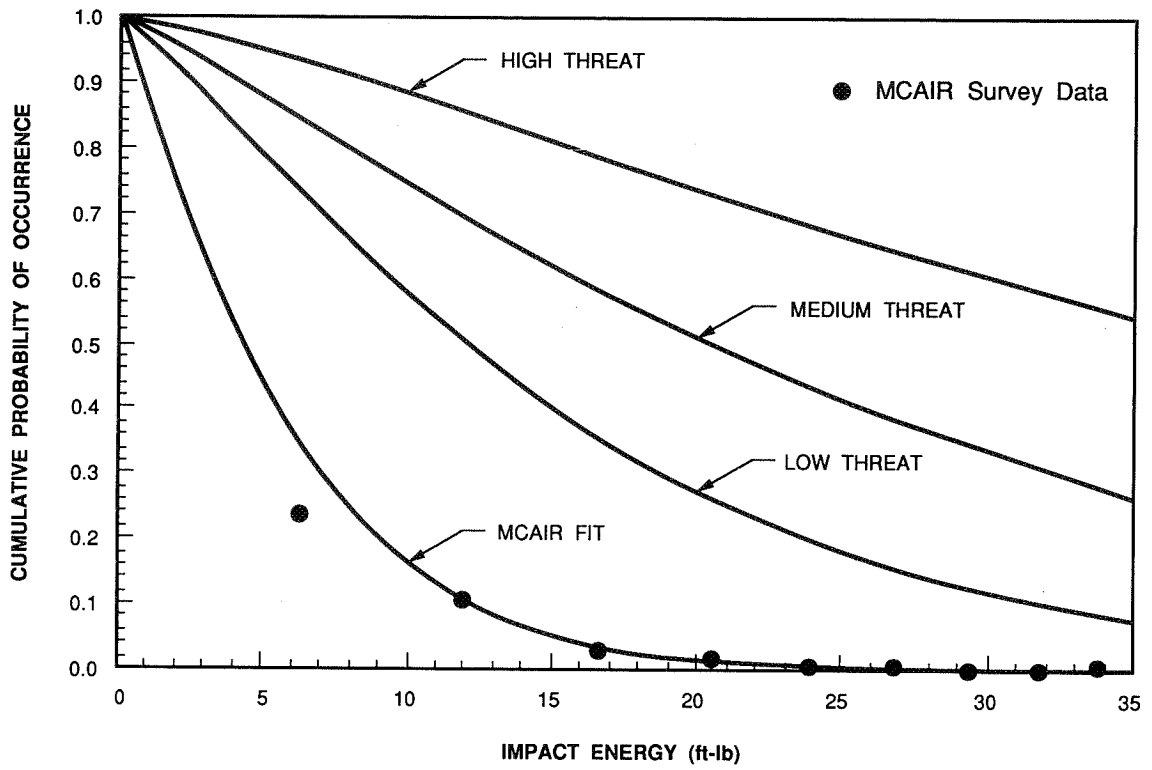
Figure 7. Comparison of Impact Threat Distributions.
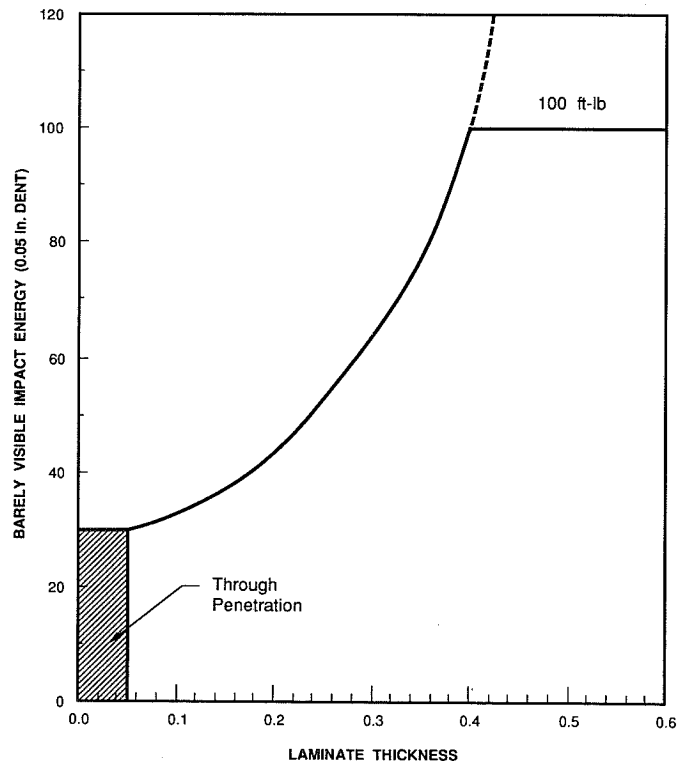
T89-24/13/A

Figure 8. Influence of Laminate Thickness on Barely Visible Impact Energy (0.05-inch Dent Depth).

492
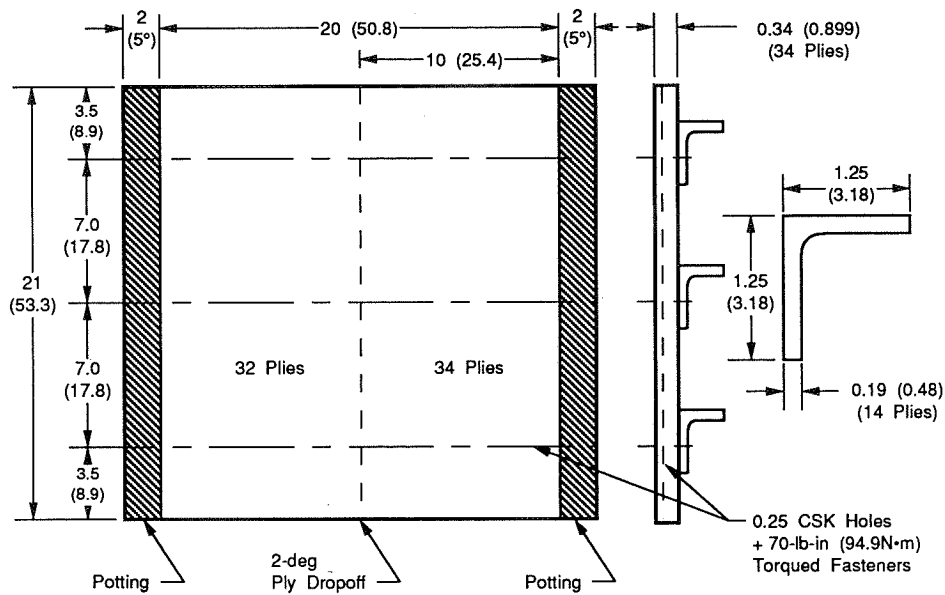
NOTES:

All dimensions in inches (centimeters)
Material: AS4/3501-6, double-ply
Nominal: 0.0104 in. (0.0264 cm)

T89-24/15/B

Figure 9. Multispar Test Panel.

APPLIED COMPRESSION STRAIN (μln/ln)
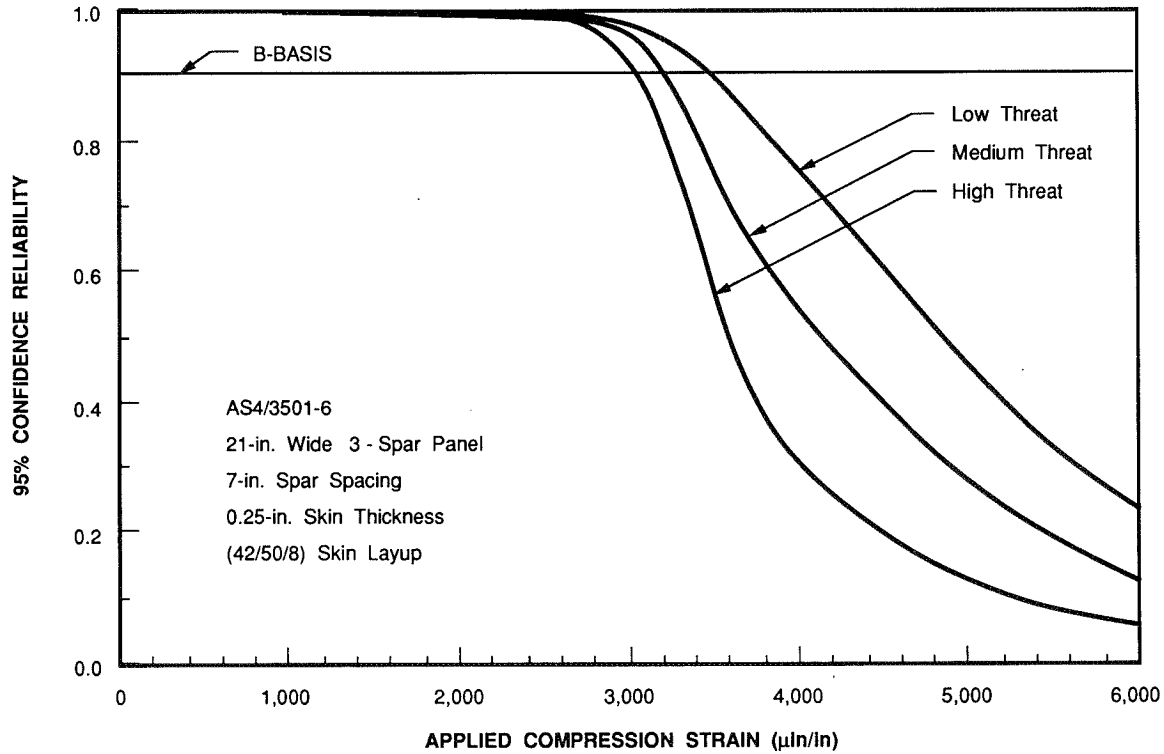
T89-24/16/B

Figure 10. Influence of Impact Threat Scenario on Post-Impact Structural Reliability.

493
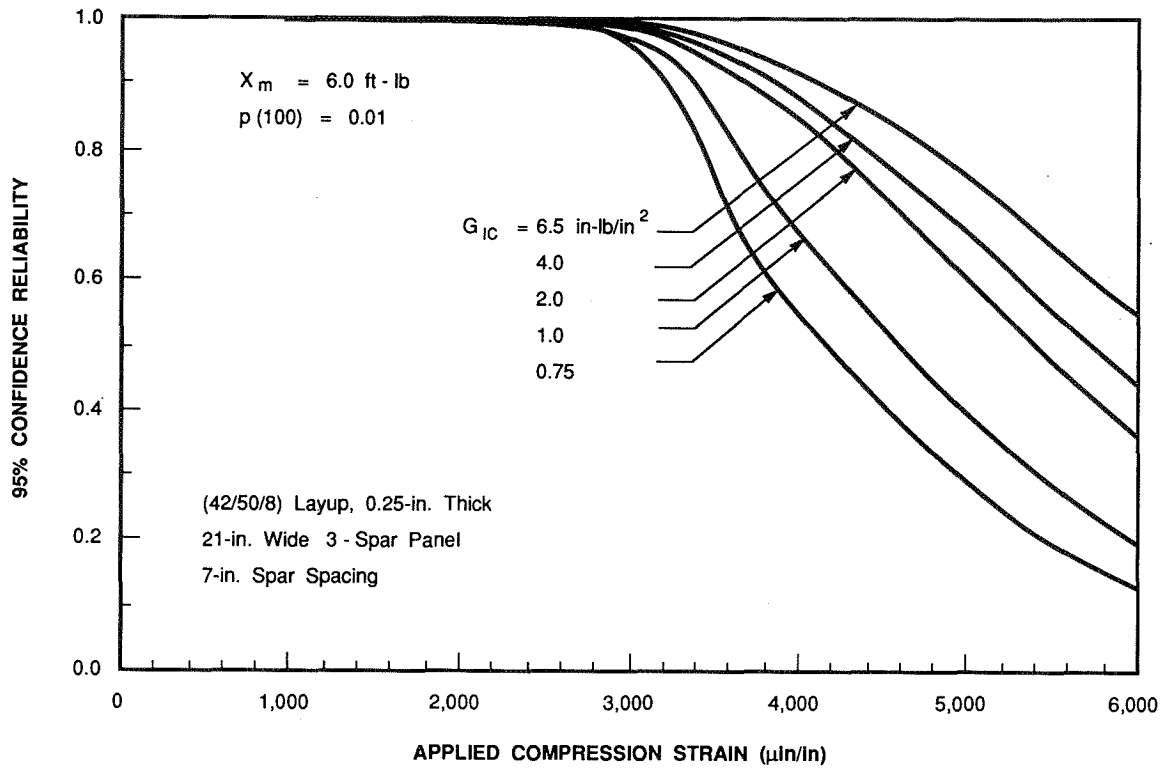
Figure 11. Influence of Fracture Toughness on Post-Impact Structural Reliability.
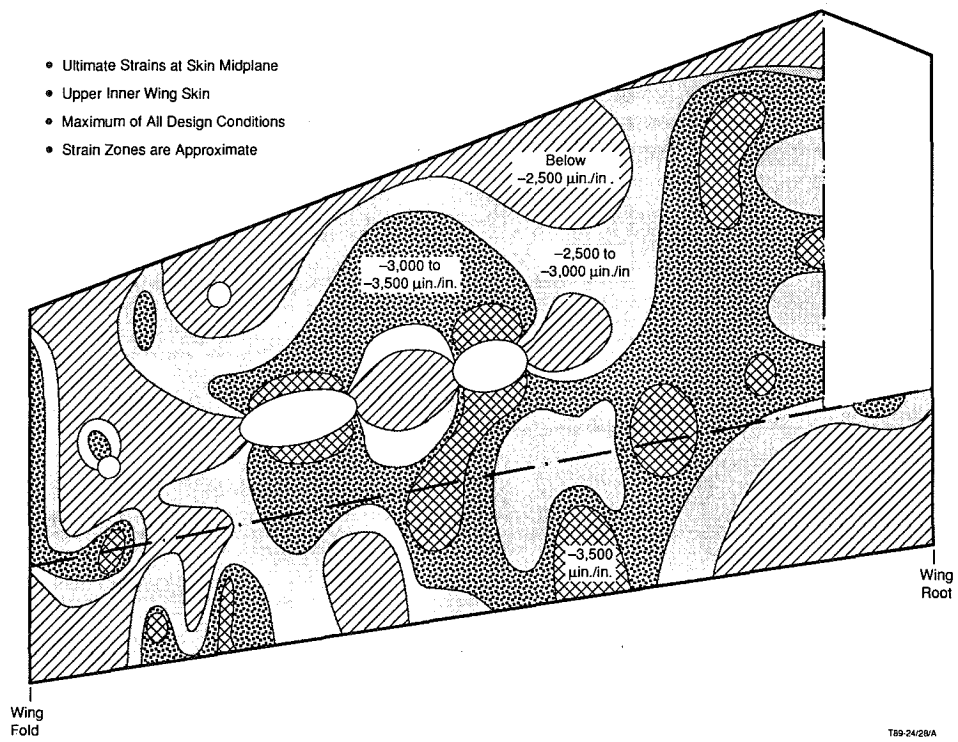
Figure 12. Maximum Spanwise Compression Strains in F/A-18 Inner Wing Upper Skin.

494

FWD

INBD

0.546/2650

0.650/3225

0.650/2975

0.608/2500

0.504/2750

0.504/3000

0.671/3350

0.504/3050

0.650/3250

0.504/3350

0.504/2600

0.442/3300

0.608/2850

0.359/2700

0.442/3450

0.671/3450

0.359/2700

0.421/3100

0.650/3300

0.504/3250

0.608/2650

0.359/2900

0.504/2725

0.359/2700

0.483/3350

0.671/3500

0.608/3400

0.650/3300

0.525/2650

0.775/3200

0.525/2850

0.671/3375

0.671/3325

0.650/2650

0.671/3350

0.525/2850

0.608/2550

0.650/2950

0.608/3400

0.608/3400

0.608/2800

0.608/3350

0.587/3300

0.525/3100

0.525/2625

Numbers Indicate t/ϵ_{DUL}

t = Skin Thickness (inch)

ϵ_{DUL} = Compression Strain at DUL (μin/in)

T89-24/18/A

Figure 13. Subdivision of the F/A-18 Inner Wing Upper Skin.

> 0.99

0.95 – 0.99

0.90 – 0.95
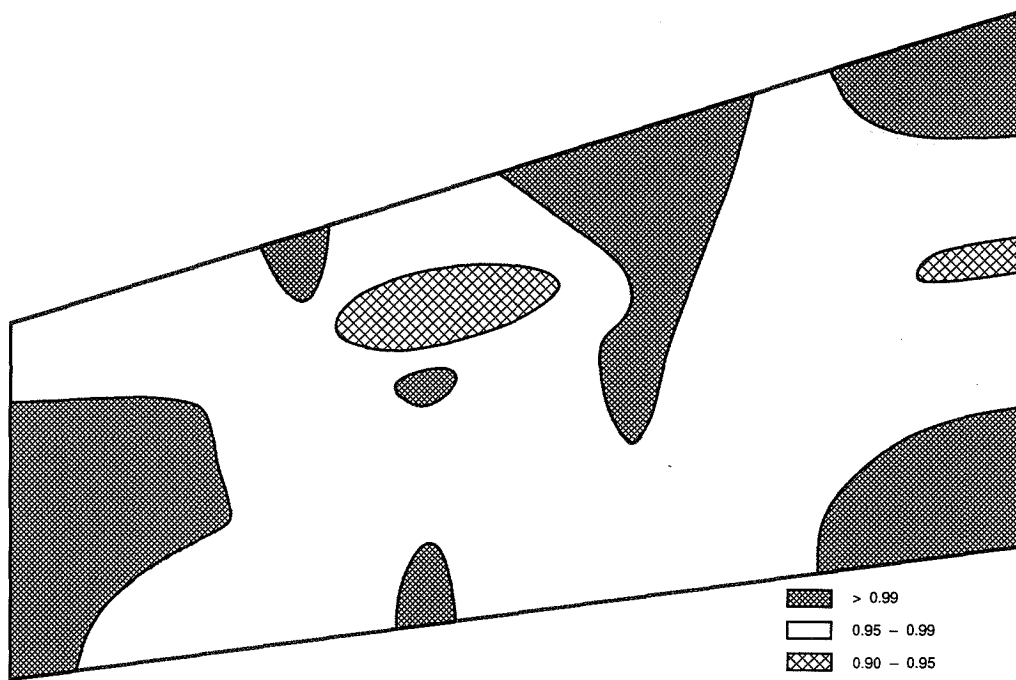
T89-24/19/A

Figure 14. Reliability at DUL of the F-A/18 Inner Wing Upper Skin Against a Medium Threat Scenario.

495
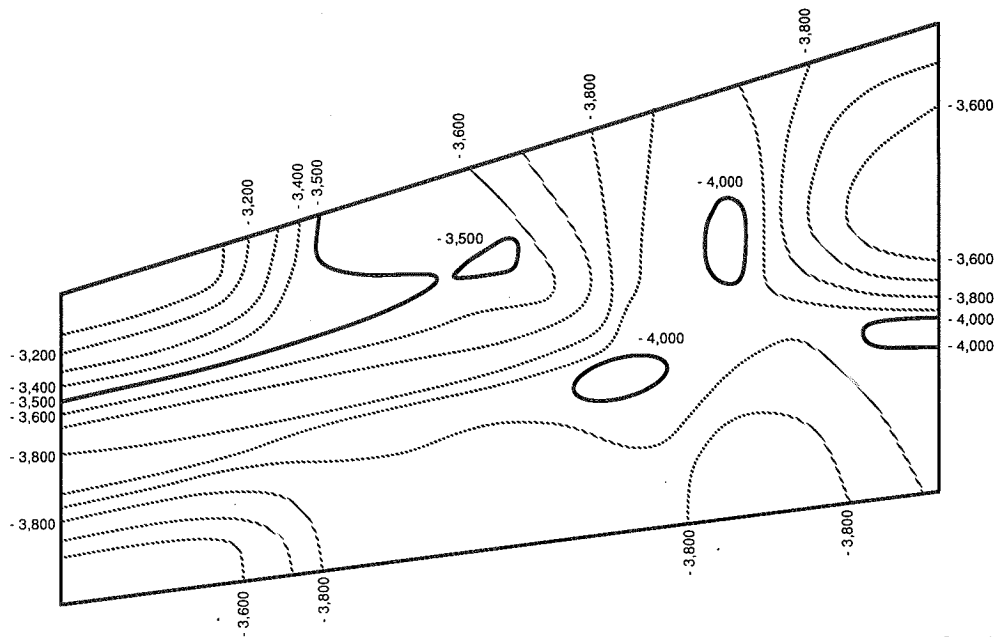
Figure 15. B-Basis Strain Allowable Contours for the F-A-18 Inner Wing Upper Skin Against a Medium Impact Threat Scenario.

Figure 16. B-Basis Margin of Safety for the F/A-18 Inner Wing Upper Skin Against a Medium Threat Scenario.
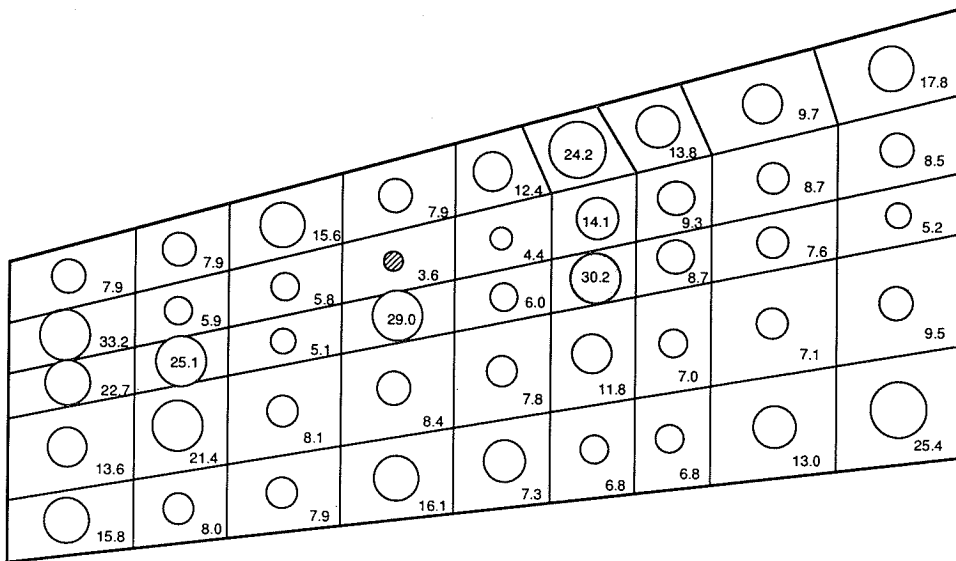
Figure 17. B-Basis Allowable Critical Damage Areas (in^2) at DUL for the F/A-18 Inner Wing Upper Skin. Medium Threat Scenario.
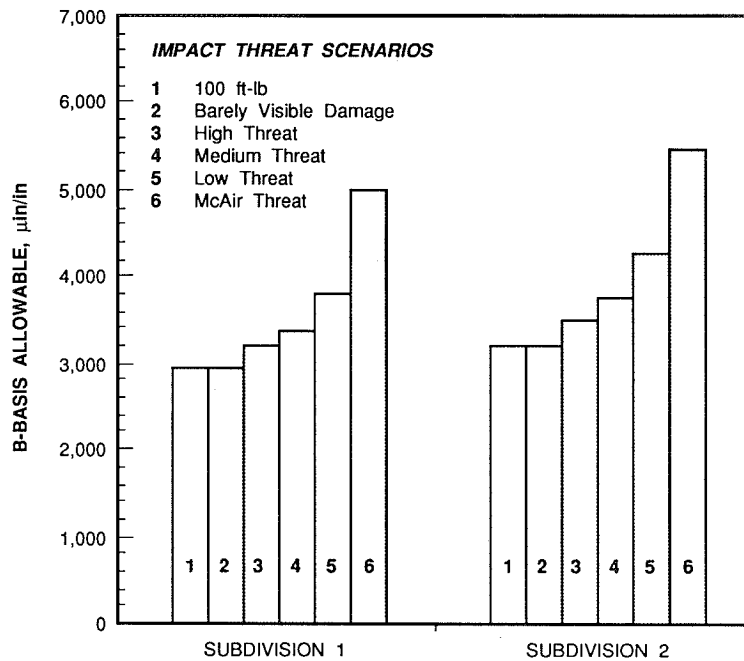
Figure 18. Sensitivity of F/A-18 Inner Wing Upper Skin B-Basis Strain Allowables to Impact Threat Scenario.
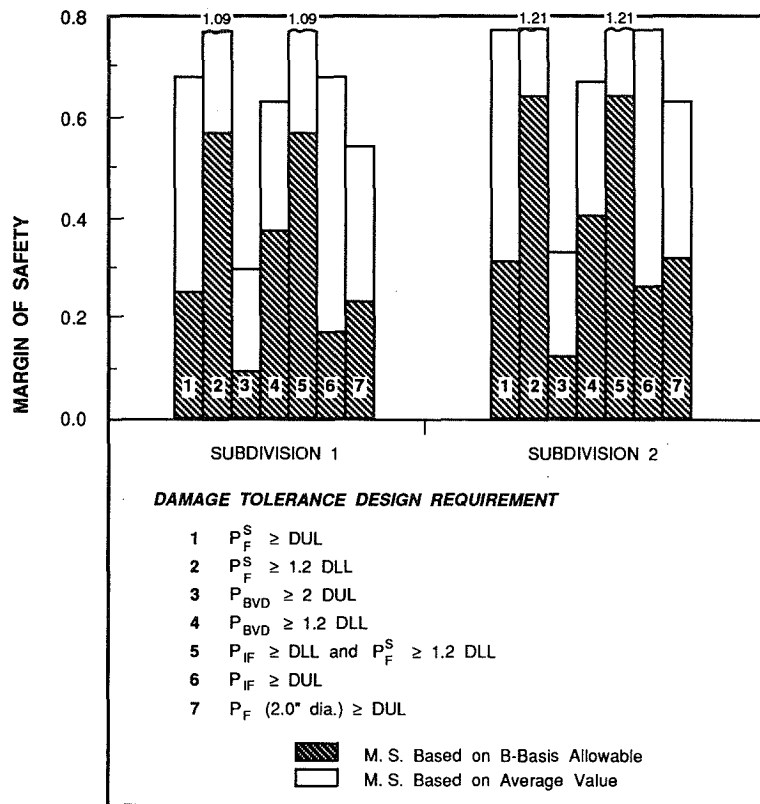
Figure 19. Sensitivity of F/A-18 Inner Wing Upper Skin B-Basis Margin of Safety to Damage Tolerance Residual Strength Load Requirement.
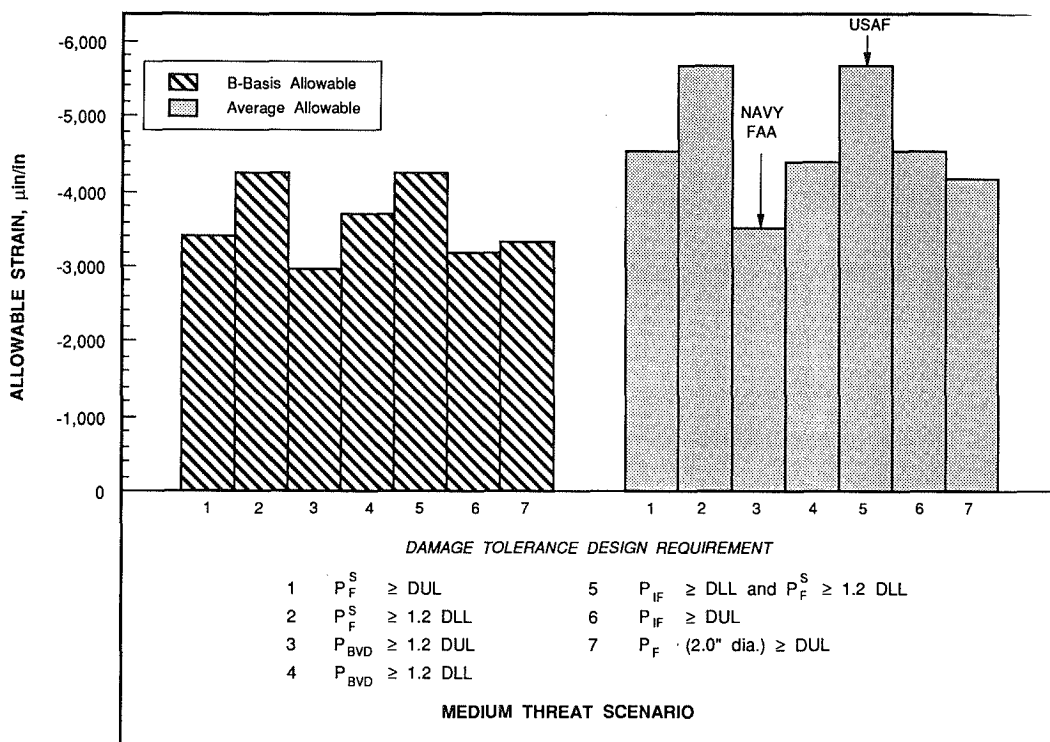
Figure 20. Influence of Damage Tolerance Residual Strength Load Design Requirement on F/A-18 Inner Wing Strain Allowables.

CERTIFICATION OF DAMAGE TOLERANT COMPOSITE STRUCTURE[1]

Andrew J. Rapoff and Harold D. Dill
McDonnell Aircraft Company
McDonnell Douglas Corporation, St. Louis, Missouri

Kenneth B. Sanger
McDonnell Douglas Technologies, Inc., San Diego, California
McDonnell Douglas Corporation, St. Louis, Missouri

Edward F. Kautz
Naval Air Development Center, Warminster, Pennsylvania

ABSTRACT

A reliability based certification testing methodology for impact damage tolerant composite structure was developed. Cocured, adhesively bonded, and impact damaged composite static strength and fatigue life data were statistically analyzed to determine the influence of test parameters on the data scatter. The impact damage resistance and damage tolerance of various structural configurations were characterized through the analysis of an industry wide database of impact test results. Realistic impact damage certification requirements were proposed based on actual fleet aircraft data. The capabilities of available impact damage analysis methods were determined through correlation with experimental data. Probabilistic methods were developed to estimate the reliability of impact damaged composite structures.

INTRODUCTION

A reliable certification testing procedure has evolved, over a period of many years, for metallic aircraft structures. The procedure encompasses two key requirements: (1) the full scale static test article must demonstrate a strength which equals or exceeds 150% design limit load (DLL), and (2) the full scale fatigue test article must demonstrate a life which equals or exceeds two times the design service life. These requirements are accepted measures of assuring structural integrity, developed mainly through experience.

These same full scale test requirements have been applied to the certification of composite structure by the aircraft industry. The Navy previously funded two certification programs [1,2] to address

bolted composite and mixed composite/metal structures. Significant
changes and additions were made in the certification process to
account for special characteristics inherent to composites. A Navy
certification methodology was thus formulated for what, at the time,
was current composite usage. In this program, the methodology was
extended to include integral (cocured or adhesively bonded) and impact
damaged composite structure.

SCATTER ANALYSIS RESULTS

The analysis of static strength and fatigue life data scatter is
an intrinsic part of the certification process. Scatter affects the
minimum strength or life a structure must exhibit to attain a specific
level of reliability. Scatter in strength and life data was analyzed
in previous certification programs [1,2] for composite structures
whose principal means of attachment was mechanical fastening. No
tests were performed in those programs. The selected sources provided
a database of over 6,000 static strength tests and 700 fatigue life
tests. Several material systems, specimen types, and environmental
conditions were included in the database. Several important
observations were made in the previous programs concerning scatter in
bolted composite test data.

The strength scatter was characterized by the coefficient of
variation, CV, which is the standard deviation divided by the mean
value. The strength scatter for bolted composites was found to be
over one and one half times that for metals, and is independent of
material system, environment, and loading direction (tension or
compression). Strength specimens with holes produce approximately one
third less scatter than unnotched specimens. Specimens with unloaded
or loaded holes have nearly identical static strength scatter, and the
scatter is independent of thickness/hole diameter and edge
distance/hole diameter ratios.

The fatigue life scatter for bolted composites, as characterized
by the standard deviation in the logarithm of life, can be up to ten
times the life scatter of metals. The life scatter for specimens with
no load transfer through the fastener is less than that for specimens
with load transfer. Life scatter increases with the applied stress
level for no load transfer specimens, but has little effect on the
life scatter for load transfer specimens. Environmental conditions
have little effect on bolted composite life scatter.

The integrally stiffened and impact damaged composite strength and
life data available in the literature were far less abundant than that
available for the bolted composite scatter analysis. Only twelve data
sources were obtained through personal contacts and a review of more
than twenty five sources. The data obtained included 373 strength and
59 fatigue tests. Although the database was limited, several
important observations can still be made.

The strength scatter of integral composite specimens is slightly
higher than that of bolted composites, and appears to be independent

500

of material system and environment. Impact damaged composite specimens, with an in plane failure mode, exhibit strength scatter that is nearly that of metal specimens, and appears to be independent of material system, environment, laminate layup, and impact energy normalized by the specimen thickness. The fatigue life scatter of integral and impact damaged composite specimens appears to be similar to that observed for bolted composites. A summary of the scatter analysis results of all of the composite data is given in Figure 1.

IMPACT DAMAGE REQUIREMENTS

To set guidelines for development testing, the threat of impact damage to composite structure must be known. Impact test data were analyzed to identify the parameters that affect the damage resistance and damage tolerance of composite structures. A summary of the database used to characterize impact damage is given in Figure 2. Damage resistance is the ability of a structure to resist damage, and is related to parameters of the impact event. Damage tolerance is the ability of a structure to perform as intended with damage present, such as retain adequate residual strength, and is related to the loading and structural configuration. The following observations were made concerning impact damage resistance and tolerance of composite structures.

Simple coupons accurately represent the midbay damage resistance and damage tolerance of more complex integral and bolted composite structures. Damage resistance is independent of laminate layups commonly used in fighter aircraft, but matrix dominated layups are more damage tolerant than fiber dominated layups. Stitching through the laminate thickness improves damage resistance, but the subsequent damage tolerance (strength) is related only to the amount of damage present; stitching provides no further benefits. Adverse environmental conditions and impact damage both reduce the damage tolerance of composites. However, their combined effect appears to be less detrimental than the effects of each taken separately.

The susceptibility of composite structures to impact damage needs to be considered in the certification process, along with the damage resistance and tolerance characteristics. Surveys of fleet aircraft impact damage were performed by MCAIR [3]. Impact damage was measured and recorded for nine F/A-18, eighteen F-4, three A-10, and three F-111 aircraft. Indentation depth exceedances per aircraft for each aircraft type are shown in Figure 3. The largest indentation depth recorded was 0.09 inch, of the more than 3,000 visible occurrences. Indentation depths of 0.01 inch deep were readily visible during the walk around surveys, making a visibility threshold of a 0.05 inch deep indentation a conservative requirement. These indentation depth data were compared to impact test data (Figure 4), and a conservative estimate of the impact energy causing the maximum indentation depth was found to be 50 ft-lbs.

IMPACT DAMAGE ANALYSES

Verified strength and life analysis capabilities reduce the amount of testing required to characterize the behavior of the myriad of configurations found in aircraft structure. Analyses also permit element test results to be related to subcomponents and full scale article tests. Promising impact damage resistance and tolerance analyses were identified through a literature search. The capabilities of each available method were evaluated through comparison with experimental data. Although some of the residual strength analyses appear promising, the complexity of integral composite structure precludes their use as a means of significantly reducing the amount of testing required to demonstrate impact damage tolerance. The current analyses may be applied within a particular development test program to identify parameters that affect strength significantly, or as a basis for empirical correlations between development and full scale test results to guide any redesigns.

CERTIFICATION METHODOLOGIES

Bolted Composite or Mixed Composite/Metal Structure

The certification methodology for these structural types can be summarized as follows:

(1) Static strength and fatigue life design allowables are developed using coupon specimens. A sufficient number of coupons are tested to obtain B-basis strain allowables for the range of expected service environmental conditions. B-basis implies that 90% of future values will be greater than the B-basis value, and that the estimate of this value will be correct 95% of the time. Fatigue life behavior is characterized using spectrum loading.

(2) The structural analysis and design of the airframe are used to select areas deemed critical for static and fatigue test verification. A series of low complexity specimens representing these critical areas are tested. Specimens simulating progressively greater design complexity, including large scale components, are then tested, usually in the critical environment for the anticipated failure mode. These specimens are strain gaged for correlation with the full scale test results.

(3) A full scale static test to failure of the entire airframe is performed, in most cases, under room temperature/ambient (RTA) conditions. For a successful static test, the measured strains at 150% design limit load (DLL) must not exceed the B-basis allowables for the most critical environmental condition. Also, the failure load of the composite structure must exceed 150% DLL by a factor equal to the RTA allowable divided by the environment allowable. Moreover, the load-strain response in critical areas of the full scale article must agree with that of the supporting element and component tests.

502

(4) A full scale fatigue test of the entire airframe is performed under RTA conditions using a severe load spectrum. The full scale article must not suffer a catastrophic failure during a test to two times the design service life.

Integral or Impact Damaged Composite Structure
Static Strength Certification

Two reliability based approaches to static strength certification of integral or impact damaged composite airframes were developed: the demonstrated strength approach and the measured strains approach. The methods were used to determine the required structural performance of an impact damaged composite airframe, including environmental effects, so as to achieve the same reliability as that of an all metal airframe with a demonstrated strength of 150% DLL.

Using the demonstrated strength approach, variations in strength, peak load, and structural response are accommodated by testing the full scale article to a load level above that expected in the service life of the aircraft. Again, the traditional load level increase has been to 150% DLL. Variation in expected peak load was estimated from load factor exceedance data, from aircraft exhibiting nominally identical usage. Variation in structural response includes variations in manufacturing and design tolerances, and was estimated from strain gage data [2].

Summarized in Figure 5 are the reliabilities at 100% DLL for a composite full scale article tested to 150% DLL, and the demonstrated strength needed to achieve the reliability of a metal full scale article. Reliabilities are given for a composite full scale article, with impact damage, tested under the critical environmental condition, and for an undamaged composite full scale article tested under RTA conditions. Reliabilities for in plane and out of plane failure modes are strongly affected by their respective static strength variations, as shown in Figure 5.

The damaged/environment reliability is calculated for the undamaged/RTA full scale article using either of two knockdown (reduction factor) approaches. One approach, the combined K_{DE} approach, is to derive strength knockdowns from specimens tested damaged, at environment, and compare these results to similar undamaged/RTA tests. The other approach, the separate $K_D K_E$ approach, uses damage and environment strength knockdowns that are derived from separate supporting element tests. The reliabilities in Figure 5 were calculated under the assumption that the critical area of the structure was subject to impact damage with the lowest failure load occurring at an environment other than RTA. It is recognized that this may not always be the case, and that the values given in Figure 5 are conservative estimates.

The estimated metal reliability decreases if the variation in expected peak load is included in the reliability calculation. With no peak load variation, the metal reliability is 99.9997%, while if

the peak load variation is included, the metal reliability decreases to 99.995%. From Figure 5, the metal reliabilities are not reached with a composite full scale test to 150% DLL. Only testing the composite full scale with impact damage at environment results in achievable demonstrated strengths; using either knockdown approach with an undamaged/RTA composite test requires unreasonably high strengths to be demonstrated. The demonstrated strength approach may not be a viable approach for certifying the static strength of an airframe subject to impact damage because of the cost and time required to environmentally condition the structure.

The recommended approach is to demonstrate that the measured strains at 100% DLL are less than the damaged/environment ultimate strain estimate by a sufficient margin so as to achieve the desired reliability. The full scale article is tested undamaged/RTA and supporting elements are tested either damaged/environment, or undamaged/RTA with one of the knockdown approaches used to accommodate damage/environment strength reductions. The required element margins are given in Figure 6, and indicate that, although in some cases somewhat high, they are nevertheless achievable.

A difficulty is anticipated when the failure mode is out of plane using the measured strains approach. Measuring out of plane strains on the full scale article are nearly impossible. Therefore, in plane strains from the full scale article and supporting element tests must be correlated with out of plane failure loads.

Integral or Impact Damaged Composite Structure
Fatigue Life Certification

Three reliability based approaches to fatigue life certification of integral or impact damaged composite airframes were developed: the scatter factor approach, the increased loads factor approach, and the ultimate strength/measured strains approach. These approaches were used to determine the required structural performance of an impact damaged composite airframe, including environmental effects. The goal was to achieve the same reliability as that of a metal airframe with a demonstrated life of two times the design service life.

Using the scatter factor approach, variations in life and expected usage are accommodated by demonstrating a test life that is greater than the design service life. Traditionally, this has been two times the design service life. Shown in Figure 7 are reliabilities of damaged composite full scale articles, with either a critical in plane or out of plane failure mode, as a function of the life demonstrated in test. Clearly, the demonstrated lives necessary to achieve the same reliability as a metal airframe are unreasonably high, ten to twenty times the design service life. This, coupled with the fact that the full scale article must be impact damaged, precludes the use of the scatter factor approach to fatigue life certification of impact damaged composite structures.

504

However, through modest increases in the spectrum fatigue loads, the desired reliability level may be attained with lower demonstrated lives. The necessary load increases for test durations of one, two, and four times the design service life are summarized in Figure 8, for various material and specimen configurations. An impact damaged composite full scale article, whose critical failure mode is in plane, must accommodate an 8% increase in loads with the traditional two lifetime test. If the failure mode is out of plane, the full scale article must accommodate a 20% load increase for the same two lifetime test. A 20% increase in loads is not practical for metallic structure, making this approach viable for all composite structure only.

The recommended approach is to compare measured strains, from the full scale static article test, to allowable strains from fatigue element tests. The advantages of this ultimate strength/measured strains approach are twofold. Only a static test of a full scale article need be performed to certify the composite structure. Also, the full scale article is undamaged. Damaging the full scale article will at best be controversial, and results could possibly be compromised should unrealistic damage be introduced in the structure. The traditional two lifetime fatigue test is still performed to certify any metallic components.

Results of this fatigue certification approach are shown in Figure 9. The supporting elements, representative of each fatigue critical area, should be impact damaged. Typically, five spectrum fatigue tests should be performed at each of two different limit load levels. These load levels should be chosen to be as different as the economics of testing will allow. If the load level is too low, life to failure will be prohibitively long. Conversely, load levels that are too high could cause quasistatic failures. From Figure 9, adequate fatigue reliability is achieved with element B-basis fatigue strain allowables that are 17% greater than the measured strain in the fatigue critical area, when the failure mode is out of plane. Only an 11% margin is necessary when the failure mode is in plane.

CONCLUSIONS AND RECOMMENDATIONS

The following conclusions are made based on this work:

(1) The static strength variation of integral composite construction appears to be independent of test conditions and specimen configuration. Population scatter estimates can then be made using generic test configurations, permitting design allowables to be determined from smaller samples, as compared to standard handbook methods. Within the test budget, more structural details can be interrogated and more accurate reliability estimations made.

(2) Coupons and elements can accurately represent the damage resistance and damage tolerance behavior of full scale composite structure. These less expensive specimens can be used to characterize static strength and fatigue life behavior of damaged composite

structure, including environmental effects. Larger, and more expensive, subcomponent tests can still be performed and increase confidence and more accurately simulate secondary effects due to damage.

(3) A good start has been made in defining the real threat of impact damage to aircraft structure through surveys of fleet aircraft. The threat does not appear to be as severe as previously conjectured, but appears to be highly dependent on maintenance actions and detail design.

(4) The multiplicity of failure modes present within the composite during the impact event has precluded the development of a quick and accurate damage resistance analysis. This portion of the impact problem is best left to empirical characterization. The damage tolerance analyses are more developed but still rest on the same semi-empirical foundation as undamaged strength and life.

Recommendations for future work are

(1) Integral and impact damaged composite fatigue life database was very limited. Not enough data existed or were published to make well supported conclusions about fatigue life scatter. Future efforts could be directed at this apparent gap in the knowledge of scatter.

(2) Impact damage on fleet aircraft with primary composite structures should be more thoroughly assessed. The threat of impact damage to current designs has been given an initial assessment and is not expected to be greater through changes in material systems. However, newer aircraft may have special servicing conditions which cause those aircraft to be subjected to a higher incidence of damage.

(3) A composite damage tolerance design guide is needed that combines the results from research efforts, production experience, and service experience. This guide should include assessments of manufacturing actions, design practice, and testing requirements.

SUMMARY

To achieve the computed reliability of metallic structures, significant changes in composite certification procedures are required; composites have comparatively large strength and life scatter, are susceptible to impact damage, and are environmentally sensitive. As summarized in Figure 10, a straightforward modification of metallic procedures would result in unrealistically large load and life increases for composite structures. Alternatives are to demonstrate that airframe strains are conservative, either by comparison to element and component test results or by modest increases in fatigue loads.

The certification process for composite structures requires a level of planning significantly greater than that used for all metal structures. The airframe contractor and contracting agency must preplan development tests and coordinate them with the full scale tests. With careful planning, all composite and mixed composite/metal aircraft structures can be reliably certified.

REFERENCES

1. Sanger, K. B., "Certification Testing Methodology for Composite Structures," NADC-87032-60, January 1986.

2. Whitehead, R. S., et al., "Certification Testing Methodology for Composite Structures," NADC-87042-60, October 1986.

3. "Improved Integrity of Composite Structures," McDonnell Aircraft Company Independent Research and Development Project No. 7-331.

4. McCarty, J. E., et al., "Damage Tolerance of Composites," AFWAL Contract F33615-82-C-3213.

5. Dominguez, J., F/A-18 Wing Skin Impact Test, Naval Air Development Center, December 1987.

6. Ramkumar, R. L., "Composite Impact Damage Susceptibility," NADC-79068-60, January 1981.

7. Bhatia, N. M., "Impact Damage Tolerance of Thick Graphite/Epoxy Laminates," NADC-79038-60, January 1979.

8. Ashford, L. W., "AV-8B Composite Structure Data Base," MDC A8814, Volume I, McDonnell Douglas Corporation, March 1985.

9. Dexter, H. B. and Funk, J. G., "Impact Resistance and Interlaminar Fracture Toughness of Through the Thickness Reinforced Graphite/Epoxy," NASA Langley Research Center.

Material/Specimen	Static Strength		Fatigue Life	
	Coefficient of Variation	Weibull Shape Parameter	Standard Deviation of Log Life	Weibull Shape Parameter
Metal	0.040	31	0.10	5.0
Composites				
Out of Plane Failure	0.078	16	0.42	1.0
Damaged In Plane Failure	0.043	29	0.32	1.4
Fastener Specimens				
No Load Transfer	0.065	19	0.30	1.5
Intermediate Load Transfer	0.064	19	0.72	0.81
Pin Bearing	0.062	20	0.55	0.66

GP93-0541-2-D

Figure 1. Summary of Static Strength and Fatigue Life Scatter Analyses

Author	Material	Specimen Description	Layup/ Thickness	Impactor	Damage Resistance Effects	Damage Tolerance Effects
McCarty, et. al. [4]	AS4/3501-6 AS4/APC-2 AS6/5245C C12000/5245C T300/V378A	Panels Stiffened With Mechanically Attached Titanium Channels (Multispar Panels)	42/50/8 0.25 in. Thickness	1 in. Dia Steel	• Impact Energy Level • Material System	• Damage Area • Multiple Impacts • Peak Spectrum Load
McCarty, et. al. [4]	AS4/3501-6	Coupons (Clamped Along Edges)	42/50/8 0.25 in. Thickness	1 in. Dia Steel	• Impact Energy Level	• Damage Area
McCarty, et. al. [4]	AS6/2220-3	Cocured Multirib Panels (With and Without Stitching Through Rib Flange)	4/28/4 0.27 in. Thickness	1 in. Dia Steel	• Impact Location • Stitching	
Dominguez [5]	AS4/3501-6	F/A-18 Wing Fully Assembled and Attached to Aircraft (Aluminum Substructure)	Various	1 in. Dia Steel	• Impact Location • Laminate Layup and Thickness	
Ramkumar [6]	AS4/3501-6	Coupons (Steel Bars Bolted Along All Edges)	42/50/8 0.25 in. Thickness 42/50/8 0.50 in. Thickness	1/8 in. Dia Steel 1/2 in. Dia Steel	• Impact Location • Laminate Layup and Thickness	
Bhatia [7]	AS4/3501-6	Coupons (Aluminum Channels Bolted Along Two Edges)	42% 0° Plies 0.44 in. Thickness 21% 0° Plies 0.50 in. Thickness	5/8 in. Dia Steel	• Laminate Layup and Thickness	• Laminate Layup
Ashford [8]	AS4/3501-6 T300/V378A	Coupons (Clamped Along All Edges)	25/50/25 0.112 in. Thickness	1/2 in. Dia Steel	• Temperature	• Temperature • Peak Spectrum Load
Dexter and Funk [9]	T300/3501-6	Coupons (Clamped Along All Edges; Various Stitch Spacings/Pitches)	Quasi-Isotropic 0.30 in. Thickness	1/2 in. Dia Aluminum	• Stitching	• Stitching

GP93-0541-1-T

Figure 2. Summary of Impact Damage Characterization Data
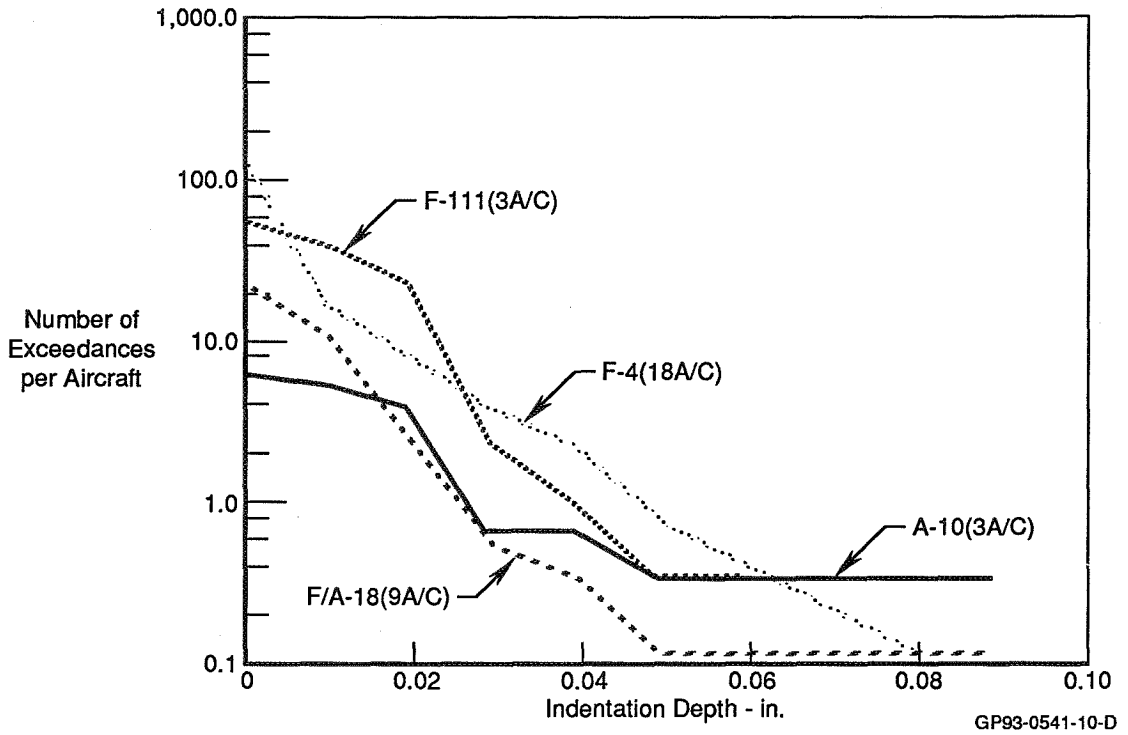
Figure 3. Indentation Depth Exceedances for Fleet Survey Aircraft
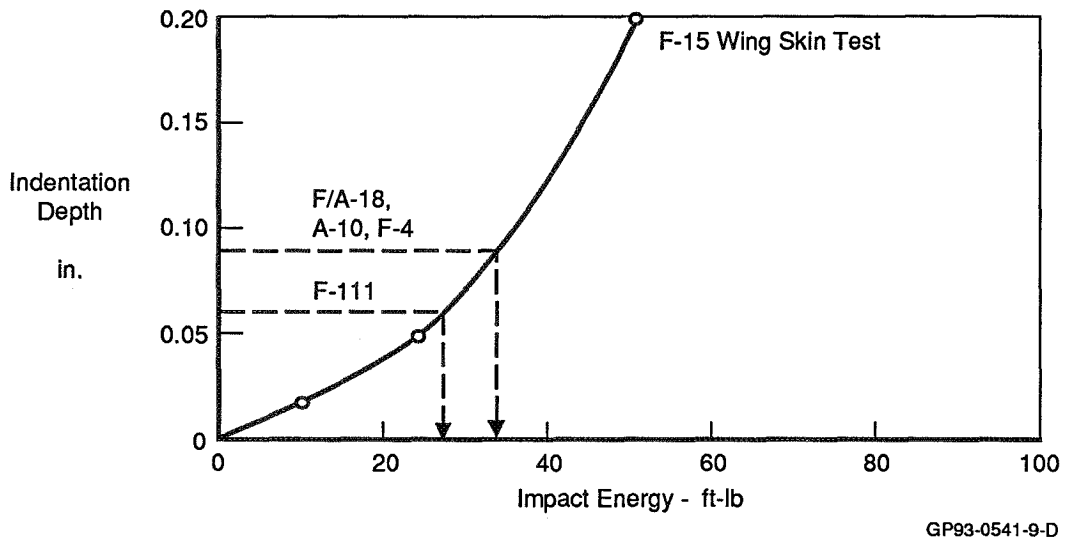
Figure 4. Maximum Damage to Fleet Aircraft Are Caused by Impact Energies of Less Than 40 ft-lb

Composite Full Scale Article and Knockdown Approach		No Peak Load Variation		Nominally Identical Usage Peak Load Variation	
		%R at 100% DLL[1]	R = 99.9997[2] (%DLL)	%R at 100% DLL[1]	R = 99.995%[2] (%DLL)
In Plane Failure Mode	Damaged/Environment	99.999	151.4	99.989	152.1
	Undamaged/RTA Combined K_{DE}	0.135	360.5	0.487	342.8
	Undamaged/RTA Separate K_D K_E	0.017	408.4	0.099	383.7
Out of Plane Failure Mode	Damaged/Environment	98.921	200.7	98.344	190.6
	Undamaged/RTA Combined K_{DE}	0.786	950.6	1.255	686.2
	Undamaged/RTA Separate K_D K_E	0.265	1,377.8	0.485	878.1

(1) Composite reliabilities are for full scale tests to 150% DLL.
(2) Reliability of metal full scale article tested to 150% DLL.

GP93-0541-8-D

Figure 5. Summary of Demonstrated Strength Approach to Impact Damaged
Composite Certification

		Damaged and Environment Ultimate Strain/Measured Strain at 100% DLL	
Composite Element and Knockdown Approach		No Peak Load Variation R = 99.9997%[1]	Nominally Identical Usage Peak Load Variation R = 99.995%[1]
In Plane Failure Mode	Damaged/Environment	167.0%	166.1%
	Undamaged/RTA Combined K_{DE}	170.7%	169.6%
	Undamaged/RTA Separate K_D K_E	174.2%	172.9%
Out of Plane Failure Mode	Damaged/Environment	225.6%	209.4%
	Undamaged/RTA Combined K_{DE}	233.9%	216.2%
	Undamaged/RTA Separate K_D K_E	242.0%	222.9%

(1) Reliability of metal full scale article tested to 150% DLL

GP93-0541-5-D

Figure 6. Summary of Measured Strains Approach to Impact Damaged Composite Certification
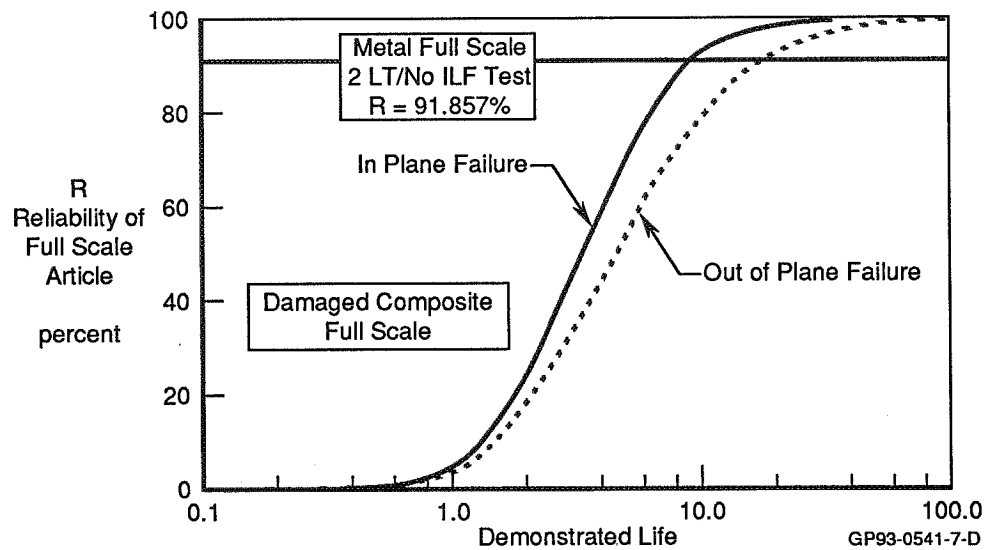
Figure 7. Required Demonstrated Lives for Composite Certification Are Unrealistic Using Scatter Factor Approach

Material/Specimen	ILF Required to Achieve Metal 2LT/ No ILF Test Reliability of 91.857%		
	$N_L = 1$	$N_L = 2$	$N_L = 4$
Metal	1.141	1.000	0.878
Composites			
Out of Plane Failure	1.263	1.196	1.132
Damaged In Plane Failure	1.119	1.081	1.045
Fastener Specimens			
No Load Transfer	1.080	1.053	1.027
Intermediate Load Transfer	1.200	1.170	1.141
Pin Bearing	1.390	1.310	1.235

1. ILF denotes increased loads factor   GP93-0541-4-D
2. LT denotes lifetimes
3. N_L denotes demonstrated life in test

**Figure 8. Increased Loads Factor to Achieve the Reliability of a
Metal Two Lifetime/No Increased Loads Factor Test**
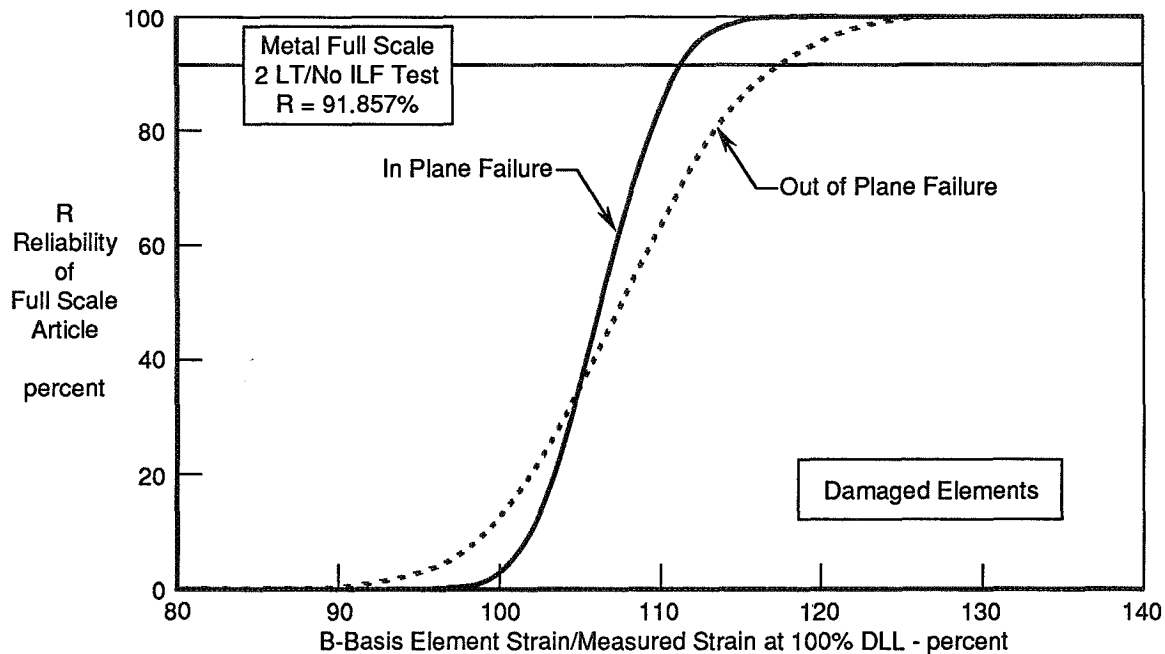
GP93-0541-6-D

**Figure 9. Fatigue Certification With Damaged Supporting Elements Using Ultimate
Strength/Measured Strains Approach**

513

Material/Specimen	Static Strength Approaches		Fatigue Life Approaches		
	Demonstrated Strength (DLL)[2]	Measured Strains at DLL/B-Basis Allowable[2]	Test Duration (LT)[3]	ILF With 2 LT Test[3]	Measured Strains at DLL/B-Basis Allowable[3]
Metal	150%	65%	2	0%	88%
Composites					
Out of Plane Failure	200%	49%	20	20%	85%
Damaged In Plane Failure	151%	64%	10	8%	90%
Fastener Specimens					
No Load Transfer	180%	55%	5	5%	91%
Intermediate Load Transfer	178%	56%	43	17%	88%
Pin Bearing	175%	57%	34	28%	84%

(1) Composite elements tested damaged/environment
(2) Required to achieve baseline metal reliability of 99.9997%
(3) Required to achieve baseline metal reliability of 91.857%

GP93-0541-3-D

Figure 10. Summary of Certification Approaches

514

STATISTICALLY BASED MATERIAL PROPERTIES
A MILITARY HANDBOOK-17 PERSPECTIVE

Donald M. Neal and Mark G. Vangel
U.S. Army Materials Technology Laboratory, SLCMT-MRS
Watertown, Massachusetts

ABSTRACT

This paper describes statistical procedures and their importance in obtaining composite material property values in designing structures for aircraft and military combat systems. The property value is such that the strength exceeds this value with a prescribed probability with 95% confidence in the assertion. The survival probabilities are the 99th percentile and 90th percentile for the A and B basis values respectively. The basis values for strain to failure measurements are defined in a similar manner. The B value is the primary concern of this paper.

INTRODUCTION

Many traditional structural materials, which are homogeneous and isotropic, differ from composite materials which have extensive intrinsic statistical variability in many material properties. This variability, particularly important to strength properties, is due not only to inhomogeneity and anisotropy, but also to the basic brittleness of many matrices and most fibers and to the potential for property mismatch between the components. Because of this inherent statistical variability, careful statistical analysis of composite material properties is not only more important but is also more complex than for traditional structures.

This paper addresses this issue by discussing the methodologies and their sequence of applications for obtaining statistical material property values (basis values). A more detailed analysis showing the various operations required for computation of the basis value is presented by the authors in the statistics chapter of the MIL-17 Handbook (ref. 1). The procedures in this handbook required substantial research efforts in order to accommodate various requirements (eg. small samples, batch to batch variability, and tolerance limits) for obtaining the basis values. Guidance in selection of the methodology came from the needs of the military, aircraft industry, and the Federal Aviation Administration (FAA). Some of the procedures include determination of outliers, selection of statistical models, tests for batch to batch variation, single and multi-batch models for basis value computation and nonparametric methods. In figure 1, a flowchart is shown outlining the sequence of operations.

An important application of the basis property value is to the design of composite aircraft structures where a design allowable is developed from this value. The process usually involves a reduction in the basis values in order to represent a specific application of the composite material in a structure (for example, a structure with a bolt hole for a particular test and environmental condition). One common approach in the design process requires the design allowable be divided by the maximum applied stress or strain and the result to be greater than one. The basis value is also used in qualifying new composite material systems to be used in the manufacture of aircraft. In this case, the values are obtained from an extensive test matrix including both loading and environmental conditions. The value also provides guidance in selecting material systems for specific design requirements.

The paper also shows how material strength variability and the number of test specimens can affect the determination of reliability numbers. Methods are presented for obtaining protection against this situation by providing a tolerance limit value on a stress corresponding to a high reliability. A comparison between deterministic and statistical reliability estimates demonstrates the inadequacy of the deterministic approach. A case study is presented describing the recommended procedures outlined in the MIL-17 Handbook for determining statistically based material property values.

RELIABILITY ESTIMATES

Sample Size - Variability

The importance of determining a tolerance limit on a percentile value is graphically displayed in figures 2 and 3. The cumulative distribution function (CDF) of the standard normal (mean equals 0, standard deviation 1) is plotted for sample sizes of 10 and 50, using 25 randomly selected sets of data. In figure 2, for n equals 10, the spread in the percentile is 2.1 for the 10th percentile. In figure 3, for n equals 50, the spread is .7 for the same percentile. The results show the relative uncertainty associated with small sample sizes when computing reliability values. The range in the percentile can also depend on the amount of variability in the data (i.e., the variance).

Often in structural design, a design allowable value is obtained from the basis value. A design allowable is an experimentally determined acceptable stress value for a material (called an allowable stress). The allowable is a function of the material basis value, layup, damage tolerance, open holes, and other factors. It is usually numerically determined for some critical stress region located within the structure. In using the allowable it is required that the critical stress be less than a proportion (margin of safety) of the allowable stress value. Determining a property value from only 10 strength tests using 90% reliability estimates without confidence in the assertion could result in a nonconservative design situation. In order to

516

prevent this occurrence and provide a guarantee of the reliability value, a tolerance limit (i.e., a lower confidence bound) on the percentile is recommended. The MIL-17 Handbook statistics chapter describes methods for obtaining basis values for a prescribed tolerance limit.

Definition of the B-Basis Value

The B-basis value is a random variable where an observed basis value from a sample (data set) will be less than the 10th percentile of the population with a probability of .95. In figures 4 and 5 a graphical display is shown of the basis value probability density functions for random samples of n equals 10 and 50 respectively. Samples are from the same population as in figures 2 and 3. The vertical dotted lines represent the location of the population 10th percentile (X_{10}). The probability density function of the population is also displayed in the figures. Note that 95% of the time the basis value is less than X_{10}. The graphical display of the basis value density function shows much less dispersion for n equals 50 than for n equals 10; therefore, small sample sizes often result in very conservative estimates of the basis value.

STATISTICAL METHODS - MATERIAL PROPERTY VALUES

Flowchart Guidelines

Since the statistical procedures and the flowchart (figure 1) have been published in the MIL-17 Handbook (ref. 1) and (ref. 2), this paper will only present a brief description of the methods, their purpose, interpretation of results, and the need for following the order of application suggested by the flowchart. The authors have written a computer code which performs the necessary computations for obtaining the basis values as described in the flowchart. The code is available on a diskette, which can be used on various computers including PC's that are IBM compatible. Both the executable and source code are on the diskette. This code is available free of charge from the authors. The flowchart capability was tested by applying the recommended procedures using both real and simulated data sets. The results of the simulations showed at least 95% of computed values were less than the known 10% point; this is consistent with the definitions of 'B'-basis value, see also (refs. 1 and 2).

The flowchart has two directions of operations, one is for the single batch (sample), and the other is for the multi-batch case. A batch could represent specimens made from a manufactured sheet of composite material representing a roll of prepreg material. Published MIL-17 Handbook basis values are usually obtained from five batches of six specimens each.

Initially, let us assume the user of the flowchart has only a single batch or more than one batch but that the batches can be pooled

so that a single sample analysis can be applied. The first operation (see figure 1) is to determine if outliers exist in the data set. A more detailed discussion of outlier detection schemes and applications is published in ref. 3. The method selected is called the Maximum Normed Residual (MNR) procedure (ref. 4) and is published in the MIL-17 Handbook. It is simple to apply and performs reasonably well, even though it assumes that the data are from a symmetric distribution. The analysis requires obtaining an ordered array of normed residuals written as

$$NR_i = (x_i - \bar{x})/s, \quad i=1, \cdots n \tag{1}$$

where $\bar{x}$ is the mean, s is the standard deviation (SD), and n is the sample size. If the maximum absolute value of NR_i (MNR) is less than some critical value (CV) (see refs. 1 and 2), then no outliers exist. If MNR is greater than CV, then an outlier X is determined from the largest NR_i value.

Outlying test results are substantially different from the primary data. For example, assume that the data set contains 16 strength values and 15 range from 150 to 200 KSI while the other is 80 KSI. The MNR method would identify the 80 KSI value to be an outlier. The 80 KSI specimen should be examined for problems in fabrication and testing. If a rationale is determined for rejecting this test result, then do not include the outlying test value in the data set when obtaining the basis value. If there is no rationale for rejection, the outlier should remain unless the test engineer believes that a non-detectable error exists.

It is important to identify the existence of outliers but also of equal importance to resist removing the values unless a rationale has been established. Leaving in or arbitrary removal of outlying values can adversely affect the statistical model selection process and consequently the basis value computation. An outlier in a data set will usually result in a larger variance and a possible shift in the mean when compared with the same data without the outlier. The amount of shift and the variance increase depends on the severity of the outlier (distance removed from the primary data set). It is suggested that for small samples (n is less than 20) critical values corresponding to a 10% significance level be used (see refs. 1 and 2) in order to identify outlying values. If the sample is greater than 20, then use the 5% level. It is often difficult to test for outliers when there is a limited amount of data; therefore, the 10% level will provide additional power to detect outliers. This level will also result in more chance of incorrectly identifying outliers. Outliers can be incorrectly identified from data sets with highly skewed distributions; therefore, it is suggested the box-plot method (refs. 1 and 3) be applied for determining outliers in this situation.

Goodness of Fit Test – Distribution Function

Referring to figure 1, the next step is to identify an acceptable model for representing the data. In the order of preference the three candidate models are Weibull, normal, and the nonparametric method. The Weibull model is

$$F_W(x) = 1 - \exp[-(x/\alpha)^\beta] \quad , \text{ where} \tag{2}$$

x is greater than 0, α is the scale parameter, and β is the shape parameter, is considered first in the ordering of the test procedures. The Anderson-Darling (AD) goodness-of-fit test statistic (refs. 1 and 5), is suggested for identifying the model because it emphasizes discrepancies in the tail regions between the cumulative distribution function of the data and the cumulative distribution function of the model. This is more desirable than evaluating the distributional assumptions near the mean since reliability estimates are usually measured in the tail regions. The Anderson-Darling test statistic and the observed significance levels computations are described in refs. 1 and 2. Example problems are also shown in ref. 1, demonstrating computational procedures for applying the AD method.

In following the flowchart, if the Weibull model hasn't been accepted as a desired model, then a test for the normal distribution is suggested,

$$F_N(x) = \frac{1}{\sigma(2\pi)^{1/2}} \int_{-\infty}^{x} \exp[-(t-\mu)^2/2\sigma^2] dt \tag{3}$$

where μ is the mean, and σ^2 is the variance. The AD test for the normal model is similar to the test for the Weibull. The procedure used to identify the normal model is also in refs. 1 and 2. It should be noted that for small samples reliable identification of a model to represent the data is difficult unless some prior information of the population is known.

If the Weibull and normal models are rejected, then a nonparametric method can be used to compute the basis value (see flowchart). This method does not assume any parametric distribution as described above. Therefore, model identification is not required, although application of the method can often result in overly conservative estimates for the basis value.

The conventional nonparametric method (ref. 6) requires a minimum of 29 values in order to obtain a 'B'-basis value, and 300 are needed for the 'A'-basis number. This paper presents a method for obtaining 'A' and 'B' basis values for any sample size. The method is a modification of the ref. 7 procedure involving the ordered data values arranged from least to largest with the basis value defined as

$$B = X_{(r)} - K(X_{(r)} - X_{(1)}), \tag{4}$$

519

where $X_{(r)}$ is r^{th} ordered value and $X_{(1)}$ is the first ordered number. In refs. 1 and 2 tables for r and K values are tabulated for sample sizes n. Note, in the case where 'A' values are required for small sample sizes, it is suggested that nonparametric methods be applied unless some prior information of the model is known. This is because of the limited information available in the lower tail region of the distribution, which can result in erroneous estimates of the reliability numbers. The 'A'-basis value is often used in design where a single load path exists; therefore, it is essential that the value be conservative.

Weibull Method - 'B'-Basis Value

Returning to the sequence of operations as outlined in the flow-chart, if the Weibull model is accepted, then determine the basis value from the following relationship

$$B = \hat{\alpha}[\ln(1/P_B)]^{1/\hat{\beta}} \tag{5}$$

where $\hat{\beta}$ and $\hat{\alpha}$ are maximum likelihood estimates of the shape β and scale α of the Weibull distribution. That is, these estimates maximize the likelihood function, which is the product of probability densities (2) evaluated at each of the n data values. Tables for P_B as a function of the sample size n and the code for determining $\hat{\alpha}$ and $\hat{\beta}$ are given in refs. 2 and 3.

Normal Method - 'B'-Basis

If the Weibull model was rejected and the normal model is an acceptable representation of the data, then compute the basis value as

$$B = \bar{X} - K_B S \tag{6}$$

where $\bar{X}$ and S are the mean and SD, and K_B is obtained from tables in refs. 1 and 2.

PROCEDURES FOR MULTIPLE BATCHES

Anderson-Darling Test

If there is more than one batch of data being analyzed, then a significance test is required in order to determine if the batches may be pooled or if a multi-batch statistical analysis is to be applied (see flowchart). Note, the outlier test is to be applied to pooled data prior to testing. The recommended test is the K-Sample Anderson-Darling Test (refs. 1 and 8) which determines if batch to batch variability exists among the K batches. This test is similar to the AD test for identifying acceptable statistical models for representing

520

data. In the K sample case, paired comparisons are made for the empirical CDF's while the other AD methods compare a parametric CDF with an empirical CDF. In all cases, this comparison involves the integration of the squared difference of the CDF's weighted in the tail region of the distribution. The K-sample AD is basically a two sample test in that each sample (i^{th} batch) is <u>individually</u> compared with the pooled K-1 other batches, repeated K times until each ith batch has been compared. The average of these K two-sample tests determines the K-sample AD test statistic. Tables of critical values and a detailed description of the method and its application is shown in refs. 1, 2, and 8.

If a significant difference is noted among the K batches, then, as shown in the flowchart, a test for equality of variance is suggested using a method in ref. 9. Application of the method, tables, and the necessary relationships for computing the test statistic are given in refs. 1 and 2. The variance test is suggested only as a diagnostic tool. Sample test results that have large variances relative to the other batches may identify possible problems in testing or manufacturing of the specimens. Equality of variance is not required when applying the Modified Lemon method, as discussed below, in the multi-batch case. Although the Modified Lemon method is based on the assumptions of equality of variance and normality, simulation results have shown that these assumptions are not necessary. After testing for equality variance, it is suggested that the basis value be obtained from application of the Modified Lemon method (see figure 1).

The Modified Lemon Method

Composite materials typically exhibit considerable variability in strength from batch to batch. Because of this variability, one should not indiscriminately pool data across batches and apply single batch procedures. The K-sample Anderson-Darling test was introduced into the MIL-17 Handbook in order to prevent the pooling of data in situations where significant variability exists between batches. For the situation where the K-sample Anderson-Darling test indicates that batches should remain distinct, a special basis value procedure has been provided. This method, referred to as the 'ANOVA' or 'Modified Lemon' method, will be discussed next. A detailed description for applying the method is shown in refs. 1 and 2. For a discussion of the underlying theory, see ref. 10, the original Lemon paper, and ref. 11, the Mee and Owen paper which modifies the Lemon method.

The Modified Lemon method considers each strength measurement to be a sum of three parts. The first part is an unknown constant mean. If one were to produce batches endlessly, breaking specimens from each batch, the average of all of these measurements would approach this unknown constant in the limit of infinitely many batches. Imagine, however, that one were to test many specimens from a single batch. The average strength approaches a constant in this situation as well, but this constant will not be the same as for the case where each specimen came from a different batch. The average converges to an overall population mean (a 'grand mean') in the first case, while the

average converges to the population mean for a particular batch in the second case. The difference between the overall population mean and the population mean for a particular batch is the second component of a strength measurement. This difference is a random quantity - it will vary from batch to batch in an unsystematic way. We assume that this random variable has a normal distribution with a mean of zero and some unknown variance which we refer to as the between batch component of variance. Finally, in order to arrive at the value of a particular strength measurement, we must add to the sum of the constant overall mean and a random shift due to the present batch a third component. This is another random component which differs for each specimen in each batch. It represents variability about the batch mean. It also is assumed to have a normal distribution with a mean of zero and an unknown variance, which is referred to as the 'within batch' component of variance.

The 'Modified Lemon' method uses the data from several batches to determine a material basis property value which provides 95% confidence on the appropriate percentile of a randomly chosen observation from a randomly chosen <u>future</u> batch. This basis property provides protection against the possibility of batch-to-batch variability resulting in future batches which have lower mean strength than those batches for which data are available.

To see what this means, imagine that several batches have been tested and that this statistical procedure has been applied to provide a 'B'-basis value. Now, imagine that you were to get another batch and test a specimen from it. After this you obtained still another batch and tested a specimen from it. If you were to repeat this process for infinitely many future batches, you would obtain a distribution of strength measurements corresponding to a randomly chosen measurement from a random batch. You can be 95% certain that the basis value which you calculated originally is less than the tenth percentile of this hypothetical population of future measurements. This is the primary reason why the Modified Lemon method is advocated by the MIL-17 Handbook - it provides protection against variability between batches which will be made in the future through the use of data which is presently available.

An illustrative example of this method applied to nine batches of material is shown below. The data sets did not pass the K-sample AD test for pooling. Let the batches be

1	2	3	4	5	6	7	8	9
61.3	66.5	66.0	61.9	68.9	75.8	72.8	71.9	68.7
68.5	64.7	72.7	68.0	65.0	75.2	75.0	71.0	76.3
62.5	64.9	67.1	63.3	70.9	71.5	66.3	69.5	76.6
66.0	65.2	67.7	74.6	65.4	69.6	69.5	69.5	66.2
66.6	70.3	65.7	66.2	66.5	66.1	71.9	72.6	72.4
64.8			68.2	64.9			74.6	72.8
69.5			69.1					109.6

with a single outlier, 109.6 determined from MNR method. Let's assume 109.6 was an incorrect test result and was replaced by 69.6, a corrected test value.

After a substantial amount of computation (see refs. 1 and 2) involving sums of squares, within batch and between batch variances, non-central t distribution, etc., the 'B'-basis value is

$$'B' = 60.93$$

The summary statistics are

Batch	n_i	$\overline{X}_i$	S_i
1	7	65.60	2.99
2	5	66.32	2.33
3	5	67.84	2.84
4	7	67.33	4.17
5	6	66.93	2.45
6	5	71.64	4.03
7	5	71.10	3.33
8	6	71.52	1.96
9	7	71.80	3.88

It should be noted the value of 60.93 is lower than 61.9 of nonparametric solution from the pooled sample. The Modified Lemon method can be overly conservative (low basis values) in order to guarantee 90% reliability with 95% confidence. The number of batches and the variability between and within the batches affect the computation of the basis value. If there are few batches and large between batch variability with small within batch variability, then this situation could result in very low basis numbers depending on the amount of variability and number of batches.

In figure 6 results from application of flowchart procedures are shown for three batches of five specimens of AS4/Epoxy material tested in compression. In this case, the mean strength values show a small amount of variability while there is a relatively large spread within each data set. 'B'-basis results from the flowchart application are for the following: ANOVA (Modified Lemon), Weibull, Normal, Lognormal, and nonparametric methods. Not included in the flowchart results are a list of assumptions that were violated. The results show a small difference in basis values except for the nonparametric solution which has the low value of 167.1. The Weibull method was suggested since it passed the K-sample AD test and the AD goodness-of-fit test. The relatively large within batch variances and small differences in mean values made it possible to pool the batches.

Figure 7 shows another result of computing the 'B'-basis values using the ANOVA, Weibull, and normal methods applied to another three selected batches from same population as in figure 6. The ANOVA result of 15.7 KSI is substantially lower than those from the other

two methods. Unfortunately, this is a result of a large difference in mean values preventing pooling of the batches resulting in the required ANOVA application. The large difference in mean values in addition to relatively small within batch variability resulted in this extremely low basis value. A 'B' value of 6.5 was obtained from the simple normal analysis using the three mean values. The result shows that for this example the ANOVA method primarily depends on the batch means. The above results would suggest obtaining more batches or investigating testing and processing procedures.

In figure 8, results are shown for the case of randomly selecting another batch from the same population described in figure 7. In this case the ANOVA result shows a value of 105.4 KSI which is substantially larger than the 15.7 KSI recorded for the three batches. The importance in having a larger number of batches is shown from these results in figures 7 and 8. Also, with more data available, the pooled results for Weibull and Normal model also resulted in less conservative values.

Figure 9 presents results showing where a substantial amount of within batch data is not necessary. In case 1, the ANOVA results for three batches of 100 data values each, resulted in 154.9 KSI while for case 2, three batches of ten each, a 'B'-basis value of 152 KSI was obtained. This result emphasizes the importance of being able to obtain more batches rather than increasing the batch size. However, the ANOVA results in figure 6 show three batches can provide reasonable results similar to pooled results if small differences in mean values relative to batch variances exist. Note that for very large batch sizes, the K-sample AD test can reject pooling of data even though there is a small difference in mean values. This rejection is statistically correct, but the user of the flowchart may consider the difference in the batch means not of engineering importance. In this case the user can make the decision of pooling or not pooling, since there will be a small difference in basis values from pooled or unpooled results. If there are large batch differences and the ANOVA method is suggested from the flowchart, then adding more batches can reduce the conservatism. The ANOVA method is a random effects model which determines a basis value representing all future values obtained from the same material system and type of test. In order to provide this guarantee in the presence of large batch to batch variability, there is the potential for it to be overly conservative which was shown in figure 7.

Reliability at Basis Stress Value

Figure 10 conceptually describes the statistical reliability of a simple structure in tension as it relates to the 'B'-basis applied stress value. In the example shown in the figure, ten percent of all the specimens (structures) will fail when subjected to load S. This statement should be incorrect at most one time in twenty (95% confidence). S is the 'B'-basis value obtained from strength (failure load) measurements from specimens of similar material and geometry. This statistical guarantee that at most 10% of the specimens will fail

can provide the engineer with a quantitative number for selecting and applying material in composite material structures. This is unlike the conventional deterministic property value approach which is an ad hoc procedure that reduces the mean strength measurements in order to obtain some design value which can result in a potentially over or under design situation. In applying the statistical basis value, it is assumed the material, geometry, and loading conditions in the structural design situation are similar to those obtained from the strength measurements. This is also true for deterministic property value applications. In the following sections the inadequacies of the deterministic approach are discussed in more detail.

Reliability Values-Statistical vs. Deterministic

In figure 11 the results of a simulation process involving the random selection of ten values from population of 191 strength measurements repeated 2,500 times are graphically displayed. For each simulation a design number or material property value is obtained from each of the three procedures $\overline{X}/2$, $(2/3)\overline{X}$, and the MIL-17 flowchart. The mean value of the data set is $\overline{X}$. The reliability values, as shown in the figure, are obtained by evaluating the population probability distribution fit to the 191 values at the design numbers.

In the case where the mean is reduced by a factor of 1/2, the strength values are very low (90 KSI), and the reliability is extremely high (1.0). The engineer may not be able to afford such a high reliability value of 1.0 (to twenty significant digits) at the expense of having design values as low as 90 KSI when mean strength is 180 KSI. The factor of 2/3 increases the design value but reduces the reliability to approximately .999. The flowchart 'B'-basis calculation provides higher strength values with acceptable reliability numbers. The other two procedures show an element of uncertainty by depending on the chosen factor. If the engineer used the factor of 1/2, this would result in an extremely over design situation requiring either rejection of the material or the design. Alternatively, if the engineer used the mean strength as design number, the reliability would be reduced to .5, although strength values would be much higher. The flowchart procedure removes the uncertainty by providing a guaranteed minimum reliability of .90 without unnecessarily reducing the basis value. The minimum reliability can be increased to .99 if necessary by using 'A'-basis computations as outlined in the MIL-17 Handbook.

Effect of Variance on Reliability Estimates

In figure 12 the effects of variance differences as they relate to reliability estimates are shown from a simulation process. This involved randomly selecting ten values from each of two separate normal distributions with same mean of 100 and different SD's of 5 and 25 repeated 2,500 times. The reliability values are obtained in a similar manner as described in the previous section, except the probability values were obtained from the normal distribution. In the case

where the SD is 5, there is very little dispersion in the reliability values. Again, the design number from $\overline{X}/2$ is substantially lower than the basis value using the flowchart process, although the reliability is very high for this number. In comparing this with the results using SD of 25, a substantial increase dispersion of the reliability values particularly for the basis results using flowchart methods. The flowchart results show similar reliability estimates for both SD's of 5 and 25, although for the $\overline{X}/2$ the reliability has been reduced substantially from twelve nines to .96. This is the result of the deterministic ($\overline{X}/2$) approach being independent of variance. This is not an issue if 50% reliability is required, but for 90% reliability, variability is important. Dividing the mean by two can be nonconservative for situation when the distribution has a large spread (long tail). In order to make adjustment for this situation, the flowchart method (basis value) is suggested. See results in the figure where the basis value adjusts to a lower level but maintains the same range for the reliability estimates. The basis value will guarantee a reliability by adjusting the design value while the safety factor approach cannot guarantee reliability. This result suggests using the basis method if it is important to maintain a certain level of reliability. The overall issue is that the flowchart methods will provide property values with specified reliability with 95% confidence while the deterministic approach is an ad hoc approach with no control of the resulting reliability estimates.

CONCLUSIONS

This paper is an exposition of the statistical procedures described in the MIL-17 Handbook for obtaining material property values. Its primary goal was to introduce the MIL-17 statistics chapter to the users so that they may use it more effectively. The methods and the sequence of operations suggested by the statistics chapter flowchart were analyzed with respect to their effectiveness, purpose, and limitations. By following the flowchart procedures, guidance is provided to the user so that reasonably accurate property values may be obtained without relying on ad hoc schemes which could potentially result in either excessively low or high values.

Each method and its order of application were discussed with respect to their specific purpose, such as model identification, batch to batch variability recognition, outlier detection, and the basis value computation. There are situations where low basis values will result, not because of limitations in the statistical procedures but are usually the result of very large or small data sets, large batch to batch variations, or model recognition.

The comparison between the statistical reliability and the deterministic approach showed a preference for statistics since it was able to guarantee a specified reliability in contrast to a deterministic method which is primarily an ad hoc process resulting in considerable uncertainty as to the corresponding reliability estimates. Finally, the authors have attempted to provide a satisfactory definition of a

statistically based material property value by introducing the tolerance limit concept and its importance. A number of illustrations were presented showing the advantage of the tolerance limit over the deterministic approach.

ACKNOWLEDGMENT

REFERENCES

1. MIL-HDBK-17B, Polymer Matrix Composites, vol. 1, February 1988. Naval Publications and Forms Center, 5801 Tabor Avenue, Philadelphia, Pennsylvania 19120.

2. Neal, D. M.; Vangel, M. G.; and Todt, F.: Determination of Statistically Based Composite Material Properties. In Engineered Materials Handbook, vol. 1, 1987, Composites, ed. Cyril A. Dostal, American Society of Metals Press, Metals Park, Ohio.

3. Neal, D. M. and Spiridigliozzi, L.: An Efficient Method for Determining "A" and "B" Allowables. ARO 83-2, in Proceedings of the 28th Conference on the Design of Experiments in Army Research, Army Research Office, 1983, pp. 199-235.

4. Stefansky, W.: Rejecting Outliers in Factorial Designs. Technometrics, vol. 14, 1972, pp. 469-479.

5. Anderson, T. W. and Darling, D. A.: A Test of Goodness-of-Fit. J. Am. Statis. Assoc., vol. 49, 1954, pp. 765-769.

6. Conover, W. J.: Practical Nonparametric Statistics. John Wiley and Sons, 1980, p. 111.

7. Hanson, D. L. and Koopmans, L. H.: Tolerance Limits for the Class of Distributions With Increasing Hazard Rates. Annals of Mathematical Statistics, vol. 35, 1964, pp. 1561-1570.

8. Scholz, F. W. and Stephens, M. A.: K-Sample Anderson-Darling Tests. J. Am. Statis. Assoc., vol. 82, 1987, p. 918.

9. Lehmann, E. L.: Testing Statistical Hypotheses. John Wiley and Sons, 1959, pp. 274-275.

10. Lemon, G. H.: Factors and One-Sided Tolerance Bounds for Balanced One-Way ANOVA Random Effects Model. J. Am. Statis. Assoc., vol. 72, 1977, pp. 676-680.

11. Mee, R. W. and Owen, D. B.: Improved Factors for One-Sided Tolerance Limits for Balanced One-Way ANOVA Random Effects Model. J. Am. Statis. Assoc., vol. 78, 1983, pp. 901-905.
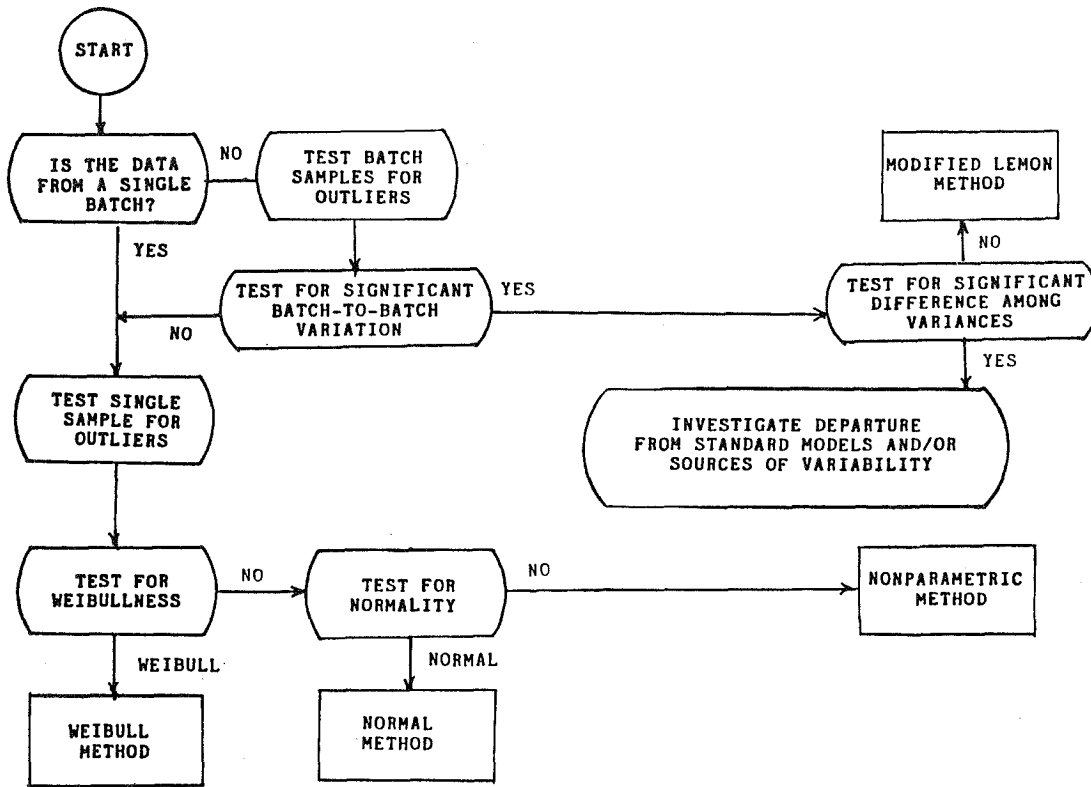
FIGURE 1   FLOW CHART ILLUSTRATING COMPUTATIONAL PROCEDURES

FOR STATISTICALLY BASED MATERIAL PROPERTIES

Random data sets of size n from a Normal distribution.

Example:
Empirical CDF

i	x	i/n (=p)
1	-2	.10
2	-1	.20
3	0	.30
4	1	.40
5	1.5	.50
6	1.8	.60
7	1.9	.70
8	2.1	.80
9	2.3	.90

mean=0

sd=1
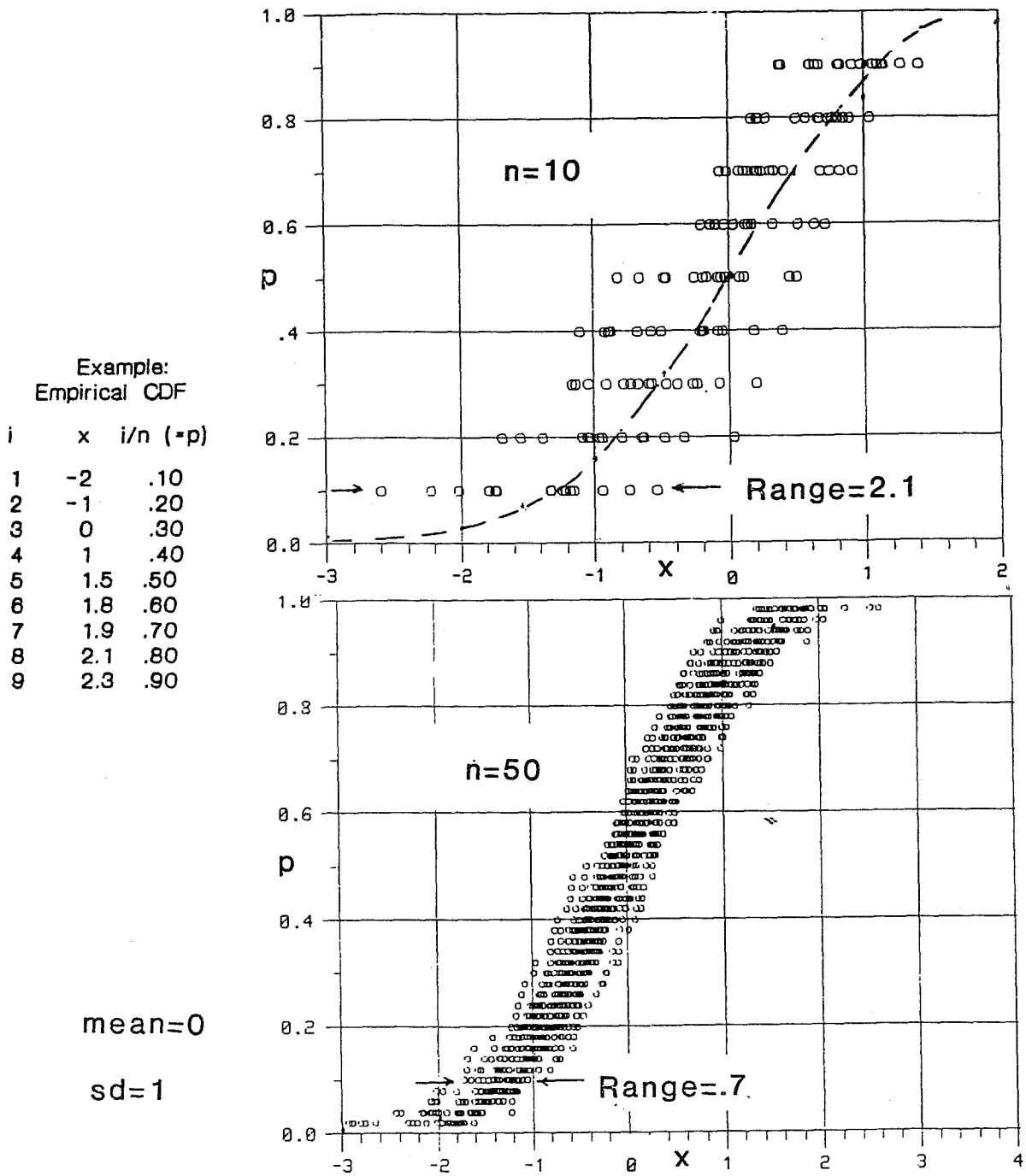
FIGURES 2 AND 3 SAMPLE SIZE EFFECT ON RELIABILITY
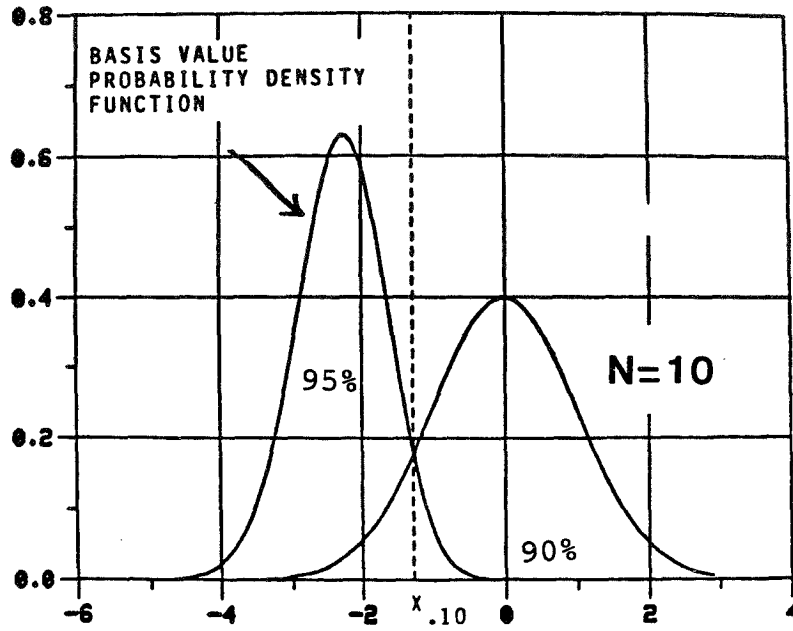
Density
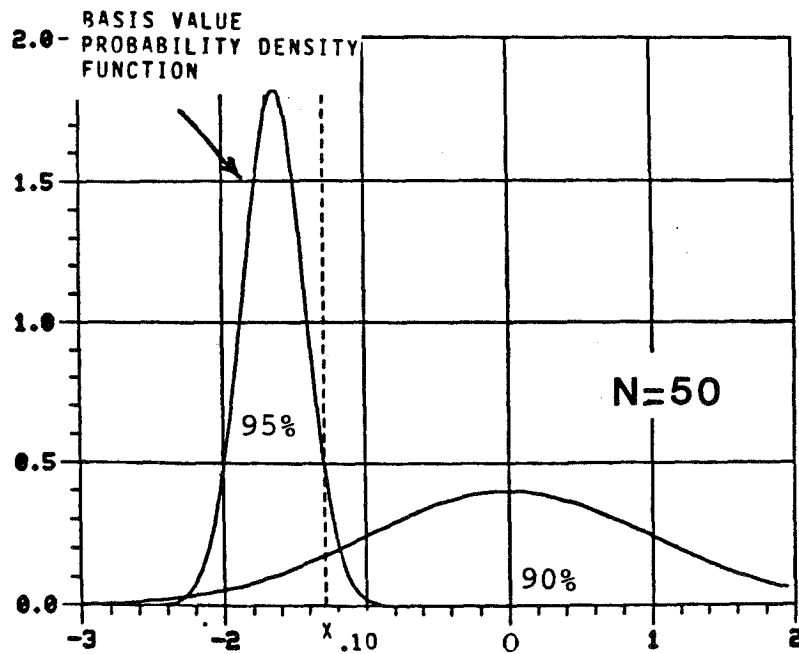
FIGURES 4 AND 5   BASIS VALUE PROB. DENSITY FUNC.

METHOD	BASIS VALUE	
ANOVA	202.6	Ksi
Weibull	196.5	Ksi
Normal	199.1	Ksi
Lognomal	199.6	Ksi
Nonparametric	167.1	Ksi

The Weibull result is recommended by the Flowchart.

(3 batches of 5, AS4/Epoxy compression)
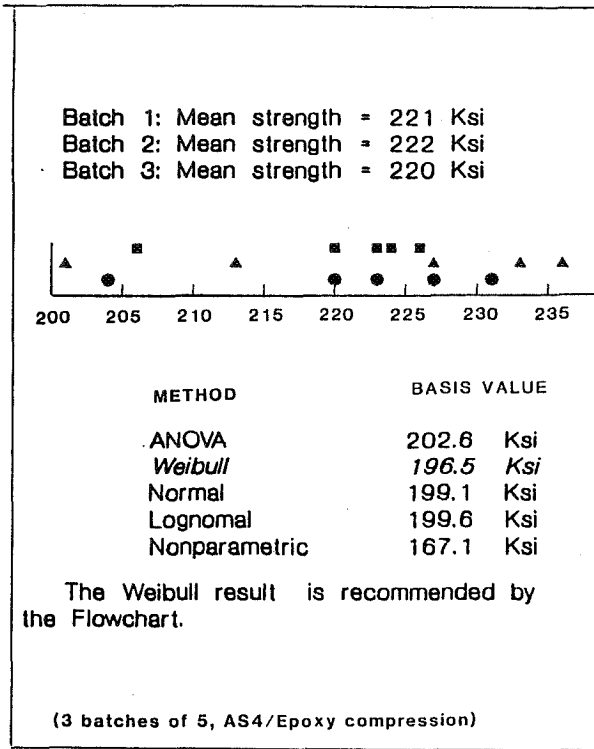
FIGURE 6 EXAMPLE OF BASIS VALUE CALCULATION
NEGLIGABLE BATCH-TO-BATCH VARIABILITY

Batch 1: Mean strength = 181 Ksi
Batch 2: Mean strength = 236 Ksi
Batch 3: Mean strength = 241 Ksi

METHOD	BASIS VALUE	
ANOVA	15.7	Ksi
Weibull	161.9	Ksi
Normal	159.3	Ksi

The ANOVA result is recommended by the Flowchart. Normal analysis using only the three mean values gives a B-basis value of 6.5. Either reject the material as too variable or obtain more batches.

(3 batches of 5, AS4/Epoxy compression)

FIGURE 7 EXAMPLE OF BASIS VALUE CALCULATION
SUBSTANTIAL BATCH-TO-BATCH VARIABILITY

Batch 1: Mean strength = 181 Ksi
Batch 2: Mean strength = 236 Ksi
Batch 3: Mean strength = 241 Ksi
Batch 4: Mean strength = 217 Ksi

METHOD	BASIS VALUE	
ANOVA	105.4	Ksi
Weibull	170.3	Ksi
Normal	170.0	Ksi

The ANOVA result is recommended by the Flowchart. A single additional batch increased the basis value from 15.7 Ksi to 105.4 Ksi.

(4 batches of 5, AS4/Epoxy compression)
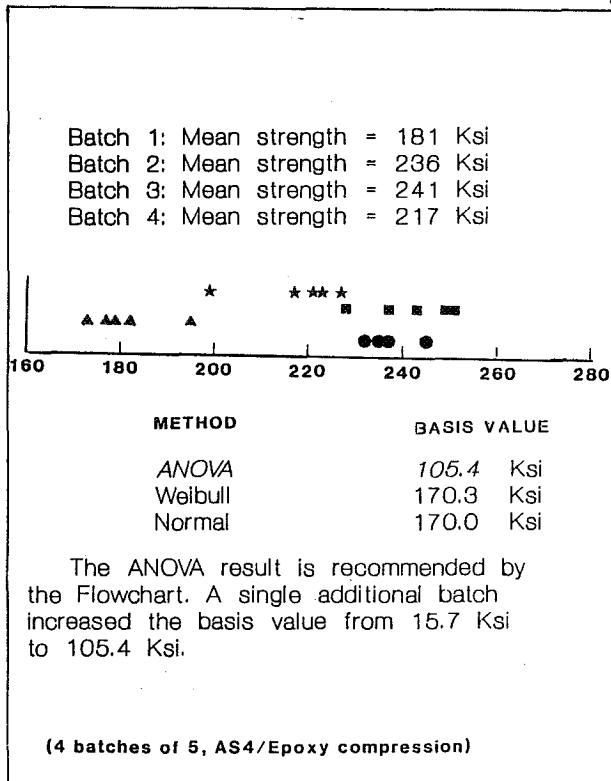
FIGURE 8 EXAMPLE OF BASIS VALUE CALCULATION
THE EFFECT OF AN ADDITIONAL BATCH

Case 1:
T300/Epoxy Unidirectional Tension
3 batches of 100 specimens each

Method	Basis Value
ANOVA	154.9
Weibull	171.7
Normal	175.7

Case 2:
One random dataset of 10 from each of the above three batches.

Method	Basis Value
ANOVA	152.0
Weibull	165.7
Normal	172.5

The ANOVA method is recommended by the Flowchart. Note that there is little difference between basis values for batch sizes of 10 and basis values for batch sizes of 100.

FIGURE 9 THE EFFECT OF INCREASED BATCH SIZE:
SUBSTANTIAL BETWEEN-BATCH VARIABILITY

The reliability of a test specimen at the B-basis stress should be high. For a statistically based B- basis value calculated from a procedure appropriate to the data, this reliability is guaranteed to be at least 90% (i,e., 90% with 95% confidence).

S = B-basis stress

$\longleftarrow$ [=====] $\longrightarrow$ **S**

N specimens of which F fail at or below stress S.

Estimated reliability at B-basis stress (N-F)/N

FIGURE 10   RELIABILITY AT BASIS STRESS:

STATISTICAL VS. DETERMINISTIC

Population: 191 strength values

Dataset: 10 specimens chosen 2500 times randomly

strength

80	100	120	140	160	180

(1.0)——(1.0)
$\overline{X}/2$

(.999)——(.998)
$\overline{X}/1.5$

(.997)———————(.918)
B-basis(Flowchart)

() Reliability Values

(T300/Epoxy Unidirectional)   TENSION
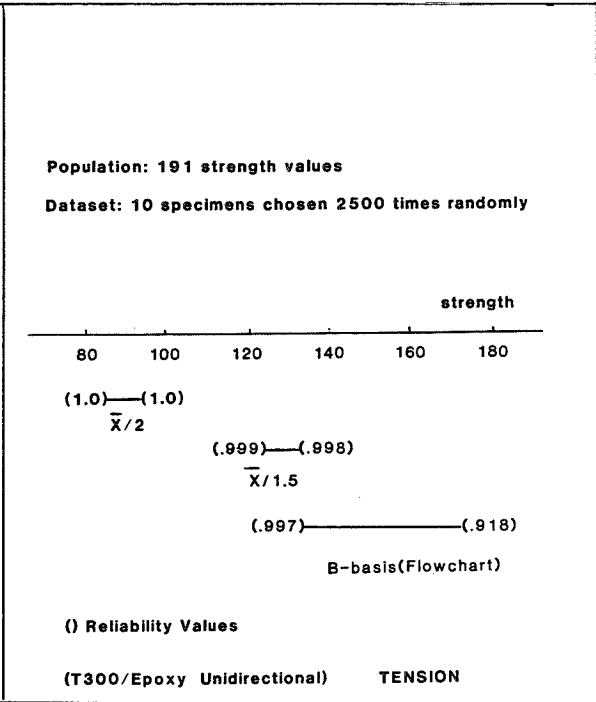
FIGURE 11   RELIABILITY / STRENGTH COMPARISON:

A CASE STUDY - STAT. VS. DETERMINISTIC

Population mean 100, 10 values per dataset

Standard Deviation 5   strength

40   50   60   70   80   . 90

                        (.999...)——(.999...)   (.99)—(.93)
                                $\overline{X}$/1.5   Basis Value

    (.999...)——(.999...)
            $\overline{X}$/2

Standard Deviation 25   strength

20   30   40   50   60   70   80

        (.99)————————————————(.93)
                Basis Value

                                (.95)————(.86)
                                    $\overline{X}$/1.5

                (.99)————(.96)
                    . $\overline{X}$/2

(2500 rand. norm. samp.)   ( ) 90% conf.
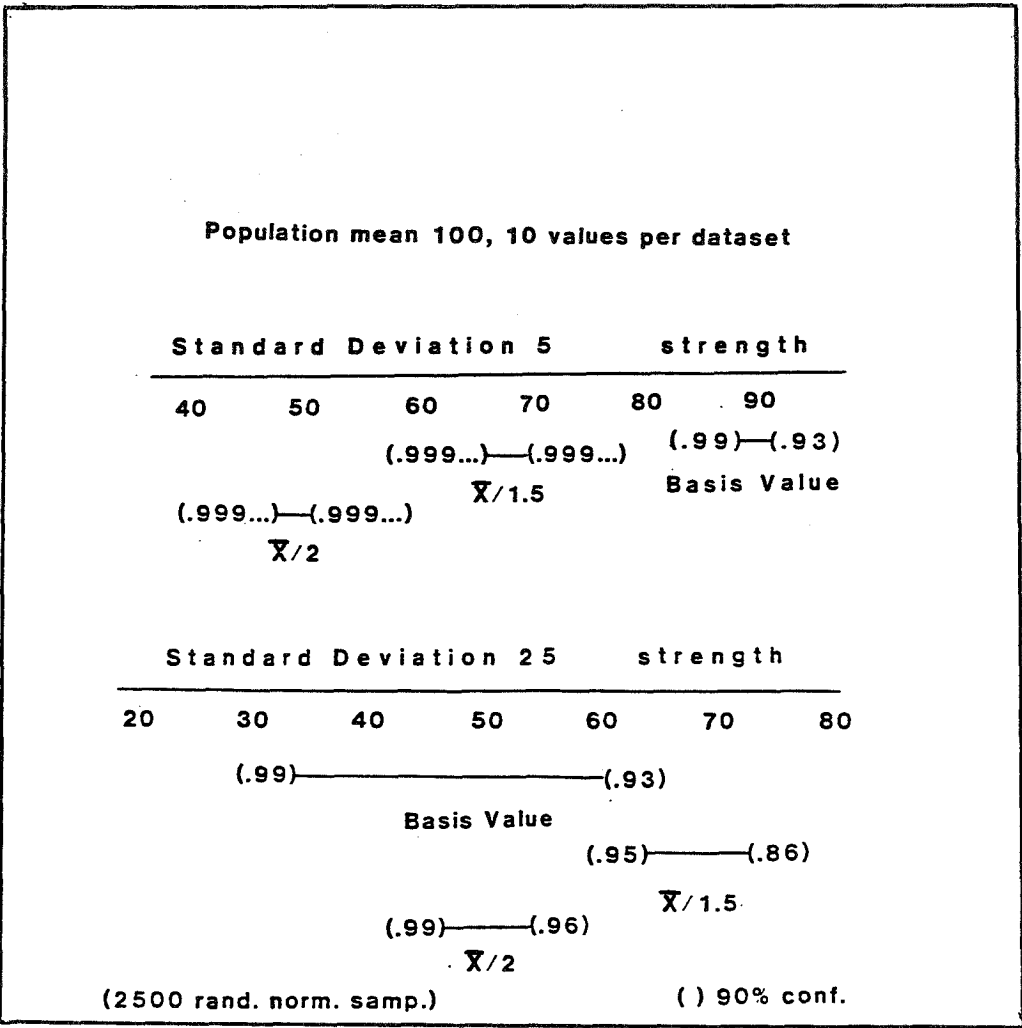
FIGURE 12   RELIABILITY / STRENGTH COMPARISON:

A CASE STUDY - STAT. VS DETERMINISTIC

Methodology in Design (B)

Chairman: Thomas Hess
Naval Air Development Center

COMPRESSION BEHAVIOR OF GRAPHITE-EPOXY AND GRAPHITE-THERMOPLASTIC PANELS WITH CIRCULAR HOLES OR IMPACT DAMAGE

N92-32582

Dawn C. Jegley
NASA Langley Research Center

SUMMARY

An experimental investigation of the compression behavior of laminated specimens made from graphite-epoxy tape (AS4-3502), graphite-thermoplastic tape (AS4-PEEK) and graphite-thermoplastic fabric (AS4-PEEK) was conducted. Specimens with five different stacking sequences were loaded to failure in uniaxial compression. Some of the specimens had central circular holes with diameters up to 65 percent of the specimen width. Other specimens were subjected to low speed impact with impact energy up to 30 J prior to compressive loading. This investigation indicates that graphite-thermoplastic specimens with holes have up to 15 percent lower failure stresses and strains than graphite-epoxy specimens with the same stacking sequence and hole size. However, graphite-thermoplastic specimens subjected to low speed impact have up to 15 percent higher failure stresses and strains than graphite-epoxy specimens with the same stacking sequence and impact energy. Compression tests of graphite-thermoplastic specimens constructed of unidirectional tape and of fabric indicate that the material form has little effect on failure strains in specimens with holes or low speed impact damage.

INTRODUCTION

Light-weight composite materials are increasingly being used in aircraft structures. The structural response of laminated composites containing thermoplastic resin must be evaluated before they can be considered for application to civil transport aircraft structures. Quasi-isotropic graphite-thermoplastic laminates have been evaluated (e.g., ref. 1), but other stacking sequences should be considered since all laminates do not exhibit the same behavior. An experimental investigation of the compression behavior of laminated specimens made from graphite-epoxy tape (AS4-3502), graphite-thermoplastic tape (AS4-PEEK) and graphite-thermoplastic fabric (AS4-PEEK) has been conducted and the results of the investigation are presented in the present paper. Results for specimens in two categories are presented, specimens with 0° plies and specimens with no 0° plies. Specimens with thicknesses ranging from .11 to .46 cm were constructed and loaded in uniaxial compression. Some specimens had central circular holes with diameters up to 65 percent of the specimen width. Other specimens were subjected to low speed impact with impact energy up to 30 J and then loaded to failure in uniaxial compression.

TEST SPECIMENS

The graphite-epoxy specimens tested in this investigation were fabricated from

commercially available Hercules Incorporated AS4^{+} graphite fiber and 3502[+] thermosetting epoxy resin. Graphite-epoxy specimens were made from unidirectional tape and are designated with the letter E in table I. The graphite-thermoplastic specimens were fabricated from commercially available Hercules Incorporated AS4^{+} graphite fiber and ICI PEEK[+] resin. Graphite-thermoplastic specimens made from unidirectional tape are designated with the letter T in table I. Graphite-thermoplastic specimens in which the $\pm45^{\circ}$ plies are made from woven fabric are designated with the letter F in table I. The five stacking sequences considered are as follows: stacking sequence 1, $[(\pm45)_2/0_4/90/\pm45/0_2/90]_s$; stacking sequence 2, $[(\pm45)_3/0_2/90/(\pm45)_2/0/\overline{90}]_s$; stacking sequence 3, $[\pm45/0_6/\pm45/0_6]_s$; stacking sequence 4, $[\pm45/0_6/\pm45/0_6/\overline{90}]_s$; and stacking sequence 5, $[(\pm45)_2/\overline{90}]_s$. Each specimen type is designated by a letter indicating the material and a number indicating the stacking sequence. Individual specimens are identified by a specimen type followed by a number 1 through 15. For example, the first specimen tested which was made from graphite-thermoplastic tape with stacking sequence $[(\pm45)_2/0_4/90/\pm45/0_2/90]_s$ is designated T1-1. The stacking sequences, specimen designations and the number of specimens tested of each type of specimen are listed in table I. All specimens were nominally 25.4 cm long and either 7.62 or 10.16 cm wide. Centrally located circular holes were machined into some of the specimens with diamond impregnated core drills. Specimen cross sectional area and hole size are listed in tables II and III. Nominal material properties of both material systems are listed in table IV. The loaded ends of each specimen were machined flat and parallel to permit uniform end displacement. All specimens were ultrasonically C-scanned to establish specimen quality prior to testing.

APPARATUS AND TESTS

Test specimens were loaded in uniaxial compression using a 1.33 MN capacity hydraulic testing machine. The loaded ends of the specimen were clamped by fixtures during testing and the sides were simply supported by restraints to prevent the specimen from buckling as a wide column. A typical specimen mounted in the support fixture is shown in figure 1. Electrical resistance strain gages were used to monitor strains and dc differential transformers were used to monitor displacements. The locations of the back-to-back strain gages used to monitor the far-field laminate strains in all specimens and along a horizontal line between the edge of the hole and the side of the specimen are shown in figure 1. All specimens were painted white on one side to give a reflective surface so that a moire fringe technique could be used to monitor out-of-plane deformation patterns.

A procedure detailed in ref. 2 was used in the current study for impacting specimens. Aluminum spheres 1.27 cm in diameter were used as impact projectiles. The projectiles were directed normal to the plane of the specimen at speeds from 15 to 153 m/s corresponding to impact energies from .35 to 34. J. All specimens were

---

[+]Identification of commercial products and companies in this paper is used to describe adequately the materials. The identification of these commercial products does not constitute endorsement, expressed or implied, of such products by the National Aeronautics and Space Administration.

538

impacted at the center of the test section. The applied load, the displacement of the loading platten and the strain gage signals were recorded at regular intervals.

RESULTS AND DISCUSSION

Test results for specimens constructed with five stacking sequences (listed in table I) are presented in this section. A comparison is made between specimens with the same stacking sequence constructed from graphite-epoxy tape and graphite-thermoplastic tape, specimens with the same stacking sequence constructed from graphite-thermoplastic tape and fabric, and specimens constructed from graphite-thermoplastic tape with clustered 0° plies and separated 0° plies. Specimen stiffness, strain concentrations around holes and the effects of holes or impact damage on failure strain are discussed. Post-buckling of thin specimens will also be discussed.

Control Specimens

Control specimens (those without holes or impact damage) were constructed with each stacking sequence studied. Control specimens made from graphite-epoxy and graphite-thermoplastic materials with stacking sequence $[(\pm 45)_2/0_4/90/\pm 45/0_2/90]_s$, designated E1-1 and T1-1 in table II, respectively, buckled prior to failure. Moire fringe patterns indicate that the control specimen E1-1 buckled into 3 half-waves while the control specimen T1-1 buckled into 1 half-wave at about 70 percent of the failure load. The stress-strain relationships for these control specimens are shown in figure 2. The slope of these curves indicates that the prebuckling stiffness of specimen E1-1 (which is 5 percent thicker than specimen T1-1) is about 8 percent higher than the prebuckling stiffness of specimen T1-1 even though they have the same stacking sequence. A slight reduction in stiffness at buckling can be seen in figure 2 at a stress of about 400 MPa. Both control specimens E1-1 and T1-1 failed near a clamped edge.

Control specimens with stacking sequence $[(\pm 45)_3/0_2/90/(\pm 45)_2/0/\overline{90}]_s$ made from graphite-thermoplastic tape and woven fabric, designated T2-1 and F2-1 respectively, buckled into 3 half-waves prior to failure near a clamped edge. The stress-strain relationships for control specimens of types T2 and F2 are shown in figure 3. Since these specimens contain 69 percent $\pm 45^{\circ}$ plies, their stress-strain relationships are nonlinear, indicating nonlinear material properties. The slope of the curves indicates that the difference in prebuckling stiffness of the two specimens is approximately the same. The fabric specimen failed at a higher stress and strain than the tape specimen.

In graphite-epoxy specimens conventional stacking sequences rarely contain many plies of the same orientation clustered together. To determine whether clustering many 0° plies in the center of a graphite-thermoplastic laminate influences failure due to uniaxial compressive loading, two stacking sequences were studied. Control specimens made from graphite-thermoplastic tape with stacking sequences $[\pm 45/0_6/\pm 45/0_6]_s$ and $[\pm 45/0_6/\pm 45/0_6/\overline{90}]_s$, designated T3-1 and T4-1, respectively, do not buckle prior to failure. Both control specimens T3-1 and T4-1 failed near a clamped edge at approximately the same failure strain. Specimen T4-1 is about 5 percent thicker and stiffer than specimen T3-1.

All previously mentioned specimens contain 28 or more plies. These relatively thick specimens display a different behavior than specimens containing significantly fewer plies. To compare relatively thin specimens, graphite-epoxy tape, graphite-thermoplastic tape and graphite-thermoplastic fabric specimens (designated as specimen types E5, T5 and F5, respectively) with stacking sequence $[(\pm 45)_2/\overline{90}]_s$ were studied. The stress-strain relationships for the control specimens of specimen types E5, T5 and F5 are shown in figure 4. The fabric specimen is about 12 percent thinner and about 10 percent less stiff than the tape specimens. The control specimens of specimen types E5, T5, and F5 buckled into 4 half-waves of approximately equal wavelength then failed at mid-length of the specimen (along a nodal line). Each specimen carried load well into the postbuckling range. Failure strain for the graphite-epoxy control specimen was 35 percent and 20 percent lower than the failure strain for the graphite-thermoplastic fabric and tape specimens, respectively. The graphite-thermoplastic fabric specimen had the highest failure strain of .0138. The prebuckling stiffness in the graphite-epoxy specimen is about 10 percent higher than the prebuckling stiffness in the graphite-thermoplastic specimens. The postbuckling stiffness in the graphite-epoxy specimen is about 25 percent higher than the postbuckling stiffness in the graphite-thermoplastic specimens. The shear stiffness of a graphite-thermoplastic $0°$ lamina is 15 percent lower than the shear stiffness of a graphite-epoxy $0°$ lamina. Since this $[(\pm 45)_2/\overline{90}]_s$ laminate is 88 percent $\pm 45°$ plies, the graphite-thermoplastic specimens have the lower laminate stiffnesses.

Specimens with $0°$ Plies

Specimens with holes

Strain distributions around holes.--An analysis was conducted using the finite element code EAL[3] to examine strain distributions around a hole for specimens of types E1 and T1. In the finite element analysis one quarter of the specimen was modeled. The finite element grids contained approximately 175 quadrilateral elements. Smaller elements were used near the hole edge than away from the hole. Specific grid configurations varied from one hole size to the next. Typical properties of AS4/3502 are shown in table IV. Properties of AS4/PEEK presented in the literature[4-6] vary somewhat. The properties shown in table IV were used in this study.

Normalized strain distributions based on strain gage measurements and analytical predictions for specimens with hole diameter .794 and 2.54 cm are shown in figure 5. For the specimens with the larger hole, the strains predicted for the graphite-thermoplastic specimens are slightly higher than those predicted for the graphite-epoxy specimens. This trend is not apparent in the experimental results. No difference between the strain distribution of the two material systems can be seen for the specimens with the smaller hole. A study of strain distributions around holes presented in reference 7 indicates that the difference in strain concentration at the edge of the hole is a finite width effect, i.e., dependent upon a/w, where a is the hole diameter and w is the plate width. The strain concentration is higher for the graphite-thermoplastic specimen than for the graphite-epoxy specimen for the larger hole size shown, indicating that the graphite-thermoplastic specimens are more notch sensitive[7] than the graphite-epoxy specimens.

Failure Characteristics.--The effect of hole size on failure strain is shown in figure 6a for graphite-epoxy and graphite-thermoplastic specimens with stacking sequence $[(\pm45)_2/0_4/90/\pm45/0_2/90]_s$ (specimens of type E1 and T1). Specimen geometry, failure stress and failure strain are shown in table II for all specimens of types E1 and T1 tested. All specimens are nominally 25.4 cm long, 7.62 cm wide and .381 cm thick.

All specimens of types E1 and T1 with holes failed through the hole and exhibited no buckling behavior. Failure strain is 5 to 30 percent higher for specimens of type E1 than for specimens of type T1 with the same hole size. Failure of each specimen involved delamination between plies and laminate failure in transverse cracking across the specimen, as shown in the photographs of specimens E1-7 and T1-5 in figure 6b. Failed fibers became wedged between other fibers during failure. The failure of the graphite-thermoplastic specimens at consistently lower stresses and strains than the graphite-epoxy specimens may be related to the lower shear stiffness of the AS4/PEEK material. However, since this $[\pm45_2/0_4/90/\pm45/0_2/90]_s$ laminate contains only 43 percent $\pm45^o$ plies, matrix shearing is not the dominate failure mode. No matrix shearing bands[8] are evident after failure. C-scans of specimens after testing indicate that off-axis (in the $\pm45^o$ directions) and longitudinal (in the 0° direction) cracking occurred during loading in both the graphite-epoxy and graphite-thermoplastic specimens. The graphite-thermoplastic specimens behaved similarly to the graphite-epoxy specimens with small hole sizes (a/w < .25) but the graphite-epoxy specimens fail at significantly higher strains than the graphite-thermoplastic specimens when larger holes were present.

The effect of hole size on failure strain is shown in figure 7 for specimens with stacking sequence $[(\pm45)_3/0_2/90/(\pm45)_2/0/\overline{90}]_s$ made from graphite-thermoplastic tape and graphite-thermoplastic woven fabric, designated as specimen types T2 and F2, respectively. Average specimen cross sectional area away from the hole and the range of hole sizes considered is presented in table III. Nominal specimen width is 7.62 cm and nominal thickness is .38 cm. All specimens of type T2 and F2 with holes failed through the hole and exhibited no buckling behavior. Failure strains are almost identical for specimens of the same hole size for the two material forms, as shown in figure 7. C-scans made of specimens after failure indicate that no off-axis cracking occurred in any of the specimens of type T2 or F2. Some longitudinal cracking occurred in the specimens with large holes.

To determine whether clustering many 0° plies in the center of a graphite-thermoplastic laminate influences the failure of specimens with holes, graphite-thermoplastic specimens made from tape with stacking sequences $[\pm45/0_6/\pm45/0_6]_s$ and $[\pm45/0_6/\pm45/0_6/\overline{90}]_s$, designated as specimen types T3 and T4, respectively, were examined. The average far field cross sectional area of these specimens and the range of hole sizes considered is presented in table III. Nominal specimen width is 7.62 cm and thickness is .43 cm. The effect of hole size on failure strain is shown in figure 8a for these specimens. A comparison of the failure strains of the specimens indicates that there is no consistent difference between specimens of the two stacking sequences. The clustered 0° plies do not induce premature failure in specimens with holes.

No specimens of type T3 or T4 buckled prior to failure. All specimens with holes failed through the hole. A photograph of the edge of the hole in specimen T4-6 with a 5.08-cm-diameter hole is shown in figure 8b. Delamination between 0° and $+45^{\circ}$ or -45° plies is the primary cause of failure. Delamination can be seen at the edge of the hole. Transverse cracks formed across the width of the specimen as the matrix failed.

Specimens with Impact Damage

The effect of impact damage on failure strain is shown in figure 9 for specimens with stacking sequence $[\pm 45_2/0_4/90/\pm 45/0_2/90]_s$ made from graphite-epoxy tape and graphite-thermoplastic tape, designated as specimen types E1 and T1, respectively. Specimen cross sectional area, impact energy, failure stress and failure strain are presented in table II for all specimens of type E1 and T1 tested. All specimens are nominally 25.4 cm long, 7.62 cm wide and .381 cm thick. Graphite-epoxy specimens not impacted or subjected to impact speed of about 30 m/sec (1.4 J of impact energy), specimens E1-1 and E1-8 in table II, buckled into 3 half-waves. Graphite-thermoplastic specimens not impacted or subjected to impact speed of about 30 m/sec, specimens T1-1 and T1-8 in table II, buckled into one half-wave. No other specimen buckled. Specimens which buckled failed at the end of the specimen. All other specimens failed through the impact site. Failure loads for specimens with end failures are about the same, independent of material or impact damage. Specimens subjected to impact speeds above 31 m/sec show significant reduction in load carrying ability due to impact damage in both materials; however, this reduction is more pronounced in the graphite-epoxy specimens. For impact speeds above 92 m/sec (12.5 J of impact energy), failure strain remains constant as impact speed increases. C-scans made of specimens after impact but before compressive loading reveal that for impact speeds less than 92 m/sec, the graphite-epoxy specimen has more damage than the graphite-thermoplastic specimen for each impact speed. However, for impact speeds greater than 92 m/sec, the graphite-thermoplastic specimen sustained more damage than the graphite-epoxy specimen. C-scans made for specimens subjected to all impact speeds indicate that damage is confined to an oval around the impact site. There is no longitudinal splitting or off-axis damage propagation for either type of material. The graphite-epoxy and graphite-thermoplastic specimens subjected to severe impact damage (impact speeds greater than 92 m/sec) failed at about 33 percent and 45 percent, respectively, of the failure strain of the undamaged specimens. The failure mode in impacted specimens which did not buckle, as in the specimens with holes, involved delaminations. The same failure mode (dominated by delamination) is seen in specimens of both material systems in this study as described in reference 9 for quasi-isotropic AS4-3502 specimens subjected to impact damage.

The effect of impact damage on failure strain is shown in figure 10 for graphite-thermoplastic specimens with stacking sequence $[(\pm 45)_3/0_2/90/(\pm 45)_2/0/\overline{90}]_s$ made from tape (specimens of type T2) and from woven fabric (specimens of type F2). The range of impact energies is presented in table III. Nominal specimen width is 10.16 cm and nominal thickness is .38 cm. All specimens subjected to impact speeds from 31 to 46 m/sec (impact energy of 1.4 to 3.3 J) buckled prior to failure. Specimens subjected to higher impact speeds did not buckle. Specimens subjected to impact speed of 31 m/sec failed at one end of the specimen. The tape specimen impacted at 47 m/sec buckled into 3 half-waves then failed at a nodal line, away from the impact site. All other impact-damaged specimens failed at the impact site. The mode of failure in all specimens involved delamination and fiber breakage. The tape specimens exhibited more delamination than the fabric specimens since each pair of

$\pm 45^\circ$ plies is woven together and cannot delaminate in the fabric specimen. Failure strains are almost the same for tape and fabric specimens, as shown in figure 10.

To determine whether clustering many 0° plies in the center of a graphite-thermoplastic laminate influences the failure of specimens subjected to low speed impact, graphite-thermoplastic specimens made from tape with stacking sequences $[\pm 45/0_6/\pm 45/0_6]_s$ (specimen type T3) and $[\pm 45/0_6/\pm 45/0_6/\overline{90}]_s$ (specimen type T4) are examined. The range of impact energies considered is outlined in table III. Nominal specimen width is 7.62 cm and specimen thickness is .43 cm. No specimens of type T3 or T4 buckled prior to failure. Those impacted with energy less than 1 J failed near a clamped edge. All other impacted specimens failed through the impact site. Delamination was the primary cause of failure. Transverse cracks formed across the specimen as the matrix failed. Despite the high percentage of 0° plies (75%), C-scans made after severe impact and compressive loading reveal no indication of longitudinal cracks as are described in reference 9 for failures of unidirectional laminates. The effect of impact damage on failure strain is shown in figure 11 for the specimens of type T3 and T4. There is no consistent difference between the failure strains of specimens of the two stacking sequences. The clustered 0° plies do not induce premature failure in specimens subjected to impact damage.

<div align="center">Specimens with No 0° Plies</div>

Specimens with Holes

Strain distributions around holes.--Normalized prebuckling strain distributions based on strain gage measurements and analytical predictions for specimens with hole diameters of .794, 2.54 and 5.0 cm are shown in figure 12. This distribution indicates that the graphite-thermoplastic tape specimens have the highest ratio of local strain to far field strain and the graphite-thermoplastic fabric specimens have the lowest ratio for all hole sizes. Material properties for fabric specimens are assumed to be the same as for tape specimens made of graphite-thermoplastic material but the thickness of the specimens differ by about 7%. The calculated strain ratios are the same for the graphite-thermoplastic fabric and tape specimens.

Failure characteristics.--The prebuckling stiffness of a finite width specimen may be affected by the size of a hole. The prebuckling stiffness of specimens with large holes is not the same as the prebuckling stiffness of control specimens or specimens with small holes. This difference in prebuckling stiffness for graphite-epoxy tape specimens with stacking sequence $[(\pm 45)_2/\overline{90}]_s$ is shown in figure 13. Specimens of this type with large holes buckle at much lower loads than specimens with smaller holes. This reduction in prebuckling stiffness and in buckling load is caused by a combination of the effect of the large hole and the significant anisotropic effects inherent in this stacking sequence. For this laminate, the ratio of the anisotropic terms to the longitudinal bending stiffness, D_{16}/D_{11} and D_{26}/D_{11}, is approximately 0.25 . All three types of specimens demonstrate a similar reduction in prebuckling stiffness as hole size increases for this stacking sequence.

The effects of hole size on failure strain are shown in figure 14 for specimens with stacking sequence $[(\pm 45)_2/\overline{90}]_s$ made from graphite-epoxy tape (specimen type E5), graphite-thermoplastic tape (specimen type T5) and graphite-thermoplastic fabric (specimen type F5). The range of hole sizes considered is presented in table III for all specimens of types E5, T5 and F5 tested. All specimens are nominally 25.4 cm

long, 7.62 cm wide and .127 cm thick. The specimens of types E5, T5 and F5 with holes buckled into 3 or more half-waves (often with different wavelengths) with one half-wave centered around the hole. Buckling became evident on moire patterns at or below 40 percent of the undamaged specimen's failure load in specimens with small holes. Buckling became evident on moire patterns at less than 20 percent of the undamaged specimen's failure load for specimens with large holes. The failure mode of all specimens involved delamination and transverse cracking. C-scans made after testing indicate that no longitudinal or off-axis cracking occurred in the graphite-thermoplastic specimens, but both types of cracks appeared in the graphite-epoxy specimens. The specimens with small holes failed at a nodal line in the top half of the specimen. Holes with a/w less than .4 have almost no effect on failure stress for all three types of specimens. The graphite-epoxy specimens with a/w less than .4 have 20 percent lower failure stresses than the graphite-thermoplastic specimens. The specimens with larger holes (a/w > .4) fail through the hole. Failure stresses for graphite-epoxy specimens with larger holes are slightly lower than those for the graphite-thermoplastic specimens. The graphite-thermoplastic fabric specimens can withstand 10-20 percent higher stress than the graphite-epoxy specimens. The failure stresses of the graphite-thermoplastic tape specimens are 5-10 percent above those of the graphite-epoxy specimens.

Specimens with Impact Damage

The effects of impact damage on failure strain is shown in figure 15 for specimens with stacking sequence $[(\pm45)_2/\overline{90}]_s$ made from graphite-epoxy tape (specimen type E5), graphite-thermoplastic tape (specimen type T5) and graphite-thermoplastic fabric (specimen type F5). The range of impact energies considered is presented in table III for all specimens of types E5, T5 and F5 tested. All specimens are nominally 25.4 cm long, 7.62 cm wide and .127 cm thick.

All impacted specimens buckled prior to failure. Specimens subjected to low impact energies (less than 5.5 J with impact speeds less than about 61 m/sec) failed the same way the control specimens failed. The specimens buckled into four half-waves with a nodal line through the impact site. The specimens failed at this nodal line by transverse cracking across the width of the specimen. Similar results are presented in reference 10 for specimens of thicknesses ranging from .20 to .33 cm and impacted at speeds up to 95 m/sec.

Specimens subjected to impact energies greater than 6 J buckled into 3, 4 or 5 half-waves with one half-wave centered on the impact site and the specimens failed through the impact site by transverse cracking. The wavelengths of each half-wave within a specimen were not necessarily the same. Off-axis cracking is evident in the specimens after impact and before compressive loading for all specimens with impact speeds more than about 61 m/sec (impact energy of 5.5 J). All impact specimens failed through the center of the specimen (impact site) except the fabric specimen impacted at 107 m/sec (impact energy of 17. J) which buckled into two half-waves then failed near the center of one of the half-waves. C-scans made after the test of this specimen indicate that no longitudinal or off-axis cracking occurred. All three types of specimens have approximately the same failure stress for impact speeds less than about 61 m/sec. Above 61 m/sec, all three types of specimens exhibit a reduction in failure stress due to impact damage.

A comparison of failure stresses for the three types of specimens, shown in figure 15, indicates that the graphite-thermoplastic specimens withstand about 30

percent more stress than the graphite-epoxy specimens for impact speeds below about 61 m/sec (impact energy of 5.5 J). Graphite-thermoplastic tape specimens withstand 10-20 percent more strain than the graphite-epoxy specimens for impact speeds below 61 m/sec. However, the reduction in failure strain due to impact damage is larger in both types of graphite-thermoplastic specimens than in the graphite-epoxy specimens. This difference may be related to the amount of damage sustained when the impactor penetrates and passes through the specimens rather than bouncing off the specimen. The impactor fully penetrates the graphite-epoxy specimens at impact speed of more than 73 m/sec (impact energy of 7.5 J), the fabric specimens at speeds of more than 84 m/sec (impact energy of 10.5 J) and the tape graphite-thermoplastic specimens at speeds of more than 99 m/sec (impact energy of 14.7 J). The filled data points in the figure represent impacts in which the impactor penetrated the specimen and the open data points represent impacts in which the impactor bounced off the specimen. C-scans of some specimens after impact indicate that the graphite-epoxy specimens have the smallest damage area for a given impact energy. In some cases the graphite-thermoplastic tape specimens have damaged areas up to three times as large as the damaged areas of the graphite-epoxy specimens for the same impact energy. The graphite-thermoplastic fabric specimens have damaged areas up to twice as large as the damaged areas of the graphite-epoxy specimens for the same impact energy. The size of the damaged area does not directly correlate to the reduction in failure stress.

CONCLUDING REMARKS

An experimental investigation of the compression behavior of laminated specimens made from graphite-epoxy tape (AS4-3502), graphite-thermoplastic tape (AS4-PEEK) and graphite-thermoplastic fabric (AS4-PEEK) was conducted. Specimens with no damage prior to compressive loading, specimens with central circular holes with diameters up to 65 percent of the specimen width and specimens subjected to low speed impact damage were loaded to failure in uniaxial compression.

Graphite-thermoplastic tape specimens with holes have up to 15 percent lower failure stresses and strains than graphite-epoxy specimens with the same stacking sequence and hole size. However, graphite-thermoplastic specimens have higher failure stresses and strains than graphite-epoxy specimens of the same stacking sequence and impact energy. Tests of graphite-thermoplastic specimens constructed from unidirectional tape and from fabric indicate that the material form has little effect on failure stresses associated with circular holes or with low speed impact damage. Compression tests of graphite-thermoplastic specimens with holes or with impact damage with many clustered plies of the same orientation indicate that having many clustered 0° plies does not influence the load carrying ability of the specimen. Postbuckled graphite-thermoplastic specimens with holes carry more load than similar postbuckled graphite-epoxy specimens.

REFERENCES

1. Williams, Jerry G.; O'Brien, T. Kevin; and Chapman, A. J. III: Comparison of
   Toughened Composite Laminates using NASA Standard Damage Tolerance Tests,
   ACEE Composite Structures Technology, NASA Conference Publication 2321, August
   1984, pp. 51-74.

2. Starnes, J. H. Jr.; Rhodes, M. D.; and Williams, J. G.: Effect of Impact Damage
   and Holes on the Compression Strength of a Graphite/Epoxy Laminate.
   Nondestructive Evaluation and Flaw Criticality for Composite Materials, edited
   by R. B. Pipes, ASTM STP 696, 1979, pp. 145-171.

3. Whetstone, W. D.: EISI-EAL System Level 2091. Engineering Information Systems,
   Inc., July 1983.

4. Malik, B.; Palazotto, A; and Whitner, J.: Notch Strength of GR/PEEK Composite
   Materials at Elevated Temperatures. AIAA Paper No. 85-0648, 1985.

5. Coquill, S. L.; and Adams, D. F.: Mechanical Properties of Several Neat Polymer
   Matrix Materials and Unidirectional Carbon Fiber-Reinforced Composites. NASA
   CR 181805, April 1989.

6. Anon.: Property Data of Aromatic Polymer Composite, APC-2/Hercules Magnamite
   AS4 Carbon Fibre. Data Sheet 3a, ICI-Fiberite, 1987.

7. Rhodes, Marvin D.; Mikulas, Martin M., Jr.; and McGowan, Paul E.: Effects of
   Orthotropy and Width on the Compression Strength of Graphite-epoxy Panels with
   Holes. AIAA Journal, vol. 22, no. 9, September 1984, pp. 1283-1292.

8. Shuart, M. J.; and Williams, J. G.: Compression Behavior of $\pm 45^{\circ}$-Dominated
   Laminates with a Circular Hole or Impact Damage. AIAA Journal, vol. 24,
   no. 1, January 1986, pp. 115-122.

9. Williams, J. G.: Effect of Impact Damage and Open Holes on the Compression
   Strength of Tough Resin/high Strain Fiber Laminates. NASA TM 85756, February
   1984.

10. Starnes, James H. Jr.; and Rouse, Marshall: Postbuckling and Failure
    Characteristics of Selected Flat Rectangular Graphite-Epoxy Plates Loaded in
    Compression. AIAA Paper No. 81-0543, 1981.

546

TABLE I.-STACKING SEQUENCE AND SPECIMEN DESIGNATION

Designation	Stacking Sequence	Material	Number of Specimens Tested
Specimens with 0° plies			
T1	$[(\pm 45)_2/0_4/90/\pm 45/0_2/90]_s$	AS4/PEEK/tape	12
T2	$[(\pm 45)_3/0_2/90/(\pm 45)_2/0/\overline{90}]_s$	AS4/PEEK/tape	14
T3	$[\pm 45/0_6/\pm 45/0_6]_s$	AS4/PEEK/tape	14
T4	$[\pm 45/0_6/\pm 45/0_6/\overline{\overline{90}}]_s$	AS4/PEEK/tape	14
E1	$[(\pm 45)_2/0_4/90/\pm 45/0_2/90]_s$	AS4/3502/tape	11
F2	$[(\pm 45)_3/0_2/90/(\pm 45)_2/0/\overline{90}]_s$	AS4/PEEK/fabric	15
Specimens with no 0° plies			
E5	$[(\pm 45)_2/\overline{90}]_s$	AS4/3502/tape	15
T5	$[(\pm 45)_2/\overline{\overline{90}}]_s$	AS4/PEEK/tape	15
F5	$[(\pm 45)_2/\overline{90}]_s$	AS4/PEEK/fabric	12

TABLE II.- DESCRIPTION OF $[(\pm 45)_2/0_4/90/\pm 45/0_2/90]_s$ SPECIMENS

Specimen	Cross-sectional area, A, cm^2	Hole diameter, a, cm	Impact energy, J	Failure	
				Stress, MPa	Strain
E1-1	2.81	0.00	0.	536.4	.00902
E1-2	2.82	0.79	0.	418.4	.00681
E1-3	2.83	1.27	0.	345.6	.00584
E1-4	2.83	1.91	0.	394.3	.00697
E1-5	2.83	2.54	0.	316.3	.00563
E1-6	2.84	3.81	0.	251.5	.00537
E1-7	2.82	5.08	0.	165.4	.00447
E1-8	2.82	0.	1.36	578.1	.01080
E1-9	2.84	0.	5.77	293.4	.00490
E1-10	2.84	0.	10.6	195.5	.00441
E1-11	2.84	0.	16.9	183.0	.00395
T1-1	2.89	0.00	0.	532.7	.01110
T1-2	2.94	0.79	0.	379.9	.00666
T1-3	2.90	1.27	0.	329.6	.00577
T1-4	2.99	1.91	0.	288.5	.00550
T1-5	2.92	2.54	0.	240.9	.00451
T1-6	2.92	3.81	0.	192.4	.00415
T1-7	2.90	5.08	0.	132.0	.00367
T1-8	2.88	0.	1.33	526.0	.00990
T1-9	2.88	0.	3.09	398.5	.00670
T1-10	2.88	0.	5.64	347.8	.00620
T1-11	2.88	0.	10.6	314.5	.00567
T1-12	2.89	0.	17.9	242.8	.00500

TABLE III. DESCRIPTION OF $[(\pm45)_3/0_2/90/(\pm45)_2/0/\overline{90}]_s$, $[\pm45/0_6/\pm45/0_6]_s$, $[\pm45/0_6/\pm45/0_6/\overline{90}]_s$ and $[(\pm45)_2/\overline{90}]_s$ SPECIMENS

Specimen Designation	Average cross sectional area, A, cm^2	Range of hole diameters, a, cm	Range of impact energies, J
T2	2.99	0-5.08	
T2	4.03		0-28.1
F2	2.85	0-5.08	
F2	3.86		0-29.0
T3	3.33	0-5.08	
T3	3.36		0-34.8
T4	3.43	0-5.08	
T4	3.41		0-33.9
E5	.965	0-5.08	
E5	.953		0-22.7
T5	.966	0-5.08	
T5	.939		0-34.8
F5	.886	0-5.08	
F5	.921		0-19.9

Table IV. Material Properties

Material	AS4-3502 graphite-epoxy	AS4-PEEK graphite-thermoplastic
Young's modulus, E_1	127.6 GPa	133.8 GPa
Young's modulus, E_2	11.3 GPa	8.9 GPa
Shear modulus, G_{12}	6.0 GPa	5.1 GPa
Poisson's ratio, μ_{12}	.3	.38
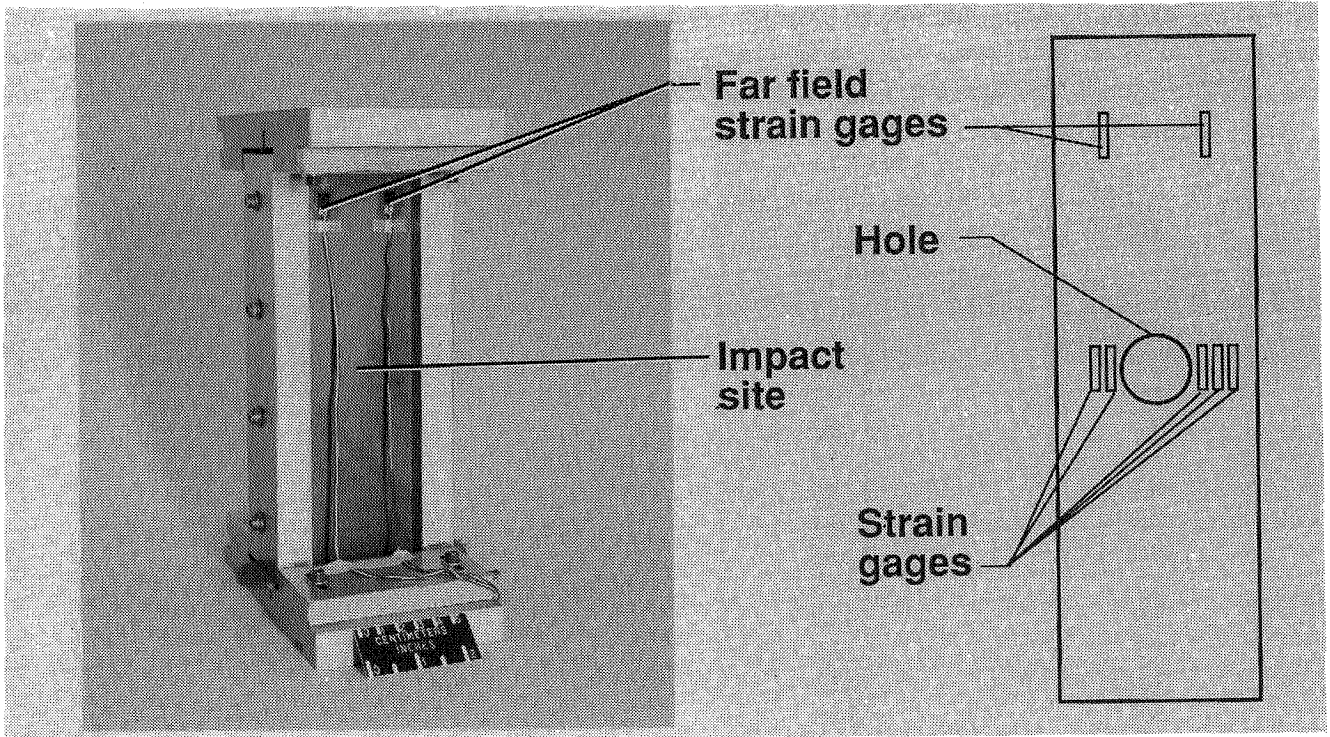
Figure 1a. Typical specimen in test fixture.

Figure 1b. Strain gage pattern for a typical specimen with a hole.

Figure 1. Specimen configuration.
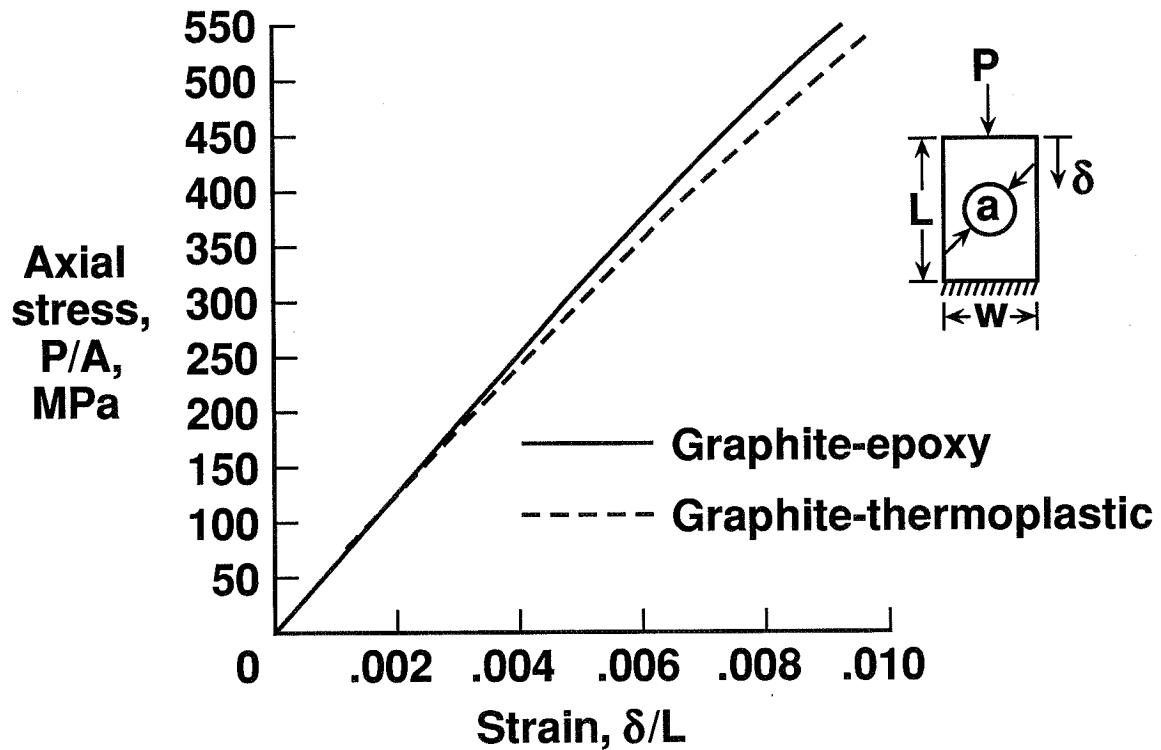
Figure 2. Compression stress-strain behavior for control specimens E1-1 and T1-1 with stacking sequence $[(\pm45)_2/0_4/90/\pm45/0_2/90]_s$.
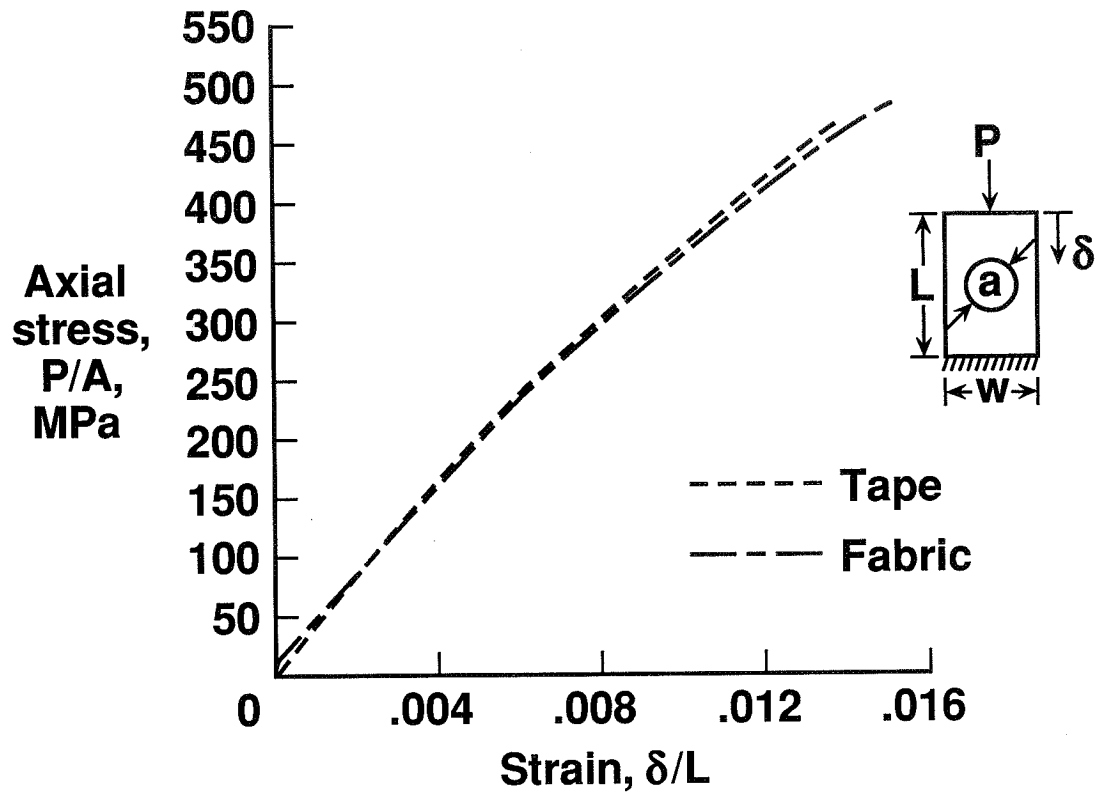
Figure 3. Compression stress-strain behavior for control specimens E2-1 and T2-1 with stacking sequence $[(\pm45)_3/0_2/90/(\pm45)_2/0/\overline{90}]_s$.
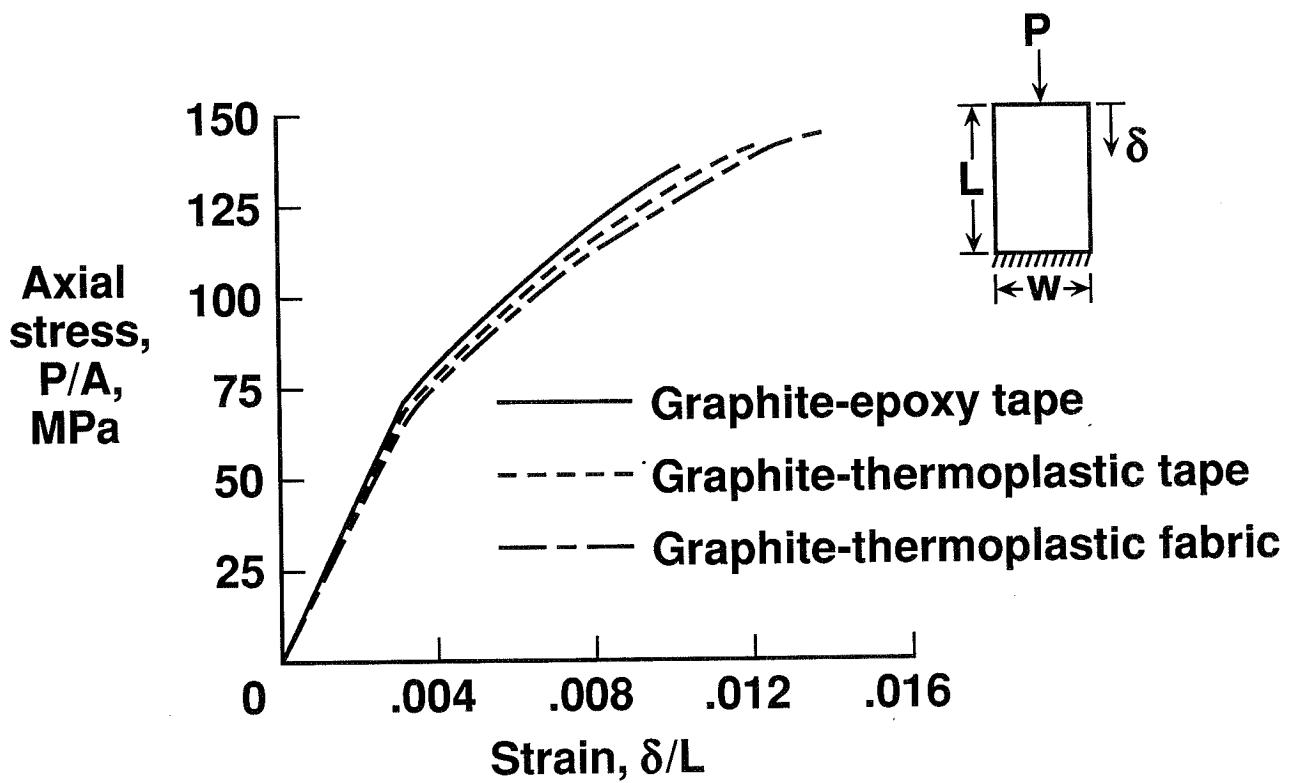
Figure 4. Compression stress-strain behavior for control specimens of type E5, T5 and F5 with stacking sequence $[(\pm45)_2/\overline{90}]_s$.
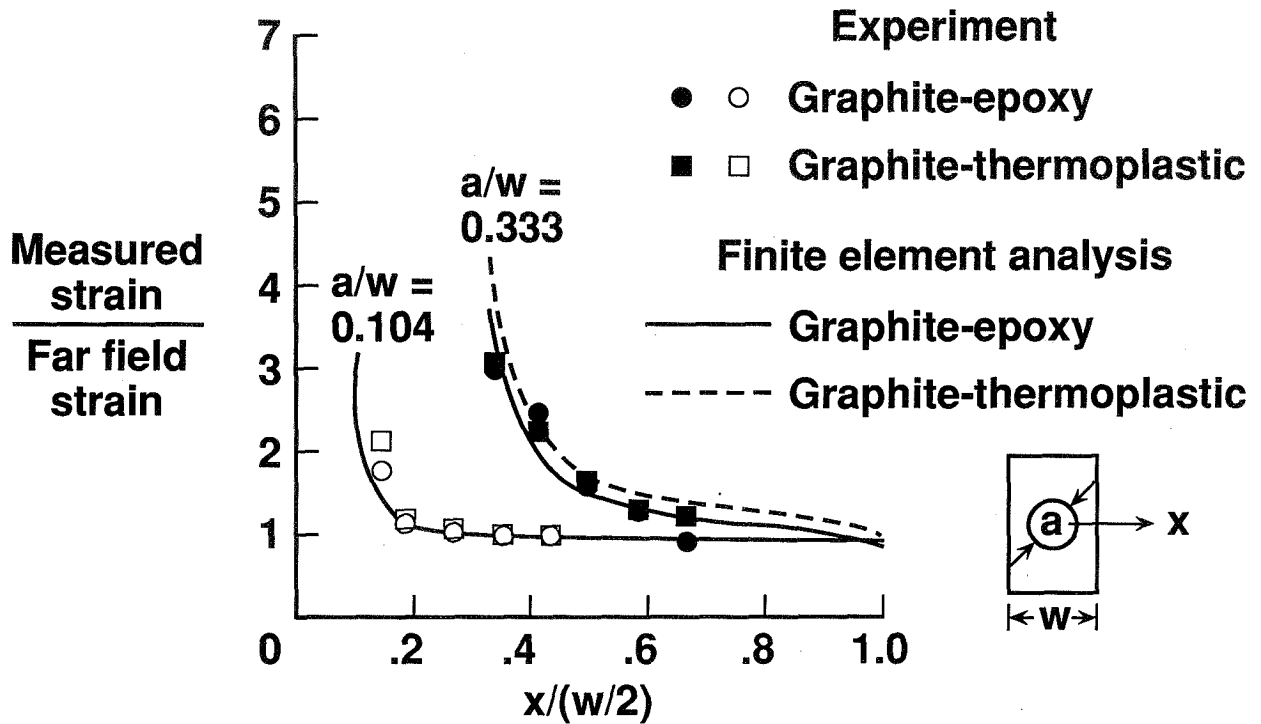
Figure 5. Longitudinal strain distribution at hole for specimens with stacking sequence $[(\pm45)_2/0_4/90/\pm45/0_2/90]_s$.
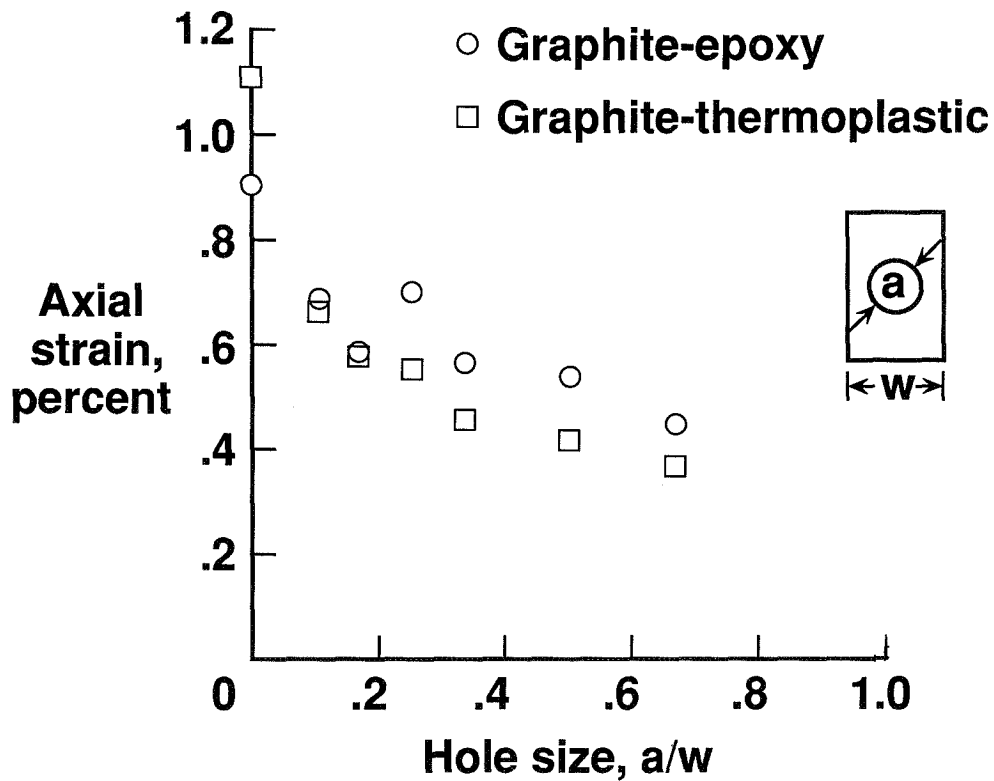
a. Failure strain as a function of hole size.
Figure 6. Results for specimens with stacking sequence $[(\pm45)_2/0_4/90/\pm45/0_2/90]_s$.

5.08
cm

2.54
cm

Specimen E1-7
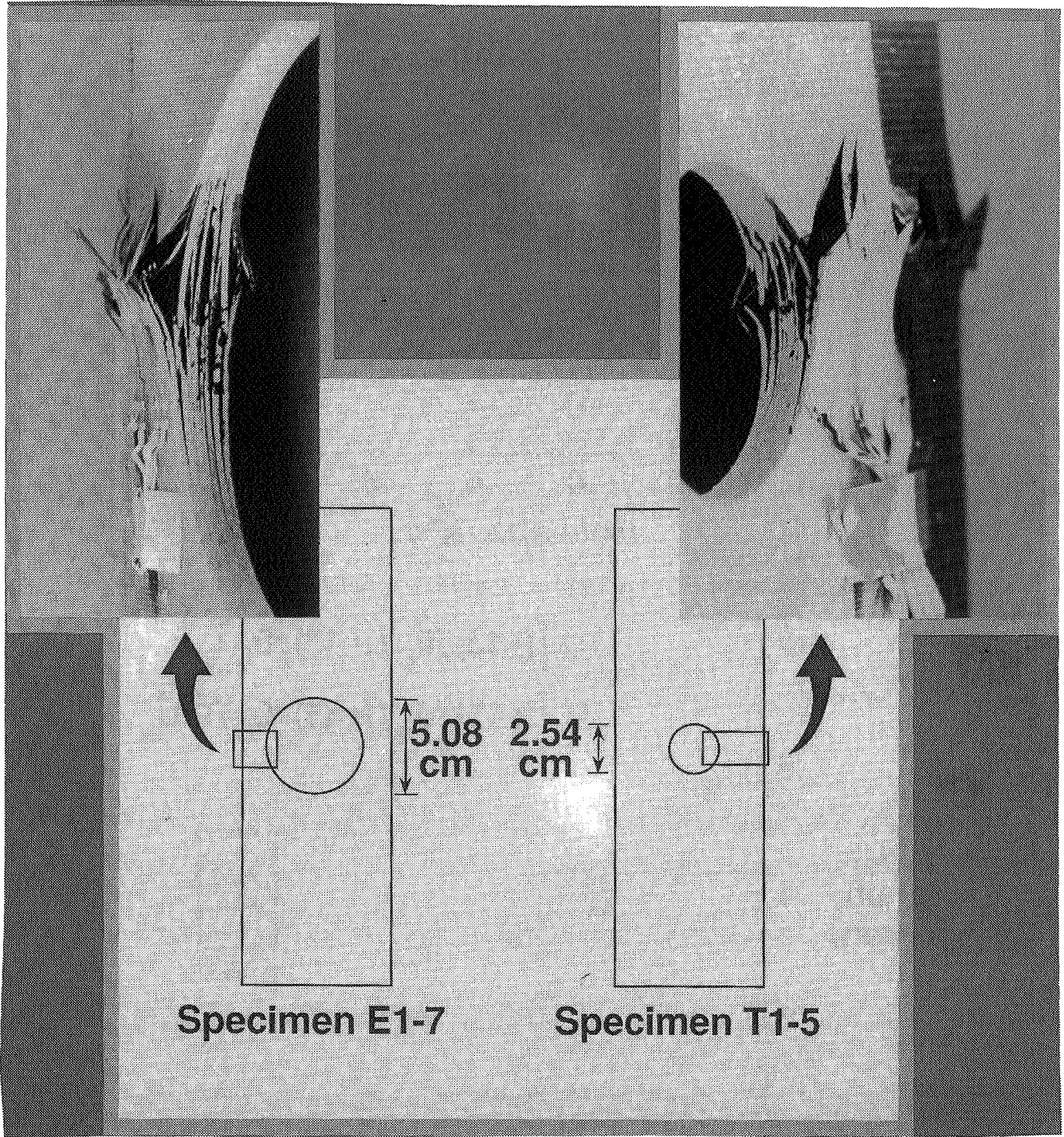
Specimen T1-5

b. Failure mode.

Figure 6. Concluded.
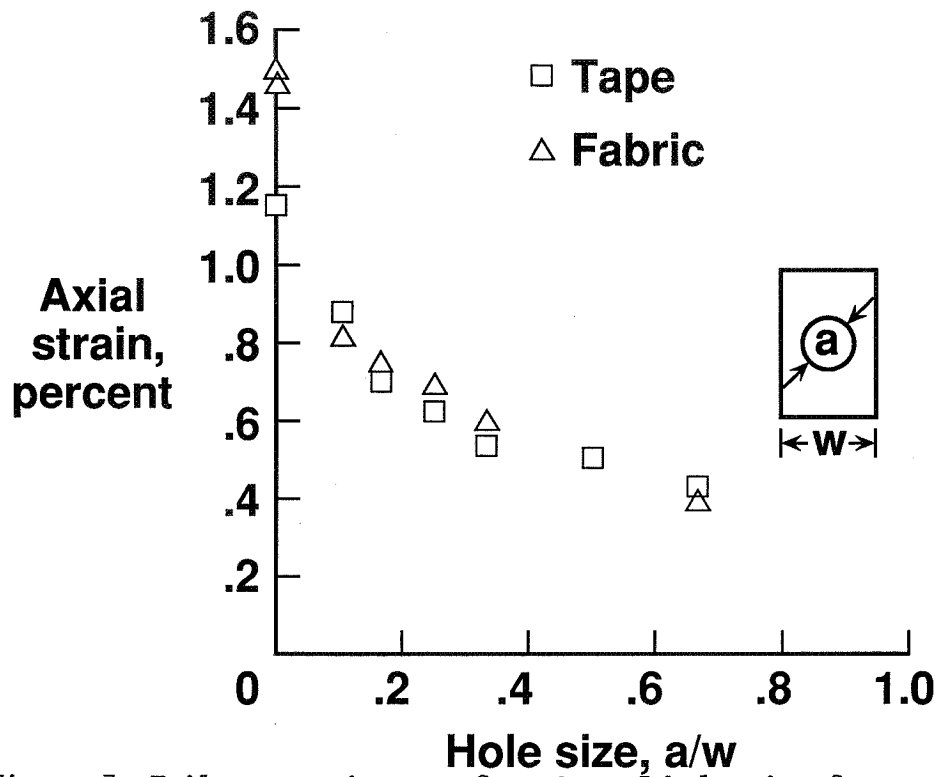
Figure 7. Failure strain as a function of hole size for graphite-thermoplastic specimens with stacking sequence $[(\pm 45)_3/0_2/90/(\pm 45)_2/0/\overline{90}]_s$.
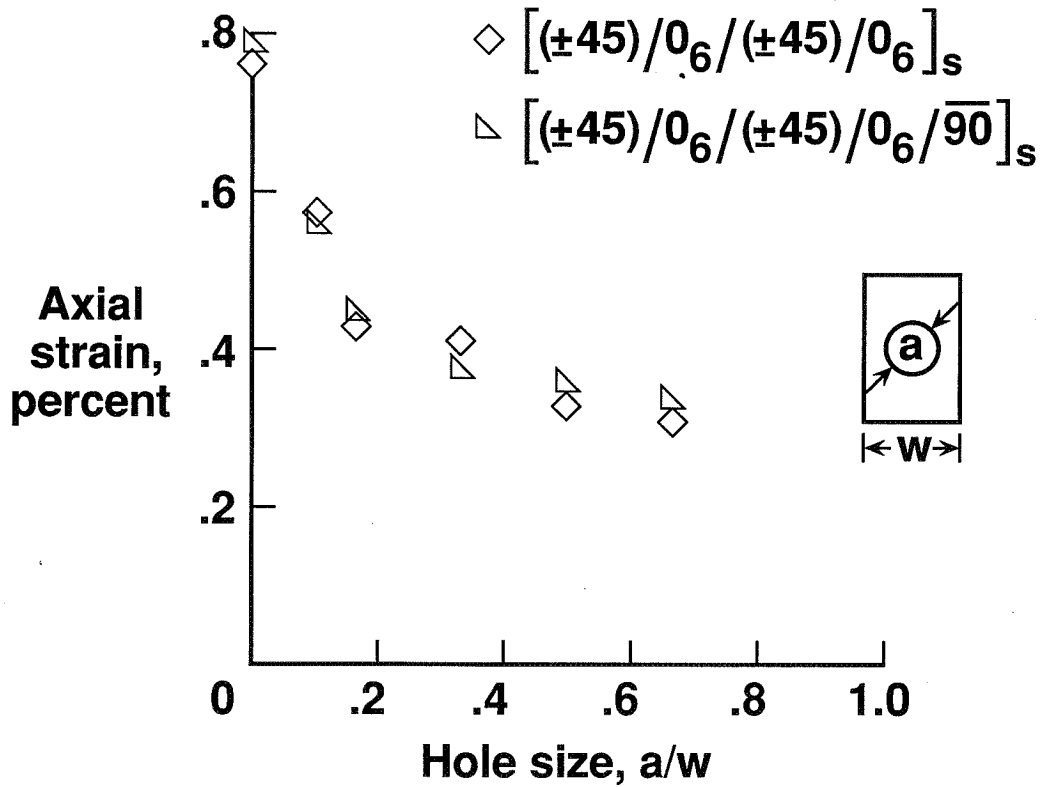
a. Failure strain as a function of hole size.

Figure 8. Results for graphite-thermoplastic specimens with stacking sequence $[\pm 45/0_6/\pm 45/0_6]_s$ and $[\pm 45/0_6/\pm 45/0_6/\overline{90}]_s$.
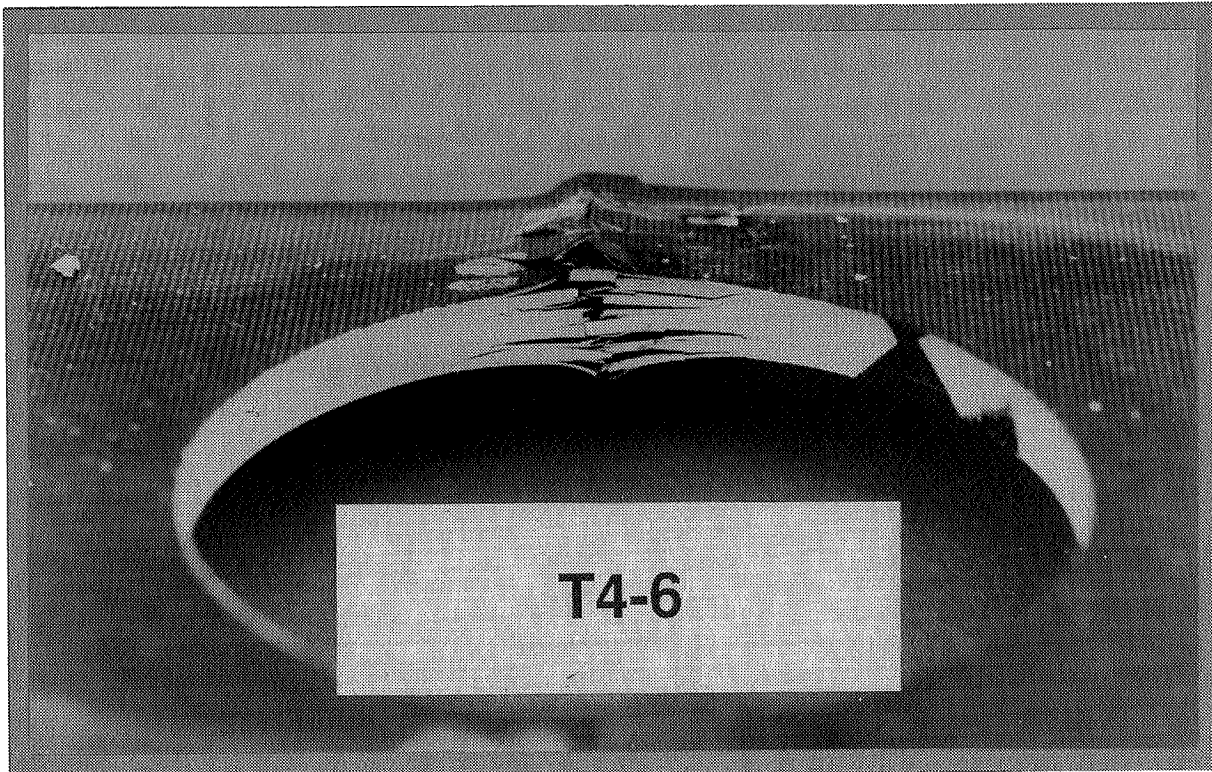
b. Failure mode.

Figure 8. Concluded.
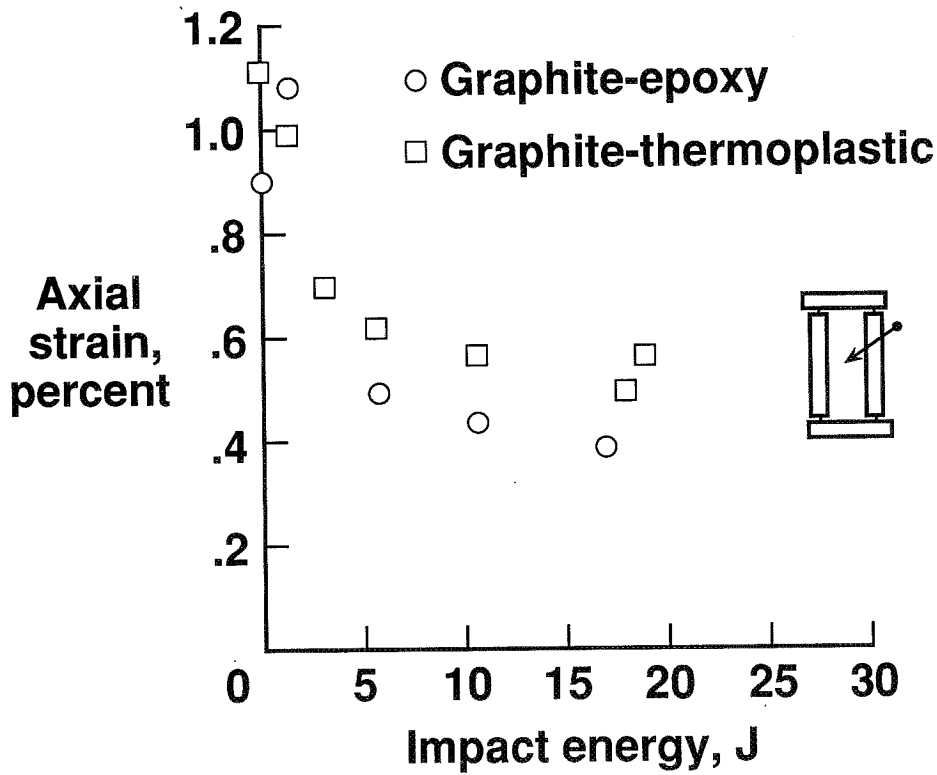
Figure 9. Failure strain as a function of impact energy for specimens with stacking sequence $[(\pm45)_2/0_4/90/\pm45/0_2/90]_s$.
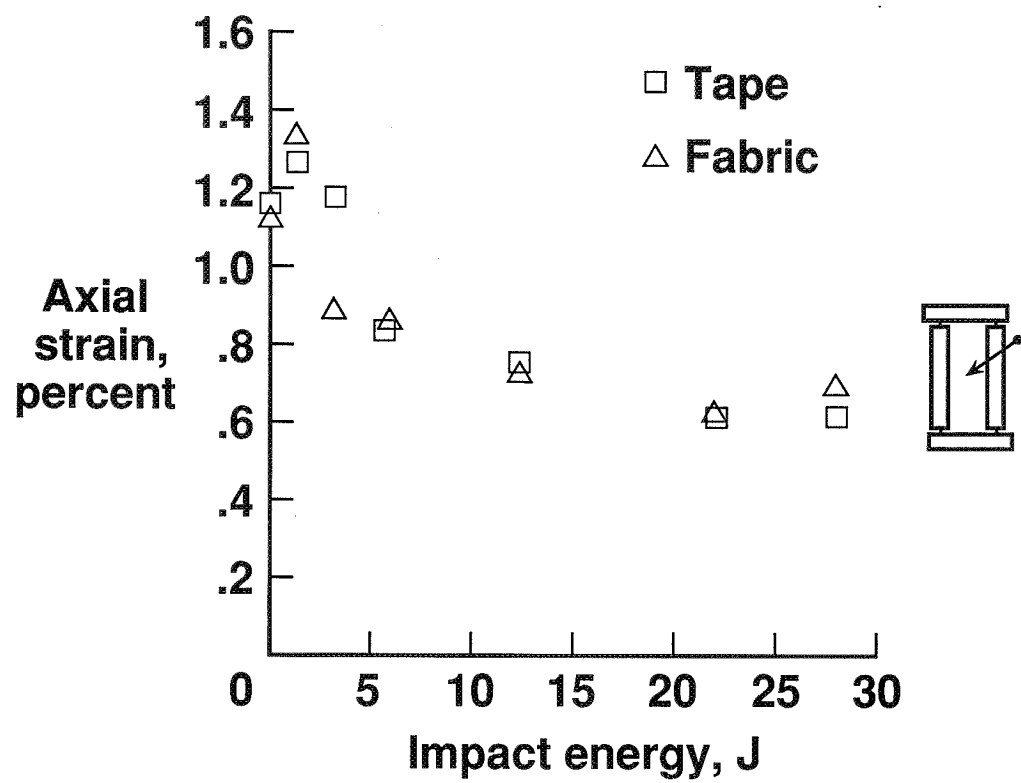
Figure 10. Failure strain as a function of impact energy for graphite-thermoplastic specimens with stacking sequence $[(\pm 45)_3/0_2/90/(\pm 45)_2/0/\overline{90}]_s$.
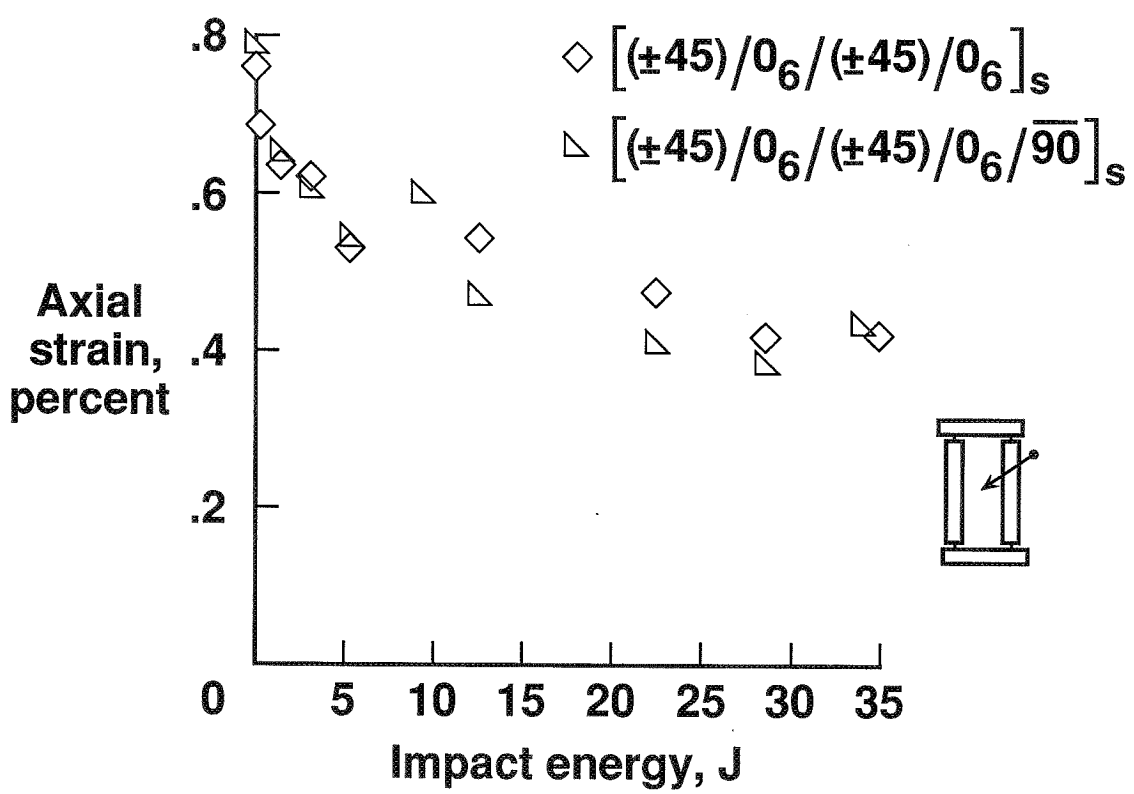
Figure 11. Failure strain as a function of impact energy for graphite-thermoplastic specimens with stacking sequences $[\pm 45/0_6/\pm 45/0_6]_s$ and $[\pm 45/0_6/\pm 45/0_6/\overline{90}]_s$.

Experiment

■ □ Graphite-thermoplastic tape

▲ △ Graphite-thermoplastic fabric

● ○ Graphite-epoxy tape

Finite element analysis

—————— Graphite-epoxy

- - - - - Graphite-thermoplastic

$\dfrac{\text{Measured strain}}{\text{Far field strain}}$

a/w = 0.5

a/w = 0.333

a/w = 0.104

x/(w/2)
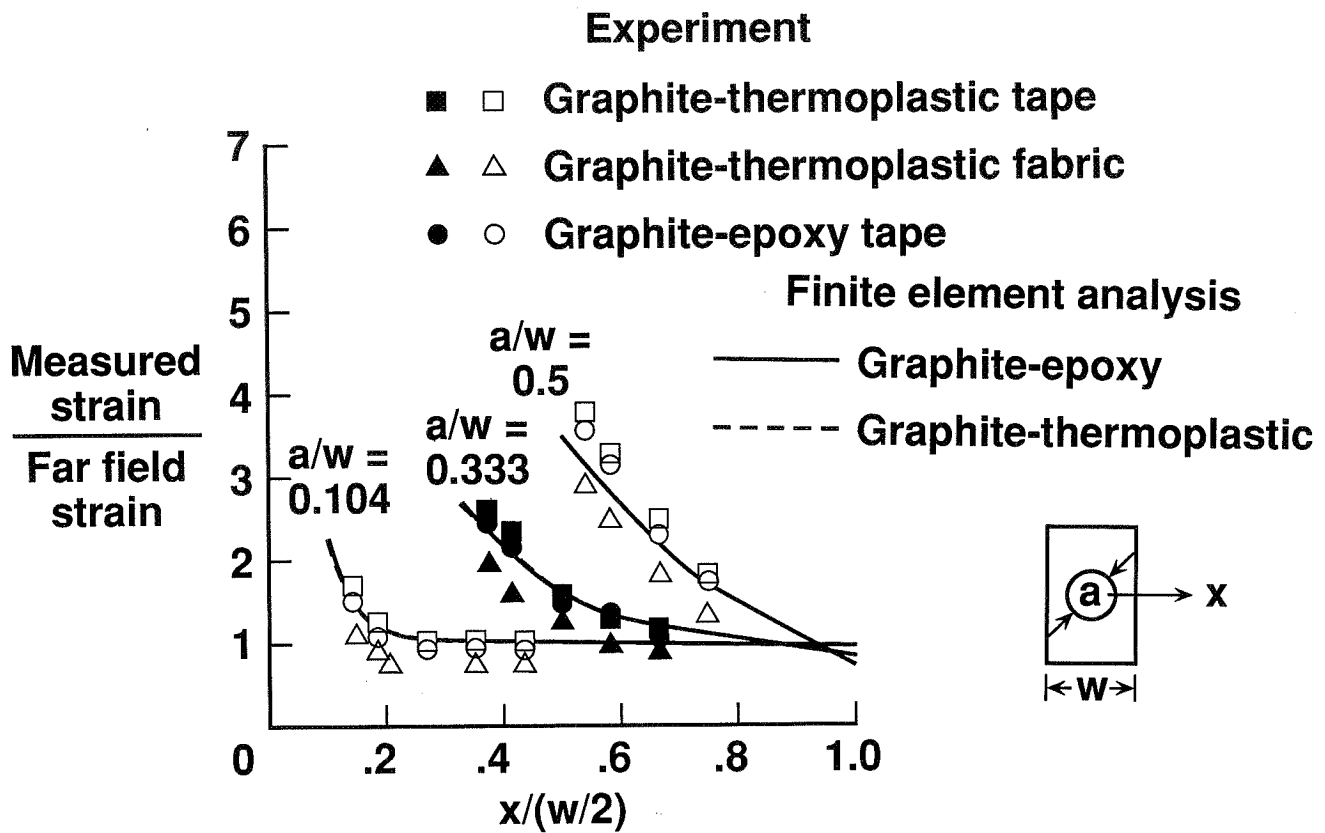
Figure 12. Longitudinal strain distribution at hole for specimens with stacking sequence $[(\pm 45)_2/\overline{90}]_s$.

Axial stress, P/A, MPa

a/w = 0

a/w = 0.333

a/w = 0.5

a/w = 0.667
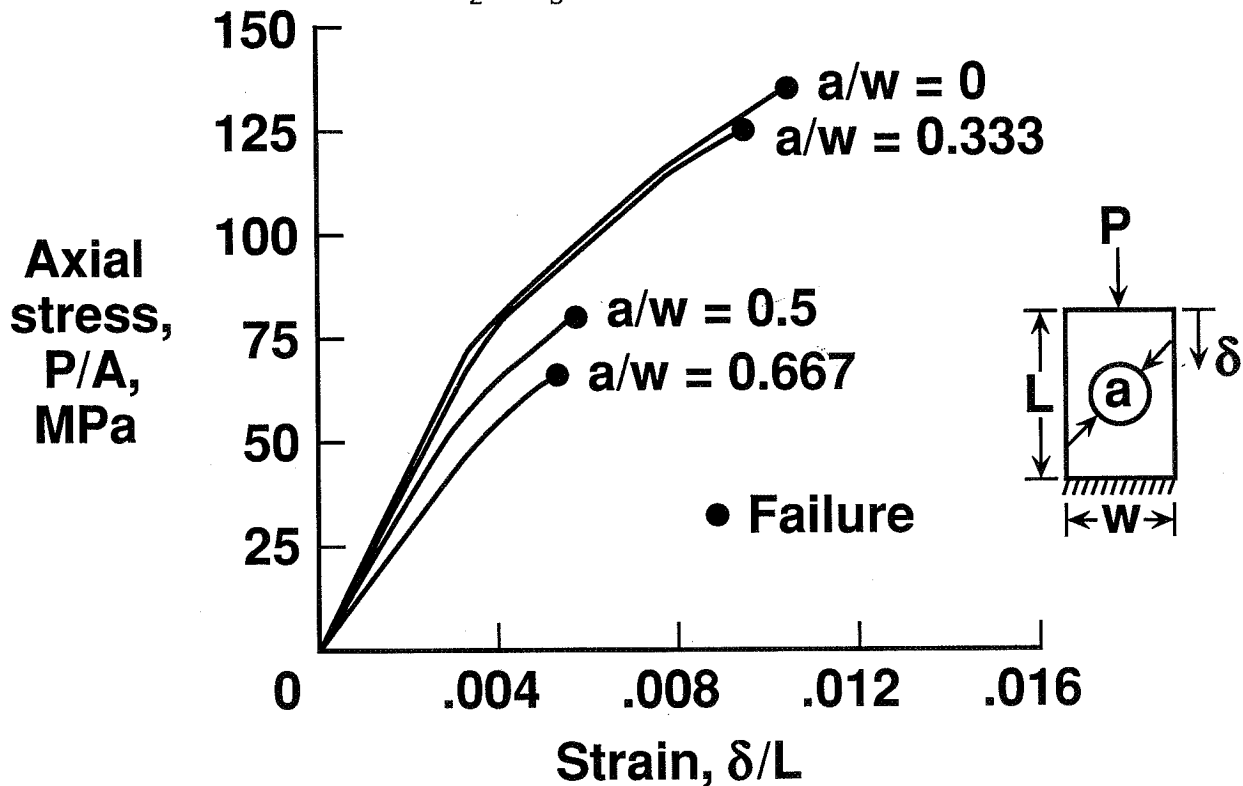
● Failure

Strain, δ/L

Figure 13. Change in stiffness of graphite-epoxy specimen with stacking sequence $[(\pm 45)_2/\overline{90}]_s$ as hole size changes.

557
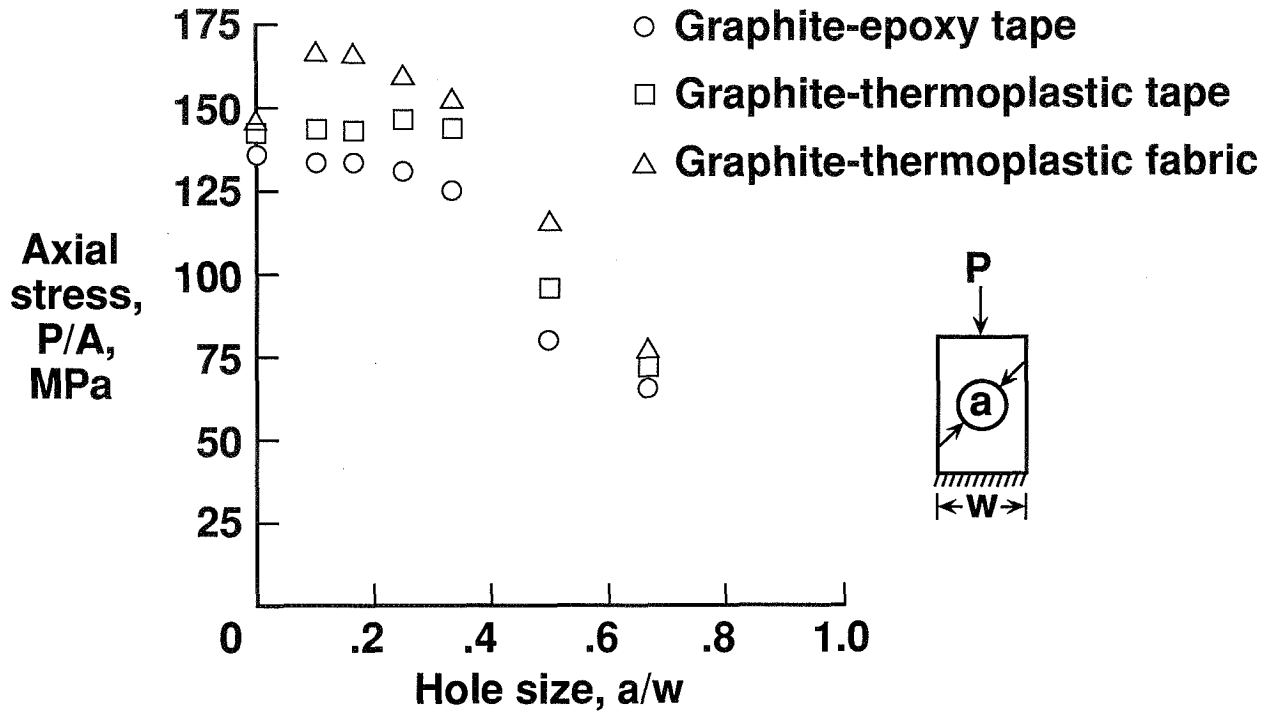
Figure 14. Failure strain as a function of hole size for specimens with stacking sequence $[(\pm45)_2/\overline{90}]_s$.
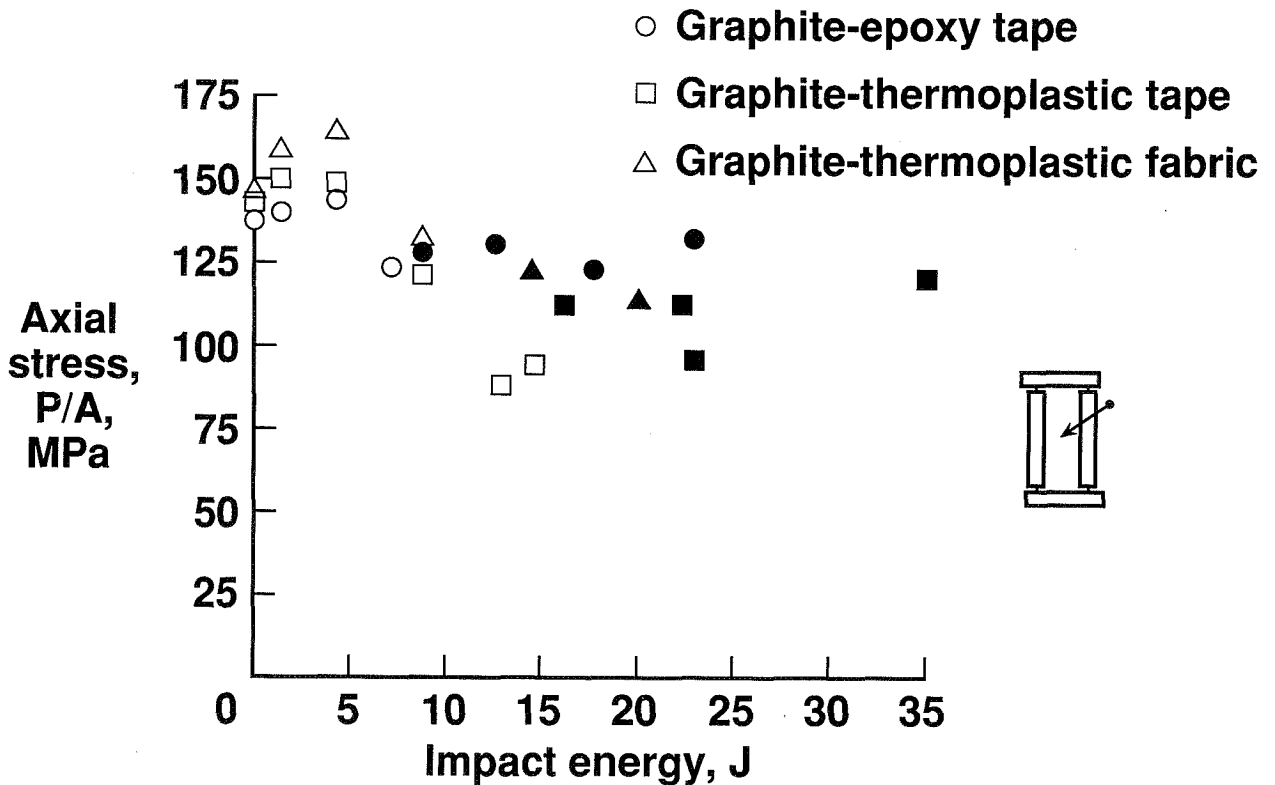
Figure 15. Failure strain as a function of impact energy for specimens with stacking sequence $[(\pm45)_2/\overline{90}]_s$ (open symbols represent cases when the impactor did not fully penetrate the specimen, filled symbols represent cases when the impactor did).

IMPACT RESPONSE OF GRAPHITE/EPOXY FABRIC STRUCTURES

Paul A. Lagace and Michael J. Kraft
TECHNOLOGY LABORATORY FOR ADVANCED COMPOSITES
Department of Aeronautics and Astronautics
Massachusetts Institute of Technology
Cambridge, Massachusetts

ABSTRACT

The impact damage resistance and damage tolerance of graphite/epoxy fabric plate (coupon) and cylinder structures were investigated and compared in an analytical and experimental study. Hercules A370-5H/3501-6 five-harness satin weave cloth in a quasi-isotropic $(0,45)_s$ laminate configuration was utilized. Specimens were impacted with 12.7 mm diameter steel spheres at velocities ranging from 10 m/s to 100 m/s. Damage resistance of the specimens was determined through the use of dye penetrant enhanced x-radiography, sectioning, epoxy burnoff, and visual methods. Damage tolerance of the flat plate structures was assessed in a residual tensile test while damage tolerance of the cylinder structures was assessed via pressurization tests. Impacted fabric laminates exhibited matrix crushing, fiber breakage, delamination, and "fiber bundle disbonds"; the latter being a unique damage mode for fabric laminates. Plate delamination and bundle disbonding was found to be more extensive around the central core area of fiber damage in the coupon specimens than in the cylinder specimens which showed a cleaner damage area due to impact. Damage resistance and damage tolerance were predicted by utilizing a five-step analysis approach previously utilized for coupon configurations. Two of the five steps were adapted to account for the effects of the structural configuration of the pressurized cylinder. The damage resistance analysis provided good correlation to the fiber damage region of both the coupon and cylinder specimens. There was little difference in the size of this region in the two specimen types. However, the analysis was not able to predict the distribution of damage through-the-thickness. This was important in assessing the damage tolerance of the cylinders as the damage causes a decrease in the local bending stiffness which allows bending strain to occur upon pressurization. The damage tolerance analysis was thus able to predict the residual tensile strength of the coupons but was not able to capture the behavior of the pressurized cylinders. A general methodology to predict the impact damage resistance and damage tolerance of composite structures utilizing coupon data is presented.

INTRODUCTION

With the increased use of advanced composite materials has come a number of issues which must be treated in the design of such structures. One of these major issues in composite laminates is impact, both due to the fact that the damage caused by impact is difficult to detect as well as the fact that laminates are particularly sensitive to the delaminations which result.

The great majority of studies on the impact behavior of laminated materials has dealt with coupon-type configurations [e.g. 1] or with design-specific configurations [e.g. 2]. However, neither of

...the ████████████ fills the need for a general design methodology to assess the impact response of composite structures. The composite coupon cannot adequately represent the stress/strain field in the particular composite configuration under the applied loadings, while a design-specific configuration provides information applicable only to that specific configuration. What is sought is an overall methodology which will allow the use of data from coupon-level specimens and take into account the specifics of the structural configuration to "correct" the data due to these structural factors. Such a methodology is illustrated in Figure 1.

Pressurized composite cylinders were chosen as the subject of this study. These represent composite fuselage membrane structure. Both damage resistance and damage tolerances issues are considered. Damage resistance is defined as the ability of a material/structure to undergo an "event" (in this case impact) without damage. Damage tolerance is defined as the ability of a material/structure to maintain "performance" (in this case to not fail/burst) with damage present.

Each of these issues has been considered to some extent in previous work. The response of orthotropic cylinders to impact has been modelled analytically [3] including the case where the cylinder is pressurized [4]. However, experimental data is lacking. The issue of damage tolerance of pressurized cylinders has also been addressed [5], but the specific case of damage tolerance for the presence of impact damage has not been considered. Thus, both damage resistance and damage tolerance issues related to impact need to be considered.

OBJECTIVES AND APPROACH

The issue of extending coupon data to a structural configuration is addressed with the overall objective of developing a general methodology as summarized in Figure 1. The relatively simple configuration of a cylinder, which represents an aircraft fuselage, was chosen for this work. Thus, the impact damage resistance and damage tolerance of graphite/epoxy fabric plate (coupon) and cylinder structures were investigated in both analytical and experimental fashions. All specimens were made from Hercules A370/3501-6 five-harness satin weave cloth in a quasi-isotropic laminate configuration of $(0,45)_S$. Specimens were impacted with 12.7 mm diameter steel spheres and the resultant damage measured through the use of dye-penetrant enhanced x-ray, sectioning, epoxy burn-off and visual methods. Damage tolerance of the flat plate structures was determined under tensile loading of the 350 mm by 70 mm coupons. The damage tolerance of the cylindrical structures was measured by internally pressurizing the 152 mm radius cylinders which were 610 mm in length.

This approach led to three specific objectives in order to achieve the overall objective of the work. One, due to the nature of the fabric material, different damage patterns are exhibited in these specimens than in specimens made from unidirectional graphite/epoxy. Thus, the first objective is to determine the damage characteristics of graphite/epoxy fabric subjected to impact. Two, the basic behavior of the plate and cylinder specimens must be established and compared in order to develop and assess a general methodology. Thus, the second objective is to determine the damage resistance and damage tolerance characteristics of fabric composite coupons and cylinders. Three, the coupon and cylinder behavior can be utilized in conjunction with analytical techniques to develop and assess a generic design methodology. Thus, the third objective is to develop a methodology to predict impact behavior of composite cylinders based on coupon data. This will allow assessment of the overall methodology for utilizing coupon data to predict structural behavior and will point to issues which must be considered in this procedure.

ANALYTICAL TECHNIQUES

The analytical approach adopted is to utilize an impact assessment methodology developed and verified for the coupon configuration [6] and to develop specific analyses to account for the

560

1. Global Analysis of Impact Event
↓
Loads on Plate
↓
2. Local Deformation and Strain Response Analysis
↓
Local Strain Field
↓
3. Failure Criteria
↓
Damage Predictions
↓
4. Degraded Property Model
↓
Damaged Stress/Strain Field
↓
5.. Failure Criteria for Component
↓
Performance Prediction

material
system
and
layup

material properties

COUPON TESTS

GENERAL IMPACT METHODOLOGY

general predictions

damage and failure prediction

SPECIFIC STRUCTURAL ANALYSIS

structural factors

structural configuration

Figure 1   Summary of methodology to assess impact damage resistance and damage tolerance of composite structures.
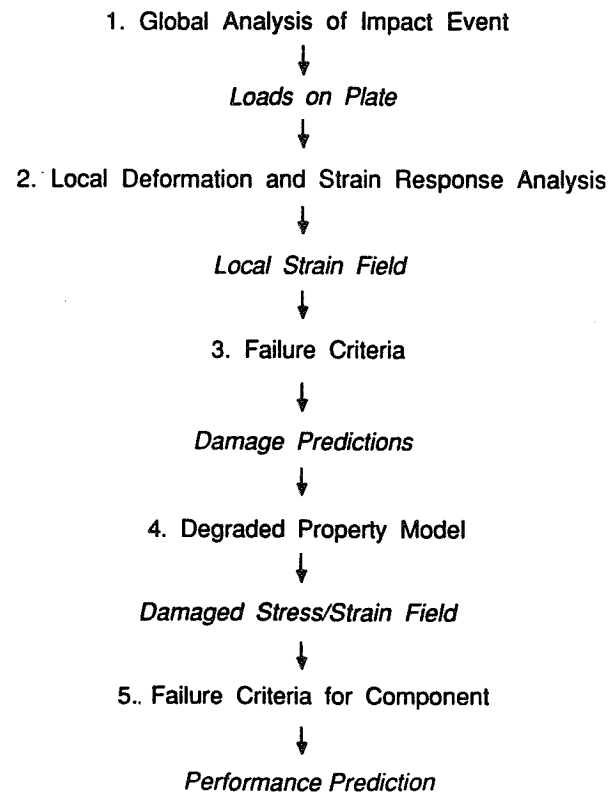
Figure 2   Approach overview of impact analysis.

structural configuration of the pressurized cylinders and the factors and behavior which are introduced due to this configuration.

General Approach

It has been shown [6} that the damage resistance and damage tolerance of coupons subjected to impact can be relatively well assessed using the five-step analysis approach illustrated in Figure 2. Separate analyses have been developed for the five modelling steps. The first three steps (global analysis of impact event, local deformation and strain response analysis, and failure criteria) deal with the damage resistance as this results in damage predictions for the particular impact event, while the latter two steps (degraded property model and failure criteria for component) assess the damage tolerance and result in a performance prediction. These five steps are subsequently summarized. In-depth descriptions can be found in References 6 through 9.

An assumed modes Rayleigh-Ritz analysis is utilized to determine the force and deflection time history of a plate subjected to an impacting mass. The forcing function is nonlinear in that the contact law is assumed to be Hertzian in nature. The effects of in-plane loading, shear deformation and bending-twisting coupling are accounted for. The maximum force caused by the impactor is passed on to a local contact analysis, step two. An axisymmetric stress function is utilized, with the constitutive properties smeared through the thickness, to determine the stress and strain fields caused by the contact. The dynamics of the situation are accounted for by including d'Alembert inertial terms in the direction transverse to the plate. The predicted strains, on a ply-by-ply basis, are passed on to step three, the failure criteria. The maximum strain failure criterion is used for all six components of strain. This allows the mode of failure to be indicated on a ply-by-ply basis and results in a damage prediction on a ply-by-ply basis.

The damage tolerance portion of this analysis begins with step four where an analysis of the damaged laminate is performed to determine the local strain around the damage when the part is subjected to a specific loading. The model is based on the complex potential analysis of Lekhnitskii and considers an anisotropic inclusion in an equivalent membrane model. The ply constitutive constants are degraded based on the predicted damage and specified degradation rules, and this effect is integrated through the thickness in the area of damage to form an elastic inclusion with different constitutive constants than the surrounding laminate. This analysis provides the local strain field which is used in the fifth and last step to predict the part performance. An average strain concept is utilized, on a laminate basis, to predict when final failure occurs.

Modifications for Cylinder Configuration

In considering the five-step approach, only two of the steps must be modified to account for a particular structural configuration. In the first three steps dealing with damage resistance, only the first step, the global analysis of the impact event, must be modified as the structural configuration has a decided effect on the dynamic response. However, the local model is not affected by the structural configuration since, by definition, it is a local model and does not "care" what the structure looks like as long as the critical structural parameters, in this case the radius of the cylinder, are much larger than the critical size parameter in the local model, the radius of the impactor. This is clearly met in the current work (152 mm to 6.3 mm). The third step is the failure criteria which is a characteristic of the material, not the structural configuration, since it is a local phenomenon.

In the latter two steps dealing with the damage tolerance, only step five dealing with the failure criteria for the component must be modified as this is clearly affected by the configuration of the component. Step four on the degraded property model does not need to be modified as long as the degradation assumptions remain valid. The critical assumption is that delaminations and isolated angle ply splits do not cause significant degradation under tensile loading and thus only fiber breakage creates a significant reduction in constitutive properties. This has been shown to apply to fabric laminates [10].

Global Analysis of Impact Event. The main difference in the case of the cylinders is that the curvature affects the deflection behavior. This is captured through the strain-curvature relations:

$$\varepsilon_x = \frac{\delta u}{\delta x} \qquad \varepsilon_y = \frac{\delta v}{\delta y} + \frac{w}{R} \qquad \gamma_{xy} = \frac{\delta u}{\delta y} + \frac{\delta v}{\delta x} \qquad \kappa_x = \frac{-\delta^2 w}{\delta x^2} \qquad \kappa_y = \frac{-\delta^2 w}{\delta y^2} + \frac{1}{R}\frac{\delta v}{\delta y} \qquad \kappa_{xy} = -2\frac{\delta^2 w}{\delta x\,\delta y} \qquad (1)$$

Kirchoff thin plate assumptions are utilized here since the length of the cylinder is much greater than the thickness. Furthermore, orthotropy is assumed in order to allow a simpler model and is pertinent due to the quasi-isotropic layup utilized for the specimens.

Given these facts, the assumed displacements are in the following form:

$$u = \sum u_{mn} \cos\left(\frac{m\pi x}{a}\right) \cos\left(\frac{ny}{R}\right) \qquad\qquad v = \sum v_{mn} \sin\left(\frac{m\pi x}{a}\right) \sin\left(\frac{ny}{R}\right)$$

$$w = \sum w_{mn} \sin\left(\frac{m\pi x}{a}\right) \cos\left(\frac{ny}{R}\right) \qquad\qquad (2)$$

where a is the cylinder length and R is the cylinder radius. The analysis from this point follows the previous analysis [8] with the potential energy expression modified

$$\Pi_p = \frac{1}{2} \int_0^a \int_{-\pi R}^{+\pi R} \left[A_{11}\,\varepsilon_x^2 + 2\,A_{12}\,\varepsilon_x\varepsilon_y + A_{22}\,\varepsilon_y^2 + A_{66}\,\gamma_{xy}^2 \right.$$

$$\left. + D_{11}\,\kappa_x^2 + 2\,D_{12}\,\kappa_x\kappa_y + D_{22}\,\kappa_y^2 + D_{66}\,\kappa_{xy}^2 \right] dx\,dy \qquad (3)$$

562

to take into account the difference in specimen geometry. The A_{ij} and D_{ij} are the laminate stretching and bending matrices as normally defined in laminated plate theory.

It should be noted that in order to allow more efficient computer run time, the generalized beam functions developed by Dugundji [11] were utilized in the coupon global analysis.

Failure Criteria for Component. A pressurized cylinder has a bidirectional membrane load in its skin. Thus, techniques utilized with coupons seem directly applicable. However, the pressurized cylinder with impact damage presents the following problem. As illustrated in Figure 3, the damaged area of the cylinder is equivalently a piece of damaged material spanning a region in the undamaged cylinder surface. If this piece has a low bending stiffness relative to the surrounding undamaged laminate, local bending will result. The impact damage may be modelled as a hole covered by a diaphragm that allows the flaw edge to deflect and rotate but transmits the pressure force to the shell in the form of a uniform transverse shear stress at the flaw edge. This interaction causes the presence of higher stress levels in the surrounding undamaged laminate, due to the internal pressure loading, than those stresses found in a similarly loaded flat plate. This is the same phenomenon modelled by Folias for the case of a through-flaw [12].

In the limit, this damaged area may be modelled as a through-notch. A stress correction factor [12] has been successfully utilized in the case of through-notches in pressurized composite cylinders to account for this localized bending and predict the failure pressure from data obtained on coupon specimens with notches [5]. This correction factor is a function of the cylinder geometry and of the material properties. The failure stress of a cylinder is thus found by dividing the flat plate solution by this factor K, yielding

$$\sigma_{f(cylinder)} = \sigma_{f(flat\ plate)} / K \qquad (4)$$

The correction factor, K, is given by the equation

$$K = (1 + 0.317\lambda^2)^{1/2} \qquad (5)$$

with the shell parameter given by

$$\lambda^4 = (Eh / R^2 D) r^4 \qquad (6)$$

where E is the longitudinal modulus of the quasi-isotropic laminate, h is the shell thickness, R is the shell radius, D is the bending stiffness of the quasi-isotropic laminate, and r is the half-crack length.
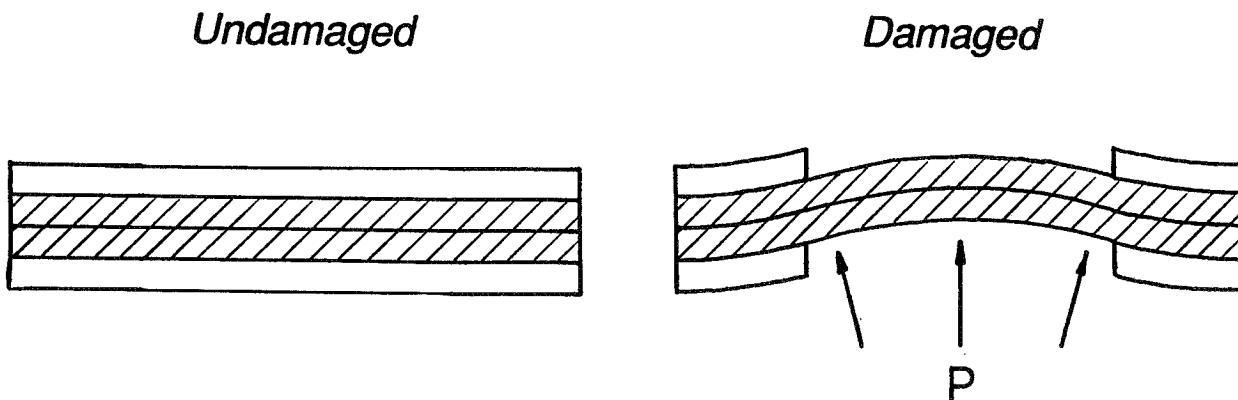
Undamaged   Damaged

Figure 3   Illustration of localized bending at location of impact damage due to internal pressure.

Implicit in this formulation is that the stress in the hoop direction controls the failure behavior and thus the longitudinal stress is not considered [13].

The strain around the inclusion, as calculated from the damage predictions, was determined and this averaged over a characteristic dimension [14]. This dimension was found to have a value of 4.7 mm for this material and layup configuration [13]. The predicted fracture stress was then degraded by the correction factor. It should be noted that this is not strictly applicable to an average strain concept since the correction factor deals with stress intensities.

The entire analysis was implemented in FORTRAN on a DEC MicroVax II computer. Run time for a typical analysis (all five steps) was about 25 CPU minutes.

EXPERIMENTAL TECHNIQUES

The experimental test program is divided into two phases. The first phase is the investigation of the characteristics of impact damage in flat plate and cylinder graphite/epoxy fabric laminates. Phase two is a determination of the residual strength of impacted flat plate and cylindrical shell structures. All work was conducted using Hercules A370/3501-6 graphite/epoxy which is a five-harness satin weave fabric prepreg system. The layup used for all specimens is $(0,45)_S$. Parentheses and commas indicates the use of fabric plies. The ply angles are measured with respect to the warp direction of the fabric.

The basic configurations of the coupon and cylinder specimens are shown in Figures 4 and 5, respectively. The coupons were laid up by hand as 300 mm by 350 mm plates and cut to the desired dimensions, after cure, with a water-cooled diamond wheel. Cylinders were laid up by hand on an aluminum mandrel. The cure cycle, as suggested by the manufacturer, begins with a 1 hour hold at 116°C and continues with a two hour hold at 177°C. A 0.59 MPa autoclave pressure is maintained throughout as well as a full vacuum. Heating and cooling rates were maintained at 3°C per minute. Specimens were postcured for eight hours at 177°C.
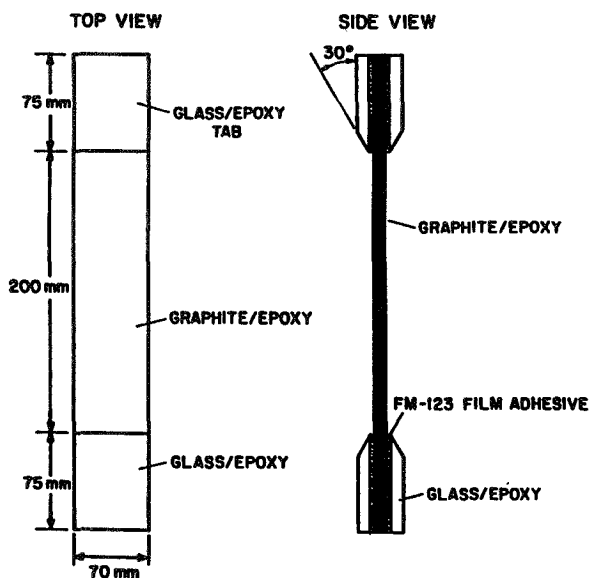
Figure 4   Physical characteristics of the coupon specimen.
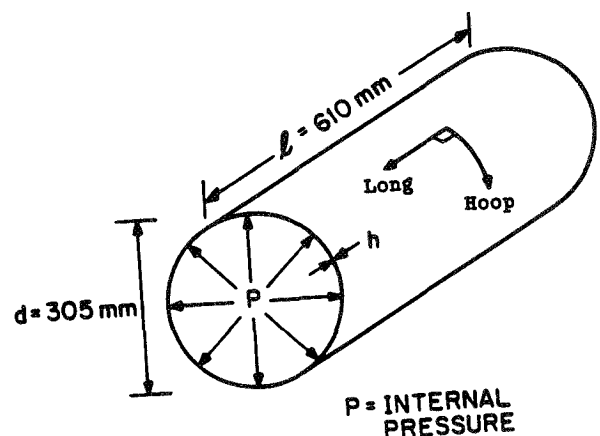
Figure 5   Physical characteristics of the cylinder specimen.

Damage Resistance Tests

A total of thirty-nine coupon specimens and two cylinder specimens were utilized in this portion of the work. Each cylinder was impacted at eighteen different locations. Impact was conducted utilizing a modified pressurized air gun [15] and a 12.7 mm diameter steel ball. The velocity of the projectile was varied between 10 and 100 m/s. The coupons were held in a special fixture to give clamped-free boundary conditions. The length of the target area in these cases is 200 mm. The cylinder specimens were placed in two endcaps with a small groove. These endcaps were then placed on a fixture manufactured from steel channels. The specimens only contacted the endcaps thus assuring simply-supported boundary conditions. The cylinder specimens were rotated after each impact so that the next impact occurred at a location of significant distance from any other impacts such that no interference occurred. These distances are 203 mm in the longitudinal direction and 160 mm in the hoop direction. After impact, the cylinder was sectioned using a hand-held jigsaw and a carbide blade to facilitate further examination.

Impacted coupon and cylinder specimens were examined visually, by dye penetrant (diiodobutane) enhanced X-ray, and by epoxy burnoff. In the case of the use of dye penetrant, the dye was sparingly injected into the damage area with a needle and syringe. The epoxy burnoff procedure required the use of an oven capable of reaching 550°C and a small amount of stainless steel mesh. This technique was easier to implement with fabric than with tape because the weave of the fabric plies prevents breakup of the specimen.

Damage Tolerance Tests

A total of thirty-seven coupon specimens and twelve cylinder specimens were tested in this portion of the experimental work. Five of the coupons were unflawed and five had 12.7 mm drilled holes. These gave boundaries for the damage tolerance response. The remaining twenty-seven coupon specimens were impacted at various velocities, inspected for damage using the dye penetrant enhanced x-radiography, and subsequently tested for residual strength. The coupons were tested using an MTS 810 hydraulic testing machine. Tests were conducted monotonically in tension at a stroke rate of 1.5 mm per second to give an approximate strain rate of 4200 microstrain per minute over the 200 mm test section.

The cylinders are tested via pressurization, thus requiring a sealed specimen. The pressure vessel test system is shown schematically in Figure 6. This consists of the graphite/epoxy test article reinforced within 160 mm of the ends with nine layers of Boatex 7781 fiberglass in a wet layup with Shell Epon V40 resin and 815 hardener cured for two hours at 100°C. The test article is then fixed in an aluminum endcap with thirty-six hardened pins. A highly flexible epoxy (3M Scotch-Weld 2216 B/A Gray Epoxy Adhesive) fills in the gaps between the test article and the endcaps. The inside of the assembly is lined with a rubber bladder attached to the two inspection port covers and is inserted after the endcaps are completely attached. The bladder prevents leakage which can occur due to slight laminate porosity at high pressure levels.

The cylinders were tested in a blast chamber. The pressurization was accomplished with bottled nitrogen via a copper tube attached to one of the endcaps with standard pipe fittings. This tube was then run outside the blast chamber to the bottled nitrogen. The other endcap was attached with similar tubing and fittings to a pressure transducer. The transducer and strain gage signals were fed to a data acquisition system and data sampled every 0.4 seconds. The output of the transducer was also fed to an X-Y plotter so that the pressure could be monitored during the test. Pressurization was performed manually, via a pressure regulator, attempting to keep a constant pressurization rate of 0.69 MPa per minute, as shown by the X-Y plotter, until catastrophic failure occurred.

A total of eight cylinder specimens were impacted, visually inspected for damage, and then tested via pressurization. Four unimpacted specimens were also tested.
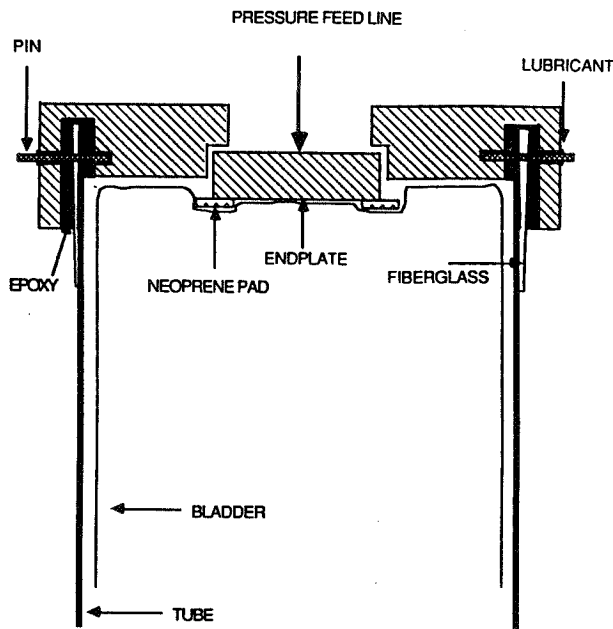
Figure 6   Endcap system for the cylinder specimen.
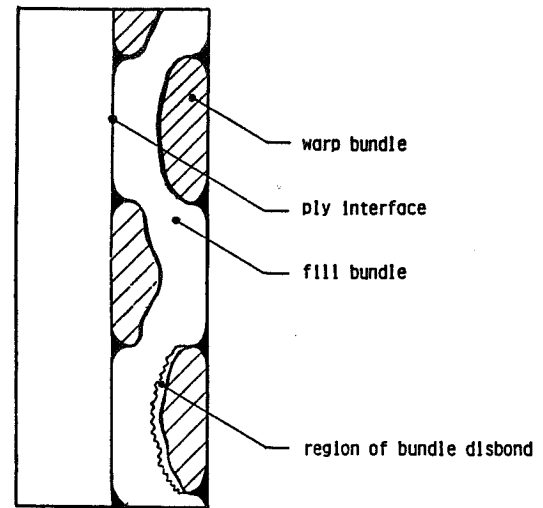
Figure 7   Illustration of a "fiber bundle disbond".

RESULTS

Damage Characteristics of Fabric Material

Four types of damage were observed in the fabric material due to the impact. The first is matrix "crushing" which occurred directly under the impactor; the second is fiber breakage; and the third is delamination. These first three are typical modes which are found in unidirectional tape laminates. However, the fourth damage mode is unique to fabric specimens. This damage mode, illustrated in Figure 7, is termed "fiber bundle disbonds". These are defined as the separation of single fiber bundles, or tows, from its associated ply. The disbonds generally occur on the face of the laminate opposite the impact surface. These disbonds were found for all impact levels and appeared first in the sequence of damage propagation in the fabric laminates and were a precursor to fiber breakage.

Fiber bundle disbonds are the fabric ply equivalent of angle ply splitting in unidirectional tape. This unique damage mode underscores the needs to characterize the damage types which can occur and to assess their criticality in damage tolerance response.

Damage Resistance

Although four types of damage were noted in the experimental work, in regards to damage tolerance,only the fiber breakage was considered important. Thus, the damage due to the impact is represented by a core region of fiber damage which could easily be identified on the X-ray photographs. In general, this region was circular and could thus be characterized by a core area diameter. This diameter is plotted versus impactor velocity for both the coupon and cylinder specimens in Figure 8. This shows that there is little difference in this integrated damage representation between the coupon and cylinder specimens.

Little difference is found in the predicted damage sizes between the two configurations as can be seen in Figures 9 and 10. The material properties used in the analysis are shown in Table 1. This similarity in predicted damage sizes can be explained by considering the step-by-step results of the analysis sequence of Figure 2. The coupon and cylinder only differ in the global analysis. Force

566

Figure 8 — Core area diameter versus impactor velocity for both the coupon (plate) and cylinder specimens.

Table 1 A370-5H/3501-6 Ply Properties

Moduli	Failure Strains[a] [microstrain]
$E_{11} = 72.5$ GPa	$\varepsilon_{11}^{t} = 11{,}300$
$E_{22} = 72.6$ GPa	$\varepsilon_{11}^{c} = 10{,}700$
$E_{33} = 10.0$ GPa	$\varepsilon_{22}^{t} = 10{,}000$
$G_{12} = 4.43$ GPa	$\varepsilon_{22}^{c} = 9{,}800$
$G_{13} = 6.0$ GPa	$\varepsilon_{33}^{t} = 5{,}000$
$G_{23} = 6.0$ GPa	$\varepsilon_{33}^{c} = 18{,}900$
$\nu_{12} = 0.059$	$\gamma_{12} = 23{,}600$
$\nu_{13} = 0.30$	$\gamma_{13} = 17{,}500$
$\nu_{23} = 0.30$	$\gamma_{23} = 18{,}900$

$t_{ply} = 0.35$ mm

$\rho = 1540$ kg/m^2

[a] superscript t indicates tension; c indicates compression.

versus time histories for a coupon and cylinder configuration for the case of a 12.7 mm steel impactor at 40 m/s are shown in Figures 11 and 12, respectively. Although the overall time signatures are considerably different, only the peak force predicted from the analysis, as well as the associated target acceleration, is passed on to the next analysis step. The peak force predicted for these two cases is virtually identical, being slightly over 2 kN. From this point on, the two analyses do not differ and thus the same predicted damage will result for the coupon and cylinder cases.

However, if the overall damage distribution is considered rather than the integrated damage representation of the core damage region, there is considerable difference between the coupon and cylinder cases. The damage area in the cylinder case was cleaner and more contained around the core area than in the coupon case with the delamination and bundle disbonding being more dominant
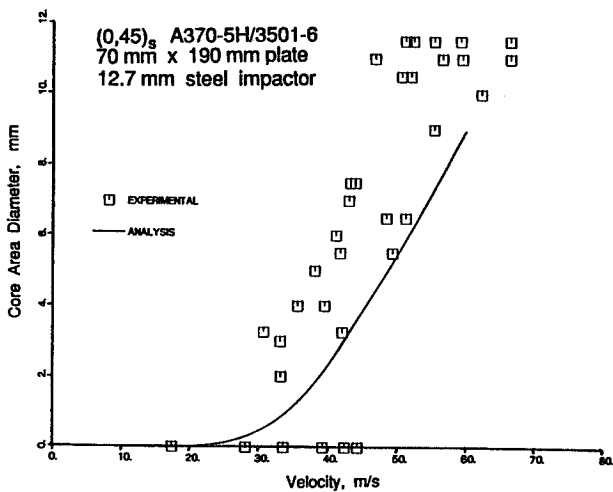
Figure 9 — Coupon (plate) damage results and prediction with impactor velocity.
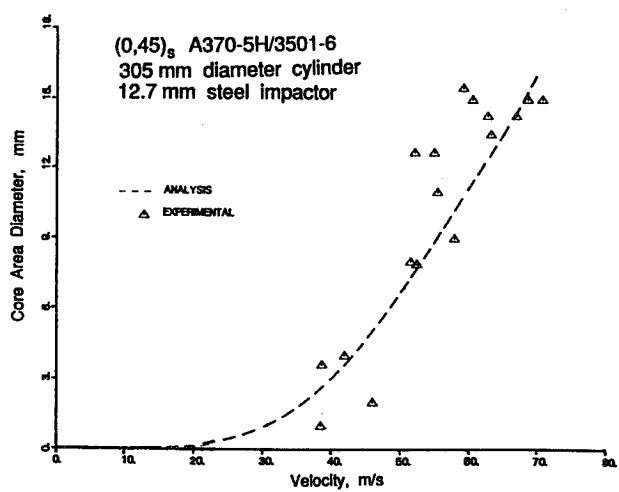
Figure 10 — Cylinder damage results and prediction with impactor velocity.

567
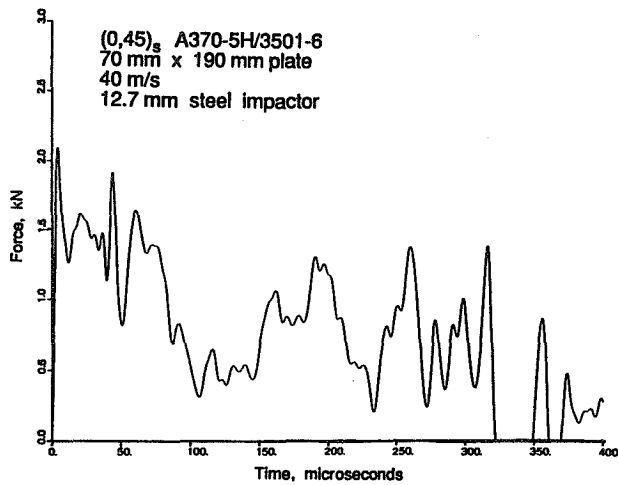
Figure 11 Predicted force versus time history for coupon (plate) specimen impacted with a 12.7 mm steel ball at 40 m/s.
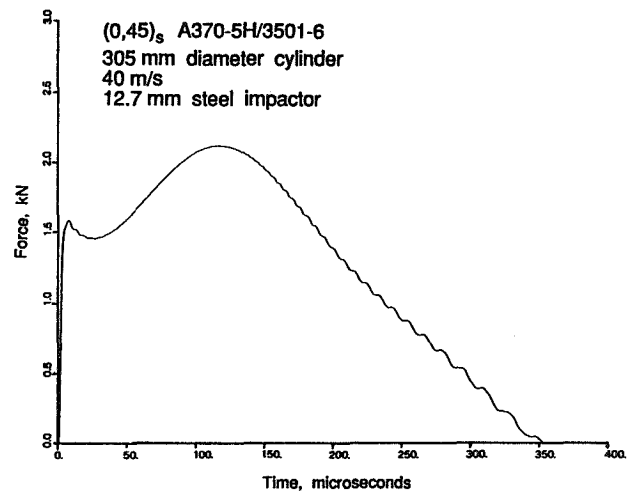
Figure 12 Predicted force versus time history for cylinder specimen impacted with a 12.7 mm steel ball at 40 m/s.

in the coupon specimens. Whether this damage distribution is important depends upon its effect on damage tolerance.

Damage Tolerance

Good results were achieved for the prediction of the damage tolerance of the coupon specimens loaded in tension using the average strain concept as shown in Figure 13. The predicted failure stress is plotted versus the core area diameter, the controlling parameter. However, the correlation was not as good for the case of the cylinder specimens as shown in Figure 14.

The first concern was that the failure patterns of the two configurations may differ. In order to utilize the coupon data for the prediction of cylinder behavior, the same failure mode must occur or the data will not represent the failure phenomena which take place. It appears that the failure in both the
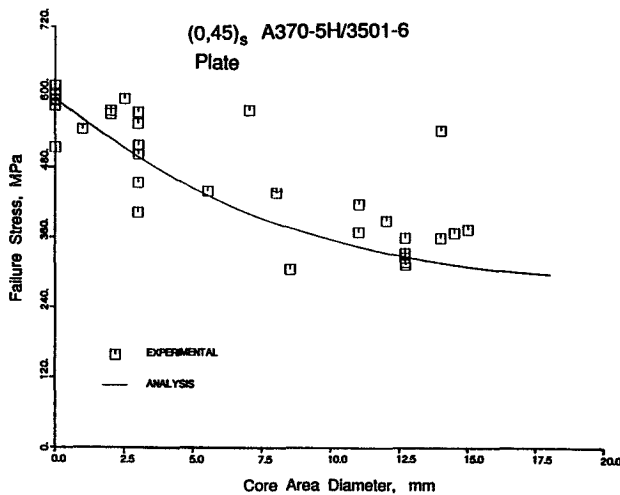
Figure 13 Tensile residual strength and predictions versus damage core diameter for coupon (plate) specimens.
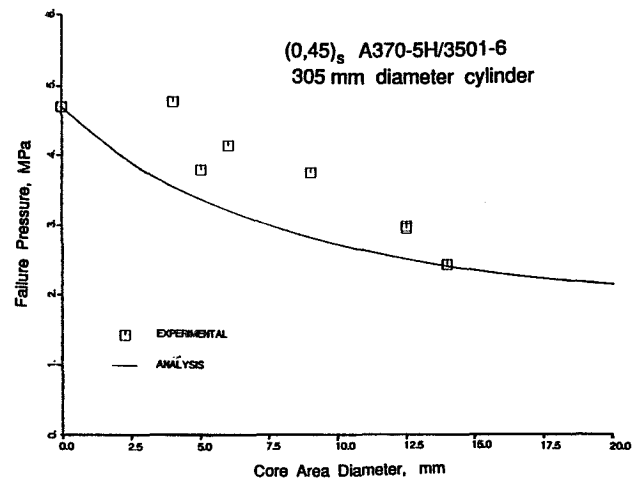
Figure 14 Failure pressure and predictions versus damage core diameter for cylinder specimens.

568
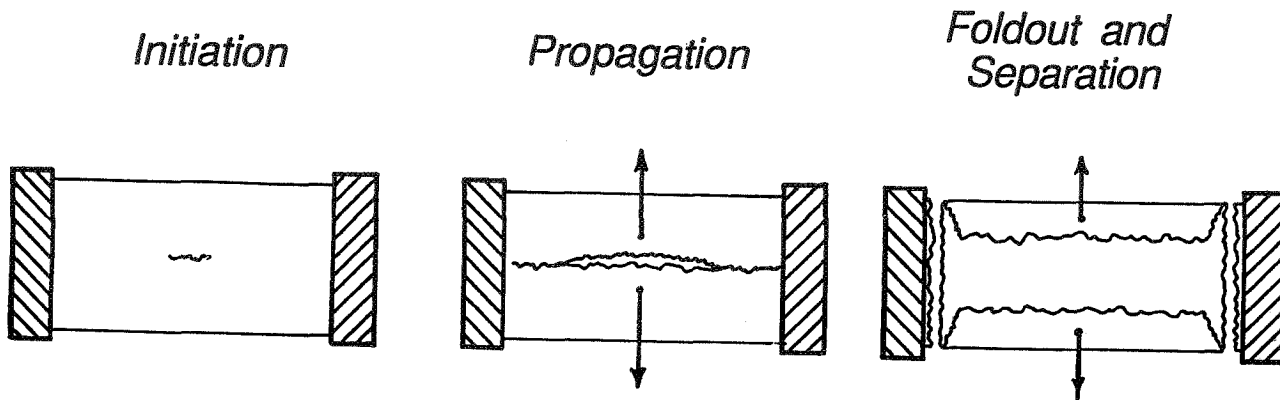
Figure 15   Typical failure sequence of impacted cylinder under pressure.

coupon and cylinder specimens is governed by failure of the 0° plies. This was clear in the coupon specimen, but required reconstruction of the cylinder after the catastrophic explosion. The reconstructed specimens indicated the failure process shown in Figure 15. Thus, in both cases, the primary fracture path was perpendicular to the highest loaded direction and was governed by 0° failure.

The second concern deals with the correction utilized for localized bending to relate the flat geometry to the pressurized cylinder. The damage area was modelled as a through-notch for this case and it was most clearly not such. Since the bending at the impact damage area is a function of the level of impact damage area, the amount of bending was overpredicted and thus the reduction in the flat plate strength was overestimated. It is interesting to note that as the core area diameter increased and approached punch-through, which is well-approximated by a through-notch, the experimental results approach the analytical prediction.

Thus, the plate inclusion analysis applied directly to the cylinder geometry to predict damage tolerance did not properly account for the structural effects associated with impact damage in pressurized cylinders. It is clear that information as to the distribution and type of damage is needed and must be modelled. Thus, a simple correction factor for bending at the impact damage edge cannot be applied. The proper analysis will require knowledge of delamination size as well as location through-the-thickness as this will affect the local bending stiffness and thus the localized bending strain which results from pressurization.

SUMMARY AND METHODOLOGY ASSESSMENT

The damage resistance and damage tolerance of coupon and pressurized cylinder fabric graphite/epoxy specimens were assessed and compared, with the overall objective being to provide a general methodology to assess the impact behavior of composite structure from coupon-level specimens. An analysis procedure previously developed to assess the impact behavior for coupon specimens was adapted to account for the structural effects introduced by the cylinder configuration.

The damage resistance of both the coupon and cylinder specimens was well-predicted in terms of a core area diameter representing the extent of fiber damage in these specimens. Furthermore, this integrated damage parameter was not affected, either in the analysis or the experiments, by the structural configuration. However, the overall distribution of damage was considerably different for the two configurations with the cylinder specimens showing a clean area with little delamination extending beyond the core damage region, while the coupon specimens showed extensive delamination away from the core damage region as well as fiber bundle disbonds. This latter damage type was found to be unique to fabric laminates and indicates the needs to first determine the damage modes which may

occur in a particular material and to assess the severity of the occurrence of such damage. Thus, the analysis can only properly model the integrated fiber damage size.

In the case of damage tolerance, predictions were made based on the core damage diameter. The analysis, utilizing an average strain concept, was able to correlate the results from the coupons extremely well. However, this was not the case for the pressurized cylinders. In this case, the damage was modelled as a through-flaw and a correction made to the plate prediction to account for localized bending which occurs due to the local change in bending stiffness. This analysis underestimated the failure pressure of the cylinders. This is attributed to the inability to model the distribution of damage at the impact site which will have an effect on the local bending stiffness and thus the amount of bending strain which occurs. It is noted that it is a necessary condition that the failure modes in the coupon and cylinder specimens be similar in order to apply the coupon data to the cylinder configuration.

Although the damage tolerance of the cylinders was not properly predicted, this is not an indictment of the general methodology, presented in Figure 1, to assess the impact response of structural configurations utilizing coupon-level results. The results clearly indicate that the ramifications of the specific structural configuration must be clearly understood and well modelled for this predictive model to be useful. Furthermore, knowledge of the damage distribution and the effect this has on the strain/stress field in the vicinity of the impact is needed. The methodology does, however, provide a working framework for the assessment of impact damage resistance and damage tolerance of structural configurations utilizing coupon data.

REFERENCES

1.   H.-Y.T. Wu and G.S. Springer, "Impact Induced Stresses, Strains, and Delaminations in Composites Plates", *Journal of Composite Materials*, Vol. 22, June, 1988, pp. 533-559.

2.   A.J. Gustafson, G.S. Ng, and G.T. Singley, "Impact Behavior of Fibrous Composites and Metal Substructures", Report No. USAAVRADCOM-TR-82-D-31, Applied Technology Laboratory, U.S. Army Research Laboratories, Fort Eustis, VA, October, 1982.

3.   H. Razi and V.E.J. Lindsay, "Analysis of Simply-Supported Orthotropic Cylinder Subjected to Low Velocity Impact", *Proceedings of the AIAA/ASME/ASCE/AHS 28th Structures, Structural Dynamics and Materials Conference*, Monterey, California, April, 1987, pp. 438-442.

4.   C.W. Bert and V. Birnam, "Response of Prestressed Cylindrically Curved Composite Structures Subjected to Low-Velocity Impact", *Proceedings of the Fourth Japan-U.S. Conference on Composite Materials*, Washington, D.C., June, 1988, pp. 43-52.

5.   P.A. Lagace and K.J. Saeger, "Damage Tolerance Characteristics of Pressurized Graphite/Epoxy Cylinders", *Proceedings of the Sixth International Symposium on Offshore Mechanics and Arctic Engineering*, ASME, Houston, Texas, March, 1987, pp. 31-37.

6.   D.S. Cairns, "Impact and Post-Impact Response of Graphite/Epoxy and Kevlar/Epoxy Structures", TELAC Report 87-15, Massachusetts Institute of Technology, August, 1987.

7.   D. S. Cairns and P.A. Lagace, "Thick Composite Plates Subjected to Lateral Loading", *Journal of Applied Mechanics*, Vol. 54, September, 1987, pp. 611-616.

8.   D.S. Cairns and P.A. Lagace, "Transient Response of Graphite/Epoxy and Kevlar/Epoxy Laminates Subjected to Impact", *AIAA Journal*, Vol. 27, November, 1989, pp. 1590-1596.

C-3

9. D.S. Cairns and P.A. Lagace, "Residual Tensile Strength of Graphite/Epoxy and Kevlar/Epoxy Laminates with Impact Damage", to appear in *ASTM STP 1059,* 1990.

10. M.J. Kraft, "Impact Damage Response of Graphite/Epoxy Fabric Structures", TELAC Report 88-9, Massachusetts Institute of Technology, July, 1988.

11. J. Dugundji, "Simple Expressions for Higher Vibration Modes of Uniform Euler Beams", *AIAA Journal,* Vol. 26, August, 1988, pp. 1013-1014.

12. E.S. Folias, "Asymptotic Approximations to Crack Problems in Shells", *Mechanics of Fracture,* Vol. 3, Noordhoff International, Leiden, the Netherlands, 1977, pp. 117-160.

13. M. Kageyama, "The Effects of Delaminations on the Failure of Pressurized Graphite/Epoxy Cylinders", TELAC Report 86-18, Massachusetts Institute of Technology, June, 1986.

14. J.M. Whitney and R.J. Nuismer, "Stress Fracture Criteria for Laminated Composites Containing Stress Concentrations", *Journal of Composite Materials,* Vol. 8, 1974, pp. 253-265.

15. J.G. Williams, M.S. Anderson, M.D. Rhodes, J.H. Starnes, Jr., and W.J. Stroud, "Recent Developments in the Design, Testing, and Impact Damage Tolerance of Stiffened Composite Panels", NASA TM 80077, April, 1979.

POSTBUCKLING BEHAVIOR OF CURVED PANELS UNDER COMBINED COMPRESSION AND SHEAR LOADS*

Ravi B. Deo, Han Pin Kan and Narain M. Bhatia
Northrop Corporation, Aircraft Division

N92-32584

SUMMARY

The objectives of the work reported in this paper were to develop a validated semiempirical design procedure and fatigue data for curved, stiffened composite panels operating in the postbuckled regime under the action of combined compression and shear loading. A previously developed design methodology for composite panels under pure shear or pure compression loading was used as the starting point for the program. Initially, the well established interaction rules for metal panels were adopted to predict buckling under combined loading. Test data were then developed to verify these rules and suggest modifications where necessary. Postbuckling failure envelopes were developed by accounting for the failure modes possible under shear loading only, and under pure compression loading. Static failure predictions under combined loading were based on test verified interaction criteria. Fatigue tests were conducted under combined loading to determine strength degradation and the possible failure modes.

INTRODUCTION

Several recent studies have demonstrated that the structural efficiency of military and commercial aircraft can be improved by taking advantage of the postbuckled strength of stiffened panels. An assessment of postbuckled stiffened panel design, analysis and applications technology (References 1 and 2) showed that several deficiencies had to be addressed to establish a systematic postbuckling design methodology. The Design Development and durability Validation of Postbuckled Composite and Metal Panels program was initiated in late 1984 by the Air Force Flight Dynamics Laboratory to specifically address the technology needs. This program followed an earlier Air Force Flight Dynamics Laboratory program (Reference 1) where a design methodology was developed for postbuckled composite and metal panels under simple loading conditions.

In Reference 1 a design and analysis methodology was developed for flat and curved stiffened panels made of either composite or metallic materials and subjected to either compression loading or shear loading. In practice, however, stiffened airframe panels are subjected to a combination of axial compression and shear loads. A semiempirical design methodology for curved metal panels under combined loading exists (Reference 3) but has seen limited verification. The present program was undertaken to extend the Reference 1 and Reference 3 methods for application to curved composite panels under combined uniaxial compression and shear loading and to further substantiate the metal panel design procedures.

The objectives of the work reported in this paper were to develop validated semiempirical design procedures and fatigue data for curved, stiffened composite postbuckled panels under combined uniaxial compression and shear loading. The specific requirements encompassed by these objectives were as follows:

1. Extend the existing semiempirical analysis methodology (Reference 1) into a design tool for curved composite panels subjected to uniaxial compression and shear loading. Account for any unique failure modes.

2. Develop a static and fatigue data base for composite panel design verification.

3. Prepare a procedural design guide. Exercise the design guide on a realistic aircraft component.

---

compression panel analysis methods of Reference 1 were used as the starting points for the semiempirical design procedure development. Initially, the interaction rules used for metal panels (Reference 3) were adopted to predict buckling under combined shear and compression loading. Test data were then used to verify these rules and suggest modifications where necessary. Postbuckling failure envelopes were developed by accounting for the failure modes possible under shear loading only, and under pure compression loading. Failure predictions under combined loading were based on test verified interaction criteria. Details of the design methodology and the fatigue behavior are described in this paper.

DESIGN METHODOLOGY

A complete static analysis of postbuckled structures consists of predicting the initial buckling loads, the failure or ultimate load of the panel after buckling, and the local skin and stiffener displacement and stress fields. The latter predictions are useful for fatigue analysis. The semiempirical methodology described here can be used to obtain the initial buckling and failure loads. The energy method based analysis described in Reference 4 is useful in predicting the local stresses and displacements needed for fatigue life prediction.

The semiempirical analysis method was selected as a design tool for postbuckled structures to provide a quick, inexpensive, and reasonably accurate but conservative design methodology. The scope of this methodology encompassed cylindrically curved stiffened panels loaded in simultaneously acting longitudinal compression and in-plane shear.

The essence of the combined loading design procedure is summarized in Figure 1. As can be seen in the figure, the curved panel is analyzed for compression and shear loads independently according to Reference 1 methods. Buckling loads under combined loading are predicted using the parabolic interaction rule developed for metal panels (Reference 3). Failure analysis requires consideration of failure modes under shear and compression acting independently and those due to the interaction of the loads. Failure prediction for panels under combined loads can be carried out by generating a failure load envelope as shown in Figure 2 and locating the failure load for a given compression to shear load ratio. Figure 2 also shows the variety of failure modes possible under combined loading. The failure modes affected by combined loading are stiffener crippling and skin rupture under tensile loading determined from a principal strain analysis and the maximum strain criterion. The following paragraphs present further details of the semiempirical analysis.

Skin Buckling Strain

Compression buckling strains for curved composite panels can be accurately determined through the use of computer codes SS8 (Reference 5) and BUCLP-2 (Reference 6), for example. However, for an approximate calculation of the skin buckling strain, the simplified Equation 1 (Reference 7) can be used.

$$\epsilon_{cr}^w = \left(\frac{m\pi}{L}\right)^2 \frac{1}{E_{xw}t_w}\left[D_{11} + 2(D_{12} + 2D_{66})\left(\frac{nL}{mb_w}\right)^2 + D_{22}\left(\frac{nL}{mb_w}\right)^4\right]$$

$$+ \frac{E_{yw}}{\left(\frac{m\pi}{L}\right)^2 R^2\left[E_{xw} - \left(2\nu_{xyw}E_{yw} - \frac{E_{xw}E_{yw}}{G_{xyw}}\right)\left(\frac{nL}{mb_w}\right)^2 + E_{yw}\left(\frac{nL}{mb_w}\right)^4\right]} \tag{1}$$

where D_{ij} are the terms of the bending stiffness matrix of the composite skin, E_{xw}, E_{yw}, G_{xyw}, ν_{xyw}, and t_w are the web elastic constants and thickness, respectively, L is the panel length, b_w is the width of the skin, R is the radius of curvature of the panel and n and m are integer coefficients representing the number of

half buckle waves in the width and length direction, respectively. The lowest value of strain for various values of n and m represents the buckling strain of the specimen.

The effective width of the skin, b_w, was assumed to be equal to the distance between the two adjacent stiffeners measured from one stiffener flange centroid to the next stiffener flange centroid. Note that b_w is less than the stringer spacing h_s.

The composite panel buckling loads obtained from program SS8 are in terms of running loads $N^0_{x_{cr}}$ and $N^0_{xy_{cr}}$ for compression and shear loading, respectively.

For combined compression and shear loading, the buckling loads can be computed from (Reference 3):

$$R_c + R_s^2 = 1 \tag{2}$$

where $R_c = N_{x_{cr}}/N^0_{x_{cr}}$ and $R_s = N_{xy_{cr}}/N^0_{xy_{cr}}$. $N^0_{x_{cr}}$ and $N^0_{xy_{cr}}$ are the pure compression and pure shear buckling loads, respectively, and $N_{x_{cr}}$ and $N_{xy_{cr}}$ are the buckling loads when the shear and compression loads are acting simultaneously. The presence of compression stresses reduces the shear buckling stress and vice versa.

Failure Analysis and Margin Computation

Failure analysis of postbuckled structures requires identification of all possible failure modes and calculating the loads corresponding to the critical failure mode. For curved panels under combined loading a failure envelope spanning the load ratio N_x/N_{xy} values of 0 (i.e., $N_x = 0$, $N_{xy} \neq 0$) to ∞ (i.e., $N_x \neq 0$, $N_{xy} = 0$) is a convenient means for identifying the critical failure mode. The procedure to develop this failure envelope is described in the following subsections.

Compression Loading Failure Analysis $(N_x/N_{xy} = \infty, \ N_{xy} = 0)$. Under compression loading the possible failure modes are

1. Euler buckling of the stiffened panel
2. Stiffener crippling
3. Stiffener/skin separation for composite panels with cocured or bonded stiffeners.

The semiempirical analysis methods for these failure modes are documented in References 1 and 8.

The compression failure load for the panel is determined as the lowest of the loads calculated for the listed modes.

Shear Loading Failure Analysis $(N_x/N_{xy} = 0; \ N_{xy} \neq 0)$. Flat or curved shear panel analysis is accomplished by means of the semiempirical tension field theory developed by Kuhn (Reference 3) for metal panels. In Reference 1 the tension field theory was modified for application to composite shear panels by taking into account material anisotropy.

The essential elements of the generalized (for application to metals as well as composites) tension field theory and its application are summarized in Figure 3. Details of the semiempirical analyses required to perform the various steps in Figure 3 are given in References 1 and 8.

Combined Loading Failure Analysis (N_x/N_{xy} = B; $N^o_{x_{cr}}/N^o_{xy_{cr}}$ = A). The effects of shear and compression loading interaction have to be accounted for in a combined loading failure analysis. For the combined loading case, the additional considerations are

1. The buckling stresses are reduced in accordance with the interaction given in Equation 2.
2. Compression stresses in the stiffeners prior to buckling are those due to the directly applied compression only. However, after buckling the compression stresses due to diagonal tension must be added to the direct compression.
3. The allowable stress calculation for the stiffeners must account for an interaction between the forced crippling (panel shear induced) and natural crippling (direct compression induced) modes of stiffener failure.
4. Calculation of the stiffener stresses due to applied shear loads is modified to account for the presence of the compression load.

The buckling interaction equation can be rewritten as

$$N_{x_{cr}}/N^o_{x_{cr}} + (N_{xy_{cr}}/N^o_{xy_{cr}})^2 = 1$$

then,

$$N_{xy_{cr}} = N^o_{xy_{cr}} \sqrt{1 - (N_{x_{cr}}/N^o_{x_{cr}})} . \tag{3}$$

The diagonal tension factor k is expressed as

$$k = \tanh \left[\left(0.5 + 300 \frac{t_w h_r}{R \, h_s} \right) \log \frac{N_{xy}}{N_{xy_{cr}}} \right] \tag{4}$$

where

$$k = \text{diagonal tension factor}$$

$$h_s = \text{strainer spacing, in.}$$

$$h_r = \text{ring or frame spacing, in.}$$

$$t_w = \text{skin thickness, in.}$$

$$R = \text{panel radius of curvature, in.}$$

$$N_{xy} = \text{applied shear load, lb/in.}$$

$$N_{xy_{cr}} = \text{Shear buckling load for combined loading as calculated from Equation 3}$$

Calculation of k using Equation 4 is subject to the auxiliary rules that if $h_s > h_r$, then replace h_r/h_s with h_s/h_r and if the resulting ratio is greater than 2, then use a value of 2 for the ratio.

The diagonal tension angle a is computed iteratively using the procedure illustrated in Figure 3 and described in Reference 1 for pure shear, but with appropriate modifications to the stiffener strain expressions. Thus, if $a = 30°$ initially then the new a is calculated using Equation 5 where, ϵ, the skin strain, is obtained from Equation 5a, ϵ_r, the ring or frame strain from Equation 5b, ϵ_s, the stiffener strain from Equation 5c, and R_f, a geometric parameter from Equation 5d.

$$\alpha_1 = \tan^{-1} \left[\frac{\epsilon - \epsilon_s}{\epsilon - \epsilon_r + R_f} \right]^{0.5} \tag{5}$$

$$\epsilon = \frac{\tau}{E_{wa}} \left[\frac{2k}{\sin 2\alpha} + \frac{E_{wa}}{2G_{rs}} (1-k) \sin 2\alpha \right] \tag{5a}$$

$$\epsilon_r = \frac{-k\tau \tan\alpha}{\left[\frac{EA_r}{h_r t_w} + 0.5 (1-k)E_{wr} \right]} \tag{5b}$$

$$\epsilon_s = \frac{-k\tau \cot\alpha}{\left[\frac{EA_s}{h_s t_w} + 0.5(1-k)E_{ws} \cdot R_L \right]} \tag{5c}$$

where

$$R_f = \frac{1}{24} \left(\frac{h_s}{R} \right)^2 \qquad \text{if } h_r > h_s$$

$$\tag{5d}$$

$$= \frac{1}{8} \left(\frac{h_r}{R} \right)^2 \tan^2\alpha \qquad \text{if } h_s > h_r$$

is a geometric parameter, and

$$R_L = -\frac{A}{2B} + \sqrt{\left(\frac{A^2}{4B^2} + 1 \right)} \tag{5e}$$

is a combined loading parameter with A and B defined as

$$N^o_{x_{cr}}/N^o_{xy_{cr}} = A$$

$$\tag{5f}$$

$$N_x/N_{xy} = B \ .$$

As in the pure shear case, sufficient iterations need to be performed so that $\alpha_{new} \approx \alpha_{old}$.

Computation of Stiffener Margin of Safety. The total stiffener load can be expressed as

$$P_s = P_x + P_{xy} \tag{6}$$

where P_x is the load in the stiffener due to direct compression and P_{xy} is the load in the stiffener due to the diagonal tension folds. The resulting stiffener strain can be expressed as (Reference 3)

$$\epsilon_s = \frac{-N_x h_s}{[(EA)_s + w\, t_w E_{ws}]} - \frac{k\, N_{xy} \cot\alpha}{t_w \left[\frac{(EA)_s}{h_s t_w} + 0.5(1-k)E_{ws}R_s \right]} \tag{7}$$

where the negative signs denote a compression strain, w is the effective width of the skin reacting the compression load after buckling and is obtained from Equations 17 or 18 in Reference 4, and R_L is given by Equation 5e. The average and maximum strains in the stiffener can be computed by analogy to the pure shear case, i.e.,

$$\epsilon_{s_{ave}} = \frac{-N_x h_s}{[(EA)_s + w\ t_w E_{ws}]} - \frac{k\ N_{xy}\ \cot\alpha}{t_w\left[\frac{(EA)_s}{h_s t_w} + 0.5(1-k)E_{ws}R_s\right]} \cdot \frac{\overline{(EA)}_s}{(EA)_s} \tag{8}$$

$$\epsilon_{s_{max}} = \frac{-N_x h_s}{[(EA)_s + w\ t_w E_{ws}]} - \frac{k\ N_{xy}\ \cot\alpha}{t_w\left[\frac{(EA)_s}{h_s t_w} + 0.5(1-k)E_{ws}R_s\right]} \cdot D_o \tag{9}$$

where

$$D_o = \left[1 - 0.775(1-k)\left(1-0.8\frac{h_r}{h_s}\right)\right] \quad \text{if } h_s > h_r$$

$$= \left[1 - 0.775(1-k)\left(1-0.8\frac{h_s}{h_r}\right)\right] \quad \text{if } h_s > h_r \tag{10}$$

and

$$\overline{(EA)}_s = (EA)_s \frac{\overline{EI}_s}{EI_s}\ .$$

In computing margins of safety for stiffener design, the above strains have to be compared against the Euler buckling strain and the stiffener crippling allowable strain. For Euler buckling, it is immaterial whether the stiffener compressive strain arises from the direct compression load, P_x, or from the diagonal tension action caused by P_{xy}. Euler buckling failure is assumed to take place when $\epsilon_{s_{ave}}$ given by Equation 8 above reaches ϵ_{SB} given in References 1 or 4. The nature of stiffener crippling under combined loading, however, requires that the interaction between the strain due to direct compression and the strain due to diagonal tension be accounted for. This is because crippling under diagonal tension is caused by forced deformation of the stiffener leg attached to the web, whereas direct compression causes crippling failure by local instability of the entire stiffener section. An empirical expression for this interaction has been given in Reference 3 for curved metal panels. For generic application to metal and composite panels the Reference 3 interaction is expressed in terms of strains as follows:

$$\frac{\epsilon_s^{co}}{\epsilon_s^{cc}} + \left(\frac{\epsilon_s^{so}}{\epsilon_{os}}\right)^{1.5} \leq 1.0 \tag{11}$$

where

ϵ_s^{co} = the direct compression strain

ϵ_s^{so} = the compression strain due to diagonal tension which cause stiffener crippling while acting simultaneously

ϵ_s^{cc} = the stiffener crippling strain under pure compression loading (Reference 1)

ϵ_{os} = the forced crippling strain of the stiffener under pure shear loading (Reference 1).

The margin of safety is computed as follows:

$$M.S. = \frac{1}{\left[\frac{\epsilon_s^c}{\epsilon_s^{cc}} + \left(\frac{\epsilon_{s_{max}}^s}{\epsilon_{os}}\right)^{1.5}\right]} - 1$$

578

where

$$\epsilon_s^c = \frac{-N_x h_s}{[(EA)_s + w\, t_w E_{ws}]}$$

and

$$\epsilon_{s_{max}}^s = \frac{-k N_{xy} \cot \alpha}{t_w \left[\frac{(EA)_s}{h_s t_w} + 0.5(1-k)E_{ws}R_L \right]} D_o \qquad (12)$$

Computation of Ring Margin of Safety. Metal panel test data show that the hoop compression stresses in the ring due to diagonal tension are unaffected by the axial compression on the curved panel as a whole. Therefore, the ring strains and margins of safety can be calculated as in the case of pure shear (Reference 1).

Automated Semiempirical Design Methodology

The design procedure outlined above has been coded in a computer program called PBUKL for use as a design tool. Detailed documentation of this program is given in Reference 9. The program is an extension of TENWEB, works interactively, and has several built-in stiffener profiles for design flexibility.

Program PBUKL was used to design the curved panels tested in this study.

METHODOLOGY VERIFICATION

Static and fatigue tests were conducted on composite panels to substantiate the semiempirical design methodology and to characterize their fatigue behavior. The test panel configuration is shown in Figure 4. The test matrix for the four static and four fatigue tests is shown in Table 1. All test panels were extensively instrumented with back-to-back strain gages to ensure uniformity of loading and to obtain data for methodology verification. A schematic of the test fixture used is shown in Figure 5.

Static Test Data Correlation

The static test data were analyzed to correlate the measured initial buckling load, ultimate strength and failure mode with predictions from the semiempirical analysis. These results are discussed in the following subparagraphs.

Initial Buckling Under Combined Loads. The correlation between initial buckling load predictions and test data for composite panels is shown in Figure 6. In the case of composite panels, the pure shear, pure compression and the combined loading initial buckling predictions were based on program SS8 (Reference 5). In Figure 6, the parabolic and linear interaction curves are also shown for comparison. The linear interaction expression provides a lower bound for the test data. For preliminary design purposes, use of the linear interaction is more appropriate for composite panels. Figure 7 shows that the test data are bounded by the linear and a fourth power (i.e., $a = 1$ and $a = 4$ in the expression $R_c + R_s^a = 1$) interaction rule (Reference 10).

Ultimate Strength Under Combined Loads. The ultimate strength of composite panels was predicted using the methodology given in the preceding section. The strength predictions were plotted as failure envelopes and are shown in Figure 8. The only change in the strength prediction methodology made after

comparison with test data was in the stiffener crippling interaction equation under combined loading. Originally the following criterion was adopted for stiffener crippling:

$$\frac{\epsilon_s^{co}}{\epsilon_s^{cc}} + \left(\frac{\epsilon_s^{so}}{\epsilon_{os}}\right)^{1.5} \leq 1.0.$$

However, the test data for composite panels show better correlation with a linear interaction, i.e.,

$$\frac{\epsilon_s^{co}}{\epsilon_s^{cc}} + \left(\frac{\epsilon_s^{so}}{\epsilon_{os}}\right) \leq 1. \tag{13}$$

The composite panel test data show good agreement with the linear interaction stiffener crippling prediction. There are two exceptions, however, in panels GR-1 and GR-2. The low failure loads obtained for these panels are plausible since these two early panels showed some load introduction problems during the static tests. Specifically, the panel load introduction area skin thickness was the same as the test section skin thickness. Due to load introduction eccentricities, the skin in the load introduction area buckled before the panel ultimate load was reached. Thus, the two panels were not subjected to a uniform axial compression load and, therefore, showed failure loads slightly lower than the predictions. In all other panels the load introduction region thickness was increased by secondarily bonding fiberglass laminates. Thus, the semiempirical design method with Equation 13 replacing Equation 11 can be used for designing curved composite panels under uniaxial compression and shear loads.

Fatigue Life Under Combined Loads. The fatigue test data for composite panels are fully documented in Reference 4.

A summary of the test results is shown in Figure 9. The two panels tested at $(N_x)_{max}/(N_{xy})_{max} = 2$ experienced no fatigue failure after 100,000 cycles of constant amplitude loading. Residual static strength tests on these panels indicated no strength reduction (See Figure 8). The static failure mode was primarily skin/stiffener separation. Panels under constant amplitude shear dominated loads, i.e., $(N_x)_{max}/(N_{xy})_{max} = 0.5$, failed under fatigue cycling. The fatigue failure mode in these panels (GR-7 and GR-8) was skin stiffener separation at stiffener and ring intersection accompanied by local skin rupture. Thus, the composite panels appear to be more sensitive in fatigue to shear dominated loading.

Figure 10 shows a plot of the number of fatigue cycles sustained by the composite panels versus the applied loads. From the four data points in Figure 10 a fatigue threshold was estimated to be approximately 80 percent of the static strength. Thus, in fatigue the composite panels could be utilized up to 200 percent of their initial buckling load for shear dominated loading. The postbuckling range for composite panels under compression dominated loading could be possibly higher.

CONCLUSIONS

The significant conclusions from this program are summarized in the following listing:

1. The semiempirical static design methodology developed in Reference 1 for postbuckled composite and metal panels under pure shear or pure compression loading was extended to panels under combined uniaxial compression and shear loads.

2. The methodology was coded in a computer program (PBUKL) for rapid iterative design of composite and metal panels.

3. Experimental verification data were used to develop a new criteria to predict the effect of shear and compression load interaction on composite panel skin buckling. A linear interaction, although conservative, seems more appropriate for the design of composite panels as opposed to the well established parabolic interaction rule for metal panels.

4. The test data showed that for composite panels a linear interaction rule for stiffener crippling prediction yields better correlation than a nonlinear interaction rule.

5. Ultimate panel strength predictions based on the semiempirical analysis for composite and metal panels were found to be very accurate and well suited for design purposes.

6. Stiffener and skin separation in composite panels was the observed failure mode under static combined uniaxial compression and shear loading.

7. Composite panels demonstrated a high fatigue threshold relative to the initial skin buckling loads. Composite panels designed for a static strength equal to 250 percent of the initial skin buckling load can be safely operated under fatigue loading up to 200 percent of the initial buckling load.

8. Composite panels tested in the program showed a greater sensitivity to shear dominated fatigue loading as compared with compression dominated fatigue loading.

9. The fatigue failure mode in composite panels was separation between the cocured stiffener and the skin. In particular, the region at the intersection of the stiffener and the ring was vulnerable to the failure mode.

REFERENCES

1. Deo, R.B., Agarwal, B.L., Madenci, E., "Design Methodology and Life Analysis of Postbuckled Metal and Composite Panels," AFWAL-TR-85-3096 Final Report, Volume I, Contract F33615-81-C-3208, December 1985.

2. Deo, R.B., and Madenci, E., "Design Development and Durability Validation of Postbuckled Composite and Metal Panels," AFWAL-TR-85-3077 Final Report, Technology Assessment, Contract F33615-84-C-3220, May 1985.

3. Kuhn, P., Peterson, M.P., and Levin, L.R., "Summary of Diagonal Tension," Parts I and II, NACA TN2661 and 2662, May 1952.

4. Deo, R.B., Kan, H.P., and Bhatia, N.M., "Design Development and Durability Validation of Postbuckled Composite and Metal Panels, Volume III — Analysis and Test Results," AFWAL-TR-89-3030, Volume III, Contract F33615-84-C-3220, September 1989.

5. Wilkins, D.J., "Anisotropic Curved Panel Analysis," General Dynamics, Convair Aerospace Division Report FZM-5567, May 1973.

6. Viswanathan, A.V., and Tamekuni, M., "Elastic Buckling Analysis for Composite Stiffened Panels and Other Structures Subjected to Biaxial Inplane Loads," NASA CR-2216, 1973.

7. Block, D.L., Card, M.F., and Mikulas, M.M., Jr., "Buckling of Eccentrically Stiffened Orthotropic Cylinders." NASA TND-29601, August 1965.

8. Deo, R.B., Agarwal, B.L., Sobota, Capt. M., "Postbuckled Composite Structures Design Technology," Paper published in the Proceedings of the Seventh Conference on Fibrous Composites in Structural Design, AFWAL-TR-85-3094, June 1985.

9. Deo, R.B., and Kan, H.P., "Design Development and Durability Validation of Postbuckled Composite and Metal Panels," WRDC-TR-89-3030, Automated Data Systems Documentation, Contract F33615-84-C-3220, December 1989.

10. Ogonowski, J.M., and Sanger, K.B., "Postbuckling of Curved and Flat Stiffened Composite Panels Under Combined Load," Report No. NADC-81097-60.

Table 1. Composite Panel Test Matrix (RTD Environment)

PANEL NO.	MATERIAL	TYPE OF TEST	LOAD RATIO N_x/N_{xy}	R-RATIO * FOR FATIGUE TESTS	MAXIMUM FATIGUE LOAD, % STATIC STRENGTH	STATIC STRAIN SURVEYS TO INITIAL BUCKLING (N_x/N_{xy})
GR1 GR2	AS4 and A370-5H/ 3501-6 Graphite-Epoxy	Static	0.5	--	--	0, 0.5, 1.0, ∞, 2.0
GR3 GR4		Static	2.0	--	--	0, 0.5, 1.0, ∞, 2.0
GR5 GR6		Fatigue	-- --	$R_x = 10$, $R_{xy} = -1.0$	70	0, 0.5, 1.0, 2.0
GR7 GR8		Fatigue	-- --	$R_x = 10$, $R_{xy} = -1.0$	70	0, 0.5, 1.0, 2.0

* R_x denotes R-ratio for compression load
R_{xy} denotes R-ratio for shear load
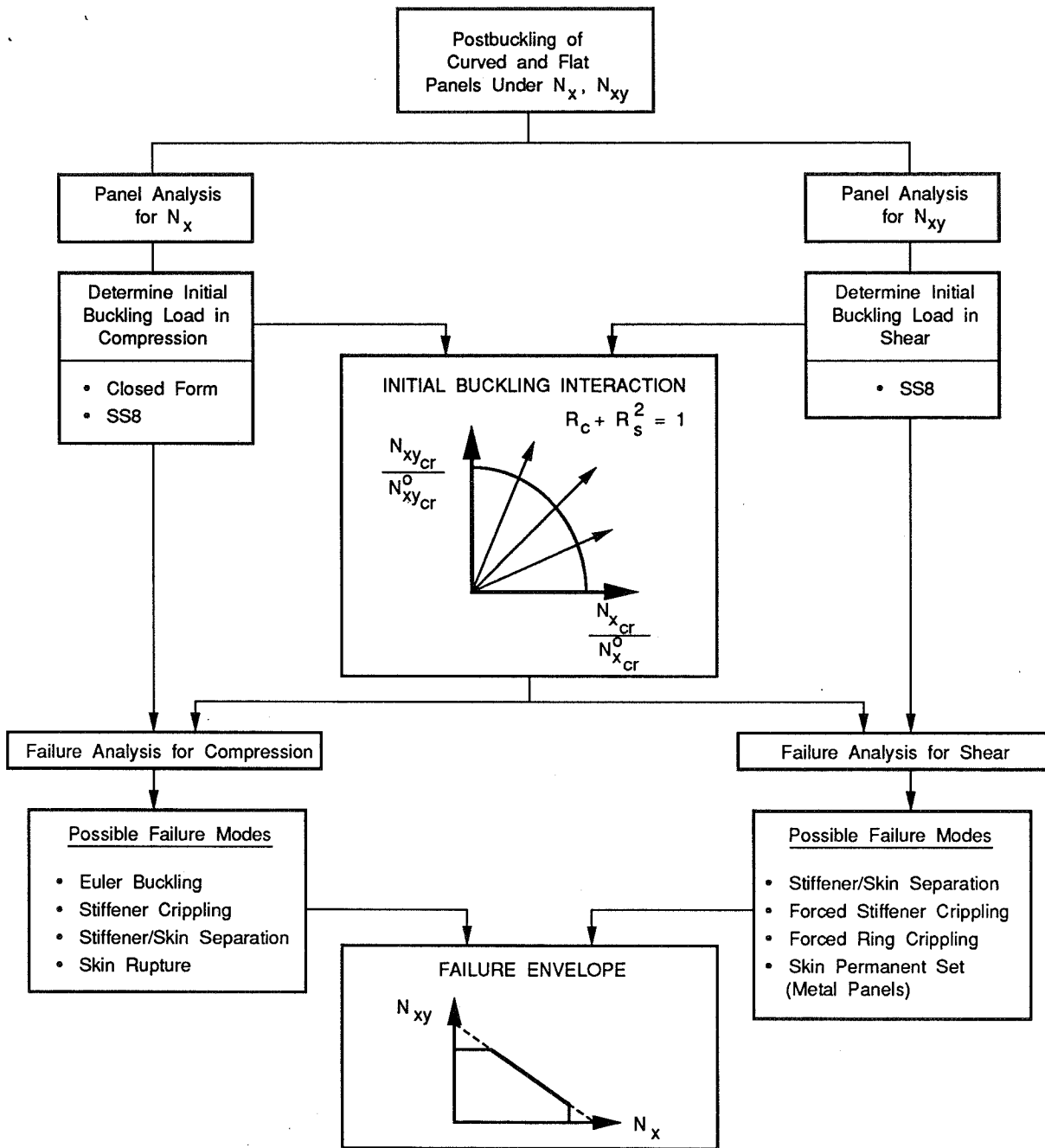
Figure 1. Semiempirical Analysis Approach for Postbuckled Stiffened Panels Under Combined Loading
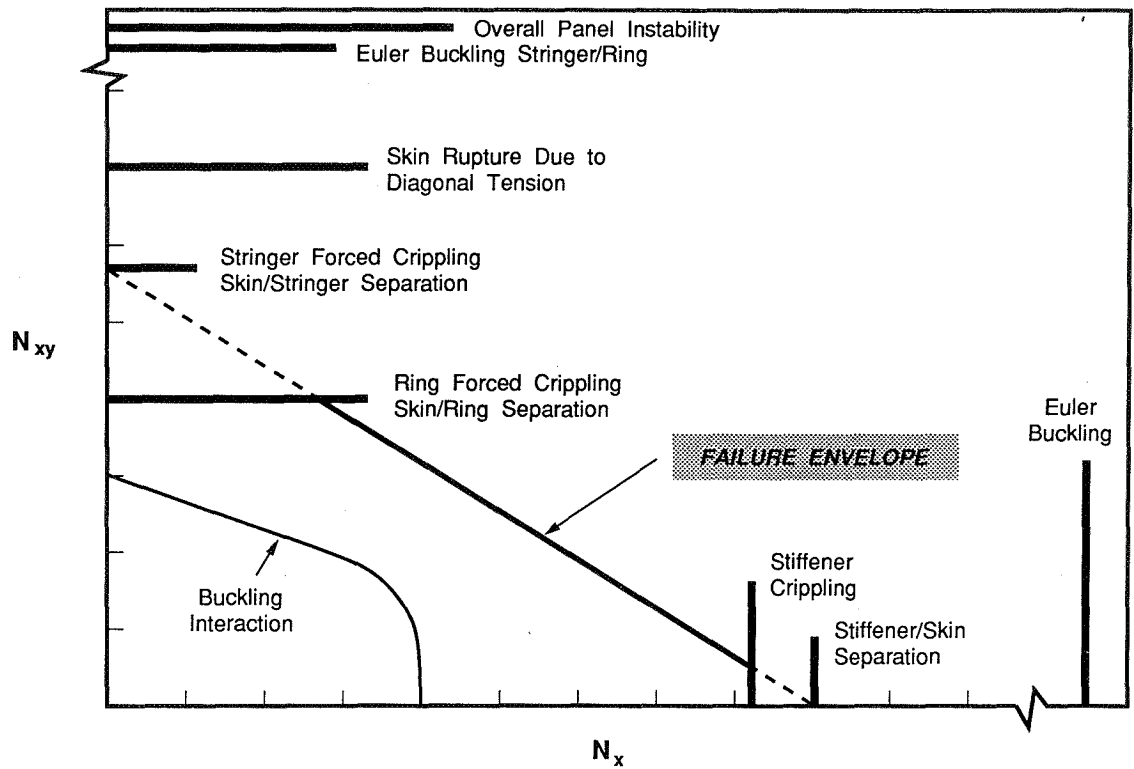
Figure 2. Schematic of a Failure Envelope for Postbuckled Composite Panels Under Combined Compression and Shear Loading
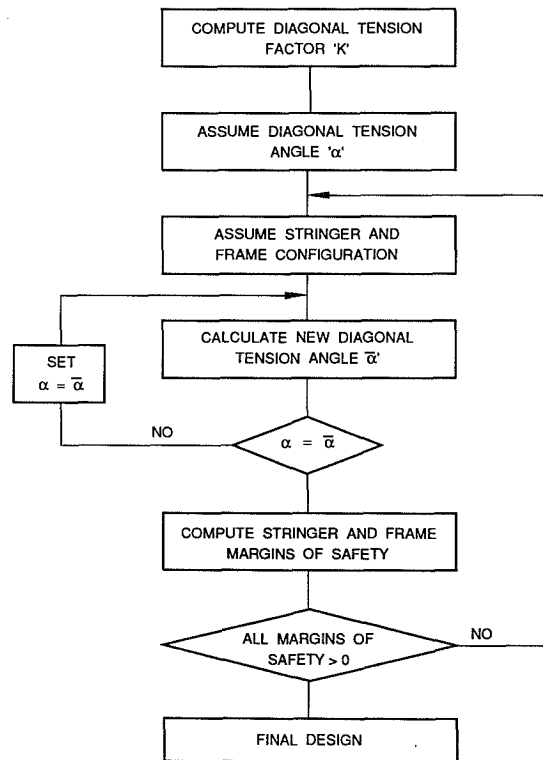
Figure 3. Application of Tension Field Theory to Shear Panels
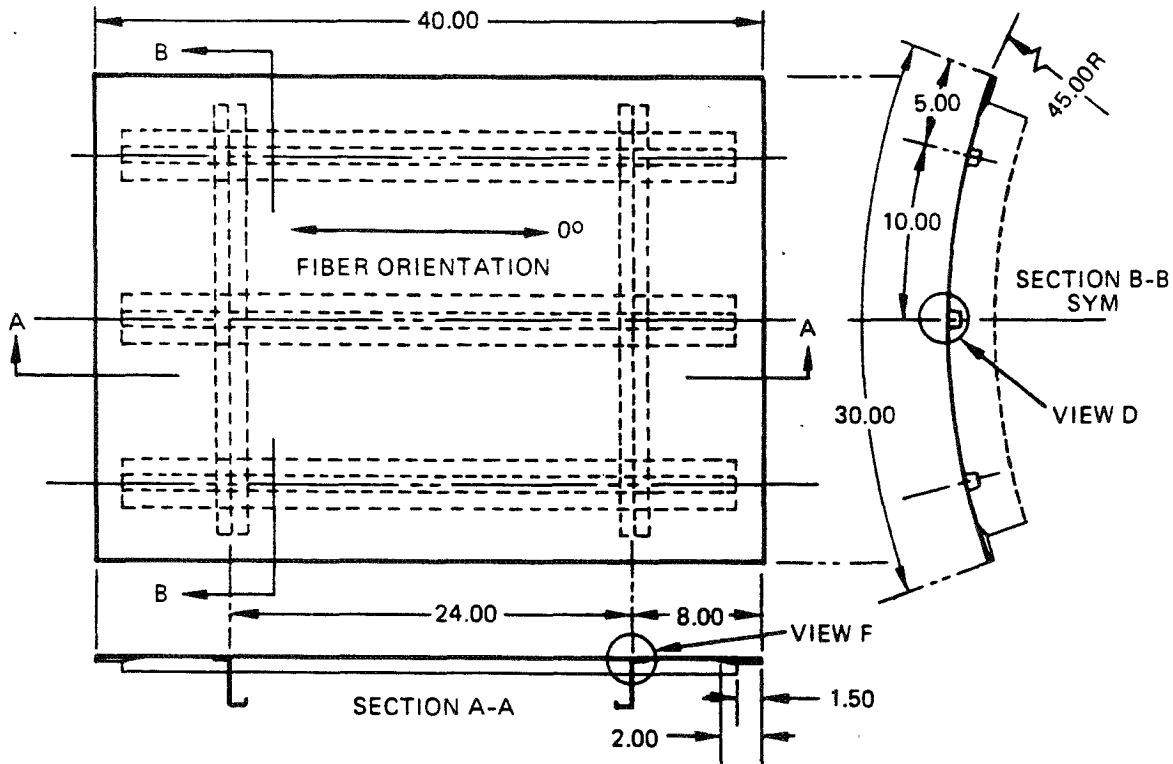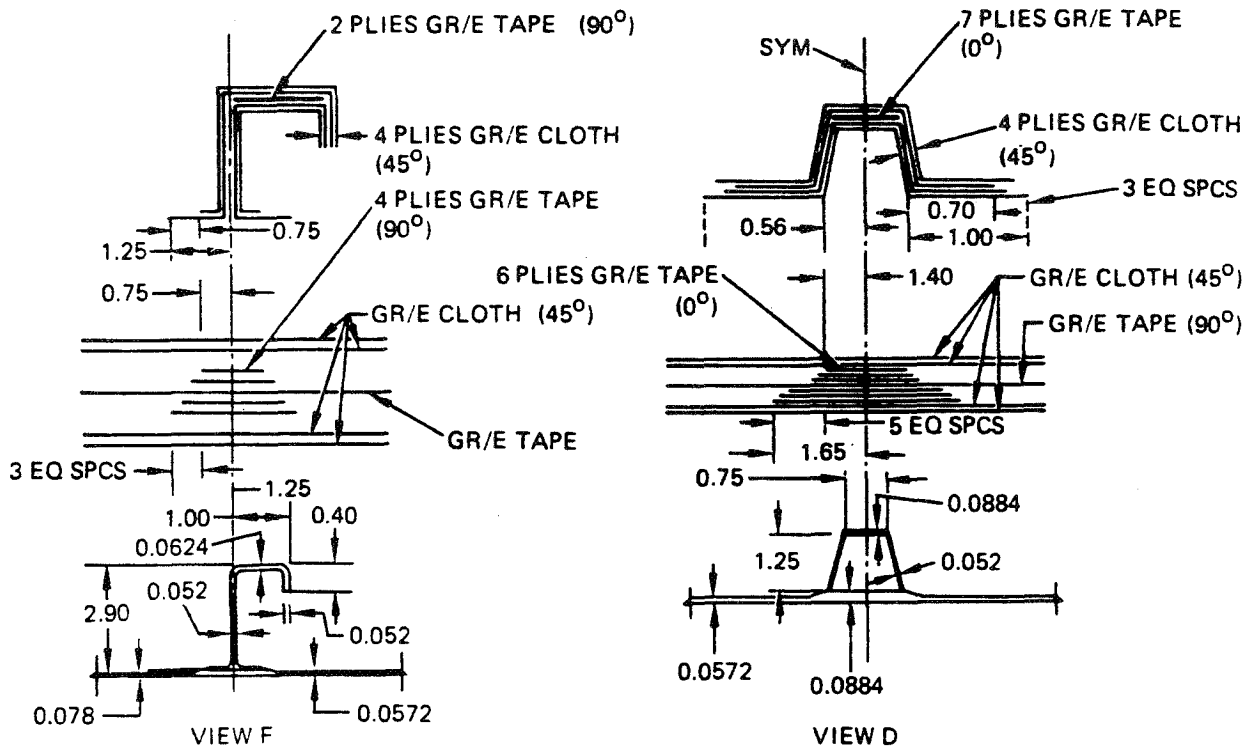
Figure 4. Composite Test Panel Configuration

585
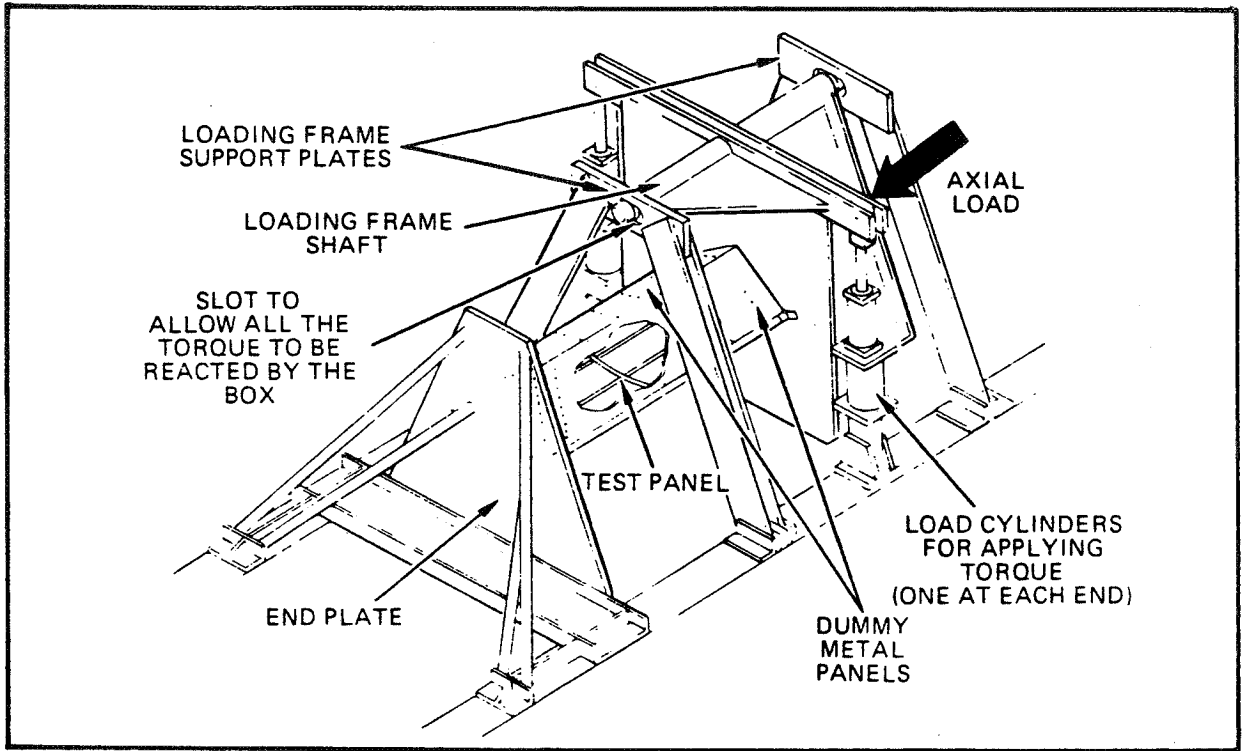
Figure 5. Schematic of the Test Fixture
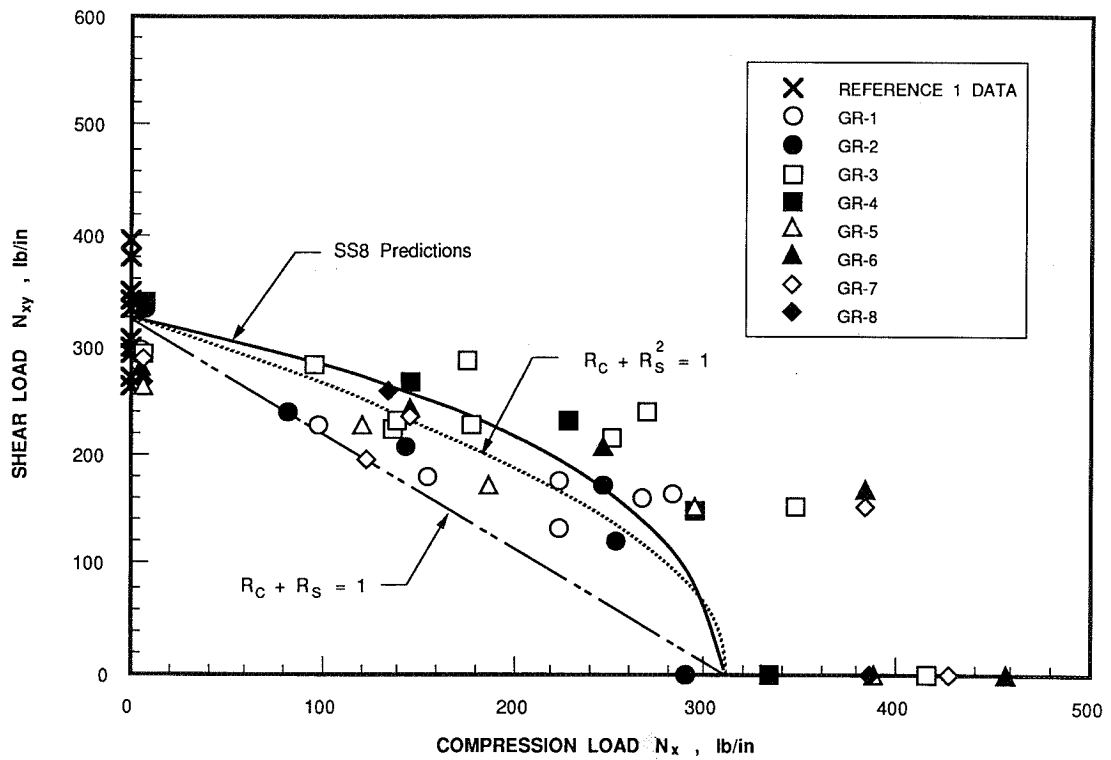
Figure 6. Comparison of Measured and Predicted Buckling Loads for Composite Panels
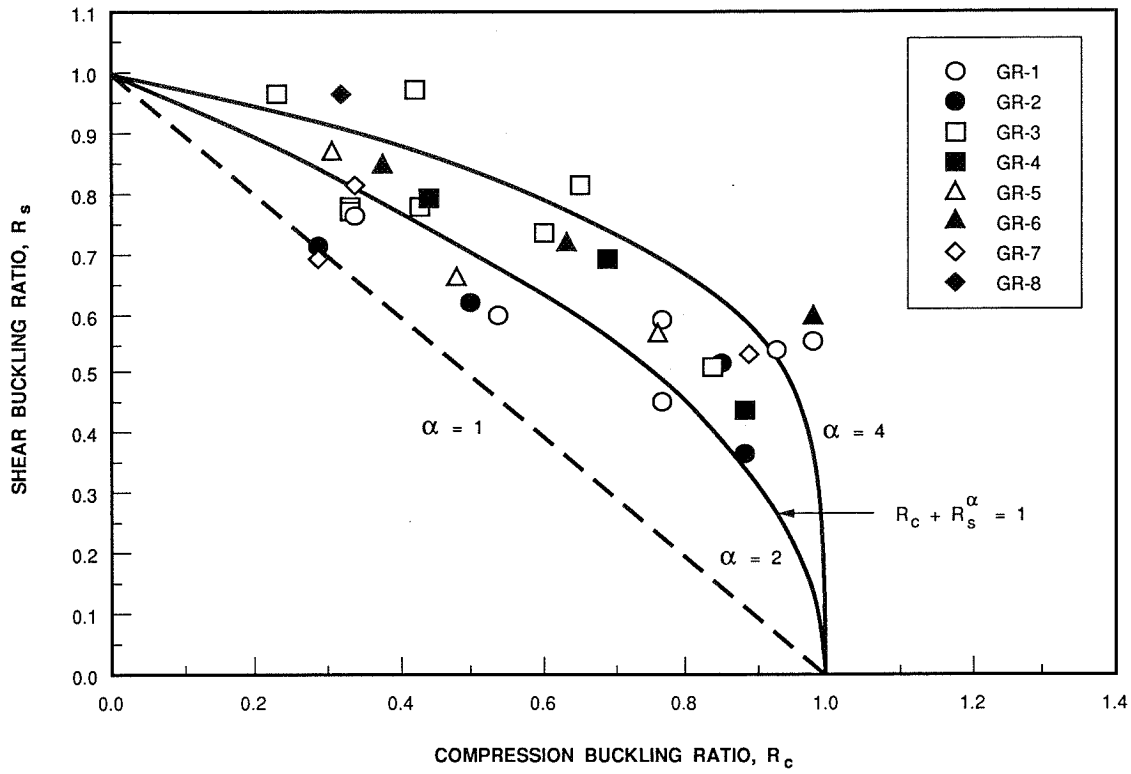
Figure 7. Comparison of Measured Buckling Loads With Predictions From Different Interaction Rules
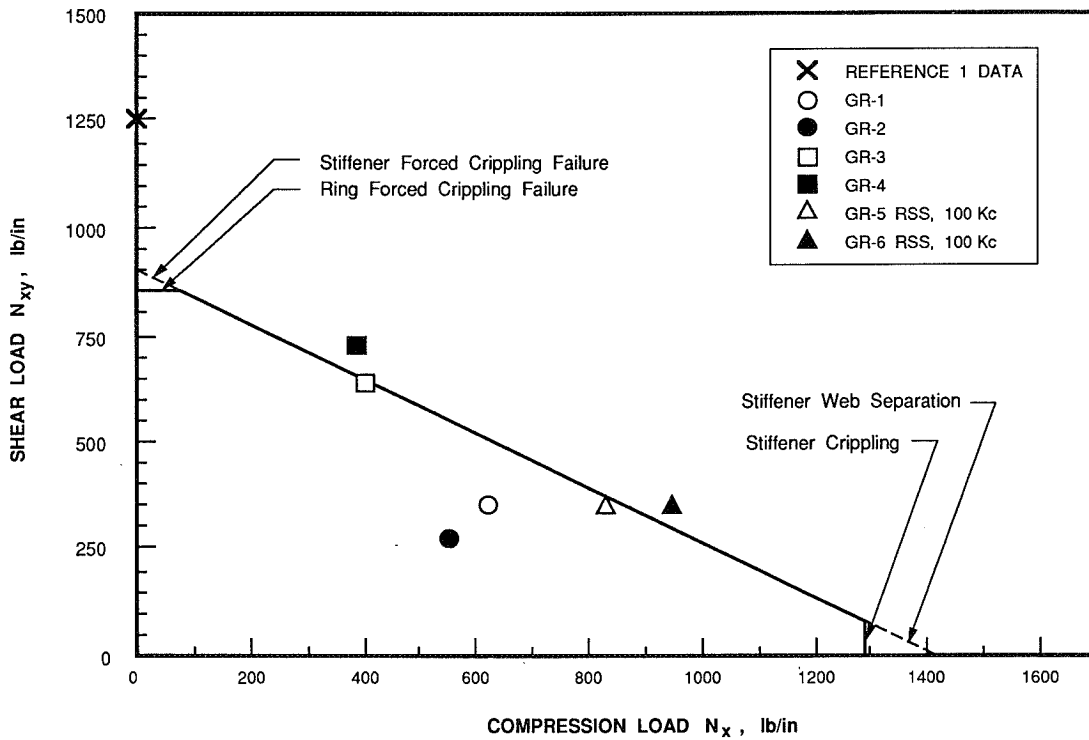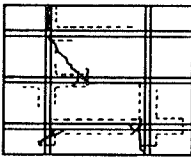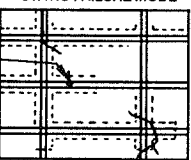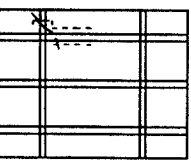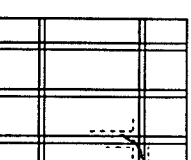
Figure 8. Failure Envelope for Composite Panels and Correlation With Test Data

PANEL No.	FATIGUE CRACKS*	MAX FATIGUE LOAD, lbs/in		$\dfrac{N_x}{N_{xy}}$	$\dfrac{N_x}{N_x^{CR}}$	$\dfrac{N_{xy}}{N_{xy}^{CR}}$	MAX. FATIGUE LOAD, % STATIC STRENGTH	FATIGUE HISTORY	STATIC OR FATIGUE FAILURE
		N_x	N_{xy}						
GR-5	STATIC FAILURE MODE	538	218	2.47	1.82	1.45	0.69	RUN OUT AT 100,000 CYCLES	RESIDUAL STATIC STRENGTH: N_x = 833 lb/in N_{xy} = 353 lb/in
GR-6	STATIC FAILURE MODE STIFF. FAILURE	590	239	2.70	1.68	1.41	0.76	RUN OUT AT 100,000 CYCLES	RESIDUAL STATIC STRENGTH: N_x = 810 lb/in N_{xy} = 356 lb/in
GR-7		334	530	0.63	2.29	2.26	0.78	FATIGUE FAILURE AS SHOWN AT 38,743 CYCLES	FATIGUE
GR-8		286	521	0.55	2.13	2.03	0.77	FATIGUE FAILURE AS SHOWN AT 62,095 CYCLES	FATIGUE

* ——— SKIN RUPTURE   ············· STIFFENER/SKIN DISBONDS

Figure 9. Fatigue Failure Modes for Composite Panels
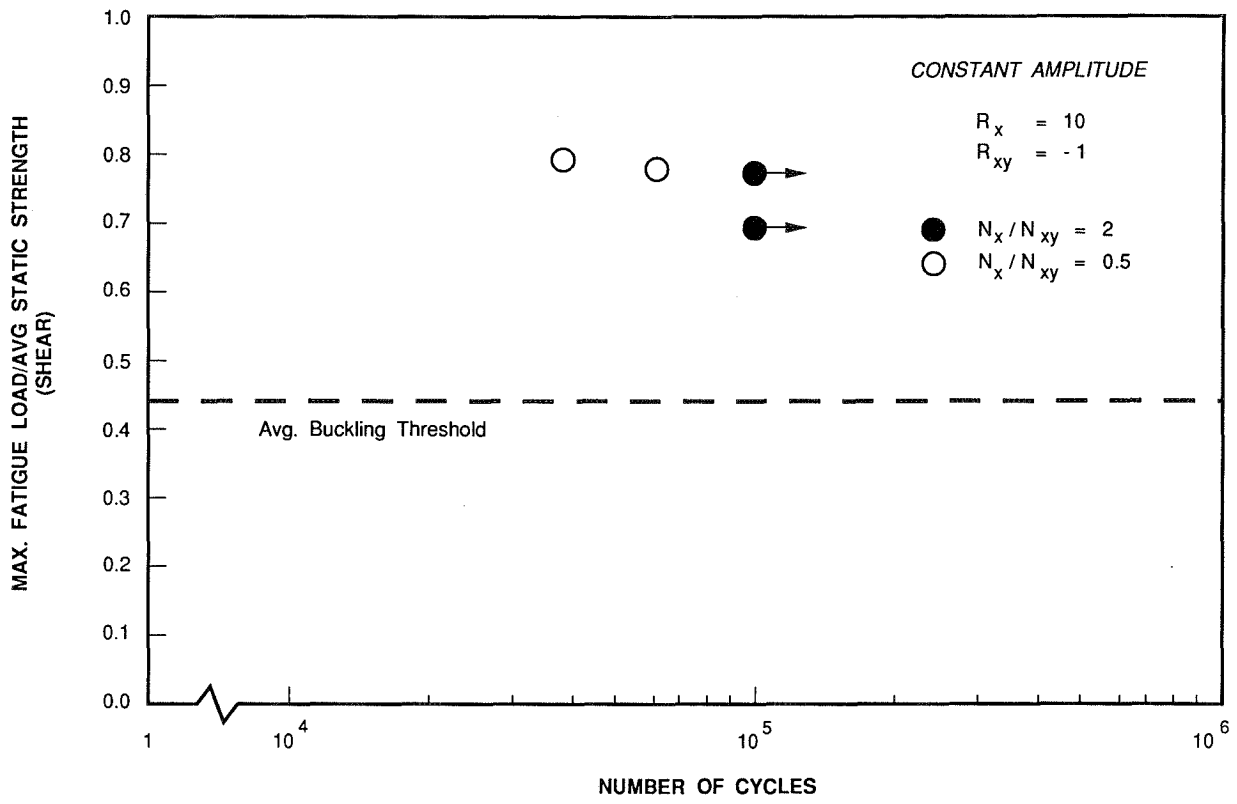
Figure 10. Composite Panel Fatigue Data

POSTBUCKLING OF STIFFENED COMPOSITE PLATES UNDER
COMBINED LOADING[1]

Richard K. Kunz
Lockheed Aeronautical Systems Company

SUMMARY

An analysis methodology for the postbuckling behavior of laminated plates under combined in-plane normal and shear loading is presented. The plates are simply supported on their ends, and elastically re-strained against rotation along their longitudinal edges. Discrete thickness changes along the plate edges are included in the formulation to account for attached stiffener flanges and/or edge pad-ups. The resulting analytical approach is suitable for inclusion in a preliminary sizing procedure for longitudinally stiffened composite panels.

INTRODUCTION

The analysis and optimum sizing of composite stiffened panels loaded in the postbuckling regime is a critical problem in the design of aircraft structures. Because plate structures can exhibit considerable load carrying capacity after the onset of buckling, the skins of such structural components as fuselage panels, spar webs, floors, and bulk-heads may be allowed to buckle under certain loading conditions. When composite materials are used, the large number of design variables involved in determining the optimum sizing of postbuckled panels poses a formidable challenge to the designer/analyst.

A computer code known as POSTOP [1,2] was developed over the course of several years to address this need. POSTOP includes a comprehensive set of analysis routines coupled with a general-purpose numerical opti-mization code resulting in an analysis and sizing code for the prelim-inary design of stiffened composite panels loaded in the postbuckling regime. Among POSTOP's analysis modules is an approach to determine the postbuckling response of the skin between stiffeners, based on a formulation due to Koiter [3]. The present paper describes a more general postbuckled plate analysis intended to extend the capabilities of the analysis currently used in POSTOP and to provide a more physi-cally consistent interface with the other analysis modules comprising the POSTOP code.

Because the postbuckling analysis is to be embedded in an optimization code, computational efficiency was an important consideration in the

---

selection of an analytical approach. The work of previous investigators was evaluated for suitability to the present application. Feng [4] and Zhang and Matthews [5] each used a Rayleigh-Ritz approach, expanding both the in-plane and out-of-plane response into double series in the in-plane coordinates. One effect of this approach is that a large number of coefficients must be calculated from the non-linear governing equations.

Stein [6] assumed the postbuckling response to be periodic in the longitudinal direction, enabling a series expansion of all three displacement components in the transverse direction only. While the specific solution procedure used by Stein was not adopted in the present work, his normal displacement function formed the basis for the one chosen for this investigation. Kudva and Agarwal [7] expressed both the normal and in-plane response in terms of only seven parameters; however, the approach was felt to lack the generality in loading and plate geometry required for the present application. In all of the above analyses [4]-[7] plate edges were either simply supported or clamped.

Rhodes and Harvey [8] adopted an approach similar to [6] for the normal response. However, the in-plane response was obtained explicitly in terms of the normal displacement expansion by direct solution of the in-plane compatibility equation governing the Airy stress function. As a result, both the normal and in-plane formulations were expressed in terms of a single set of coefficients. This approach had the advantage of reducing the number of coefficients to be determined while retaining generality in plate geometry. The analysis also included the effects of elastically restrained longitudinal edges, but was restricted to isotropic plates loaded in uniaxial compression.

The present work uses the basic approach of [8], while generalizing to anisotropic plates under combined loading. In addition, the present geometric configuration includes regions of discrete stiffness changes along the longitudinal edges of the plate, to account for attached stiffener flanges and/or pad-up under the stiffeners, allowing the resulting stiffness tailoring effects on buckling and postbuckling to be determined.

SYMBOLS

a	Plate length
$[A_{ij}]$, $[B_{ij}]$, $[D_{ij}]$	In-plane, coupling, and bending stiffnes matrices
A_n, B_n	Coefficients in series for w, eqn. (3)
$[a_{ij}]$	$[A_{ij}]^{-1}$
b	Plate width
b_o	Width of center portion of plate
K_R	Torsional spring constant, eqn. (6)

M_x, M_y, M_{xy}	Moment resultants
N, M	Limit of summations for w, eqn. (3)
N_{cr}, ε_{cr}	Critical load, strain for a uniform, simply-supported plate under uniaxial compression
N_x, N_y, N_{xy}	In-plane stress resultants
$\bar{N}_x$, $\bar{N}_y$, $\bar{N}_{xy}$	Average in-plane edge stress resultants
t	Plate thickness
u, v, w	Longitudinal, transverse, and normal displacements
U_b, U_m, U_s	Strain energy due to bending, membrane, spring
V	Potential of applied loads
w_c	Normal displacement along the crest of a buckle
x, y, z	Longitudinal, transverse, and normal coordinates
α_n, β_n	Parameters in series for w, eqn. (3)
ε_1, ε_2, γ_{12}	Imposed edge strains, Fig. 2
λ	Half-wavelength of buckles in x-direction
Π	Total potential
ψ	Airy stress function
*	Quantities referred to the edge region

ANALYTICAL FORMULATION

Fundamental Considerations

The plate geometry for the present analysis is shown in Figure 1. The following are the major assumptions incorporated into the analysis:

   i)   The plate is geometrically and elastically symmetric about y = 0.

  ii)   The plate is simply supported at x = 0, a.

 iii)   Plate edges are assumed to remain straight under the in-plane loading, due to the presence of the stiffeners and required continuity with similar adjacent skin regions; in-plane edge boundary conditions consist of imposed displacements characterizing biaxial normal and shear loading.

  iv)   At y = $\pm b_s$, the transverse displacement is zero. Rotations at y = $\pm b_s$ are restrained by the adjacent stiffeners, which are assumed to act as linear torsional springs.

   v)   The skin is a balanced symmetric laminate, so that there is no extensional-shear or bending-extensional coupling. Bending-torsional coupling is included in the analysis. To approximately account for the eccentricity in the edge regions b_o < |y| < b_s, the reduced bending stiffness matrix is used in this region.

vi) Transverse shear deformations are neglected. The von Karman nonlinear kinematic formulation is used.

Additional approximations and restrictions are noted in the sequel as they are encountered.

Consistent with the above assumptions, the constitutive and kinematic relations for the plate may be combined to relate in-plane stress and moment resultants to the plate displacements:

$$
\begin{Bmatrix} N_x \\ N_y \\ N_{xy} \end{Bmatrix} = \begin{bmatrix} A_{11} & A_{12} & 0 \\ A_{12} & A_{22} & 0 \\ 0 & 0 & A_{66} \end{bmatrix} \begin{Bmatrix} u_{,x} + \frac{1}{2} w_{,x}^2 \\ v_{,y} + \frac{1}{2} w_{,y}^2 \\ u_{,y} + v_{,x} + w_{,x} w_{,y} \end{Bmatrix} \tag{1}
$$

$$
\begin{Bmatrix} M_x \\ M_y \\ M_{xy} \end{Bmatrix} = - \begin{bmatrix} D_{11} & D_{12} & D_{16} \\ D_{12} & D_{22} & D_{26} \\ D_{16} & D_{26} & D_{66} \end{bmatrix} \begin{Bmatrix} w_{,xx} \\ w_{,yy} \\ 2w_{,xy} \end{Bmatrix} \tag{2}
$$

Because of the possiblity of a thickness change along the plate edges, the A and D matrices may assume different values in the center and edge regions. In the following discussion, a superscript * will be used to denote values in the edge region $b_o < |y| < b_s$ when the distinction is necessary. Furthermore, since the edge region may in general be unsymmetric, the reduced bending stiffness matrix [9]

$$
D^* = D - BA^{-1}B
$$

will be used in eqn. (2) for the D matrix in the edge region, where B is the bending-extensional coupling matrix.

Normal Displacement Function

The transverse displacement $w(x,y)$ is represented by the series expansion

$$
w(x,y) = \sin\frac{\pi x}{\lambda} \sum_{n=0}^{N} A_n \cos\frac{\alpha_n y}{b_s} + \cos\frac{\pi x}{\lambda} \sum_{n=1}^{M} B_n \sin\frac{\beta_n y}{b_s} \tag{3}
$$

where λ is the half-wavelength of buckles in the x-direction. The first term in eqn. (3) represents deformations symmetric about the longitudinal centerline; the second is the skew-symmetric component. Hence, for an isotropic or orthotropic plate subject to normal loading only, the B_n will be zero. The B_n become important for cases of shear loading and in the presence of bending-torsional coupling. This functional form permits curved nodal lines in the presence of shear. Coefficients A_n and B_n represent the primary unknowns to be determined by the postbuckling analysis.

594

Boundary conditions governing normal displacements on $y = \pm b_s$ enable the determination of parameters α_n and β_n, as well as coefficients A_0 and B_1. The zero displacement boundary condition,

$$w(x, \pm b_s) = 0 \tag{4}$$

gives

$$A_0 = -\frac{1}{\cos\alpha_0} \sum_{n=1}^{N} A_n \cos\alpha_n$$

$$\tag{5}$$

$$B_1 = -\frac{1}{\sin\beta_1} \sum_{n=2}^{M} B_n \sin\beta_n$$

The condition of elastic rotational restraint is represented by requiring that the y-direction curvature be proportional to the slope at the plate edges:

$$-\frac{w_{,yy}}{w_{,y}} = \pm \frac{K_R}{b_s} \qquad y = \pm b_s \tag{6}$$

where K_R is a non-dimensional torsional spring constant. Substituting eqn. (3) into (6) yields the following two conditions:

$$\tan\alpha_n = -\frac{1}{K_R}\alpha_n \qquad\qquad \cot\beta_n = \frac{1}{K_R}\beta_n \tag{7}$$

Equations (7) have multiple roots for α_n and β_n; they may be solved iteratively for as many values as are required for terms in the series (3).

Determination of In-plane Response

The Airy stress function approach is used to determine the in-plane response of the plate. By directly solving the governing differential equation, the in-plane response can be determined in terms of the previously introduced coefficients A_n and B_n. This has the advantages of keeping the number of unknown quantities to a minimum, as well as assuring that the in-plane solution is consistent with the assumed form of the normal response.

The Airy stress function $\psi(x,y)$ is defined implicitly by the relations

$$N_x = \psi_{,yy}$$

$$N_y = \psi_{,xx} \tag{8}$$

$$N_{xy} = -\psi_{,xy}$$

such that the in-plane equilibrium equations are identically satisfied. The equation assuring compatibility of in-plane displacements becomes

the governing differential equation for ψ; for the present case, in which the nonlinear terms are included in the kinematic formulation, this equation assumes the form

$$a_{22}\psi_{,xxxx} + (2a_{12} + a_{66})\psi_{,xxyy} + a_{11}\psi_{,yyyy} = w_{,xy}^2 - w_{,xx}w_{,yy} \qquad (9)$$

where

$$[a] = [A]^{-1}$$

By substituting eqn. (3) into the right-hand side of (9), it is seen that the general solution for ψ has the form

$$\psi(x,y) = \psi_c(x,y) + \psi_1(y) + \psi_2(y)\cos\frac{2\pi x}{\lambda} + \psi_3(y)\sin\frac{2\pi x}{\lambda} \qquad (10)$$

where $\psi_c(x,y)$ represents the complementary solution, and the remaining three terms are particular integrals.

The particular solutions are obtained by substituting eqn. (11) into (10) and equating coefficients of like terms in x. The result is an ordinary differential equation for each of ψ_1, ψ_2, and ψ_3, which may be readily solved. The terms in the complementary solution which are necessary to satisfy the in-plane boundary conditions may also be readily obtained. The results may be expressed as

$$\psi_c(x,y) = Qy^2 + \frac{1}{2}\bar{N}_y x^2 - \bar{N}_{xy}xy$$

$$\psi_1''(y) = \frac{\pi^2}{8\lambda^2 a_{11}} \sum_{n=0}^{N}\sum_{m=0}^{N} A_n A_m \left[\cos\frac{(\alpha_n - \alpha_m)y}{b_s} + \cos\frac{(\alpha_n + \alpha_m)y}{b_s}\right]$$

$$+ \frac{\pi^2}{8\lambda^2 a_{11}} \sum_{n=1}^{M}\sum_{m=1}^{M} B_n B_m \left[\cos\frac{(\beta_n - \beta_m)y}{b_s} + \cos\frac{(\beta_n + \beta_m)y}{b_s}\right]$$

$$\psi_2(y) = \frac{\pi^2}{4\lambda^2 b_s^2} \sum_{n=0}^{N}\sum_{m=0}^{N} A_n A_m \left[\gamma_{nm}\cos\frac{(\alpha_n - \alpha_m)y}{b_s} + \delta_{nm}\cos\frac{(\alpha_n + \alpha_m)y}{b_s}\right] \qquad (11)$$

$$+ \frac{\pi^2}{4\lambda^2 b_s^2} \sum_{n=1}^{M}\sum_{m=1}^{M} B_n B_m \left[\xi_{nm}\cos\frac{(\alpha_n - \alpha_m)y}{b_s} + \eta_{nm}\cos\frac{(\alpha_n + \alpha_m)y}{b_s}\right]$$

$$+ \bar{C}_{21}F_1(y) + \bar{C}_{22}F_2(y) + \bar{C}_{23}F_3(y) + \bar{C}_{24}F_4(y)$$

596

$$\psi_3(y) = \frac{\pi^2}{4\lambda^2 b_s^2} \sum_{n=0}^{N} \sum_{m=1}^{M} A_n B_m \left[\phi_{nm} \sin \frac{(\alpha_n - \beta_m)y}{b_s} + \zeta_{nm} \sin \frac{(\alpha_n + \beta_m)y}{b_s} \right]$$

$$+ \bar{C}_{31} F_1(y) + \bar{C}_{32} F_2(y) + \bar{C}_{33} F_3(y) + \bar{C}_{34} F_4(y)$$

In the above expressions, the coefficients γ_{nm}, δ_{nm}, ξ_{nm}, η_{nm}, ϕ_{nm}, and ζ_{nm} represent known quantities involving the a_{ij}, α_n, β_n, and λ. Similarly, the form of the $F_i(y)$, $i = 1,4$ depend on the a_{ij}. All of these quantities are detailed in Appendix A. Because of their dependence on the a_{ij}, these quantities will assume different values in the center ($|y| < b_o$) and edge ($b_o < |y| < b_s$) regions of the plate. The integration constants Q, $\bar{N}_y$, $\bar{N}_{xy}$, $\bar{C}_{2i}$, and $\bar{C}_{3i}$ must be determined from the in-plane boundary conditions.

In-plane Boundary Conditions

With the Airy stress function ψ determined to within the constants defined in the previous section, the in-plane stress resultants and displacements may be determined to within these same parameters. Equations (8) are used to directly obtain the stress resultants, and the displacements are obtained from integration of equations (1). Because the in-plane compatibility equation (9) has been explicitly satisfied, we are assured that (1) has a solution for u and v.

Because the plate under consideration forms a portion of a panel between stiffeners (Figure 1), the boundary conditions applied to this plate are taken in the form of edge displacements. That is, all plate edges are required to remain straight under the action of the applied in-plane loading, and undergo displacements characteristic of biaxial normal and shear deformation (Figure 2). Consistent with the definitions in Figure 2, the following boundary conditions are imposed:

$$u(x+2\lambda,y) - u(x,y) = 2\lambda\varepsilon_1$$

$$v(x,b_s) = -v(x,-b_s) = b_s\varepsilon_2$$

$$u(x,b_s) = b_s\gamma_{12} + \varepsilon_1 x \qquad u(x,-b_s) = b_s\gamma_{12} - \varepsilon_1 x$$

$$v(x+2\lambda,y) - v(x,y) = 0$$

(12)

In addition, continuity of displacements u, v and force resultants N_y and N_{xy} at the interfaces $y = \pm b_o$ between the edge and center regions of the plate must be enforced.

The above boundary and interface conditions provide enough information to determine all of the integration constants in the solution (11) for the Airy stress function ψ, in terms of the applied deformation parameters ε_1, ε_2, and γ_{12}, and the normal displacement coefficients A_n and B_n. The form of these results is given in Appendix B. It is not difficult to show, with the aid of equations (8), (10), and (11) that the constants $\bar{N}_y$ and $\bar{N}_{xy}$ have the physical interpretation of the average normal and shear stress resultants, respectively, applied to the edge

$y = \pm b_s$. In addition, the average normal stress resultant applied to the ends of the plate, $\overline{N}_x$, may also be obtained from quantities introduced previously, and is recorded in Appendix B.

Total Potential

In the preceding sections, all quantities related to the response of the plate under the specified deformation conditions were obtained in terms of the normal displacement amplitudes A_n and B_n. To determine the amplitudes, the total potential of the plate is minimized with respect to these parameters.

The total potential of the plate consists of the strain energy and the potential of the specified external loads.

$$\Pi = U + V \tag{13}$$

The strain energy can be broken down into membrane energy, bending energy, and the energy stored in the torsional springs along the edges.

$$U = U_b + U_m + U_s \tag{14}$$

The bending energy may be written down in terms of the normal displacement,

$$U_b = \frac{1}{2}\int_0^{2\lambda}\int_0^{b_s}\left[D_{11}w^2_{,xx} + D_{22}w^2_{,yy} + D_{66}w^2_{,xy} + 2D_{12}w_{,xx,yy}\right.$$

$$\left. + 4D_{16}w_{,xx}w_{,xy} + 4D_{26}w_{,yy}w_{,xy}\right]dy\ dx \tag{15}$$

In eqn. (15), and in all subsequent energy expressions, integrals are taken over one full wavelength in the x-direction due to periodicity, and over half the width due to symmetry. The membrane energy is expressible in terms of the Airy stress function,

$$U_m = \frac{1}{2}\int_0^{2\lambda}\int_0^{b_s}\left[a_{22}\psi^2_{,xx} + a_{11}\psi^2_{,yy} + 2a_{12}\psi_{,xx}\psi_{,yy} + a_{66}\psi^2_{,xy}\right]dy\ dx \tag{16}$$

The strain energy stored in the spring may be expressed in terms of the normal displacement, using eqn. (6):

$$U_s = \frac{1}{2}\int_0^{2\lambda}M_y w_{,y}\bigg|_{y=b_s} = -\frac{1}{2}D^*_{22}\int_0^{2\lambda}w_{,yy}w_{,y}\bigg|_{y=b_s}dx \tag{17}$$

For convenience of problem solution and ease of integration with the POSTOP code, the independent variables to be specified describing the in-plane loading on the plate are chosen to be the longitudinal edge-

shortening parameter, ε_1, and the average stress resultants on the longitudinal edges, $\bar{N}_y$ and $\bar{N}_{xy}$. The associated parameters ε_2, γ_{12}, and $\bar{N}_x$ may be determined via the relations of Appendix B in terms of the amplitude coefficients, A_n and B_n. The potential of the applied stress resultants on these two edges may be expressed as

$$V = -\lambda b_s\left[\bar{N}_y\varepsilon_2 + \bar{N}_{xy}\gamma_{12}\right] \tag{18}$$

Equation (3) w is substituted into eqns. (15) and (17); the result for ψ is used in (16); and the expressions for ε_2 and γ_{12} are entered into (18). The integrals indicated in eqns. (15-17) may be evaluated in closed form. When the results of (15)-(18) are incorporated into the expression for the total potential, the latter may be written in the form

$$
\Pi = \sum_{i=0}^{N}\sum_{j=0}^{N}\sum_{k=0}^{N}\sum_{l=0}^{N}A_iA_jA_kA_l[A4]_{ijkl} + \sum_{i=1}^{M}\sum_{j=1}^{M}\sum_{k=1}^{M}\sum_{l=1}^{M}B_iB_jB_kB_l[B4]_{ijkl}
$$

$$
+ \sum_{i=0}^{N}\sum_{j=0}^{N}\sum_{k=1}^{M}\sum_{l=1}^{M}A_iA_jB_kB_l[A2B2]_{ijkl} + \sum_{i=0}^{N}\sum_{j=0}^{N}A_iA_j\left[\varepsilon_1[EA]_{ij}\right.
$$

$$
\left. + \bar{N}_y[NA]_{ij} + [A2]_{ij}\right] + \sum_{i=1}^{M}\sum_{j=1}^{M}B_iB_j\left[\varepsilon_1[EB]_{ij} + \bar{N}_y[NB]_{ij} + [B2]_{ij}\right] \tag{19}
$$

$$
+ \sum_{n=0}^{N}\sum_{m=1}^{M}A_iB_j\left[\bar{N}_{xy}[NAB]_{ij} + [AB]_{ij}\right]
$$

$$
+ \varepsilon_1^2[E2] + \bar{N}_y^2[N2] + \varepsilon_1\bar{N}_y[EN] + \bar{N}_{xy}^2[NS]
$$

In the above equation, all quantities in [ ] are expressible in terms of quantities previously introduced.

SOLUTION PROCEDURE

Equation (19) expresses the total potential of the plate in terms of the amplitude coefficients of the normal displacements as explicit unknowns. The solution to the postbuckling problem requires determination of the A_n and B_n such that Π is a minimum. There are two alternative approaches for obtaining this solution. One is to set the derivatives of Π with respect to each of the unknowns to zero; because the total potential is a quartic function of the coefficients, the resulting set of (N + M − 1) algebraic equations is nonlinear.

An alternative approach is to adopt a numerical direct search method to determine the minimum value of Π. In part because the postbuckling

analysis is to be embedded in a numerical optimization routine for the sizing of the stiffened panel, it was decided to use the same optimization code for numerically determining the unconstrained minimum of the total potential for the solution of the postbuckling problem. The Automated Design Synthesis (ADS) system [10] was selected to perform this dual function. ADS is a comprehensive set of numerical optimization algorithms, capable of handling both equality and inequality constraints.

The following procedure was adopted to determine the solution to the postbuckling problem for a specified set of loading parameters ε_1, N_y, N_{xy}:

1. The initial buckling problem, corresponding to load parameters in the same ratio as the actual applied loads, is solved. The critical load condition is obtained by solving the linear eigenvalue problem which results from omitting the fourth degree terms in equation (19). Note that the half-wavelength λ appears implicitly in the expression for the total potential, and there must be an integral number of half-waves over the length of the plate. Therefore, the eigenvalue problem may have to be solved for several values of λ before the lowest eigenvalue is found.

2. The total potential, equation (19), is minimized numerically via ADS, using the same value of λ as was obtained in step 1. The initial value for the normal displacement components is chosen as a multiple of the eigenvector obtained from the initial buckling solution. The solution is comprised of the values of A_n and B_n which minimize Π for the specified value of λ.

3. The load/displacement parameters N_x, ε_2, and γ_{12} corresponding to the solution obtained in step 2 are determined from eqns. (B1), (B2), and (B5).

4. Because the number of half-waves may increase from the number at initial buckling as one goes further into the postbuckling regime, the procedure returns to step 2, using the next lower admissible value of λ. The process continues until the external load resultant reaches a minimum for a given value of the in-plane displacement.

It should be pointed out that, for a plate free of imperfections, the value of λ chosen would be that for which the total potential has its smallest value. It is found that this results in a "ratcheting" appearance to the postbuckled load-displacement response. Choosing the wavelength which results in the smallest load for a given deformation in effect provides an envelope to this ratcheted curve from below, and therefore provides a more realistic response considering initial plate imperfections and load eccentricities.

Once the normal displacement amplitude coefficients have been determined by the above procedure, displacements and stress and moment resultants may be otained throughout the plate through the use of equations presented in preceding sections.

600

To verify the validity and to establish the limitations of the analysis approach outlined above, comparisons of results with existing analytical solutions were made. An in-house Lockheed code enables the determination of the initial buckling load for simply supported plates with discrete thickness discontinuities along the edges. Additional comparisons were made with classical solutions for the initial buckling of isotropic plates under combined loading, and with both clamped and simply supported edges.

For cases in which the shear loading is zero, and for which the bending-torsional coupling terms are small, excellent agreement (within 1%) in the initial buckling load was obtained. On the other hand, for pure shear loading, and a plate aspect ratio $(a/2b_s)$ near 1.0, the critical load predicted by the present analysis is up to 40% too low. This is because the skew-symmetric terms in the expansion for the normal displacement (corresponding to the B_n) do not satisfy the zero dispacement boundary conditions at the ends $x = 0,a$. The result is that the model is more flexible than the actual case of simple end supports. When the dominant loading is shear, the skew-symmetric terms become important; when the aspect ratio is small, the effects of the boundary conditions at the ends become important. For cases of combined loading in which the normal and shear loads are comparable in magnitude and/or when the plate aspect ratio is 2.5 or greater, agreement within 5% was obtained in all cases investigated. It is expected that similar results would be obtained for the postbuckling response.

As a check of the validity of the postbuckling analysis, and to examine the effects of the rotational restraint, the case of an isotropic plate with aspect ratio 4.0 subjected to uniaxial compressive load was investigated. A non-dimensional plot of the load vs. compression is shown in Figure 3, where N_{cr} and ε_{cr} are the load and axial compression, respectively, for the simply supported case at initial buckling. The figure shows the increase in both buckling load and postbuckling stiffness due to the increasing rotational restraint coefficient, K_R. The results compare well with those given in [8]. The postbuckling stiffness shown in Figure 3 is somewhat higher than that of [8] as expected, due to a difference in boundary conditions in the two formulations. In [8], the longitudinal edges were unloaded; in the present analysis, these edges are constrained to remain straight, resulting in increased stiffness in the postbuckling range.

Figure 4 shows the normal displacement profile across the width of the plate at the crest of a buckle for the simply supported case of Figure 3 at several points in the postbuckled region. The characteristic flattening of the buckles as one proceeds into the postbuckled regime is demonstrated by these results. It is this flattening effect which led Koiter [3] to the formulation which was used in the original version of POSTOP [1].

The stiffening effect of attached stiffener flanges is demonstrated in Figure 5 for a simply supported 24-ply graphite-epoxy plate under uniaxial compression. The attached flanges are 12 plies each, with vary-

ing widths. In this case N_{cr} and ε_{cr} represent the critical condition for the plate with no attached flanges. It is felt that, by including the flanges as part of the plate in the analysis of stiffened panels, the effect of these flanges, as well as any pad-ups under the flanges, is more accurately represented.

Finally, Figure 6 shows the longitudinal response of a uniform plate under combined longitudinal and shear loading. It demonstrates that, while the presence of shear has a marked destabilizing effect on initial buckling, the postbuckled longitudinal stiffness increases slightly for increasing shear loading, due to the buckles being increasingly skewed to the plate axes.

In the above cases, as well as additional cases which have been run, the maximum number of terms required for satisfactory convergence of the normal displacement was 11 (N=5, M=5). Note that, since A_0 and B_1 are dependent variables by eqn. (5), this corresponds to 9 independent variables to be determined. In general, the number of terms required for convergence increased as the loading progressed further into the postbuckled regime.

CONCLUSIONS

An efficient and effective approach has been developed for the analysis of laminated plates loaded into the postbuckled regime. Because the computational resources required are minimal, the approach is suitable for embedding in an optimization code for the analysis and sizing of stiffened composite panels. Features of the analysis include the ability to consider the effect of rotational restraints at the plate edges; the inclusion of discrete thickness discontinuities along the longitudinal edges to model the effects of edge pad-ups or attached stiffener flanges; and the ability to handle cases of combined normal and shear loading.

The analysis approach described herein is currently being integrated with POSTOP [1,2], a preliminary design tool for the analysis and sizing of stiffened composite panels.

REFERENCES

1. Dickson, J. N.; and Biggers, S. B.: POSTOP: Postbuckled Open-Stiffener Optimum Panels - Theory and Capability. NASA CR-172259, January 1984.

2. Biggers, S. B.; and Dickson, J. N.: POSTOP: Postbuckled Open-Stiffener Optimum Panels - Users Manual. NASA CR-172260, January 1984.

3. Koiter, W. T.: Het Schuifplooiveld by Grote Overschrydingen van de Knikspanning. National Luchtvaart Laboratorium, Report S295, November 1946 (in Dutch).

4. Feng, M.: An Energy Theory for Postbuckling of Composite Plates Under Combined Loading. Computers and Structures, Vol. 16, No. 1-4, pp. 423-431, 1983.

5. Zhang, Y.; and Matthews, F. L.: Postbuckling Behavior of Anisotropic Laminated Plates Under Pure Shear and Shear Combined with Compressive Loading. AIAA Journal, Vol. 22, No. 2, pp. 281-286, February 1984.

6. Stein, Manuel: Postbuckling of Long Orthotropic Plates in Combined Shear and Compression. AIAA Paper No. 83-0876, presented at the AIAA/ASME/ASCE/AHS 24th Structures, Structural Dynamics, and Materials Conference, Lake Tahoe, NV, May 1983.

7. Kudva, N. J.; and Agarwal, B. L.: Postbuckling Analysis of Stiffened Composite Shear Panels - Theoretical Analysis and Comparison with Experiments. Proceedings, ASME Winter Annual Meeting, pp. 221-229, December 1981.

8. Rhodes, J.; and Harvey, J. M.: The Postbuckling Behaviour of Thin Flat Plates in Compression with the Unloaded Edges Elastically Restrained Against Rotation. Journal of Mechanical Engineering Science, Vol. 13, no. 2, pp. 82-91, 1971.

9. Ashton, J. E.; and Whitney, J. M.: Theory of Laminated Plates. Technomic Publishing Co., Stamford, CT, 1970.

10. Vanderplaats, G. N.: ADS - A Fortran Program for Automated Design Synthesis. Engineering Design Optimization, Inc., Santa Barbara, CA, January 1987.

APPENDIX A

The following quantities were introduced in equations (11). Results are given explicitly for the center region $|y| < b_o$. For the edge region $b_o < |y| < b_s$, replace a_{ij} by a_{ij}^*.

$$\gamma_{nm} = \frac{\alpha_m(\alpha_n + \alpha_m)}{\left(\frac{\alpha_n - \alpha_m}{b_s}\right)^4 a_{11} + \left(\frac{2\pi(\alpha_n - \alpha_m)}{\lambda b_s}\right)^2 (2a_{12} + a_{66}) + \left(\frac{2\pi}{\lambda}\right)^4 a_{22}}$$

$$\delta_{nm} = \frac{-\alpha_m(\alpha_n - \alpha_m)}{\left(\frac{\alpha_n + \alpha_m}{b_s}\right)^4 a_{11} + \left(\frac{2\pi(\alpha_n + \alpha_m)}{\lambda b_s}\right)^2 (2a_{12} + a_{66}) + \left(\frac{2\pi}{\lambda}\right)^4 a_{22}}$$

$$\xi_{nm} = \frac{-\beta_m(\beta_n + \beta_m)}{\left(\frac{\beta_n - \beta_m}{b_s}\right)^4 a_{11} + \left(\frac{2\pi(\beta_n - \beta_m)}{\lambda b_s}\right)^2 (2a_{12} + a_{66}) + \left(\frac{2\pi}{\lambda}\right)^4 a_{22}}$$

(A1)

$$\eta_{nm} = \frac{-\beta_m(\beta_n - \beta_m)}{\left(\frac{\beta_n + \beta_m}{b_s}\right)^4 a_{11} + \left(\frac{2\pi(\beta_n + \beta_m)}{\lambda b_s}\right)^2 (2a_{12} + a_{66}) + \left(\frac{2\pi}{\lambda}\right)^4 a_{22}}$$

$$\phi_{nm} = \frac{(\alpha_n\beta_m + \beta_m^2 + \alpha_n^2)}{\left(\frac{\alpha_n - \beta_m}{b_s}\right)^4 a_{11} + \left(\frac{2\pi(\alpha_n - \beta_m)}{\lambda b_s}\right)^2 (2a_{12} + a_{66}) + \left(\frac{2\pi}{\lambda}\right)^4 a_{22}}$$

$$\zeta_{nm} = \frac{(\alpha_n\beta_m - \beta_m^2 - \alpha_n^2)}{\left(\frac{\alpha_n + \beta_m}{b_s}\right)^4 a_{11} + \left(\frac{2\pi(\alpha_n + \beta_m)}{\lambda b_s}\right)^2 (2a_{12} + a_{66}) + \left(\frac{2\pi}{\lambda}\right)^4 a_{22}}$$

If: Then:

$$\frac{4a_{11}a_{22}}{(2a_{12} + a_{66})^2} < 1$$

$F_1(y) = \cosh c_1 y \qquad F_3(y) = \cosh c_1 y$

$F_2(y) = \sinh c_1 y \qquad F_4(y) = \sinh c_2 y$

where   (A2)

$$c_1, c_2 = \left\{ \left(\frac{2\pi}{\lambda}\right)^2 \frac{1}{2a_{11}}(2a_{12} + a_{66}) \left[1 \pm \sqrt{1 - \frac{4a_{11}a_{22}}{(2a_{12} + a_{66})^2}}\right]\right\}^{1/2}$$

If: Then:

$$\frac{4a_{11}a_{22}}{(2a_{12} + a_{66})^2} < 1$$

$F_1(y) = \cosh k_1 y \cos k_2 y$

$F_2(y) = \cosh k_1 y \sin k_2 y$

$F_3(y) = \sinh k_1 y \sin k_2 y$

$F_4(y) = \sinh k_1 y \cos k_2 y$

where   (A3)

$$k_1, k_2 = \frac{2\pi}{\lambda}\sqrt{\frac{2a_{12} + a_{66}}{2a_{11}}}\left[\frac{\sqrt{a_{11}a_{22}}}{2a_{12} + a_{66}} \pm \frac{1}{2}\right]^{1/2}$$

APPENDIX B

The form of the relations between the constants of integration from the in-plane solution, equation (11), and the applied edge displacement parameters are given below.

$$\bar{N}_y^* = \bar{N}_y \qquad\qquad \bar{N}_{xy}^* = \bar{N}_{xy}$$

$$\frac{1}{b_s}\left[\frac{a_{11}^* a_{22}^* - a_{12}^{*2}}{a_{11}^*}(b_s - b_o) + \frac{a_{11}a_{22} - a_{12}^2}{a_{11}}b_o\right]\overline{N}_y = \varepsilon_2 -$$

(B1)

$$\frac{1}{b_s}\left[\frac{a_{12}^*}{a_{11}^*}(b_s - b_o) + \frac{a_{12}}{a_{11}}b_o\right]\varepsilon_1 + \sum_{n=0}^{N}\sum_{m=0}^{N}A_n A_m[YA]_{nm} + \sum_{n=1}^{M}\sum_{m=1}^{M}B_n B_m[YB]_{nm}$$

$$\frac{1}{b_s}\left[a_{66}^*(b_s - b_o) + a_{66}b_o\right]\overline{N}_{xy} = \gamma_{12} + \sum_{n=0}^{N}\sum_{m=1}^{M}A_n B_m[XY]_{nm} \qquad (B2)$$

$$Q = \frac{1}{a_{11}}\varepsilon_1 - \frac{a_{12}}{a_{11}}\overline{N}_y \qquad\qquad Q^* = \frac{1}{a_{11}^*}\varepsilon_1 - \frac{a_{12}^*}{a_{11}^*}\overline{N}_y \qquad (B3)$$

$$\overline{C}_{22} = \overline{C}_{24} = \overline{C}_{31} = \overline{C}_{33} = 0$$

Let $\qquad \overline{C}_{21}^* = C_{21} \qquad\qquad \overline{C}_{22}^* = C_{22} \qquad\qquad \overline{C}_{23}^* = C_{23}$

$\qquad\qquad \overline{C}_{24}^* = C_{24} \qquad\qquad \overline{C}_{21} = C_{25} \qquad\qquad \overline{C}_{23} = C_{26}$

$\qquad\qquad \overline{C}_{31}^* = C_{31} \qquad\qquad \overline{C}_{32}^* = C_{32} \qquad\qquad \overline{C}_{33}^* = C_{33}$

$\qquad\qquad \overline{C}_{34}^* = C_{34} \qquad\qquad \overline{C}_{32} = C_{35} \qquad\qquad \overline{C}_{34} = C_{36}$

Then $\qquad C_{2i} = \sum_{n=0}^{N}\sum_{m=0}^{N}A_n A_m[CA]_{nmi} + \sum_{n=1}^{M}\sum_{m=1}^{M}B_n B_m[CB]_{nmi} \qquad i=1,6$

(B4)

$$C_{3i} = \sum_{n=0}^{N}\sum_{m=1}^{M}A_n B_m[C3]_{nmi} \qquad\qquad i=1,6$$

$$\overline{N}_x = \left[\frac{b_s - b_o}{b_s a_{11}^*} + \frac{b_o}{b_s a_{11}}\right]\varepsilon_1 - \left[\frac{(b_s - b_o)a_{12}^*}{b_s a_{11}^*} + \frac{b_o a_{12}}{b_s a_{11}}\right]\overline{N}_y$$

(B5)

$$+ \sum_{n=0}^{N}\sum_{m=0}^{N}A_n A_m[XA]_{nm} + \sum_{n=1}^{M}\sum_{m=1}^{M}B_n B_m[XB]_{nm} + \sum_{i=1}^{6}C_{2i}[XC]_i$$

In the above equations, the coefficients in [ ] are all known in terms of quantities previously introduced. Because of the length of the expressions involved, they are not recorded here.
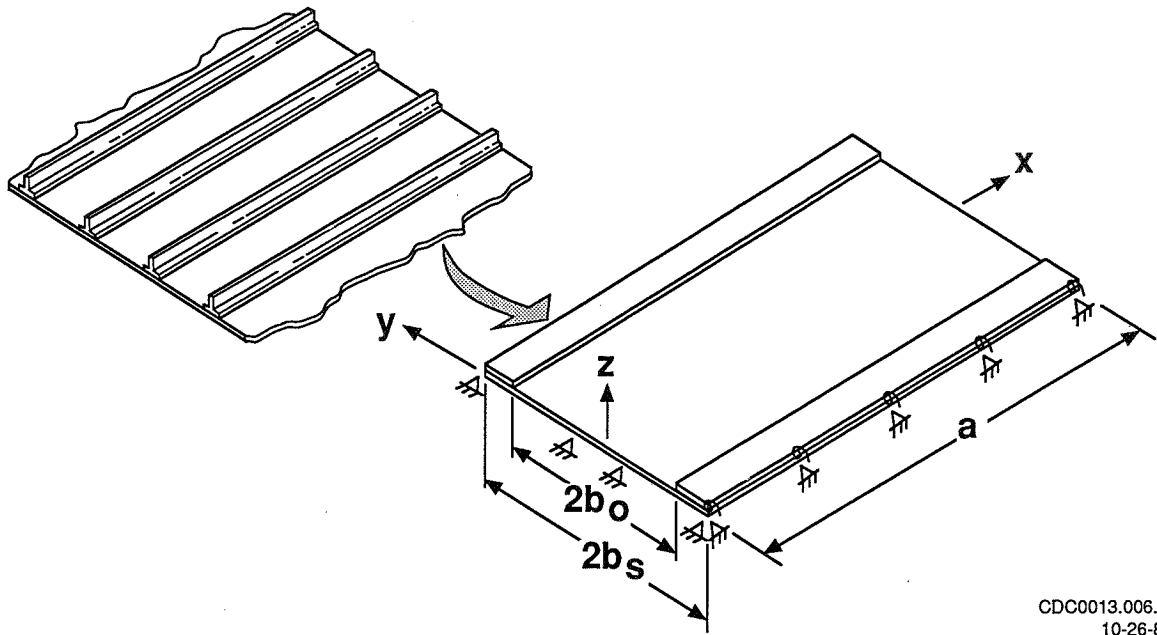
Figure 1. Geometric Configuration
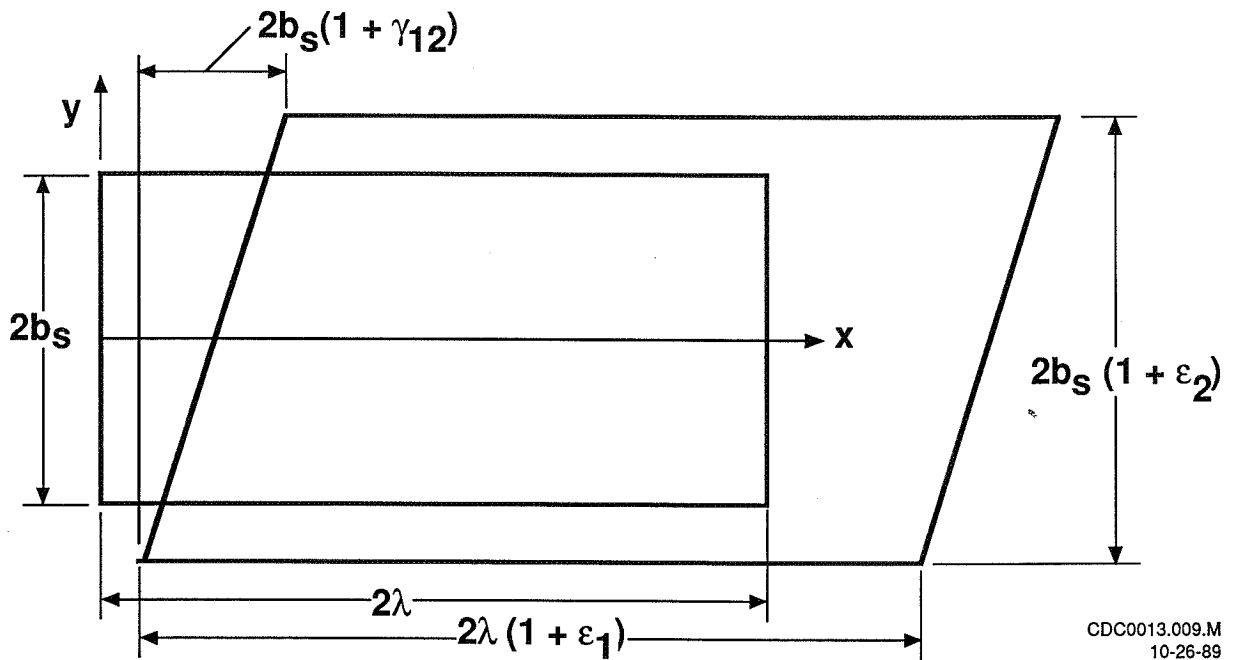
Figure 2. Definition Of In-plane Displacement Boundary Conditions
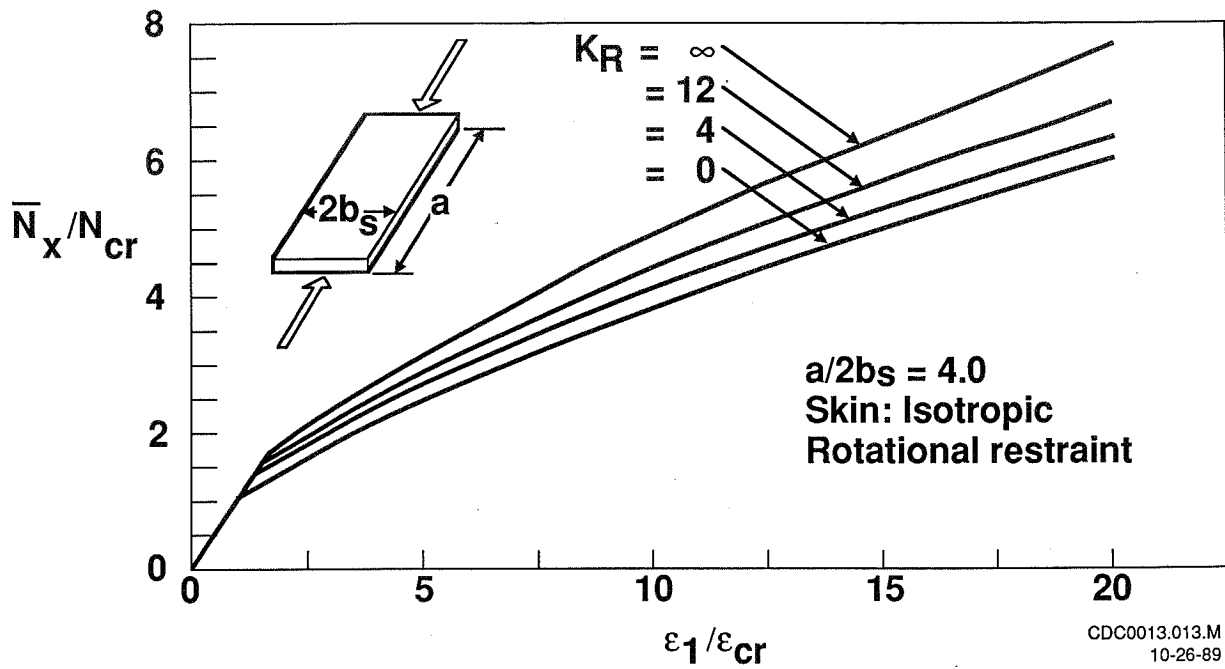
Figure 3. Effect of Rotational Edge Restraint
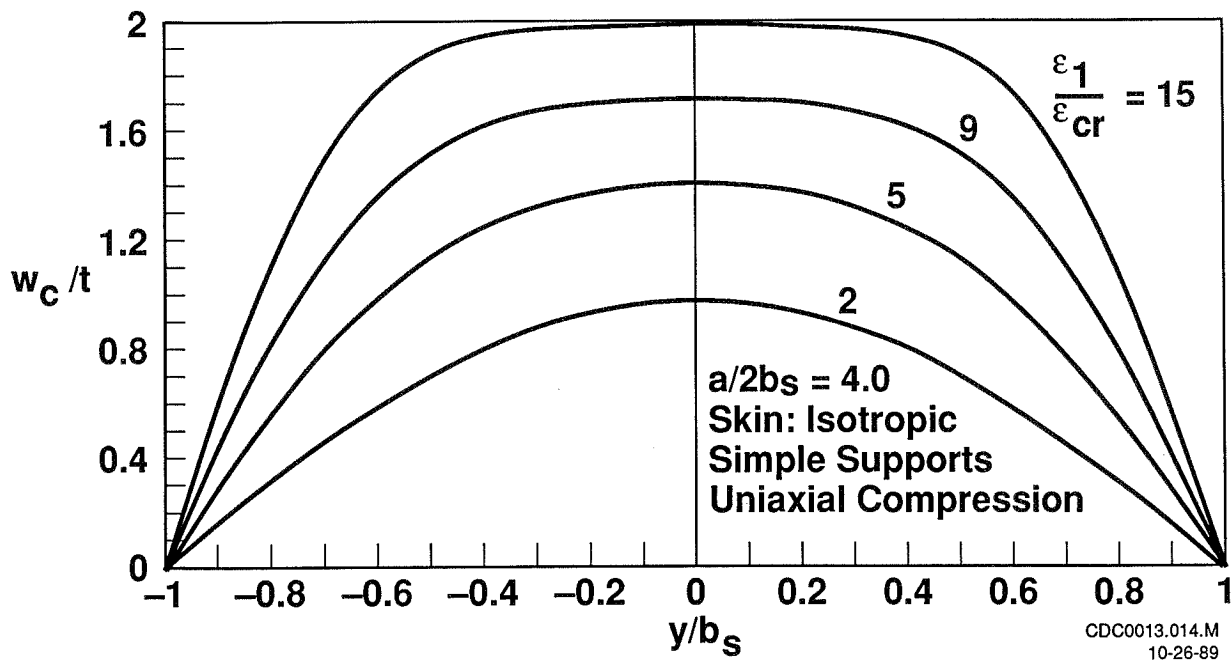
Figure 4. Normal Displacement Profiles
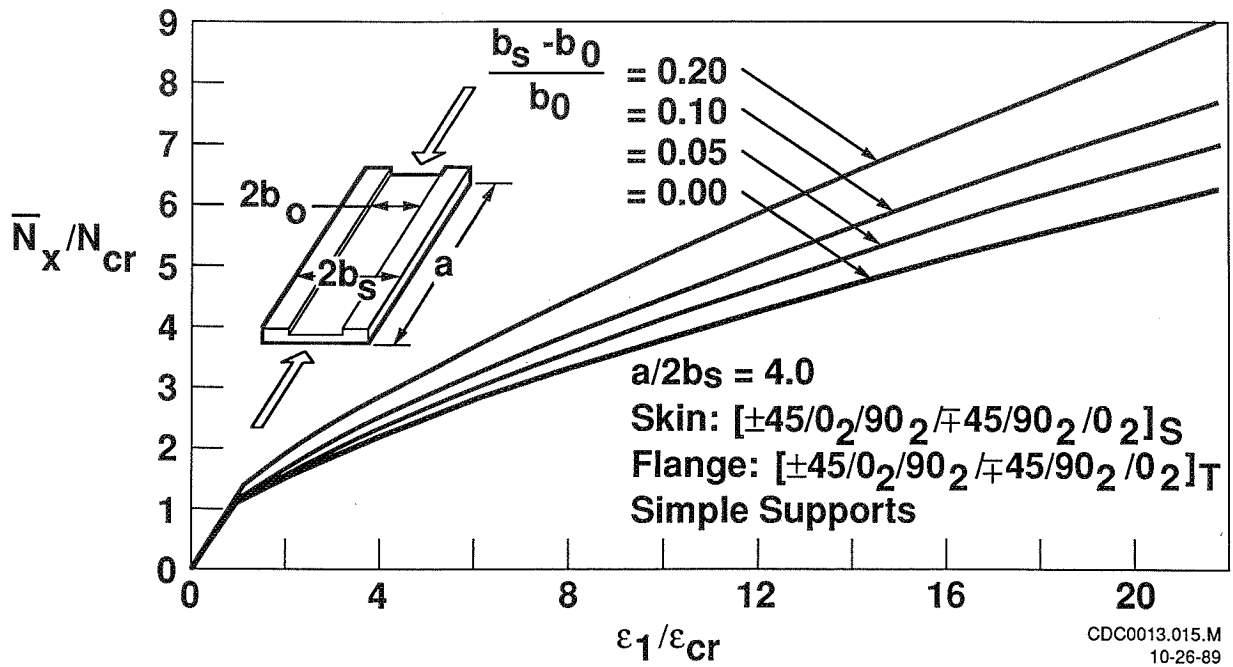
Figure 5. Effect of Attached Stiffener Flanges
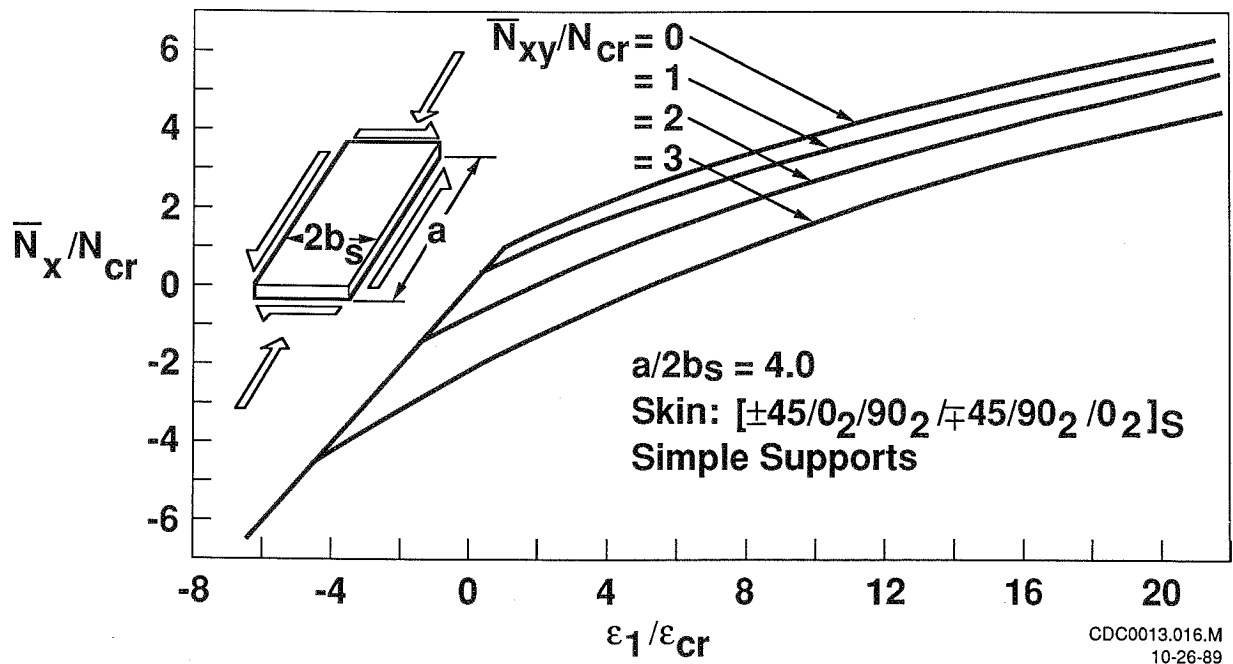
Figure 6. Effect of Shear Loading

Initial Postbuckling Response of an Unsymmetrically Laminated Rectangular Plate

Raphael T. Haftka and Eric R. Johnson

Virginia Polytechnic Institute and State University

ABSTRACT

It has been shown that anisotropic plates can have unstable postbuckling behavior resulting in potential imperfection sensitivity. The present paper quantifies the degree of instability for rectangular simply supported cross-ply laminated plates. The analysis is based on asymptotic Koiter-type expansion of postbuckling response. The degree of postbuckling instability is quantified in terms of the reduction in load carrying capacity in the immediate postbuckling range. For graphite-epoxy plates it is found that this measure of instability is very small. Only a low aspect ratio plate with a high degree of anisotropy can have any significant reduction in its buckling load.

INTRODUCTION

There has been recent interest in the postbuckling behavior of anisotropic plates, both analytically and experimentally (e.g. Jeffrey, 1987, Jensen and Lagace, 1988, Hui and Du, 1987, Cohen and Haftka, 1989). Hui (1986) has shown that unlike orthotropic plates, anisotropic plates can have unstable postbuckling behavior resulting in imperfection sensitivity. However, the severity of the postbuckling instability which depends on the ratio of the cubic and quartic terms in the energy expression has not been quantified. The objective of the present paper is to investigate the severity of the instability for cross-ply laminated plates.

The paper first shows that it is possible to obtain a membrane prebuckling state for a general anisotropic plate by adjusting the loading on the plate. The postbuckling analysis associated with this membrane prebuckling state is greatly simplified as compared to the more general case.

Next the asymptotic postbuckling behavior of a rectangular simply supported anisotropic plate is analyzed, and results are obtained for cross-ply graphite-epoxy plates. The severity of the postbuckling instability is presented in terms of the maximum reduction in the load in the postbuckling regime.

ANALYSIS

General Formulation

The static buckling and initial postbuckling theory of elastic structures, whose prebuckling equilibrium state is governed by linear theory was presented by Budiansky (1966) and extended by Cohen (1968) to the case of nonlinear prebuckling. In the following we specialize Budiansky's and Cohen's formulation to generally laminated plates.

The generalized field variables for the theory are the displacement vector u (with components u, v, w), the generalized strain tensor ϵ, and the generalized stress tensor σ. For a flat plate, the field variables are defined on a reference plane S enclosed by an edge curve C. Cartesian coordinates x and y lie in the reference plane S, while coordinate z is normal to S. Hence for plates governed by Kirchhoff-Love theory

$$\mathbf{u} = [u(x,y), v(x,y), w(x,y)]^T \tag{1}$$

$$\epsilon = [\mathbf{e}^T, \mathbf{k}^T]^T = [\epsilon_x, \epsilon_y, \gamma_{xy}, k_x, k_y, k_{xy}]^T \tag{2}$$

$$\sigma = [\mathbf{N}^T, \mathbf{M}^T]^T = [N_x, N_y, N_{xy}, M_x, M_y, M_{xy}]^T \tag{3}$$

in which superscript T denotes the transpose; $\epsilon_x, \epsilon_y,$ and γ_{xy} are the components of the membrane strain vector $\mathbf{e}$; k_x, k_y, k_{xy} are the components of the curvature vector $\mathbf{k}$ of the deformed reference plane; N_x, N_y and N_{xy} are the components of the membrane stress resultant tensor $\mathbf{N}$, and M_x, M_y and M_{xy} are the components of the bending moment tensor $\mathbf{M}$.

The strain displacement relations are written in the general form

$$\epsilon = L_1(\mathbf{u}) + \frac{1}{2}L_2(\mathbf{u}) \tag{4}$$

where L_1 and L_2 are linear and quadratic functionals, respectively. For the plate problem equation (4) can be written separately for the membrane and bending components. For the membrane strains

$$\mathbf{e} = \left\{ \begin{array}{c} \epsilon_x \\ \epsilon_y \\ \gamma_{xy} \end{array} \right\} = \left\{ \begin{array}{c} u_{,x} \\ v_{,y} \\ u_{,y} + v_{,x} \end{array} \right\} + \frac{1}{2} \left\{ \begin{array}{c} w_{,x}^2 \\ w_{,y}^2 \\ 2w_{,x}w_{,y} \end{array} \right\} \tag{5}$$

which can be written as

$$\mathbf{e} = \mathbf{E}\,\mathbf{u} + \frac{1}{2}\mathbf{F}_2(w) \tag{6}$$

where $\mathbf{E}$ is the matrix linear operator defined as

$$\mathbf{E}(\ ) = \begin{bmatrix} (\ )_{,x} & 0 & 0 \\ 0 & (\ )_{,y} & 0 \\ (\ )_{,y} & (\ )_{,x} & 0 \end{bmatrix} \tag{7}$$

and the quadratic functional $\mathbf{F}_2(w)$ is the second term in Equation (5). Similarly, for the bending strains

$$\left\{ \begin{array}{c} k_x \\ k_y \\ k_{xy} \end{array} \right\} = \mathbf{k} = \mathbf{G}w = \left\{ \begin{array}{c} -w_{,xx} \\ -w_{,yy} \\ -2w_{,xy} \end{array} \right\} \tag{8}$$

so that altogether

$$L_1(\mathbf{u}) = \left\{ \begin{array}{c} \mathbf{E}\mathbf{u} \\ \mathbf{G}w \end{array} \right\} \qquad L_2(\mathbf{u}) = \left\{ \begin{array}{c} \mathbf{F}_2(w) \\ 0 \end{array} \right\} \tag{9}$$

The generalized Hooke's Law is

$$\sigma = \mathbf{H}\,\epsilon \tag{10}$$

where the elastic stiffness matrix $\mathbf{H}$ is obtained from classical lamination theory in terms of the matrices $\mathbf{A}, \mathbf{B},$ and $\mathbf{D}$, that is

$$\mathbf{N} = \mathbf{A}\,\mathbf{e} + \mathbf{B}\,\mathbf{k} \tag{11}$$

$$\mathbf{M} = \mathbf{B}\,\mathbf{e} + \mathbf{D}\,\mathbf{k} \tag{12}$$

The equilibrium of the structure is written via the principle of virtual work as

$$\sigma \cdot \delta\epsilon = \mathbf{q} \cdot \delta\mathbf{u} \tag{13}$$

in which the dot notation refers to the virtual work of the stresses (or loads) acting through the strains (or displacements) integrated over the structure. In the virtual work principle, the kinematically admissible variations in the displacements, δu, are accompanied by the variations in the strains from Equations (4) by the expression

$$\delta\epsilon = \delta L_1(\mathbf{u}) + \frac{1}{2}\delta L_2(\mathbf{u}) = L_1(\delta\mathbf{u}) + L_{11}(\mathbf{u}, \delta\mathbf{u}) \tag{14}$$

since $\frac{1}{2}\delta L_2(\mathbf{u})$ is a bilinear form in $\mathbf{u}$ and $\delta\mathbf{u}$ (which we call L_{11}). For the plate problem the bilinear functional is given as

$$L_{11}(\mathbf{u}, \delta\mathbf{u}) = [w_{,x}\delta w_{,x}, \ w_{,y}\delta w_{,y}, \ w_{,x}\delta w_{,y} + w_{,y}\delta w_{,x}, \ 0, 0, 0,]^T. \tag{15}$$

Alternatively, we may separate the bending and membrane components of Equation (14) as

$$\delta\mathbf{e} = \delta(\mathbf{E}\,\mathbf{u}) + \frac{1}{2}\delta\mathbf{F}_2(w) = \mathbf{E}\delta\mathbf{u} + \mathbf{F}_{11}(w, \delta w) \tag{16}$$

$$\delta\mathbf{k} = \mathbf{G}\delta w \tag{17}$$

where the bilinear functional $\mathbf{F}_{11}$ is given as

$$\mathbf{F}_{11}(w, \delta w) = [w_{,x}\delta w_{,x}, \ w_{,y}\delta w_{,y}, \ w_{,x}\delta w_{,y} + w_{,y}\delta w_{,x}]^T \tag{18}$$

Altogether the left side of Equation (13) may be written as

$$\sigma \cdot \delta\epsilon = \mathbf{N} \cdot \delta\mathbf{e} + \mathbf{M} \cdot \delta\mathbf{k} = \mathbf{N} \cdot [\mathbf{E}\delta\mathbf{u} + \mathbf{F}_{11}(w, \delta w)] + \mathbf{M} \cdot \mathbf{G}\delta w$$

We assume the plate is subjected to edge loading only, such that the external virtual work term on the right hand side of Equation (13) is

$$\mathbf{q} \cdot \delta\mathbf{u} = \int_C (q_n\delta u_n + q_t\delta u_t + q_z\delta w + M_n\delta w_{,n})ds \tag{19}$$

where subscripts n and t designate components in the normal and tangential directions to the edge curve C, s is the arc length coordinate on C, and M_n is an applied bending moment per unit arc length

Prebuckling State

Let $\mathbf{u}_0, \epsilon_0$ and σ_0 denote the field variables prior to buckling. Assuming proportional loading $\mathbf{q} = \lambda\mathbf{q}_0$, in which λ is a load amplitude parameter and $\mathbf{q}_0$ a fixed load distribution, a linear prebuckling state with $\mathbf{u}_0$ proportional to λ is realized if

$$L_{11}(\mathbf{u}_0, \delta\mathbf{u}) = 0 \tag{20}$$

This condition is satisfied for our plate problem when the out-of-plane displacement w_0 vanishes identically in prebuckling. The equilibrium configuration in prebuckling is then governed by (see Equations (13), (14), (20))

$$\sigma_0 \cdot L_1(\delta\mathbf{u}) = \lambda\mathbf{q}_0 \cdot \delta\mathbf{u} \tag{21}$$

In order not to have an overdetermined system of equations for u and v from Equation (21), we take $M_x = M_y = M_{xy} = 0$. This momentless condition requires from Hooke's Law that

$$\mathbf{B}\, \mathbf{e}_0 = 0 \tag{22}$$

The momentless prebuckling equilibrium state defined by Equation (22) can be achieved for nonzero membrane strain only if $\mathbf{B}$ is singular. The bending-extension coupling matrix is singular for particular choices of the reference plane. To see this, we use the parallel axis theorem from classical lamination theory. If $\mathbf{A}, \mathbf{B},$ and $\mathbf{D}$ denote the reference matrices defined for the z-axis normal to the reference plane, and $\bar{\mathbf{A}}, \bar{\mathbf{B}},$ and $\bar{\mathbf{D}}$ are the matrices defined for a parallel reference plane $\bar{z}$, where $\bar{z} = z + d$, then these matrices are related by

$$\begin{aligned}
\bar{\mathbf{A}} &= \mathbf{A} \\
\bar{\mathbf{B}} &= \mathbf{B} + d\mathbf{A} \\
\bar{\mathbf{D}} &= \mathbf{D} + 2d\mathbf{B} + d^2\mathbf{A}
\end{aligned} \tag{23}$$

We substitute the second equation of (23) into equation (22) to get

$$(\bar{\mathbf{B}} - d\mathbf{A})\mathbf{e}_0 = 0 \tag{24}$$

Thus, the shift d in the position of the reference surface from an arbitrarily selected position ($\bar{z} = 0$) is an eigenvalue of Equation (24). Associated with each of the three eigenvalues for d is an eigenvector of membrane strains. This eigenstrain vector determines a stress resultant eigenvector via Hooke's law. Finally, the virtual work principle (21) is satisfied in prebuckling if the applied loading q_0 is equal to the spatially uniform stress resultant eigenvector.

For the cross-ply laminates considered here the one-six and two-six terms in the $\mathbf{A}, \mathbf{B},$ and $\mathbf{D}$ matrices are zero. Then the eigenproblem of Equation (24) decouples into two eigenproblems. One solution is for $B_{66} = 0$ and a shear loading N_{xy0}, with $N_{y0} = N_{x0} = 0$. The other solution has no shear and represents bi-axial loading.

Buckling Analysis

Following Budiansky and Cohen the field variables are expanded in terms of a scalar buckling-mode amplitude parameter ξ as follows

$$\begin{aligned}
\mathbf{u} &= \lambda \mathbf{u}_0' + \xi \mathbf{u}_1 + \xi^2 \mathbf{u}_2 + \dots \\
\epsilon &= \lambda \epsilon_0' + \xi \epsilon_1 + \xi^2 \epsilon_2 + \dots \\
\sigma &= \lambda \sigma_0' + \xi \sigma_1 + \xi^2 \sigma_2 + \dots
\end{aligned} \tag{25}$$

in which $\mathbf{u}_0' = \dfrac{\partial \mathbf{u}_0}{\partial \lambda} = \dfrac{\mathbf{u}_0}{\lambda}$, etc.,

$$\epsilon_1 = L_1(\mathbf{u}_1), \quad \epsilon_2 = L_1(\mathbf{u}_2) + \frac{1}{2}L_2(\mathbf{u}_1), \dots \tag{26}$$

and

$$\sigma_i = \mathbf{H}\, \epsilon_i, \quad i = 1, 2, \dots \tag{27}$$

612

Equations (25) are substituted into the virtual work equation (13) to obtain an expansion of Equation (13) in terms of ξ. Equations (20) and (21) are used in this expansion process, and in the resulting expression $o(\xi)$ terms govern buckling. The variational statement for the buckling eigenvalue problem is

$$\lambda_{cr}\sigma_0' \cdot L_{11}(\mathbf{u}_1, \delta\mathbf{u}) + \sigma_1 \cdot L_1(\delta\mathbf{u}) = 0 \tag{28}$$

The lowest eigenvalue is the critical load λ_{cr}, and the associated eigenfunction $\mathbf{u}_1$ is the buckling mode. In the plate problem Equation (28) becomes

$$\lambda_{cr}\mathbf{N}_0' \cdot \mathbf{F}_{11}(w_1, \delta w) + \mathbf{N}_1 \cdot \mathbf{E}\delta u + \mathbf{M}_1 \cdot \mathbf{G}\delta w$$
$$= \lambda_{cr}\mathbf{N}_0' \cdot \mathbf{F}_{11}(w_1, \delta w) + (\mathbf{A}\,\mathbf{E}\,\mathbf{u}_1 + \mathbf{B}\,\mathbf{G}w_1) \cdot \mathbf{E}\delta u$$
$$+ (\mathbf{B}\,\mathbf{E}\,\mathbf{u}_1 + \mathbf{D}\,\mathbf{G}w_1) \cdot \mathbf{G}\,\delta w = 0 \tag{29}$$

Two recurring terms in Equation (29) are of the form $\mathbf{E}\,u$ and $\mathbf{G}w$. Recall from Equation (7) and (8) that

$$\mathbf{E}\,u = [u_{,x},\ v_{,y},\ u_{,y} + v_{,x}]^T \text{ and } \mathbf{G}w = -[w_{,xx},\ w_{,yy},\ 2w_{,xy}]^T$$

For the buckling mode we assume

$$\mathbf{u}_1 = \sum_{i=1}^{N} \mathbf{V}^i(x,y)\alpha^i \tag{30}$$

in which the vectors α^i with components $\alpha^{i1}, \alpha^{i2}, \alpha^{i3}$ are the unknown amplitudes and $\mathbf{V}^i$ is a 3x3 diagonal matrix of shape functions, i.e.,

$$\mathbf{V}^i = diag[u^i(x,y), v^i(x,y), w^i(x,y)] \tag{31}$$

Futhermore, we assume that $\mathbf{V}^i$ is kinematically admissible, and the virtual displacements can, therefore, be expressed in the same form as $\mathbf{u}_1$

$$\delta\mathbf{u} = \mathbf{V}^j(x,y)\delta\alpha^j \qquad j = 1, 2, \ldots, N \tag{32}$$

Substituting Equations (30) and (32) into Equation (29) we get $3N$ equations (three equations for each value of j in (32)) for the $3N$ components of $\alpha^i, i = 1, 2, \ldots, N$. These equations may be written as

$$\sum_{j=1}^{N}(\mathbf{K}_{ij} - \lambda_{cr}\mathbf{K}_{Gij})\alpha^j = 0 \qquad i = 1, 2, \ldots, N \tag{33}$$

where $\mathbf{K}_{ij}$ is a 3x3 matrix given by

$$\mathbf{K}_{ij} = (\mathbf{A}\,\mathbf{E}\,\mathbf{V}^j + \mathbf{B}\hat{\mathbf{G}}w^j) \cdot \mathbf{E}\,\mathbf{V}^i + (\mathbf{B}\,\mathbf{E}\,\mathbf{V}^j + \mathbf{D}\hat{\mathbf{G}}w^j) \cdot \hat{\mathbf{G}}w^i \tag{34}$$

where the "dot" operation between matrices is defined as the transpose of the left matrix times the right matrix followed by integration, for example

$$\mathbf{A}\,\mathbf{E}\,\mathbf{V}^j \cdot \mathbf{E}\,\mathbf{V}^i = \int_S (\mathbf{A}\,\mathbf{E}\,\mathbf{V}^j)^T \mathbf{E}\,\mathbf{V}^i dS \tag{35}$$

and $\hat{\mathbf{G}}w$ is a 3x3 matrix with two zero columns and the third column equal to $\mathbf{G}w$. All the components of the 3x3 matrix $\mathbf{K}_{Gij}$ are zero except for the 33 component which is

$$(K_{Gij})_{33} = \lambda_{cr}\mathbf{N}_0' \cdot \mathbf{F}_{11}(w^i, w^j) = \lambda_{cr}[N_{xo}'w_{,x}^i w_{,x}^j + N_{yo}'w_{,y}^i w_{,y}^j + N_{xyo}'(w_{,x}^i w_{,y}^j + w_{,y}^i w_{,x}^j)] \tag{36}$$

Postbuckling analysis

The field variables $u_2, \epsilon_2, \sigma_2$ in Equation (25) are governed by

$$\lambda_{cr}\sigma_0' \cdot L_{11}(u_2, \delta u) + \sigma_2 \cdot L_1(\delta u) + \sigma_1 \cdot L_{11}(u_1, \delta u) + \hat{a}\lambda_{cr}\sigma_0' \cdot L_{11}(u_1, \delta u) \tag{37}$$

where

$$\hat{a} = \frac{1.5\sigma_1 \cdot L_2(u_1)}{\sigma_1 \cdot \epsilon_1} \tag{38}$$

Using Equations (26) and (27) this may be rearranged in the form

$$\lambda_{cr}\sigma_0' \cdot L_{11}(u_2, \delta u) + HL_1(u_2) \cdot L_1(\delta u) =$$
$$-\frac{1}{2}HL_2(u_1) \cdot L_1(\delta u) - HL_1(u_1) \cdot L_{11}(u_1, \delta u)$$
$$-\hat{a}\lambda_{cr}\sigma_0' \cdot L_{11}(u_1, \delta u) \tag{39}$$

which for the plate problem becomes

$$\lambda_{cr}N_0' \cdot F_{11}(w_2, \delta w) + (A\,E\,u_2 + B\,G w_2) \cdot E\delta u + (B\,E\,u_2 + D\,G w_2) \cdot G\delta w$$
$$= -\frac{1}{2}[A\,F_2(w_1) \cdot E\delta u + B\,F_2(w_1) \cdot G\delta w]$$
$$-(A\,E\,u_1 + B\,G w_1) \cdot F_{11}(w_1, \delta w) - \hat{a}\lambda_{cr}N_0' \cdot F_{11}(w_1, \delta w) \tag{40}$$

The relation between the load and the buckling mode amplitude ξ is

$$\frac{\lambda}{\lambda_{cr}} = 1 + \hat{a}\xi + \hat{b}\xi^2 + \dots \tag{41}$$

where $\hat{a}$ is given by Equation (38) and

$$\hat{b} = \frac{2\sigma_1 \cdot L_{11}(u_1, u_2) + \sigma_2 \cdot L_2(u_1)}{\sigma_1 \cdot \epsilon_1} \tag{42}$$

The u_2 field is assumed to be of the same form as the u_1 field plus possible additional terms

$$u_2 = \sum_{l=1}^{N} V^l(x, y)\beta^l + P(x, y)\gamma \tag{43}$$

where P is a matrix of shape functions and γ a vector of amplitudes. The u_2 field is typically also required to satisfy an orthogonality condition of the form

$$\sigma_0 \cdot L_{11}(u_1, u_2) = 0 \tag{44}$$

We consider now the special case where the V^i in Equation (30) can represent the buckling mode with a single term of the expansion, that is the buckling mode is given as

$$u_1 = V^i(x, y)\alpha^i \tag{45}$$

614

for some i. In that case the orthogonality of the buckling modes would result in $\mathbf{K}_{ij}$ and $\mathbf{K}_{Gij}$ being zero for $i \neq j$. The buckling load calculation reduces to solving N 3x3 eigenproblems

$$(\mathbf{K}_{jj} - \lambda_{cr}\mathbf{K}_{Gij})\alpha^j = 0 \qquad j = 1, 2, \ldots, N \tag{46}$$

and choosing the one with the lowest λ_{cr}, here assumed to be the i-th one. Because the homogeneous part of the $\mathbf{u}_2$ equation is identical to that of the $\mathbf{u}_1$ equation, the terms involving β's in Equation (43) decouple into diagonal 3x3 blocks and are coupled only through the γ's. Substituting from Equations (43) and (45) into Equation (40), with the virtual displacements represented by every choice of $\delta\beta^l$ and $\delta\gamma$ in (43), we get

$$(\mathbf{K}_{ll} - \lambda_{cr}\mathbf{K}_{Gll})\beta^l + \mathbf{K}_l^{\beta\gamma}\gamma = \alpha^{i3}\mathbf{R}^l\alpha^i \tag{47}$$

$$(\mathbf{K}_l^{\beta\gamma})^T\beta^l + \mathbf{K}^{\gamma\gamma}\gamma = \alpha^{i3}\mathbf{R}^\gamma\alpha^i \tag{48}$$

where the components of the 3x3 matrix $\mathbf{R}^l$ are given as

$$R_{11}^l = R_{12}^l = R_{21}^l = R_{22}^l = 0$$

$$R_{13}^l = -0.5\mathbf{A}\,\mathbf{F}_2(w^i) \cdot \mathbf{E}\left\{\begin{array}{c} u^l \\ 0 \\ 0 \end{array}\right\}$$

$$R_{23}^l = -0.5\mathbf{A}\,\mathbf{F}_2(w^i) \cdot \mathbf{E}\left\{\begin{array}{c} 0 \\ v^l \\ 0 \end{array}\right\}$$

$$R_{31}^l = -\mathbf{A}\,\mathbf{E}\left\{\begin{array}{c} u^i \\ 0 \\ 0 \end{array}\right\} \cdot \mathbf{F}_{11}(w^i, w^l) \tag{49}$$

$$R_{32}^l = -\mathbf{A}\,\mathbf{E}\left\{\begin{array}{c} 0 \\ v^i \\ 0 \end{array}\right\} \cdot \mathbf{F}_{11}(w^i, w^l)$$

$$R_{33}^l = -0.5\mathbf{B}\,\mathbf{F}_2(w^i) \cdot \mathbf{G}w^l - \mathbf{B}\,\mathbf{G}w^i \cdot \mathbf{F}_{11}(w^i, w^l)$$

and where the terms associated with the γ's are defined later for the specific choice of $\mathbf{P}$.

Simply-supported Rectangular Plate

For the simply supported rectangular plate shown in Figure 1 the buckling mode is in the form

$$\begin{aligned} u_1 &= \alpha^{i1}\cos\bar{r}x\sin\bar{s}y \\ v_1 &= \alpha^{i2}\sin\bar{r}x\cos\bar{s}y \\ w_1 &= \alpha^{i3}\sin\bar{r}x\sin\bar{s}y \end{aligned} \tag{50}$$

where $\bar{r} = r\pi/a$, $\bar{s} = s\pi/b$, and r, s are integers that depend on i. Then

$$\begin{aligned} \mathbf{V}^i &= diag[\cos\bar{r}x\sin\bar{s}y,\ \sin\bar{r}x\cos\bar{s}y,\ \sin\bar{r}x\sin\bar{s}y] \\ &= diag[u^i, v^i, w^i] \end{aligned} \tag{51}$$

We assume that the one-six and two-six terms in the elastic matrices are zero, and then Equation (34) yields the components of $\mathbf{K}_{ii}$ as

$$(K_{ii})_{11} = \int (A_{11}u^{i2}_{,x} + A_{66}u^{i2}_{,y})dS = (A_{11}\bar{r}^2 + A_{66}\bar{s}^2)(ab/4)$$

$$(K_{ii})_{12} = \int (A_{12}u^{i}_{,x}v^{i}_{,y} + A_{66}u^{i}_{,y}v^{i}_{,x})dS = (A_{12} + A_{66})\bar{r}\bar{s}(ab/4)$$

$$(K_{ii})_{13} = \int [-B_{11}u^{i}_{,x}w^{i}_{,xx} - B_{12}u^{i}_{,x}w^{i}_{,yy} - 2B_{66}u^{i}_{,y}w^{i}_{,xy}]dS$$
$$= [-B_{11}\bar{r}^3 - (B_{12} + 2B_{66})\bar{r}\bar{s}^2](ab/4)$$

$$(K_{ii})_{22} = \int (A_{22}v^{i2}_{,y} + A_{66}v^{i2}_{,x})dS = (A_{22}\bar{s}^2 + A_{66}\bar{r}^2)(ab/4) \tag{52}$$

$$(K_{ii})_{23} = \int (-B_{12}v^{i}_{,y}w^{i}_{,xx} - B_{22}v^{i}_{,y}w^{i}_{,yy} - 2B_{66}v^{i}_{,x}w^{i}_{,xy})dS$$
$$= -[B_{22}\bar{s}^3 + (B_{12} + 2B_{66})\bar{r}^2\bar{s}](ab/4)$$

$$(K_{ii})_{33} = \int (D_{11}w^{i2}_{,xx} + 2D_{12}w^{i}_{,xx}w^{i}_{,yy} + D_{22}w^{i2}_{,yy} + 4D_{66}w^{i2}_{,xy})dS$$
$$= [D_{11}\bar{r}^4 + 2(D_{12} + 2D_{66})\bar{r}^2\bar{s}^2 + D_{22}\bar{s}^4](ab/4)$$

For $\mathbf{u}_2$ the $\mathbf{p}$ terms in Equation (43) are selected as the $\mathbf{u}_2$ solution for the isotropic plate (Koiter, 1970) so that

$$u_2 = \sum_{l=1}^{N} \beta^{l1} \cos \bar{p}x \sin \bar{q}y + \gamma_1 x/a + \gamma_2 \sin 2\bar{r}x + \gamma_3 \sin 2\bar{r}x \cos 2\bar{s}y$$

$$v_2 = \sum_{l=1}^{N} \beta^{l2} \sin \bar{p}x \sin \bar{q}y + \gamma_4 y/b + \gamma_5 \sin 2\bar{s}y + \gamma_6 \cos 2\bar{r}x \sin 2\bar{s}y \tag{53}$$

$$w_2 = \sum_{l=1}^{N} \beta^{l3} \sin \bar{p}x \sin \bar{q}y, \quad \text{and } \beta^{l3} = 0 \text{ if } p = r \text{ and } q = s$$

where $\bar{p} = p\pi/a$, $\bar{q} = q\pi/b$ and p and q are integers that depend on l. The coefficient in the expression for w_2 that corresponds to the buckling mode is prescribed to vanish so that the orthogonality condition, Equation (44), is satisfied by the $\mathbf{u}_2$ field. Also, the virtual displacement δw in the governing equilibrium Equation (40) is represented by each shape function of the w_2 expansion, so that the term with $\hat{a}$ as a coefficient in Equation (40) vanishes. Cohen showed that the orthogonality condition (44) assumed by Budiansky is not necessary, but if employed it simplifies the expression for $\hat{b}$ to that given by Budiansky, which is repeated in our Equation (42).

The components of the matrix R^l in Equation (49) are given in terms of three integrals.

$$I_{1x}(r,p) = \int_0^a \cos^2 \bar{r}x \sin \bar{p}x \, dx = \frac{1}{2\bar{p}}(1 - \cos \pi p)$$

$$+ \frac{1}{4(2\bar{r} - \bar{p})}[1 - \cos(2r - p)\pi] + \frac{1}{4(2\bar{r} + \bar{p})}[1 - \cos(2r + p)\pi] \quad (54)$$

if $2r \neq p$ and $I_{1x}(r,p) = 0$ if $2r = p$

$$I_{2x}(r,p) = \int_0^a \sin^2 \bar{r}x \sin \bar{p}x \, dx = \frac{1}{2\bar{p}}(1 - \cos \pi p)$$

$$- \frac{1}{4(2\bar{r} - \bar{p})}[1 - \cos(2r - p)\pi] + \frac{1}{4(2\bar{r} + \bar{p})}[1 - \cos(2r + p)\pi] \quad (55)$$

if $2r \neq p$ and $I_{2x}(r,p) = 0$ if $2r = p$

$$I_{3x}(r,p) = \int_0^a \sin \bar{r}x \cos \bar{r}x \cos \bar{p}x \, dx = \frac{1}{4(2\bar{r} - \bar{p})}[1 - \cos(2r - p)\pi]$$

$$+ \frac{1}{4(2\bar{r} + \bar{p})}[1 - \cos(2r + p)\pi] \quad (56)$$

if $2r \neq p$ and $I_{3x}(r,p) = 0$ if $2r = p$ with similar definition for integrals in the y direction. For example

$$I_{1y}(s,q) = \int_0^b \cos^2 \bar{s}y \sin \bar{q}y \, dy \quad (57)$$

Using these integrals we can write the components of $\mathbf{R}^l$ in Equation (47) as

$$R_{13}^l = -\int [0.5(A_{11}w_{,x}^{i^2} + A_{12}w_{,y}^{i^2})u_{,x}^l + A_{66}w_{,x}^i w_{,y}^i u_{,y}^l]dS$$

$$= 0.5A_{11}\bar{r}^2\bar{p}I_{1x}(r,p)I_{2y}(s,q) + 0.5A_{12}\bar{s}^2\bar{p}I_{2x}(r,p)I_{1y}(s,q)$$
$$- A_{66}\bar{r}\bar{s}\bar{q}I_{3x}(r,p)I_{3y}(s,q)$$

$$R_{23}^l = -\int [0.5(A_{12}w_{,x}^{i^2} + A_{22}w_{,y}^{i^2})v_{,y}^l + A_{66}w_{,x}^i w_{,y}^i v_{,x}^l]dS$$

$$= 0.5A_{12}\bar{r}^2\bar{q}I_{1x}(r,p)I_{2y}(s,q) + 0.5A_{22}\bar{s}^2\bar{q}I_{2x}(r,p)I_{1y}(s,q)$$
$$- A_{66}\bar{r}\bar{s}\bar{p}I_{3x}(r,p)I_{3y}(s,q)$$

$$R_{31}^l = -\int [A_{11}u_{,x}^i w_{,x}^i w_{,x}^l + A_{12}u_{,x}^i w_{,y}^i w_{,y}^l$$
$$+ A_{66}u_{,y}^i(w_{,x}^i w_{,y}^l + w_{,y}^i w_{,x}^l)]dS$$

$$= A_{11}\bar{r}^2\bar{p}I_{3x}(r,p)I_{2y}(s,q) + A_{12}\bar{r}\bar{s}\bar{q}I_{2x}(r,p)I_{3y}(s,q)$$
$$- A_{66}[\bar{r}\bar{s}\bar{q}I_{1x}(r,p)I_{3y}(s,q) + \bar{s}^2\bar{p}I_{3x}(r,p)I_{1y}(s,q)]$$

$$R_{32}^l = -\int [A_{12}v_{,y}^i w_{,x}^i w_{,x}^l + A_{22}v_{,y}^i w_{,y}^i w_{,y}^l \qquad (58)$$
$$+ A_{66}v_{,x}^i(w_{,x}^i w_{,y}^l + w_{,y}^i w_{,x}^l)]dS$$

$$= A_{12}\bar{r}\bar{s}\bar{p}I_{3x}(r,p)I_{2y}(s,q) + A_{22}\bar{s}^2\bar{q}I_{2x}(r,p)I_{3y}(s,q)$$
$$- A_{66}[\bar{r}^2\bar{q}I_{1x}(r,p)I_{3y}(s,q) + \bar{r}\bar{s}\bar{p}I_{3x}(r,p)I_{1y}(s,q)]$$

$$R_{33}^l = \int \frac{1}{2}[(B_{11}w_{,x}^{i^2} + B_{12}w_{,y}^{i^2})w_{,xx}^l + (B_{12}w_{,x}^{i^2} + B_{22}w_{,y}^{i^2})w_{,yy}^l$$
$$+ 4B_{66}w_{,x}^i w_{,y}^i w_{,xy}^l] + (B_{11}w_{,xx}^i + B_{12}w_{,yy}^i)w_{,x}^i w_{,x}^l + (B_{12}w_{,xx}^i + B_{22}w_{,yy}^i)w_{,y}^i w_{,y}^l$$
$$+ 2B_{66}w_{,xy}^i(w_{,x}^i w_{,y}^l + w_{,y}^i w_{,x}^l)dS$$

$$= -\frac{1}{2}(B_{11}\bar{r}^2\bar{p}^2 + B_{12}\bar{r}^2\bar{q}^2)I_{1x}(r,p)I_{2y}(s,q) - \frac{1}{2}\bar{s}^2(B_{12}\bar{p}^2 + B_{22}\bar{q}^2)I_{2x}(r,p)I_{1y}(n,q)$$
$$+ 2B_{66}\bar{r}\bar{s}\bar{p}\bar{q}I_{3x}(r,p)I_{3y}(s,q)$$
$$- \bar{r}\bar{p}(B_{11}\bar{r}^2 + B_{12}\bar{s}^2)I_{3x}(r,p)I_{2y}(s,q) - \bar{s}\bar{q}(B_{12}\bar{r}^2 + B_{22}\bar{s}^2)I_{2x}(r,p)I_{3y}(s,q)$$
$$+ 2B_{66}\bar{r}\bar{s}[\bar{r}\bar{q}I_{1x}(r,p)I_{3y}(s,q) + \bar{s}\bar{p}I_{3x}(r,p)I_{1y}(s,q)]$$

The elements of the matrices associated with the γ-terms in Equations (47) and (48) are determined by the particular choice of matrix $\mathbf{P}(x,y)$. For $\mathbf{P}(x,y)$ given by Equations (53), the elements of $\mathbf{K}^{\beta\gamma}, \mathbf{K}^{\gamma\gamma}$, and $\mathbf{R}^{\gamma}$ are

$$(K_l^{\beta\gamma})_{11} = -A_{11}(1 - \cos p\pi)(1 - \cos q\pi)/\bar{q}a$$

$$(K_l^{\beta\gamma})_{12} = -A_{11}2\bar{r}\bar{p}[I_{1x}(r,p) - I_{2x}(r,p)](1 - \cos q\pi)/\bar{q}$$

$$(K_l^{\beta\gamma})_{13} = -A_{11}2\bar{r}\bar{p}[I_{1x}(r,p) - I_{2x}(r,p)][I_{1y}(s,q) - I_{2y}(s,q)]$$
$$- 8A_{66}\bar{s}\bar{q}I_{3x}(r,p)I_{3y}(s,q)$$

$$(K_l^{\beta\gamma})_{14} = -A_{12}(1 - \cos p\pi)(1 - \cos q\pi)/\bar{q}b$$

$$(K_l^{\beta\gamma})_{15} = -2A_{12}\bar{s}[I_{1y}(s,q) - I_{2y}(s,q)](1 - \cos p\pi)$$

$$(K_l^{\beta\gamma})_{16} = -2A_{12}\bar{s}\bar{p}[I_{1x}(r,p) - I_{2x}(r,p)][I_{1y}(s,q) - I_{2y}(s,q)]$$
$$- 8A_{66}\bar{r}\bar{q}I_{3x}(r,p)I_{3y}(s,q)$$

$$(K_l^{\beta\gamma})_{21} = -A_{12}(1 - \cos p\pi)(1 - \cos q\pi)/\bar{p}a$$

$$(K_l^{\beta\gamma})_{22} = -2A_{12}\bar{r}[I_{1x}(r,p) - I_{2x}(r,p)](1 - \cos q\pi)$$

$$(K_l^{\beta\gamma})_{23} = -2A_{12}\bar{r}\bar{q}[I_{1x}(r,p) - I_{2x}(r,p)][I_{1y}(s,q) - I_{2y}(s,q)]$$
$$- 8A_{66}\bar{s}\bar{p}I_{3x}(r,p)I_{3y}(s,q)$$

$$(K_l^{\beta\gamma})_{24} = -A_{22}(1 - \cos p\pi)(1 - \cos q\pi)/\bar{p}b \tag{59}$$

$$(K_l^{\beta\gamma})_{25} = -2A_{22}\bar{s}\bar{q}[I_{1y}(s,q) - I_{2y}(s,q)](1 - \cos p\pi)/\bar{p}$$

$$(K_l^{\beta\gamma})_{26} = -2A_{22}\bar{s}\bar{q}[I_{1x}(r,p) - I_{2x}(r,p)][I_{1y}(s,q) - I_{2y}(s,q)]$$
$$- 8A_{66}\bar{r}\bar{p}I_{3x}(r,p)I_{3y}(s,q)$$

$$(K_l^{\beta\gamma})_{31} = \left(B_{11}\frac{\bar{p}}{\bar{q}a} + B_{12}\frac{\bar{q}}{\bar{p}a}\right)(1 - \cos p\pi)(1 - \cos q\pi)$$

$$(K_l^{\beta\gamma})_{32} = 2\bar{r}(B_{11}\bar{p}^2 + B_{12}\bar{q}^2)[I_{1x}(r,p) - I_{2x}(r,p)](1 - \cos q\pi)/\bar{q}$$

$$(K_l^{\beta\gamma})_{33} = 2\bar{r}(B_{11}\bar{p}^2 + B_{12}\bar{q}^2)[I_{1x}(r,p) - I_{2x}(r,p)][I_{1y}(s,q) - I_{2y}(s,q)]$$
$$+ 16B_{66}\bar{s}\bar{p}\bar{q}I_{3x}(r,p)I_{3y}(s,q)$$

$$(K_l^{\beta\gamma})_{34} = (B_{12}\bar{p}^2 + B_{22}\bar{q}^2)(1 - \cos p\pi)(1 - \cos q\pi)/(\bar{p}\bar{q}b)$$

$$(K_l^{\beta\gamma})_{35} = 2\bar{s}(B_{12}\bar{p}^2 + B_{22}\bar{q}^2)[I_{1y}(s,q) - I_{2y}(s,q)](1 - \cos p\pi)/\bar{p}$$

$$(K_l^{\beta\gamma})_{36} = 2\bar{s}(B_{12}\bar{p}^2 + B_{22}\bar{q}^2)[I_{1x}(r,p) - I_{2x}(r,p)][I_{1y}(s,q) - I_{2y}(s,q)]$$
$$+ 16B_{66}\bar{r}\bar{p}\bar{q}I_{3x}(r,p)I_{3y}(s,q)$$

$$(K^{\gamma\gamma})_{11} = A_{11}\frac{b}{a}$$

$$(K^{\gamma\gamma})_{12} = (K^{\gamma\gamma})_{13} = 0$$

$$(K^{\gamma\gamma})_{14} = A_{12}$$

$$(K^{\gamma\gamma})_{15} = (K^{\gamma\gamma})_{16} = 0$$

$$(K^{\gamma\gamma})_{22} = 2ab\bar{r}^2 A_{11}$$

$$(K^{\gamma\gamma})_{23} = (K^{\gamma\gamma})_{24} = (K^{\gamma\gamma})_{25} = (K^{\gamma\gamma})_{26} = 0$$

$$(K^{\gamma\gamma})_{33} = (A_{11}\bar{r}^2 + A_{66}\bar{s}^2)ab \qquad (60)$$

$$(K^{\gamma\gamma})_{34} = (K^{\gamma\gamma})_{35} = 0$$

$$(K^{\gamma\gamma})_{36} = (A_{12} + A_{66})\bar{r}\bar{s}ab$$

$$(K^{\gamma\gamma})_{44} = A_{22}\frac{a}{b}$$

$$(K^{\gamma\gamma})_{45} = (K^{\gamma\gamma})_{46} = 0$$

$$(K^{\gamma\gamma})_{55} = 2\bar{s}^2 ab A_{22}$$

$$(K^{\gamma\gamma})_{56} = 0$$

$$(K^{\gamma\gamma})_{66} = (A_{22}\bar{s}^2 + A_{66}\bar{r}^2)ab$$

and

$$R^\gamma_{j1} = R^\gamma_{j2} = 0 \qquad j = 1,\dots,6$$

$$R^\gamma_{13} = -(A_{11}\bar{r}^2 + A_{12}\bar{s}^2)\frac{b}{8}$$

$$R^\gamma_{23} = (-\bar{r}^3 A_{11} + \bar{r}\bar{s}^2 A_{12})\frac{ab}{8}$$

$$R^\gamma_{33} = [A_{11}\bar{r}^3 + (A_{12} + 2A_{66})\bar{r}\bar{s}^2]\frac{ab}{16} \qquad (61)$$

$$R^\gamma_{43} = -(A_{12}\bar{r}^2 + A_{22}\bar{s}^2)\frac{a}{8}$$

$$R^\gamma_{53} = (A_{12}\bar{r}^2\bar{s} - A_{22}\bar{s}^3)\frac{ab}{8}$$

$$R^\gamma_{63} = [A_{22}\bar{s}^3 + (A_{12} + 2A_{66})\bar{r}^2\bar{s}]\frac{ab}{16}$$

The terms appearing in the calculation of the postbuckling coefficients $\hat{a}$ and $\hat{b}$ are given as

$$\sigma_1 \cdot \epsilon_1 = \mathbf{H}L_1(\mathbf{u}_1) \cdot L_1(\mathbf{u}_1) = (\alpha^i)^T \mathbf{K}_{ii}(\alpha^i) \qquad (62)$$

$$\sigma_1 \cdot L_2(\mathbf{u}_1) = \mathbf{H}L_1(\mathbf{u}_1) \cdot L_2(\mathbf{u}_1) = \int [(A_{11}u_{1,x} + A_{12}v_{1,y})w^2_{1,x}$$

$$+ (A_{12}u_{1,x} + A_{22}v_{1,y})w^2_{1,y} + 2A_{66}(u_{1,y} + v_{1,x})w_{1,x}w_{1,y}$$

$$- (B_{11}w_{1,xx} + B_{12}w_{1,yy})w^2_{1,x} - (B_{12}w_{1,xx} + B_{22}w_{1,yy})w^2_{1,y}$$

$$- 4B_{66}w_{1,xy}w_{1,x}w_{1,y}]dS = -\sum_{k=1}^{3} R^i_{3k}(\alpha^{i3})^2\alpha^{ik} \qquad (63)$$

$$2\sigma_1 \cdot L_{11}(\mathbf{u}_1, \mathbf{u}_2) + \sigma_2 \cdot L_2(\mathbf{u}_1) = 2\mathbf{H}L_1(\mathbf{u}_1) \cdot L_{11}(\mathbf{u}_1, \mathbf{u}_2)$$
$$+ \mathbf{H}L_1(\mathbf{u}_2) \cdot L_2(\mathbf{u}_1) + \frac{1}{2}\mathbf{H}L_2(\mathbf{u}_1) \cdot L_2(\mathbf{u}_1) \quad (64)$$

The first two terms can be seen from Equations (39) and (47) to be

$$2\mathbf{H}L_1(\mathbf{u}_1) \cdot L_{11}(\mathbf{u}_1, \mathbf{u}_2) + \mathbf{H}L_1(\mathbf{u}_2) \cdot L_2(\mathbf{u}_2) = -2\sum_{l=1}^{N}\sum_{m=1}^{3}\sum_{n=1}^{3} R_{mn}^{l}\alpha^{in}\alpha^{i3}\beta^{lm} \quad (65)$$

and the last term is

$$\frac{1}{2}\mathbf{H}L_2(\mathbf{u}_1) \cdot L_2(\mathbf{u}_1) = \frac{1}{2}\int[(A_{11}w_{1,x}^2 + A_{12}w_{1,y}^2)w_{1,x}^2 + (A_{12}w_{1,x}^2 + A_{22}w_{1,y}^2)w_{1,y}^2 + 4A_{66}w_{1,x}^2 w_{1,y}^2]dS$$
$$= \frac{ab}{128}[9A_{11}\bar{r}^4 + 8(A_{12} + 2A_{66})\bar{r}^2\bar{s}^2 + 9A_{22}\bar{s}^4] \quad (66)$$

One additional constraint imposed on the u_2 solution is that it does not alter the resultant N_x on the loaded edge nor the result N_y on the unloaded edge

$$\int_0^a N_{x2}(0,y)dy = 0 \quad (67)$$

$$\int_0^b N_{y2}(x,0)dx = 0 \quad (68)$$

RESULTS AND DISCUSSION

The postbuckling coefficients $\hat{a}$ and $\hat{b}$ were calculated for a number of cross-ply graphite-epoxy plates. When $\hat{a}$ is not zero then some degree of postbuckling instability is indicated. The effect of this instability can be quantified by $\dfrac{\lambda_m}{\lambda_{cr}}$ where λ_m is the minimum load obtained by differentiating Equation (41) with respect to ξ and setting the result to zero

$$1 - \frac{\lambda_m}{\lambda_{cr}} = \frac{\hat{a}^2}{4\hat{b}} \quad (69)$$

Table 1 presents results for a $0°/90°$ graphite-epoxy (T300/5208, Tsai 1985) plate as a function of the aspect ratio. The aspect ratio is the length of the plate, which is parallel to the N_x-load axis, divided by the width of the plate, which is parallel to the N_y-load axis. All numerical results reported used $N = 20$ in Equation (53), and for each aspect ratio in Table 1 the buckling mode consists of one half wave in the length and width ($r = s = 1$ in Equations (50)). It is seen that the instability associated with the anisotropy is very small except for low aspect ratios where $\hat{b}$ becomes small because the plate behaves like a wide column. Table 2 presents results for a low-aspect-ratio plate of $(0°/90°)_n$ construction. For each n in Table 2 the ratio N_y/N_x is also equal to 0.015. It is clear that the effect of anisotropy dwindles rapidly with increasing n. Based on these results it appears that the instability associated with plate anisotropy should have very little effect on practical configurations.

CONCLUDING REMARKS

The paper presented an asymptotic Koiter-type analysis based on expansion of the initial postbuckling response for rectangular, simply-supported, anisotropic laminated plates. It was shown that by properly choosing the reference surface and the in-plane loading it is possible to have membrane prebuckling response. The degree of postbuckling instability was quantified by the reduction in the load carrying capacity. For graphite-epoxy cross-ply plates it was found that this measure of instability is negligible except for very low aspect-ratio plates and highly anisotropic stacking sequences. Thus the instability associated with anisotropy appears to have little practical significance

ACKNOWLEDGMENT

REFERENCES

Budiansky B., "Dynamic Buckling of Elastic Structures: Criteria and Estimates", in <u>Dynamic Stability of Structures</u>, proceedings of an International Conference held at Northwestern University, Evanston, Illinois, October 18–20, 1965, Pergamon Press, pp. 83–106, 1966.

Cohen, G.A., "Effect of a Nonlinear Prebuckling State on the Postbuckling Behavior and Imperfection Sensitivity of Elastic Structures", AIAA Journal, 6, 8, pp. 1616–1619, 1968.

Cohen, G.A., and Haftka, R.T., "Sensitivity of Buckling Loads of Anisotropic Shells of Revolution to Geometric Imperfections and Design Changes", Computers and Structures, 31, 6, pp. 985–995, 1989.

Hui, D., "Imperfection Sensitivity of Axially Compressed Laminated Flat Plates Due to Bending-Stretching Coupling", International Journal Solids Structures, 22, 1, pp. 13–22, 1986.

Hui, D., and Du, I.H.Y., "Imperfection Sensitivity of Long Axisymmetric Cross-Ply Cylindrical Panels Under Shear Loads", Journal of Applied Mechanics, 54, pp. 292–298, 1987.

Jeffrey, Glenda, L., "Postbuckling of Laminated Anisotropic Panels", NASA Technical Memorandum 100509, October, 1987.

Jensen, David, W., and Lagace, Paul, A., "Influence of Mechanical Couplings on the Buckling and Postbuckling of Anisotropic Plates", AIAA Journal, 26, 10, pp. 1269–1277, 1988.

Koiter, W.T., "A Translation of the Stability of Elastic Equilibrium", Air Force Flight Dynamics Laboratory, Wright-Patterson Air Force Base, Ohio, Technical Report AFFDL-TR-70-25, p.239, February 1970.

Tsai, S.W., "Composite Design-1985", Think Composites, Dayton Ohio, pp. 6–8, 1985.

Table 1: Postbuckling coefficients and load reduction for a $0°/90°$ graphite-epoxy plate (buckling mode normalized to the plate thickness).

Aspect ratio	N_y/N_x	$\hat{a}$	$\hat{b}$	$1 - \lambda_m/\lambda_{cr}$
1/3	0.015	0.0857	0.0302	0.0607
1/2	0.015	0.0904	0.0952	0.0215
1	0.015	0.	0.294	0.
1 1/3	0.015	-0.0530	0.324	0.0022
2	0.015	0.	0.449	0.

Table 2: Postbuckling coefficients and load reduction for a $(0°/90°)_n$ graphite-epoxy plate of aspect ratio 1/2 (buckling mode normalized to plate thickness).

n	$\hat{a}$	$\hat{b}$	$1 - \lambda_m/\lambda_{cr}$
1	0.0904	0.0952	0.0215
2	0.0232	0.0488	0.00275
4	0.0103	0.0435	0.00061
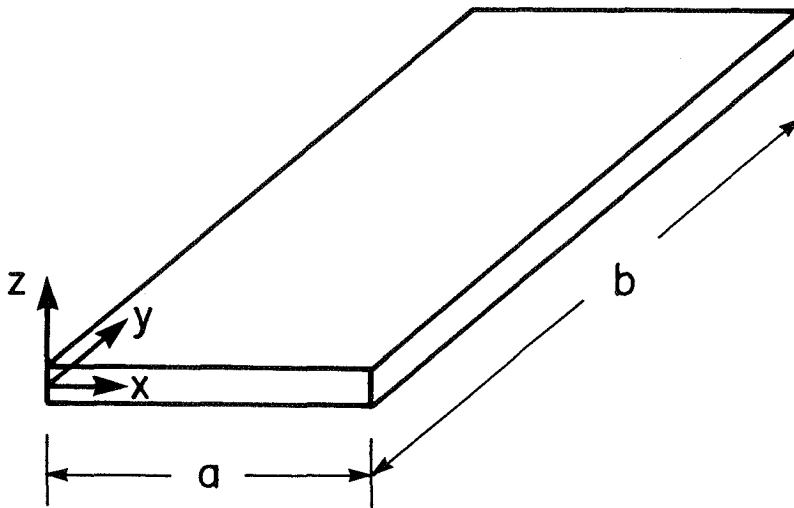
Figure I: Simply-Supported Plate Geometry

BUCKLING AND POSTBUCKLING BEHAVIOR OF SQUARE COMPRESSION-LOADED

GRAPHITE-EPOXY PLATES WITH CIRCULAR CUTOUTS

Michael P. Nemeth
Structural Mechanics Division
NASA Langley Research Center
Hampton, Virginia

SUMMARY

An experimental study of the postbuckling behavior of square compression-loaded graphite-epoxy plates and isotropic plates with a central circular cutout is presented. Results are presented for unidirectional $[0_{10}]_s$ and $[90_{10}]_s$ plates, $[(0/90)_5]_s$ plates, and for aluminum plates. Results are also presented for $[(\pm\theta)_6]_s$ angle-ply plates for values of $\theta = $ 30, 45, and 60 degrees.

The experimental results indicate that the change in axial stiffness of a plate at buckling is strongly dependent upon cutout size and plate orthotropy. The presence of a cutout gives rise to an internal load distribution that changes, sometimes dramatically, as a function of cutout size coupled with the plate orthotropy. In the buckled state, the role of orthotropy becomes more significant since bending in addition to membrane orthotropy is present. Most of the plates with cutouts exhibited less postbuckling stiffness than the corresponding plate without a cutout, and the postbuckling stiffness decreased with increasing cutout size. However, some of the highly orthotropic plates with cutouts exhibited more postbuckling stiffness than the corresponding plate without a cutout. These results suggest that the complex interaction of cutout size and plate orthotropy on the internal load distribution in plates needs further investigation. These results also suggest the possibility of tailoring the cutout size and the stacking sequence of a composite plate to optimize postbuckling stiffness. An important finding of this experimental study is that plates with large radius cutouts do exhibit some postbuckling strength.

The experimental results presented in the paper also indicate that a cutout can influence modal interaction in a plate. Specifically, results are presented that show a plate with a relatively small cutout buckling at a higher load than the corresponding plate without a cutout, due to modal interaction. Other results are presented that indicate the presence of nonlinear prebuckling deformations, due to material nonlinearity, in the angle-ply plates with $\theta = 45$ and 60 degrees. The nonlinear prebuckling deformations are more pronounced in the plates with $\theta = 45$ degrees, and become even more pronounced as the cutout size increases. Results are also presented that show how load-path eccentricity due to improper machining of the test specimens affects the buckling behavior. Some of the plates with cutouts and eccentricity exhibited a snap-through type of buckling behavior.

INTRODUCTION

The technical challenges associated with the development of military and civilian aerospace vehicles for the twenty-first century have identified several key areas that need further development. One important area is the design technology and analysis of large-scale composite structures. The high performance requirements of these structures has led to a search for ways to exploit their tailorability to meet specific mission goals.

An important structural component used in practically all aerospace vehicles is the rectangular plate with a central circular cutout. Cutouts commonly appear in plates as access ports for mechanical and electrical systems, or are included to reduce the structural weight in components such as wing ribs and spars. Often during flight, these members experience compression loads, and thus their buckling and postbuckling behavior are important factors that must be considered in their design.

Investigations of the buckling behavior of plates with cutouts have appeared in the technical literature since 1943. A summary of these investigations, for both isotropic and laminated composite plates, is given in reference 1. In-depth parametric studies of the buckling behavior of square and rectangular plates with central circular cutouts are presented in references 1 through 3. Analytical and experimental results are presented in these studies that indicate buckling behavior trends for a wide range of plate parameters. The results and physical insight presented in these references indicate that the buckling behavior of compression-loaded isotropic and orthotropic plates with cutouts is well understood.

Substantially fewer studies on the postbuckling behavior of plates with cutouts are available in the technical literature. Some of the first studies were presented by Yu and Davis in reference 4, by Martin in reference 5, by Yu and Davis in reference 6, and by Ritchie and Rhodes in reference 7. The results presented in references 4 and 6 address the postbuckling collapse of steel beams, columns, and plate girder structures with cutouts in their webs. The results presented in references 5 and 7 focus specifically on square isotropic plates with central circular cutouts. In addition, buckling and postbuckling results are also presented in reference 5 for square laminated composite plates with central circular cutouts.

More recently, selected results for the postbuckling and failure characteristics of compression-loaded rectangular graphite-epoxy plates with central circular cutouts have been presented in reference 8. Additional recent studies of the postbuckling collapse of square isotropic plates with square and circular cutouts are presented in references 9 and 10. A study of the imperfection sensitivity and postbuckling strength of compression-loaded square isotropic and laminated composite plates with central circular cutouts is presented in reference 11.

Review of the studies presented in references 4 through 11 indicates that the effects of cutout size, plate aspect ratio, and laminate stacking sequence on the postbuckling behavior of plates are still not well understood. This paper examines the behavior of selected isotropic and graphite-epoxy compression-loaded square plates, and attempts to establish

overall trends indicating the effects of cutout size and plate orthotropy on plate postbuckling behavior. The paper focuses on an experimental study of unidirectional $[0_{10}]_s$ and $[90_{10}]_s$ plates, $[(0/90)_5]_s$ plates, and aluminum plates. These plates represent extreme cases of orthotropy and moderate orthotropy, as well as isotropy. Results are also presented for $[(\pm\theta)_6]_s$ angle-ply plates for values of θ = 30, 45, and 60 degrees.

SYMBOLS

d	hole diameter, in. (see figure 2)
H	nominal plate thickness, in. (see Table VIII)
L	plate length, in. (see figure 2)
P	axial load, lb
P_{cr}^{o}	axial load at buckling for d/W = 0 case, lb (see Table VIII)
W	plate width, in. (see figure 2)
Δ	end-shortening, in. (see figure 2)
Δ_{cr}^{o}	end-shortening at buckling for d/W = 0 case, in. (see Table VIII)
θ	fiber orientation angle (see figure 4)
δ	transverse deflection at edge of cutout, in. (see figure 3)

SPECIMENS, APPARATUS, AND TESTS

The aluminum specimens tested in this investigation were machined out of 6061-T6 aluminum sheets having a nominal thickness of .0625 inches. Several thickness measurements were made on each specimen, and the average thickness was determined to be 0.0647 inches. Nominal material properties were assumed to include a Young's modulus $E = 11.0 \times 10^6$ psi and a Poisson's ratio $\nu = 0.33$.

The composite specimens tested in this investigation were fabricated from commercially available 450 K (350°F) cure Hercules AS4/3502 graphite-epoxy preimpregnated tapes. Nominal lamina properties were assumed to include a longitudinal modulus $E_1 = 18.5 \times 10^6$ psi, a transverse modulus $E_2 = 1.6 \times 10^6$ psi, an inplane shear modulus $G_{12} = 0.832 \times 10^6$ psi, a major Poisson's

ratio $\nu_{12} = 0.35$, and a nominal ply thickness of 0.005 inches. The tapes
were laid up to form 20-ply-thick laminates having $[0_{10}]_s$, $[(0/90)_5]_s$, and
$[90_{10}]_s$ stacking sequences, and to form 24-ply-thick laminates having
$[(\pm30)_6]_s$, $[(\pm45)_6]_s$, and $[(\pm60)_6]_s$ stacking sequences.

The laminates were cured in an autoclave using the manufacturer's
recommended procedures. After curing, the laminates were ultrasonically C-
scanned to assess specimen quality and then machined into test specimens.
All specimens were 10-inches-long by 10-inches-wide, and the loaded edges
were machined flat and parallel to permit uniform compressive loading.
Central circular cutouts were machined into the aluminum panels using a
milling machine, and machined into the composite panels using diamond
impregnated core drills. The circular cutout diameters ranged from 0 to
6.25 inches. One side of each specimen was painted white to reflect light
so that a moire-fringe technique could be used to monitor the out-of-plane
deformations. A total of 40 specimens were tested. The specimens have the
following designations: A1 through A7 for the aluminum specimens, B1 through
B7 for the $[0_{10}]_s$ specimens, C1 through C6 for the $[90_{10}]_s$ specimens, D1
through D7 for the $[(0/90)_5]_s$ specimens, E1 through E5 for the $[(\pm30)_6]_s$
specimens, F1 through F4 for the $[(\pm45)_6]_s$ specimens, and G1 through G4 for
the $[(\pm60)_6]_s$ specimens. The cutout sizes for each specimen are given in
Tables I through VII. Several thickness measurements were also made on each
composite specimen. The average thickness values were determined to be
0.107 inches for the $[0_{10}]_s$ laminates, 0.106 inches for the $[90_{10}]_s$
laminates, 0.110 inches for the $[(0/90)_5]_s$ laminates, 0.1176 inches for the
$[(\pm30)_6]_s$ and $[(\pm60)_6]_s$ laminates, and 0.1307 inches for the $[(\pm45)_6]_s$
laminates.

The specimens were loaded gradually in axial compression using a 300-
kip-capacity hydraulic testing machine. The loaded ends of the specimens
were clamped by fixtures during testing, and the unloaded edges were simply
supported by restraints that prevent the specimen from buckling as a wide
column. Most specimens were loaded to approximately twice the buckling
load, and then the test was stopped. Some specimens were loaded until
failure. A typical specimen mounted in the test fixture is shown in figure
1.

Electrical resistance strain gages were used to measure strains, and
direct-current differential transformers were used to measure axial
displacements and displacements normal to the specimen surface. Electrical
signals from the instrumentation and the corresponding applied loads were
recorded on magnetic tape at regular time intervals during the tests.

RESULTS AND DISCUSSION

Results are presented in this section for several different aluminum
and graphite-epoxy plates. First, the methods used to obtain the

experimental values of the prebuckling stiffnesses, buckling loads, and initial postbuckling stiffnesses are presented. Results are then presented for the aluminum plates; the $[0_{10}]_s$, $[90_{10}]_s$, and $[(0/90)_5]_s$ specially orthotropic plates; and the $[(\pm30)_6]_s$, $[(\pm45)_6]_s$, and $[(\pm60)_6]_s$ symmetrically laminated angle-ply plates in separate subsections. Failure results are then presented for the specimens that were loaded to failure. After these subsections, results indicating the overall stiffness trends exhibited by the specimens, and results indicating the effects of cutout size and plate orthotropy on the distribution of the out-of-plane displacement fields in the specimens are presented. Finally, results showing modal interaction in a plate with a cutout, and results indicating the effects of load-path eccentricity due to improper machining of some of the specimens are presented.

Analysis and Representation of the Test Data

To illustrate the postbuckling behavior of plates with cutouts, nondimensional load versus end-shortening curves and nondimensional load versus transverse deflection curves are presented in this paper. The nondimensional load versus end-shortening curve for each specimen was obtained by first performing a least squares fit of a straight line to the most linear part of the primary branch of the actual load versus end-shortening plot recorded during the test. Using the equation of the line obtained from the least squares fit of the test data, the prebuckling stiffness was obtained directly, and the initial irregularity in the actual load versus end-shortening plot, associated with initial slack in the test fixture, was eliminated. The elimination was performed by translating the coordinate system of the actual load versus end-shortening plot such that the line obtained from the least squares fit passed through the origin.

In a similar manner, the initial postbuckling stiffness was obtained directly by performing a least squares fit of a straight line to the most linear part of the secondary branch of the load versus end-shortening plot recorded during testing. The experimental buckling load and associated end-shortening were then obtained by computing the intersection of the two straight lines fitted to the primary and secondary branches of the load versus end-shortening test data.

Finally, the curves were nondimensionalized by dividing the load and end-shortening of a given specimen by analytical values of the buckling load P_{cr}^0 and end-shortening Δ_{cr}^0, respectively, of the corresponding plate without a hole. These analytical values were obtained using an in-house computer program for buckling analysis, and are based on the nominal material properties given in this paper previously and on nominal plate thicknesses. The nominal plate thicknesses used in the buckling calculations were based on the average values of the measured plate thicknesses previously described. Moreover, the analytical values were based on square-plate geometry, and on a uniaxial loading condition in which two opposite edges of the plate are uniformly displaced toward one another. The loaded edges were assumed to be clamped, and the unloaded edges were assumed to be simply supported. In all of the calculations, the buckling load and corresponding end-shortening were based on the 9.5-inch unsupported length between knife

edge supports of the test fixture. The nominal thicknesses used in these calculations and the corresponding analytical values are given in Table VIII.

The experimental load versus end-shortening results are presented in subsequent sections of the paper by two straight lines obtained from the least squares fits to the primary and the initial part of the secondary branches of the test data. The intersection of the two straight lines is marked with a solid circular symbol in the figures to denote the experimental buckling load. The nondimensional transverse deflection shown in the figures presented herein was obtained by dividing the actual transverse deflection by the nominal plate thickness that was used to compute P_{cr}^0 and Δ_{cr}^0.

Differences between the analytical values and experimental values of the buckling loads and displacements of the plates without cutouts are noted. These differences are attributed to differences between the actual thicknesses of the plates and assumed nominal thickness used in the calculated values, and the assumption of ideal clamped and simply supported boundary conditions in the analysis. The differences between analysis and experiment are also attributed to the difference between the 9.5-inch unsupported length between the ends of the test fixture that was used as the plate width in the buckling calculations and the true plate width of 10 inches.

The experimental results for some of the angle-ply laminates exhibited secondary branches of the load versus end-shortening plots recorded during testing that were totally nonlinear. This attribute made it difficult to establish the experimental buckling load in the manner previously described. For these cases, the experimental buckling load was estimated from the load versus transverse deflection data and from strain gage data. The initial postbuckling stiffness was taken to be the slope of a line tangent to the secondary branch of the load versus end-shortening plot and intersecting the straight line least squares fit of the primary branch at the estimate of the buckling load. It is important to point out that for these cases, the value of the initial postbuckling stiffness is sensitive to the estimate of the buckling load.

Aluminum Plates

Experimental results were obtained for a square aluminum plate without a cutout and for square aluminum plates having six different cutout sizes. The cutout size, buckling load, prebuckling stiffness, and postbuckling stiffness of each plate are presented in Table I. Nondimensional load versus end-shortening curves and nondimensional load versus transverse deflection curves are presented in figures 2 and 3, respectively.

The results presented in Table I and figure 2 indicate that the prebuckling stiffnesses of the isotropic plates decrease monotonically with increasing cutout size. This trend is consistent with the fact that an increase in cutout size gives rise to a decrease in the cross-sectional area at the net section of the plate. The maximum decrease in prebuckling

630

stiffness compared to the stiffness of the plate without a cutout is approximately 42% for the plate with d/W = 0.6.

The results in Table I also indicate that the buckling loads of the plates decrease at first and then tend to increase with increasing cutout size. Analytical results indicating a similar trend for the buckling loads are presented in reference 1, and suggest that increase in experimental buckling load with increasing cutout size presented herein is not due entirely to scatter in the test data. The buckling mode shapes for all the plates consisted of one half-wave along both their length and width.

Additional results presented in Table I and figure 2 indicate that the initial postbuckling stiffnesses of the plates decrease monotonically with increasing cutout size. The largest decrease is approximately 43% for d/W = 0.6. Comparing the prebuckling stiffness to the postbuckling stiffness given in Table I for each specimen indicates that, as the cutout size increases, the change in axial stiffness due to buckling varies between 35% and 40% for the full range of cutout sizes.

The nondimensional load versus transverse deflection curves shown in figure 3 give an indication of the relative size of the initial imperfection in the geometry of each plate. Moreover, these results give an indication of the nature of the postbuckling deformations near the cutout. For the plates with d/W less than 0.6, the transverse deflection was measured on the top edge of the cutout as indicated in figure 3. For the plate with d/W = 0.6, the measurement was made on the right edge of the cutout. The curves shown in this figure can not be compared directly since the location of the transverse deflection measurement is different for each value of d/W. However, the curves do give some indication of the postbuckling deformation near the cutout since the transverse deflection measurements for two adjacent cutout sizes (e.g., d/W = 0.3 and 0.4) are near one another, and since the plates possess similar deformation shapes (one half-wave along their length and width). Comparing the relative sizes of the transverse deflections of the specimens with d/W = 0.5 and 0.6 suggests that as the cutout size increases the amount of bending in the top central region of the plate is less than the amount of bending in the right central region of the plate.

Specially Orthotropic Plates

Experimental results were obtained for unidirectional $[0_{10}]_s$, unidirectional $[90_{10}]_s$, and cross-ply $[(0/90)_5]_s$ square plates having up to seven different cutout sizes ranging from d/W = 0 to 0.66. The cutout size, buckling load, prebuckling stiffness, and postbuckling stiffness of each $[0_{10}]_s$, $[90_{10}]_s$, and $[(0/90)_5]_s$ plate are presented in Tables II, III, and IV, respectively. Nondimensional load versus end-shortening curves and nondimensional load versus transverse deflection curves are presented in figures 4 and 5, respectively, for the $[0_{10}]_s$ plates; presented in figures 6 and 7, respectively, for the $[90_{10}]_s$ plates; and presented in figures 8 and 9, respectively, for the $[(0/90)_5]_s$ plates.

Results for $[0_{10}]_s$ plates.- The results presented in Table II and figure 4 indicate that the prebuckling stiffnesses of the $[0_{10}]_s$ plates decrease monotonically with increasing cutout size, with the exception of the d/W = 0.32 case. For this particular case, it was found that the loaded edges of the specimen had not been properly machined. This observation suggests that improper machining of the loaded edges of the test specimen may have produced an edge effect that increased the prebuckling stiffness (see subsequent section entitled Anomalous behavior.). The maximum decrease in prebuckling stiffness is approximately 74% for the plate with d/W = 0.66.

The results presented in Table II also indicate that the buckling loads of the plates decrease monotonically with increasing cutout size. Analytical results showing essentially the same trend are presented in reference 2. The maximum reduction is approximately 33% for the plate with d/W = 0.66. The buckling mode shapes for all the plates consisted of one half-wave along both the plate lengths and widths.

The results presented in Table II and figure 4 also indicate that the initial postbuckling stiffnesses of the $[0_{10}]_s$ plates decrease monotonically with increasing cutout size, with the exception of the d/W = 0.11 and 0.32 cases. The largest decrease is approximately 24% for d/W = 0.66. Comparing the prebuckling stiffness to the postbuckling stiffness given in Table II for each specimen indicates, that as the cutout size increases, the change in axial stiffness due to buckling decreases monotonically from approximately a 76% stiffness reduction for the plate with d/W = 0 to a 31% stiffness reduction for the plate with d/W = 0.66.

The nondimensional load versus transverse deflection curves shown in figure 5 indicate that the plates with d/W = 0.21 and 0.11 had the largest initial imperfections. In addition, the results in figure 5 suggest that, for the buckled plates, the region adjacent to the cutout (where the transverse deflection was measured) generally becomes more flexible in bending as the cutout size increases.

Results for $[90_{10}]_s$ plates.- The results presented in Table III and figure 6 indicate that the prebuckling stiffnesses of the $[90_{10}]_s$ plates decrease with increasing cutout size, for the most part, with the exception of the d/W = 0.42 case. For this particular case, the prebuckling stiffness was determined to be approximately 16% higher than the prebuckling stiffness of the corresponding plate without a cutout. The reduction in prebuckling stiffnesses exhibited by the plates with d/W < 0.42 was less than 10% of the prebuckling stiffness of the corresponding plate without a cutout. The maximum decrease in prebuckling stiffness is approximately 54% for the plates with d/W = 0.66. These results suggest that a complex interaction between the plate geometry and the degree of plate orthotropy may be present.

The results presented in Table III also indicate that the buckling loads of the $[90_{10}]_s$ plates do not decrease monotonically with increasing cutout size. The buckling load of the plate with d/W = 0.11 is approximately 9% higher than the buckling load of the corresponding plate

without a cutout. The lowest buckling load, approximately 30% of the
buckling load for d/W = 0, is exhibited by the plate with d/W = 0.42. The
plate with d/W = 0.66 buckles at a load approximately 18% less than the
buckling load for the corresponding plate without a cutout. Analytical
results showing the same trend are also presented in reference 2, and
suggest that the unusual trend exhibited by the plates is not due entirely
to scatter in the test data.

In addition, the results presented in Table III and figure 6 indicate
that the initial postbuckling stiffnesses of the plates do not typically
decrease with increasing cutout size. In fact, the experimental results
indicate initial postbuckling stiffnesses approximately 36% larger than the
stiffness of the corresponding plate without a cutout for the plate with d/W
= 0.21, and as high as 56% larger for the plate with d/W = 0.42. The plate
with d/W = 0.66 exhibited a stiffness reduction of approximately 43% of the
initial postbuckling stiffness of the corresponding plate without a cutout.
Comparing the prebuckling stiffness to the postbuckling stiffness given in
Table III for each specimen indicates that the change in axial stiffness due
to buckling is typically less than that of the d/W = 0 case, and ranges
between 28% and 54% of their respective prebuckling stiffnesses.

The nondimensional load versus transverse deflection curves shown in
figure 7 for the $[90_{10}]_s$ plates indicate that the plates with d/W = 0.42 and
0.32 exhibit the largest initial imperfections. The results in this figure
also suggest that the region adjacent to the cutout in the buckled plates
with d/W > 0.11 generally becomes more flexible in bending as the cutout
size increases. The largest amount of flexibility is exhibited by the plate
with d/W = 0.42. The results presented in this figure for the plate with
d/W = 0 indicate that the plate has a relatively large geometric
imperfection and deforms out-of-plane somewhat before moving in the
opposite direction to form a nodal line at the center of the plate (where
the transverse deflection was measured). The results presented in this
figure for the plate with d/W = 0.11 indicate that the plate has a very
small geometric imperfection and that the central region of the plate
deforms initially out-of-plane as if to form a distinct mode shape, and then
moves in the opposite direction as if a different mode shape is forming.
This observation is directly related to another interesting result presented
in Table III and shown in figure 6 for the plate with d/W = 0.11; i.e., the
plate with d/W = 0.11 buckles at a higher load than the corresponding plate
without a cutout.

The buckle mode shape for the $[90_{10}]_s$ plate without a cutout consisted
of one half-wave in the direction normal to the loading and two half-waves
in the direction parallel to the loading. The buckle mode shape for the
$[90_{10}]_s$ plate with d/W = 0.11 is shown in figure 10 by the moire fringe
patterns photographed during the test. The fringe pattern for $P/P_{cr}^o = 0.99$
indicates that the plate is beginning to buckle into a mode that lies
between the mode observed for the plate with d/W = 0 and a mode consisting
of one half-wave in each direction. The fringe pattern for $P/P_{cr}^o = 1.14$
shown in figure 10 indicates that as the load increases the plate is moving
closer to the mode with two half-waves along the loading direction. The

buckling mode shapes for all the plates with d/W > 0.11 consisted of one half-wave along both the plate length and width.

To gain insight into this phenomenon, some buckling analyses were performed using the BUCKO computer code described in reference 12. Analytical results were obtained for $[90_{10}]_s$ plates, based on nominal lamina properties and ply thicknesses, for plate aspect ratios ranging from L/W = 0.4 to 2.0, and for cutout sizes of d/W = 0 and 0.1. These analytical results are shown in figure 11.

The analytical results shown in figure 11 are the usual festooned curves that relate buckling coefficient K to plate aspect ratio L/W. The equation defining the buckling coefficient is given in figure 11. The terms D_{11} and D_{22} appearing in the equation are the usual orthotropic plate bending stiffnesses. At the first set of cusps in these curves, the buckle mode changes from one half-wave along the loading direction to two half-waves. The analytical results indicate that the plate with L/W = 1 and d/W = 0.10 is on the cusp of the intersecting dashed-line curve. This analytical result and the experimental results previously described suggest that a modal interaction was present during the test of the $[90_{10}]_s$ plate with d/W = 0.11. Moreover, the resulting interaction gave rise to a slight increase in buckling load.

Results for $[(0/90)_5]_s$ plates.- The results presented in Table IV and figure 8 indicate that the prebuckling stiffnesses of the $[(0/90)_5]_s$ plates decrease with increasing cutout size, with the exception of the plate with d/W = 0.42. This plate exhibits a prebuckling stiffness almost equal to that of the plate with d/W = 0.32. The maximum decrease in prebuckling stiffness is approximately 61% for the plate with d/W = 0.66.

The results presented in Table IV also indicate that the buckling loads of the plates decrease monotonically as d/W increases up to 0.32, and then the buckling loads change very little as d/W increases. The buckling loads of the plate with d/W = 0.32 and 0.66 are approximately 11% less and 5% less than the buckling load of the corresponding plate without a cutout, respectively. Analytical results indicating a somewhat similar trend are also presented in reference 2. The buckling mode shapes for all the plates consisted of one half-wave along both the plate length and width.

The results presented in Table IV and figure 8 indicate that the initial postbuckling stiffnesses of the plates decrease monotonically with increasing cutout size. The largest decrease is approximately 51% for d/W = 0.66. Comparing the prebuckling stiffness to the postbuckling stiffness given in Table IV for each specimen indicates that as the cutout size increases the change in axial stiffness due to buckling decreases from approximately a 53% stiffness reduction for d/W = 0 to a 31% stiffness reduction for d/W = 0.32. The stiffness reduction for d/W = 0.66 is approximately 41%.

The nondimensional load versus transverse deflection curves shown in figure 9 for the $[(0/90)_5]_s$ plates indicate that the plates with d/W = 0.32

634

and 0.21 had the largest initial imperfections. The results presented in this figure for the plate with d/W = 0.66 indicate that the plate initially deforms in the direction of its geometric imperfection shape, and then buckles into a similar mode shape in the opposite direction. This behavior is manifested in figure 8 by the small jump in the load versus end-shortening curve (similar to what is encountered when a change in buckle mode occurs) near the buckling load, for the plate with d/W = 0.66.

Symmetrically Laminated Angle-ply Plates

Experimental results were also obtained for $[(\pm30)_6]_s$, $[(\pm60)_6]_s$, and $[(\pm45)_6]_s$ square plates having up to five different cutout sizes ranging from d/W = 0 to 0.66. The cutout size, buckling load, prebuckling stiffness, and postbuckling stiffness of each $[(\pm30)_6]_s$, $[(\pm60)_6]_s$, and $[(\pm45)_6]_s$ plate are presented in Table V, VI, and VII, respectively. Nondimensional load versus end-shortening curves and nondimensional load versus transverse deflection curves are presented in figures 12 and 13, respectively, for the $[(\pm30)_6]_s$ plates; presented in figures 14 and 15, respectively, for the $[(\pm60)_6]_s$ plates; and presented in figures 16 and 17, respectively, for the $[(\pm45)_6]_s$ plates.

Results for $[(\pm30)_6]_s$ plates.- The results presented in Table V and figure 12 indicate that the prebuckling stiffnesses of the $[(\pm30)_6]_s$ plates decrease monotonically with increasing cutout size. The maximum decrease in prebuckling stiffness is approximately 54% for the plate with d/W = 0.66.

The results presented in Table V also indicate that the buckling loads of the plates decrease monotonically with increasing cutout size up to d/W = 0.60. The buckling load of the plate with d/W = 0.60 is approximately 16% less than the buckling load of the corresponding plate without a cutout. The plate with d/W = 0.66 exhibits a buckling load approximately 13% less than the buckling load of the corresponding plate without a cutout. Analytical results that indicate a somewhat similar trend are presented in reference 3. The buckling mode shapes for all the plates consisted of one half-wave along both their length and width.

The results presented in Table V and figure 12 indicate that the initial postbuckling stiffnesses of the plates with d/W = 0.11 and 0.32 are approximately 4% higher than the postbuckling stiffness of the plate with d/W = 0. The plates with d/W = 0.6 and 0.66 exhibit initial postbuckling stiffnesses that are approximately 16% and 27% less than the stiffness of the corresponding plate without a cutout, respectively. Comparing the prebuckling stiffness to the postbuckling stiffness given in Table V for each plate indicates that, as the cutout size increases, the change in axial stiffness due to buckling decreases monotonically from approximately a 66% stiffness reduction for d/W = 0 to a 46% stiffness reduction for d/W = 0.66.

The nondimensional load versus transverse deflection curves shown in figure 13 indicate that the plates with d/W = 0.11 and 0 had the largest initial imperfections. The results also suggest that the region adjacent to the cutout in the buckled plates with d/W ≤ 0.32 becomes more flexible in bending as the cutout size increases. The results presented in this figure for the plates with d/W = 0.60 and 0.66 indicate that the plates failed at loads much lower in the postbuckling range than the other plates.

Results for $[(\pm 60)_6]_s$ plates.- The results presented in Table VI and figure 14 indicate that the prebuckling stiffnesses of the $[(\pm 60)_6]_s$ plates decrease monotonically with increasing cutout size. The maximum decrease in prebuckling stiffness is approximately 60% to 69% for the plate with d/W = 0.66. The nondimensional load versus end-shortening curve shown in figure 14 for the plate with d/W = 0.66 exhibits a nonlinear prebuckling path. Neglecting the nonlinearity gives a prebuckling stiffness reduction due to the cutout of approximately 60%, whereas including the nonlinearity accounts for another 9% reduction in stiffness. Because of the nonlinear path, the buckling load was estimated using the corresponding nondimensional load versus transverse deflection curve presented in figure 15. At the buckling load, the secondary branch of the load versus end-shortening curve is linear. Strain gage data (for back-to-back pairs of gages located near the edge of the cutout) recorded during testing of the plate with d/W = 0.66 corroborated the presence of material nonlinearity. This fact is illustrated in figure 18 by the nonlinear shape of the initial part of the curves giving nondimensional load versus axial strain. The strain gage data for the plates with the smaller cutout sizes showed no indication of material nonlinearity prior to buckling.

The results presented in Table VI also indicate that the buckling loads of the plates decrease monotonically with increasing cutout size up to d/W = 0.32. The buckling load of the plate with d/W = 0.32 is approximately 16% less than the buckling load of the corresponding plate without a cutout. The plate with d/W = 0.66 exhibits a buckling load 23% greater than the buckling load of the corresponding plate without a cutout. These buckling loads exhibit a trend that is similar to the analytically obtained buckling loads presented in reference 3. The buckling mode shapes for all the plates consisted of one half-wave along both the plate length and width.

The results presented in Tables VI and figure 14 indicate that the initial postbuckling stiffnesses of the plates decrease with increasing cutout size. The largest reduction in stiffness is exhibited by the plate with d/W = 0.66 and is approximately 74% of the stiffness of the corresponding plate without a cutout. The plates with d/W = 0 and 0.11 also exhibit a change in buckle pattern from one half-wave along the loading direction to two half-waves along the loading direction at approximately P/P_{cr}^0 = 1.4. Associated with these changes in buckle pattern are additional reductions in postbuckling stiffness of 26% and 34% of the corresponding prebuckling stiffnesses for the plates with d/W = 0 and 0.11, respectively. Comparing the prebuckling stiffness to the postbuckling stiffness given in Table VI for each specimen with d/W < 0.66 indicates that as the cutout size increases, the axial stiffness due to initial buckling decreases about 33%

to 39%. The plate with d/W = 0.66 exhibits a stiffness reduction (including the effects of material nonlinearity) of approximately 60%.

The nondimensional load versus transverse deflection curves shown in figure 15 suggest that the region adjacent to the cutout (where the displacement was measured) becomes more flexible in bending as the cutout size increases, for all cutout sizes except d/W = 0.66. The results in this figure also show a change in buckle pattern for the plates with d/W = 0 and 0.11 at approximately $P/P_{cr} = 1.4\overset{0}{}$.

Results for $[(\pm45)_6]_s$ plates.- The results presented in Table VII and figure 16 indicate that the prebuckling stiffnesses of the $[(\pm45)_6]_s$ plates decrease monotonically with increasing cutout size. The maximum decrease in prebuckling stiffness is approximately 62% to 88% for the plate with d/W = 0.66. The nondimensional load versus end-shortening curve shown in figure 16 for the plate with d/W = 0.66 exhibits a substantial nonlinear prebuckling path. Neglecting the nonlinearity gives a prebuckling stiffness reduction due to the cutout of approximately 62%, whereas including the nonlinearity accounts for another 26% reduction in stiffness.

Because of the nonlinear prebuckling path of the plate with d/W = 0.66, the buckling load was estimated using the corresponding nondimensional load versus transverse deflection curve presented in figure 17. At the buckling load, the secondary branch of the load versus end-shortening curve is not linear like that of the $[(\pm60)_6]_s$ plate with d/W = 0.66. Placing a tangent line through the buckling load indicates that the initial postbuckling stiffness and the prebuckling stiffness just prior to buckling are the same. This observation suggests that significant nonlinear material behavior was present during buckling. Strain gage data (from back-to-back pairs of gages located near the edge of the cutout) recorded during testing of the $[(\pm45)_6]_s$ plates indicate the presence of very small amounts of material nonlinearity in the plates with d/W < 0.66. These small amounts of material nonlinearity account for the shape of the nondimensional load versus end-shortening curves shown in figure 16; i.e., the curves start out linear and then become substantially nonlinear just after buckling.

The results presented in Table VII also indicate that the buckling loads of the $[(\pm45)_6]_s$ plates decrease monotonically with increasing cutout size up to d/W = 0.32. The buckling loads of the plate with d/W = 0.32 and 0.66 are approximately 14% less and 14% greater, respectively, than the buckling load of the corresponding plate without a cutout. For all the plates, the buckling load was estimated from the appropriate load versus transverse deflection curve and associated strain gage data due to the rapid onset of nonlinear behavior immediately after buckling. The buckling mode shapes for all the plates consisted of one half-wave along both the plate length and width.

The results presented in Tables VII and figure 16 indicate that the initial postbuckling stiffnesses of the plates decrease with increasing cutout size. The largest reduction in stiffness is exhibited by the plate

with d/W = 0.66 and is approximately 73% (including substantial material nonlinearity) of the stiffness of the corresponding plate without a cutout. Comparing the prebuckling stiffness to the postbuckling stiffness given in Table VII for each $[(\pm45)_6]_s$ plate with d/W < 0.66 indicates that as the cutout size increases, the reduction in axial stiffness due to initial buckling is around 45% to 55%. The plate with d/W = 0.66 exhibits a stiffness reduction of approximately 68% that includes the effects of material nonlinearity. An important point to note is that the postbuckling stiffness presented herein for each specimen is dependent upon the estimate of the buckling load, due to the nonlinear shape of the nondimensional load versus end-shortening curves.

The nondimensional load versus transverse deflection curves shown in figure 17 for the $[(\pm45)_6]_s$ plates with d/W < 0.66 indicate that the region adjacent to the cutout (where the displacement was measured) of the buckled plates becomes more flexible in bending as the cutout size increases. The results presented in this figure for the plate with d/W = 0.32 indicate that the plate initially deforms in the direction of its geometric imperfection shape, and then buckles into a similar mode shape in the opposite direction. However, no indication of this behavior is given by the corresponding load versus end-shortening curve. The plate with d/W = 0.66 failed before getting very far into the postbuckling range.

Failure Tests

Most of the specimens tested in the experimental study described in this paper were loaded gradually to approximately twice their buckling loads. However, some of the specimens were loaded to failure. The particular specimens loaded to failure, their failure loads and average axial strains at failure are listed in Table IX. The average strains recorded in Table IX are obtained by dividing the end-shortening at failure by the true 10-inch length of the plates.

Three $[90_{10}]_s$ plates with cutout-diameter-to-plate-width ratios of d/W = 0.32, 0.42, and 0.66 were loaded to failure. The plate with d/W = 0.32 failed at the highest load. The plates with d/W = 0.42 and 0.66 failed at loads approximately 19% and 15% less, respectively, than the failure load of the plate with d/W = 0.32. Similarly, the plates with d/W = 0.42 and 0.66 failed at average strains approximately 40% smaller and 17 times larger, respectively, than the failure strain of the plate with d/W = 0.32. In all cases, the $[90_{10}]_s$ specimens failed at the net section of the plate, along the fibers in a matrix failure mode. The nondimensional load versus transverse deflection curves presented in figure 7 for the $[90_{10}]_s$ plates with d/W = 0.42 and 0.66 show an abrupt change in bending stiffness near the cutout that is associated with the onset of matrix cracking. Moreover, the curves shown in figure 7 indicate that all three of the plates failed at roughly the same magnitudes of transverse deflection.

Two $[(\pm30)_6]_s$ plates - d/W = 0.60 and 0.66 - were loaded to failure. The failure loads and average failure strains for the two plates are nearly the same. The plate with d/W = 0.60 failed along a line that is parallel to

the plus 30-degree fibers, and that runs from the edge of the cutout at the net section to the unloaded edge of the plate. The specimen appeared to have a clean break of the minus 30-degree fibers along the failure line just described. The plate with d/W = 0.66 failed along a line that is parallel to the plus 30-degree fibers, and that runs from the edge of the cutout to the corner of the plate. This specimen also appeared to have a clean break of the minus 30-degree fibers along the failure line just described, but did not intersect the cutout at the net section.

One $[(\pm 60)_6]_s$ plate - d/W = 0.66 - was loaded to failure. The failure load of the $[(\pm 60)_6]_s$ plate was approximately 29% less than the failure load of the $[(\pm 30)_6]_s$ plate. However, the average failure strain of the $[(\pm 60)_6]_s$ plate was approximately 3.3 times that of the $[(\pm 30)_6]_s$ plate. In the $[(\pm 60)_6]_s$ plate, the failure appeared to be due to delaminations that started at the unloaded edges of the plate, near the net section, and propagated to the free edge of the cutout. The delaminations also appeared to propagate along plus 60-degree fiber direction.

One $[(\pm 45)_6]_s$ plate - d/W = 0.66 - was also loaded to failure. The failure load of the $[(\pm 45)_6]_s$ plate was approximately 4% higher than the failure load of the $[(\pm 30)_6]_s$ plate, and the average failure strain of the $[(\pm 45)_6]_s$ plate was approximately 3.6 times larger than that of the $[(\pm 30)_6]_s$ plate. In the $[(\pm 45)_6]_s$ plate the failure also appeared to be due to delaminations that started at the unloaded edges of the plate, near the net section, and propagated to the free edge of the cutout. The delaminations also appeared to propagate along the plus 45-degree fiber direction.

Discussion of Results

Overall stiffness trends.- The experimental results presented in this paper include a wide range of cutout sizes, and include a broad spectrum of plate orthotropy (in addition to plate isotropy). Only one specimen was tested for each combination of cutout size and plate orthotropy. Due to the limited amount of testing on each specimen type, the degree of scatter in the experimental data is not well known. However, the experimental data presented in this paper are useful in identifying overall trends exhibited by each family of plates studied. To indicate the overall trends, results showing the reduction in prebuckling stiffness due to cutouts, results showing the change in postbuckling stiffness due to cutouts, and results showing the change in axial stiffness the plates experience in going from an unbuckled state to a buckled state are presented in Tables X, XI, and XII, respectively, for all 40 specimens tested.

The results presented in Table X indicate the reduction in axial stiffness prior to buckling, with respect to the prebuckling stiffness of the corresponding plate without a cutout, as a function of inplane plate orthotropy. The results presented in this table indicate a complex interaction between cutout size and plate orthotropy on the stiffness

reduction. For example, the $[0_{10}]_s$ plates lose a substantial amount of inplane stiffness (approximately 27%) when small cutouts are present, whereas the $[90_{10}]_s$ and $[(\pm 30)_6]_s$ plates retain a substantial amount of stiffness (approximately 88%) until d/W becomes greater than 0.32. The largest stiffness reductions are exhibited by the $[0_{10}]_s$ and $[(0/90)_5]_s$ plates for the full range of cutout sizes. The smallest stiffness reductions are exhibited by the $[90_{10}]_s$ plates for most of the cutout sizes. In all cases, the reduction in axial stiffness due to the cutout is generally not equal to the reduction in cross-sectional area at the net section of the plate.

The results presented in Table XI indicate the reduction in initial postbuckling stiffness, with respect to the initial postbuckling stiffness of the corresponding plate without a cutout, as a function of cutout size and plate orthotropy (inplane and bending orthotropy). These results also indicate a complex interaction between cutout size and plate orthotropy that influences the change in postbuckling stiffness. The general trend for the most part is a monotonic reduction in postbuckling stiffness with increasing cutout size. The isotropic and the $[(0/90)_5]_s$ plates exhibit the largest losses in postbuckling stiffness for cutout sizes up to d/W = 0.60. The $[(\pm 45)_6]_s$ and $[(\pm 60)_6]_s$ plates with d/W = 0.66, which deform inelastically prior to buckling, exhibit the largest reductions in postbuckling stiffness. In contrast, the $[90_{10}]_s$ plates with d/W = 0.21, 0.32, and 0.42 exhibit postbuckling stiffnesses between 25% and 56% higher than the postbuckling stiffness of the corresponding plate without a cutout. The magnitude of these increases suggests that the increases in stiffness noted are not due entirely to scatter in the experimental data, and suggest that further investigation of the importance of plate orthotropy on the postbuckling behavior of plates with cutouts should be performed. Moreover, these results suggest the possibility of tailoring the cutout size and the stacking sequence of a composite plate to optimize postbuckling stiffness.

The results presented in Table XII indicate the reduction in axial stiffness associated with changing from an unbuckled state to a buckled state, as a function of cutout size and plate orthotropy. The stiffness changes presented in this table correspond to the percentage difference between the prebuckling stiffness and the initial postbuckling stiffness of each plate. The results presented in this table indicate that the isotropic plates lose between 35% and 40% of their stiffness due to buckling, for the full range of cutout sizes. The specially orthotropic plates, however, have a much larger spread in the stiffness reductions with respect to the cutout sizes, than the isotropic plates. The $[(\pm 60)_6]_s$ plates exhibit a trend similar to that of the isotropic plates (less than 6% variation), with the exception of the plate with d/W = 0.66. These plates deform inelastically prior to buckling. The largest stiffness reduction is exhibited by the $[0_{10}]_s$ plate without a cutout, and the smallest stiffness reduction is exhibited by the $[90_{10}]_s$ plate with d/W = 0.21.

<u>Behavior of the out-of-plane displacement field</u> .- Results showing the effects of cutout size and plate orthotropy on the shape of the out-of-plane displacement field (transverse deflection) are presented in figure 19 for $[0_{10}]_s$, $[(0/90)_5]_s$, $[90_{10}]_s$, and $[(\pm 60)_6]_s$ plates with d/W = 0.11, 0.32, 0.42, and 0.66. The out-of-plane displacement contours shown in this figure are photographs of moire fringe patterns that were taken during testing and correspond to load levels that were well into the postbuckling range. The out-of-plane displacement patterns shown in the figure consist of one half-wave in both the length and width directions of the plate, with the exception of the $[90_{10}]_s$ plate with d/W = 0.11. In this case, the displacement pattern consists of two half-waves along the plate length and one half-wave across the plate width.

The results shown in figure 19 indicate that cutout size and plate orthotropy have a pronounced effect on the distributions of the out-of-plane displacements of the plates. The results shown in figure 19a for the $[0_{10}]_s$ plate with d/W = 0.11 indicate that lines of constant out-of-plane displacement are somewhat oval in appearance, but substantially elongated, with the longest axis of the oval being normal to the loading direction. The out-of-plane displacement distributions are typical of those that usually occur in a highly orthotropic plate. As the cutout size inceases, the out-of-plane displacement field redistributes to become more concentrated in the lateral regions of the plate near the unloaded edges, and fully envelops the full length of the plate.

The results shown in figure 19b for the $[(0/90)_5]_s$ plates (plates with a more moderate degree of orthotropy) indicate out-of-plane displacement patterns that are more evenly distributed than the displacement patterns of the $[0_{10}]_s$ plates. The displacement patterns shown for the $[(0/90)_5]_s$ plates with d/W = 0.11 and 0.42 are typical of an overall plate type of bending mode as opposed to a mode in which the out-of-plane displacement field becomes concentrated in the lateral regions of the plate near the unloaded edges. For the cutout size of d/W = 0.66, the out-of-plane displacement field in the $[(0/90)_5]_s$ plate also becomes concentrated in the lateral regions of the plate near the unloaded edges, but not to the extent that is exhibited by the highly orthotropic $[0_{10}]_s$ plates. Results obtained for the isotropic plates and $[(\pm 30)_6]_s$ plates indicated behavior very similar to the behavior of the $[(0/90)_5]_s$ plates.

The results presented in figure 19c for the $[90_{10}]_s$ plates indicate out-of-plane displacement patterns that are evenly distributed. The results shown in figure 19c for the $[90_{10}]_s$ plate with d/W = 0.66 appear to be more evenly distributed over the plate than the corresponding results for the $[0_{10}]_s$ and $[(0/90)_5]_s$ plates, but, in addition, the lines of constant out-of-plane displacement along the edges of the cutout appear to be more densely spaced.

The results presented in figure 19d for the $[(\pm 60)_6]_s$ plates indicate out-of-plane displacement patterns that are somewhat evenly distributed for the plates with d/W = 0.11 and 0.32. However, the results shown in figure 19d for the $[(\pm 60)_6]_s$ plate with d/W = 0.66 indicate that the out-of-plane displacement field is much more localized around the vicinity of the net section of the plate, unlike the out-of-plane displacement fields of the other plates with the large cutouts. This more localized distribution of the out-of-plane displacements may be related to the fact that the $[(\pm 60)_6]_s$ stacking sequence tends to relocate the inplane load outboard of the cutout much more than the isotropic, specially-orthotropic, and $[(\pm 30)_6]_s$ plates relocate the inplane load. This more localized distribution of the out-of-plane displacements may also be related to the nonlinear (material) prebuckling deformations exhibited by this plate. The corresponding $[(\pm 45)_6]_s$ plates exhibited behavior very similar to the behavior of the $[(\pm 60)_6]_s$ plates.

Modal interaction.- Another important topic briefly investigated in this paper that may be important in preliminary design of structures is the relationship between cutout size and modal interaction in plates. The results presented in figures 6, 7, 10, and 11 for the $[90_{10}]_s$ plates indicate that increasing the cutout size can cause a buckling mode shape change to occur in a plate. For example, the $[90_{10}]_s$ plate without a cutout buckled into a mode that consisted of one-half wave normal to the loading direction and two half-waves in the loading direction, whereas the corresponding plate with d/W = 0.21 buckled into a mode that consisted of one-half wave in each direction. Moreover, the results show that a cutout size can exist for which a modal interaction occurs at the onset of buckling. Specifically, the $[90_{10}]_s$ plate with d/W = 0.11 exhibited an interaction between the mode shapes of the corresponding plates with d/W = 0 and d/W = 0.21 (see figure 10). None of the other 39 plates tested exhibited modal interaction at the onset of buckling.

Insight into the behavior of the plates with cutouts tested can be obtained by examining the buckling behavior of rectangular orthotropic plates that are simply supported on the unloaded edges, in accordance with the test fixture used in the experimental study. The standard plot of buckling coefficient K versus plate aspect ratio L/W found in most text books on stability of plates is composed of a series of curves, referred to as festooned curves, that intersect at cusps. Two examples are shown in figure 11. Each independent curve between cusps represents a specific buckling mode for a certain group of plate aspect ratios. As the plate aspect ratio increases past a certain value, the number of longitudinal half-waves in the buckling mode changes. Furthermore, at the cusps, a unique buckling mode is indeterminant, since two distinct modes possess the same buckling load.

The location of these cusps is directly related to buckling behavior of the corresponding infinitely long plate. Analysis shows that the minimum points on the festooned curves occur at integer multiples of the aspect

ratio of the repetitive buckle mode of the infinitely long plate. For other aspect ratios, the plate buckles at a higher load. This relationship accounts for the festooned nature of the buckling load versus plate aspect ratio curves. The particular value of the aspect ratio of the buckling mode shape of the infinitely long plate is directly related to the inplane stresses acting in the plate, the boundary conditions acting on the unloaded edges, and the plate bending orthotropy. For the simply supported $[90_{10}]_s$ and $[0_{10}]_s$ plates without cutouts investigated in the present study, the aspect ratios of the buckling mode of infinitely long $[90_{10}]_s$ and $[0_{10}]_s$ plates are approximately 0.54 and 1.85, respectively. Thus, minimum points and cusps in a festooned curve plot of buckling coefficient versus plate aspect ratio are more closely spaced for $[90_{10}]_s$ plates than for $[0_{10}]_s$ plates. The close spacing of the cusps of the festooned curves of the $[90_{10}]_s$ plates, and the close proximity of the first cusp to the unit plate aspect ratio (see figure 11 for d/W = 0), indicates that a $[90_{10}]_s$ square plate is more likely to change buckle mode shape when a small perturbation in the buckle mode aspect ratio occurs, than the other square plates investigated herein.

In a $[90_{10}]_s$ plate with d/W = 0.11, the cutout causes redistribution of the inplane prebuckling stresses and causes a decrease in bending stiffness in the central region of the plate. The decrease in bending stiffness results from the fact that material has been removed from the plate, and from the fact that a free interior boundary is present. These effects (inplane and bending) associated with the cutout result in perturbing the aspect ratio of the buckle (or buckles) forming the mode shape and effectively shift the festooned curves until the first cusp is at a plate aspect ratio of one, as indicated by the dashed line in figure 11. As the cutout size increases, the associated festooned curves shift more until the first cusp occurs at a plate aspect ratio significantly larger than one. This observation accounts for the fact that the $[90_{10}]_s$ plates with d/W > 0.11 had buckle modes that consisted of one-half wave in each direction.

Analysis indicates that the other plates investigated in this study all possess festooned curves in which the first cusp, corresponding to a change in buckle pattern from one longitudinal half-wave to two half-waves, occurs at a plate aspect ratio substantially larger than one. Specifically, the first cusp for these plates occurs at aspect ratios far enough removed from a value of one such that perturbations in the aspect ratio of the buckle mode due to cutout sizes as big as d/W = 0.66 do not cause a change in mode shape or a modal interaction at the onset of buckling. This observation accounts for the fact that the other 39 plates tested buckled into distinct mode shapes that consisted of one half-wave in each direction, for the full range of cutout sizes. Analytical results supporting this discussion can be found in references 1 and 3 for specially-orthotropic plates and symmetrically laminated angle-ply plates with cutouts, respectively. The results reported in these references and results used to support the previous discussion, were obtained using the computer program described in reference 12.

643

<u>Anomalous behavior</u>.- Results were obtained for the $[0_{10}]_s$ plate with d/W = 0.32 that indicated buckling behavior atypical of orthotropic plates. More specifically, the results presented in figures 4 and 5 for this plate indicate that the plate deforms initially in the direction of its geometric imperfection shape and then rapidly buckles into a similar mode shape in the opposite direction. During the testing of this plate, a snapping sound was heard when the plate buckled. This observation is supported by the jump in the corresponding load versus end-shortening curve shown in figure 4, and by the discontinuity in the corresponding load versus transverse deflection curve shown in figure 5. These results indicate that the onset of buckling occurred in a manner similar to a change in buckle pattern.

For this particular test specimen, it was found that the loaded edges of the specimen had not been properly machined which resulted in an eccentric loading. The eccentricity produced bending moments that increased in magnitude as the applied loading increased, and acted to move the plate in the direction opposite to the geometric imperfection. Buckling occurred when these bending moments overcame the tendency of the plate to deform in the direction of its geometric imperfection.

Similar behavior was exhibited by the $[(0/90)_5]_s$ plate with d/W = 0.66. The load versus transverse deflection curve shown in figure 9 for this case did not have a sharp discontinuity like that shown in figure 5 for the $[0_{10}]_s$ plate with d/W = 0.32. However, a jump is present in the load versus end-shortening curve shown in figure 8 for the $[(0/90)_5]_s$ plate with d/W = 0.66, and a snapping sound was heard during the test when the plate buckled.

The load versus transverse deflection curve shown in figure 17 for $[(\pm 45)_6]_s$ plate with d/W = 0.32 indicates that the plate also deformed initially in the direction of its geometric imperfection. However, no jump in the corresponding load versus end-shortening curve (see figure 16) is present, and no snapping sound was heard when the plate buckled. The absence of these effects may be associated with the nonlinear material behavior.

In the investigation of buckling and postbuckling behavior of asymmetrically laminated plates, such as the work reported in reference 13, the inherent mechanical coupling between membrane and bending action in the plate produces out-of-plane deformations as the applied axial loading increases, in a manner similar to that associated with the load-path eccentricity previously described. The intensity of the prebuckling moments due to mechanical coupling, and the direction of the associated out-of-plane deformation, are determined by the plate stacking sequence. When the prebuckling moments produce out-of-plane deformations that act in a direction opposite to the plate's geometric imperfection, a snap-through buckling similar to that exhibited by the $[0_{10}]_s$ plate with d/W = 0.32 may occur. In such cases it is important to understand the two mechanisms, mechanical coupling (material induced eccentricity) and edge effects (geometry induced eccentricity), responsible for the plate behavior.

CONCLUDING REMARKS

An experimental study of the postbuckling behavior of square compression-loaded graphite-epoxy plates and isotropic plates with central circular cutouts has been presented. A wide range of cutout sizes and a broad spectrum of plate orthotropy has been investigated. Specifically, results have been presented for unidirectional $[0_{10}]_s$ and $[90_{10}]_s$ plates, $[(0/90)_5]_s$ plates, and for aluminum plates. Results have also been presented for $[(\pm\theta)_6]_s$ angle-ply plates for values of $\theta = 30$, 45, and 60 degrees. The circular cutout-diameter-to-plate-width ratios ranged from 0 to 0.66.

Experimental results have been presented in the paper that indicate that the change in axial stiffness of a plate at buckling is strongly dependent upon cutout size and plate orthotropy. The presence of a cutout gives rise to an internal load distribution that changes, sometimes dramatically, as a function of cutout size coupled with the plate orthotropy. Moreover, results that have been presented indicate that the reduction in prebuckling axial stiffness, associated with a cutout, is not generally equal to the reduction in cross-sectional area of the plate at the net section.

In the buckled state, the role of orthotropy increases to include bending in addition to membrane orthotropy. Experimental results have been presented that indicate that most of the plates tested with cutouts exhibit less postbuckling stiffness than the corresponding plate without a cutout, and that the amount of postbuckling stiffness generally decreases with increasing cutout size. However, the experimental results also indicate that some of the highly orthotropic plates with cutouts exhibit higher postbuckling stiffness than the corresponding plate without a cutout. In all these cases, it has been found that the cutout size and plate orthotropy dramatically affect the distribution of the out-of-plane displacement field that occurs in a buckled plate. These results suggest that the complex interaction of cutout size and orthotropy on the internal load distribution in plates needs further investigation. These results also suggest that the cutout size and the stacking sequence of a composite plate could be tailored to optimize postbuckling stiffness.

Experimental results have been presented in the paper that also indicate that a cutout can influence modal interaction in a plate. Specifically, results have been presented that show a plate with a relatively small cutout buckling at a higher load than the corresponding plate without a cutout, due to modal interaction. Other results have been presented that indicate the presence of nonlinear prebuckling deformations, due to material nonlinearity, in the angle-ply plates with $\theta = 45$ and 60 degrees. The nonlinear prebuckling deformations are more pronounced in the plates with $\theta = 45$ degrees and become even more pronounced as the cutout size increases. An important finding of this experimental study is that plates with large radius cutouts do exhibit some postbuckling strength.

REFERENCES

1. Nemeth, M. P.: Buckling Behavior of Orthotropic Composite Plates With
    Centrally Located Cutouts. Ph.D. Diss., Virginia Polytech. Inst. &
    State Univ., May 1983.

2. Nemeth, M. P.; Stein, M.; and Johnson, E. R.: An Approximate Buckling
    Analysis for Rectangular Orthotropic Plates With Centrally Located
    Cutouts. NASA Technical Paper 2528, February, 1986.

3. Nemeth, M. P.: Buckling Behavior of Compression-Loaded Symmetrically
    Laminated Angle-Ply Plates with Holes. AIAA Journal, Vol. 26, No. 3,
    March 1988, pp. 330-336.

4. Yu, W. W. and Davis, C. S.: Buckling Behavior and Post-Buckling
    Strength of Perforated Stiffened Compression Elements. Proceedings of
    the First Speciality Conference on Cold-Formed Steel Structures,
    University of Missouri-Rolla, Rolla, Mo., August 19-20, 1971.

5. Martin, J.: Buckling and Postbuckling of Laminated Composite Square
    Plates with Reinforced Central Circular Holes. Ph.D. Diss., Case
    Western Reserve University, January 1972.

6. Yu, W. W. and Davis, C. S.: Cold-Formed Steel Members with Perforated
    Elements. ASCE Journal of the Structural Division, ST10, October 1973,
    pp. 2061-2077.

7. Ritchie, D. and Rhodes, J.: Buckling and Post-buckling Behavior of
    Plates with Holes. Aeronautical Quarterly, Vol. 26, 1975, pp. 281-296.

8. Starnes, J. H., Jr. and Rouse, M.: Postbuckling and Failure
    Characteristics of Selected Flat Rectangular Graphite-Epoxy Plates
    Loaded in Compression. AIAA Paper No. 81-0543, Presented at the
    AIAA/ASME/ASCE/AHS 22nd Structures, Structural Dynamics, and Materials
    Conference, Atlanta, Georgia, April 6-8, 1981.

9. Roberts, T. M. and Azizian, Z. G.: Strength of Perforated Plates
    Subjected to In-plane Loading. Thin-Walled Structures, Vol. 2, 1984,
    pp. 153-164.

10. Narayanan, R. and Chow, F. Y.: Ultimate Capacity of Uniaxially
    Compressed Perforated Plates. Thin-Walled Structures, Vol. 2, 1984, pp.
    241-264.

11. VandenBrink, D. J. and Kamat, M. P.: Post-Buckling Response of
    Isotropic and Laminated Composite Square Plates with Circular Holes.
    Proceedings of the Fifth International Conference on Composite
    Materials, San Diego, California, July 29 - August 1, 1985, pp. 1393-
    1409.

12. Nemeth, M. P.: A Buckling Analysis for Rectangular Orthotropic Plates
    With Centrally Located Cutouts. NASA Technical Memorandum 86263,
    December, 1984.

13. Jensen, D. W. and Lagace, P. A.: influence of Mechanical Coupling on the Buckling and Postbuckling of Anisotropic Plates. AIAA Journal, Vol. 26, No. 10, October 1988, pp. 1269-1277.

Table I. Experimental buckling loads, prebuckling stiffnesses, and initial postbuckling stiffnesses for isotropic plates.

[All plates buckled into one half-wave in each coordinate direction]

Specimen	Ratio of cutout diameter to plate width, d/W [a]	Cutout diameter, in.	Buckling load, lb	Prebuckling stiffness, lb/in.	Initial Postbuckling stiffness, lb/in.
A1	0	0	1872	541,139	329,201
A2	0.1	0.95	1828	477,341	309,093
A3	.2	1.90	1736	464,290	301,479
A4	.3	2.85	1656	426,445	277,715
A5	.4	3.80	1808	390,573	244,838
A6	.5	4.75	2007	326,186	204,760
A7	.6	5.70	1995	312,527	188,885

[a] Width equals distance between test fixture supports (9.5 in.).

Table II. Experimental buckling loads, prebuckling stiffnesses, and initial postbuckling stiffnesses for $[0_{10}]_s$ laminates.

[All plates buckled into one half-wave in each coordinate direction]

Specimen	Ratio of cutout diameter to plate width, d/W[a]	Cutout diameter, in.	Buckling load, lb	Prebuckling stiffness, lb/in.	Initial Postbuckling stiffness, lb/in.
B1	0	0	9256	2,020,460	481,792
B2	0.11	1.00	8975	1,473,710	487,362
B3	.21	2.00	8767	1,194,500	458,587
B4	.32	3.00	7689	1,266,500	494,835
B5	.42	4.00	6842	724,460	394,351
B6	.60	5.70	6464	641,878	376,653
B7	.66	6.25	6158	526,781	365,660

[a] Width equals distance between test fixture supports (9.5 in.).

Table III. Experimental buckling loads, prebuckling stiffnesses, and initial postbuckling stiffnesses for $[90_{10}]_s$ laminates.

[All plates buckled into one half-wave in each coordinate direction unless otherwise noted]

Specimen	Ratio of cutout diameter to plate width, d/W[a]	Cutout diameter, in.	Buckling load, lb	Prebuckling stiffness, lb/in.	Initial Postbuckling stiffness, lb/in.
C1	0	0	2292[b]	133,066	63,445
C2	0.11	1.00	2494[c]	132,428	61,114
C3	.21	2.00	2041	120,639	86,517
C4	.32	3.00	1690	125,131	79,401
C5	.42	4.00	1607	154,529	98,959
C6	.66	6.25	1868	60,955	36,444

[a] Width equals distance between test fixture supports (9.5 in.).
[b] Mode shape consists of two half-waves in the axial direction and one half-wave in the other direction.
[c] Mode shape influenced by modal interaction (see figure 10).

Table IV. Experimental buckling loads, prebuckling stiffnesses, and initial postbuckling stiffnesses for $[(0/90)_5]_s$ laminates.

[All plates buckled into one half-wave in each coordinate direction]

Specimen	Ratio of cutout diameter to plate width, d/W[a]	Cutout diameter, in.	Buckling load, lb	Prebuckling stiffness, lb/in.	Initial Postbuckling stiffness, lb/in.
D1	0	0	6950	955,427	447,631
D2	0.11	1.00	6729	646,670	397,654
D3	.21	2.00	6407	586,874	391,869
D4	.32	3.00	6207	532,187	368,960
D5	.42	4.00	6510	535,595	330,118
D6	.60	5.70	6467	391,619	244,138
D7	.66	6.25	6581	370,703	220,011

[a] Width equals distance between test fixture supports (9.5 in.).

Table VII. Experimental buckling loads, prebuckling stiffnesses, and initial postbuckling stiffnesses for $[(\pm45)_6]_s$ laminates.

[All plates buckled into one half-wave in each direction]

Specimen	Ratio of cutout diameter to plate width, d/W [a]	Cutout diameter, in.	Buckling load [b], lb	Prebuckling stiffness, lb/in.	Initial Postbuckling stiffness, lb/in.
F1	0	0	9651	388,964	174,152
F2	0.11	1.00	9188	317,706	174,016
F3	.32	3.00	8314	275,011 [c]	145,899
F4	.66	6.25	11,020	145,951 (46,155)	46,155

[a] Width equals distance between test fixture supports (9.5 in.).
[b] Buckling loads estimated from out-of-plane displacements.
[c] Tangent stiffness at the bifurcation point.

Table VIII. Analytic buckling loads, critical end-shortenings, and nominal thicknesses for plates without cutouts.

Plate Type	Buckling Load P^0_{cr}, lb	Critical End-shortening Δ^0_{cr}, in.	Nominal Thickness H, in.
Aluminum	1773	0.002740	0.0647
$[0_{10}]_s$	9272	.004556	.1100
$[90_{10}]_s$	2473	.014050	.1100
$[(0/90)_5]_s$	6544	.005875	.1100
$[(\pm30)_6]_s$	9898	.011759	.1176
$[(\pm45)_6]_s$	10962	.029268	.1300
$[(\pm60)_6]_s$	5944	.027752	.1176

Table XI. Change in initial postbuckling stiffness due to cutout.

CHANGE IN POSTBUCKLING STIFFNESS [a], %							
	Isotropic Plates	Specially Orthotropic Plates			Symmetrically Laminated Angle-Ply Plates		
d/W[b]		$[0_{10}]_s$	$[90_{10}]_s$	$[(0/90)_5]_s$	$[(\pm30)_6]_s$	$[(\pm45)_6]_s$	$[(\pm60)_6]_s$
0	0	0	0	0	0	0	0
.10	-6	-	-	-	-	-	-
.11	-	+1	-4	-11	+4	-1	-1
.20	-8	-	-	-	-	-	-
.21	-	-5	+36	-12	-	-	-
.30	-16	-	-	-	-	-	-
.32	-	+3	+25	-18	+3	-16	-22
.40	-26	-	-	-	-	-	-
.42	-	-18	+56	-26	-	-	-
.50	-38	-	-	-	-	-	-
.60	-43	-22	-	-45	-16	-	-
.66	-	-24	-43	-51	-27	-73	-74

[a] Change in stiffness is with respect to the corresponding d/W=0 case. Negative values indicate reductions.
[b] Cutout-diameter-to-plate-width ratio (W=9.5 in.)

Table XII. Reduction in axial stiffness in going from prebuckling state to initial buckled state.

REDUCTION IN AXIAL STIFFNESS DUE TO BUCKLING, %							
	Isotropic Plates	Specially-Orthotropic Plates			Symmetrically-Laminated Angle-Ply Plates		
d/W[a]		$[0_{10}]_s$	$[90_{10}]_s$	$[(0/90)_5]_s$	$[(\pm30)_6]_s$	$[(\pm45)_6]_s$	$[(\pm60)_6]_s$
0	39	76	52	53	66	55	39
.10	35	-	-	-	-	-	-
.11	-	67	54	39	64	45	33
.20	35	-	-	-	-	-	-
.21	-	62	28	33	60	47	36
.30	35	-	-	-	-	-	-
.32	-	61	37	31	-	-	-
.40	37	-	-	-	-	-	-
.42	-	46	36	38	-	-	-
.50	37	-	-	-	-	-	-
.60	40	41	-	38	48	-	-
.66	-	31	40	41	46	68[b]	60[b]

[a] Cutout-diameter-to-plate-width ratio
[b] Includes material nonlinearity.
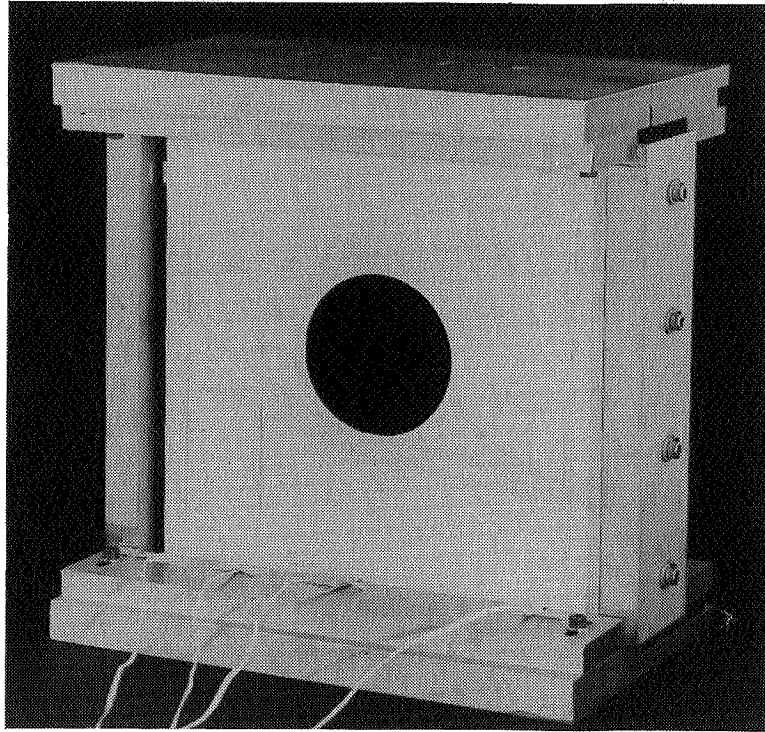
Figure 1.   Specimen mounted in test fixture.
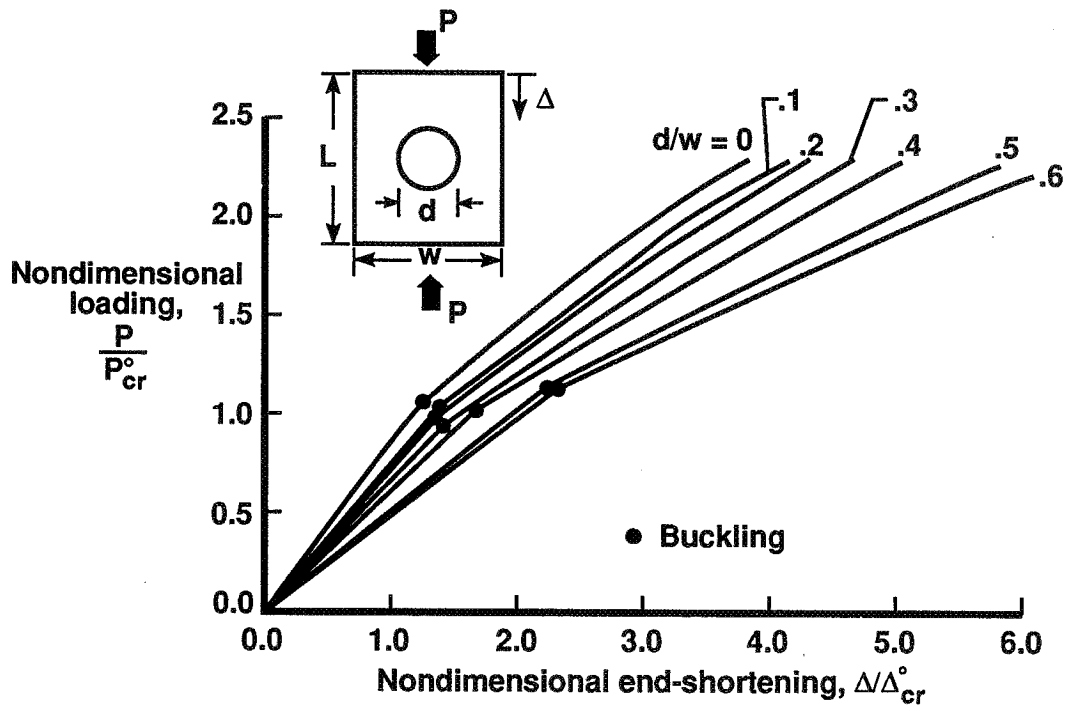
Figure 2.   Nondimensional load versus end-shortening experimental results
for isotropic square plates with central circular cutouts.
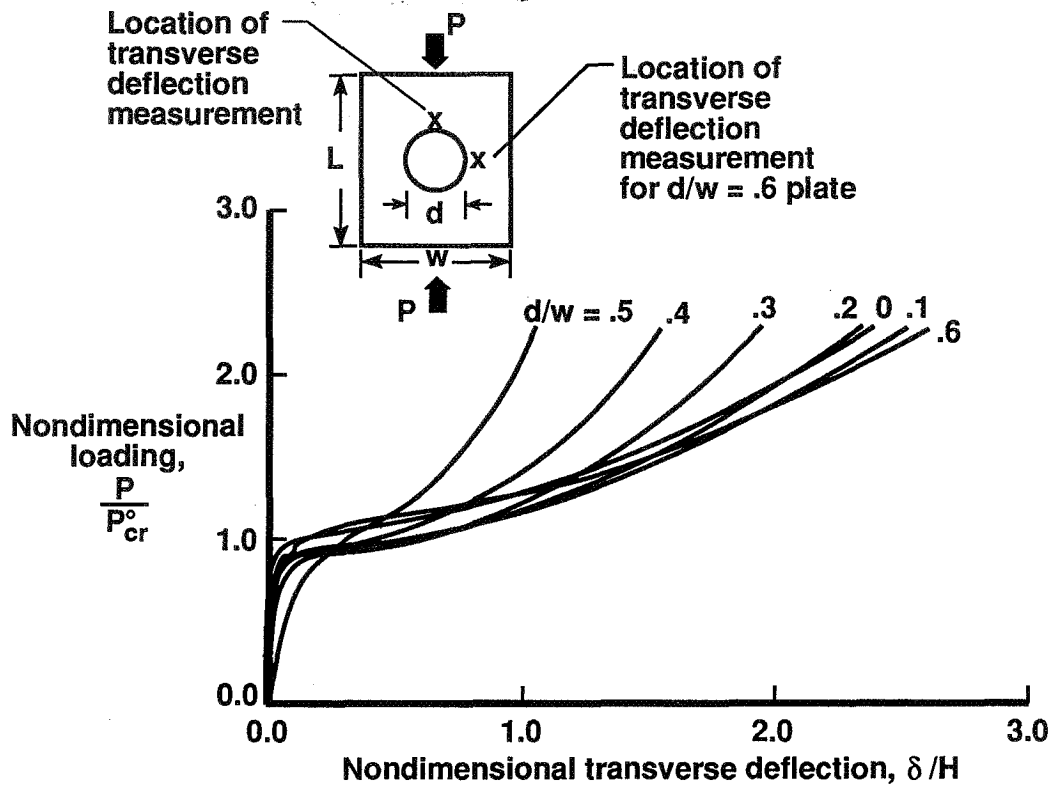
Figure 3. Nondimensional load versus transverse deflection experimental results for isotropic square plates with central circular cutouts.
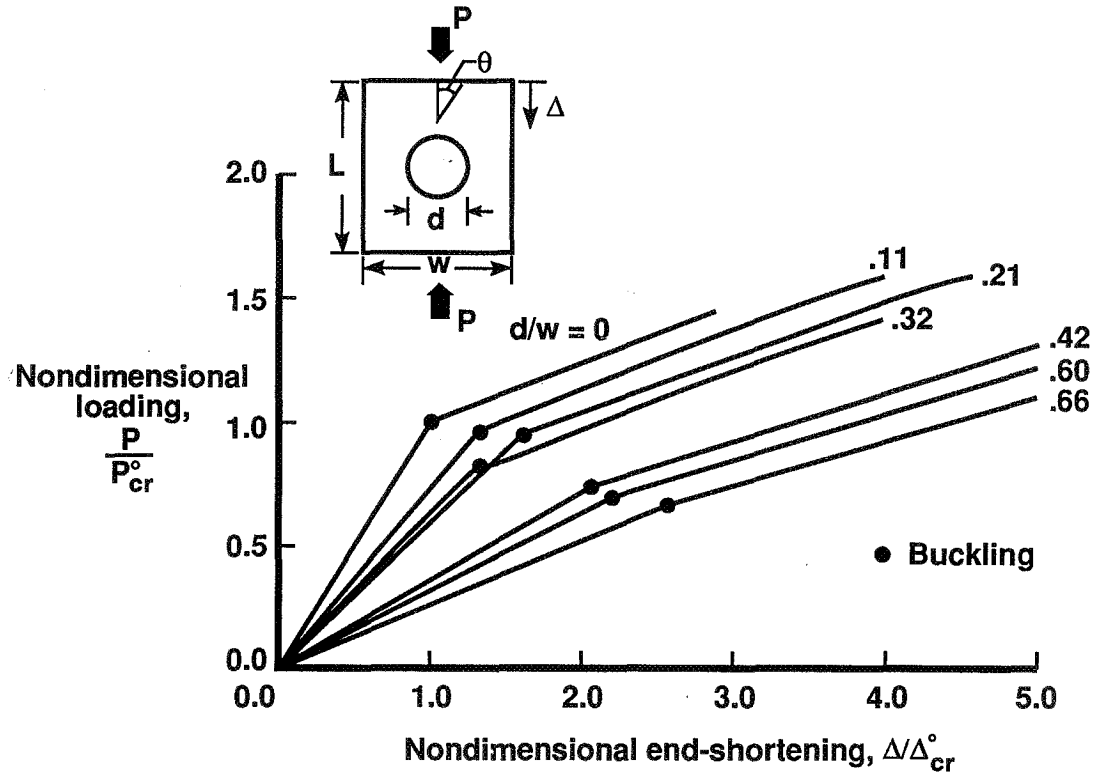
Figure 4. Nondimensional load versus end-shortening experimental results for $[0_{10}]_s$ square plates with central circular cutouts.
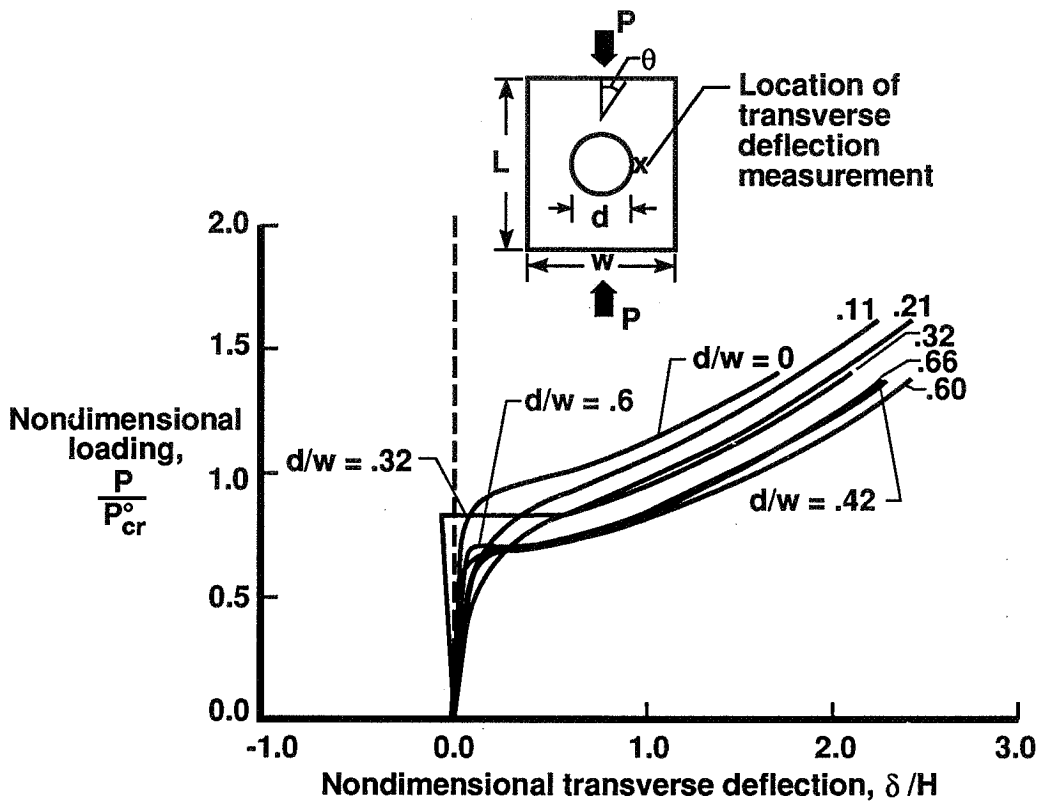
Figure 5. Nondimensional load versus transverse deflection experimental results for $[0_{10}]_s$ square plates with central circular cutouts.
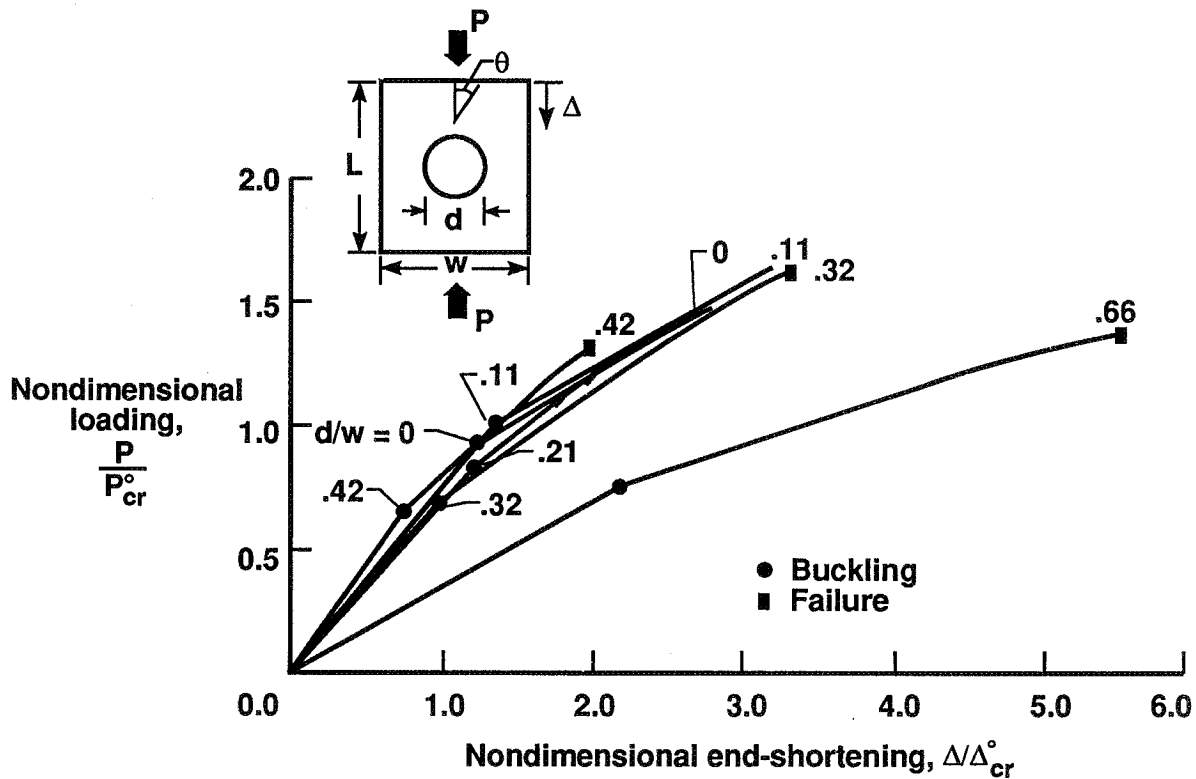
Figure 6. Nondimensional load versus end-shortening experimental results for $[90_{10}]_s$ square plates with central circular cutouts.
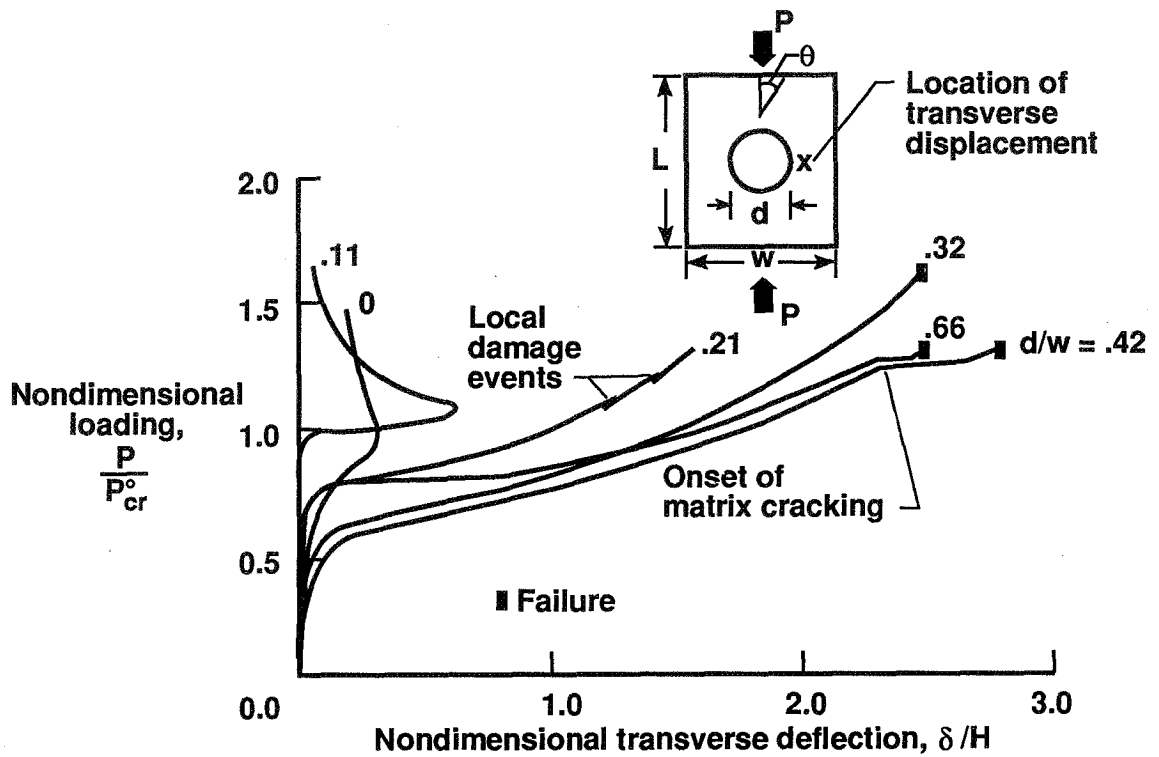
Figure 7. Nondimensional load versus transverse deflection experimental results for $[90_{10}]_s$ square plates with central circular cutouts.
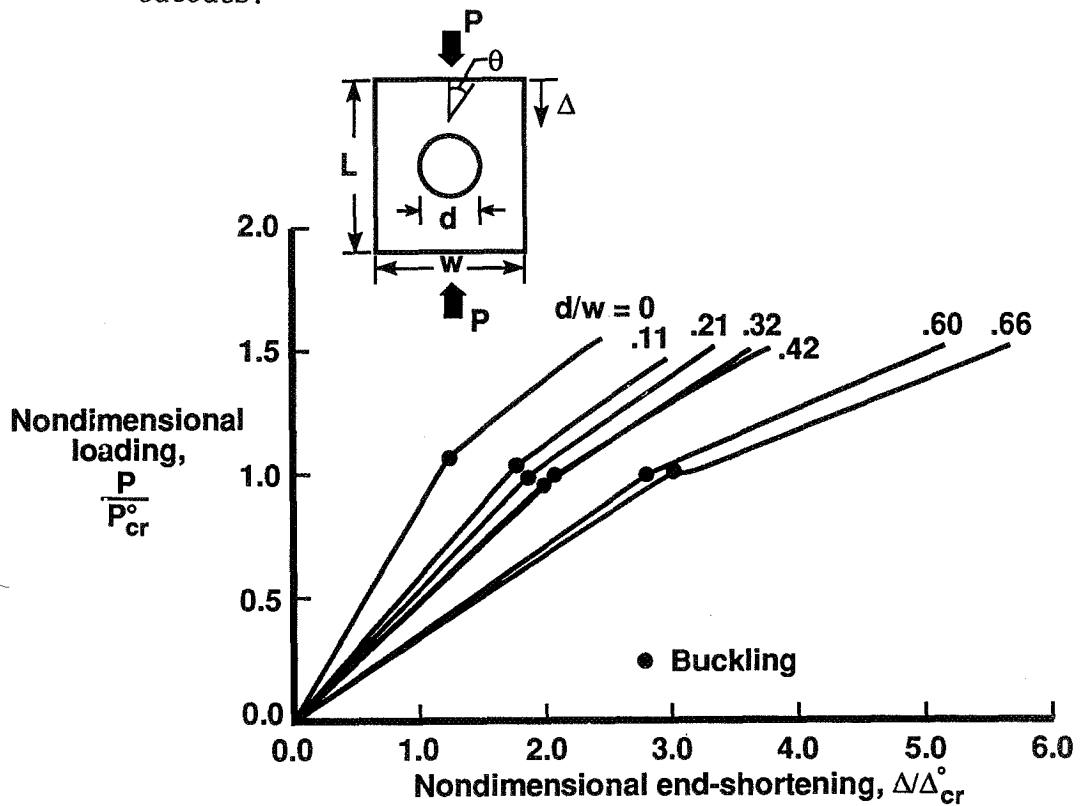
Figure 8. Nondimensional load versus end-shortening experimental results for $[(0/90)_5]_s$ square plates with central circular cutouts.
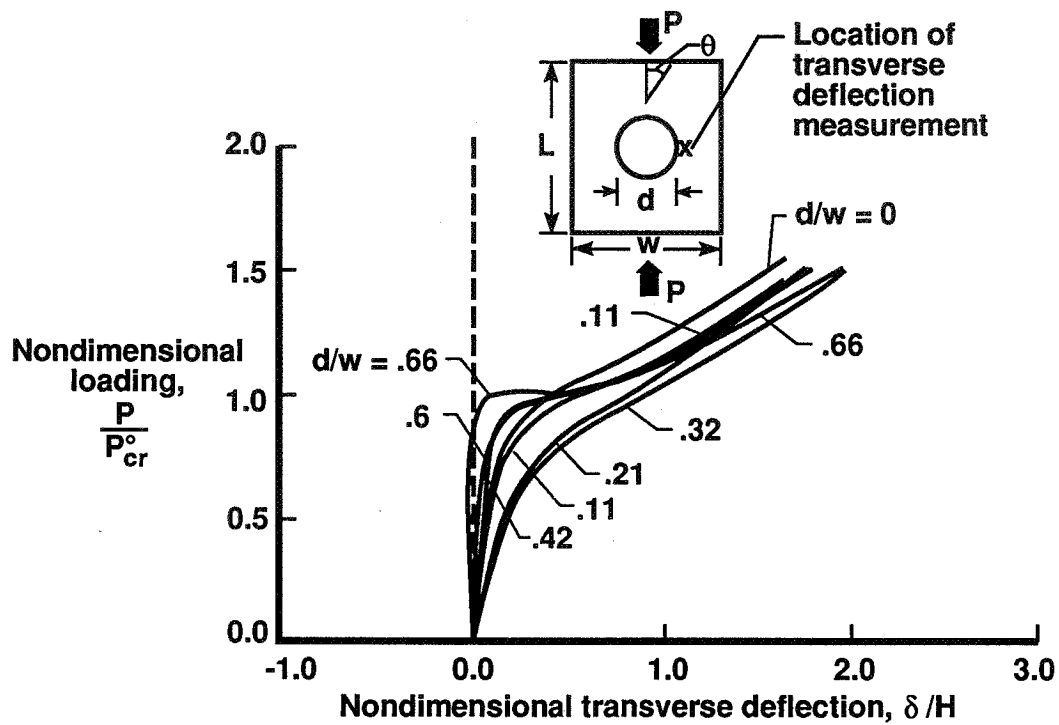
Figure 9. Nondimensional load versus transverse deflection experimental results for $[(0/90)_5]_s$ square plates with central circular cutouts.
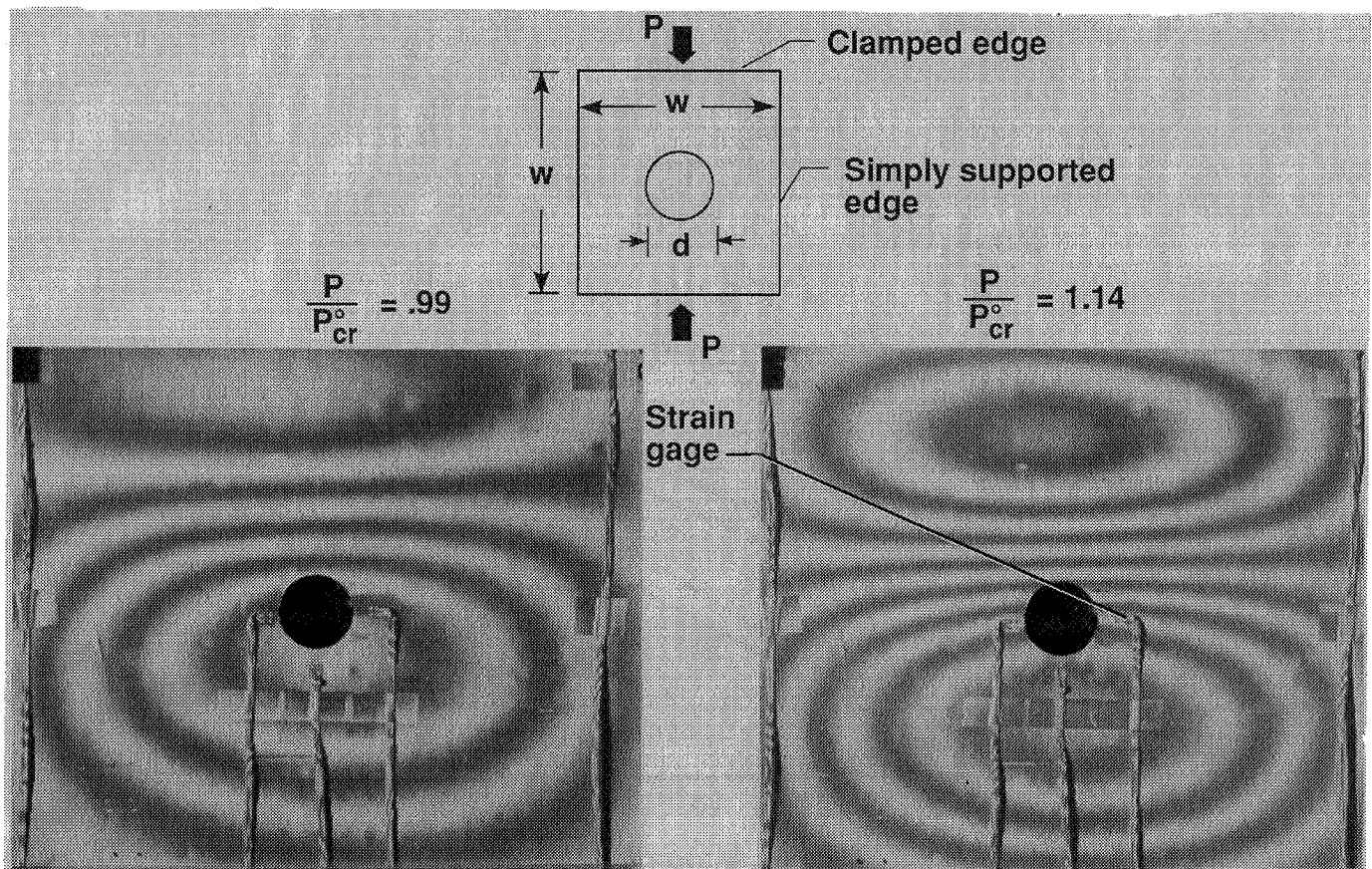
Figure 10. Interacting mode shapes for $[90_{10}]_s$ square plates with d/W = 0.11.
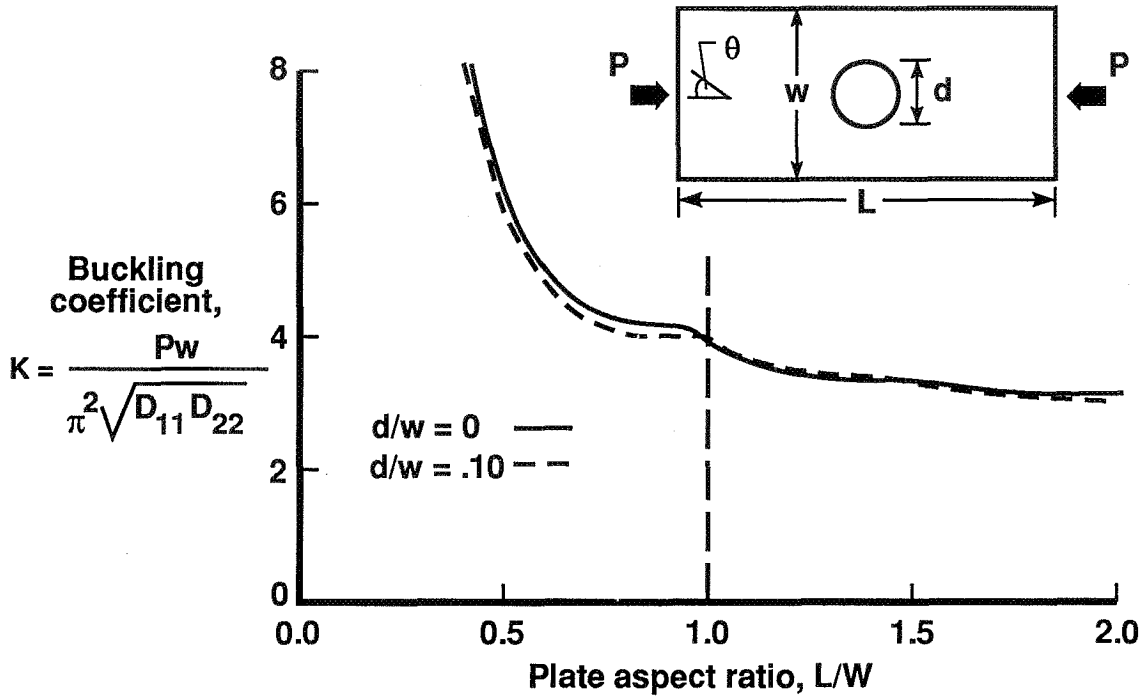
Figure 11. Buckling coefficients for $[90_{10}]_s$ rectangular plates with d/W = 0 and 0.10 (loaded edges clamped and unloaded edges simply supported).
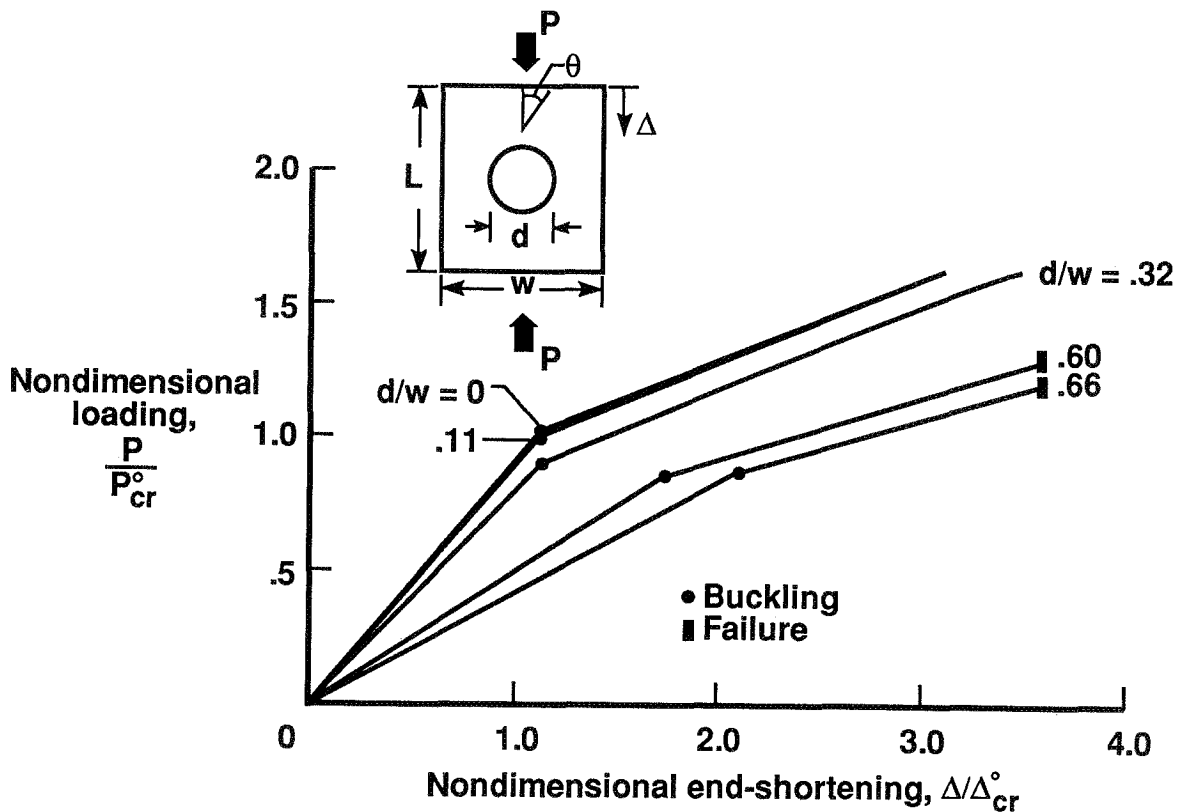
Figure 12. Nondimensional load versus end-shortening experimental results for $[(\pm30)_6]_s$ square plates with central circular cutouts.
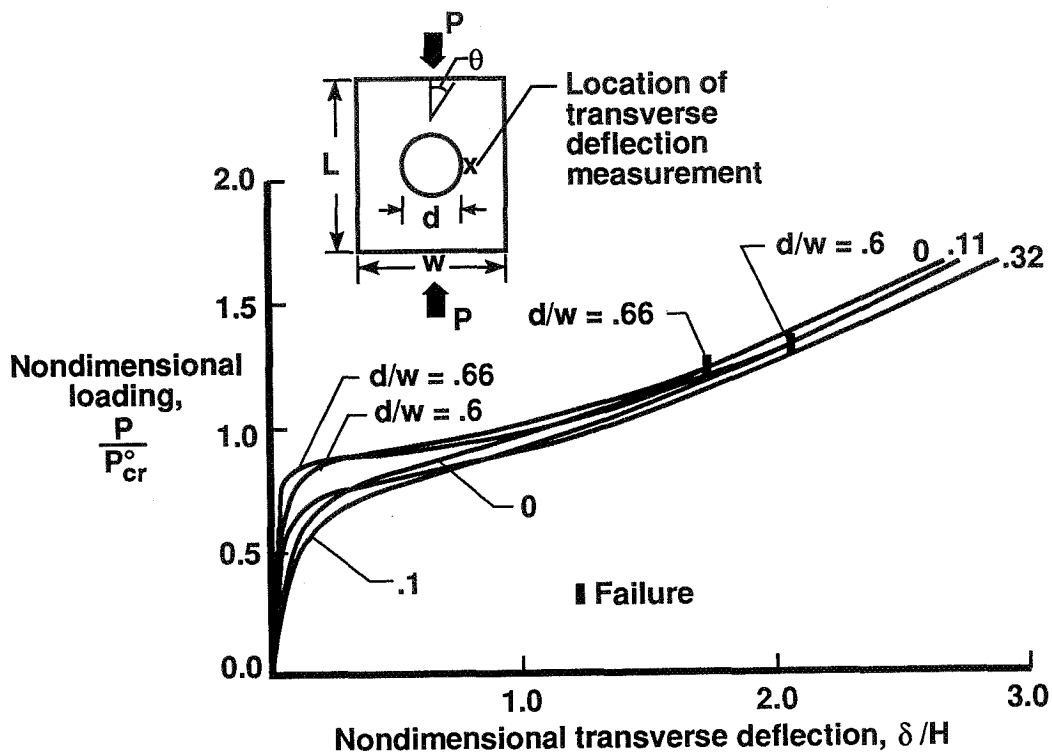
Figure 13. Nondimensional load versus transverse deflection experimental results for $[(\pm 30)_6]_s$ square plates with central circular cutouts.
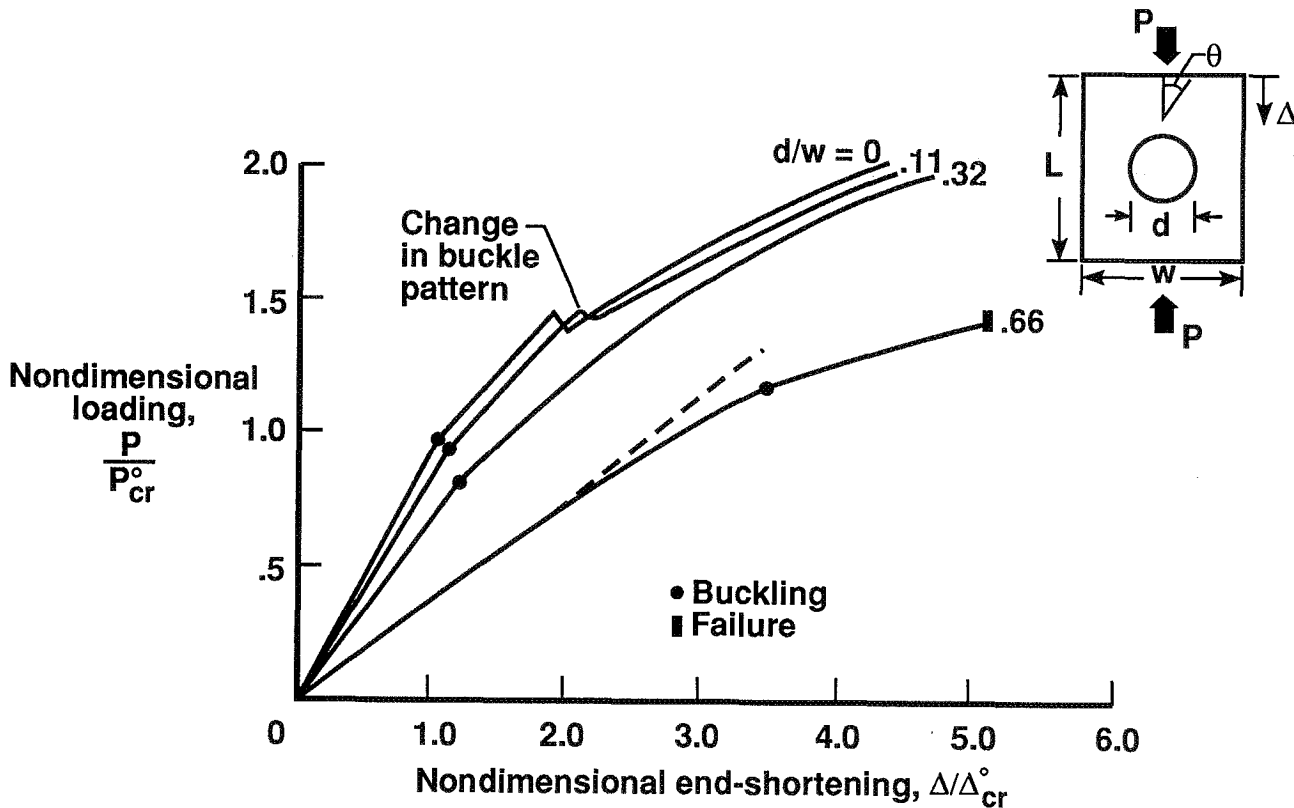
Figure 14. Nondimensional load versus end-shortening experimental results for $[(\pm 60)_6]_s$ square plates with central circular cutouts.
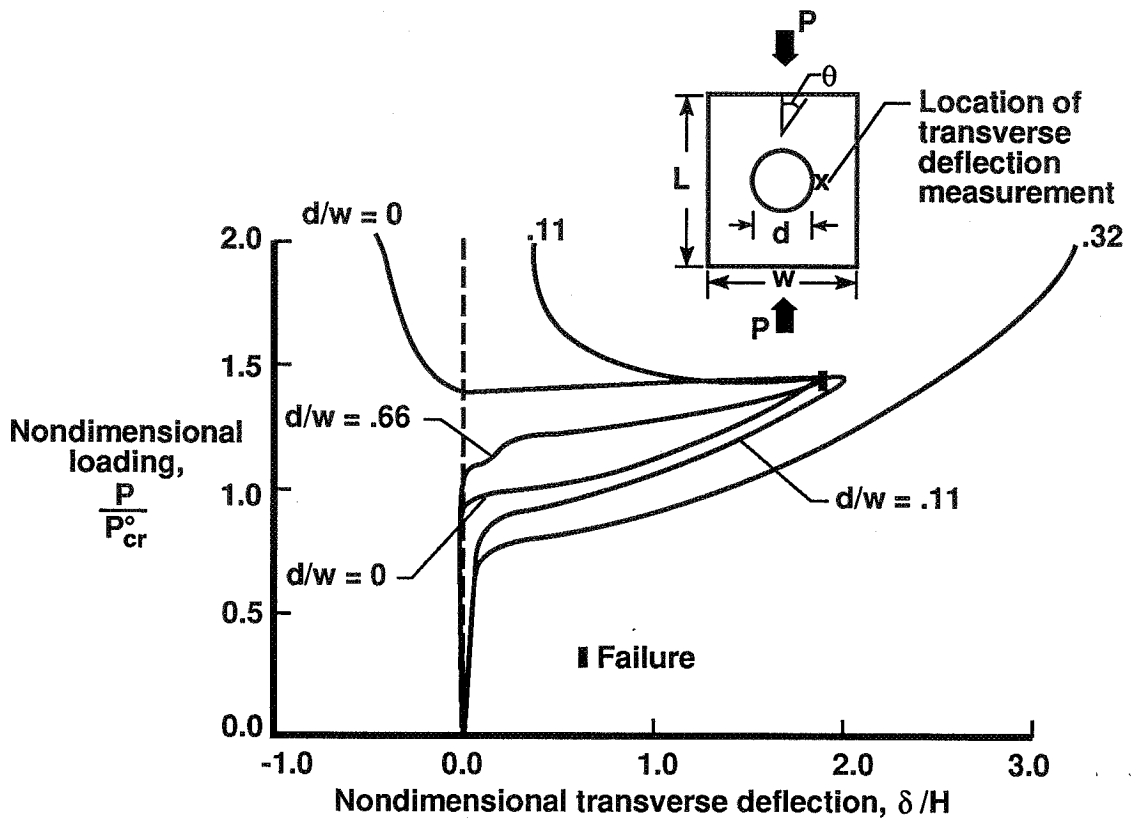
Figure 15. Nondimensional load versus transverse deflection experimental results for $[(\pm 60)_6]_s$ square plates with central circular cutouts.
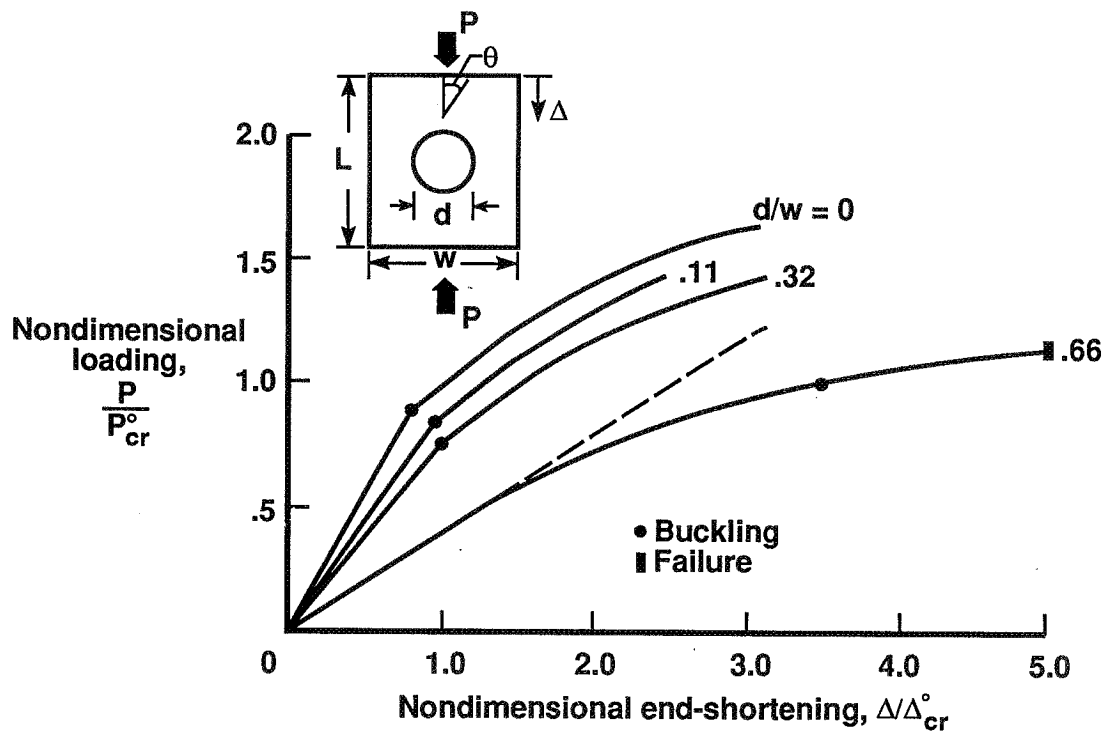
Figure 16. Nondimensional load versus end-shortening experimental results for $[(\pm 45)_6]_s$ square plates with central circular cutouts.
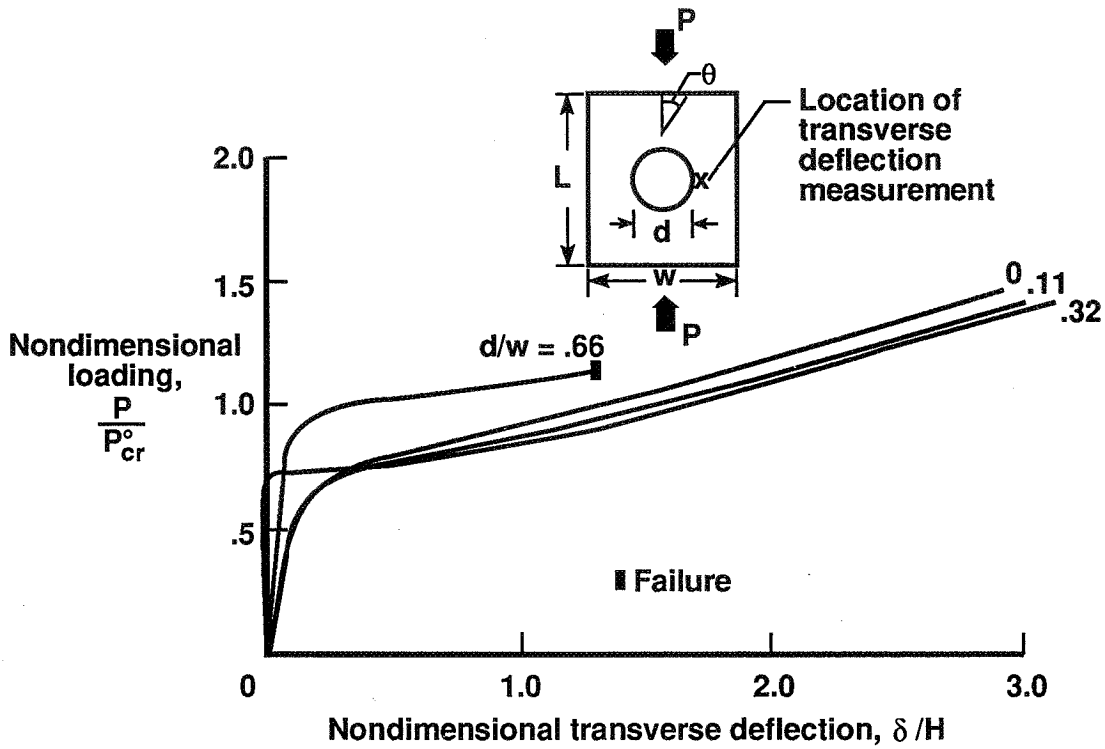
Figure 17. Nondimensional load versus transverse deflection experimental results for $[(\pm 45)_6]_s$ square plates with central circular cutouts.
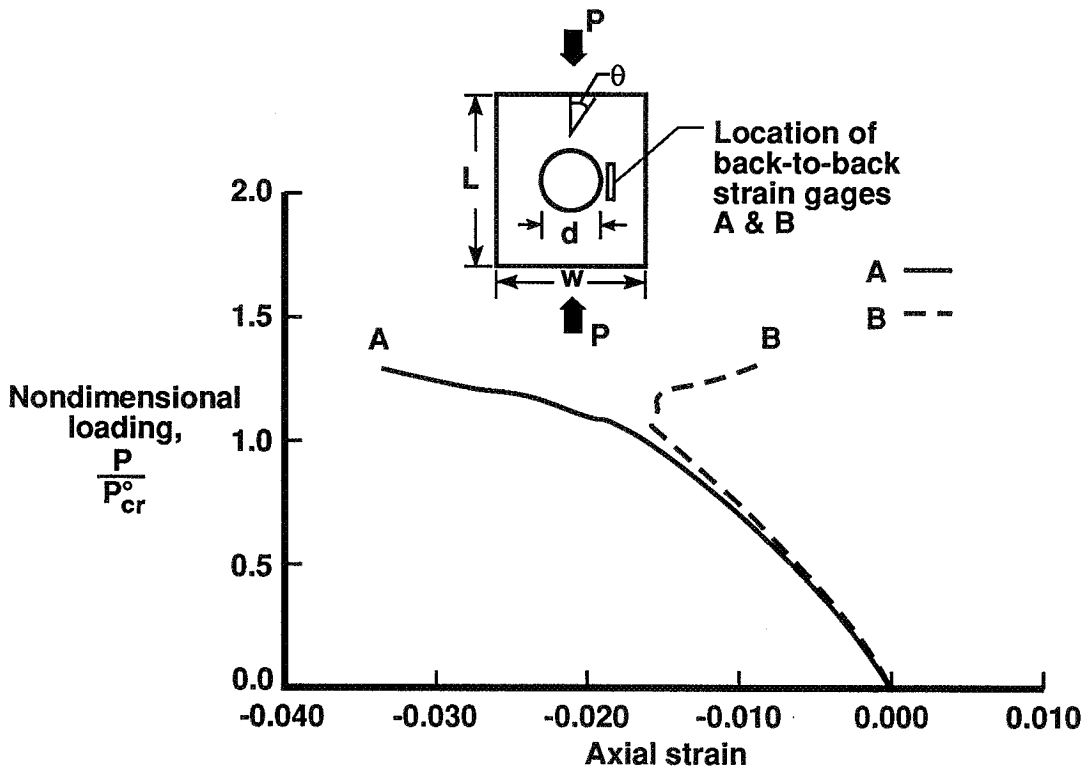
Figure 18. Strain near the cutout in the $[(\pm 60)_6]_s$ square plate with d/W = 0.66.

d/w = 0.11   P/P$^\circ_{cr}$ = 1.40   d/w = 0.42   P/P$^\circ_{cr}$ = 1.40   d/w = 0.66   P/P$^\circ_{cr}$ = 1.40
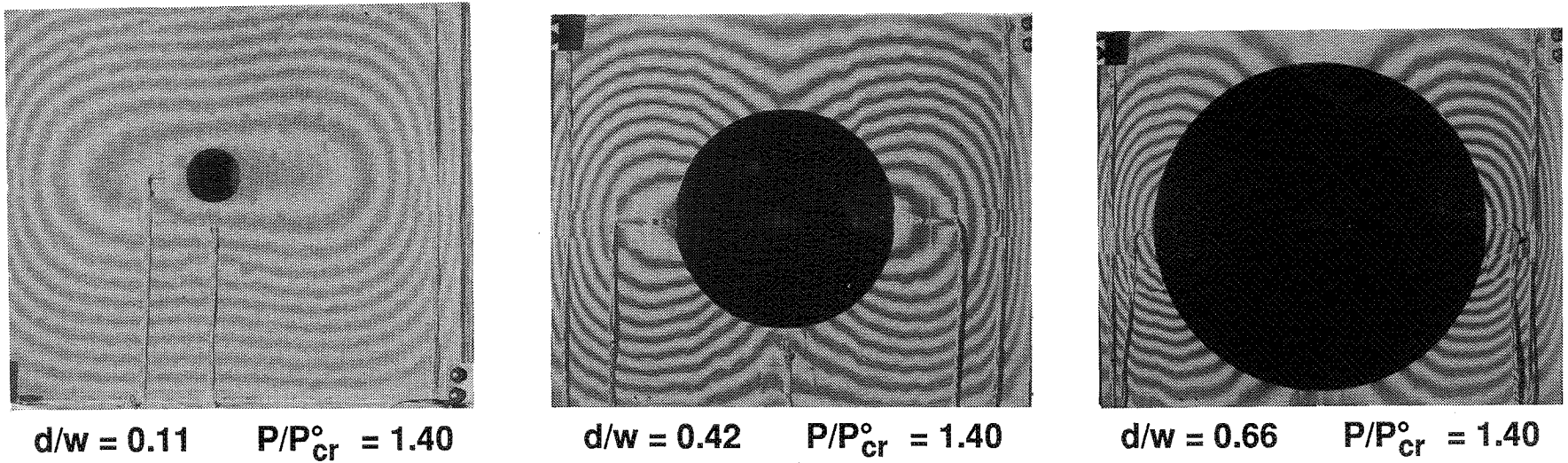
(a) Moire fringe patterns of out-of-plane displacements for $[0_{10}]_s$ plates.

d/w = 0.11   P/P$^\circ_{cr}$ = 1.53   d/w = 0.42   P/P$^\circ_{cr}$ = 1.53   d/w = 0.66   P/P$^\circ_{cr}$ = 1.53
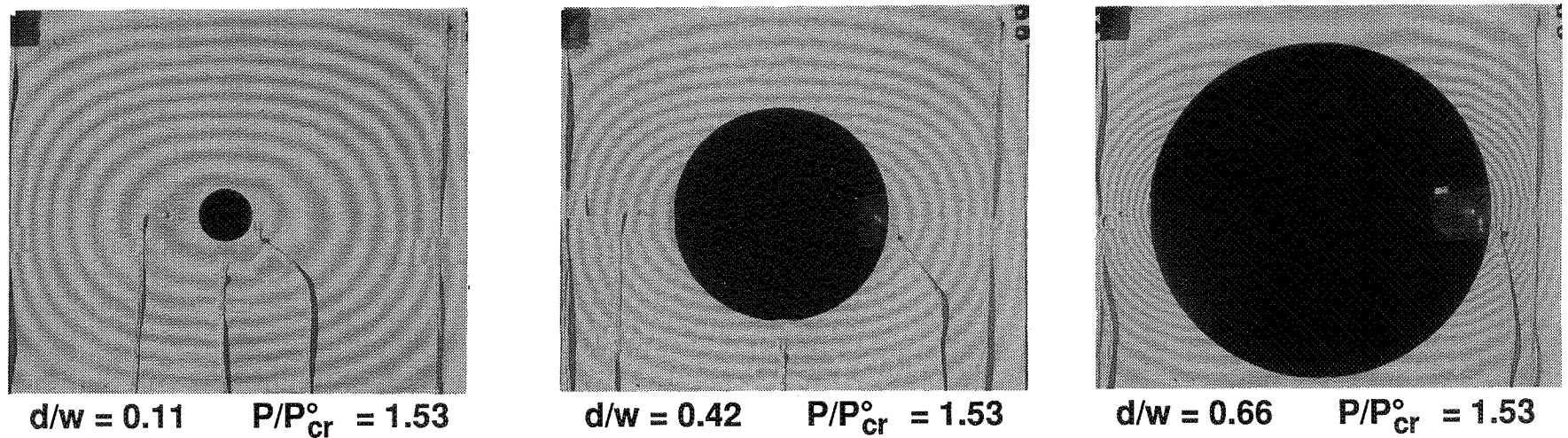
(b) Moire fringe patterns of out-of-plane displacements for $[(0/90)_5]_s$ plates.

Figure 19. Out-of-plane displacement patterns for $[0_{10}]_s$, $[(0/90)_5]_s$,
$[90_{10}]_s$, and $[(\pm60)_6]_s$ square plates with central circular
cutouts.
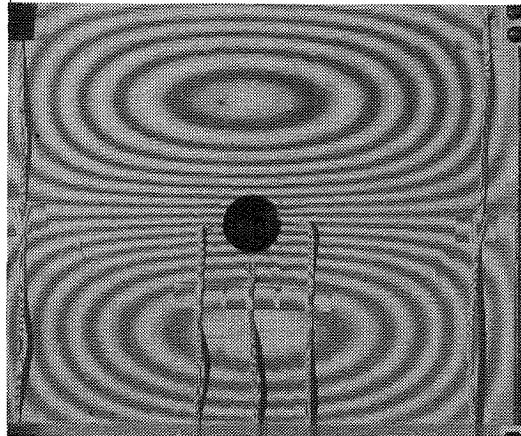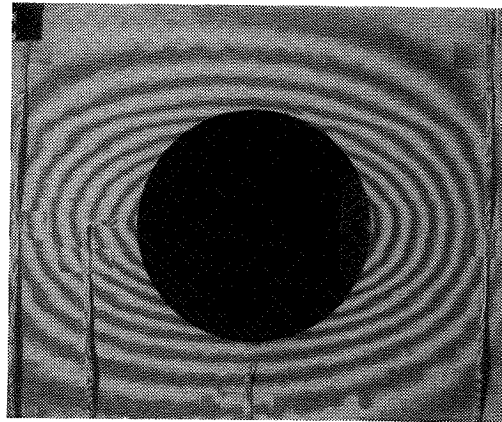
d/w = 0.11 $P/P_{cr}^\circ = 1.62$ d/w = 0.42 $P/P_{cr}^\circ = 1.21$ d/w = 0.66 $P/P_{cr}^\circ = 1.31$
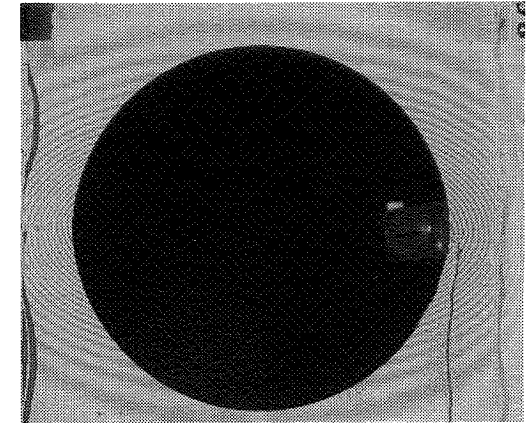
(c) Moire fringe patterns of out-of-plane displacements for $[90_{10}]_s$ plates.
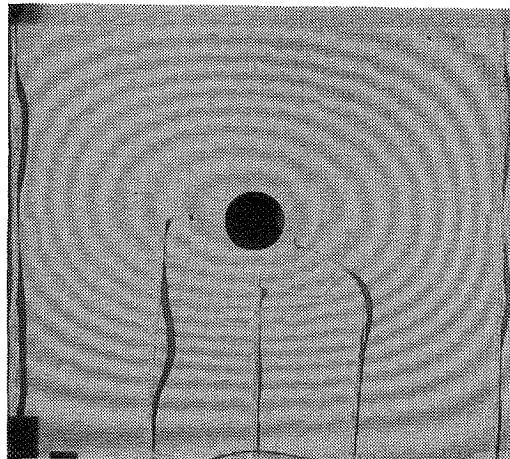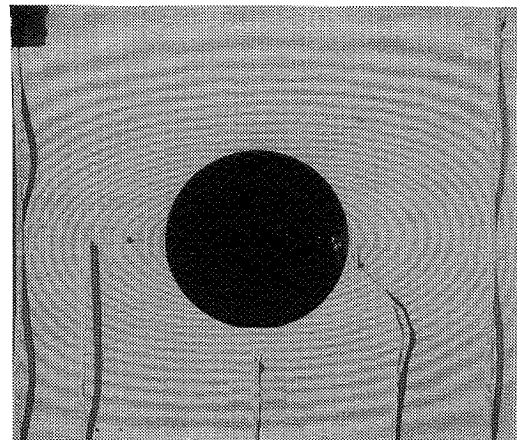
d/w = 0.11 $P/P_{cr}^\circ = 1.35$ d/w = 0.32 $P/P_{cr}^\circ = 1.68$ d/w = 0.66 $P/P_{cr}^\circ = 1.26$
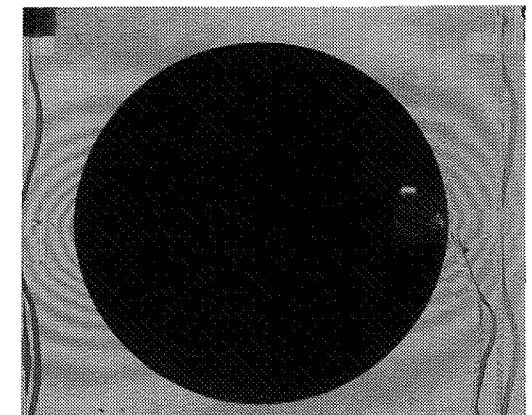
(d) Moire fringe patterns of out-of-plane displacements for $[(\pm 60)_6]_s$ plates.

Figure 19. Concluded.

A NEW APPROACH TO FIBROUS COMPOSITE LAMINATE STRENGTH PREDICTION

L. J. Hart-Smith
©Douglas Aircraft Company
McDonnell Douglas Corporation, 1989

N92-32588

P-31

ABSTRACT

A new method of predicting the strength of cross-plied fibrous composite laminates is based on expressing the classical maximum-shear-stress failure criterion for ductile metals in terms of strains. Starting with such a formulation for classical isotropic materials, the derivation is extended to orthotropic materials having a longitudinal axis of symmetry, to represent the fibers in a unidirectional composite lamina. The only modification needed to represent those same fibers with properties normalized to the lamina rather than fiber is a change in axial modulus. A mirror image is added to the strain-based "lamina" failure criterion for fiber-dominated failures to reflect the cutoffs due to the presence of orthogonal fibers. It is found that the combined failure envelope is now identical with the well-known maximum-strain failure model in the tension-tension and compression-compression quadrants but is truncated in the shear quadrants. The successive application of this simple failure model for fibers in the 0°/90° and ± 45° orientations, in turn, is shown to be the necessary and sufficient characterization of the fiber-dominated failures of laminates made from fibers having the same tensile and compressive strengths. When one such strength is greater than the other, the failure envelope is appropriately truncated for the lesser direct strain. The shear-failure cutoffs are now based on the higher axial strain to failure since they occur at lower strains than and are usually not affected by such mechanisms as microbuckling. Premature matrix failures can also be covered by appropriately truncating the fiber failure envelope. Matrix failures are excluded from consideration for conventional fiber/polymer composites but the additional features needed for a more rigorous analysis of exotic materials are covered. The new failure envelope is compared with published biaxial test data. The theory is developed for unnotched laminates but is easily shrunk to incorporate reductions to allow for bolt holes, cutouts, reduced compressive strength after impact, and the like.

INTRODUCTION

Failure or yield of metals has traditionally been characterized in terms of applied stresses. It makes little difference for isotropic materials whether such expressions are formulated in terms of stress or strain. However, it makes a tremendous difference in predicting failure of orthotropic materials such as fibrous composites. Indeed, the almost universal preference for a stress-based reference has handicapped failure prediction for composites for a quarter of a century. In stress formulations, it has been incorrectly assumed that the longitudinal and transverse properties of the unidirectional lamina, which have served as the basis of laminated composite analysis, are independent quantities that need to be specified separately for use in an interactive type of failure criterion.

If the formulation had been in terms of strain, the dependence between longitudinal and transverse strengths would have been apparent. The characterization of failure or yield in terms of strain rather than stress permits a single universal criterion to cover *all* materials, isotropic and orthotropic. In the

case of fibrous composites, the current longitudinal tests (tension and compression) are sufficient to characterize correctly the fiber-dominated failures while the measured transverse strengths, which have nothing to do with the failure of the fibers, can serve as the basis of a separate failure criterion for the resin matrix.

This paper explains how failure can be characterized in terms of strain rather than stress. The conversion for isotropic materials — metal alloys, for example — is derived first to show the tie-in to established methods. The formulation in terms of strain is then extended to orthotropic materials. That nonsymmetric failure criterion for a unidirectional fibrous composite lamina is next simplified by superposition with an equivalent strength cutoff for any orthogonal layer of the *same* composite material since, for most practical structural laminates, some orthogonal fibers will always be present.

The reduced envelope is then recognizable as a truncation in the in-plane shear quadrants of the well-known maximum-strain failure model. Whenever there are orthogonal fibers present, such an envelope is not an arbitrary truncation but is directly equivalent to the generalized maximum-shear-stress failure criterion developed earlier by the author. But now it is simplified to the point where it should be more appealing to designers and, more important, it is so formulated that there is no need to specify any transverse properties. Consequently, researchers and analysts need not be skilled in the art to make realistic laminate strength predictions.

THE MAXIMUM-SHEAR-STRESS FAILURE CRITERION
IN TERMS OF STRAIN FOR ISOTROPIC HOMOGENEOUS MATERIALS

Since the shear stresses and strains are related for isotropic materials by the simple relation

$$\tau = G\gamma \tag{1}$$

there is a one-to-one match between stress τ and strain γ. The characterization of failure in terms of Mohr circles of stress and strain (Figures 1 and 2, respectively) is as follows.

For uniaxial tension, for example, failure can be expressed by the following equations.

$$\sigma_{crit} = 2\tau_{crit} \tag{2}$$

or

$$\gamma_{crit} = (1 + \nu)\epsilon_{crit} \tag{3}$$

Similarly, for pure shear, the equal and opposite orthogonal principal stresses at failure are equal to the shear strength of the material.

$$\sigma = \tau_{crit} \tag{4}$$

and

$$\epsilon = \pm \gamma_{crit}/2 \tag{5}$$
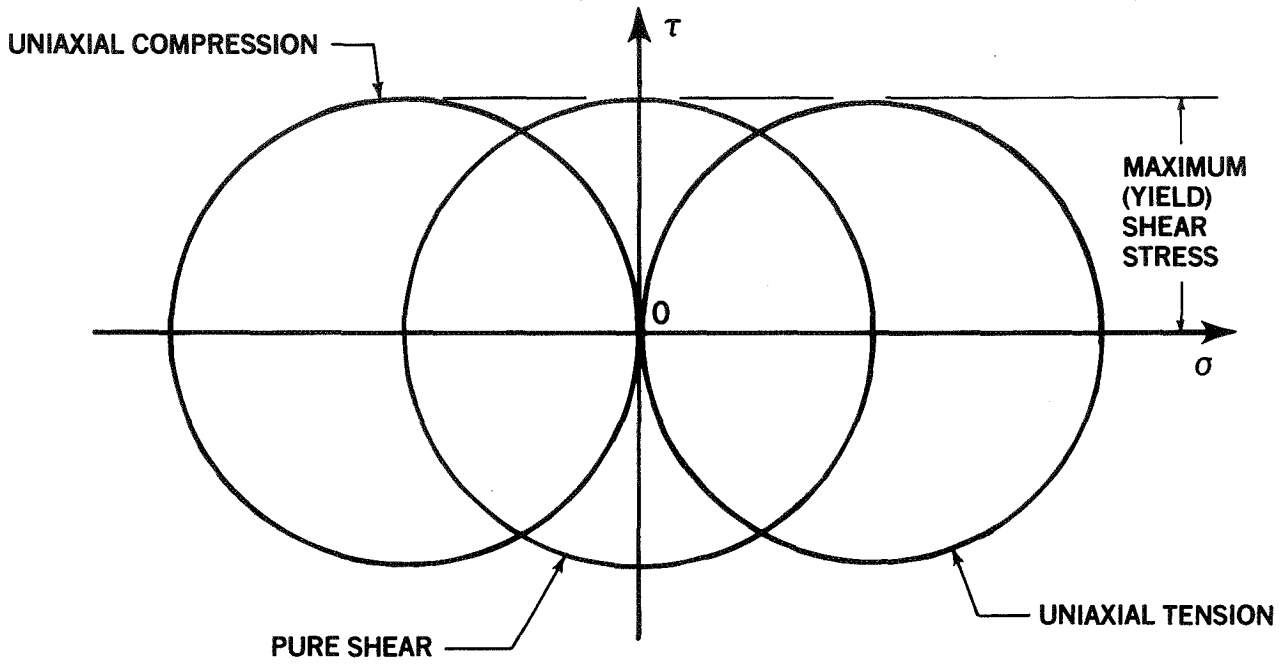
FIGURE 1. MOHR STRESS CIRCLES FOR ISOTROPIC MATERIALS
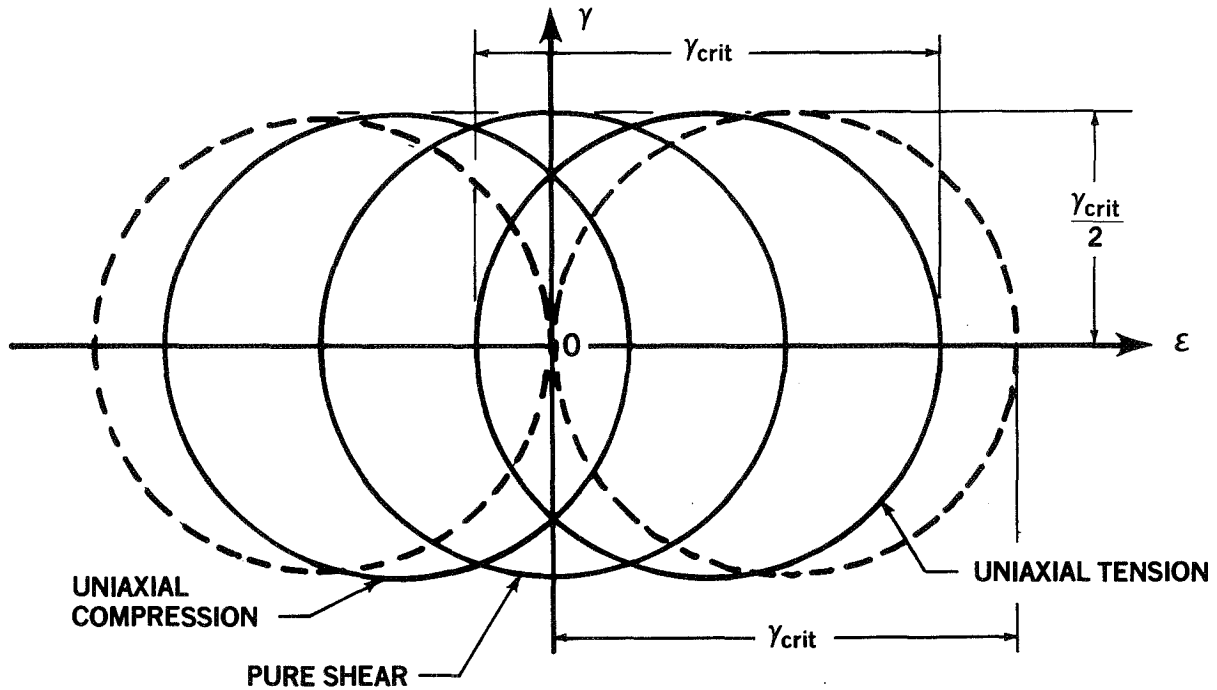
FIGURE 2. MOHR STRAIN CIRCLES FOR ISOTROPIC MATERIALS

The general stress-strain relations for isotropic materials, using x and y as principal in-plane references and z as the thickness (normal) direction, are as follows.

$$\epsilon_x = \frac{1}{E}(\sigma_x - \nu\sigma_y - \nu\sigma_z) \tag{6}$$

$$\epsilon_y = \frac{1}{E}(-\nu\sigma_x + \sigma_y - \nu\sigma_z) \tag{7}$$

and

$$\epsilon_z = \frac{1}{E}(-\nu\sigma_x - \nu\sigma_y + \sigma_z) \tag{8}$$

Failure would occur when any of the three principal strain differentials $(\epsilon_x - \epsilon_y)$, $(\epsilon_x - \epsilon_z)$, $(\epsilon_y - \epsilon_z)$, exceeded the material allowable shear strain γ_{crit}. This condition is expressed in Figure 3. The figure is unbounded along the diagonal because, with triaxial (hydrostatic) stresses all having the same sign (positive or negative), the *differences* between the principal strains can remain too small to cause failure. That open-endedness can be eliminated for the special two-dimensional load case of interest here, in which there are no normal or through-the-thickness shear stresses. For this case,

$$\sigma_z = \tau_{xz} = \tau_{yz} \equiv 0 \tag{9}$$

and Equations (6) to (8) reduce to the following.

$$\epsilon_x = \frac{1}{E}(\sigma_x - \nu\sigma_y) \tag{10}$$

$$\epsilon_y = \frac{1}{E}(-\nu\sigma_x + \sigma_y) \tag{11}$$

and

$$\epsilon_z = -\frac{\nu}{E}(\sigma_x + \sigma_y) \tag{12}$$

Figure 3 represents the critical differences between the in-plane (x and y) strains. The missing characteristics refer to the differences between the other pairs of strains. For the case $\epsilon_x - \epsilon_z = \gamma_{crit}$, the additional cutoffs are defined by

$$\epsilon_x = (1 - \nu)\gamma_{crit} - \nu\epsilon_y \tag{13}$$

while, for $\epsilon_y - \epsilon_z = \gamma_{crit}$, the remaining cutoffs (for positive and negative strains) are given as follows.

$$\epsilon_y = (1 - \nu)\gamma_{crit} - \nu\epsilon_x \tag{14}$$

Together with the cutoff $\epsilon_x - \epsilon_y = \gamma_{crit}$ shown in Figure 3, the complete failure envelope in the absence of surface stresses is as shown in Figure 4.

Figure 5 adds to the failure envelope the traces for the uniaxial load lines $\sigma_y = \sigma_z = 0$ and $\sigma_x = \sigma_z = 0$, inclined from the reference axes by an angle defined by the Poisson's ratio, as shown.

C - 4
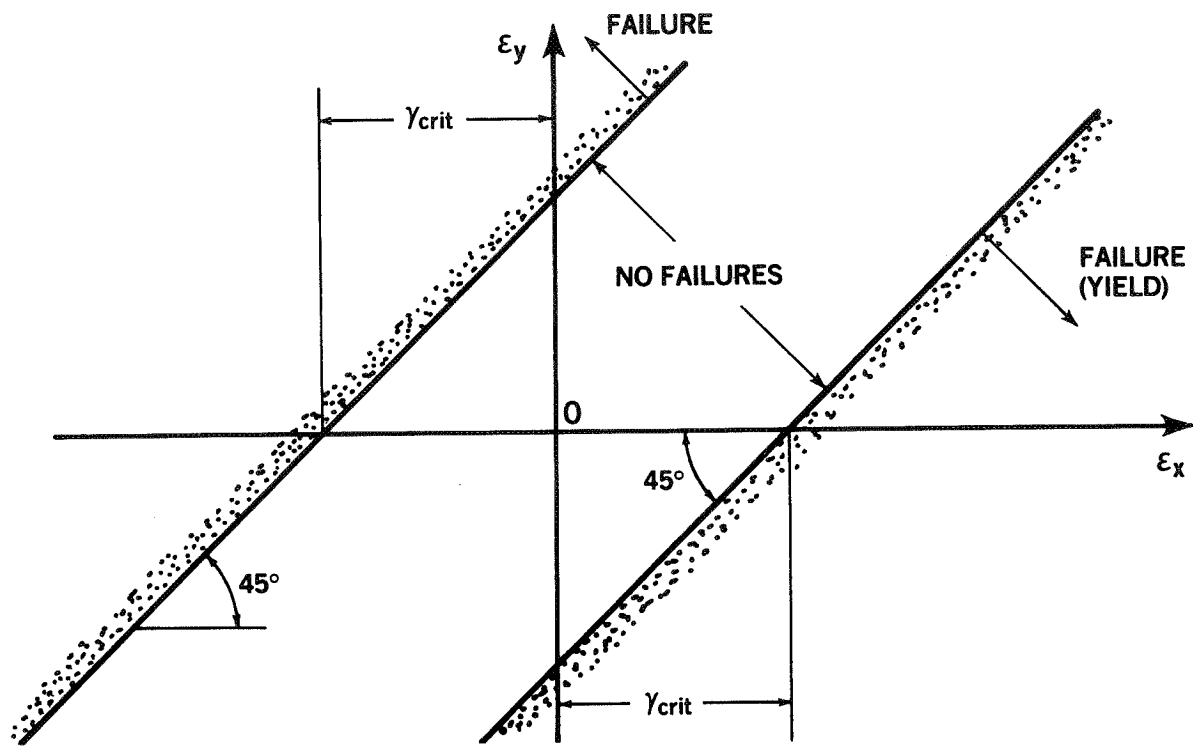
FIGURE 3. MAXIMUM-SHEAR-STRESS FAILURE CRITERION FOR ISOTROPIC MATERIALS
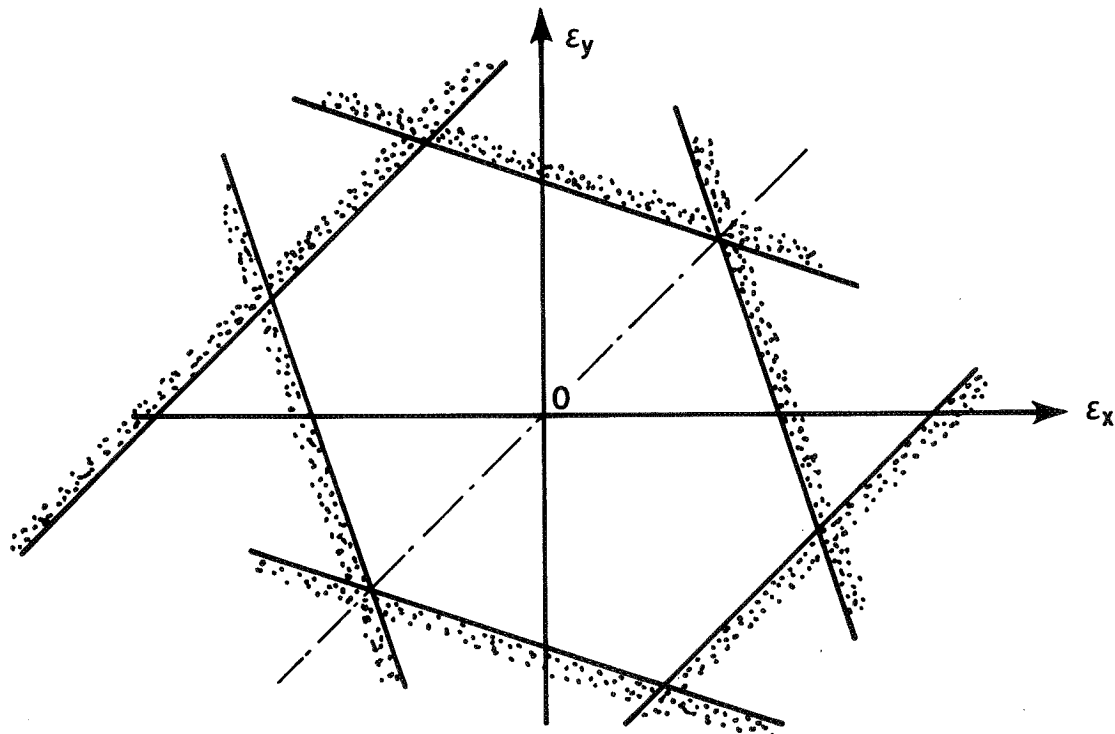
FIGURE 4. ADDITIONAL CUTOFFS DUE TO ABSENCE OF NORMAL STRESSES $(\sigma_z = 0)$
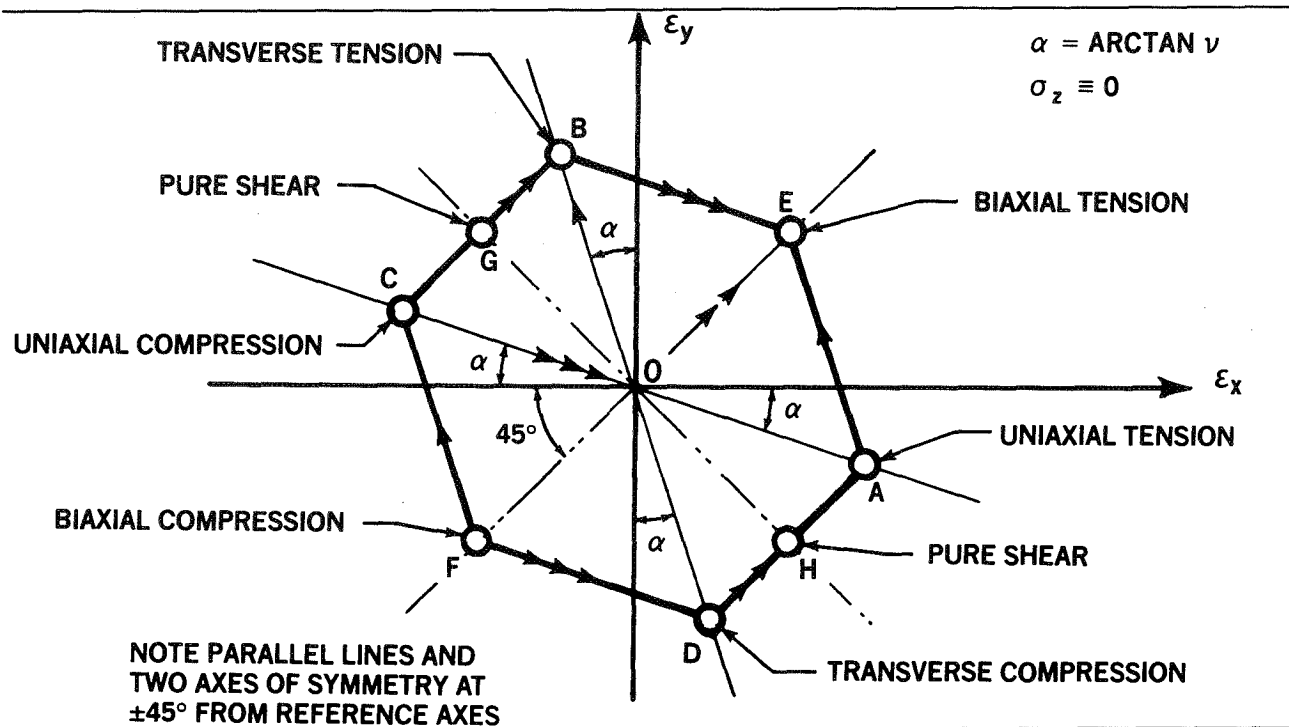
FIGURE 5. TWO-DIMENSIONAL MAXIMUM-SHEAR-STRESS FAILURE CRITERION FOR ISOTROPIC MATERIALS

These uniaxial load lines intersect the failure envelope at points A, B, C, and D. At the biaxial points E and F, $\sigma_x = \sigma_y$ in tension and compression, respectively. G and H indicate the points of pure in-plane shear, for which $\sigma_x = -\sigma_y$.

All but the in-plane shear failure lines AB and CD in Figures 4 and 5 have precisely the same length and one of only two orientations, with slopes defined by the Poisson's ratio.

The uniaxial strain at failure is given by

$$\epsilon_0 = \gamma_{crit}/(1 + \nu) \tag{15}$$

and it is now apparent that the critical shear strain, or principal direct strain *difference*, is the primary quantity and that the axial strain ϵ_0 is secondary. The critical strain combination at the biaxial points is defined by

$$\epsilon_x = \epsilon_y = \left(\frac{1-\nu}{1+\nu}\right)\gamma_{crit} = (1-\nu)\epsilon_0 \tag{16}$$

while the in-plane strains at the shear failure points can be seen to be as follows.

$$\epsilon_x = -\epsilon_y = \pm\ \gamma_{crit}/2 = \pm\ (1+\nu)\epsilon_0/2 \tag{17}$$

Before generating equivalent failure criteria for orthotropic materials, it is useful to interpret some of the less obvious lines in Figure 5. The radial lines OA, OB, OC, and OD are easily interpreted as uniaxial load lines. At point A, $\sigma_y = \sigma_z = 0$ and $\sigma_x \neq 0$. Along the line AE, the stress σ_y is increased in

668

such a way that the stress *difference* $\sigma_x - \sigma_z$ is held constant because the application of σ_y stresses cannot possibly induce any stresses in the $x - z$ plane — only compatible Poisson strains. Therefore, the axial and normal strains ϵ_x and ϵ_z must decrease by an amount $\nu\epsilon_y$ as σ_y increases. Since σ_z is zero at point A, σ_x is constant all along the lines AE and DF. The normal stress σ_z is zero throughout Figure 5, so the stress difference $\sigma_x - \sigma_z$ is also constant along the lines AE and DF. Similarly, σ_y is constant along the lines CE and BF.

The lengths of all the sides of the hexagon in Figures 4 and 5 would be identical only for one particular value of the Poisson's ratio. That value is obtained by equating the lengths of the usually different sides, as in the following equation.

$$\frac{\sqrt{(1 + \nu^2)}}{(1 + \nu)} = \sqrt{2}\left(\frac{1 - \nu}{1 + \nu}\right)$$

$$(1 + \nu^2) = 2(1 - 2\nu + \nu^2)$$

or

$$1 - 4\nu + \nu^2 = 0 \tag{18}$$

The result, $\nu = 0.2679$ is typical for metals, so that the sides of most hexagons would be nearly equal.

THE (ISOTROPIC) MAXIMUM-SHEAR-STRESS FAILURE CRITERION FORMULATED IN TERMS OF STRAINS FOR ORTHOTROPIC LAMINAE

The next step is to generalize the preceding analysis to orthotropic layers. The failure criterion to be derived should actually refer to the fiber, for fiber-dominated failures, *not* the lamina. However, the fibers and matrix obviously share a common strain along the fiber axis. For the usual case, in which strong, stiff fibers are embedded in a soft matrix, it is possible to bypass the micromechanical calculations relating the transverse strains of the fiber to those of the lamina because of the greater criticality of the fiber failure criterion. Such a simplification may not be realistic for some of the more exotic advanced composites, and a more comprehensive theory would be needed then.

It is assumed again that there are no normal or through-the-thickness shear stresses acting on the laminate. Using the subscripts L, T, and N to denote the longitudinal, transverse (in-plane), and normal directions, respectively, Equations (10) to (12) can be generalized for transversely isotropic materials to read as follows when the axis of symmetry is longitudinal.

$$\epsilon_L = \frac{1}{E_L}(\sigma_L - \nu_{LT}\sigma_T) \tag{19}$$

$$\epsilon_T = \frac{1}{E_T}(\sigma_T - \nu_{TL}\sigma_L) = -\nu_{LT}\sigma_L/E_L + \sigma_T/E_T \tag{20}$$

and

$$\epsilon_N = \frac{1}{E_T}(-\nu_{TL}\sigma_L - \nu_{TN}\sigma_T) \tag{21}$$

For a uniaxial load along the fibers, with neither lateral nor normal applied stress, the axial strain in both the fiber and lamina will be ϵ_0 at failure and the associated lateral and normal strains will be

$-\nu_{LT}\epsilon_0$ in the *lamina*. The corresponding orthogonal strain in the *fiber*, which can be presumed to have a different Poisson's ratio from the homogenized lamina, is undefined. However, for typical carbon-epoxy composites, the similarity of the Poisson's ratio ν_{LT} for the unidirectional lamina and for an isotropic resin matrix, implies that the corresponding Poisson's ratio for the fiber must also be similar. If a substantial difference is expected between the Poisson's ratios for the fiber and monolayer, one would need to complete the micromechanical analyses relating the two before proceeding with the formulation of the failure criteria. And the appropriate distinction would need to be made for all states of stress being considered.

Figure 6 shows the traces of these uniaxial load lines, in tension and compression, on the $\epsilon_L - \epsilon_T$ in-plane strain plane. If the tension and compression strengths are the same, it is possible to locate the 45-degree sloping shear-failure lines on which the uniaxial failures are represented by individual points. If the tensile and compressive strengths differ, the numerically greater value defines both shear-failure lines, as shown in Figure 6, while the lesser strength defines a cutoff due to some other failure mechanism, such as microbuckling under compression.

For a uniaxial in-plane load perpendicular to the fibers, a different Poisson's ratio, ν_{TL}, is involved and the uniaxial load line is no longer symmetric as it was for isotropic materials in Figure 4. The traces of this unidirectional load condition can be added to Figure 6, and wherever they cross the shear-failure lines denotes the points of failure of the *fibers*.[*]
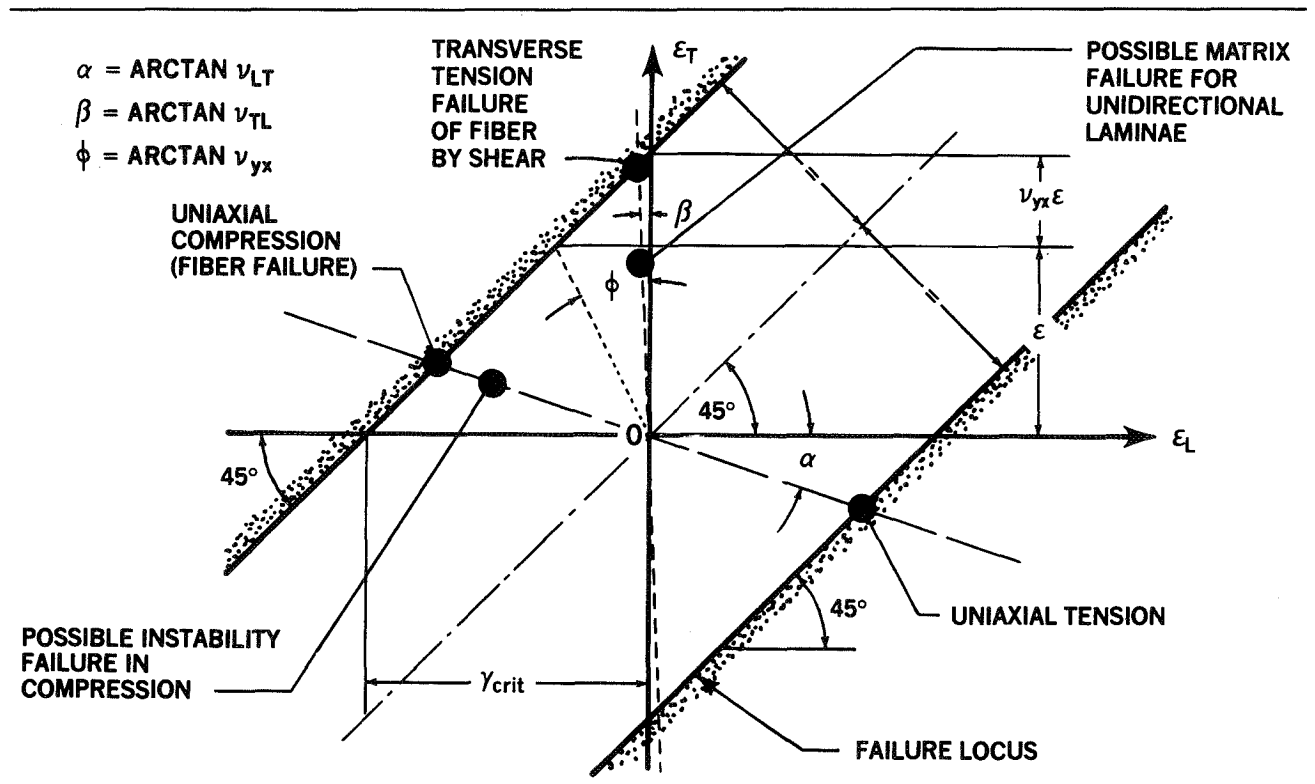
FIGURE 6. SHEAR FAILURE LOCI FOR ORTHOTROPIC MATERIALS

---

[*] With unidirectional laminae, the matrix may fail prematurely under transverse tension at a lower strain, but that is normally suppressed for any typical cross-plied structural laminate and may be considered as a special case.

670

It is apparent that the same critical shear strain holds throughout the entire region of interest in Figure 6 since the sum of longitudinal and orthogonal strains is always

$$\epsilon_0 + \nu\epsilon_0 = \gamma_{crit} \tag{22}$$

no matter what the value of the Poisson's ratio ν for any particular cross-plied laminate.

To complete Figure 6, and make it equivalent to Figure 5, constant-stress lines are added through the uniaxial stress points associated with shear failures of the fibers. Or, if there are premature failures under other modes, the additional lines must be placed where the missing shear failures would have occurred. Consider, for example (Figure 6) the addition of transverse stress to the point of uniaxial tension loading, while holding the longitudinal stress in the fibers and lamina constant without altering the stress-free state in the normal direction. Doing so would require that the additional strains be in the same relation as those following the purely transverse tension line in Figure 6. Along that line, with a slope defined by ν_{TL}, only the transverse stress varies. There are no incremental longitudinal and normal stresses, so no shear stress can be induced in the L–N plane. Likewise, the missing line from the transverse tension to the biaxial tension points must be parallel to the original longitudinal tension line in Figure 6. The entire envelope is shown completed in Figure 7 for the special case in which the tensile and compressive strengths of the unidirectional laminae are equal. Unlike Figures 4 and 5, which are
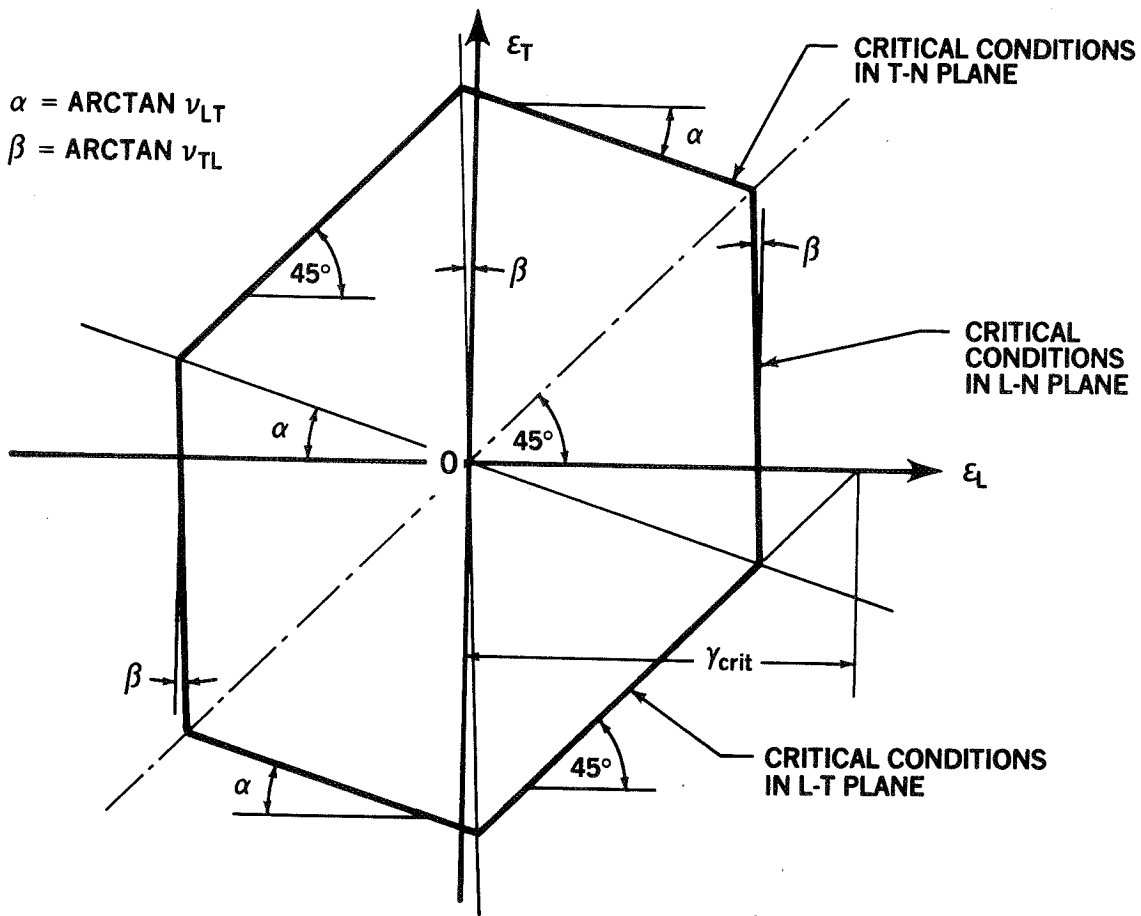
FIGURE 7. SHEAR FAILURE ENVELOPE FOR ORTHOTROPIC MATERIALS HAVING EQUAL TENSILE AND COMPRESSIVE STRENGTHS

doubly symmetric, Figure 7 is skewed because of the difference between the two in-plane Poisson's ratios. The third Poisson's ratio is involved in establishing the compatible normal strains, but does not appear in the in-plane failure envelope shown in Figure 7.

Figures 8 and 9 show the effect of fiber-dominated cutoffs at either end of the failure envelope. The cutoff representing microbuckling of the new (small-diameter) high-strain carbon fibers is drawn perpendicular to the strain axes because compression buckling is not usually sensitive to orthogonal stresses. The other cutoff, representing a lower tensile than compressive strength, is drawn parallel to the unidirectional load line since it is more likely to be a stress-imposed limit than not.
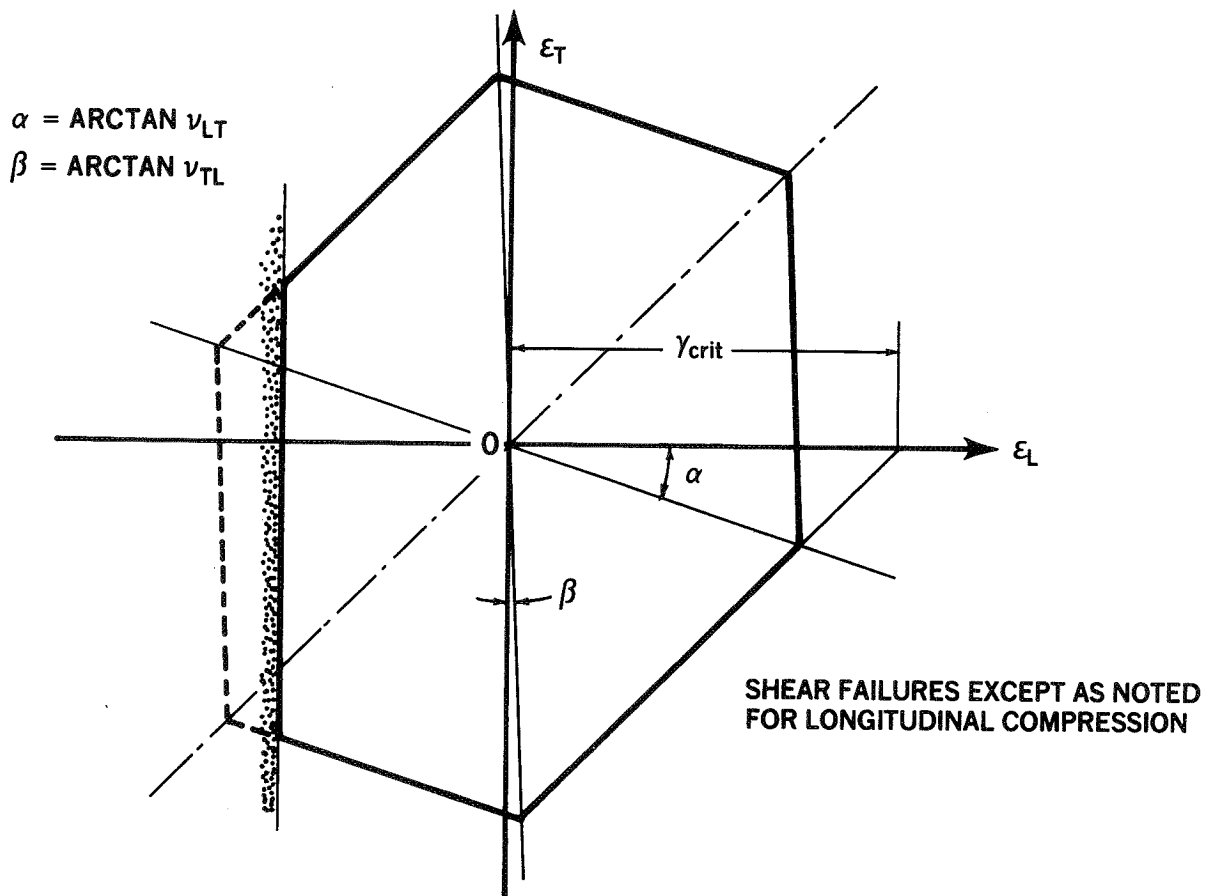
FIGURE 8. FAILURE ENVELOPE FOR ORTHOTROPIC MATERIALS WHICH ARE STRONGER IN TENSION THAN IN COMPRESSION

Figure 10 shows a postulated cutoff for matrix-dominated transverse tension failures. Since this would appear to be a stress rather than strain limit, the cutoff is drawn parallel to the constant transverse stress line on the basis that any longitudinal load would not induce any stress in the T–N plane.

Figures 7 through 9 refer to a fiber-dominated unidirectional lamina and could be used directly as a ply-by-ply failure criterion for analyzing cross-plied structural laminates. However, many simplifications ensue from reinterpreting this criterion in the context of laminates *before* it is used as a strength check, as discussed in the next section.

672

SHEAR FAILURES EXCEPT AS NOTED
FOR LONGITUDINAL TENSION

$$\alpha = \text{ARCTAN } \nu_{LT}$$
$$\beta = \text{ARCTAN } \nu_{TL}$$
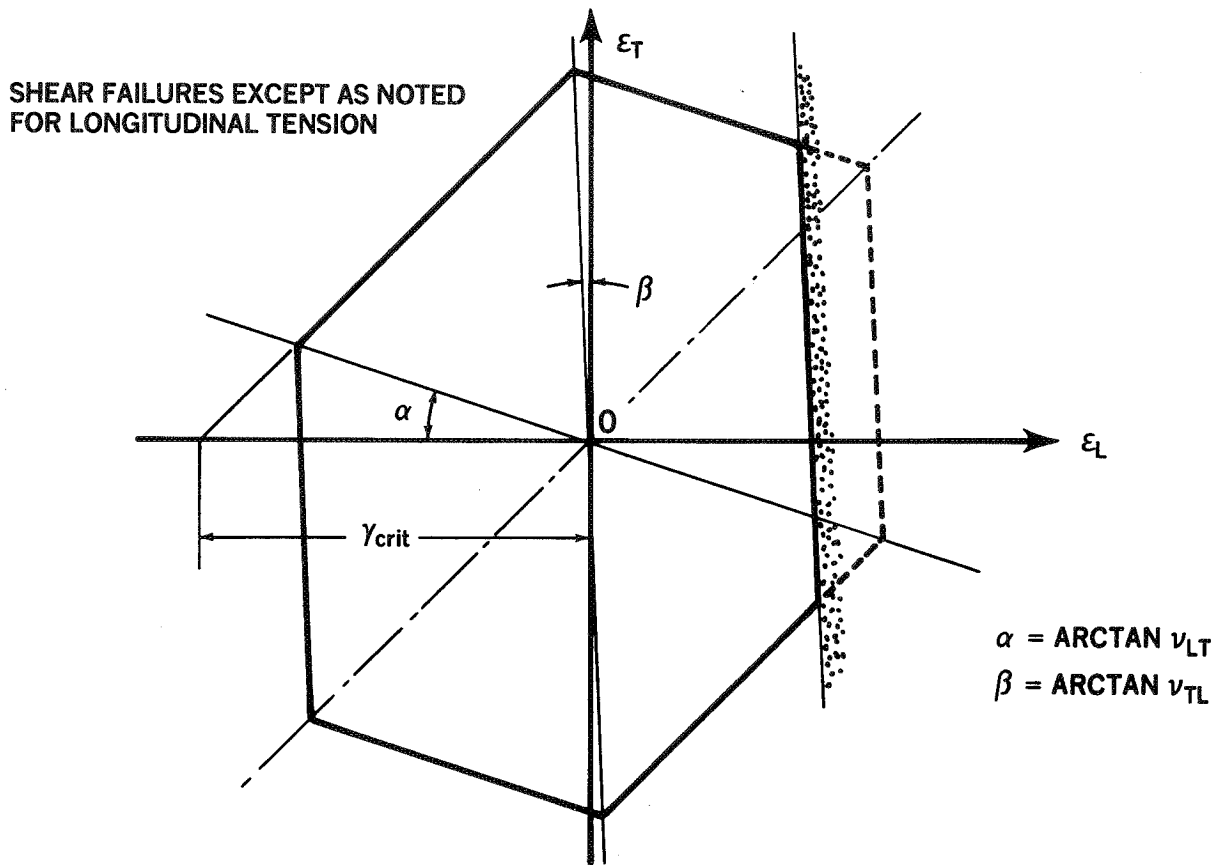
FIGURE 9. FAILURE ENVELOPE FOR ORTHOTROPIC MATERIALS WHICH ARE STRONGER IN
COMPRESSION THAN IN TENSION

THE "MAXIMUM-SHEAR-STRAIN" FAILURE CRITERION
FORMULATED FOR CROSS-PLIED STRUCTURAL LAMINATES

It is now apparent that the generalization of the classical maximum-shear-*stress* failure criterion for ductile metals is actually most conveniently expressed as a maximum-shear-*strain* criterion for orthotropic materials, encompassing the classical hypothesis as a special case. Care is needed to exclude shear strains caused by factors other than stress: as, for example, by nonuniform thermal expansion or swelling due to absorbing moisture. Even when attention is paid only to the mechanically caused shear strains, there are still some difficulties since some of the Poisson-induced strains have no corresponding stresses, as discussed in the next section.

In design of composite aircraft structures, it is customary to have a minimum percentage of fibers in *all* of the four standard directions — 0°, +45°, 90°, and -45°. That being the case, the greater strains in Figures 7 through 9 in the transverse rather than longitudinal direction would be truncated by longitudinal failures in orthogonal plies. So, if there were really orthogonal plies for each fiber direction, these figures could be simplified with no loss of accuracy. This has been done in Figure 11 by adding a mirror image to Figure 7 about the biaxial strain diagonal axis and taking the smaller strength cutoffs for each segment of the envelope. The new figure is doubly symmetric, just as Figures 4 and 5 were for isotropic materials. More importantly, the corner points are defined by the Poisson's ratios for the
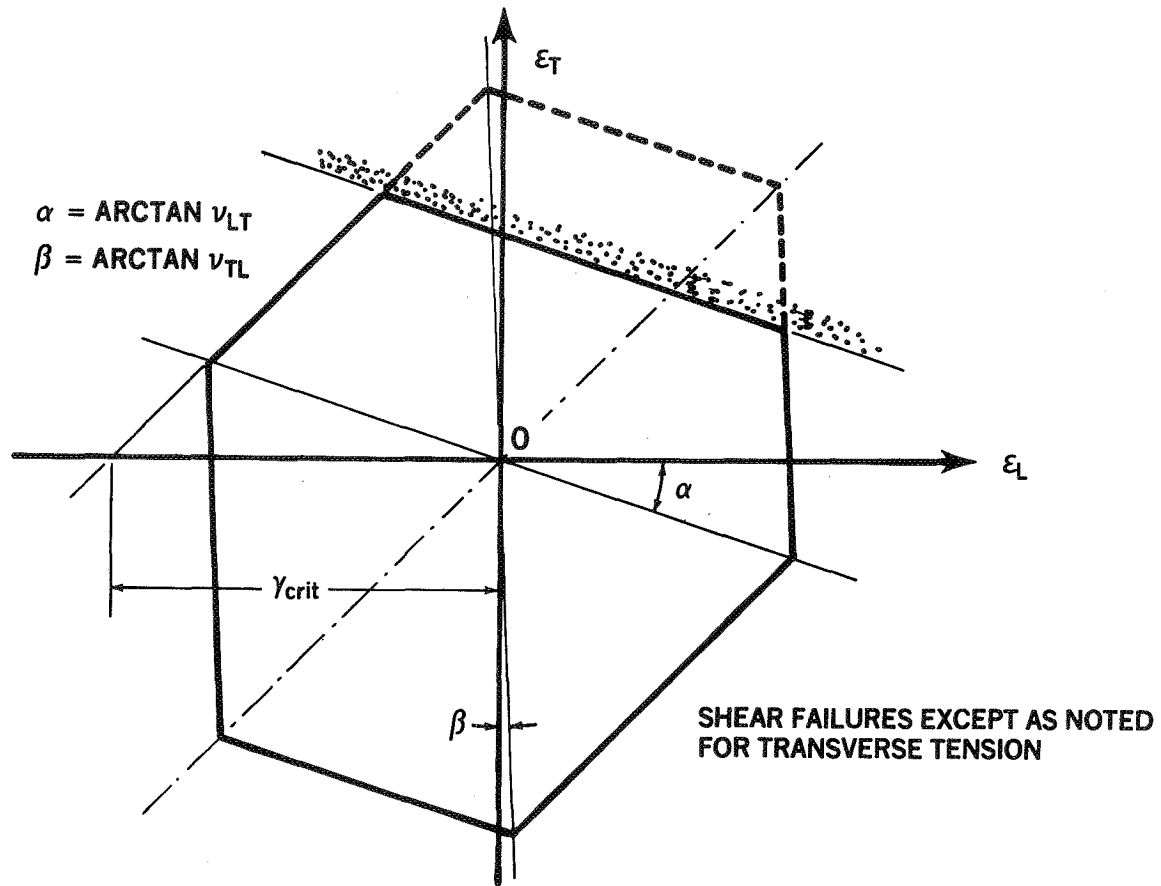
FIGURE 10. FAILURE ENVELOPE FOR ORTHOTROPIC MATERIALS WHICH HAVE A WEAKNESS IN TRANSVERSE TENSION

unidirectional laminae on which the failure envelope is based. This is of vital importance because, as shown below, those corner points remain fixed for *all* cross-plied laminates, regardless of the Poisson's ratios of the actual laminate.

Because Figure 11 is drawn in strain space rather than stress space, it remains doubly symmetric even if the percentages of 0° and 90° fibers are *not* the same. The two laminate Poisson's ratios ν_{xy} and ν_{yx} would vary with the proportion of 0° and 90° fibers, but the failure envelope would *not* do so.

Consider the case of a laminate containing equal percentages of 0° and 90° fibers, with no ± 45° fibers, for which both in-plane Poisson's ratios are approximately 0.05. Figure 12 shows where the uniaxial load lines in the longitudinal and transverse directions would intersect the failure envelope in Figure 11. No intersections fall on the 45-degree sloping shear-failure lines, and the associated maximum shear strain $(1 + \nu_{yx})\epsilon_0$ appears insufficient to have caused failure.

The explanation of this apparent anomaly is that failure is actually caused by the stress states in the planes perpendicular to the fibers, involving the normal rather than in-plane direction. A longitudinally stretched all -0° laminate contracts as much laterally as it does through the thickness. However, the presence of the orthogonal in-plane fibers in the 0°/90° laminate restricts the in-plane lateral contraction, and hence the in-plane shear stress developed in both the lamina and fiber, so that this
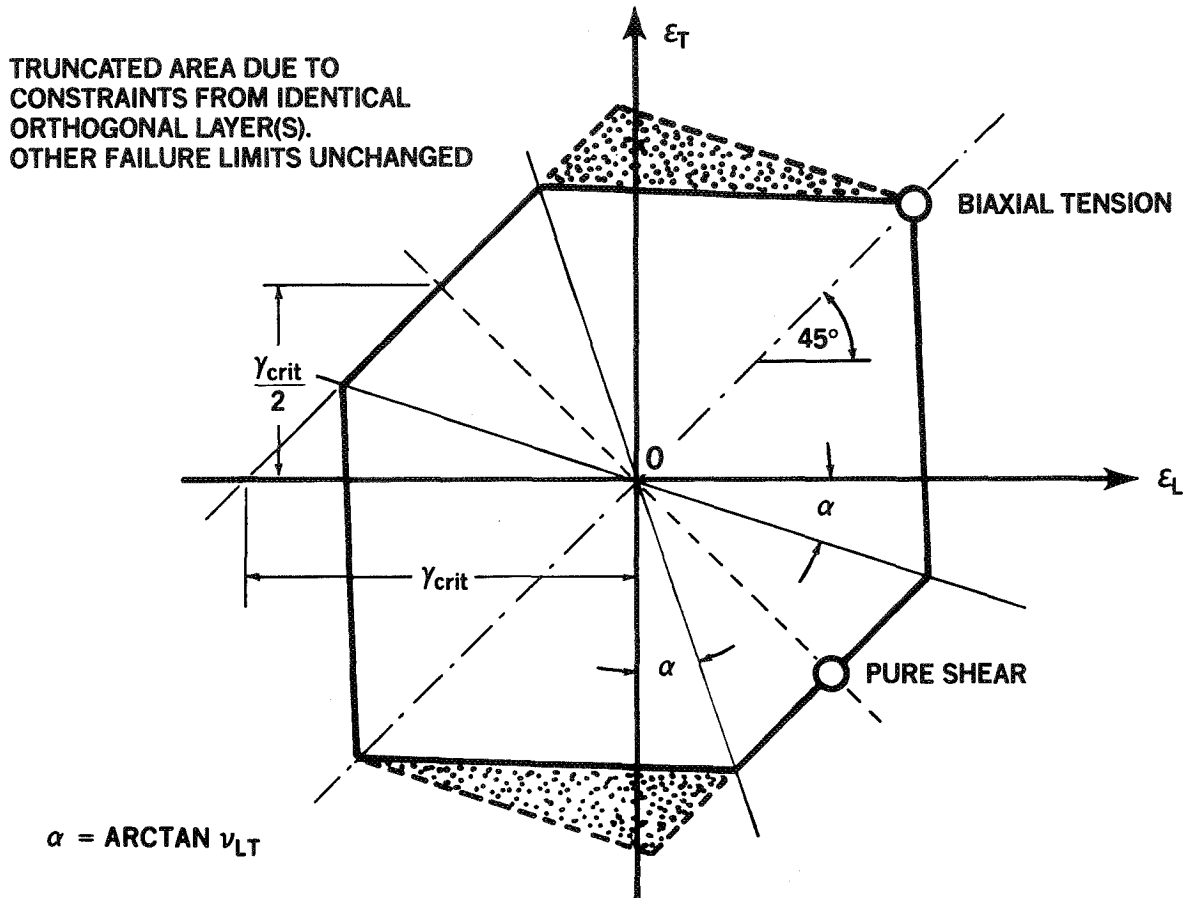
FIGURE 11. SUPERIMPOSED FAILURE ENVELOPES FOR ORTHOGONAL LAYERS OF ORTHOTROPIC MATERIALS

plane becomes less critical than the one defined by the fiber axis and the normal direction. Failure is still predicted to occur on the diagonal shear failure line in Figure 6, only now the failure point is located on Figure 12 by a radial line with a slope defined by ν_{LT} rather than by ν_{xy}. This is generally true for all laminate patterns for which $\nu_{xy} > \nu_{LT}$ for the unidirectional lamina on which Figure 6 is based.

What is happening may better be understood by drawing the appropriate Mohr circles, as has been done in Figure 13. Yet, for all practical purposes, the lines with slopes defined by ν_{yx} in Figure 12 and ν_{xy} (not shown) also correctly identified the failure strains ϵ_0 for the 0°/90° laminate. Similarly, the biaxial failure strains, which obviously are not associated with in-plane shear strains, are also correctly located.

If, for this same 0°/90° laminate, biaxial rather than uniaxial loads were to be applied, one could easily envisage a little transverse compression combined with a predominantly longitudinal tension load so that the transverse strains were made to coincide with those developed by a uniaxial load on a unidirectional lamina. In such a case, failure would occur precisely on the corner point in Figure 7 because those would be the applied strains in the laminate, only they would have been developed partly by orthogonal loads instead of entirely by Poisson contractions.

675
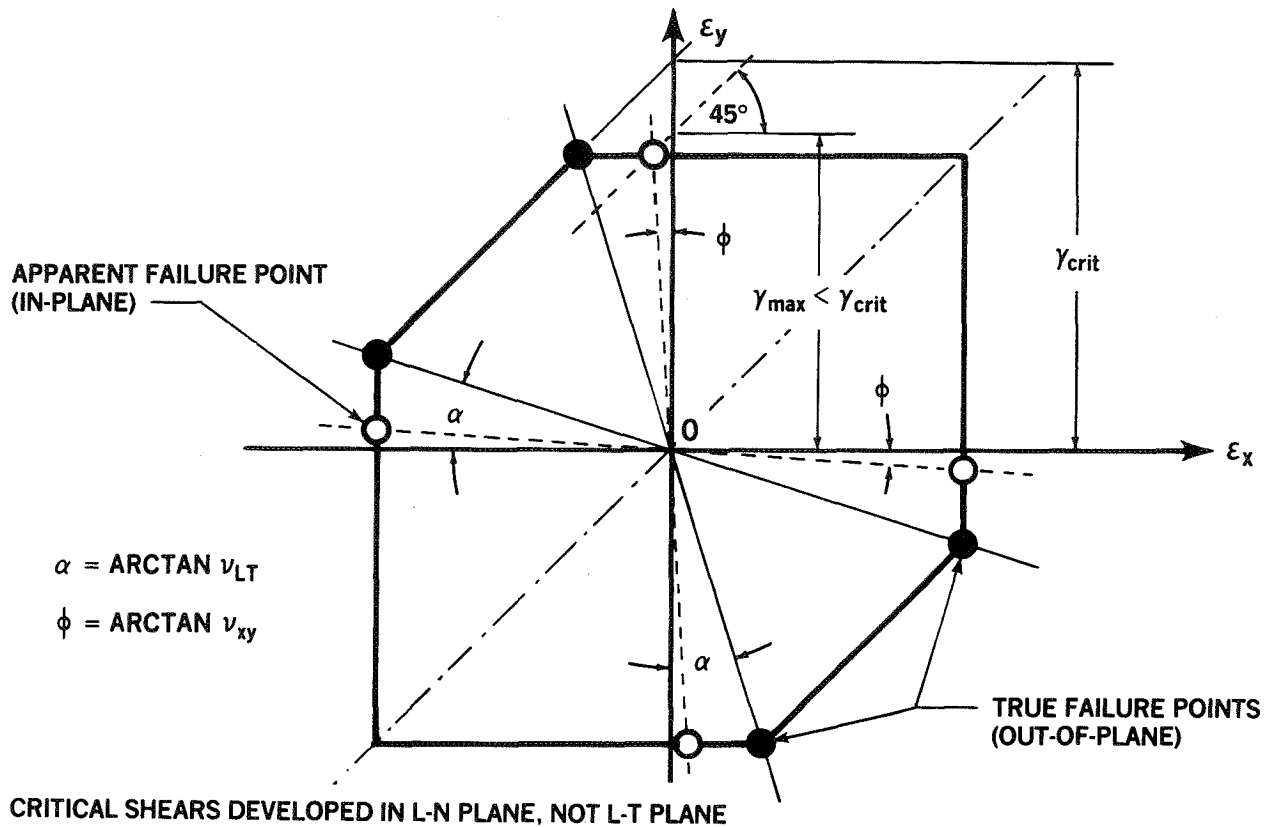
FIGURE 12. UNIAXIAL FAILURE POINTS FOR 0°/90° CROSS-PLIED LAMINATES WITH LOW POISSON'S RATIOS

Likewise, one could apply equal and opposite loads in the 0° and 90° fibers. This would induce equal and opposite strains, and failure would be predicted to occur at an axial strain of $\gamma_{crit}/2$, as noted in Figure 11. Indeed, that is the point where *all* purely in-plane-shear failures will occur, regardless of the particular Poisson's ratios for any particular cross-plied laminate.

Consider next a nonstructural cross-plied laminate consisting of 33 percent of the fibers in the 0° direction, and the remaining 67 percent shared equally between the ±45° directions. For this laminate, the Poisson's ratio ν_{xy} will be about 0.67, much higher than the typically 0.25 for a unidirectional lamina and the 0.33 for a quasi-isotropic laminate. In the absence of 90° fibers, one should ideally draw the unidirectional load lines on Figure 7 rather than Figure 11. The other Poisson's ratio ν_{yx} should be about 0.2. Figure 14 shows these radial uniaxial load lines added to Figure 7. It is significant that, in the longitudinal direction, the shear-failure line is intercepted at a *lower* axial strain than was the case for the unidirectional lamina. The critical difference between strains does occur *in-plane* in this case and the longitudinal strain at failure is expected to be less than that of the unidirectional lamina in the following ratio:

$$\epsilon_{laminate} = \epsilon_{lamina} \times (1 + \nu_{LT})/(1 + \nu_{xy}) \tag{23}$$
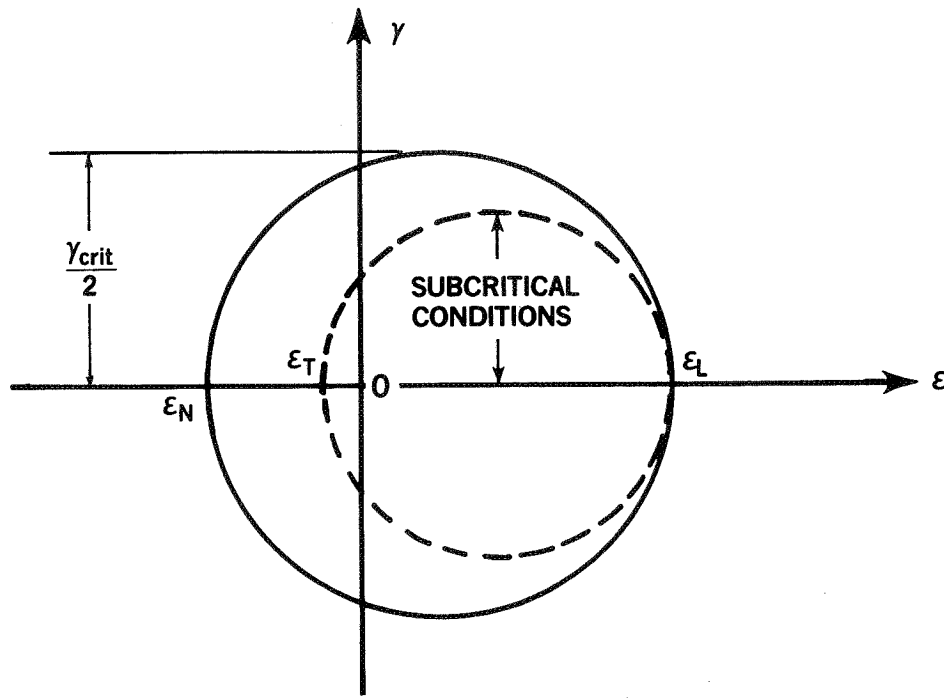
FIGURE 13. EXPLANATION OF APPARENT PREMATURE FAILURE PREDICTION

In this case, the reduction is to only 75 percent of the nominal value. Thus, this laminate without any 90° fibers is not only impractical because of its disproportionately small transverse (90°) strength and stiffness, but also because it does not allow the load-carrying 0° fibers to work to their full extent.

Actually, the loss of efficiency is probably overestimated slightly because no distinction has been made between the lateral strains in the fiber and the lamina. With a truly soft matrix, the fibers would not compress quite as much as the lamina would shrink; with a lower lateral strain experienced by the fibers, the appropriate values of transverse stress would need to be reduced. Doing so would violate the standard assumption that plane sections remain plane throughout the laminate. The maximum-strain failure model for composites may be looked upon as an overcorrection for this problem inasmuch as no allowance is made for any loss of fiber strength caused by a lateral stress of the opposite sign to the axial stress in the fiber. This issue can be resolved only by micromechanics; the same problem also exists with all the pseudo-scientific laminate strength theories.

For a quasi-isotropic laminate, the strain to failure would be predicted by Equation (23) as 94 percent of that of the unidirectional lamina. Again, in reality it would be slightly higher but, with good test specimens and test technique, it should be possible to detect a statistically significant small reduction from the unidirectional value.

If one were to test a cross-plied laminate that had the *same* Poissin's ratios as the unidirectional lamina because of the particular mixture of 90° and ±45° fibers, the longitudinal strains to failure would logically be identical and the unidirectional load lines would be the same as in Figure 7.

Now, even though Figure 11 can be applied to woven fabric laminates as well as to cross-plied tape ones, the Poisson's ratios defining the corner points *must* be those of the *unidirectional* lamina, which

677
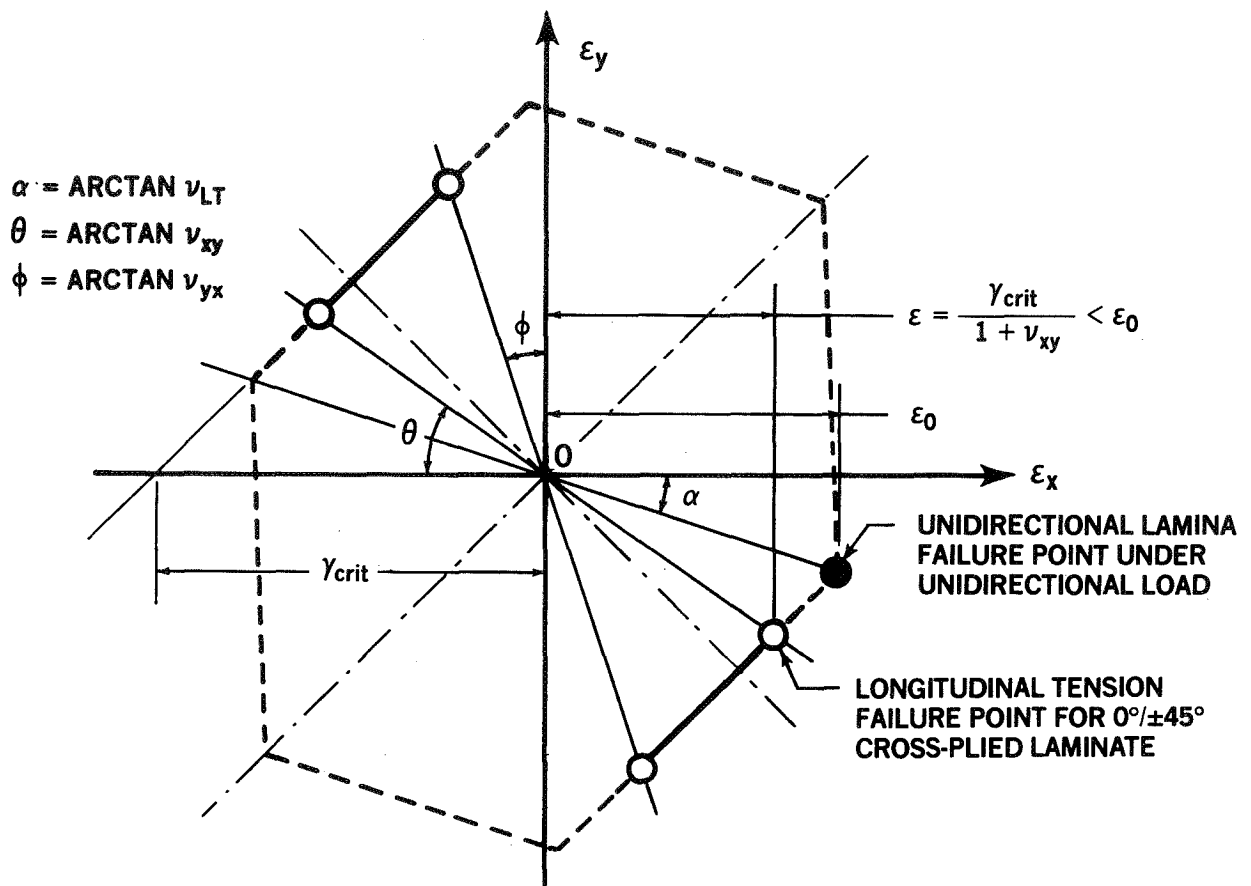
FIGURE 14. UNIAXIAL FAILURE POINTS FOR 0°/±45° LAMINATES WITH HIGH POISSON'S RATIOS

may be difficult to measure on a woven fabric. However, they can be easily related and the required values can be deduced reliably from measurements of the Poisson's ratio of a ±45° woven laminate. (The direct use of the 0°/90° laminate is not recommended for this purpose since its Poisson's ratio is so small as to be difficult to measure.)

The failure envelopes in Figures 7 through 9 would be applied, in turn, to the 0°/90° combination of fibers and the ±45° set. This would be necessary and sufficient to assess the strength of such laminates for fiber-dominated failures of in-plane loads. These are not unreasonable limitations since resin matrices are traditionally so weak that designers should always avoid applying direct transverse shear loads. Also, normal pressure loads must always be small in comparison with the in-plane stresses for any thin-shelled structures, although such might not be the case for deep submersible vehicles. Further, if the matrix is so weak as to prevent the fibers from developing their full strengths before failure of the laminate under in-plane loads, the matrix or the fiber pattern should be changed rather than the analysis method.

THE TRUNCATED MAXIMUM-STRAIN FAILURE MODEL

The transverse monolayer Poisson's ratio ν_{TL} is only about 0.025 for the usual case of carbon, boron, or glass fibers embedded in polymeric matrices like epoxies, polyester, and phenolics. It is not

678

unreasonable under such circumstances to approximate the almost horizontal and vertical lines joining the uniaxial and biaxial load points in Figure 11 by exactly horizontal and vertical lines, as in Figure 15. If that is done, the new failure criterion appears as a close approximation of the now classical maximum-strain failure model for fibrous composites (see Reference 1), but with the latter's overestimated strengths in the shear quadrants eliminated. A sample of these unconservative predictions is presented in Figure 16.

α = ARCTAN ν_{LT} FOR UNIDIRECTIONAL LAMINA

MATERIAL WEAKER
IN COMPRESSION
THAN IN TENSION

MATERIAL EQUALLY
STRONG IN TENSION
AND COMPRESSION

MATERIAL STRONGER
IN COMPRESSION
THAN IN TENSION
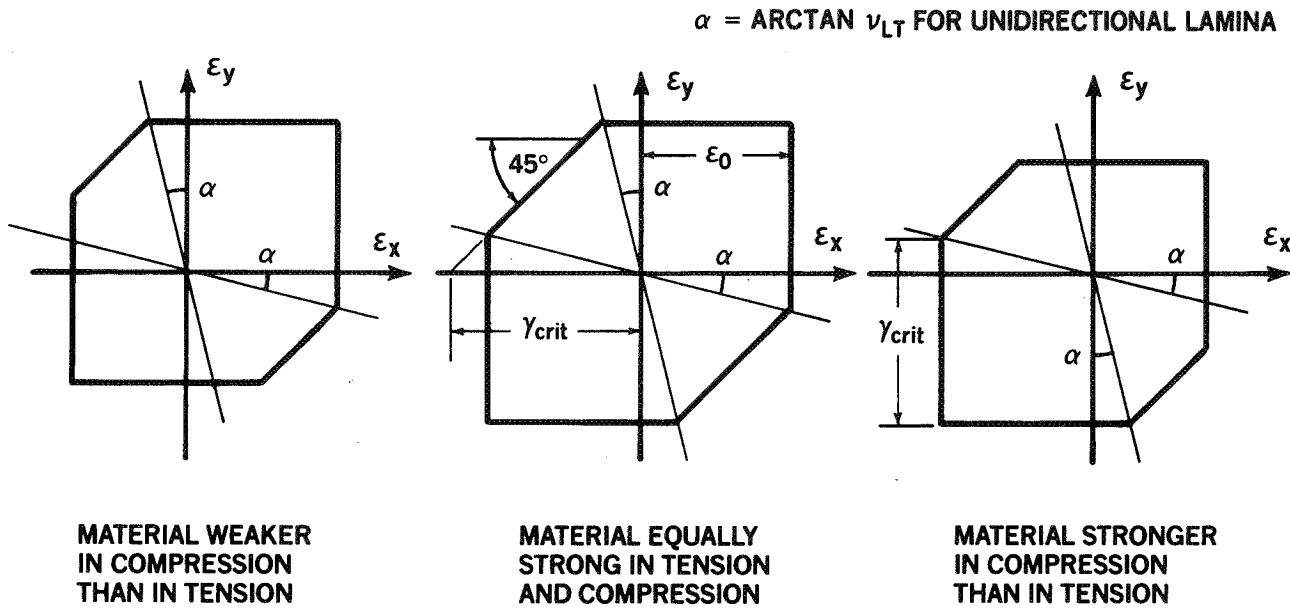
FIGURE 15. TRUNCATED MAXIMUM-STRAIN FAILURE MODELS FOR FIBER-DOMINATED FAILURES OF CROSS-PLIED COMPOSITE LAMINATES

Obviously, this type of simplification should not be expected to be valid for such composites as whisker-reinforced metal matrices for which the assumption of strong and stiff fibers and a soft and weak matrix would no longer be valid. But many of the structural applications of fiber/polymer composites would be well characterized by the simple failure models shown in Figure 15. Basing the application of the new failure criterion — that of the generalized maximum-shear-stress recommended by the author in References 2 through 4 — on an improvement in the well-known maximum-strain model for analyzing composite structures should have the effect of making the physics of the phenomena easier to understand. And, since it is now seen to be directly equivalent to the truly classical ductile-yield failure theory for metals, few designers and analysts should feel the kinds of insecurity and concern that have been associated with earlier composite failure criteria.

Nevertheless, the author again cautions that until a proper two-phase failure theory is developed to characterize the in situ strengths of the fibers and matrix separately, even this theory is capable of misapplication. It is unlikely to be improved upon for general-purpose analyses of today's fiber-reinforced polymer matrices, except for Kevlar (aramid) fibers that exhibit more than the two modes of failures observed in carbon fibers, so long as designs are confined within the outer shaded area in Figure 17. However, matrix failures prevail outside that area and *no* failure analyses are currently available for matrix-dominated failures of cross-plied laminates. The problem is that this new theory, like all prior theories, is capable of being misapplied without any restrictions on permissible fiber patterns, and without warning the user that he should not believe the predictions. This problem is critical

AREA OF UNCONSERVATISM
BETWEEN PLATEAU AND PEAK

τ_{xy}

σ_y

σ_x

AREA OF UNCONSERVATISM,
ON BOTH SIDES OF FIGURE

QUASI-ISOTROPIC HTS CARBON-EPOXY LAMINATE SHOWN
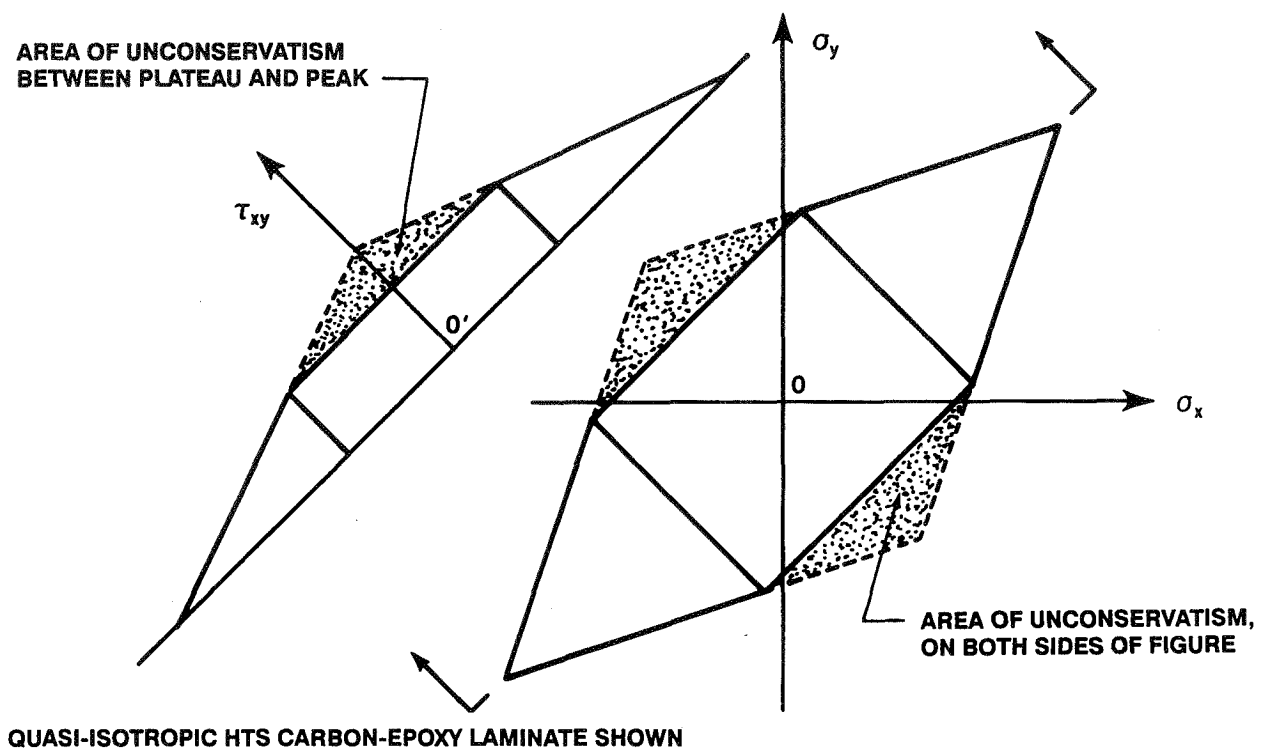
FIGURE 16. UNCONSERVATISM OF UNTRUNCATED MAXIMUM-STRAIN FAILURE MODEL

for laminate selection by computer optimization codes which are not programmed to reduce the laminate strengths for matrix-dominated failures, merely because no one has derived the necessary equations.

Ironically, a better theory for state-of-the-art fiber/polymer composites should merely discourage the use of impractical fiber patterns that have already been identified on the basis of accumulated experience but are still very much in vogue because oversimplified analyses have failed to condemn them. A better theory should not be expected to improve the strengths predicted for practical fiber patterns. However, the author believes that such improvements, from the derivation of a truly two-phase theory with possibly interface failures as well, will be vital to the use of the more exotic composites on which research has already begun.

In comparison with the "generalized maximum-shear-stress" failure criterion coded in the BLACK-ART computer program (see Reference 4), the new strain-based formulation will predict the *same* composite laminate strengths whenever input data for BLACKART have been appropriately selected to make them represent the behavior of the unidirectional lamina within a cross-plied laminate, rather than in the isolated circumstances in which it has customarily been tested. The real beauty of the present strain-based formulation is that there is no opportunity to enter transverse properties that are incompatible with the longitudinal properties. The only data needed are the lamina effective strain-to-failure in tension and compression and the Poisson's ratios of the lamina and laminate. Conversion to the corresponding strengths requires the addition of only the laminate stiffnesses, which have been calculated reliably for a long time.
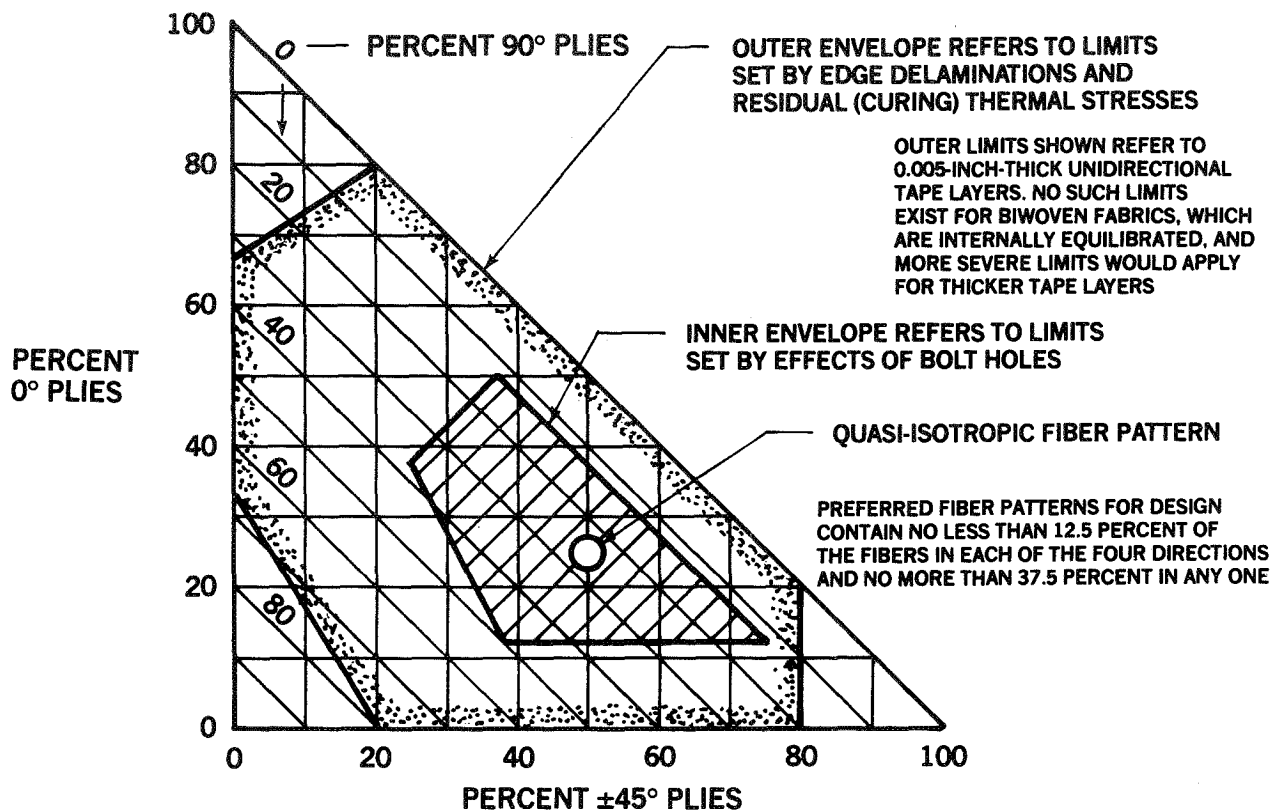
FIGURE 17. FIBER PATTERNS TO AVOID PREMATURE MATRIX FAILURES IN UNNOTCHED CROSS-PLIED CARBON-EPOXY COMPOSITE LAMINATES

It may appear that the author has made precisely the same mistake that he criticized others for; that is homogenizing the fibers and matrix into a single orthotropic composite material. It is true that the material properties are expressed at the lamina level, but the new failure criterion is really a normalized expression of the failure of the fibers alone. Actually, one should perform micromechanical analyses of the lamina and its constituents to relate the Poisson contractions of the fibers to those of the lamina because the transverse strains of the fibers need not be the same as for the lamina. And it is possible that, when this is done, pure-shear failures will be found to lie slightly off the –45-degree line in Figure 7, but still on the *same* shear failure line as for fiber failure under longitudinal tension or compression.

However, in the context of Figure 15, if the longitudinal Poisson's ratios of the fiber and lamina differed significantly, an *equivalent* failure envelope could be prepared for the Poisson's ratio of the fiber. There would be a compensatory shift in the location of the uniaxial failure points, but the *form* of the failure envelope would not change at all because the transverse strains were expressed at the lamina rather than fiber level. (Obviously, the longitudinal strains must be the same except for edge effects not normally addressed by laminate analysis.) Nevertheless, this simplification is appropriate *only* for those laminate patterns that are associated with fiber-dominated failures. The precise two-phase analysis would be required for matrix-dominated failures.

As is explained later, in order to superimpose fiber and matrix failure criteria, it is first necessary to use a common strain base — that of the laminate and hence of each lamina — rather than the strains of

the constituents. So, the failure envelopes should always be expressed at the lamina rather than constituent level. The net effect of a micromechanics analysis distinguishing between constituent and macrostrains would then appear as a change in slope of the line relating longitudinal to transverse strains within each lamina. The Poisson's ratio slopes given by ν_{LT} and ν_{TL} in Figure 7 would not change, but those defined by ν_{xy} and ν_{yx} in Figures 12 and 14 could. Likewise, the pure-shear point at the laminate level might not be precisely on the $-45°$ sloping line when assessed from the point of view of either the fiber or matrix.

EFFECTS OF IN-PLANE SHEAR ON THE "LAMINA" FAILURE CRITERION

If the principal directions of stress or strain do not coincide with the fiber axes, a question arises as to the validity of the preceding failure criteria that makes no provision for such a situation. In the case of ductile *homogeneous* materials, the maximum-shear-stress failure (or yield) criterion in Figure 5 can *always* be used by a simple rotation of reference axes to coincide with the principal stress and strain directions, so this criterion is inherently complete. However, for fibrous composites, such a rotation of reference axes would invalidate the use of the simple stress-strain relations in Equations (19) through (21). Many more terms would then be needed to characterize the stress-strain relations. And the seemingly simple alternative of computing separate principal strains, applying them to the fiber directions instead of the real strains, would be incorrect in such a case.

Fortunately, a simple physically realistic resolution of this problem is available for the cases of most common interest in which stiff strong fibers are embedded in soft matrices. It is apparent that any shear stresses with respect to the fiber axes can cause neither longitudinal nor transverse stresses between those same axes. The principal effect of such shear stresses is to cause longitudinal and transverse direct stresses in those fibers inclined at 45° to the fibers under consideration. Such an effect is easily accounted for when checking the strength of those other fibers under a combination of only axial and transverse loads. Likewise, any shear between axes inclined at $\pm 45°$ with respect to the (0°) reference fibers is accounted for in the form of direct longitudinal and transverse stresses in the 0° and 90° fibers.

Nevertheless, the "minor" effect of the shear deformation is of potential concern. If the composite were truly homogeneous, both the fibers and the matrix would undergo the same shear strain in addition to any direct longitudinal and transverse strains. It would not be permissible to ignore the effects of such shear strains on the strength of the fibers. However, when the matrix is much softer than the fibers, most of the shear strain will be confined to the (resin) matrix and the fibers will not experience significant shear stresses. In such a case, it is reasonable to complete the "lamina" characteristic in the form shown in Figure 18. The in-plane shear strain cutoff shown for 0°/90° shear on the resin matrix would normally be truncated by prior failure of the $\pm 45°$ fibers carrying the shear load. However, there would be no difficulty in applying the matrix shear strain as the dominant limit for very brittle matrices.

Unless there is a compelling reason to do otherwise, it is recommended here that the minor in-plane shear effects be ignored and consideration be given only to the associated direct loads in the $\pm 45°$ fibers and possibly the matrix-dominated 0°/90° strength under those shear loads. Materials for which this simplification is reasonable include carbon, fiberglass and boron reinforced organic matrices like the epoxies.

α = ARCTAN ν_{LT}
β = ARCTAN ν_{TL}
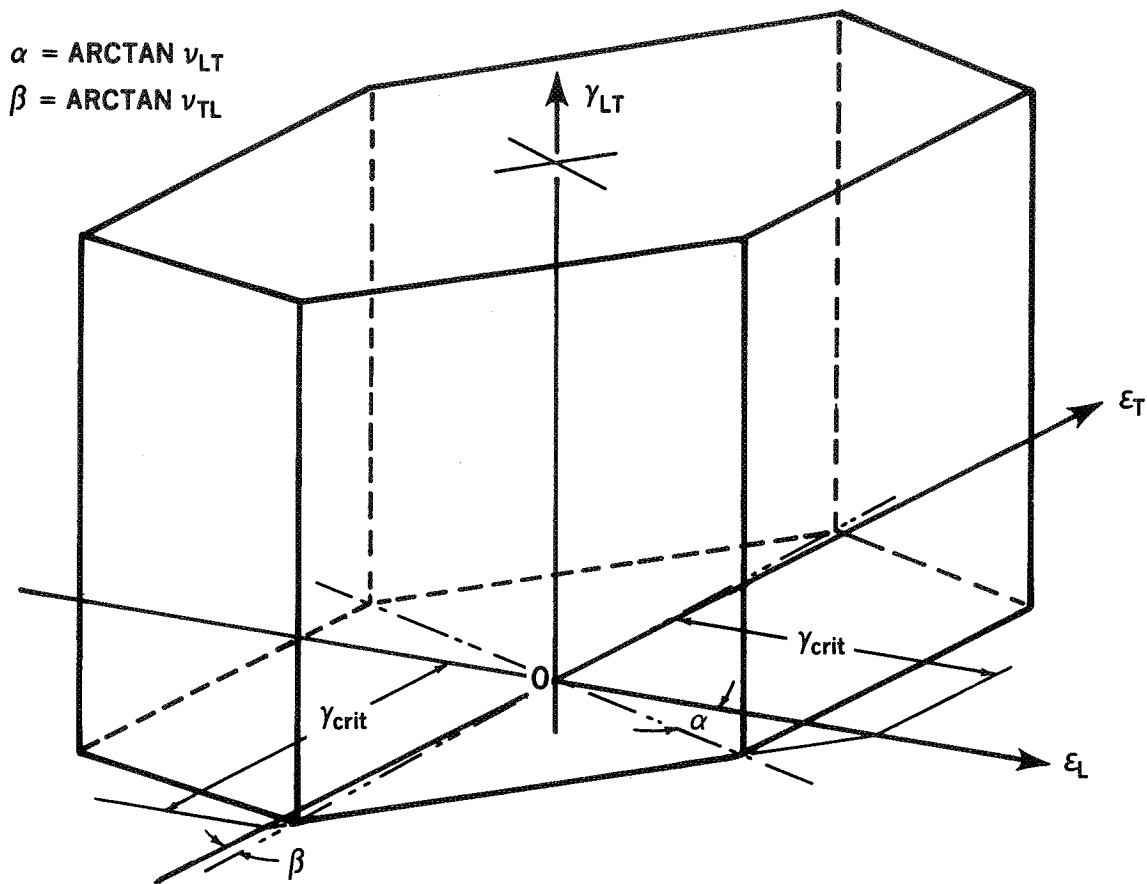
FIGURE 18. STRAIN-BASED LAMINA FAILURE CRITERION

Although Figure 18 refers to each individual lamina within the laminate, it is possible to deduce a universal failure envelope for any membrane state of stress (as opposed to bending) in any cross-plied laminate containing two axes of material symmetry. This means that the percentages of the 0° and 90° plies may differ but that there must be the same number of +45° plies as –45° plies. Such a failure envelope is illustrated in Figure 19. It should be noted that this figure may be applied only with respect to the 0° and 90° axes, not with respect to the ±45° axes. The single application of this form of failure criterion, however, encompasses all *four* fiber directions. Failure of either a 0° or 90° fiber occurs on the vertical "walls" of the failure envelope, while failure of the +45° or –45° fibers is predicted to occur somewhere on the roof. The zero-shear-strain $(\epsilon_x - \epsilon_y)$ plane is easily understood because it is taken directly from Figure 11. The height of the shear-strain plateau, likewise, follows from Figure 11, which shows that the equal and opposite direct strains in the ±45° fibers then have a magnitude of $\gamma_{crit}/2$.

The size of the plateau in Figure 19 can be established by examining the strains in the +45° and –45° fibers at the points of uniaxial load. As shown in References 2 and 4, the strain in those fibers is less than in the 0° fibers, in the ratio of $(1 - \nu)/2$ to 1. That would leave a longitudinal strain capacity of $[(1 + \nu)/2]\epsilon = \gamma_{crit}/2$ to resist any simultaneously applied in-plane shear load. This is sufficient to accommodate an in-plane shear strain of precisely γ_{crit} with respect to the 0°/90° fiber axes. The ±45° fibers are critical in the L–N and T–N planes for this combination of 0° uniaxial tension and 0°/90° shear. The L–T plane is not critical because the associated in-plane strain perpendicular to the more

683
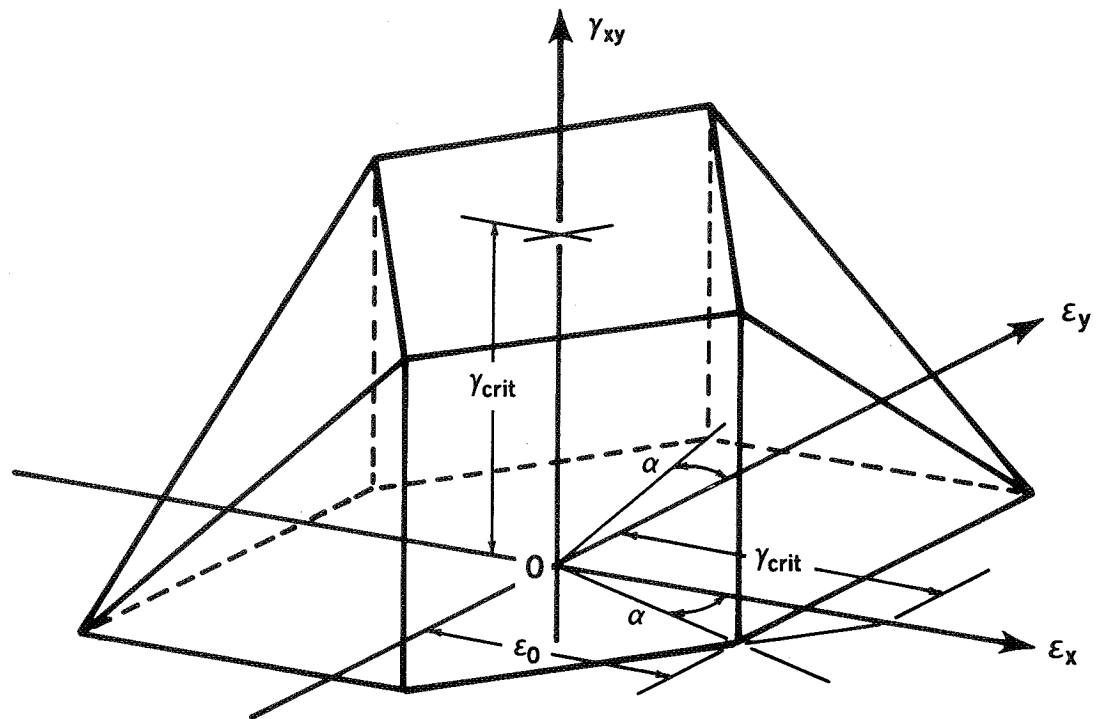
α = ARCTAN ν_{LT} FOR UNIDIRECTIONAL LAMINA

FIGURE 19. UNIVERSAL STRAIN-BASED LAMINATE FAILURE CRITERION

highly loaded fiber has the same sign as the axial strain. Since the governing Poisson's ratio is for the unidirectional lamina, this result applies for *all* cross-plied laminates, regardless of their particular Poisson's ratios. (Obviously, for this combination of loads, only one of the $\pm 45°$ fiber directions will be critical, not both).

Of course, there is no shear strength capacity at the points of biaxial tension or compression in the $\epsilon_x - \epsilon_y$ plane because *all* fibers are equally and fully strained there. The shear strength capacity varies linearly between those corner points and the edge of the shear strength plateau.

The applicability of Figure 19 to all cross-plied fiber patterns with the same percentages of $+45°$ and $-45°$ plies is the reason why, in Figure 21 *of Reference 4, the edges of the shear stress plateaus were at the same location for all three fiber patterns considered; $0°/90°$, $\pm 45°$, and quasi-isotropic.

While Figure 19 encompasses the great majority of failure envelopes for typical fibrous composites, there appears to be no justification for making similar simplifications for Kevlar (aramid) fibers that are weak in transverse shear or for metal-matrix or carbon-carbon composites with relatively stiff matrices. It would appear that the use of the maximum shear strain calculated from Mohr circles would then be more appropriate as a lower bound estimate of the failure of the fibers. However, this technique is complicated because the maximum shear strain could occur either in the L-T or L-N plane, or possibly in some other plane altogether, depending on the combination of applied loads. Moreover, not all shear strains in orthotropic materials are associated with any stresses (as is discussed later), and it is the stresses, not the strains, that cause failure of the material.

* (Figure 20 is shown on the following page.)

684

The author advises caution in applying *any* simplified failure criteria to the more exotic composites under investigation today, and reminds the readers again that the very useful simple methods presented here should be applied only to conventional fibrous composites such as carbon epoxies, in which strong, stiff fibers are embedded in relatively soft matrices.

EXPERIMENTAL VERIFICATION

The author's research into predicting the strength of cross-plied composite laminates was motivated by the development over 15 years ago of a reliable in-plane shear test specimen, shown in Figure 20. The laminate strengths achieved on that specimen, which were twice as high as had been obtained on more customary contemporary shear test coupons, were still only about half as high as predicted by contemporary failure criteria. Almost another decade passed before the author could determine what was wrong with those theories. With a fuller understanding of the subject, it became apparent that unidirectionally loaded test coupons were so completely dominated by the behavior of fibers aligned in the same direction as the load that they could never invalidate faulty strength-prediction theories. Only biaxial tests were sufficiently sensitive to other properties as well to be able to validate theories. Accordingly, the author prepared a series of papers on biaxial test specimens (see References 5 through 7) to make it possible to discriminate between failure theories that were suitable for fibrous composites and those that were not.

Fortunately, other researchers felt the same way. Swanson, in particular, generated biaxial test data on carefully fabricated and tested pressurized axially loaded tubes. The results of Swanson and his

SIZE OF COMPOSITE PANEL IS
3.0 INCHES LONG BY 2.3 INCHES WIDE

REUSABLE RAILS
MACHINED FROM STEEL

COMPRESSIVE LOAD IS APPLIED VIA
RODS RESTING IN VEE-BLOCK GROOVES
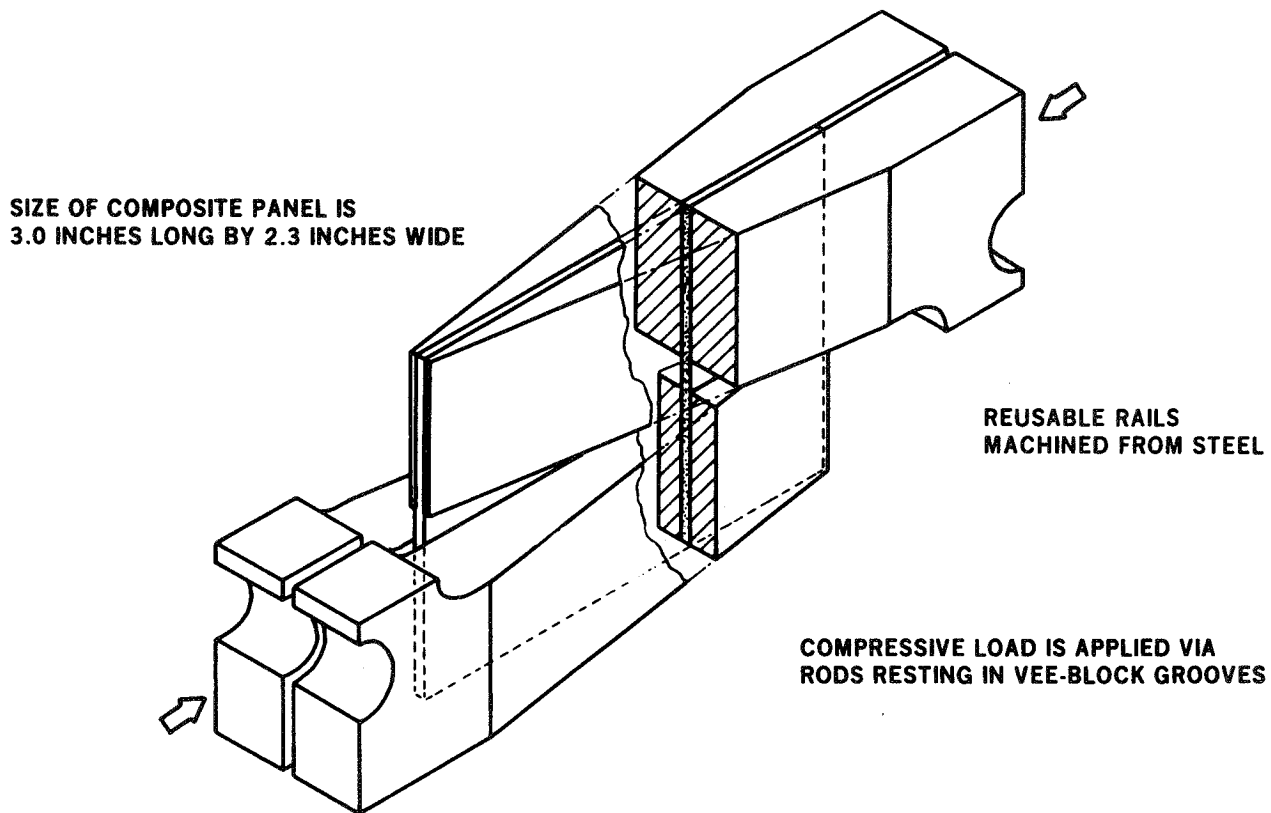
FIGURE 20. DOUGLAS BONDED, TAPERED RAIL-SHEAR TEST SPECIMEN

co-workers (Reference 8) are reproduced here in Figure 21 and compared with the present theory. The agreement is obviously excellent for the tension-tension biaxial loads, covered by the first series of tests and identified by the solid symbols.

However, the author suspects that the second batch of tubes were either made with more precision or of stronger material since the open symbols display a higher strength at the uniaxial hoop load point. The predicted shear failures, based on the earlier tensile strengths, seem to be premature, but would agree well if the 45-degree sloping lines were moved outward to pass through the higher unidirectional strain-to-failure for the later tests (identified by the open symbols). It was obvious to Swanson and his colleagues that the predominantly compressively loaded specimens were failing prematurely, even though they were unable to find reasons for this.
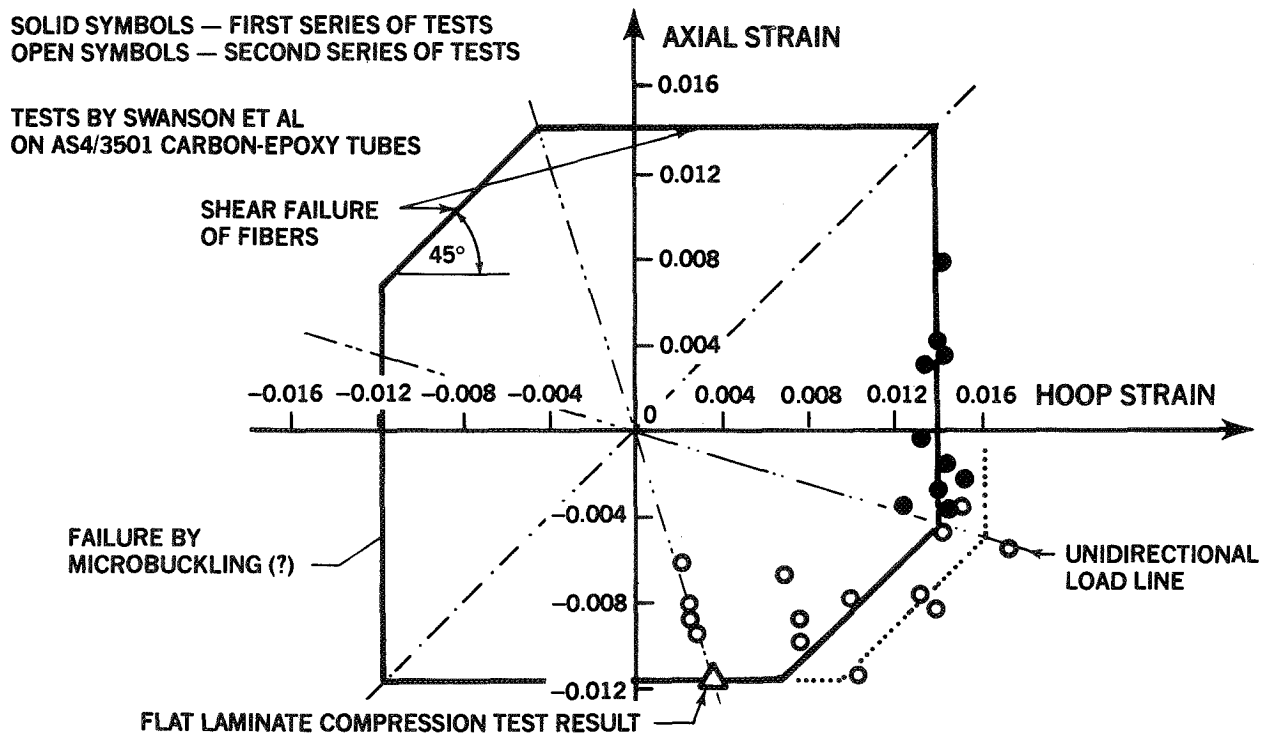
FIGURE 21. COMPARISON BETWEEN TEST AND THEORY FOR TRUNCATED MAXIMUM-STRAIN FAILURE MODEL FOR CARBON-EPOXY COMPOSITES

The predicted compressive strengths shown in Figure 21 are based on the unidirectional compressive strain-to-failure cited by Swanson but, even so, the tubes failed at a still lower strain. Some, but not all, of the most premature failures were associated with compression of the thinnest tubes tested. Even when all these premature failures are explained, it is likely that the cause would recur in real structures subject to the same kind of loading, submersible vehicles, for example.

It is evident that some mechanism other than shear failures of the fibers must have governed those compression failures. However, as shown in Figure 15, the present theory makes provision for such a possibility, and it is not at all difficult to add a cut-off representing a different compressive failure mode in part of a predominantly shear-failure envelope. Indeed, Figure 21 makes such a distinction.

Unfortunately, tests of biaxially loaded composite specimens are often conducted without analysis of probable failure modes and strengths, and most of these data are generally regarded as unreliable.

686

Therefore, such tests failed to influence researchers developing composite failure criteria. And, since the far more numerous uniaxially loaded test specimens were incapable of exposing defective theories, analytical improvements were not forthcoming. Indeed, as explained in Reference 9, none of the standard test coupons, with one exception, the tension test of a $\pm 45°$ laminate, could even be relied upon to generate reliable lamina data from which to calculate the strength of cross-plied laminates.

However, since the standard composite failure theories were incapable of making consistently correct predictions, even if they were given good input properties, such shortcomings of the standard test specimens were not as bad as they seemed at first sight. Composite designs are customarily carried out at reduced strain allowables to allow for stress concentrations at bolt holes and for damage tolerance. Barely 1 percent of typical commercial aircraft composite structures are sized by unnotched allowable strengths.

A BROADER PERSPECTIVE

As shown in this paper, a failure criterion can be based on a single shear *strain* allowable if hygrothermal strains that do not cause any stresses are eliminated from consideration. Shear strains induced by Poisson contractions in the absence of any shear stress must also be eliminated. There is no counterpart of this phenomenon for isotropic materials that have only one Poisson's ratio. However, for materials having different Poisson's ratios with respect to different material reference axes, the presence of strain in the absence of equivalent stress is quite possible. Heating an unrestrained homogeneous isotropic material cannot create either shear stresses or strains. For an orthotropic material, on the other hand, if the coefficient of thermal expansion varies with orientation, the principal thermally induced strains will differ so that shear strains must be developed. However, since the orthotropic object is presumed to be unrestrained while being heated, there can be no stresses. In a strict mathematical sense, this phenomenon and the equivalent one involving Poisson contractions are covered by assigning the value zero to the appropriate coefficients in the thermo-elastic relations.

In the absence of applied normal stresses, an axial load in a unidirectional lamina will cause the same Poisson contractions in both the transverse and normal directions. Therefore this load cannot possibly contribute to any shear strains in the plane of isotropy perpendicular to the fiber axes. This is confirmed by rearranging Equations (20) and (21) for transversely isotropic materials to express the difference between normal and transverse contractions for any combination of axial and transverse loads. It is found that

$$\epsilon_T - \epsilon_N = (1 + \nu_{TN})\sigma_T/E_T \qquad (24)$$

no matter what longitudinal stress is applied.

The corresponding principal strain differences between the other pairs of axes follow similarly from Equations (19) to (21). First,

$$\epsilon_L - \epsilon_N = \left(\frac{1 + \nu_{LT}}{E_L}\right)\sigma_L + \left(\frac{\nu_{TN} - \nu_{TL}}{E_T}\right)\sigma_T \qquad (25)$$

687

in which the second term cannot contribute to the stresses in the L-N plane and must therefore be omitted from the failure criterion. Finally,

$$\epsilon_L - \epsilon_T = \left(\frac{1 + \nu_{LT}}{E_L} \right) \sigma_L - \left(\frac{1 + \nu_{TL}}{E_T} \right) \sigma_T \tag{26}$$

in which *both* terms contribute fully to the stresses in the *L–T* plane, but the first has no effect on the *T–N* plane.

With reference to Figure 15, the 45-degree sloping lines are defined by both terms in Equation (26) while the vertical lines are defined by the first term on the right side of Equation (25) and the horizontal lines are defined by the mirror images of the vertical lines. Equation (24) is assumed here not to be a governing strength limit for strong, stiff fibers in a soft matrix.

The general theory of elasticity for anisotropic materials could probably be applied to reduce the failure criterion to an unambiguous state without needing logic to drop certain terms from the simpler formulation given here. However, the end result should be the same for fiber-dominated failures of the composite materials considered here, but this approach might be incredibly complex.

What concerns the author most is not good designs in today's composite materials; it is the identification of impractical fiber patterns that lead to weak structures with matrix-dominated failures. Fiber-dominated failures can be analyzed using a theory as simple as the present one. The more complex theories accounting properly for matrix-dominated failures are needed only to identify fiber patterns that should not be used and for which, therefore, there should be no need to predict the strengths. There is also a concern that the present theory is probably inadequate for the more exotic composite materials of the future. It is time to stop pretending that there is a scientific validity to the majority of the methods used to predict the strength of fibrous composite materials, no matter how elegant the mathematics, and it is time to acknowledge the need for much new work on a secure foundation. There are opportunities for tremendous contributions to this field, provided that they have the scientific realism needed for such analyses.

Since the presentation of his first papers on composite failure theory (References 2 and 3) the author has been progressively deriving various pieces of the theory needed for a completely rigorous two-phase composite strength-prediction theory. The intent had been that, on its completion, that work would be simplified for the customary fibrous composites in use today and any approximations made would be justified by comparison with the more general theory. As fate would have it, the second step has been completed first. Nevertheless, a summary of certain features of the more precise analyses, may help to guide future researchers.

Figure 22 indicates the features needing to be included in a proper two-constituent (phase) characterization of the strength of cross-plied fibrous composite laminates. One or the other envelope may dominate, depending on the particular state of stress. And, although the shear-strain plateaus are not shown, the same consideration of one or the other being dominant is just as applicable as for the interaction between the direct in-plane loads.

In order that the individual failure envelopes for each constituent (or phase) of the composite material may be superimposed as shown, all strains must be expressed at some common level, for example, that
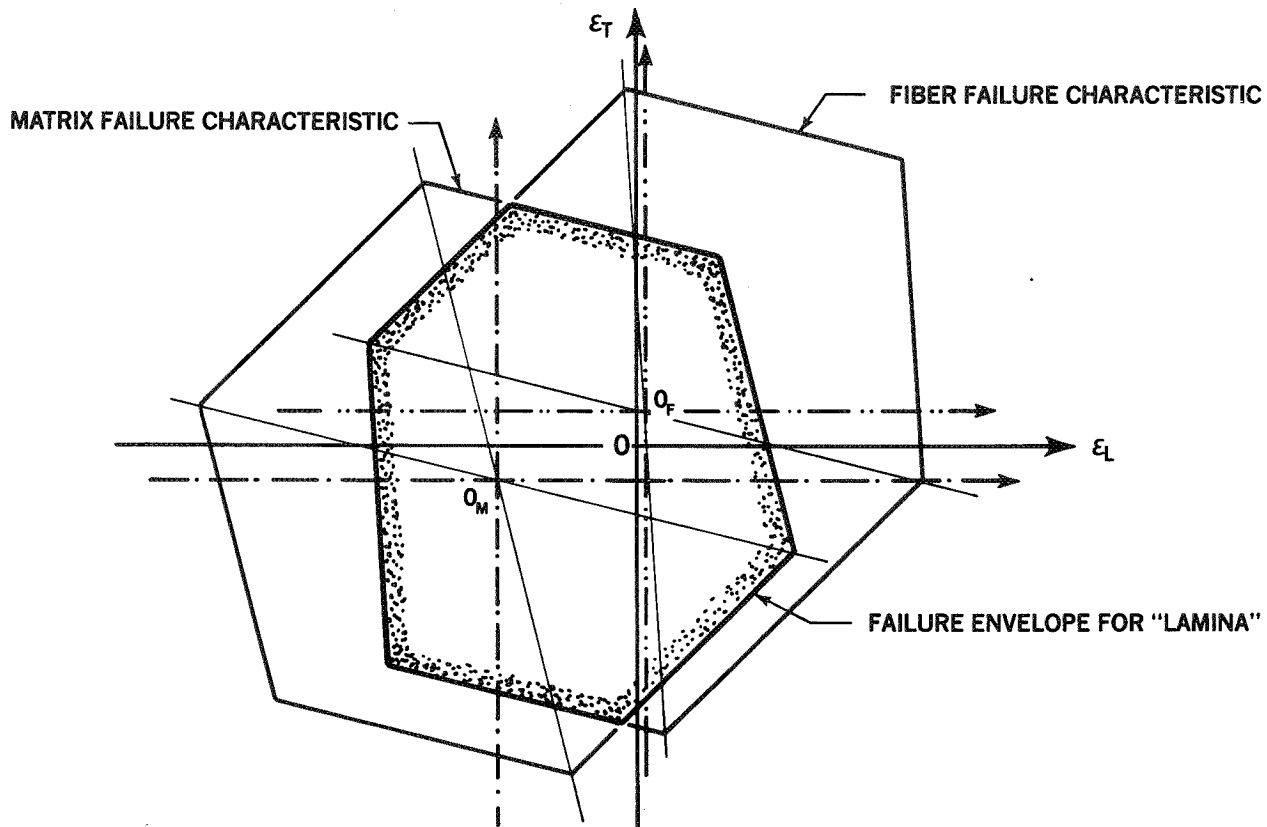
FIGURE 22. SEPARATE FAILURE CHARACTERISTICS FOR FIBERS AND MATRIX

of the lamina rather than at the constituent level. For example, longitudinal strains parallel to fibers are inevitably the same for both fibers and matrix, except for a minute edge zone. On the other hand, the strains perpendicular to the fibers need not be common and are usually not. Therefore, the fiber failure characteristic in Figure 22 could appear to have a different Poisson's ratio than an isolated fiber, for example. Likewise, for the resin matrix in which the transverse strains vary considerably because of the fibrous "inclusions," the transverse strains in Figure 22 would have to be averaged over a small but finite distance. The "failure" strain shown would correspond to some different strain at the micro-scopic level that was actually associated with the stress at which failure occurred.

This difference between constituent and equivalent "lamina" behavior is explained in Figure 23, where there are two shear failure lines drawn for the fiber failure envelope. The fiber is presumed to have a higher transverse stiffness than the resin matrix so, for a common axial strain under a unidirectional load, two different lateral contractions (corresponding to two different Poisson's ratios) are estab-lished. It is, of course, the same failure characteristic, but it can be superimposed on matrix failures in only one form. Figure 23 shows also the corresponding locations of the pure in-plane shear failure locations. It is apparent that, in this case, the blind use of the "lamina" rather than the "fiber" Poisson's ratio would result in an underestimate of the axial strain in the fiber at which in-plane shear failure occurred. (But the converse could happen for titanium-matrix composites, for example.)

Figure 23 is not only designed to explain how the generalization of the classical maximum-shear-stress failure criterion can still be applied in combination with micromechanics analysis for the more exotic composite materials, but to reinforce the suggestion that there is no need to go to such lengths for

FIGURE 23. EQUIVALENT SHEAR FAILURE CRITERIA AT FIBER AND LAMINA LEVEL

conventional fiber/resin composites in which the differences between the Poisson contractions of the fiber and lamina are small enough to be neglected.

The shape of the individual failure envelopes in Figure 22 for the fibers and matrix could change with the operating temperature. Similarly, there could be a shift in the origins O_F and O_M which are offset appropriately to allow for residual thermal stresses in each constituent from curing at an elevated temperature and operating the structure at high temperatures, where it is very cold. The amount of shift between the origins can be computed on the basis of micromechanical analysis, as in Reference 10. Since the origin shifts and the matrix failure envelope would vary with operating temperature, the form of the overlapping region of the individual failure envelopes would correspondingly change with service temperature as well. Such an effect cannot be accounted for in any homogenized model supposedly characterizing any composite material.

There is no evidence to suggest that these residual thermal stresses can creep out and relieve themselves significantly. When the residual stress intensity is high at room temperature or below, the matrix is highly resistant to creep. And, when the creep resistance is reduced at elevated temperatures, so are the stresses that would cause the creep. Moreover, the suggestion that the residual thermal stresses can be nullified by swelling stresses due to moisture absorption, merely clouds the issue by making the stress-free temperature vary with the manufacturing and service history for each particular structure. In any event, the rate of diffusion is typically so slow that reliance on any absorbed moisture to relieve curing stresses would in turn introduce the problem of how to treat the effects of that water during a rapid change in temperature.

690

It should be noted that the residual stresses are definitely *not* a lamina property. Most prior treatments of residual thermal stresses have started with the false premise that the individual lamina is homogeneous and inherently stress-free in isolation, no matter what its temperature. Such an oversimplification cannot possibly explain matrix cracking. It is even questionable for use in characterizing edge delaminations resulting from stacking together too many parallel layers of unidirectional material, whether these delaminations be caused by thermal or mechanical stresses. It was actually these edge-delamination stresses that led to the outer fiber-pattern limits in Figure 17 (for typical carbon-epoxy composites), so there are really *three* potential failure modes to consider for typical fibrous composite laminates.

Matrix failures, either intraply or interply, *always* represent an inability to develop the full strength of the fibers and should therefore be avoided by choice of an appropriate fiber pattern and layer sequence for each laminate. Mathematical composite failure theories have not adequately addressed matrix failures and, until they do, one should use good judgment to exclude the inferior arrangements rather than believe that such constraints do not exist merely because one's computer program is not smart enough to advise users of its weaknesses. Actually, far more restrictive limits on fiber patterns arise when one considers bolt holes, which introduce even further matrix-dominated influences on the degree of stress-concentration relief, as shown by the inner fiber pattern limits in Figure 17. The author believes that matrix-dominated failures will continue to require empiricism even after rigorous two-phase theories have been developed for unnotched laminates. So, the use of a simple failure model that adequately characterizes only fiber-dominated failures can be just as reliable as more elaborate theories, provided that it is used in conjunction with realistic constraints on fiber patterns.

IMPLEMENTATION OF MAXIMUM-SHEAR-STRESS FAILURE CRITERION FOR FIBROUS COMPOSITE LAMINATES

TESTS:

RECORD COMPLETE LOAD-DEFLECTION CHARACTERISTICS:

1. 0° LAMINATE — MODULUS AND POISSON'S RATIO
2. 0°/90° LAMINATE — MODULUS, TENSILE AND COMPRESSIVE STRENGTHS, AND STRAINS TO FAILURE
3. ±45° LAMINATE — MODULUS, POISSON'S RATIO, AND TENSILE STRENGTH

UNIDIRECTIONAL (ALL 0°) LAMINA PROPERTIES:

WOVEN FABRICS SHOULD BE CONSIDERED A COMBINATION OF TAPE LAYERS:

1. LONGITUDINAL MODULUS E_L — FROM TEST 1
2. TRANSVERSE MODULUS E_T — FROM DIFFERENCES BETWEEN TESTS 1 AND 2
3. LONGITUDINAL POISSON'S RATIO v_{LT} — FROM TEST 1 (OR DEDUCED FROM TEST 3 FOR WOVEN FABRICS)
4. IN-PLANE SHEAR MODULUS G_{LT} — FROM TEST 3
5. LONGITUDINAL TENSILE AND COMPRESSIVE MONOLAYER STRENGTHS F_L^{tu} AND F_L^{cu} (OR STRAINS TO FAILURE) — DETERMINED FROM TEST 2 USING PROPERTIES 1 AND 2
6. IN-PLANE SHEAR STRENGTH F_{LT}^{su} — FROM TEST 3
7. TRANSVERSE STRENGTH F_T^{tu} — IRRELEVANT FOR CROSS-PLIED STRUCTURAL LAMINATES OF TYPICAL FIBER/POLYMER COMPOSITES

APPLICATION:

CHECK COMBINATION OF LONGITUDINAL AND TRANSVERSE STRAINS FOR EACH FIBER DIRECTION OR FOR ORTHOGONAL SETS OF FIBERS

CONCLUSIONS

A simple and physically realistic method for predicting the strength of cross-plied fibrous composite laminates has been shown here to follow from a generalization of the classical maximum-shear-stress yield criterion for ductile metal alloys.

The generalization to orthotropic materials has required that the failure criterion be expressed in terms of strains rather than the more customary stresses, even though the actual governing criterion is one of stress.

The new failure criterion is shown to be similar to a simple truncation in the in-plane shear quadrants of the well-known maximum-strain empirical failure model for composites. Therefore, this new work is closely related to the best known classical failure models for both ductile metals and composite laminates. The new theory has also been compared favorably with biaxial test data of other researchers.

While the new theory is unlikely to be improved upon for state-of-the-art fiber/polymer composites, there remains a need for a proper two-phase strength analysis. Separate accounting for failures in the fiber or in the matrix will be needed both for matrix-dominated failures in impractical fiber patterns with today's composites and for predicting any failures of the more exotic composites that are as yet only in the research and early applications stage.

ACKNOWLEDGMENT

REFERENCES

1. Waddoups, M. E., "Characterization and Design of Composite Materials," in *Composite Materials Workshop*, edited by S. W. Tsai, J. C. Halpin, and N. J. Pagano, Technomic, Connecticut (1968), pp. 254-308.

2. Hart-Smith, L. J., "Simplified Estimation of Stiffness and Biaxial Strengths for Design of Laminated Carbon-Epoxy Composite Structures," Douglas Aircraft Company, Paper 7548, unlimited distribution. Presented to Seventh DoD/NASA Conference on Fibrous Composites in Structural Design, Denver, Colorado, June 17-20, 1985; published in Proceedings, AFWAL-TR-85-3094, pp. V(a)-17 to V(a)-52.

3. Hart-Smith, L. J., "Simplified Estimation of Stiffnesses and Biaxial Strengths of Woven Carbon-Epoxy Composites," Douglas Aircraft Company, Paper 7632, unlimited distribution. Presented to 31st National SAMPE Symposium and Exhibition, Las Vegas, Nevada, April 7-10, 1986; published in Closed-Session Proceedings, pp. 83-102.

4. Peterson, D. A., and Hart-Smith, L. J., "A Rational Development of Lamina-to-Laminate Analysis Methods for Fibrous Composites," Douglas Aircraft Company, Paper 7928, presented to 9th ASTM Symposium on Composite Materials: Testing and Design, Sparks, Nevada, April 27-29, 1988; to be published in ASTM STP 1059.

5. Black, J. B. Jr., and Hart-Smith, L. J., "The Douglas Bonded Tapered Rail-Shear Test Specimen for Fibrous Composite Laminates," Douglas Aircraft Company, Paper 7764, presented to 32nd International SAMPE Symposium and Exhibition, Anaheim, California, April 6-9, 1987; published in Proceedings, pp. 360-372.

6. Hart-Smith, L. J., "A Radical Proposal for In-Plane Shear Testing of Fibrous Composite Laminates," Douglas Aircraft Company, Paper 7761, presented to 32nd International SAMPE Symposium and Exhibition, Anaheim, Califonria, April 6-9, 1987; published in Proceedings, pp. 349-359.

7. Hart-Smith, L. J., "A Biaxial Test for Composite Laminates Using Circular Honeycomb Samndwich Panels," Douglas Aircraft Company, Paper 7974, presented to 33rd International SAMPE Symposium and Exhibition, Anaheim, California, March 7-10, 1988; published in Proceedings, pp. 1485-1498.

8. Swanson, S. R., and Nelson, M., "Failure Properties of Carbon/Epoxy Laminates under Tension-Compression Biaxial Stress," in *Composites '86: Recent Advances in Japan and the United States*, edited by K. Kawata, S. Umekawa, and A. Koyabashi, Proceedings of the Third Japan-U.S. Conference on Composite Materials, Tokyo, Japan, June 23-25, 1986, pp. 279-286.

9. Hart-Smith, L. J., "Some Observations About Test Specimens and Structural Analysis for Fibrous Composites," Douglas Aircraft Company, Paper 7929, presented to 9th ASTM Symposium on Composite Materials: Testing and Design, Sparks, Nevada, April 27-29, 1988; to be published in ASTM STP 1059.

10. Hart-Smith, L. J. "A Simple Two-Phase Theory for Thermal Stresses in Cross-Plied Composite Laminates," Douglas Aircraft Company, Report MDC K0337, December 1986.

SHEAR BUCKLING OF SPECIALLY ORTHOTROPIC PLATES

WITH CENTRALLY LOCATED CUTOUTS*

Vicki L. Owen & Eric C. Klang
North Carolina State University

SUMMARY

There is significant industry demand for a method of analyzing the shear buckling of composite plates with cutouts. This method should be able to easily accomodate frequent changes in model design; inflexibility being the major drawback to current finite element methods. The approach taken here is broken into two problems, prebuckling and buckling. To solve for the prebuckling stresses, complex variable equations are used in conjunction with boundary collocation. The least squares approach is utilized to improve the accuracy of the results. The buckling problem is solved using the Ritz method. A product of the Ritz method is a complicated integral equation which is solved using numerical integration. To date, the aforementioned method of determining the prebuckling stresses has been verified against infinite plate theory and finite elements. Preliminary results from the buckling portion of the analysis are currently being compiled and tested against finite elements.

INTRODUCTION

Laminated composite plates with cutouts are found in many structural applications of aerospace technology. Often structures need cutouts to form access ports for mechanical and electrical systems. Cutouts are also needed in such places as ribs to produce a light airframe. The load carrying capability of plates with cutouts is affected by their prebuckling and buckling performance; therefore, investigations in this area are essential in designing optimal structural components. The problem of compressive buckling of plates with cutouts has been addressed successfully (ref. 1), but shear buckling evaluations have been confined to a limited number of specialized finite element analyses (ref. 2). Although finite element analyses produce accurate results, they do not lend themselves to frequent changes in design.

In this paper, a new method for solving the shear buckling problem is introduced. The analysis is based on Lekhnitskii's (ref. 3) complex variable equations, boundary collocation, and the Ritz method. When using finite elements, one must model the entire plate with a large mesh of elements and solve the appropriate equations for each element. Creating the input file which describes the mesh is a tedious and time consuming procedure for the analyst. In applying boundary collocation, it is only necessary to choose points along the plate boundaries at which to solve complex variable equations that describe the applied forces and displacements. By

eliminating the need for a complex mesh structure, both manpower time and computer time are reduced. The body of this paper describes in depth the procedure used to analyze the shear buckling problem and gives results which are verified through finite element analyses.

SYMBOLS

a	-	plate width
A_{kn}	-	constant coefficients of Laurent series
b	-	plate height
c_{kn}	-	real component of A_{kn} where $A_{kn} = c_{kn} + id_{kn}$
d_{kn}	-	real component of A_{kn}
D_{ij}	-	bending stiffness constants
E_x	-	average elastic modulus in x-direction
E_y	-	average elastic modulus in y-direction
F	-	Airy stress function
G_{xy}	-	average shear modulus
N_x	-	prebuckling stress in x-direction
N_y	-	prebuckling stress in y-direction
N_{xy}	-	prebuckling shear stress
p_k	-	constant in applied displacement equation (eq. 10)
q_k	-	constant in applied displacement equation (eq. 10)
s	-	arc length
u	-	applied displacement in x-direction
U_b	-	bending energy
U_{is}	-	initial stress energy
v	-	applied displacement in y-direction
w	-	out of plane displacement
W_{mn}	-	out of plane displacement function constant
X_n	-	x-component of boundary traction
Y_n	-	y-component of boundary traction
z_k	-	complex variable defined as $z_k = x + \mu_k y$

μ_k	-	complex roots of the characteristic equation
ν	-	Poisson's ratio
ϕ_k	-	functions of z_k which make up the force function
Φ_k	-	first derivative of ϕ_k
σ_{xx}	-	normal stress in the x-direction
σ_{yy}	-	normal stress in the y-direction
τ_{xy}	-	shear stress
Π	-	total strain energy

ANALYSIS

The assumptions made in the analysis presented here are as follows. The x,y coordinate system is located at the center of the plate with the x-axis oriented horizontally. The plate is constructed of a specially orthotropic material. Each edge of the plate can be described as either simply supported or clamped. The cutout is centrally located, is in the form of an ellipse or rectangle, and can be rotated at a given angle from the x-axis. It is possible to load the plate in compression, tension, shear, or any combination of the three, but the main emphasis is on shear loading. The load can be implemented using an applied force or an applied displacement. To solve the problem, the analysis is broken into two separate problems, prebuckling and buckling.

Prebuckling Analysis

The prebuckling part of this analysis is based on Lekhnitskii's (ref. 3) complex variable equations. For a two dimensional stress analysis, the equilibrium equations are

(1)

$$\frac{\partial \sigma_{xx}}{\partial x} + \frac{\partial \tau_{xy}}{\partial y} = 0$$

$$\frac{\partial \sigma_{yy}}{\partial y} + \frac{\partial \tau_{xy}}{\partial x} = 0$$

The solutions for the stresses in terms of a function F (Airy stress function) are

(2)

$$\sigma_{xx} = \frac{\partial^2 F}{\partial y^2} \qquad \sigma_{yy} = \frac{\partial^2 F}{\partial x^2} \qquad \tau_{xy} = -\frac{\partial^2 F}{\partial x \partial y}$$

Writing the generalized biharmonic equation in terms of F gives

(3)

$$\frac{1}{E_x}\frac{\partial^4 F}{\partial y^4} - \left(\frac{2\nu_{xy}}{E_x} - \frac{1}{G_{xy}}\right)\frac{\partial^4 F}{\partial y^2 \partial x^2} + \frac{1}{E_y}\frac{\partial^4 F}{\partial x^4} = 0$$

Defining

(4)

$$z_1 = x + \mu_1 y \qquad z_2 = x + \mu_2 y$$

$$\frac{\partial}{\partial z} = \frac{\partial}{\partial y} - \mu_k\frac{\partial}{\partial x} \qquad\qquad k=1,2$$

where μ_k are the roots of the characteristic equation

(5)

$$\mu^4 + \left(\frac{E_x}{G_{xy}} - 2\nu_{xy}\right)\mu^2 + \frac{E_x}{E_y} = 0$$

The generalized biharmonic equation can be represented as

(6)

$$\frac{\partial}{\partial z_1} \frac{\partial}{\partial z_2} \frac{\partial}{\partial z_1} \frac{\partial}{\partial z_2} F = 0$$

the solution for F being

(7)

$$F = \phi_1(z_1) + \phi_2(z_2) + \phi_1(z_1) + \phi_2(z_2)$$

Substituting F into the stress equations and letting $\Phi_k(z_k) = \partial \phi_k / \partial z_k$ gives

(8)

$$\sigma_x = \frac{\partial^2 F}{\partial y^2} = 2*\text{Re} \, (\mu_1^2 \, \Phi_1' + \mu_2^2 \Phi_2')$$

$$\sigma_y = \frac{\partial^2 F}{\partial x^2} = 2*\text{Re} \, (\Phi_1' + \Phi_2')$$

$$\tau_{xy} = -\frac{\partial^2 F}{\partial x \partial y} = -2*\text{Re} \, (\mu_1 \Phi_1' + \mu_2 \Phi_2')$$

Two force equations can be written as

(9)

$$2*\text{Re} \, [\Phi_1(z_1) + \Phi_2(z_2)] \, |_{\xi_o}^{\xi} = \pm \left(-\int_0^S Y_n ds\right)$$

$$2*\text{Re} \, [\mu_1 \Phi_1(z_1) + \mu_2 \Phi_2(z_2)] \, |_{\xi_o}^{\xi} = \pm \int_0^S X_n ds$$

where the upper sign applies to external contours, the lower sign applies to internal contours, and s is the arclength of a segment on the boundary originating at ξ and ending at ξ_0. X_n and Y_n are the forces applied to the boundary in the x and y directions respectively.

Two displacement equations can be written as

(10)

$$2*\text{Re} \, [p_1 \Phi_1(z_1) + p_2 \Phi_2(z_2)] = u$$

$$2*\text{Re} \, [q_1 \Phi_1(z_1) + q_2 \Phi_2(z_2)] = v$$

where

$$p_k = \frac{1}{E_x}\mu_k^2 - \frac{v_{xy}}{E_x} \qquad q_k = \frac{-v_{xy}}{E_x}\mu_k + \frac{1}{E_y}\frac{1}{\mu_k}$$

and u and v are the applied displacements in the x and y directions respectively. For this analysis, a Laurent series of 2*N+1 terms will be assumed as follows:

(11)

$$\Phi_k(z_k) = \sum_{-N}^{N} A_{kn} z_k^n$$

where A_{kn} is a complex number, $c_{kn} + id_{kn}$.

Substituting the Laurent series representation into the force equation and evaluating from i to i-1 gives

(12 & 13)

$$2*\text{Re}\left[\sum_{-N}^{N}\{(c_{1n} + i\,d_{1n})(z_{1i}^n - z_{1(i-1)}^n) + (c_{2n} + i\,d_{2n})(z_{2i}^n - z_{2(i-1)}^n)\}\right] = \pm (-Y_n S)$$

$$2*\text{Re}\left[\sum_{-N}^{N}\{\mu_1(c_{1n} + i\,d_{1n})(z_{1i}^n - z_{1(i-1)}^n) + \mu_2(c_{2n} + i\,d_{2n})(z_{2i}^n - z_{2(i-1)}^n)\}\right] = \pm X_n S$$

Multiplying out the left hand side of equation (12) and finding the real part of the expression gives

(14)

$$\sum_{-N}^{N}\{c_{1n}(2*\text{Re}\,(z_{1i}^n - z_{1(i-1)}^n)) + d_{1n}(-2*\text{Im}\,(z_{1i}^n - z_{1(i-1)}^n)) +$$

$$c_{2n}(2*\text{Re}\,(z_{2i}^n - z_{2(i-1)}^n)) + d_{2n}(-2*\text{Im}\,(z_{2i}^n - z_{2(i-1)}^n))\} = \pm (-Y_n S)$$

Similarly for equation (13)

(15)

$$\sum_{-N}^{N}\{c_{1n}(2*\text{Re}\,(\mu_1(z_{1i}^n - z_{1(i-1)}^n))) + d_{1n}(-2*\text{Im}\,(\mu_1(z_{1i}^n - z_{1(i-1)}^n))) +$$

$$c_{2n}(2*\text{Re}(\mu_2(z_{2i}^n - z_{2(i-1)}^n))) + d_{2n}(-2*\text{Im}(\mu_2(z_{2i}^n - z_{2(i-1)}^n)))\} = \pm X_n S$$

The same procedure can be followed for the displacement boundary equations.

For n=0, $(z_{1i})^0 - (z_{1(i-1)})^0 = 1-1 = 0$ and the same for z_2; therefore, the coefficients A_{10} and A_{20} are arbitrary. Thus the Laurent series becomes
(16)

$$\Phi_k(z_k) = \sum_{-N}^{-1} A_{kn} z_k^n + \sum_{1}^{N} A_{kn} z_k^n$$

Solving the force boundary conditions or the displacement boundary conditions around the internal and external boundaries of the plate results in a system of equations which can be arranged in matrix form as follows:

$$[\, C_{mkn} \,] \, \{ A_{kn} \} = \{ F_m \}$$

where the A_{kn} are the unknown Laurent series constants, C_{mkn} contains the coefficients of the Laurent series constants, and F_m are the resultant applied forces or applied displacements. To improve the solution of this system of equations, a least squares approach is taken. Using this method, twice as many equations will be used as there are unknowns. Therefore

[C_{mkn}] is a 16*N x 8*N matrix
{ A_{kn} } is a 8*N vector
{ F_m } is a 16*N vector

To solve this system, each side of the system is multiplied by [C_{mkn}]^T as follows:

$$[\, C_{mkn} \,]^T [\, C_{mkn} \,] \, \{ A_{kn} \} = [\, C_{mkn} \,]^T \{ F_m \}$$

Now there are an equal number of equations and unknowns and the system can be solved directly for the unknown constants. Once the Laurent series constants are calculated, the stress equations (8) can be solved at any given point on the plate.

Prebuckling Results

A computer program was written to calculate the prebuckling stresses in a plate with a cutout. The preliminary results were first compared with infinite plate theory. The comparison was made by looking at the shear stress along the x-axis from the edge of a circular cutout to the edge of the plate. At the edge of the hole, the shear stress should equal zero, and at the plate edge, the shear stress should equal the value of the applied load. As the hole size decreases, the complex variable solution should converge to the infinite plate solution. Figure 1 shows the stress distribution for a square plate with a hole radius that is 15% of the plate width. A 100 lb shear stress is applied to the edges of the plate. Figure 2 shows the same plate size and loading conditions with a hole radius that is only 5% of the plate width. For the case of the smaller radius, the infinite solution and the complex variable solution are much closer in value than for the larger cutout. This indicates the expected convergence of the complex variable solution to the infinite plate solution.

700

To examine the effect of truncating the number of terms in the Laurent series expansion, a comparison was made with finite elements as exhibited in figure 3. In figure 3, the net section shear stress is shown as in figures 1 and 2. The hole radius in this example is 15% of the plate width. The number of terms in the truncated Laurent series is 2*N. As N increases, the net section stress, as approximated by the complex variable method, approaches the finite element solution. Several contour plots of the stress distribution in plates of varying geometries and material properties were also compared with finite element results and indicated good agreement.

Figures 4 and 5 exhibit the most important advantage of the complex variable method over finite elements. Figure 4 is a contour plot of the shear stress in a rectangular plate with a circular cutout. The length to width ratio of the plate is 2, and the hole radius is 15% of the plate width. The ply layup is $[0]_{24}$. By changing four lines in the input file, the situation shown in figure 5 can be created and analyzed. Figure 5 shows the shear stress distribution in a square plate with an elliptical cutout rotated 45° to the x-axis. The ply layup here is $[(0/90/+45/-45)_3]_s$. In order for finite elements to accommodate these same changes, two separate meshes of several hundred elements would have to be created by the analyst. This procedure would take considerably more time than changing 4 lines of input.

Buckling Analysis

The determination of the buckling load is based on the Ritz energy method (ref. 4). The strain energy of a structure is represented by

(17)
$$\Pi = U_{is} + U_b$$

where

(18 & 19)

$$U_{is} = \frac{1}{2} \iint_A \left\{ \lambda \left[N_x^o \left(\frac{\partial w}{\partial x} \right)^2 + N_y^o \left(\frac{\partial w}{\partial y} \right)^2 + 2 N_{xy}^o \left(\frac{\partial w}{\partial x} \right) \left(\frac{\partial w}{\partial y} \right) \right] \right\} dA$$

$$U_b = \frac{1}{2} \iint_A \left\{ D_{11} \left(\frac{\partial^2 w}{\partial x^2} \right)^2 + 2 D_{12} \left(\frac{\partial^2 w}{\partial x^2} \right) \left(\frac{\partial^2 w}{\partial y^2} \right) + 4 D_{66} \left(\frac{\partial^2 w}{\partial x \partial y} \right)^2 \right.$$
$$\left. + D_{22} \left(\frac{\partial^2 w}{\partial y^2} \right)^2 \right\} dA$$

U_{is} is the energy due to the initial stress in the system and U_b is the energy due to bending.

To solve the strain energy equation, assume the out of plane displacement function, w, to represent the buckle mode of the plate:

(20)
$$w(x,y) = \sum_{m=1}^{M} \sum_{n=1}^{N} W_{mn} f_m(x) g_n(y)$$

The displacement function is chosen according to the boundary conditions. Due to the shear loading on the plate, these displacement functions must contain symmetric and antisymmetric modes. For a simply supported plate

(21)

$$w(x,y) = \sum_{m=1}^{M} \sum_{n=1}^{N} W_{mn} \sin(m\pi x/a) \sin(n\pi y/b)$$

For a clamped plate

(22)

$$w(x,y) = \sum_{m=1}^{M} \sum_{n=1}^{N} W_{mn} [\cos\{(m-1)\pi x/a\}-\cos\{(m+1)\pi x/a\}]*$$

$$[\cos\{(n-1)\pi y/b\}-\cos\{(n+1)\pi y/b\}]$$

The total energy of the system is stationary, therefore

(23)

$$\frac{\partial \Pi}{\partial W_{mn}} = 0$$

Therefore

(24)

$$\sum_{m=1}^{M} \sum_{n=1}^{N} \iint_{A} \{ [D_{11}f_m''f_i''g_j g_n + D_{12}[f_m f_i''g_j g_n'' + f_m''f_i g_j''g_n]$$

$$+D_{22}f_m f_i g_j''g_n'' + 4D_{66}f_m'f_i'g_j'g_n' +$$

$$\lambda N_x^o f_m'f_i'g_j g_n + \lambda N_y^o f_m f_i g_j'g_n' +$$

$$\lambda N_{xy}^o[f_m f_i'g_j g_n' + f_m'f_i g_j'g_n] \}dA] W_{mn} = 0$$

The form of the displacement function coupled with the complicated form of the prebuckling stress equation makes integrating the energy equation extremely difficult; therefore, numerical integration is used. The resulting system of equations constitutes an eigenvalue problem. Solving for the lowest eigenvalue gives the critical buckling load of the system.

Buckling Results

The buckling portion of the analysis has been implemented for an out of plane displacement function with a minimum of terms. Reasonable results have been obtained for these cases, but a significant increase in the number of waves represented by the displacement function is necessary for an accurate approximation of the buckling loads. Work is in progress obtaining results using higher numbers of terms in the displacement function. These improved results will be then compared to finite elements.

CONCLUDING REMARKS

Lekhnitskii's complex variable equations were used with boundary collocation to determine the prebuckling stresses of composite plates with centrally located cutouts loaded in shear. This method was in good agreement with infinite plate theory and finite element solutions. The extremely small input files necessary to instruct the complex variable program, as opposed to the lengthy finite element mesh files, saves significant manpower time. The easy adaption of the method proposed herein to several plate and cutout geometries allows for frequent structural design changes and is appropriate for parametric studies.

The Ritz energy method was chosen to analyze the buckling problem. An out of plane displacement function was assumed according to the boundary conditions. The complicated form of the out of plane displacement function and the prebuckling stress equation led to the use of numerical integration to simplify the energy equation. The resulting system of equations constituted an eigen value problem which was solved for the buckling loads. Preliminary results using a low number of waves in the displacement function gave reasonable results, but a higher number of waves will be necessary to achieve accurate results.

REFERENCES

1. Nemeth, Micheal P.: A Buckling Analysis for Rectangular Orthotropic Plates with Centrally Located Cutouts, NASA Technical Memorandum 86263, December, 1984.

2. Sabir, A. B. and Chow, F. Y.: Elastic Buckling of Flat Panels Containing Circular and Square Holes, Proceedings of The Micheal R. Horne Conference.

3. Lekhnitshii, S. G.: Theory of Elasitcity of an Anisotropic Body, MIR Publishers, Moscow, 1981.

4. Whitney, James M.: Structural Analysis of Laminated Anisotropic Plates, Technomic Publishing Co., Lancaster, Pennsylvania, 1987.
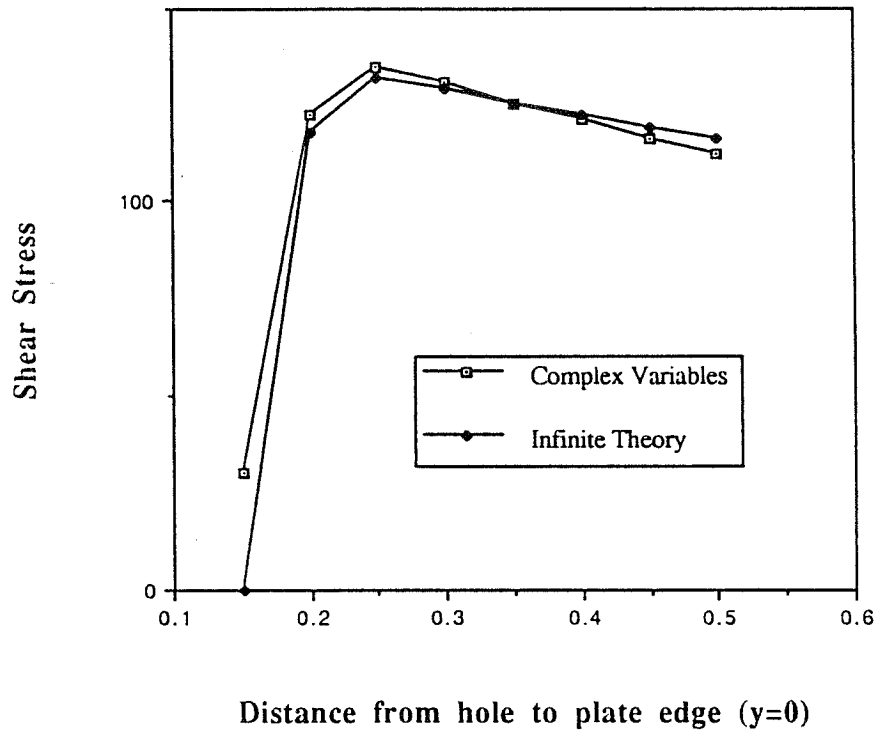
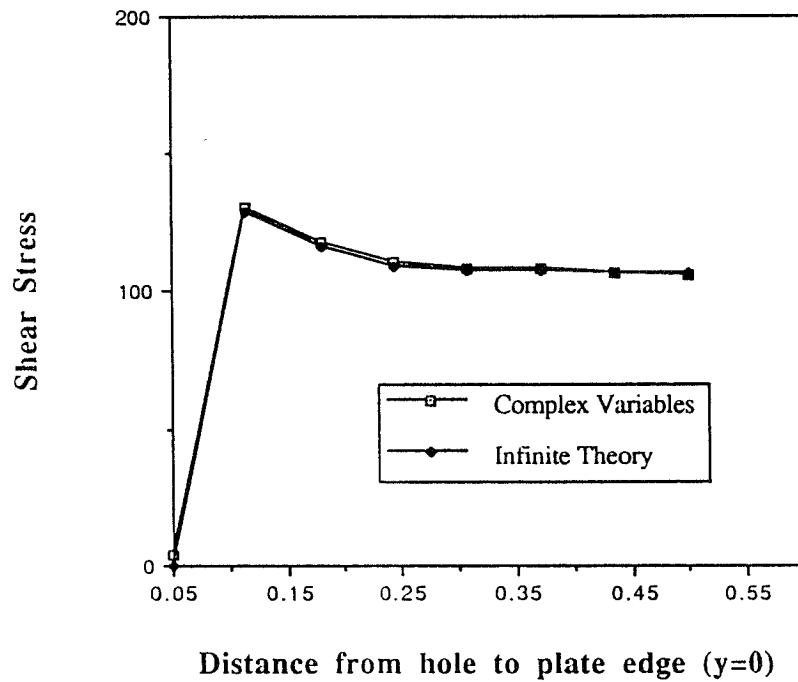Fig. 1, Shear Stress along the X-axis
Hole Radius = 0.15

Fig 2, Shear Stress along the x-axis
Hole Radius = 0.05

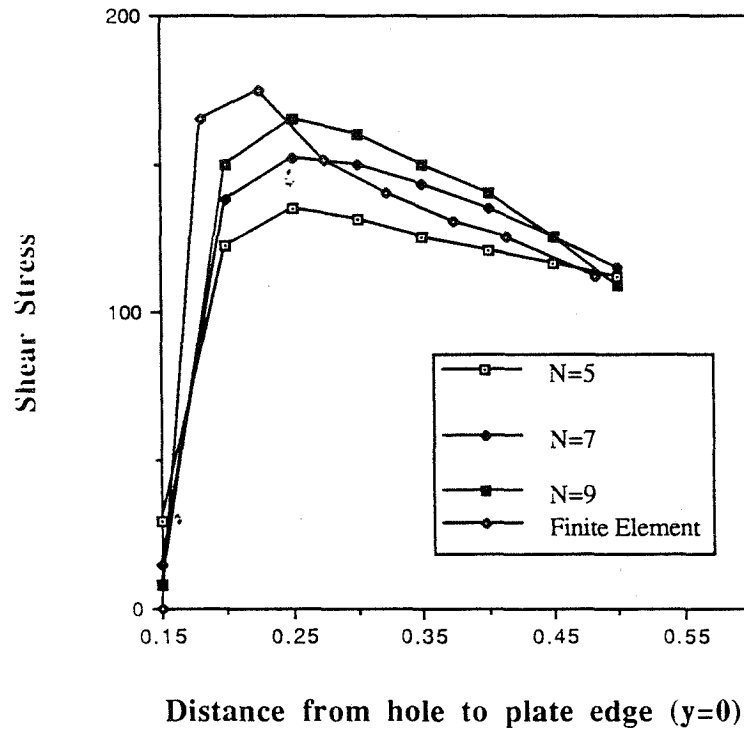Distance from hole to plate edge (y=0)

Fig. 3, Shear Stress along the x-axis
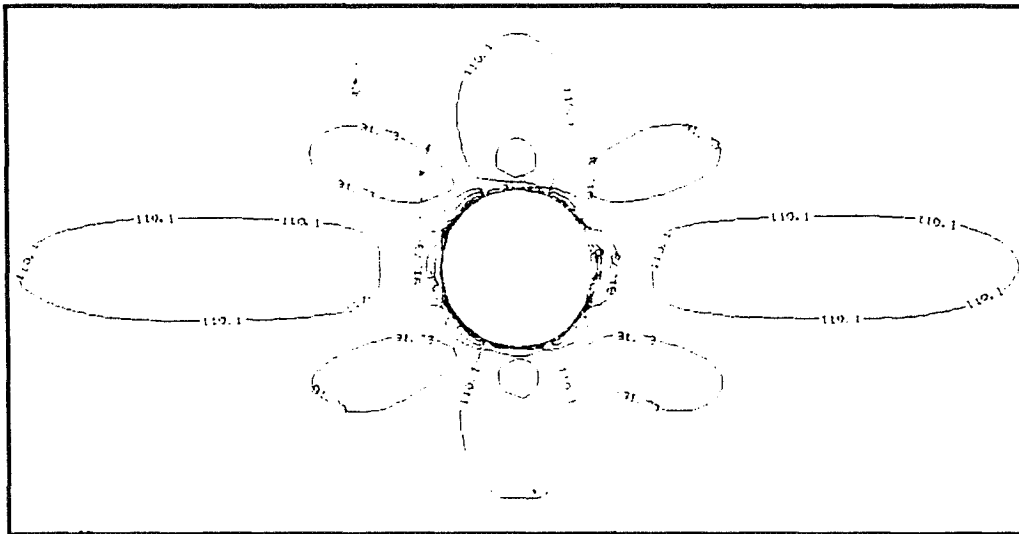Varying the # of Series Terms

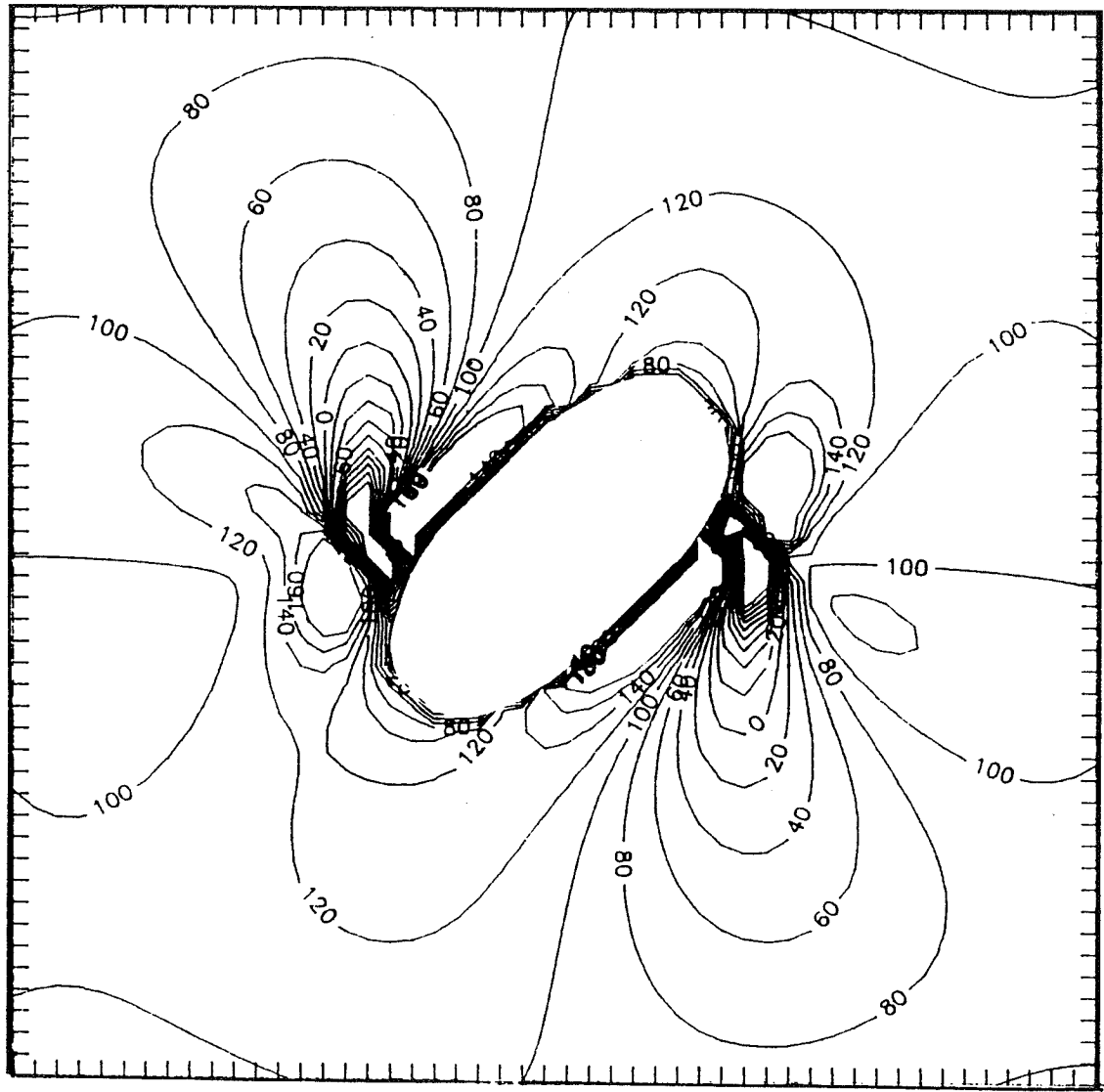Fig. 4, Shear Stress Distribution in Rectangular Plate with Circular Cutout

Fig. 5, Shear Stress Distribution in Square Plate with Rotated Elliptical Hole

1. Report No. NASA CP-3087, Part 2	2. Government Accession No.	3. Recipient's Catalog No.	
4. Title and Subtitle Eighth DoD/NASA/FAA Conference on Fibrous Composites in Structural Design		5. Report Date September 1990	
		6. Performing Organization Code	
7. Author(s) James H. Starnes, Jr., Herman L. Bohon, and Sherry B. Garzon, Compilers		8. Performing Organization Report No. L-16832	
9. Performing Organization Name and Address NASA Langley Research Center Hampton, VA 23665		10. Work Unit No. 505-63-01-09	
		11. Contract or Grant No.	
12. Sponsoring Agency Name and Address National Aeronautics and Space Administration Washington, DC 20546, Department of Defense, Washington, DC 20301, and Federal Aviation Administration, Washington, DC 20553		13. Type of Report and Period Covered Conference Publication	
		14. Sponsoring Agency Code	

15. Supplementary Notes

James H. Starnes, Jr.: Langley Research Center, Hampton, Virginia.
Herman L. Bohon: Lockheed Engineering & Sciences Company, Hampton, Virginia.
Sherry B. Garzon: Langley Research Center, Hampton, Virginia.

16. Abstract

This conference publication contains the proceedings of the Eighth DoD/NASA/FAA Conference on Fibrous Composites in Structural Design held in Norfolk, Virginia during November 28-30, 1989. Presentations were made in the following areas of composite structural design: perspectives in composites; applications in design; concepts in design; methodology in design, and reliability in design.

17. Key Words (Suggested by Authors(s)) Composite structural design Composite airframe applications Composite armament applications Composite analysis methods Composite reliability	18. Distribution Statement REVIEW for general release September 30, 1992 Subject Category 24		
19. Security Classif. (of this report) Unclassified	20. Security Classif. (of this page) Unclassified	21. No. of Pages 713	22. Price

NASA FORM 1626 OCT 86